Western Australian School of Mines
Department of Mining Engineering and Metallurgical Engineering

An Investigation of the Segregation Process Applied to Western Australian Nickel Laterites

Volume 1

David Eric Grimsey

This thesis is presented for the Degree of
Doctor of Philosophy
of
Curtin University

October 2015

Declaration of Originality

To the best of my knowledge and belief this thesis contains no material previously published by any other person except where due acknowledgment has been made.

This thesis contains no material which has been accepted for the award of any other degree or diploma in any university.

David Eric Grimsey

October 2015

Abstract

This work represents the first detailed study undertaken since the 1970's on the application of the segregation process to nickel laterite ores. Western Australian laterite deposits account for ~20% of the world's laterite nickel resource and largely remain undeveloped. This study was focused on the segregation of nickel from nontronite, an ore uniquely dominant within the WA laterite profile. Limonite and garnierite ores were also studied to provide a mineralogical contrast.

The main aim of this work was to provide a better understanding of the potentially useful but relatively complex segregation process through a study of its fundamental aspects; equipment and techniques were developed for this purpose. The kinetics of Ni, Fe and Co segregation and carbon gasification were measured for all three ores within a genuine segregation system, and quantified through development and application of appropriate equations. The system was continuously monitored through measurements of the bulk gas oxygen pressure, evolved carbonaceous gas volume, carbon consumption, oxygen removal and HCl in the off-gas. The residual chlorides within the reaction bed were measured and the efficiency of the HCl recycle was quantified. Comparable measurements were made for a chloride free carbon reduction system. Analysis and understanding of these data were enhanced through thermodynamic simulations using FACTSage software and an examination of ores, calcines and segregation products using EDS-SEM and XRD.

Factors examined and assessed included: the mineralogy of the ores, and calcines and their Ni distributions, the rate controls for Ni, Fe and Co segregation, mineralogical controls on the oxygen pressure in the gas, the impact of roasting conditions on Ni recovery, chloride deportment, the effects of mineralogy and chloride addition on reduction rate and carbon consumption, and the nature of the ferronickel product and factors which determine the ferronickel grade.

Segregation and chloride free carbon reduction were compared. Segregation was found to be superior for Ni recovery under virtually all conditions examined. Maximum Ni recoveries of ~80% were achieved for nontronite and limonite and 65% for garnierite using the standardised conditions adopted for the study. Increased recoveries to 85% seem possible for nontronite and likely for garnierite using optimisation strategies that are suggested.

Acknowledgements

This thesis represents the conclusion of a very rewarding but challenging period of my life. There have been no other significant studies of the segregation process since the 1970's. As such, design and commissioning of the experimental equipment, as well as development of the experimental method, were particularly demanding but exceptional learning experiences. The experimental program and theoretical aspects were also diverse and relatively complex. Given these challenges, this work could not have been completed without the assistance of many people to whom I am deeply grateful.

I would firstly like to express special appreciation and thanks to my technical supervisor and father Emeritus Professor Eric Grimsey. You have patiently guided me through this difficult process and helped me to develop a broad technical skillset. I now have a logical framework to solve complex problems. I feel confident that I can analyse processes from thermodynamic and kinetic standpoints, and can present clear and concise written arguments. I also appreciate the time you spent teaching me laboratory skills. I was lucky to work with a world-class researcher such as you. Thank you for sharing your skills and immense knowledge. Thanks also to my mother Robyn; I could not have got through this without your constant support.

I would also like to thank my supervisor Associate Professor Don Ibana. Your encouragement, advice and unwavering support to me, and other students, are well appreciated and acknowledged. Thanks also to my thesis committee chairperson, Associate Professor Nimal Subasinghe, for your support and assistance throughout.

Thanks to Anusha Shantha Kumara and particularly Mujesira Vukanic for assistance with chemical analysis; I feel much more confident in a laboratory now. I also thank Doctor Angela Halfpenny for teaching the use of, and assistance with, the Scanning Electron Microscope. This is an invaluable tool and I am thankful to have had the opportunity to use it.

Thanks also to Harley Davies, Peng Zhou and Yafeng Guo for allowing me to supervise your undergraduate projects. It was an excellent opportunity for me, and your work assisted in developing an understanding of the segregation process, as well as the experimental method used for this study.

I also thank the other metallurgy PhD students for their camaraderie. It was always a relief to be able to share frustrations and talk through our unique issues. I particularly thank fellow PhD student and ex-housemate Doctor Simon Assmann. I have learnt a lot from your professional approach to study and life.

Thanks also go to MERIWA and the Australian Government for supporting me financially with scholarships, and to Herron Resources for providing the nickel laterite samples. Lastly, thanks to my current employer, BHP Billiton Nickel West, and particularly my boss Anthony Rich. I sincerely appreciate your support through the final stages of this work.

Table of Contents

List of Figures

List of Tables

Chapter 1

Introduction

Global production of primary nickel was 2.22 million tonnes in 2012 (Kuck, 2014), with future production predicted to rise to meet increasing steel demand from developing economies such as China, India and Brazil. Economic nickel deposits are associated with either oxide (laterite) or sulphide host rock, with global nickel reserves estimated at ~24 billion tonnes, 73% of which are contained within laterites; however laterites only account for ~48% of global primary nickel production (Pariser and Pariser, 2010).

Sulphide ores contain nickel within discrete minerals that can be readily concentrated and then processed using proven technologies which utilise the sulphur content as an energy source. For these reasons, sulphides are the preferred source of nickel. However, the extraction of nickel from sulphides is now a mature industry, with the output from major regions optimised and the average deposit quality steadily decreasing (Dalvi et al., 2004); thus the majority of future growth in nickel production is expected to come from lateritic ores.

Efficient processing of nickel laterites has been an on-going challenge as the nickel is widely dispersed throughout a complex profile of weathered and hydrated minerals, the characteristics of which change with the depth of the deposit. These factors complicate materials handling, physical upgrading and chemical extraction; in addition, a relatively high energy input can be required to process the whole of the mined ore.

1.1 Nickel Laterite Deposits

Nickel laterite deposits are formed after prolonged weathering of Ni containing olivine-rich igneous rocks including peridotite, pyroxenite and dunite (Golightly, 1979; Alcock, 1988; Brand et al., 1998; Elias, 2002). The weathering process involves the drainage of acidic ground water, resulting in the dissolution of Mg, Fe, Co and Ni, with silica being colloidally suspended in the solution. A portion of the dissolved Fe is oxidised to ferric and precipitates along with some Co as goethite in the upper region of the laterite profile. As the Fe-depleted acidic ground water percolates further into the underlying rock, it is partially neutralised by magnesia, resulting in the precipitation of hydrous, nickel-magnesium silicates. Figure 1.1

shows the distribution profile of Ni, Fe, Co, MgO and SiO_2 throughout the vertical length of a generic nickel laterite deposit.

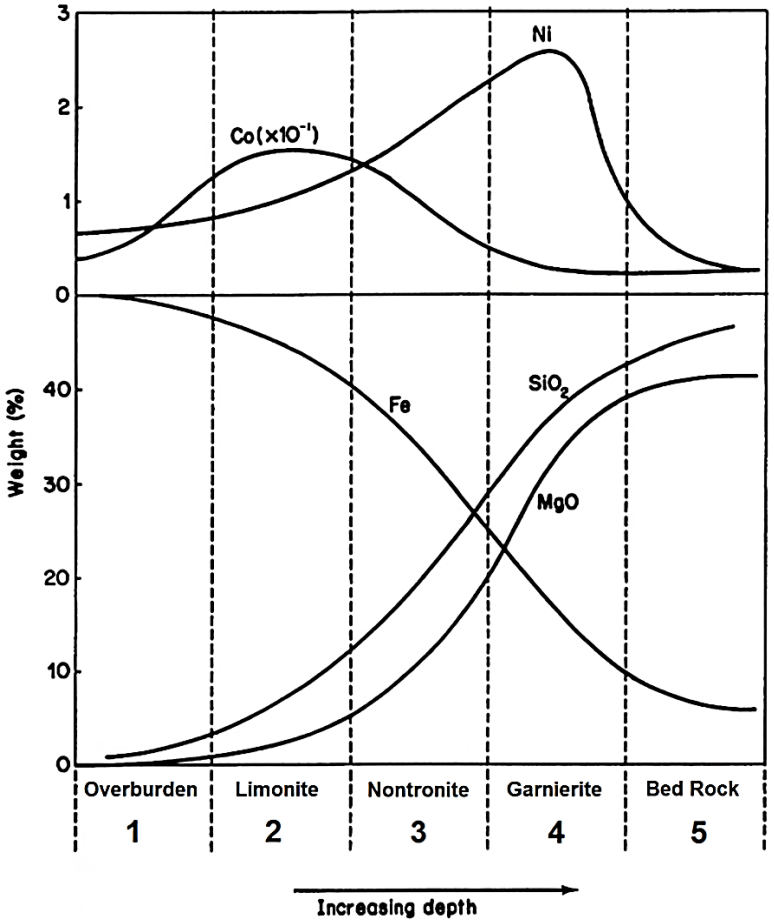

Figure 1.1 Vertical Nickel Laterite Profile (Monhemius, 1987).

The exact composition of a laterite profile is highly variable in terms of thickness, grade, chemistry and mineralogy, being dependent upon the mineralogy of the parent rock, and phenomena that influence water drainage characteristics such as tectonic setting, climate, topography and geomorphic history.

There are five vertical zones recognised in a laterite profile, as represented across the x-axis of Figure 1.1. The zones from the top to the bottom of the laterite profile are: (1) overburden, (2) limonite, (3) nontronite, (4) garnierite and (5) bed rock. Each zone is referred to by a variety of terms, with the nontronite zone also referred to as the transition, smectite or clay zone, while the garnierite zone is also referred to as the saprolite or serpentine zone. Ores from zones 2, 3 and 4 have been studied in this work, and will be referred to as limonite, nontronite and garnierite respectively. The position and approximate chemical composition of each zone is shown in Figure 1.2, alongside the applicable commercial extraction processes.

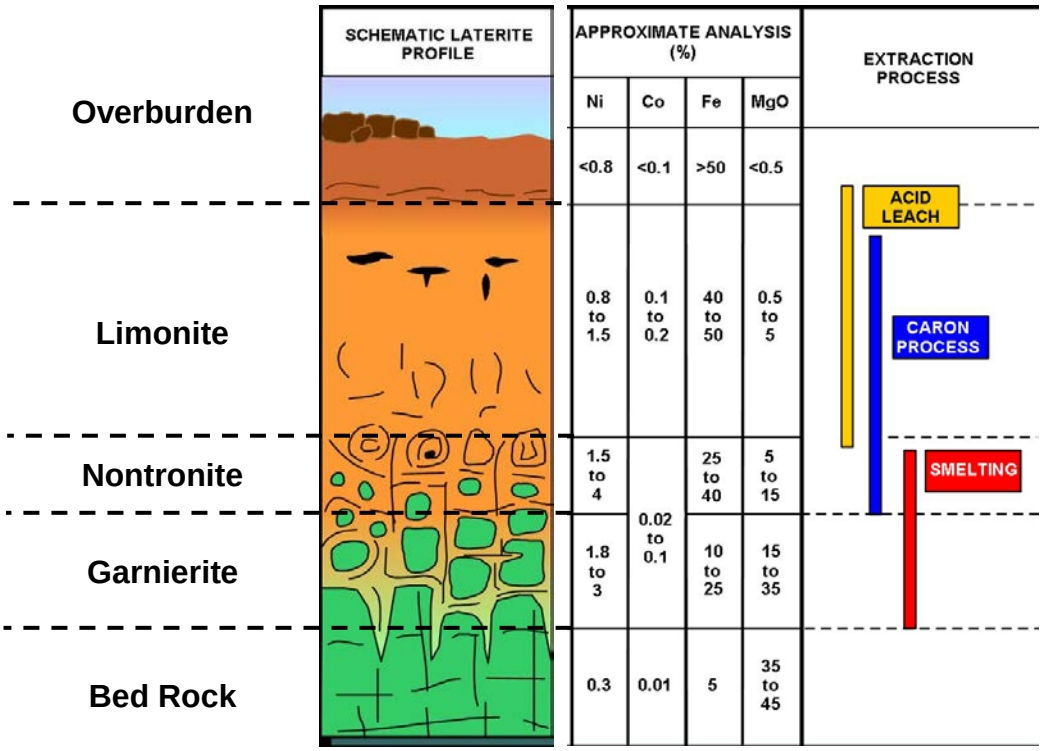

Figure 1.2 Nickel Laterite Profile and Processing Methods (Elias, 2002)

The limonite zone accounts for ~50% of global Ni laterite resources and mainly contains Fe oxyhydroxides in the form of goethite. The nontronite zone accounts for ~15% of global Ni laterite resources and contains the smectite clay called nontronite; it only develops in poorly drained regions such as in Western Australia. The garnierite zone accounts for ~35% of global Ni resources and mainly contains hydrous nickel-magnesium silicates, such as serpentine, talc and chlorite.

1.2 Processing Methods

Three main commercial processes are used to extract Ni from laterites, specifically: smelting, reduction roast/ammonia leaching (Caron process) and the high pressure sulphuric acid leach (HPAL). These processes have been extensively reviewed elsewhere (Monhemius, 1987; Simons, 1988; Dalvi et al., 2004; Butt, 2007) and only a brief summary will be presented here.

1.2.1 Smelting

Nickel laterite smelting accounts for ~60% of the world's primary Ni production from laterites and typically delivers recoveries of 90-95% Ni and 50% Co. The process involves drying the mined ore in a rotary dryer, calcining and pre-reducing the dried

ore in a rotary kiln at 973-1173 K (700-900°C)[1], and then smelting and further reducing the calcine in an electric furnace at approximately 1873 K (1600°C). The smelting plant must have access to an inexpensive and reliable electricity supply since removing the free and combined water from the laterite and melting the calcine are energy intensive processes. The smelter product is usually ferronickel but can be sulphide matte if sulphur is added to the calcine prior to smelting.

Traditionally, the laterite feedstock requires both a SiO_2/MgO ratio lower than 2.5 to prevent excessive attack on the furnace refractories, and a Ni/Fe ratio high enough to produce ferronickel with at least 20% Ni, as preferred for stainless steel production. Smelting is therefore most applicable to garnierite ores since they are generally higher grade with a relatively low %Fe and high %MgO (Figure 1.2).

Recently however, lower grade laterites containing up to 40% Fe have been smelted to produce so-called 'nickel pig iron', a ferronickel which contains 3-15% Ni and is now accepted by some plants as feed for steel production (Kruger et al., 2010).

1.2.2 The Caron Process

The Caron process accounts for ~25% of the world's primary Ni production from laterites and typically delivers recoveries of 75-80% Ni and 50% Co. This process involves drying the mined ore in a rotary dryer, calcining the ore and selectively pre-reducing Ni and Co to their metallic state (along with ~10% of the Fe) in a multiple hearth furnace at 973-1123 K (700-850ºC). The cooled calcine then undergoes leaching with an ammonia/ammonium carbonate solution in air-blown agitated tanks to oxidise and dissolve the ferronickel, after which the Fe waste (as ferric hydroxide), Co/Ni (as mixed sulphide) and Ni products (as basic carbonate) are sequentially precipitated.

The energy inputs for the Caron process are high due to the requirement to dry, calcine and reduce the ore prior to leaching. The furnace throughput is also limited by a low heating rate (commonly 5°C/min), as required to ensure maximum Ni reduction prior to the formation of forsterite (Mg_2SiO_4), which begins at ~1023 K (750°C) and tends to capture Ni within a leach resistant silicate matrix.

The feedstock must have a relatively low %MgO to minimise forsterite formation and to minimise MgO dissolution during leaching since this can lead to ammonia loss

[1] Temperatures in this work will normally be given in Kelvin (K). However, since Centigrade (ºC) is commonly used in literature, the conversion will be given in the initial chapters of this work.

through precipitation of magnesium ammonium carbonate. The Caron process is therefore most applicable to limonite and nontronite ores since these contain relatively small amounts of SiO_2 and MgO (Figure 1.2). However, the process is now considered economically uncompetitive compared to smelting and HPAL and is unlikely to be used in new projects.

1.2.3 High Pressure Acid Leach (HPAL)

The HPAL process accounts for ~10% of the world's primary Ni production from laterites, and typically delivers recoveries of 95% Ni and Co. The process involves digesting the mined ore in autoclaves with sulphuric acid at 523 K (250°C) and 33-35 atm, oxidising and re-precipitating the Fe, separating the waste solids from the pregnant liquor and then extracting the Co and Ni using either direct solvent extraction/electrowinning, mixed hydroxide precipitation or mixed sulphide precipitation.

The use of acid at relatively high temperatures and pressures, and highly saline water in the case of Western Australian laterite plants, requires expensive special materials of construction, for example, titanium lined autoclaves. Material handling issues are encountered on the front end of the process because of the undesirable rheology characteristics of the undried laterites; this limits slurries to 25% solids for smectite and 40% for limonite, which affects throughput. The feedstock must also contain relatively low amounts of acid-consuming components (Mg, Al and Ca oxides) since acid is the highest cost component of the process. The HPAL process is therefore most applicable to limonite and some nontronite ores (Figure 1.2), since garnierite ores contain uneconomic portions of acid consuming minerals.

1.3 Nickel Laterite in Western Australia (WA)

Australia accounts for ~20% of global nickel laterite resources (Dalvi et al., 2004); the majority are located in WA, where dry conditions and poor drainage have resulted in laterites which are characterised by a relatively large nontronite zone that is dominant in several WA deposits, such as Murrin Murrin and Bulong. A typical WA nickel laterite profile is shown on the left in Figure 1.3, with profiles formed in more tropical climates displayed on the right. Descriptions of specific WA deposits have been given by Elias et al. (1981) for Bulong, Hellsten et al. (1998) for Cawse, Fazakerley and Monti (1998) for Murrin Murrin and Miller et al. (2004) for Ravensthorpe.

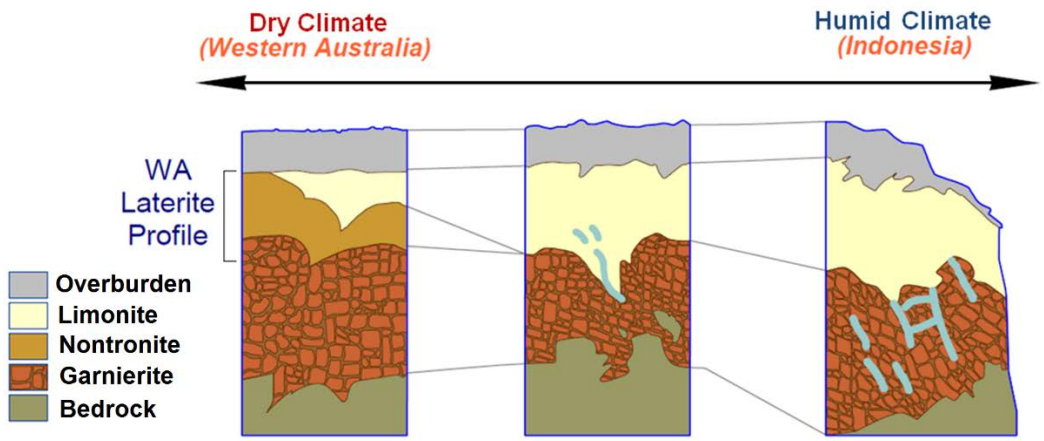

	%Ni	%Co	%Mg	%Fe	%Ni	%Co	%Mg	%Fe	%Ni	%Co	%Mg	%Fe
Overburden	.2 -.5	.02	.6	35+	.2 -.5	.02	.6	35+	.2 -.5	.02	.6	35+
Limonite	.6-1.4	.1-.2	1-2	45	1.2-1.7	.1-.2	1-2	45	1.2-17	.1-.2	1 -4	45
Nontronite	1.2	.08	3.5	18								
Garnierite	.4	.02	12.0	9	1.5 -3	.05-.1	10-20	10-25	1.5-3	.05-.1	10-30	10-20

Figure 1.3 Nickel Laterites Formed in Various Climates (Dalvi et al., 2004)

Four commercial nickel laterite extraction plants using the HPAL process have operated periodically in WA, specifically: Cawse (1998-2008), Bulong (1998-2003), Murrin Murrin (1998-present) and Ravensthorpe (2008-2009, 2011-present). These plants have experienced significant process issues (Sudol, 2005; Taylor, 2007) resulting in the permanent closure of Cawse and Bulong, and the temporary closure of Ravensthorpe. It is therefore timely to investigate promising alternative processing methods, particularly those capable of treating the WA-predominant nontronite zone. The segregation process is one such method (Piper, 2009) and will be the focus of this work.

Chapter 2

Literature Review

Segregation involves reacting a material containing valuable metal oxide at 973-1273 K (700-1000°C) in the presence of a particulate carbonaceous reductant and chloride salt. During segregation, the valuable metal is transported as a volatile chloride and reduced onto the carbon surface to form a metal coating. The metal can then be separated from the gangue into a concentrate using flotation or magnetic separation. This results in a lowering of energy costs associated with downstream processing, especially when treating initially low grade material (Kwatara et al., 2011).

Prior to segregation, ore is normally roasted[2] in air for dehydration, dehydroxylation, carbonate decomposition and sulphide oxidation, all of which may be necessary to improve the efficiency of the subsequent process.

The segregation process is relatively complex since it utilises multiple coupled reactions involving gas, solid and liquid. However, it manages to combine extraction; 'the chloridisation of metal oxide in the ore', with concentration; 'the transport of metal chloride vapour from the surface of the ore to the carbon surface, where it is reduced to metal'. This makes it potentially attractive for the treatment of ores such as nickel laterite, in which the valuable metal is highly disseminated.

2.1 Background

The segregation process was discovered by Moulden and Taplin (1924) and has since been utilised to recover metals from a variety of materials, in particular, Cu oxide and silicate ores, dead-roasted Cu sulphide concentrate and Ni laterite ore (Rey, 1967; Iwasaki et al., 1973; Wright, 1973; Rey, 1980; Rey, 1985). Segregation was first applied to Cu oxide ores that were refractory to conventional flotation and sulphuric acid leaching (Rey, 1967). Commercial plants operated periodically from 1931 to 1975 and achieved recoveries of over 85%. Although the process chemistry appeared sound, plant closures occurred due to mechanical, economic, political and workforce related issues. Throughout the late 1970's and early 1980's, segregation was investigated for the treatment of dead-roasted[3] Cu sulphide concentrates (Marcuson, 1980). Segregation was thought to offer several advantages over

[2] The roasted ore will usually be referred to in this study as the calcine.
[3] A dead-roast is designed to completely oxidise all sulphides, however, a small percentage of sulphur usually remains.

smelting, specifically: improved SO_2 control through the generation of a single concentrated gas stream, lower capital costs, and improved energy efficiency (Opie, 1976). Although showing promise, the dead-roast/segregation process has never been commercialised.

In parallel with interest in Cu segregation, work was carried out during the 1960's on the segregation of Ni from low grade nickel oxide laterite ores, especially by Japanese researchers (Iwasaki et al., 1966; Nagano et al., 1970). An increase in the Ni price during the 1970's prompted further interest in the process (Iwasaki, 1972a). Subsequent work on the segregation of Ni from laterites ores, both at laboratory and pilot scale, showed that it was possible to achieve high Ni recoveries (80-95%) from all sections of the laterite profile (Iwasaki et al., 1966; Dor, 1972; Rey et al., 1972a; Chermak et al., 1973; Ericson et al., 1984).

From 1981 to 1983, a one t/h segregation pilot plant was built in the Philippines using the MINPRO-PAMCO process in which heating was delivered using a novel mechanical kiln. The process achieved up to 90% Ni extraction from a garnierite ore containing 2.3% Ni but was discontinued due to a sharp drop in the Ni price during the 1980's (Ericson et al., 1987). This also caused general interest in the Ni segregation process to wane, leaving the process not fully understood or optimised.

In addition to Cu oxide and silicate ores, dead-roasted Cu concentrates and Ni laterites, the segregation process has also been used to extract Cu, Ni, Co, Fe, Sb, Ti, Pb and Ag from various other materials, as summarised in Table 2.1.

2.2 Segregation Overview

The chemical steps which are considered to take place during the segregation process have been mainly reviewed for Cu segregation by Brittan (1970), Brittan and Liebenberg (1971) and Rey (1985), and for Ni segregation by Brittan and Liebenberg (1972), Dor (1972), Hanf (1972a) and Rey et al. (1972a). Thermodynamics aspects of segregation have been reviewed mainly by Hanf (1972a) for Ni segregation and by Iwasaki (1972b) and Yazawa (1979) for Ni and Cu segregation.

The segregation process is understood to be a carbon reduction process that utilises chloride as an intermediary to extract and transport the metal from the calcine to the carbon surface. The process requires a supply of hydrogen and chloride in the presence of particulate carbon at temperatures between ~973-1273 K

(700-1000ºC). The process involves: (1) the generation of gaseous HCl; (2) the formation of gaseous metal chlorides; (3) the reduction of chlorides and deposition of metal on the surface of the carbonaceous reductant; and (4) the parallel reduction of metal oxides within the ore mainly with carbon monoxide[4]. Hydrogen and chloride are recycled between these various stages.

Table 2.1 Novel Applications of the Segregation Process

Material Treated	Targeted Metal	References
Copper-Cobalt Ore	Cu, Co	(Ferron et al., 1992; Ferron et al., 1993)
Deep Sea Nodules	Cu, Co, Ni	(Hoover et al., 1975; Djohari et al., 1989; Parekh et al., 1988)
Furnace Bricks	Cu	(Bear and Moresby, 1978)
Oxidised Ni Matte	Cu	(Bear et al., 1983)
Slags	Cu	(Satapathy et al., 1986; Tomášek et al., 1995)
Molybdenum Leaching Residue	Ni	(Chu et al., 2012)
Iron Ore	Fe	(Schulz and Lex, 1968; Fenson, 1981; Saly and Abdul Wahab, 2006)
Antimony Raw Materials	Sb	(Imris, 1977)
Ilmenite	Ti	(Battle et al., 1996)
Lead sulphate/sulphide	Pb	(Bear and Merrit, 1975; Bear et al., 1976; Bear et al., 1977)
Maganiferous Silver Ore	Ag	(Chase, 1981; Flores and Jordan, 1993; Flores et al., 1994; Flores et al., 1995)

A simplified representation of a segregation system is presented in Figure 2.1. This figure highlights the reactions involving the calcine, chloride salt and solid carbonaceous reductant, as well as the flow of gaseous species within the process.

Hydrogen is mainly supplied by the release of residual water from within the calcine at the segregation temperature (Equation 2.1), but lesser amounts enter as water with the chloride salt and as hydrogen within volatiles associated with the carbon.

$$H_2O(ore) \rightarrow H_2O(g) \qquad 2.1$$

Chloride is supplied through hydrolysis of an added salt, commonly NaCl in Cu segregation and $CaCl_2$ in Ni segregation, as shown in Equation 2.2 for the simplest case of hydrolysis of $CaCl_2$ to give CaO. Silica is usually present within the ore such that the product is $CaSiO_3$ rather than CaO.

[4] While the parallel reduction of metal oxides with carbon monoxide is not necessarily required for segregation, it occurs alongside segregation and has important impacts on the system.

$$H_2O(g) + CaCl_2(l) \rightarrow 2HCl(g) + CaO(s) \quad 2.2$$

After hydrogen and chloride are supplied to initiate the segregation reactions, they are largely recycled between the ore and chloride salt by exchange of HCl and H_2O, and between the ore and the carbon by exchange of H_2O, HCl, and MCl_2 (M represents a generic metal ion), as shown in Figure 2.1.

The HCl gas is ultillised to chloridise the metal oxide, as represented in Equation 2.3 for a generic metal oxide MO:

$$MO(s) + 2HCl(g) \rightarrow MCl_2(g) + H_2O(g) \quad 2.3$$

The metal chloride is then transported through the gas phase to the surface of the solid carbonaceous reductant where it is reduced by hydrogen (Equation 2.4).

$$H_2(g) + MCl_2(g) \rightarrow 2HCl(g) + M(s) \quad 2.4$$

The hydrogen is produced at the carbon surface by the water gas reaction, as represented by Equation 2.5.

$$H_2O(g) + C(s) \rightarrow H_2(g) + CO(g) \quad 2.5$$

The gasification of carbon with CO_2 via the Boudouard reaction (Equation 2.6) also occurs at the carbon surface. This generates CO, some of which reacts with H_2O via the water gas shift reaction (Equation 2.7) to produce additional hydrogen.

$$CO_2(g) + C(s) \rightarrow 2CO(g) \quad 2.6$$

$$H_2O(g) + CO(g) \rightarrow H_2(g) + CO_2(g) \quad 2.7$$

CO is largely responsible for the reduction of higher to lower valence metal oxides in the ore, such as M_3O_4 to MO (typically Fe_3O_4 to FeO) as represented by Equation 2.8, and for the reduction of metal oxides to metal as represented by Equation 2.9.

$$M_3O_4(s) + CO(g) \rightarrow 3MO(s) + CO_2(g) \quad 2.8$$

$$MO(s) + CO(g) \leftrightarrow M(s) + CO_2(g) \quad 2.9$$

Reduction of metal oxides also occurs with H_2; however, the amount present in the gas is usually very small compared to the amount of CO. If the moisture content of

the calcine is relatively high, increased levels of H_2 can be present in the gas as a result of the water gas shift reaction (Equation 2.7).

The reduction of metal oxides within the ore is known as in-situ reduction. When this results in ferronickel formation, it is detrimental to segregation, since once reduced in-situ the metal does not readily chloridise and take part in segregation. Instead, the metal usually remains finely spread throughout the ore such that any valuable metal alloyed within the in-situ deposit can be lost during downstream concentration processes.

The average composition of the gas generated within the segregation bed will depend on the thermodynamic favourability and comparative rates of the reactions that produce the species within the gas and those which consume them, as illustrated by Equations 2.1 through to 2.9. As a result, the bulk gas[5] will contain a mixture of CO, CO_2, HCl, H_2O, H_2 and metal chlorides, mainly Cu_3Cl_3 for Cu segregation and $FeCl_2$ with minor $NiCl_2$ and $CoCl_2$ for Ni segregation. All chlorides are represented in Figure 2.1 as MCl_2.

2.3 Copper and Nickel Segregation Systems

Relevant aspects of the Cu and Ni segregation systems will be reviewed and contrasted in this section, with the focus mainly on Ni segregation. In general, two types of segregation studies have been carried out for these metals. The first type examines reactions within the segregation process in isolation; such studies relating to Cu and Ni segregation are summarised in Table 2.2 and Table 2.3 respectively. The second type examines the segregation system as a whole; such studies relating to Cu and NI segregation are summarised in Table 2.4 and Table 2.5 respectively.

[5] The term 'bulk gas' is used to describe the gas which fills the space between the particles within the bed, in contrast to gas at the carbon surface; since the bed is well-mixed by vibration, the bulk gas is assumed to have a uniform composition.

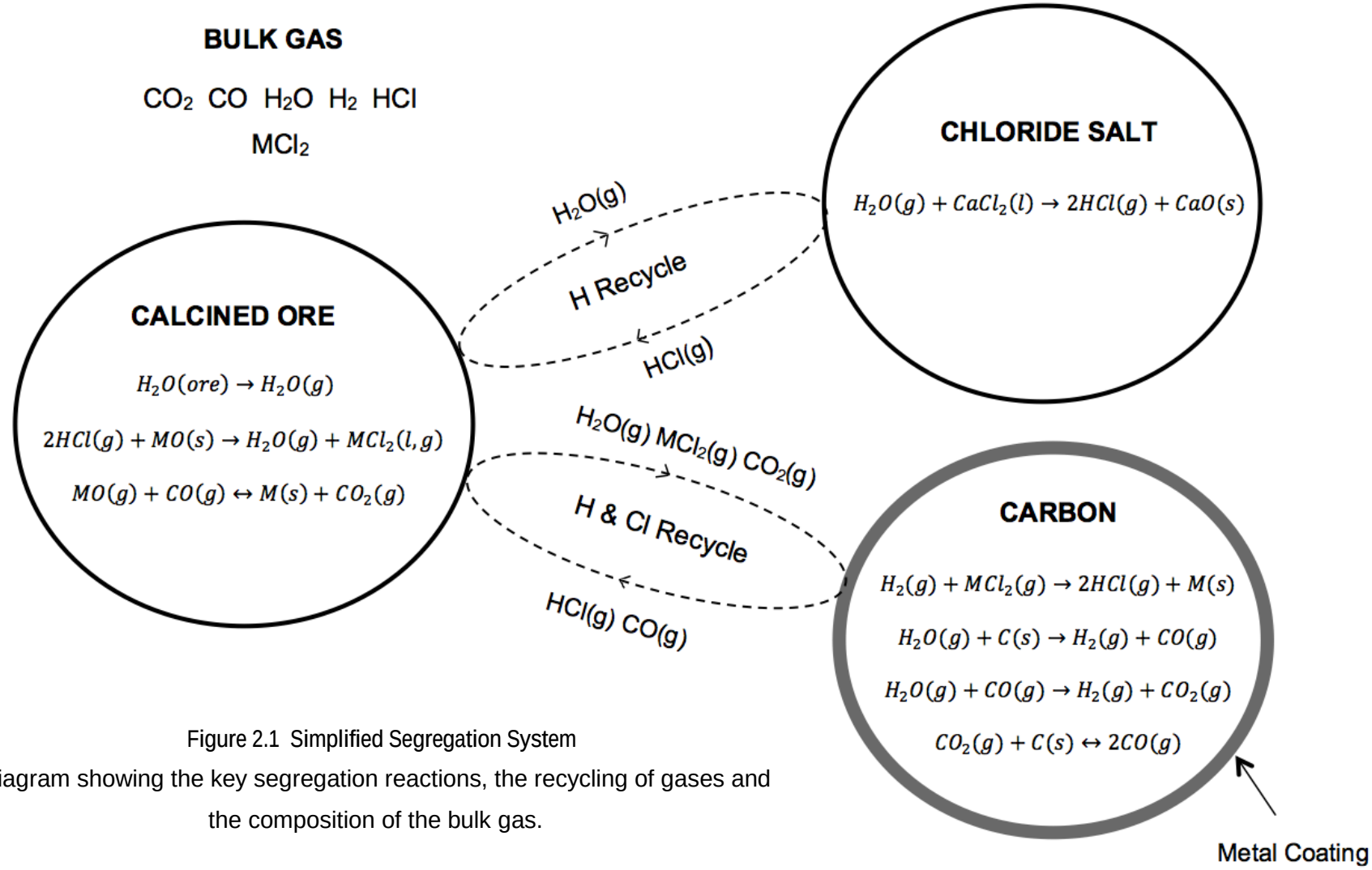

Figure 2.1 Simplified Segregation System

Diagram showing the key segregation reactions, the recycling of gases and the composition of the bulk gas.

Table 2.2 Studies of Isolated Copper Segregation Reactions

Authors(s)	Description
Hadjiat (1969)	Study of Cu segregation reactions using pure mixtures
Hanf and Sole (1970)	Hydrolysis of NaCl at 873-1273 K
Brittan and Liebenberg (1971)	Chloridisation of a siliceous ore (1.84% Cu & 3.18% Fe) with HCl(g) at 1023-1173 K, with the resulting Cu_3Cl_3(g) passed through a separate bed of coke for reduction
Hanf and Sole (1972)	Hydrolysis of NaCl in the presence of SiO_2 at 873-1273 K
Titi-Manyaka and Iwasaki (1972)	Thermal analysis during the chloridisation of Cu oxide, iron oxide, $CaCO_3$, CaO and MgO with HCl(g) from 272-1273 K

Table 2.3 Studies of Isolated Nickel Segregation Reactions

Author(s)	Description
Okamoto et al. (1971b)	Separate chloridisation with HCl(g) and reduction with H_2(g) of two garnierite ores (3% Ni, 11-18% Fe, 32-43% SiO_2 & 21-22% MgO), with an independent study of the reduction of metal chloride vapours onto various substrates with H_2(g) and examination of the resulting ferronickel
Brittan and Liebenberg (1972)	Chloridisation of a garnierite ore (1.3% Ni, 9% Fe & 16% Mg) with HCl(g) at 1273 K, with the resulting $NiCl_2$(g) and $FeCl_2$(g) passed through separate bed of coke for reduction
Hanf (1972b)	Hydrolysis of $NiCl_2$, $FeCl_2$, $MgCl_2$ and $CaCl_2$ from 873–1093 K
Fruehan and Martonik (1973a)	Chloridisation of Fe from 810-1173 K and Ni from 850-1340 K with HCl(g)
Fruehan and Martonik (1973b)	Chloridisation of Fe_2O_3, NiO, $NiFe_2O_4$ at 1073-1473 K with HCl(g) and Cl_2(g)
Webb (1973)	Chloridisation of a garnierite ore (1.1% Ni, 13% Fe, 26% MgO, 40% SiO_2) at 1123-1273 K with HCl(g)
Seaborn (1976)	Chloridisation of Fe_2O_3, Fe_3O_4, and a garnierite ore (1.1% Ni, 13% Fe, 26% MgO, 40% SiO_2) with HCl(g) at 1173 K
Kondo et al. (1978)	Hydrolysis of $CaCl_2$ at 1113-1223 K

Table 2.4 Studies of Copper Segregation

Author(s)	Material	Description
Rampacek et al. (1959)	Ore	Batch segregation of 16 ores (0.8-5% Cu, 1-24% Fe, 35-90% SiO_2, 0.3-18% $CaCO_3$, 0.1-17% MgO & 0.6-15% Al_2O_3) in a rotating retort and continuous segregation-flotation of two ores (1.3-2.2% Cu, 15-24% Fe, 40-50% SiO_2, 7% $CaCO_3$, 6.4% MgO & 4.5-5.5% Al_2O_3) in an indirectly fired rotary kiln
Pollandt and Pease (1960)	Ore	Development of a commercial segregation reactor for the treatment of a silver-Cu ore (1.5% Cu, 0.015-0.06% Ag, 14% Fe_2O_3, 22% SiO_2, 32% MnO_2, 22% $CaCO_3$) from the Berenguela Mine (Peru)

Table 2.4. Studies of Copper Segregation (cont'd)

Author(s)	Material	Description
McKinney and Waddleton (1962)	Ore	Batch segregation of a siliceous and calcareous ore in a rotating steel retort, testing various chloride salts
McKinney and Evans (1963)	Ore	Continuous segregation-flotation of four ores (sandstone, quartzite, limonite & limestone) in a directly fired kiln
Martinez (1967)	Ore	Thermal analysis during segregation of a chrysocolla ore (Cu silicate)
Pinkney and Plint (1967)	Ore	Description of the development of the commercial TORCO (Treatment of Refractory Cu Ore) Cu segregation process
Mackay and Gibson (1968)	Ore	Description of the development of a 450 t/d TORCO pilot plant in Zambia treating a sandstone and siliceous ore
Brittan (1971)	Ore	Kinetic modelling of the TORCO system
Iwasaki (1972b)	-	Thermodynamic analysis of the Cu-HCl-H_2 system using predominance area diagrams
Cathro (1973)	Ore	Batch segregation of 1 kg samples of two siliceous ores (containing minor Cu sulphide) using a rotating steel kiln
Opie (1976)	Con	Description of the dead roast-segregation process
Marcuson and Kellogg (1977)	Con	Batch segregation of 50 g samples of a high grade (37.5% Cu, 27% Fe & 0.1% S) concentrate in a quartz reactor with continuous CO_2 (g) analysis. Effect of moisture, SiO_2 and CuCl addition examined.
Marcuson (1978)	Con	Batch segregation of 50 g samples of a high grade (37.5% Cu, 27% Fe & 0.1% S) concentrate in a quartz reactor with continuous CO_2 (g) analysis. Effect of various additives examined.
Opie et al. (1979)	Con	Batch segregation of 50 g and 600 g samples of four dead-roasted Cu-Ni concentrates (14-19% Cu, 2.4-3.1% Ni, 33-45% Fe & 0.12-0.18% S) in a quartz reactor, investigating conditions for selective Cu segregation
Yazawa (1979)	Ore	Thermodynamic and mass balance analyses of the segregation of a theoretical Cu ore (2% Cu & 20% Fe)
Avraamides (1982)	Con	Batch segregation of 50 g samples of dead-roasted sulphides produced during the 'boiling' stage of Sherrit-Gordon process (80% CuO, 7% Fe_2O_3, 3% NiO & 3% SiO_2) using covered crucibles
Lu et al. (1983)	Con	Batch segregation of 4-8 g samples of a dead-roasted Cu-Ni (17% Cu, 6% Ni, 30% Fe, 10% SiO_2, 7% Al_2O_3 & 0.2% S) and a Cu (33% Cu, 34% Fe, 7% SiO_2, 2% Al_2O_3 & 0.1% S) concentrate in covered crucibles followed by acetonitrile leaching
Twidwell and Beuerman (1984)	Con	Batch segregation using a quartz tube reactor with 100 g samples of concentrate (20% Cu & 23% Fe) dead-roasted to either 1 or 2.3% S
Grotowski and Żmudziński (1987)	Ore	Batch segregation of 500 g samples of a sulphide-oxide ore (3.8% Cu, 5.5% Fe, 35% SiO_2 & 1.7% S, with 75% of the Cu associated with sulphides) in a steel retort
Grotowski and Grotowska (1990)	Pure Oxide	Batch segregation of 500 g samples of pure Cu oxide, chloride and sulphate mixtures in a steel retort, specifically investigating Cu sulphide formation during segregation
Datta et al. (1992)	Con	Batch segregation of a dead-roasted concentrate (30% Cu, 30% Fe, 1% S, 6% SiO_2) with gas analysis

Table 2.5 Studies of Nickel Segregation

Author(s)	Description
Iwasaki et al. (1966)	Batch segregation of 100-200 g samples of garnierite ore (2.9% Ni, 0.11% Co, 12% Fe, 41% SiO_2 & 24% MgO) and three limonite ores (0.4-1.1% Ni, 0.06-0.1% Co, 48-50% Fe & 2.2-9.7% SiO_2) in a quartz tube reactor
Jagolino (1970)	Batch segregation of 130 g samples of pelletised limonite ore (0.7% Ni, 0.28% Co, 52% Fe, 6% Al_2O_3, 1.7% SiO_2 & 3.0% Cr) and garnierite ore (2.1% Ni, 24% Fe, 0.03% Co, 1.5% Al_2O_3, 43% SiO_2 & 14% MgO) in a steel tube reactor
Nagano et al. (1970)	Batch segregation of 1 kg and 100 kg samples of garnierite ore (2.9% Ni, 0.11% Co, 12% Fe, 41% SiO_2 & 24% MgO) and three limonite ores (0.44-1.13% Ni, 47.5-50% Fe, 2.2-9.7% SiO_2) in two differently sized stainless steel rotary kilns
Okamoto et al. (1971a)	Detailed examination of ferronickel after batch segregation of a garnierite ore (4.3% Ni) with NH_4Cl and charcoal and also a garnierite ore (2.9% Ni, 11% Fe, 0.6% Cr, 36% SiO_2 & 19% MgO) with $CaCl_2$ and coal
Davidson (1972)	Batch segregation in a vibrating quartz tube reactor using 20 g samples of Fe_2O_3 blended in various ratios with seven garnierite ores (0.7-1.4% Ni, 6.5-14% Fe_2O_3 & 22-36% Mg)
Dor (1972)	Extensive test program (batch segregation of 200 g samples in a crucible, rotary kiln and vibrating tube reactor) carried out on six garnierite ores (0.9-3.1% Ni, 0.1-2% Fe, 12-30% MgO & 39-43% SiO_2) and a limonite ore (1.6% Ni, 53% Fe & 2.5% SiO_2), mainly investigating the use of a novel mixed iron-carbon reductant
Hanf (1972a)	Thermodynamic calculations for the overall segregation process and various segregation reactions
Iwasaki (1972b)	Thermodynamic analysis of the Ni-HCl-H_2 system using predominance area diagrams
Pietsch (1972)	Potential issues associated with treating Ni laterite segregation off-gas
Rey et al. (1972a)	Batch segregation of 15 g samples of garnierite ore (3.3% Ni, 20% Fe, 6% Mg) in a quartz tube reactor with gas analysis, including a discussion on the chemical reactions and kinetics and an estimation of process energy requirements
Rey et al. (1972b)	Batch segregation ten garnierite ores (1.4-2% Ni, 0.02-0.1% Co, 5.4-14% Fe, 38-58% SiO_2 & 23-34% MgO), with specific tests investigating the chloride reactions, effect of H_2O and structure of the ferronickel
Sole and Taylor (1972)	Batch segregation in a vibrating quartz tube reactor using 20 g samples of three limonite ores (1-1.5% Ni, >60% Fe_2O_3), nine garnierite/serpentine ores (0.7-2.3% Ni, 7-20% Fe_2O_3, 15-36% MgO & 36-60% SiO_2), three clays/altered serpentine ores (1.2-1.8% Ni, 13-30% Fe_2O_3, 6-12% MgO & 35-52% SiO_2), four talc ores (0.9-1.4 Ni< 15-45% Fe_2O_3, 10-36% MgO & 30-42% SiO_2), two mixed ores (1-1.5% Ni, 35-50% Fe, <15% MgO & 19-25% SiO_2) and a magnetite ore (> 90% Fe_3O_4), with correlation of the mineralogical, chemical, thermal and infrared properties of the ore with segregation performance
Warner et al. (1972)	Theoretical energy calculations and combustion gas volume calculations coupled with actual batch segregation results using a rotary kiln for 150 g samples of a limonite ore (1.5% Ni, 48% Fe, 0.17% Co, 4.4% SiO_2, 6% Al_2O_3 & 3.6% Cr_2O_3), a garnierite ore (2.5% Ni, 31% Fe, 0.16% Co, 21% SiO_2, 14% MgO, 3.6% Al_2O_3, 3% Cr_2O_3), a 50:50 blend of the limonite/garnierite ores, a surface crust from weathered boulders (2.4% Ni, 7.3% Fe, 0.15% Co, 42% SiO_2 & 33% MgO) and a Cu ore (2.5% Cu & 46.9%) for comparison
Chermak et al. (1973)	Batch segregation of a nontronite (%Ni not reported, 14% Fe, 44% SiO_2, 8% MgO & 7% Al_2O_3)
Webb (1973)	Batch segregation of 80-160 g samples of a garnierite ore (1.1% Ni, 13% Fe, <0.1% Co, 40% SiO_2 & 26% MgO) in a silica tube reactor

Table 2.5. Studies of Nickel Segregation (cont'd)

Author(s)	Description
Wright and Gooden (1973)	Batch segregation of 1 kg samples of five garnierite ores (1-1.9% Ni, 11-21% Fe, 30-45% Fe, 9-26% MgO & 4.5-5.1% Al_2O_3) and three limonite ores (0.7-1.2% Ni, 33-47% Fe, 12-20% SiO_2, 0.5-6.2% MgO & 8-10% Al_2O_3) using a rotating kiln
Kimura and Kondo (1975)	Thermodynamic modelling assuming sequential equilibrium of various reactions
Titova et al. (1975)	Batch segregation of 200 g samples of a mixed Ni laterite (1.1% Ni, 0.1% Co, 30% Fe, 25% SiO_2, 4% MgO, 5% Al_2O_3 & 2.5% Cr_2O_3) in a steel reactor using two-stage heating with gas analysis
Yazawa (1979)	Thermodynamic and mass balance analyses for the segregation of a theoretical Ni ore (2% Ni & 20% Fe)
Ishii and Svensson (1980)	Description of the development of the 'Mechanical Kiln' reactor and presentation of results from the segregation of a garnierite ore (2.6% Ni, 12% Fe, 43% SiO_2, 26% MgO & 0.6% Cr) using a 60 kg/h pilot reactor
Hudyma (1981)	Batch segregation of synthetic samples (0.65% Ni as $NiCl_2$, 2% coal, 2-8% $CaCl_2$ with the balance being SiO_2) in a quartz tube reactor with examination of the metallic formed on coal
Ericson et al. (1984)	Description of the development of the MINRO-PAMCO 1 t/h Mechanical kiln, with process results and proposed flow sheet
Hudyma (1984)	Batch segregation of synthetic samples (0.65% Ni as $NiCl_2$, 2% coal, 2-8% $CaCl_2$ with the balance being SiO_2) in a quartz tube reactor with examination of the metal formed on SiO_2
Ericson and Svensson (1985)	Description of the development of the 'Mechanical Kiln', with a proposed flow sheet
Ericson et al. (1987)	Description of the operation of a 1 t/h Mechanical kiln, with results from the segregation of a garnierite ore (2.3% Ni, 13% Fe, 0.04% Co, 43% SiO_2, 26% MgO & 0.7% Cr)
Titova et al. (1988)	Results from batch and continuous segregation of five garnierite ores (0.9-2.4% Ni, 0.03-0.1% Co, 11-32% Fe, 21-37% SiO_2 & 6-30% MgO), with three proposed reactor designs
Hudyma (1993a)	Batch segregation of 3 g samples of a silica-magnesite ore (0.4% Ni, 5% Fe, 22% Si, 3% Al, 9% Mg & 9% CO_2), a silicate ore (0.9% Ni, 22% Fe, 22% Si, 5% Mg & 5.4% CO_2) and a magnesite ore (0.18% Ni, 10% Fe, 21% Si, 10.5% Mg & 19.0% CO_2) in a quartz tube reactor, with the p_{CO2}/p_{CO} being related to the ferronickel grade
Tomášek et al. (1995)	Batch segregation of 50 g samples of nine Ni laterite ores with a variety of compositions (1-3% Ni, 6-42% Fe, 0.03-0.083% Co, 0.4-1.7% Cr, 2.5-45% MgO, 0.6-9.8% Al_2O_3) in a quartz reactor using sulphur containing 'activators'
Johansson and Zander (1997)	Reflections on the development of the Mechanical Kiln
Reznik et al. (1998); Reznik et al. (2003)	Thermodynamic analysis of chloride salt hydrolysis, metal oxide chloridisation and metal chloride reduction, and comparison with segregation results from other Russian researchers
Ma and Pickles (2003)	Microwave heating during batch segregation of a garnierite ore (2.4% Ni, 20% Fe, 0.15% Co, 32% SiO_2, 16% MgO, 1% Cr & 2.3% Al_2O_3)
Kwatara et al. (2011)	Batch segregation of 500 g garnierite ore samples (composition not specified) using a rotary kiln with microprobe analysis of the ferronickel

2.3.1 Copper Segregation

Copper has been segregated from mainly siliceous ores containing 1-6% Cu. The metal is usually widely dispersed within the ore as either cupric oxide (tenorite), and/or hydrated Cu silicate (chrysocolla), Cu carbonate (malachite) and sometimes copper sulphide. After dehydration, dehydroxylation, carbonate decomposition and sulphide oxidation, achieved by roasting in air to ~973-1173 K (700-900°C), the calcine contains Cu mainly as CuO and Fe mainly as Fe_2O_3 (typically < 10%), along with variable amounts of other oxide impurities such as SiO_2 (up to 60%), MgO (up to 15%) and Al_2O_3 (up to 15%).

Copper has also been segregated from dead-roasted Cu concentrates containing up to 40% Cu, 30% Fe and 2.5% S, with Cu and Fe being present as discrete CuO and Fe_2O_3, plus remnant sulphides.

Segregation temperatures for Cu ores and dead-roasted concentrates are typically 973-1123 K (700-850°C). A relatively fine reactive carbon of 75-300 µm (+200-48 Tyler mesh) in size is commonly added, usually as petroleum coke or coal. The carbon addition depends on the amounts of Cu and Fe present and ranges from 0.5-1.5% for Cu ores and 5-15% for concentrates; reaction times range from 5-60 minutes for ores and 1-3 hours for concentrates. The chloride recycle is efficient and the amount of NaCl required is significantly less than stoichiometric, with 0.1-1.5% commonly added, depending on the quality of the contact between the ore, gas phase and reagents (Rey, 1980).

During Cu segregation, the CuO within the calcine is reduced to Cu_2O by CO within the bulk gas, before being chloridised to form Cu_3Cl_3(g), which is subsequently reduced to Cu at the carbon surface, as described by Marcuson (1980). This researcher segregated roasted Cu concentrates and carried out several measurements of the oxygen pressure (p_{O_2}) of the bulk gas using a zirconium oxide sensor. It was found that while CuO remained in the calcine, the equilibrium for the CuO/Cu_2O reduction controlled the p_{O_2} and buffered the value above that necessary for the undesirable in-situ reduction of Cu_2O to Cu throughout the ore.

Figure 2.2 shows the equilibrium p_{O_2} versus temperature (973-1273 K; 700-1000°C) for the reduction of the oxides of importance in segregation. The figure confirms that the equilibrium pressure for the pure CuO/Cu_2O reaction lies well above that for the pure Cu_2O/Cu reaction. As roasted concentrates contain more CuO compared

to ores, the p_{O_2} buffering period will be longer, making in-situ reduction to Cu even less likely when segregating concentrates.

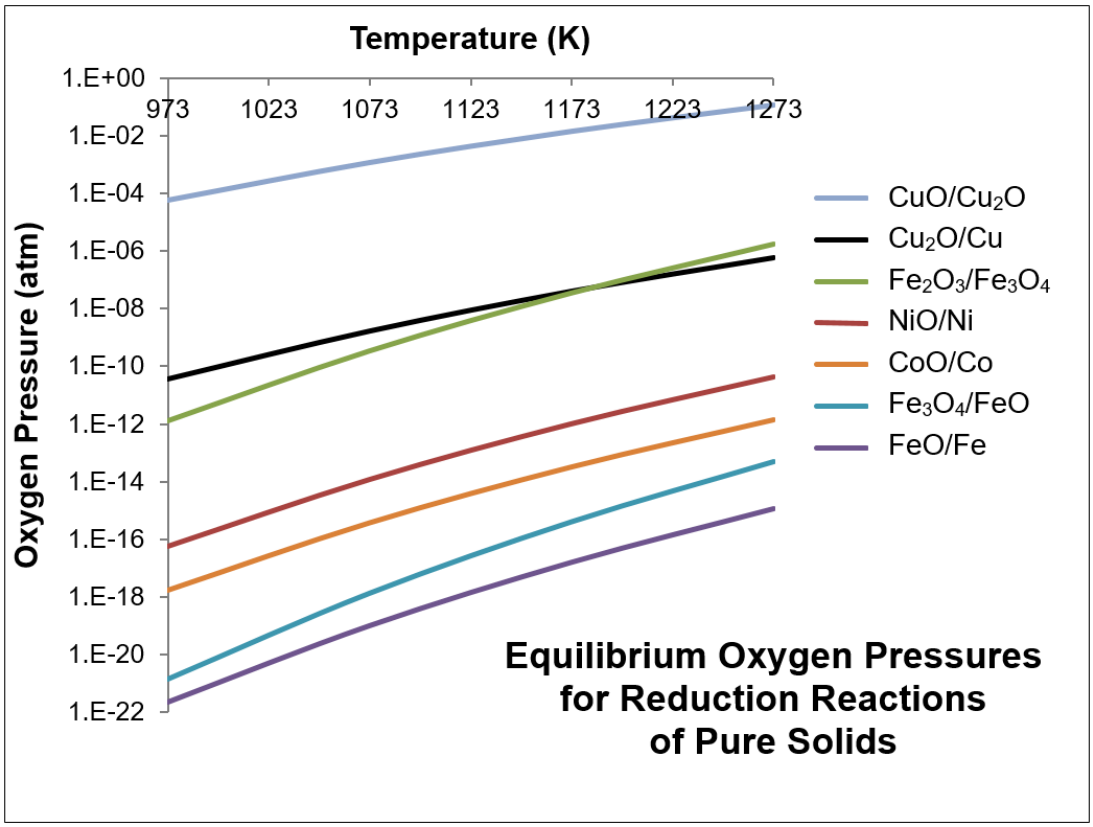

Figure 2.2 Equilibrium Oxygen Pressures for Pure Oxide Reduction Reactions

Equilibrium constants per mole of O_2, obtained from the FACTSage v6.4 'Reaction' program. All solids are pure with an activity of 1.

The p_{O_2} within the bulk gas, as determined by the CuO/Cu_2O equilibrium is sufficient to oxidise Cu for the majority of the segregation period. Marcuson (1977) therefore determined that a separate zone of lower p_{O_2}, at least compatible with the Cu_2O/Cu equilibrium, must exist at the carbon surface to prevent re-oxidation of the segregated Cu product.

Figure 2.2 shows that the equilibrium p_{O_2} for the CuO/Cu_2O reaction lies above that for the Fe_2O_3/Fe_3O_4 reaction; thus Fe_2O_3 reduction is suppressed during Cu segregation, which minimises the consumption of carbon. Reduction of Fe_2O_3 only begins after the disappearance of CuO towards the end of segregation (Marcuson, 1980), when the p_{O_2} becomes controlled by the Cu_2O/Cu equilibrium, which lies very close to the Fe_2O_3/Fe_3O_4 equilibrium (Figure 2.2). Throughout the majority of the Cu segregation process, Marcuson (1980) recognised that the off-gas is virtually 100%

CO_2. He was therefore able to measure the evolution of CO_2 to monitor the extent of Cu reduction during segregation.

The final segregation product from both Cu ore and dead-roasted concentrate is a relatively pure metallic Cu that coats the carbon, with no co-segregation of Fe. Between 60-95% of Cu from ore and 85-100% of Cu from roasted concentrate can be recovered into a high grade concentrate containing up to 80% Cu using conventional flotation (Marcuson, 1977).

2.3.2 Nickel Segregation

Nickel has been segregated mainly from garnierite (siliceous) and limonite (ferruginous) lateritic ores containing 1-3.5% Ni. Table 2.6 provides a summary of ore compositions (in order of increasing %Fe), key segregation parameters and maximum Ni recoveries for all studies that have reported Ni recovery data. Garnierite, nontronite and limonite ores are studied in this work, and their compositions, maximum obtained Ni recoveries and corresponding segregation parameters are given in Table 2.6 for reference. Only one study (Chermak et al., 1973) reports on the segregation of Ni from nontronite lateritic ore, which is the main focus of this work.

Nickel is widely dispersed within lateritic ores, mainly substituted for Fe or Mg within siliceous clays, or for Fe within hydrated iron oxides. A detailed consideration of the nature of Ni laterites and their mineralogy is given in 0.

Segregation of Ni ores usually begins with a roast in air to ~1173-1273 K (900-1000^{o}C) mainly to remove all free moisture and most chemically bound water, and to decompose any carbonates and to oxidise any sulphides. The calcine likely contains Ni as NiO within hematite, silicates or amorphous siliceous material. The amorphous material also contains Fe and Mg oxides and other minor oxides (Section 4.1). Calcine compositions vary widely depending on the composition of the original ore (Table 2.6). They can contain up to 50% Fe mainly as hematite, 55% SiO_2 both free and combined, and up to 35% MgO and 10% Al_2O_3 both usually as silicates.

Table 2.6 Nickel Segregation Parameters from the Literature

Ore compositions, $CaCl_2$ and carbon additions, carbon types (BCoal = bituminous coal), segregation temperatures, segregation times and maximum Ni recoveries, all arranged by increasing Fe content of the ore. Only includes studies reporting Ni recovery; NR is not reported)

Reference	Ore	Ni (%)	Fe (%)	SiO_2 (%)	MgO (%)	Al_2O_3 (%)	$CaCl_2$ (%)	C (%)	Temp K (°C)	Time min	Ni % Rec.
Davidson (1972)	Garnierite	1.07	4.6	NR	32.5	NR	5	Coke 3	1173 (900)	90	52
Davidson (1972)	Garnierite	1.02	4.7	NR	22.9	NR	5	Coke 3	1173 (900)	90	75
Davidson (1972)	Garnierite	1.0	5.3	NR	35.6	NR	5	Coke 3	1173 (900)	90	50
Davidson (1972)	Garnierite	1.50	5.8	NR	29.7	NR	5	Coke 3	1173 (900)	90	78
Davidson (1972)	Garnierite	0.85	5.8	NR	29.3	NR	5	Coke 3	1173 (900)	90	50
Davidson (1972)	Garnierite	0.70	7.2	NR	30.8	NR	5	Coke 3	1173 (900)	90	70
Warner et al. (1972)	Unspecified	2.43	7.3	41.2	33.0	0.5	5	Coke 7	1273 (1000)	60	61
Dor (1972)	Riddle Blend	1.1	8	43	29	NR	8	BCoal 2	1223 (950)	90	57
Brittan and Liebenberg (1972)	Garnierite	1.20	9	NR	26.6	NR	5	Coke 3	1173 (900)	90	75
Wright and Gooden (1973)	Garnierite	1.20	9	NR	26.6	NR	5	Coke 3	1273 (1000)	90	84
Wright and Gooden (1973)	Serpentine	1.16	10.7	32.0	26.4	5.0	5	Coke 2	1273 (1000)	60	81
Davidson (1972)	Garnierite	1.43	10.9	NR	22.3	NR	5	Coke 3	1173 (900)	90	83
This Work	WA Garnierite	1.27	11.7	53.3	14.8	2.58	5	Coke 5	1223 (900)	60	65
Iwasaki et al. (1966)	Garnierite	2.89	12.0	40.8	24.3	0.75	7	Coke 3.5	1273 (1000)	60	93
Ericson et al. (1984)	Saprolite	2.30	13.2	42.6	22.6	0.8	4	Coke 2	1223 (950)	~5 hrs	90

Table 2.6 Nickel Segregation Parameters from the Literature (cont'd)

Reference	Ore	Ni (%)	Fe (%)	SiO_2 (%)	MgO (%)	Al_2O_3 (%)	$CaCl_2$ (%)	C (%)	Temp K (°C)	Time min	Ni % Rec.
Wright and Gooden (1973)	Serpentine	1.85	14.1	40.5	9.4	4.7	5	Coke 2	1273 (1000)	60	84
Chermak et al. (1973)	Nontronite	NR	14.4	44	8.3	7.2	5	Coke 4	1273 (1000)	60	70
Chermak et al. (1973)	Nontronite	NR	14.4	44	8.3	7.2	5	Coal 4	1273 (1000)	60	66
Wright and Gooden (1973)	Serpentine	1.35	14.7	45.3	12.3	5.1	5	Coke 2	1273 (1000)	60	77
Wright and Gooden (1973)	Serpentine	1.70	15.8	30.1	20.3	4.5	5	Coke 2	1273 (1000)	60	80
Rey et al. (1972a)	Siliceous	3.3	19.6	NR	NR	NR	6	Coke 2	1223, 1273	70	77, 95
Wright and Gooden (1973)	Serpentine	0.98	20.6	31.1	19.4	4.6	5	Coke 2	1273 (1000)	60	71
Dor (1972)	Silicate Blend	3.1	22	43	14	NR	8	BCoal 3	1223 (950)	90	70
This Work	WA Nontronite	1.21	24.4	40.7	2.02	3.96	5	Coke 5	1273 (1000)	60	79
Warner et al. (1972)	Saprolite	2.52	31.0	21.2	13.8	3.6	5	Coke 7	1273 (1000)	60	87
Wright and Gooden (1973)	Limonite	1.20	33.3	18.2	6.2	8.6	5	Coke 2	1273 (1000)	60	60
Wright and Gooden (1973)	Limonite	1.03	41.6	20.3	1.65	8.1	5	Coke 2	1273 (1000)	60	31
Wright and Gooden (1973)	Limonite	0.67	46.7	12.3	0.51	10.2	5	Coke 2	1273 (1000)	60	17
Iwasaki et al. (1966)	Limonite	0.85	47.6	9.68	0	2.78	4.6	Coke 5.8	1223 (950)	60	83
Warner et al. (1972)	Limonite	1.47	48.2	4.4	1.0	6.0	5	Coke 7	1273 (1000)	60	81
Iwasaki et al. (1966)	Limonite	0.97	50.9	2.24	0	6.46	4.6	Coke 5.8	1223 (950)	60	78
This Work	WA Limonite	0.93	51.2	3.10	0.41	4.47	5	Coke 5	1173 (900)	90	80

There are two notable thermodynamic differences between Cu and Ni segregation (Dor, 1972). Firstly, the overall process of reduction of NiO to Ni requires a significantly lower p_{O_2} than for the reduction of Cu_2O to Cu, as shown in Figure 2.2. Secondly, the intermediate process of chloridisation of NiO is significantly less favourable than the chloridisation of Cu_2O, since the equilibrium vapour pressure of $NiCl_2$ is significantly less than Cu_3Cl_3 under similar chloridising conditions (Figure 2.4). As a result, different segregation conditions are required for Ni segregation compared to Cu segregation, as outlined by Rey et al. (1972a).

Nickel segregation requires comparatively higher temperatures of 1173-1273 K (900-1000^{o}C), as shown in Table 2.6, compared to 973-1173 K (700-900^{o}C) for Cu segregation. Higher temperatures are needed to generate more reducing conditions in the presence of carbon, as required for NiO reduction compared to Cu_2O reduction. For Ni segregation, the on-set of ore sintering limits the upper temperature to within the range 1173-1373 K (900-1100^{o}C).

The partial pressure of HCl generated through hydrolysis of the chloride salt also has to be higher to produce an adequate pressure of $NiCl_2$, compared with that required to produce an adequate pressure of Cu_3Cl_3. This is typically achieved by adding 4-6% $CaCl_2$ (Table 2.6) in place of 0.1-1.5% NaCl and by using higher temperatures. Hanf (1972b) confirmed that HCl pressures from the hydrolysis of NaCl are 2-10 times lower than from the hydrolysis of $CaCl_2$ at Ni segregation temperatures, and are too low for adequate chloridisation of NiO.

The roast conditions also have to be more carefully controlled for Ni segregation compared to Cu segregation, such that the majority of free and combined H_2O is removed from the calcine (Section 2.4.6). This is required because $NiCl_2$(g) is much more easily hydrolysed in the presence of water vapour than Cu_3Cl_3(g). The use of $CaCl_2$ in place of NaCl is also beneficial in controlling the pressure of H_2O in the bulk gas, since the favourable hydrolysis reaction reduces the pressure of H_2O while enhancing the pressure of HCl. This protects $NiCl_2$ from hydrolysis (Rey et al., 1972a).

In contrast, the Cu segregation system is insensitive to H_2O, with successful segregation of ore being reported (Rampacek et al., 1959) when the off-gas contained 74-83% H_2O. A high pressure of H_2O may even be beneficial to Cu segregation since it suppresses the chloridisation of competing species such as Fe, Mg and Ca (Brittan and Liebenberg, 1971).

The higher temperatures and more reducing conditions required for Ni segregation also result in significant reduction of iron oxides in the calcine. This does not occur in Cu segregation. Figure 2.2 indicates that within a system of pure solids with activities of one, all Fe_2O_3 will be reduced to Fe_3O_4 before the reduction of NiO to Ni. This is because the equilibrium p_{O_2} for the Fe_2O_3/Fe_3O_4 reaction lies well above that for the NiO/Ni reaction. However, since NiO is likely present as part of silicates or oxide solid solutions within the segregation calcine (Section 4.1), the activity of NiO is less than one, and requires a lower p_{O_2} for reduction than shown on the diagram[6]. As a result, extensive co-reduction of Fe_3O_4 to FeO is unavoidable during Ni segregation.

This co-reduction of iron oxides requires higher carbon additions than used for Cu ores; typically 2-6% (Table 2.6) depending on the Fe content of the Ni ore, compared to 0.5-1.5% for Cu ores. This increased carbon usage is accompanied by higher carbonaceous gas evolution and stronger reducing conditions, with increased likelihood of undesirable in-situ reduction to ferronickel throughout the ore. A less reactive carbon, commonly metallurgical coke, is normally used for Ni segregation (Table 2.6) to minimise the impact of in-situ reduction. A more highly reactive carbon such as petroleum coke or coal is normally used for Cu segregation since it is carried out at lower temperatures.

The endothermic nature of iron oxide reduction with carbon, coupled with higher reaction temperatures, results in energy requirements that can be eight times those necessary for the segregation of a Cu ore with comparative Fe content (Warner et al., 1972). The method by which the required heat energy can be delivered to the segregation process is also constrained, since burner combustion gases contain H_2O and should not come in direct contact with the segregation charge to minimise chloride hydrolysis. It has been suggested (Nagano et al., 1970) that use of a pelletised charge can minimise direct contact with combustion gases.

In addition to the more extensive reduction of iron oxides, the higher temperatures used for Ni segregation also make the co-segregation of Fe more favourable and unavoidable, resulting in a segregation product of ferronickel rather than relatively pure metal, as is produced in Cu segregation. The chloridisation of FeO is thermodynamically favourable (Figure 2.4), such that the Ni segregation gas can

[6] For $2Ni(s) + O_2(g) \rightarrow 2NiO(s)$, rearrangement of the expression for the equilibrium constant K gives $p_{O_2} = a^2{}_{NiO}/(Ka^2{}_{Ni})$ where a is activity relative to the pure solid; thus if a_{NiO} is lower, the p_{O_2} required for reduction is also lower.

contain up to 23% $FeCl_2$ (Rey et al., 1972a, Table 2.8). Coupled with a high carbonaceous gas evolution from iron oxide reduction, this results in loss of $FeCl_2$ from the bed, and higher chloride salt requirements of 4-8% of ore compared to 0.1-1.5% for Cu ores (Rey et al., 1972b). The higher HCl pressure required for Ni segregation also adds to the chloride loss. It thus seems that the chloride recycle within the Ni segregation system is relatively inefficient compared to Cu segregation.

The ferronickel segregation product is coated onto carbon particles that can be concentrated by magnetic separation from the siliceous gangue from garnierite ores, or by flotation from the magnetite rich gangue from limonite ores. Both methods produce concentrates containing 5-20% Ni; however, when subjected to multiple concentration stages with fine grinding, the production of high grade concentrates containing relatively pure ferronickel (65-70% Ni) is possible (Ericson et al., 1987). Nickel laterite segregation reaction times range from 60-90 minutes in the laboratory and up to 5 hours within a one t/h pilot plant (Ericson et al., 1987); reported Ni recoveries vary between 50-90% (Table 2.6) for a range of Ni laterite ores.

2.4 Aspects of Nickel Segregation

The findings from previous studies relating to specific aspects of the Ni segregation process will now be reviewed. In order of review, these are: generation of HCl, formation of gaseous metal chlorides, reduction of chlorides at the carbon surface, the ferronickel deposit, the role of the solid carbonaceous reductant; gas composition; impact of H_2O, impact of the roast, and impact of ore composition and mineralogy.

2.4.1 Generation of HCl

HCl gas supplied from the hydrolysis of $CaCl_2$ has been established as the primary chloridising agent in the Ni segregation process, with, for example, 100 times more HCl evolved in comparison to Cl_2 during segregation of a garnierite ore (Iwasaki et al., 1973).

Chloride salts other than $CaCl_2$ have been tested for their ability to provide a sufficiently high and sustainable pressure of HCl, as required for successful Ni segregation (Table 2.7). These alternative salts were found either to yield a lower p_{HCl} than required (NaCl), or a higher but unsustainable p_{HCl} resulting from too rapid decomposition (NH_4Cl) or too rapid hydrolysis and/or gaseous loss ($MgCl_2$, $AlCl_3$, $FeCl_2$, $FeCl_3$).

Table 2.7 Chloride Salts tested for Nickel Segregation

Salts Tested	Reference
$CaCl_2$, NH_4Cl, $MgCl_2$ & NaCl	Iwasaki et al. (1966)
$CaCl_2$, $FeCl_2$, $FeCl_3$, $MgCl_2$ & $AlCl_3$	Dorr (1972)
$CaCl_2$, $MgCl_2$ & NaCl	Davidson (1972)
NaCl, $CaCl_2$	Hanf (1972b)
$CaCl_2$ & NH_4Cl	Webb (1973)

The hydrolysis of $CaCl_2$ in the presence of silica and also roasted garnierite ore has been studied by Hanf (1972b). It was found that equilibrium is achieved very rapidly when water vapour is passed over $CaCl_2$ in the presence of SiO_2 at 873-1223 K (600-950°C), with the p_{HCl} being enhanced through the reaction of CaO to form diopside according to:

$$CaCl_2(l) + SiO_2(s) + H_2O(g) \rightarrow CaSiO_3(s) + 2HCl(g) \qquad 2.10$$

After a time, a $CaSiO_3$ layer formed around the SiO_2 particles which caused the HCl evolution rate to decrease. However, it was found that the p_{HCl}/p_{H_2O} ratios generated by $CaCl_2$/roasted garnierite mixtures did achieve the equilibrium values as measured for the pure $CaCl_2$-SiO_2-H_2O system, indicating that equilibrium was likely to be achieved at segregation temperatures for silica containing ores.

It has been reported that $CaCl_2$ rapidly hydrolyses while maximum water is being released from the calcine during the initial stages of segregation, resulting in the high pressures of HCl. Canterford (1975) reported that 33% of $CaCl_2$ was lost from the reacting charge, mainly as HCl, during the first few minutes of segregation of various Australian laterites at 1273 K (1000°C). Rey et al. (1972a) reported that HCl appears in the gas before CO and CO_2, with up to 37% HCl being recorded during the first few minutes of segregation of roasted garnierite ore at 900°C (1173 K); after segregation all CaO had reacted to form silicates within the gangue. It was also found that 25-40% of the $CaCl_2$ (originally 6% of ore) still existed after a garnierite had been segregated for 120 minutes at 1173-1253 K (900-980°C), confirming that $CaCl_2$ remained a source of chloride for the entire Ni segregation process.

Rey et al. (1972b) reported that $CaCl_2$ hydrolysis is slower and less complete when segregating roasted limonite ore compared to when segregating roasted garnierite, and that the extent of hydrolysis depended on the acidity (or silica content) of the ore. Hanf (1972b) found that the p_{HCl}/p_{H_2O} ratios generated by $CaCl_2$/roasted limonite mixtures were lower than for the $CaCl_2$-SiO_2-H_2O system, though higher

than predicted in the absence of SiO_2. He suggested that the hydrolysis of $CaCl_2$ in the presence of limonitic ores might be enhanced by iron oxides that react to form calcium ferrite, as represented by:

$$CaCl_2(l) + Fe_2O_3(s) + H_2O(g) \rightarrow CaFe_2O_4(s) + 2HCl(g) \qquad 2.11$$

It seems accepted that the generation of HCl gas through hydrolysis of $CaCl_2$ is a rapid reaction with relatively low kinetic resistance[7] within the Ni segregation process, such that it operates very near equilibrium (Brittan and Liebenberg; 1972, Hanf, 1972b). As a result, when segregating siliceous ores, the p_{HCl}^2/p_{H_2O} within the bulk gas is likely set by the equilibrium constant for Equation 2.10 as given below:

$$K_{2.10} = \frac{a_{CaSiO_3}}{a_{CaCl_2}a_{SiO_2}}\frac{p_{HCl}^2}{p_{H_2O}} \qquad 2.12$$

The p_{HCl}^2/p_{H_2O} from hydrolysis will thus depend on the activities of the condensed phases, according to:

$$\frac{p_{HCl}^2}{p_{H_2O}} = K_{2.10}\frac{a_{CaCl_2}a_{SiO_2}}{a_{CaSiO_3}} \qquad 2.13$$

In the ideal case where all condensed phases are pure, the activities are one and the equilibrium constant expression reduces to:

$$\frac{p_{HCl}^2}{p_{H_2O}} = K_{2.10} \qquad 2.14$$

Figure 2.3 shows the p_{HCl}^2/p_{H_2O} in the presence of pure condensed phases, as determined by the equilibrium constants of the respective $CaCl_2$ hydrolysis reactions, specifically, as represented by: Equation 2.2 for hydrolysis in the absence of SiO_2, Equation 2.10 for hydrolysis in the presence of SiO_2 and Equation 2.11 for hydrolysis in the presence of Fe_2O_3.

The figure illustrates the very significant enhancement in p_{HCl}^2/p_{H_2O} which occurs in the presence of SiO_2 when the product is $CaSiO_3$, compared to when the hydrolysis product is pure CaO; a lesser enhancement occurs in the presence of Fe_2O_3 when the hydrolysis product is $CaFe_2O_4$.

[7] Kinetic resistance is defined as $\frac{1}{kA}$ where k is the rate constant and A is the available area of the reacting species.

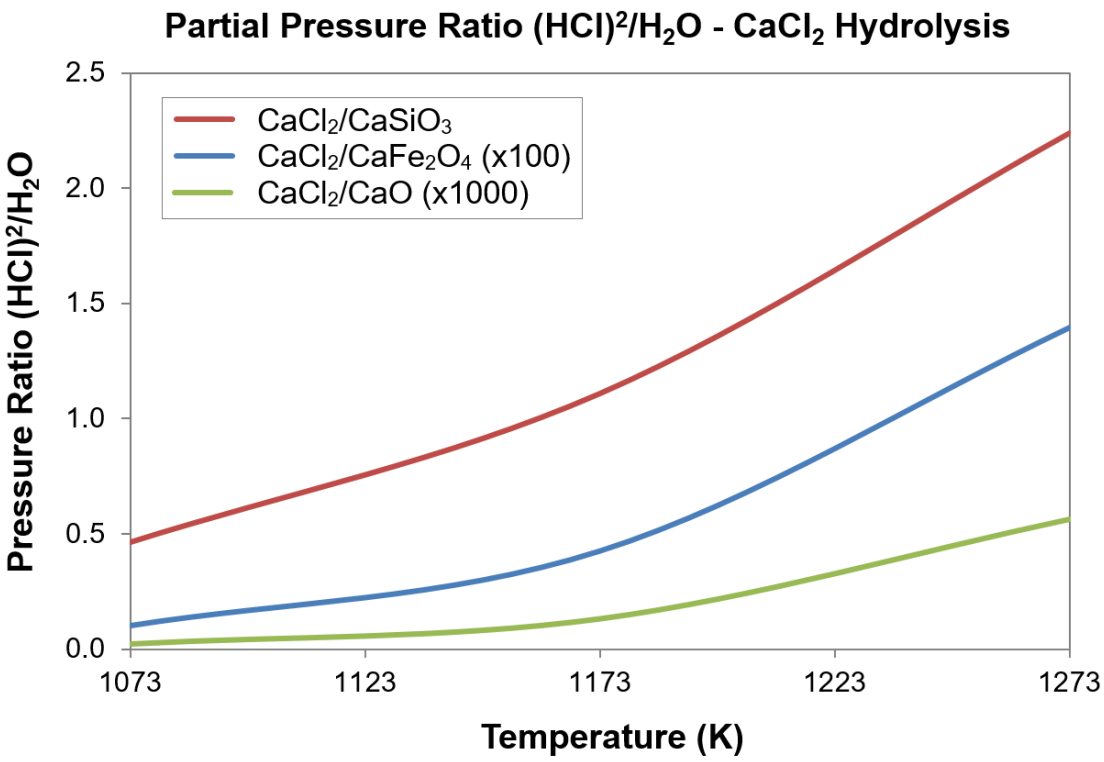

Figure 2.3 Equilibrium Partial Pressure Ratio from $CaCl_2$ Hydrolysis

The p_{HCl}^2/p_{H_2O} gas ratio produced from the hydrolysis of $CaCl_2$ to form either diopside ($CaSiO_3$), calcium ferrite ($CaFe_2O_4$) or calcia (CaO), for pure condensed phases. Data are from the FACTSage v6.4 'Reaction' program.

2.4.2 Formation of Gaseous Metal Chlorides

Chloridisation of Ni, Fe and Co oxides is considered to occur during the majority of the Ni segregation process through reverse hydrolysis reactions (also referred to as chloridisation reactions), as represented by:

$$NiO(s) + 2HCl(g) \rightarrow NiCl_2(g) + H_2O(g) \quad 2.15$$

$$Fe_2O_3(s) + 6HCl(g) \rightarrow 2FeCl_3(g) + 3H_2O(g) \quad 2.16$$

$$FeO(s) + 2HCl(g) \rightarrow FeCl_2(g) + H_2O(g) \quad 2.17$$

$$CoO(s) + 2HCl(g) \rightarrow CoCl_2(g) + H_2O(g) \quad 2.18$$

For each metal, the maximum possible chloride pressure will be achieved if the reverse hydrolysis reaches equilibrium with the p_{HCl}^2/p_{H_2O} ratio established by the

$CaCl_2$ hydrolysis equilibrium. This is illustrated by considering the equilibrium constant for the formation of $NiCl_2$ gas via Equation 2.15:

$$K_{2.15} = \frac{p_{NiCl_2}}{a_{NiO}} \frac{p_{H_2O}}{p_{HCl}^2} \quad 2.19$$

The maximum (equilibrium) partial pressure of $NiCl_2$ in the presence of pure solid NiO ($a_{NiO} = 1$) exists when the p_{HCl}^2/p_{H_2O} ratio is given by $K_{2.10}$. It may be calculated by:

$$p_{NiCl_2} = K_{2.15} \frac{p_{HCl}^2}{p_{H_2O}} = K_{2.15} K_{2.10} \quad 2.20$$

The maximum partial pressures of $FeCl_2$, $CoCl_2$, $NiCl_2$ and $FeCl_3$ which can exist when the p_{HCl}^2/p_{H_2O} is controlled by $CaCl_2$ hydrolysis in the presence of a siliceous ore are shown in Figure 2.4, calculated for example as per Equation 2.20 for the chloridisation of NiO. The temperature range of 1073-1273 K (800-1000°C) on the figure covers the potential temperature range for Ni segregation. The calculated values are for an idealised Ni segregation system consisting of pure condensed phases. The figure shows that the maximum partial pressure of $FeCl_2$ is significantly greater than for $NiCl_2$, while the $CoCl_2$ partial pressure is intermediate and the $FeCl_3$ partial pressure is comparatively negligible.

Towards the end of Ni segregation, Rey et al. (1972a) observed that the H_2O content of the gas may become negligible such that HCl in gas is also negligible (see Table 2.8), even though $FeCl_2$ is still entering the gas and excess $CaCl_2$ remains in the bed. During this period when $CaCl_2$ hydrolysis appears negligible, Rey et al. (1972a) suggested that a direct chloridisation of oxides could occur through the reaction of $CaCl_2$ with FeO, NiO and SiO_2 within the ore, according to reactions of the type shown in Equations 2.21 and 2.22. These represent the combination of the $CaCl_2$ hydrolysis reaction (Equation 2.10) with the reaction for the chloridisation of FeO by HCl (Equation 2.17) or for NiO chloridisation (Equation 2.15). This mechanism was also suggested by Reznik et al. (2003).

$$CaCl_2(l) + FeO(s) + SiO_2(s) \rightarrow FeCl_2(g) + CaSiO_3(s) \quad 2.21$$

$$CaCl_2(l) + NiO(s) + SiO_2(s) \rightarrow NiCl_2(g) + CaSiO_3(s) \quad 2.22$$

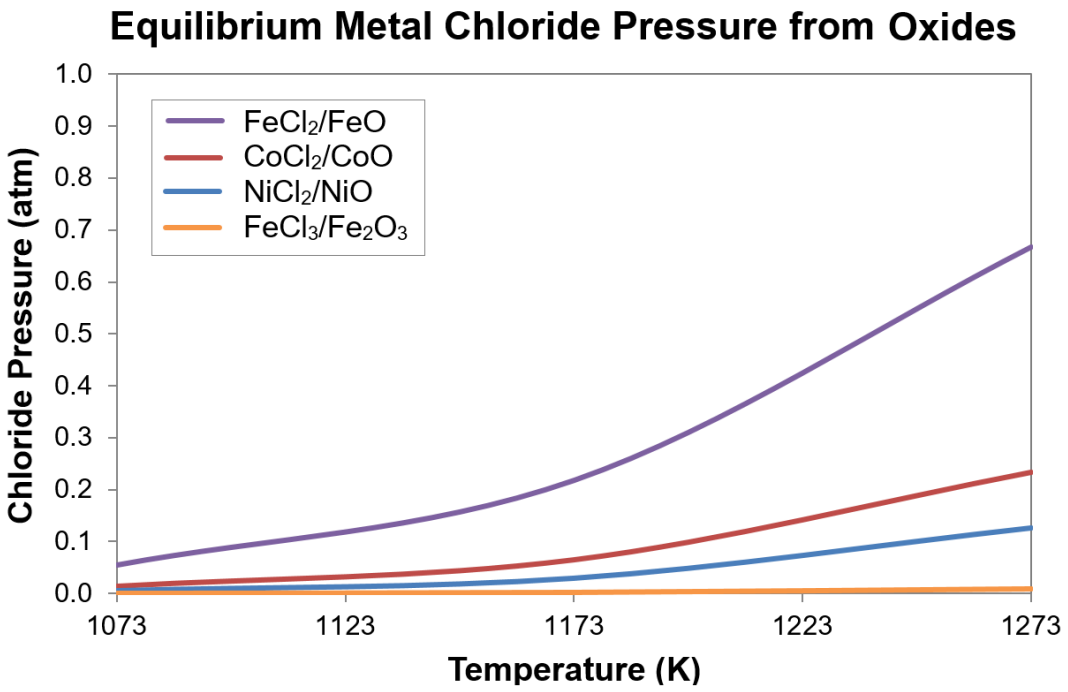

Figure 2.4 Equilibrium Metal Chloride Pressure from Pure Oxides

Maximum chloride pressure in equilibrium with oxides when the p_{HCl}^2/p_{H_2O} in the gas is controlled by $CaCl_2$ hydrolysis with siliceous ore. All condensed phases are pure with activity of 1. Data are from the FACTSage v6.4 'Reaction' program.

Chloridisation of Nickel Oxide, Silicate and Ferrite

Pure NiO is readily chloridised in an atmosphere of HCl gas (Iwasaki et al., 1973). Chloridisation begins at ~643 K (370°C) with volatilisation of $NiCl_2$ commencing at ~773 K (500°C). Both processes appear very rapid at the higher temperatures required for optimum Ni segregation (Fruehan and Martonik, 1973b), which indicates that optimum Ni segregation temperatures are more than adequate for rapid chloridisation of pure NiO (Hanf, 1972b).

NiO within roasted laterite likely mainly exists at low concentrations substituted within the lattice of iron oxide, or dissolved within silicate or spinel solid solutions (Section 4.1); thus the activity of NiO can be significantly less than one. Optimum Ni segregation temperatures must therefore be high enough to generate a p_{HCl}^2/p_{H_2O} from $CaCl_2$ hydrolysis that is sufficient to chloridise the lower activity NiO (Hanf, 1972b), in addition to providing adequate reducing conditions.

Figure 2.5 shows the maximum $NiCl_2$ pressure which can coexist with pure Ni oxide, silicate and ferrite when the $CaCl_2$ hydrolysis equilibrium is established for siliceous ores, calculated as per Equation 2.20. The figure shows that the maximum $NiCl_2$

pressure is moderately decreased when NiO is combined as a pure silicate and greatly decreased when combined as a pure ferrite. The maximum chloride pressure will be even less if Ni silicate is present in solid solution with iron and magnesium silicates, or if Ni ferrite is present as a solid solution with magnetite or substituted within hematite, as found in roasted laterite ores (Section 4.1).

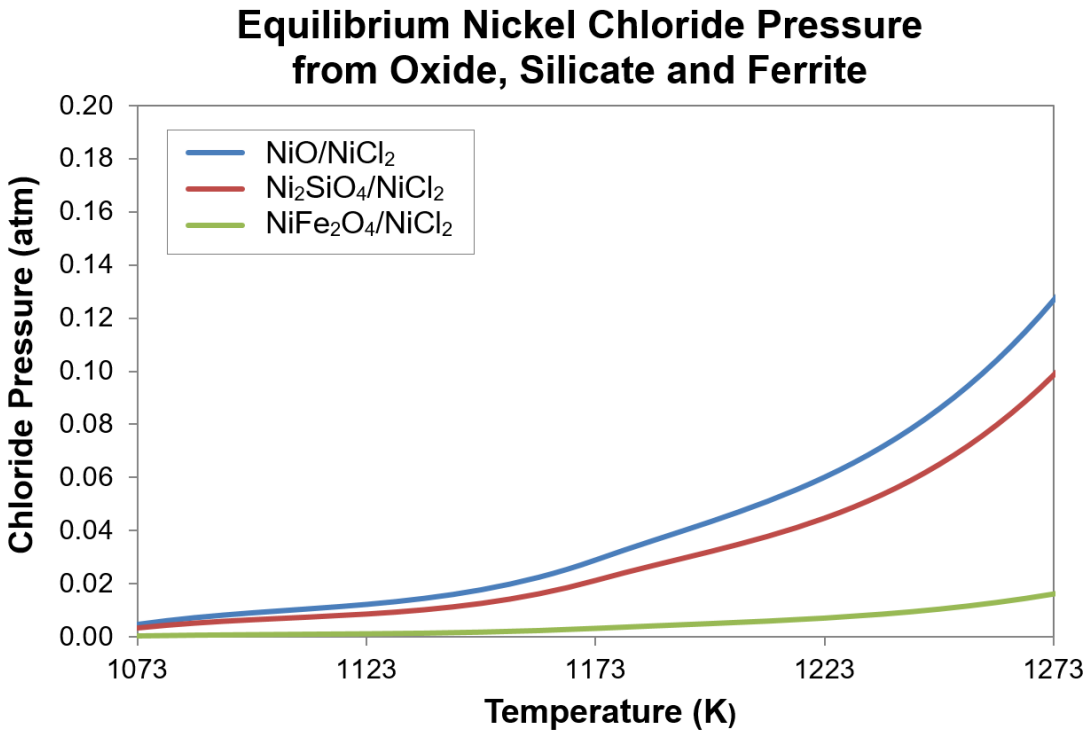

Figure 2.5 Equilibrium $NiCl_2$ Pressure from Oxide, Silicate and Ferrite

Maximum $NiCl_2$ pressure when p_{HCl}^2/p_{H_2O} in segregation gas is controlled by $CaCl_2$ hydrolysis with siliceous ore. All condensed phases are pure with activity of 1. Data are from FACTSage v6.4 'Reaction' program.

The lower NiO activity present within roasted laterite ores will not only lower the pressure of $NiCl_2$ in the gas, it will also decrease the rate of the NiO chloridisation process (Hallet, 1997). However, the chloridisation of NiO within laterites is not necessarily a slow process relative to the other segregation reaction steps, especially when the pressure of HCl is high (Brittan and Liebenberg, 1972).

Brittan and Liebenberg (1972) found that the chloridisation of a garnierite ore at 1223 K (950°C) with moist N_2 gas containing 40% HCl was equilibrium limited until 60% of the initial NiO was chloridised. The rate then decreased significantly over time, with both Brittan and Liebenberg (1972) and Seaborn (1976) suggesting that the NiO with higher activity reacts over the initial period, while the NiO of lower

activity reacts more slowly over the latter period. Rey et al. (1972b) also reported that the rate of chloridisation of NiO by HCl(g) passed through a plug of roasted garnierite at segregation temperatures was initially very fast, but decreased over time. This was considered to result from a decreased activity of NiO within the ore (due to the presence of silicates), or insufficient contact between ore and gas, or slow diffusion in and out of the grains, or a combination of several of these factors.

Chloridisation of Ferrous Oxide, Silicate (Fayalite) and Magnetite

The chloridisation of FeO is relatively favourable and seemingly unavoidable under Ni segregation conditions. Pietsch (1972), for example, was unable to determine any conditions that allow for selective NiO chloridisation in the presence of iron oxides when testing a variety of ores and synthetic mixtures over a range of oxygen pressures, temperatures and times.

Figure 2.6 shows the maximum $FeCl_2$ pressure which can coexist with ferrous oxide[8], silicate and magnetite when the $CaCl_2$ hydrolysis equilibrium is established for siliceous ores. The figure shows that the equilibrium $FeCl_2$ pressure decreases progressively and significantly from ferrous oxide, to silicate (fayalite), to spinel (magnetite).

At a given temperature, the partial pressure of $FeCl_2$ is significantly higher than $NiCl_2$ when chloridising an equivalent mineral species; at 1173 K (900°C) for example, the p_{FeCl_2}/p_{NiCl_2} is 7.5 for oxide, 3.2 for silicate and 3.1 for spinel, as calculated from the data within Figure 2.5 and Figure 2.6. The partial pressure of $FeCl_2$ is also much higher than for $FeCl_3$ under similar conditions (Figure 2.4), indicating $FeCl_2$ will be much more significant than $FeCl_3$ within the segregation process.

Hanf (1972b) showed that the chloridisation equilibrium for FeO, like NiO, is rapidly established when FeO is reacted with HCl gas in moist air at segregation temperatures. Brittan and Liebenberg (1972) reported that the chloridisation of FeO when segregating a garnierite ore appeared faster than the chloridisation of NiO. They, along with Rey et al. (1972b), passed a gas containing HCl and H_2O through segregation bed containing garnierite. Both researchers identified system characteristics consistent with the FeO chloridisation reaction being at equilibrium, specifically; $FeCl_2$ made up a significant portion of the gas, and when the HCl/H_2O gas ratio was altered, the corresponding concentrations of $FeCl_2$ in the gas and of Fe in the ferronickel changed rapidly in response.

[8] The data are based on pure FeO as used in the FACTSage database, however, it is recognised that FeO is nonstoichiometric and always contains an amount of ferric ions.

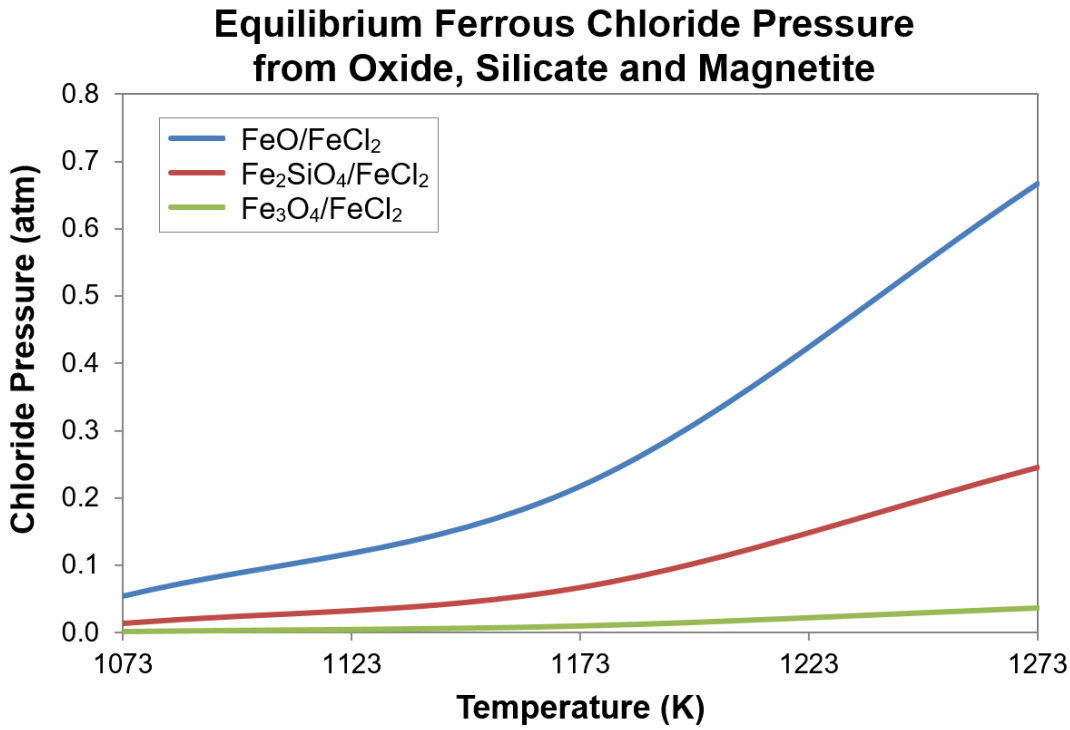

Figure 2.6 Equilibrium $FeCl_2$ Pressure from Oxide, Silicate and Magnetite

Maximum chloride pressure when p_{HCl}^2/p_{H_2O} in segregation gas is controlled by $CaCl_2$ hydrolysis with siliceous ore. All condensed phases are pure with activity of 1. Data are from FACTSage v6.4 'Reaction' program.

The presence of relatively high $FeCl_2$ gas pressures throughout the segregation bed may be beneficial. Hanf (1972a) and Brittan and Liebenberg (1972) both considered that $FeCl_2$ is likely an additional chloridising agent for NiO via the following reaction, which is thermodynamically more favourable than the reaction with HCl; at 1173 K, for example, $K_{2.23} = 0.13$ for chloridisation with $FeCl_2$, compared to $K_{2.15} = 0.026$ for chloridisation with HCl (FactSage v6.4).

$$NiO(s) + FeCl_2(g) \rightarrow NiCl_2(g) + FeO(s) \qquad 2.23$$

Brittan and Liebenberg (1972) also suggested that because the partial pressure of $FeCl_2$ is significantly higher than $NiCl_2$, the larger amount of FeO chloridised might disrupt the mineral lattice and potentially facilitate the chloridisation of NiO contained within it.

2.4.3 Reduction of Chlorides at the Carbon Surface

The reduction of chlorides with carbon or carbonaceous gases is thermodynamically prohibited and hydrogen has been confirmed experimentally as the reducing agent

for Ni and Fe chlorides at or near the surface of carbon in the segregation process (Hanf, 1972a). More recently, Reznik et al. (1998) confirmed that reduction of Ni and Fe chlorides by solid carbon in a dry gas at 1273 K (1000°C) is impossible in the absence of a source of hydrogen.

In Cu segregation, a reactive carbon such as coal is normally the reductant. This type of carbon can contain significant hydrogen within volatiles that is released during segregation to provide H_2 for the reduction of chlorides (Hanf, 1972a). In Ni segregation, a less reactive, low volatile carbon such as coke is normally used as the reductant; the supply of hydrogen directly from the carbon is therefore reduced. According to Hanf (1972a) the reduction of metal chlorides during Ni segregation is sustained throughout the process by hydrogen generated at the carbon surface by gasification with H_2O by the water gas reaction (Equation 2.5).

Rey et al. (1972a) believed that the water gas shift reaction (Equation 2.7) is the major source of hydrogen, since its rate is not restricted by the relatively small mass of carbon present. However, the CO reacting with H_2O in the water gas shift reaction also comes from the gasification of the same "small amount" of carbon via the Boudouard reaction (Equation 2.6) and ultimately the hydrogen must originate from the gasification of carbon.

Although the supply of H_2O to the Ni segregation system appears essential for the generation of H_2 for metal chloride reduction, the amount must be minimised to avoid adverse hydrolysis effects (Section 2.4.6). However, it appears that Ni segregation can be successfully carried out in the presence of trace amounts of hydrogen due to a relatively efficient H recycle. Rey et al. (1972a) found that segregation continued when HCl, H_2O and H_2 were undetectable in the off-gas (Section 2.4.7). Rey et al (1972b) also found that residual H_2O in roasted garnierite ore was capable of supplying hydrogen for a significant period, since it took from 80 minutes at 1173 K (900°C) and 40 minutes at 1253 K (980°C) to release the residual 0.8-0.9 % H_2O from a garnierite under segregation conditions.

The reduction of $NiCl_2$ and $FeCl_2$ gases by H_2 at the carbon surface can be represented by the equations:

$$NiCl_2(g) + H_2(g) \rightarrow 2HCl(g) + Ni(s) \qquad 2.24$$

$$FeCl_2(g) + H_2(g) \rightarrow 2HCl(g) + Fe(s) \qquad 2.25$$

The reduction of $NiCl_2$ is much more thermodynamically favourable than the reduction of $FeCl_2$; at 1173 K (900°C), for example, $K_{2.24} = 5500$ for the reduction of $NiCl_2$ compared to $K_{2.25} = 2.84$ for the reduction of $FeCl_2$ (FACTSagev6.4 data). This substantial difference enables the preferential reduction of Ni over Fe from a segregation gas that has a high ratio of $FeCl_2$ to $NiCl_2$ resulting from the more favourable chloridisation of FeO relative to NiO (Brittan and Liebenberg, 1972).

The reduction of both $FeCl_2$ and $NiCl_2$ is rapid under Ni segregation conditions, as demonstrated by Brittan and Liebenberg (1972). These researchers passed a moist gas containing $NiCl_2$ and $FeCl_2$ through a plug of carbon at 1273 K (1000°C) and found that both metal chlorides were reduced from the gas immediately upon contact with the carbon. The deposit of ferronickel was formed on its leading edge, and when the height of the coke bed was halved, the reduction of $NiCl_2$ and $FeCl_2$ was unaffected. It thus appeared that H_2 generated at the carbon surface through reaction with H_2O in the moist gas immediately reduced the metal chlorides. The proportion of $NiCl_2$ converted to metal was also significantly higher than $FeCl_2$, consistent with the higher K value for the reduction of $NiCl_2$ with H_2. It was therefore concluded that the chloride reduction operated very close to equilibrium.

Brittan and Liebenberg (1972) and Hanf (1972a) considered that the rapid and thermodynamically favourable reduction of $NiCl_2$(g) will maintain a low $NiCl_2$ pressure in the gas and, in doing so, provide a significant driving force for the chloridisation of NiO from the ore. In contrast, the thermodynamically favourable chloridisation of FeO (Figure 2.6) combined with the thermodynamically unfavourable reduction of $FeCl_2$(g) will maintain a relatively high $FeCl_2$ pressure in the segregation gas (Hanf, 1972a).

These views are consistent with experimental observations. Iwasaki et al. (1966) observed a plume of $FeCl_2$ during the segregation of a limonite ore at 1273 K (1000°C) but noted insignificant volatilisation loss of Ni. Rey et al. (1972a) recorded up to 23% $FeCl_2$ in the off-gas from garnierite segregation, while $NiCl_2$ was below the detection limit of their gas chromatograph (see Table 2.8). Rey et al. (1972a) calculated that the off-gas contained from 3.8×10^{-2}-8.8×10^{-2} vol% $NiCl_2$ at 1173-1253 K (900-980°C), which represented Ni volatilisation losses of only 0.08-0.25%.

Since both metal chloride reduction reactions are likely to operate near equilibrium during segregation due to their relatively low kinetic resistances, the equilibrium

formation of ferronickel alloy on the carbon surface can be described through a combination of Equation 2.24 minus Equation 2.25 to give:

$$NiCl_2(g) + Fe(s) \rightarrow FeCl_2(g) + Ni(s) \quad 2.26$$

where

$$K_{2.26} = \frac{p_{FeCl_2}}{p_{NiCl_2}} \frac{a_{Ni}}{a_{Fe}} \quad 2.27$$

and

$$\frac{p_{FeCl_2}}{p_{NiCl_2}} = K_{2.26} \frac{a_{Fe}}{a_{Ni}} \quad 2.28$$

This relationship shows that at any temperature, the composition of the alloy being formed, as represented by the activity ratio of Fe to Ni, is dependent on the partial pressure ratio of $FeCl_2$ to $NiCl_2$ near the carbon surface. Since the value of $K_{2.26}$ is relatively high at Ni segregation temperatures (for example, at 1173 K (1000°C) the value of $K_{2.26}$ is 1936), the ratio p_{FeCl_2}/p_{NiCl_2} near the carbon surface will be much higher than the ratio a_{Fe}/a_{Ni}.

The p_{FeCl_2}/p_{NiCl_2} ratio within the reduction gas for a given Fe content of ferronickel was calculated using Equation 2.28. Values of $K_{2.26}$ were taken from the FACTSage (V6.4) 'Reaction' program and metal activities from the 'Equilib' program using the FTmisc-FCCS database which contains a solution model for fcc Ni-Fe alloys.

The calculated p_{FeCl_2}/p_{NiCl_2} ratios in equilibrium with ferronickel alloys containing up to 20% Fe are presented in Figure 2.7. The p_{FeCl_2}/p_{NiCl_2} in gas is shown to increase significantly as the Fe content of alloy increases, although less so at higher temperatures. For example, the ratio increases to ~600 at 1073 K (800°C) and to ~200 at 1273 K (1000°C) as the Fe content in alloy increases to 20%. These respective ratios increase to 10,500 and 2,500 when the Fe content reaches 60%.

2.4.4 The Ferronickel Deposit

Hudyma (1981) studied the nucleation and growth of ferronickel particles deposited on coal in the presence of $NiCl_2$ and $CaCl_2$ at 1123-1323 K (850-1050°C). It was concluded that reduction takes place via chlorides which are adsorbed onto the carbon or an existing alloy surface.

The form of the ferronickel deposit may depend on the type and size of the solid carbonaceous reductant. Webb (1973) found that coke would retain its original

shape and maintain relatively larger alloy deposits; in contrast, coal would decompose because of a higher proportion of volatiles and give smaller sized alloys.

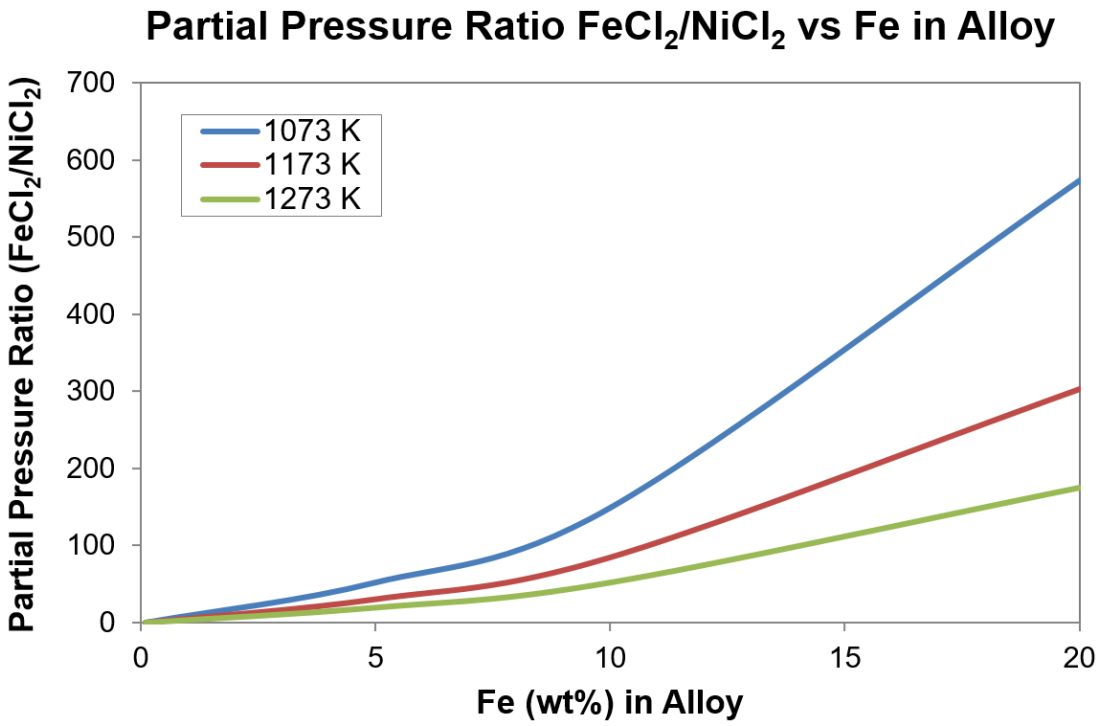

Figure 2.7 Equilibrium $FeCl_2/NiCl_2$ in Gas versus Ferronickel Composition
Fe(wt%) in ferronickel and equilibrium ratio of $FeCl_2$ and $NiCl_2$ in reduction gas, as calculated from FACTSage V6.4 using Equation 2.28.

Rey et al. (1972b) observed that the ferronickel deposits were either loosely associated with carbon particles, or independently present as 5-10 µm or sometimes coarser spheres. Dor (1972) observed independent alloy aggregates up to 60-80 µm; these deposits were thought to initially form on carbon, and then detach through either gasification of the carbon or mechanical abrasion. Narrow gaps in the metal coating were always present such that the carbon surface remained in contact with the gas.

Ferronickel nucleates on the carbon surface with a cubic crystal structure (Rey et al., 1972b; Iwasaki et al., 1973). After nucleation, new deposition tends to take place upon exisiting ferronickel in the form of whisker/dendritic shapes (Rey et al., 1972b; Iwasaki et al., 1973; Webb, 1973), likely forming through reducton of chloride absorbed on the metal (Hudyma, 1981). Rey et al. (1972a) found that the grains of ferronickel were coarser when segregation began at a lower temperature since there was less nucleation of the alloy and more growth of the existing nuclei.

At lower temperatures of ~1123 K (850°C), the ferronickel retained a crystalline structure, while at higher temperatures of ~1273 K (1000°C), the alloy formed as irregular lumps (Rey et al., 1972b; Iwasaki et al., 1973). Grain growth likely occurred at higher temperatures via the evaporation and condensation mechanism, whereby Ni evaporates from the smaller radius grains (which have a higher Ni vapour pressure) and condenses on larger particles (Hudyma, 1981).

If sulphur was present, either from the calcine, coke or coal, it formed a low melting point sulphide which bordered the ferronickel (Rey et al., 1972b). This may lower the surface tension of the alloy and facilitate migration, coalescence and agglomeration (Valix and Cheung, 2002). It could also lower the activities of Ni and Fe in the alloy and facilitate reduction. Tomášek et al. (1995) found that additions of either 9% pyrite or sulphur prior to segregation increased Ni recovery by up to 20%.

Alloy deposition begins with the formation of relatively pure nickel (Iwasaki et al., 1973). The Ni grade decreases with increases in both time and temperature as an increasing proportion of Fe is added to the alloy (Rey et al., 1972a); the p_{FeCl_2}/p_{NiCl_2} within the segregation gas contacting the alloy must also increase substantially as this occurs (Figure 2.7).

Nickel recovery increases as the grade of alloy decreases (Warner et al., 1972), with the final grades ranging from 30-70% Ni. This represents a significantly larger portion of nickel oxide being reduced to metal compared to iron oxide, since iron oxide is present at a much higher concentration that nickel oxide in laterite ores (Rey et al., 1972a). Hudyma (1993) studied the nucleation and growth of ferronickel particles under segregation conditions and concluded that the final grade of ferronickel was closely related to the CO_2/CO ratio of the bulk gas.

Rey et al. (1972b) reported that the distribution of Ni and Fe across a ferronickel particle was relatively uniform, even though newly deposited alloy became increasingly richer in Fe as the reaction proceeded; hence both Ni and Fe must diffuse within the ferronickel during segregation. Webb (1973) reported that ferronickel particles can be slightly richer in Ni in the centre, and that grade can vary from particle to particle, indicating that gas composition can also vary from particle to particle.

In addition to alloy segregated onto carbon, ferronickel can form through the in-situ reduction of nickel and iron oxides in the ore with CO or H_2 from the bulk gas.

According to Dor (1972), an in-situ reduced alloy forms as relatively small grains which are widely disseminated throughout the ore. Brittan and Liebenberg (1972) reported that such ferronickel has a higher Ni/Fe ratio than segregated alloy, consistent with direct reduction from the bulk gas, rather than from reduction at the carbon surface where the atmosphere is more reducing.

Ericson et al. (1987) confirmed that in-situ reduction of laterite in the absence of chloride can yield small ferronickel particles throughout the ore, down to micron size, with highly variable compositions. If the temperature could be raised several hundred degrees, more readily recoverable larger particles could be grown from in-situ reduced alloys, but sintering of ore at ~1273-1373 K (1000-1100^{o}C) prevents this. In contrast, the segregation product from their MINPRO-PAMCO pilot plant yielded readily recoverable ferronickel aggregates of 100-200 µm; some individual grains up to 80 µm were also found embedded in a crystalline silicate matrix.

2.4.5 The Role of the Solid Carbonaceous Reductant

In addition to providing solid nuclei for the initial deposition of the reduced ferronickel, carbon is also the primary reducing agent for the removal of oxygen from the roasted laterite.

While H_2 is directly responsible for the reduction of metal chlorides, the following sequence of reactions from within the segregation process (Section 2.2) highlights the primary reduction role played by carbon:

$$MO(s) + 2HCl(g) \rightarrow MCl_2(g) + H_2O(g) \quad 2.3$$

$$H_2(g) + MCl_2(g) \rightarrow 2HCl(g) + M(s) \quad 2.4$$

$$H_2O(g) + C(s) \rightarrow H_2(g) + CO(g) \quad 2.5$$

The addition of these three equations yields the overall reduction reaction as:

$$MO(s) + C(s) \rightarrow M(s) + CO(g) \quad 2.29$$

In the segregation of Ni ores, the CO in the gas reduces hematite (Fe_2O_3) in the calcine to magnetite (Fe_3O_4) and potentially to wustite ('FeO'),. and when in-situ reduction to ferronickel occurs, through to Fe. The reduction of magnetite to wustite occurs via the following reactions (Section 2.2):

$$Fe_3O_4(s) + CO(g) \rightarrow 3FeO(s) + CO_2(g) \quad 2.8$$

$$CO_2(g) + C(s) \rightarrow 2CO(g) \quad 2.6$$

Carbon is also the primary reductant, as illustrated by a combination of Equations 2.6 and 2.8 to give:

$$Fe_3O_4(s) + C(s) \rightarrow 3FeO(s) + CO(g) \quad 2.30$$

In reality, the segregation bulk gas will contain both CO_2 and CO. This is because Equations 2.6 and 2.8 represent a coupled process in which reaction 2.8 consumes CO and generates CO_2 while reaction 2.6, the Boudouard reaction, consumes CO_2 and generates CO.

At the temperatures (973-1273 K, 700-1000°C) and carbon sizes (<300 µm) used in segregation, the rate of reduction of iron oxide should be dominantly controlled by the rate of generation of CO through the Boudouard reaction (Rao, 1971; Fruehan, 1977). As a result, the iron oxide reduction reactions should operate close to equilibrium and hence mainly determine the p_{CO_2}/p_{CO} of the segregation bulk gas. They should also control the oxygen pressure (p_{O_2}) within the gas through the equilibrium:

$$2CO + O_2(g) \rightarrow 2CO_2(g) \quad 2.31$$

where

$$p_{O_2} = \frac{1}{K_{2.31}}\left(\frac{p_{CO_2}}{p_{CO}}\right)^2 \quad 2.32$$

The amount of carbon reductant and its surface area should be controlled to minimise in-situ reduction to alloy while allowing $NiCl_2$ reduction via H_2 at the carbon surface. It is generally accepted that metallurgical coke is more suitable than coal for this purpose, with the amounts used ranging from 2-7% of the ore (Table 2.6) and sizes ranging from 75-300 µm (+200-48 Tyler mesh). Ultimately, an amount of carbon must remain throughout the process to protect the deposited ferronickel from reoxidation by the bulk gas.

2.4.6 Impact of H_2O

H_2O enters the segregation system primarily as bonded water retained within the calcine. The amount present is considered to have an important influence on the nickel segregation system since both $FeCl_2$ and $NiCl_2$ are susceptible to hydrolysis

at segregation temperatures. The effect of retained water on nickel segregation has been considered in a number of studies.

Brittan and Liebenberg (1972) passed a N_2 gas containing 40 vol% HCl and 10 vol% CO through a fluid bed of roasted garnierite at 1273 K (1000°C). When the steam content of the gas was increased from 0 to 10 vol%, the chloridisation of Fe from the ore decreased from 90 to 50%, and the chloridisation of Ni decreased from 70 to 30%; both effects were attributed to hydrolysis of the metal chlorides.

Rey et al. (1972b) passed a wet gas equivalent to combusted propane (11 vol% CO_2, 15 vol% H_2O and 74 vol% N_2) through the reaction bed during garnierite segregation. As the gas flow rate was increased, it was found that both the $FeCl_2$ in the gas and the recovery of Ni to the alloy decreased significantly but neither was affected when a dry gas (20 vol% CO_2, 80 vol% N_2) was passed through the charge. It was concluded that $FeCl_2$ was more affected by hydrolysis than $NiCl_2$, such that the grade of concentrate increased when the gas contained more water vapour. Wright (1994) also found that injecting steam during the segregation of various laterites increased the ferronickel grade but decreased the Ni recovery.

Brittan and Liebenberg (1972) considered that the presence of carbon within the segregation system protects $NiCl_2$ from hydrolysis by maintaining a very low $NiCl_2$ partial pressure because of the highly favourable reduction with H_2 at the carbon surface (Section 2.4.3). Okamoto et al. (1971b) also suggested that the presence of carbon is important to suppress hydrolysis of $NiCl_2$ since it removes H_2O through the water gas reaction (Equation 2.5).

Rey et al. (1972a) and Rey et al. (1972b) determined that once the amount of H_2O retained within a calcine exceeded a critical level, the recovery of Ni by segregation decreased dramatically. When segregating a garnierite ore with 6% $CaCl_2$ at 1253 K (980°C), the highest Ni recovery was achieved when 0.1-0.8% H_2O was retained in the calcine; but recovery fell once the H_2O exceeded 1% and segregation proved impossible with >3% H_2O. It was concluded that provided $CaCl_2$ could absorb the retained H_2O such that the p_{HCl}/p_{H2O} ratio in the gas was determined by the $CaCl_2$ hydrolysis equilibrium, then Ni segregation was feasible; otherwise, it was not.

Once the critical H_2O limit was exceeded, the ferronickel grade increased, the Ni recovery decreased and the segregated product contained a fine speckle of in-situ reduced ferronickel distributed throughout the ore. It appears that when excess H_2O is present, the $NiCl_2$ and more so the $FeCl_2$ gas pressures are decreased through

hydrolysis. This decreases the p_{FeCl_2}/p_{NiCl_2} ratio in the gas and thus increases the grade of segregated alloy (Figure 2.7). However, excess H_2O also decreases the pressure of HCl and the generation of chlorides, which both decrease the yield of segregated alloy and exposes nickel and iron oxides in the ore to in-situ reduction by CO in the gas.

2.4.7 Gas Composition

The gas from Cu segregation is dominantly CO_2 (Section 2.3.1). The gas resulting from Ni segregation is significantly larger in volume (Sections 2.3.2), and contains variable amounts of CO and CO_2, significant HCl and $FeCl_2$, and minor H_2O.

Rey et al. (1972a) measured the total amounts of CO_2, CO, $FeCl_2$, HCl and H_2O in the off-gas, over four progressive time intervals, during the segregation of a garnierite ore at 1253 K (980°C). The gas was less voluminous than normal since a mildly reducing roast in the presence of 2.5% coke was used prior to segregation, rather than a roast in air.

The amounts of gas evolved, as m^3/t ore (STP), and the gas compositions (vol %) were measured over the time intervals 0-20, 20-40, 40-60 and 60-96 minutes, as presented in Table 2.8 The total amount of gas evolved decreased with time which is indicative of a decrease in the overall Boudouard reaction rate.

Table 2.8 Gas Analysis: Laboratory Scale Garnierite Segregation

15 g samples segregated in a quartz tube reactor; 6% $CaCl_2$, 1.9% coke (0.6% consumed in roast), 1253 K (980°C). Gas sampled in batches and analysed by gas chromatography (Rey et al., 1972a).

Period (min)	Gas Evolved (m^3/t ore) STP						Gas Evolved (vol%)					
	CO_2	CO	$FeCl_2$	HCl	H_2O	Total	CO_2	CO	CO_2/CO	$FeCl_2$	HCl	H_2O
0 - 20	9.4	1.14	2.4	6	4.67	23.61	39.9	4.8	8.3	10.1	25.4	19.8
20 - 40	2.38	1.64	1.73	1.06	0.8	7.61	31.3	21.6	1.5	22.7	13.9	10.5
40 - 60	1.6	2.17	0.94	0	0	4.71	33.9	46.1	0.74	20.0	0	
60 - 96	1.5	3.85	0.26	0	0	5.61	26.8	68.6	0.39	4.60	0	

Table 2.8 shows that the amount of CO_2 decreased while the amount of CO increased as the reaction proceeded. As a result, the p_{O_2} of the gas decreased (Equation 2.32) and the atmosphere became more reducing with time. According to Rey et al. (1972a), the CO content of carbonaceous gas increased as the easily

reducible nickel and iron oxides disappeared and the CO_2/CO ratio adjusted towards equilibrium with the FeO/Fe/C system.

The $FeCl_2$ in the gas remained relatively constant ~20 vol% from 20-60 minutes (Table 2.8). The majority of HCl and H_2O were released within the first 20 minutes, consistent with a very rapid hydrolysis of $CaCl_2$. No H_2 was detected over the entire reaction time (within a <1% limit) and both HCl and H_2O were undetectable in the gas after 40 minutes. Even so, production of $FeCl_2$ and some segregation continued after the amount of H_2O and H_2 in the gas appeared negligible, indicating that nickel segregation was possible when very little hydrogen was present (Rey et al., 1972a).

The p_{HCl}^2/p_{H_2O} ratio calculated from the HCl and H_2O vol% values, assuming 1 atm total pressure, is 0.33 for 0-20 minutes[9] and 0.18 for 20-40 minutes, compared to a value of $K_{2.10} = 2 = p_{HCl}^2/p_{H_2O}$ for the ideal hydrolysis of $CaCl_2$ in the presence of SiO_2 at 1253 K (980°C) (Equation 2.14). The lower calculated values do not necessarily mean that the chloride hydrolysis equilibrium was not achieved, since the a_{SiO_2} and the a_{CaSiO_3} are not necessarily one within the silicates present in the ore.

Ericson et al. (1987) published the average gas compositions from the one t/h MINPRO-PAMCO pilot plant (Table 2.9). These showed a CO_2/CO ratio of 0.27, in reasonable agreement with final value of 0.39 from Rey et al. (1972a) (Table 2.8).

Table 2.9 Gas Analysis: Pilot Scale Garnierite Segregation

One t/h segregation in a Mechanical Kiln, as developed for the MINPRO-PAMCO segregation process; gas sampled in batches and analysed by gas chromatography (Ericson et al., 1987).

Species in Off-Gas (%)						
HCl	CO	CO_2	CO_2/CO	O_2	H_2	N_2
6.0	56.5	15	0.27	<0.1	1.5	21

A number of investigators have passed gas through a segregation bed to test the effects of various imposed gas compositions on the segregation process.

[9] $p_{HCl}^2/p_{H_2O} = 0.254^2/0.198 = 0.33$

Dor (1972) passed gases with compositions from pure N_2 to N_2/CO_2 (21/79 vol% ratio), to N_2/CO_2 containing 1-5 vol% of either CO, H_2 or O_2 through a rotating drum reactor, to test the effect of mildly oxidising or reducing atmospheres on Ni segregation. These gases had no significant effect on the total segregation of Ni and Fe. However, there was a significant drop in Ni recoveries when humidified N_2 gas was used, consistent with the impact of $NiCl_2$ hydrolysis (Section 2.4.6).

Warner et al. (1972) passed gases with compositions from pure N_2 to mixtures of N_2, CO, CO_2, H_2, H_2O and HCl through a rotating drum reactor, to assess the effects of direct-fired combustion gases on Ni segregation. The Ni and Fe segregation recoveries both decreased as the gas flow rate or H_2O in the gas was increased; however, the total reduction to metal (segregated plus in-situ alloy) remained largely unaffected.

Warner et al. (1972) considered that the gas swept away volatile chlorides thus promoting in-situ reduction to alloy over segregation, with the total reduction controlled more by the amount of carbon than the composition of the purge gas. In all cases, the passage of gas decreased the Ni recovery to a magnetic concentrate and increased the in-situ alloy in the tails.

2.4.8 Impact of the Roast

The amount of H_2O retained in the calcine should be minimised prior to Ni segregation (Section 2.4.6). However, the higher temperatures and longer roasting times sometimes necessary to achieve this may also cause a portion of the Ni to become refractory because of mineralogical changes, particularly for garnierite ores.

Rey et al. (1972a) carried out roasting and segregation tests at 1173-1423 K (900-1150^{o}C) on a garnierite ore in which the retained H_2O was reduced to 0.8%. The ore was first roasted in the presence of 2.5% coke at the segregation temperature to remove H_2O and convert Fe_2O_3 to Fe_3O_4 under mildly reducing conditions. Segregation was initiated by adding 6% $CaCl_2$ to the calcine, which retained 1.94% coke after the roast. The Ni recovery is shown in Figure 2.8 as a function of time at each segregation temperature (in centrigrade).

A maximum recovery of ~83% was achieved at 1223 K (950^{o}C); the recovery then decreased to ~55% as the roasting/segregation temperature was increased to 1423 K (1150^{o}C). The decrease in Ni recovery at higher temperatures was attributed to the formation and growth of olivine (mainly Mg_2SiO_4) which entrapped NiO within its lattice.

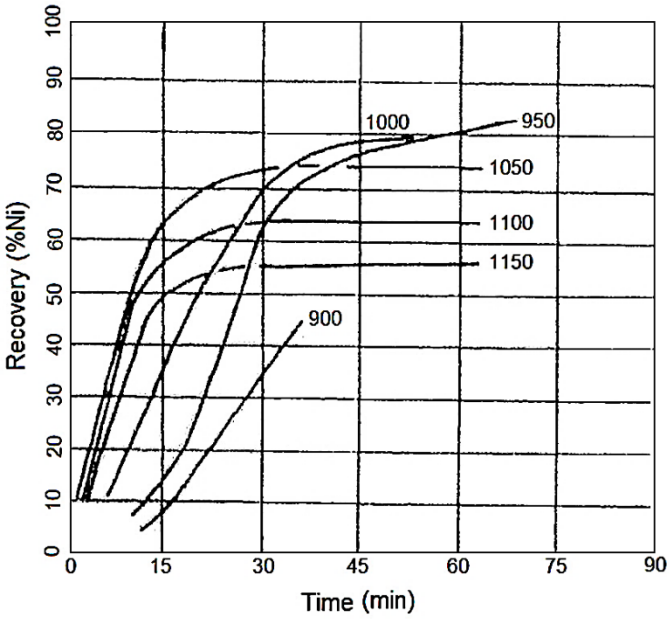

Figure 2.8 Nickel Recovery from Garnierite using a Static Bed (Rey et al., 1972a)

Rey et al. (1972a) used an alternative roast to minimise the capture of NiO within olivine, in which moisture was rapidly removed from the ore by heating under fluidised (rather than static) conditions for 5 minutes at 1273 K (1000°C). This improved Ni recoveries for segregation at 1273 K (1000°C) from 80 to 95%, at 1323 K (1050°C) from 75 to 93% and at 1373 K (1100°C) from 65 to 93%.

Further consideration on the impact of roasting on the decomposition of minerals within limonite, nontronite and garnierite lateritic ores and the potential impact on nickel segregation is given in 0.

2.4.9 Impact of Ore Composition and Mineralogy

Sole and Taylor (1972) examined the segregation performance of 20 laterite ores, ranging from high iron oxide limonites, to high magnesium silicate garnierites. Segregation behaviour was assessed under comparable conditions at either 1173 or 1273 K (900 or 1000°C) using both Ni recovery (R) and concentrate grade (G). These were combined to calculate segregation efficiency, expressed as $RxG^{0.5}$. It was found that the concentration of iron oxides had a major influence on segregation efficiency, with ~25% Fe_2O_3 (17.5% Fe) at 1173 K (900°C) being optimum.

Dor (1972) tested one limonite (53% Fe, 2.5% SiO_2), two intermediate ores (~20% Fe, 14% MgO, 40% SiO_2) and five garnierite ores (~8% Fe, 30% MgO, 40% SiO_2)

using a wide range of segregation conditions and chloridising agents. It was found that the amount of Ni lost to the tails increased as the silica content of ore increased, with the final tails containing from 0.1-0.4% Ni. Under conditions that produced the maximum Ni recovery, the amount of reductant required increased as the iron oxide content of ore increased. Overall, segregation was considered most suited to higher grade (1.5-2% Ni) transition or blended ores containing relatively low MgO (<15%) and intermediate Fe (10-20%).

Warner et al. (1972) segregated four ores ranging from limonite (48% Fe, 4.4% SiO_2) to a weathered high magnesium silicate (7.3% Fe, 33% MgO, 42% SiO_2) using various conditions and combustion gas atmospheres. Ores with higher Fe and lower MgO gave the highest recoveries as less Ni was considered lost within the magnesium silicate phase.

Davidson (1972) found that Ni recovery from seven segregated garnierites was maximised in ores that contained the highest iron oxide (16% Fe_2O_3; 11% Fe) and lowest magnesia (22% MgO). Blending of the iron oxide rich ore with high MgO ore substantially improved the Ni recovery from the high MgO ore.

Davidson (1972) reported that upon addition of iron oxides, the silicates formed during segregation were changed from Mg_2SiO_4 (forsterite) and $MgSiO_3$ (enstatite), to Mg_2SiO_4 and Fe_2SiO_4 (fayalite) within an olivine solution. These solid-solid interactions were considered to release Ni from the silicate and enhance recovery. The addition of iron oxides also greatly decreased the quantity of ferronickel present as small inclusions within the olivine particles.

Davidson (1972) also reported that using $CaCl_2$ as a chloridiser, rather than NaCl or $MgCl_2$, increased the fayalite content of olivine and this further enhanced Ni recovery. A similar enhancement by $CaCl_2$ was noted by Brittan and Liebenberg (1972) but the exact nature of this effect remains unexplained.

Wright and Gooden (1973) segregated eight ores ranging from garnierites to limonites, with compositions of 11-47% Fe, 26-0.5% MgO and 45-12% SiO_2. Standardised rather than optimised conditions were used and segregation was assessed at 1273 K (1000^{o}C) using Ni recovery (R), concentrate grade (G) and feed grade (F). These were combined to calculate segregation efficiency expressed as $Rx(C/F)^{0.5}$. This efficiency factor decreased almost linearly with increase in Fe content, with limonites showing the poorest response.

Scott and Dyson, as reported by Canterford (1975), found no correlation between Ni recovery and the Fe and MgO contents of segregated Australian laterites, and that the addition of 10% Fe_2O_3 to high MgO ores did not improve Ni recovery. These authors considered that a simple correlation between ore composition and segregation performance could not necessarily be expected due to underlying variations in mineralogy.

The mineralogy of the ore also has a significant impact on the grade of concentrate produced during segregation (Iwasaki et al., 1966; Dor, 1972; Rey et al., 1972a). Roasted limonite ores predominantly contain hematite, which cannot be reduced beyond magnetite during segregation without excess use of carbon. As such, the use of magnetic separation to recover ferronickel from segregated limonites will produce very low-grade concentrates, leaving flotation as the preferred concentration method for segregated limonite ores.

Roasted garnierite ores contain a relatively small amount of Fe (5-20%) as hematite. This is readily reduced to FeO and likely present after segregation as Fe_2SiO_4 (fayalite) within olivine, $FeSiO_3$ (ferrosilite) within pyroxene, neither of which is magnetic. However, ferronickel from garnierite segregation can be efficiently concentrated using magnetic separation and this is the preferred method.

2.5 Discussion

It is well established that segregation utilises multiple reactions involving gas, solid and liquid, a number of which are coupled and occur simultaneously. Cu segregation is simpler than Ni segregation since it has more favourable thermodynamics and produces a relatively pure metal. Ni segregation requires higher temperatures combined with stronger chloridisation and reducing conditions that bring about the co-segregation of Fe with Ni, an increased likelihood of unfavourable in-situ reduction to ferronickel, and the production of a greater volume of dominantly carbonaceous off-gas.

Fundamental studies on individual aspects of the Ni segregation process have provided valuable data on the nature of the ferronickel product and on thermodynamic and kinetic aspects. These include the generation of HCl from hydrolysis of $CaCl_2$, the chloridisation with HCl of Ni and Fe oxides, both pure and within ores, and the reduction of Ni and Fe chlorides with H_2.

Valuable fundamental data are also available from non-segregation specific studies on the reduction of oxides and silicates with CO in the presence of carbon, the gasification of carbon with CO_2 through the Boudouard reaction and with H_2O through the water gas reaction, and the reaction of CO with H_2O through the water gas shift reaction.

Studies on Ni segregation as a complete process are mainly industrial in nature, with a focus on Ni recovery and concentrate grade and some additional fundamental aspects. These studies provide valuable data notably on the effectiveness of various chloride salts and carbon reductants, the impact of H_2O on Ni recovery and ferronickel grade, the relationship between ferronickel grade with carbon addition and reaction time, the composition of the segregation off-gas and the impact of the roast and ore mineralogy on Ni recovery.

While much valuable knowledge has been accumulated in relation to Ni segregation, a more fundamental understanding of the whole process is required to predict how a particular ore will respond.

Marcuson (1977) carried out an exemplary fundamental study on the Cu segregation process as applied to dead-roasted concentrates. This study clarified the underlying factors that affected the process, through a series of experiments in which: Cu recovery was recorded versus time, oxygen pressure within the segregation bed was for some experiments measured using a zirconia sensor, and the evolution of CO_2 from the reaction bed was continuously measured through absorption in Ascarite®.

The primary aim of this work was to complete a comparable but more extensive fundamental study for the Ni segregation process, as applied to three ores from a Western Australian Ni laterite deposit. This work primarily focuses on the response of a nontronite ore; however, comparable data were also determined for both a limonite and garnierite ore to enable the impact of mineralogy on segregation performance to be assessed.

The segregation experiments were designed: to measure the Ni, Fe and Co recoveries from segregation over time; to continuously measure the oxygen pressure in the segregation bed, the evolution of carbonaceous gases from the bed, and the HCl content of the segregation off gas; and to monitor to residual chlorides within the segregation product. The metal recoveries, oxygen pressures and

carbonaceous gas volumes were also measured for equivalent chloride-free carbon reduction systems to provide a baseline comparison with segregation.

The data obtained were used to: fit rate expression for Ni, Fe and Co segregation recoveries and to assess the potential rate controls for the process, determine the cumulative carbon consumption during reduction and to assess the rate of carbon gasification with CO_2 via the Boudouard reaction under segregation conditions, determine the cumulative oxygen removed during reduction to assess the background reduction of iron oxides, and to determine the rate of HCl loss in the off-gas and assess the efficiency of the HCl recycle within the segregation bed.

The interpretation of these data were greatly aided by the utilisation of the FACTSage v6.4 thermodynamic software package (Bale et al., 2009) to provide thermodynamic data and enable equilibrium simulations of the iron oxide reduction reactions, and by the utilisation of Energy Dispersive Spectroscopy-Scanning Electron Microscopy (EDS-SEM) for the detailed analysis of calcine and segregation products.

Chapter 3

Experimental

3.1 Experimental Design

Each experiment involved a sequence of procedures with multiple steps within each procedure (see Figure 3.11); as a result, some scatter in the data was inevitable. All steps were carried out as carefully as possible but it was expected that multiple repetitions for most experiments would be needed to establish credible trends.

Three laterite ore types were to be studied. The approach adopted to give the most meaningful comparison with the least number of experiments was to use standardised rather than optimised segregation conditions for all ores. For this reason, reagent addition of 5% coke or activated carbon and 5% $CaCl_2$ (relative to the total mass of the dried ore), was used in all tests; by comparison, additions of 2-7% of carbonaceous reductant and 4.6-8% $CaCl_2$ have been used in previous Ni laterite segregation studies covering a range of ore types (Table 2.6).

3.1.1 Ore and Reagents

Relatively fine ore (-212 µm), carbon (125-300 µm) and calcium chloride (300-500 µm) were used in this work, in common with many other studies. The use of fine reagents minimises the kinetic resistance from inter and intra particle diffusion. This maximises the reaction rate and increases the likelihood of a chemical rate control. The size of the calcium chloride is not critical as it will break up on heating (Pinkney and Plint, 1967).

After drying, the nickel laterite ores contained 11-13% of bonded H_2O, most of which was removed by roasting in air using a large, open crucible within a muffle furnace. Control of the water content is important before segregation, so the ores and reagents were either stored under argon in desiccators, or kept at 110°C (383 K) in a furnace, as appropriate to minimise aerial absorption of moisture. Procedures were also adopted to minimise handling time within air prior to a segregation test.

3.1.2 Reactor Selection

Previous segregation work in the laboratory has been carried out using a number of different configurations to contain the charge. These include placing the charge within: covered crucibles in a muffle furnace (Dor, 1972), quartz or steel tube

reactors in a horizontal or vertical tube furnace (Iwasaki et al., 1966; Jagolino, 1970; Davidson, 1972; Mehrotra and Srinivasan, 1994), or a rotating drum reactor in a muffle furnace (Nagano et al., 1970).

A laboratory batch reactor based on the design of Davidson (1972) was chosen for this work. The reactor consisted of a vertical, closed-end quartz tube in which the charge could be mechanically fluidised using a vibrator located under the furnace and attached to the reactor tube via a support rod.

The reactor was chosen because it: enabled the testing of relatively small amounts of ore in the range 20-25 grams, could easily be moved in and out of a vertical tube furnace, provided a readily accessible top entry for the delivery of reagents (C and $CaCl_2$) to the hot ore, and allowed for the convenient collection of the segregation off-gas without the need for a carrier gas, thus avoiding undesirable dilution of the segregation gas arising from the bed.

The vibration of the segregation bed was considered important because it: enabled the reagents to be rapidly mixed with the ore at temperature to define a zero time for the reaction, provided mechanical fluidisation of the segregation bed which minimised any temperature gradients, provided mixing of the solids and gas within the segregation bed to homogenise the bulk gas composition and to minimise diffusional effects, and facilitated the rapid release of gas from the segregation bed.

Davidson (1972) found that provided the reagents and ore were initially well mixed by vibration, continuous mechanical fluidisation of the reaction bed had little effect on segregation recoveries over the first 30 minutes of reaction; however the use of vibration did improve Ni recoveries by ~5% over longer reaction times. Dor (1972) also reported slightly higher Ni recoveries from a Davidson-type vibrated tube compared to static bed or a rotating drum reactor.

In this work, the effect of vibration on metal recovery was assessed using two tests for each calcine (Appendix B.12). It was found that mechanical fluidisation of the bed had little impact on Ni recovery when segregating limonite, a small negative impact when segregating nontronite (decrease from 61% to 57%) and a larger negative impact when segregating garnierite (decrease from 60% to 51%), under the specific conditions used.

This negative impact may be the result of an enhancement of in-situ reduction to alloy over segregation when better mixing is provided between the bulk gas and the

ore, because in-situ reduction was particular prevalent when segregating garnierite (Section 8.2.5). This result contrasts the minor improvements found by Davidson (1972) and Dor (1972) but it is not clear to what extent these researchers distinguished between segregated and in-situ ferronickel in determining Ni recovery. Although possibly not optimum for garnierite, vibration was used throughout this work for the reasons previously stated, especially the ability to mix the reagents with calcine at temperature to define a zero time for segregation.

3.1.3 Gas Analysis

It is generally understood that the gas composition at the carbon surface is more reducing than the gas composition at the ore surface during Ni segregation; thus, the segregation gas composition cannot be uniform throughout the entire bed. However, no experimental method was available to measure the oxygen pressure at specific locations within the segregation bed.

In this work, the objective was to measure the average (homogenised) composition of the gas within the reaction bed at any time[10], in addition to the rate of evolution of gas from the bed and the cumulative total volume of the evolved gas. These goals could only be partially achieved due to experimental limitations.

A number of methods were used for the gas analysis: an industrial zirconium oxide oxygen sensor was placed just above the reaction bed to continuously measure the oxygen pressure and allow for calculation of the CO_2/CO ratio in the gas; a liquid displacement meter was used to continuously measure the rate of evolution of the carbonaceous (CO_2 + CO) gas and the cumulative total carbonaceous gas volume; and for dedicated tests, the off-gas was held above 373 K (100^{o}C) to prevent condensation before bubbling through an aqueous solution; the HCl content was then determined from the pH change of the solution.

The above measurements provided continuous data for the CO_2, CO, HCl contents of the gas. Measurements were not made for the $FeCl_2$, $NiCl_2$ and H_2O or H_2 contents of the gas because of experimental limitations.

3.1.4 Obtaining a Concentrate

A Davis Tube Tester was chosen for the production of magnetic concentrates from segregation as others had successfully used it for this purpose (Dor, 1972; Warner

[10] The homogenised gas within the reaction bed will be referred to as the ‘bulk gas’ throughout this work.

et al., 1972; Wright and Gooden, 1973; Wright, 1994). Magnetic concentrates were obtained from the segregation of the nontronite and garnierite ores but not from the limonite since the majority of the product was magnetite. Previous researchers have concentrated segregated limonite using flotation (Iwasaki et al., 1966); however, flotation could not be reliably employed in this study since the mass of product (18-24 grams) was too small.

3.1.5 Analysis of Segregated Material

Selective dissolution with bromine-methanol solutions is an established method for analytical determination of metallic Ni, Fe and Co in the presence of their oxides and silicates (Kison et al., 1968; Young, 1986). This method was selected for the determination of the metals within the magnetic concentrates from nontronite and garnierite segregation, and directly from limonite segregation products, for which a magnetic concentrate could not be obtained.

3.2 Equipment

Five key pieces of equipment were used in this work: (1) the segregation reactor assembly, (2) the argon gas train, (3) the carbonaceous gas flow measurement assembly, (4) the apparatus for measurement of HCl in the off-gas, and (5) the data logging system.

3.2.1 Segregation Reactor Assembly

The segregation reactor and furnace assembly are shown in Figure 3.1. Key components are labelled and numbered within the figure; these components will be described throughout this section in the order in which they are numbered.

A typical segregation reaction bed (1) weighed ~22-28 g and consisted of the calcine mixed with 5% coke and 5% $CaCl_2$. The reaction bed was contained within a vertical 25 mm ID, 28 mm OD closed-end tube reactor (2) (custom made from fused quartz by Precision Glass Blowing, California, USA), supported at the base by a 600 mm long x 6 mm diameter quartz rod (3). This was attached to a variable speed ChemAp AG Vibromixer (4) to allow for continuous mixing of the reaction bed through mechanical fluidisation.

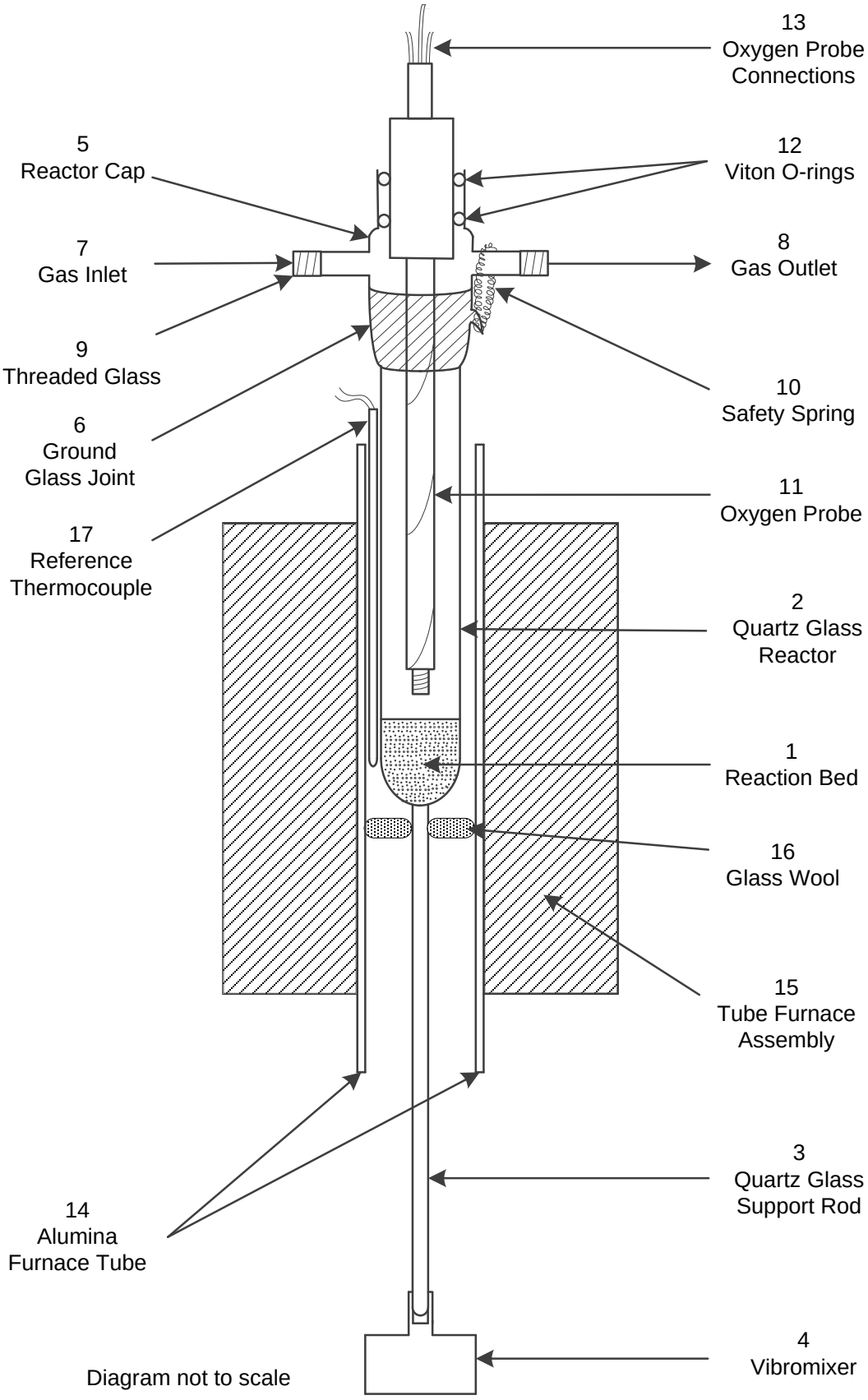

Figure 3.1 The Segregation Reactor Assembly

The top of the 360 mm high reactor tube was sealed with a Pyrex® cap (5) via a 24/40 ground glass joint (6). The cap was fitted with gas inlet (7) and outlet tubes (8), with threaded ends for the attachment of various gas trains via Quickfit® screw thread connectors (9). A safety spring was wrapped around the gas outlet and looped onto a hook attached near the top of the reactor tube (10). This was designed to compress the ground glass seal to prevent complete ejection of the cap in case of a pressure increase. The cap housed an industrial DS oxygen probe supplied by Ceramic Oxide Fabricators (11). The main body of the probe consisted of a 8mm OD x 350 mm long alumina tube, extended at the top by a 13 mm OD x 50 mm long stainless steel sheath. Two Viton® O-rings were used to form a seal within the 16 mm ID entry hole through the cap (12). A more detailed drawing of the custom made Pyrex® cap housing the oxygen probe is shown in Figure 3.2.

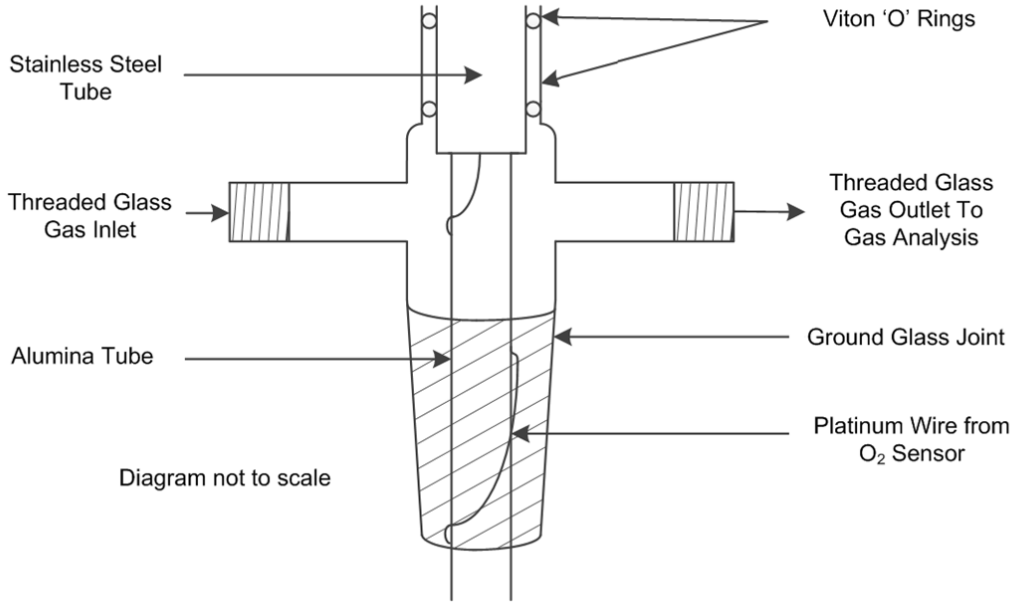

Figure 3.2 Pyrex Reactor Cap housing Oxygen Probe

Custom made by JR and SJ Davis Glassblowing (Perth).

The oxygen probe sensor was located ~10 mm above the surface of the reaction bed and consisted of a $SIRO_2$ C700® 7% yttria stabilised zirconia (YSZ) solid electrolyte plug bonded into the base of the alumina support tube. The leads for the probe's thermocouple (type R, Pt/Pt 13% Rh) and oxygen sensor (Pt/Pt) exited the top of the probe through a shrink wrapped seal, along with a 1.5 mm ID Teflon® tube (13) used for passing air down through an alumina tube to the standard electrode at the inner surface of the sensor plug.

The quartz reactor tube was located within a 30 mm ID, 36 mm OD alumina furnace tube (14), heated by a Pyroco silicon carbide vertical tube furnace (15). A plug of glass wool (16) was packed around the base of the reactor support rod within the furnace tube to act as a heat shield. The furnace temperature was controlled by a UT150 Yokogawa PID controller via a type R thermocouple located near the furnace heating elements (not shown in Figure 3.1).

The reaction temperature was monitored by a chromel–alumel K type thermocouple (the reference thermocouple), located in the space between the outer wall of the 28 mm OD quartz reactor and the 30 mm ID furnace tube, and positioned centrally relative to the 35 mm furnace hot zone (± 5 K at 1173 K) (17). The reaction bed of ~45 mm extended beyond the constant temperature zone; however calibration showed that the bed temperature was uniform due to fluidisation, and ~3 K above that measured by the reference thermocouple.

The base of the supporting rod for the quartz reactor was clamped into the head of the Vibromixer, whereas an untightened stand clamp loosely supported the top of the reactor such that the vibration was not suppressed. The power setting of the Vibromixer was calibrated to ensure that the ore was fluidised, as determined by visual observation of the bed while the reactor was outside of the reactor. Limonite required a slightly higher power setting than nontronite and garnierite due to its higher density.

A more detailed drawing of the 'off the shelf' oxygen probe is shown in Figure 3.3. The probe was used to measure continuously both the oxygen pressure (p_{O_2}) and the temperature in the segregation gas just above the reaction bed. The probe temperature was measured by a type R thermocouple with its head resting against the inside of the sensor plug at the base of the alumina support tube. The e.m.f. generated across the Pt wire electrodes attached either side of the YSZ oxygen sensor plug was used to measure the p_{O_2}. The e.m.f. developed because of the oxygen pressure difference between normal air in contact with the inside electrode and the segregation gas in contact with the outside electrode (Section 3.4.1).

The sensor e.m.f. and temperature were used to calculate the p_{O_2} and the average p_{CO_2}/p_{CO} for the segregation bed, as explained in Section 3.4.1, on the assumption that equilibrium is achieved for the CO_2/CO reaction with O_2 according to:

$$2CO + O_2(g) \rightarrow 2CO_2(g) \qquad 2.31$$

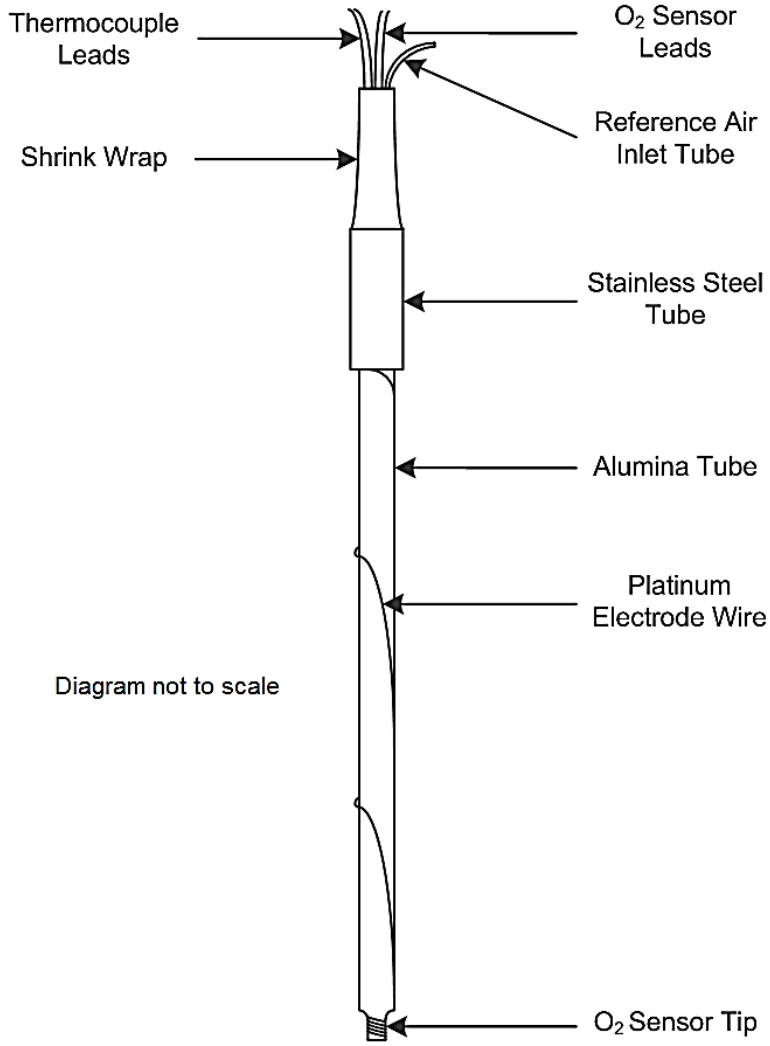

Figure 3.3 DS Oxygen Probe

A DS industrial oxygen probe with a yttria stabilized zirconia (YSZ) solid electrolyte sensor (Ceramic Oxide Fabricators, Melbourne

The DS oxygen probe is manufactured for the measurement of oxygen pressures of 1 to 10^{-24} atm from 823-1973 K (550-1700^{o}C) in industrial gas environments (COF, 2015) with an accuracy of up to ±2 mV. At 1173 K (900^{o}C) for example, this equates to an error of up to ±7% at an oxygen pressure of 10^{-10} atm. During a standard segregation test, the oxygen probe was introduced just above the hot bed at the start of the reaction. As a result, the initial recorded p_{O_2} was lower than actual, until the probe heated to the reaction temperature within a few minutes or less.

Initially, the sensor failed after ~10 tests due to breakage of the external Pt electrode wire (Figure 3.3) because of the vibration applied to fluidise the reactor bed. The

probe was returned to the manufacturer who repaired the wire and confirmed that the accuracy of the sensor was otherwise unaffected, even though the exterior became contaminated with iron oxides etc. from the reaction bed. Breakage of the external Pt wire continued to be a problem throughout the tests, although the life of the probe was extended significantly by covering the wire near the sensor with a high purity alumina adhesive (Resbond® 898) and also encasing the outer electrode in a fine alumina sheath, bound to the probe support tube with a Pt wire.

Frequent cracking of the fused quartz reactors during cooling in air after segregation was an issue at the commencement of the work. Scanning Electron Microscopic (SEM) analysis by CSIRO (Perth) of a cracked section revealed the cracks initiated at locations where $CaCl_2$ contacted the wall of a new reactor and formed spots of silicate that penetrated into the glass. The silicate penetration appeared to initiate devitrification of the fused quartz on cooling which resulted in cracking of the reactor.

The problem of frequent cracking of the reactors was overcome by coating the exposed wall of each new reactor with a fine, evenly dispersed, protective layer of silicate prior to it being used for segregation testing. To achieve this, 50 g of calcine was well mixed at room temperature with 1-2% $CaCl_2$, loaded into a new reactor tube, and heated under argon to 1173 K. A satisfactory protective coating of silicate developed after 3 hours under mechanical agitation at this temperature. This pre-treatment extended reactor life to ~10 tests before cracking occurred.

Other steps were also necessary to prolong reactor life. The reactors were not washed with water between tests, as washing tended to cause the reactors to devitrify and crack more easily. To keep the reactors dry and minimise 'shock' heating, they were held at 573 K (300^{o}C) and then 873 K (500^{o}C) before being placed in the reaction furnace held at the segregation temperature.

The reactor was flushed with high purity argon as it heated up to the segregation temperature. Ore was then added using a method developed to minimise any dust loss. The pre-weighed calcine was loaded into an argon filled, 300 mm long Pyrex tube with a 20 mm OD and 1 mm wall thickness, sealed at one end with a very thin plastic film of Glad Wrap® (Figure 3.4). The end of the Pyrex tubing (containing the ore) was then moved rapidly into the hot reactor to melt the Glad Wrap® and release the ore into the reaction bed. This method reduced dust loss to less than 2%.

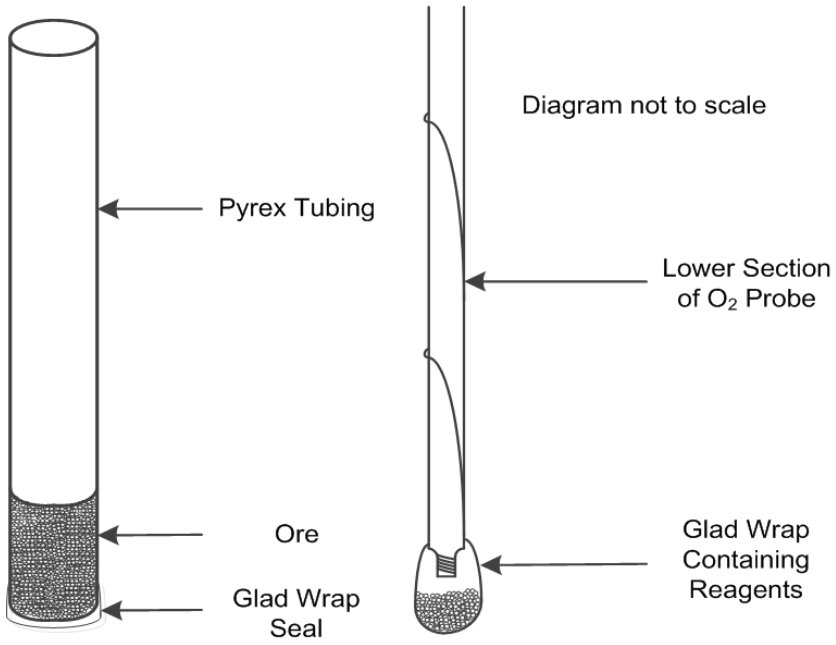

Figure 3.4 Equipment used for Addition of Ore and Reagents

Left: 300 mm long Pyrex tube with a 20 mm OD and 1 mm wall thickness, sealed at one end with Glad Wrap® used for insertion of ore and reagents.

Right: End of oxygen probe showing pod of Glad Wrap® used for insertion of reagents in two-step segregation.

In one-step segregation tests, both the carbon and $CaCl_2$ reagents were pre-mixed with the ore and added together to the hot reactor. In two-step segregation, the ore was added to the hot reactor and then allowed to heat to the segregation temperature under argon before the carbon and $CaCl_2$ were added to initiate segregation. Two-step segregation was used for the majority of tests since it provided a more accurate zero time for kinetic studies

In the two-step method, the carbon and $CaCl_2$ were secured onto the tip of the oxygen probe using Glad Wrap® (Figure 3.4). The reagents were then added to the reaction bed of ore by rapidly inserting the oxygen probe into the reactor and sealing the reactor cap in place via the 24/40 ground glass joint (Figure 3.2). Upon insertion, the reagents dropped cleanly onto the bed from the end of the probe as the Glad Wrap® melted.

The argon gas inlet at the top of the reactor was sealed and the gas outlet connected to the off-gas volume analysis train (Section 3.2.3) using threaded Teflon® connectors; this process took ~5-10 seconds. Care was taken to maintain

a gas tight seal at the connectors because the vibration applied to the reactor tended to loosen them. This was achieved by using Teflon® tape on the glass threads, silicon grease on the ground glass joint and compressing the joint with the spring secured to the reactor top.

3.2.2 Inlet Argon Gas Train

High purity argon was used to purge the reactor of air, moisture and any remnant chlorides between tests, and to provide an inert atmosphere within the reactor during heat up and cool down. The argon was passed into the reaction zone using a quartz tube housed within a Pyrex® reactor cap (Figure 3.5), linked via a screw thread connecter to the inlet argon gas train Figure 3.6.

The gas train consisted in sequence of an argon gas bottle, a mineral oil bubbler (used to visually monitor flow rate) and a 20 litre ($20x10^{-3}$ m^3) buffer tank. The buffer tank was included to facilitate cooling of the reaction product under argon. After segregation was complete, the outlet of the Pyrex® reactor cap was sealed and the inlet was connected to the argon gas train. The buffer tank was necessary to increase the volume of the reaction system to prevent the reactor cap jamming from the pressure drop created by gases contracting during cool down.

3.2.3 Carbonaceous Gas Flow Measurement Assembly

The gas evolved during nickel segregation is known to contain multiple species, specifically: CO_2, CO, $FeCl_2$, HCl and H_2O. Small to negligible amounts of H_2 (<1%) and $NiCl_2$ (<0.1%) and are also present (Rey et al., 1972a), along with trace $CoCl_2$. The carbonaceous species are CO_2 and CO; thus the $FeCl_2$, HCl and H_2O must be removed to allow the carbonaceous gas volume to be measured.

Both the $FeCl_2$ and H_2O condense as they cool while passing upwards from the hot reaction bed (1123-1223 K, 850-950^oC) before exiting through the outlet in the reactor cap at ~313 K (~40^oC). The $FeCl_2$ was seen to condense as a yellow solid on the upper walls of the reactor and on part of the cap, as confirmed by chemical analysis. $FeCl_2$ is a solid at the gas exit temperature with a very low vapour pressure; thus the amount leaving the reactor in the off-gas is expected to be negligible.

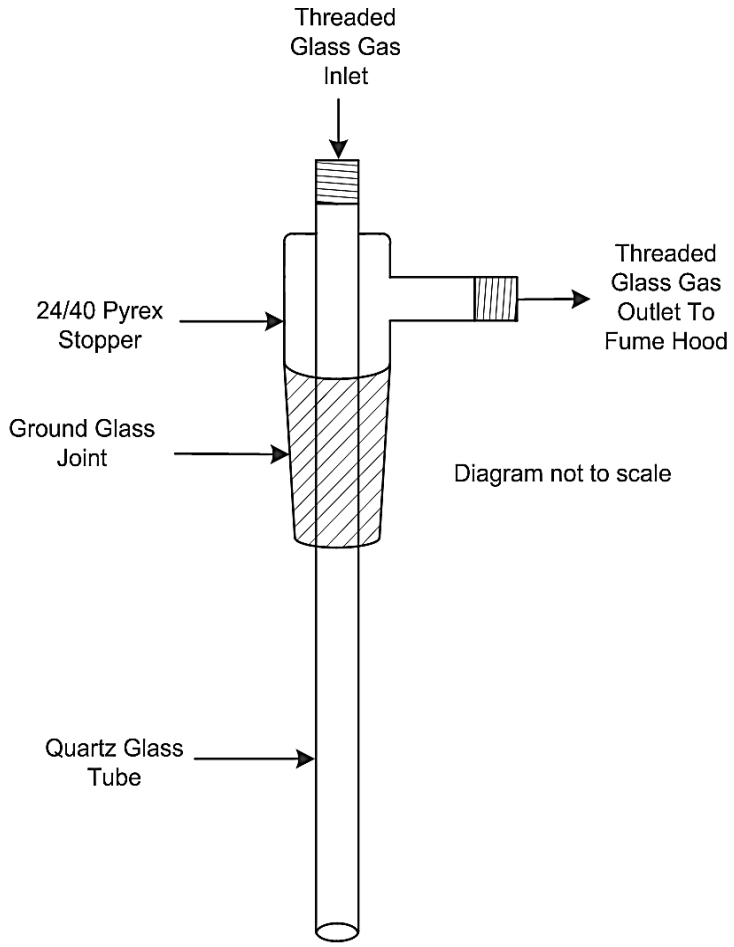

Figure 3.5 Pyrex Reactor Cap with Quartz Gas Injection Tube

Custom made by JR and SJ Davis Glassblowing (Perth)

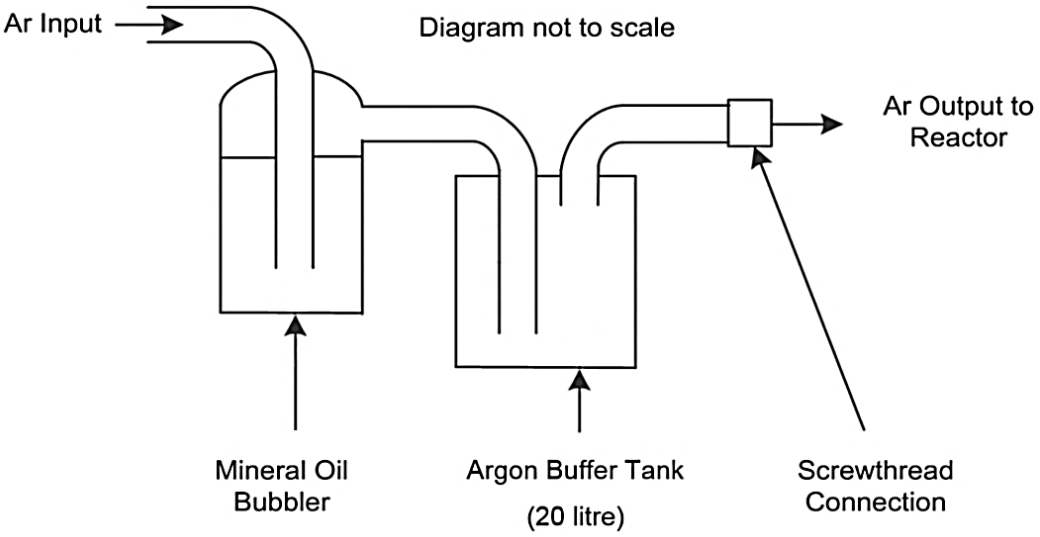

Figure 3.6 Inlet Argon Gas Train

Water condensed as a clear liquid on the upper tube wall and the reactor cap over the initial reaction period; thus the gas exiting the reactor would contain H_2O up to the saturation limit of 7.2 vol% H_2O at 313 K. Over time, the liquid would dissolve chloride species and turn yellow (from $FeCl_2$). The solubility of HCl in water at 313 K is 630 kg/m^3 (g/l); thus most of the HCl could dissolve within the condensed water, with very little in the off-gas leaving the reactor.

The actual amounts of $FeCl_2$, $NiCl_2$, $CoCl_2$ and HCl exiting the reactor within the off-gas were assessed by bubbling the gas through acidified, but initially de-ionised water, to capture and solubilise the chlorides. The apparatus used is shown in Figure 3.7. Analysis of the solution using Induction Coupled Plasma Mass Spectrometry (ICP-MS) confirmed that negligible Fe, Ni and Co were present after segregation at 1173 K, indicating that little or no $FeCl_2$, $NiCl_2$ or $CoCl_2$ was carried in the off-gas beyond the reactor cap. The de-ionised water was acidified to a pH of ~2 to buffer the acidification effect from the dissolution of CO_2 and subsequent carbonic acid dissociation (Appendix A.1), so that any HCl absorbed could be detected (Section 3.2.4). No change in pH was detected after passing the gas; thus little or no HCl was carried in the off-gas beyond the reactor cap.

It was concluded that the gas exiting the reactor would contain up to 7% H_2O, <1% H_2, with the remainder being CO_2 and CO. The H_2O was removed by passing the gas through anhydrous calcium sulphate (Drierite®). The calcium sulphate absorbs small amounts of CO_2 (Elia et al., 1986). However, this amount was considered negligible, since no change volume change was observed after repeatedly passing 50 ml of CO_2 back and forth through a Drierite® tube with syringes attached to each end of the tube; the volume was determined through examination of the volumetric markings on the syringes. The dried gas was thus assumed to contain only CO_2 and CO within an error of <1% associated with the H_2 remaining in the gas[11].

The dry gas was passed into the bottom of a 50 litre (1 litre = 10^{-3} m^3) argon filled buffer tank, with the gas outlet at the top of the tank connected to a Ritter TG05 drum type liquid displacement gas flow meter (Figure 3.8). The tank was designed to minimise any potential measurement error by facilitating the preferential displacement of a gas highly concentrated in argon (rather than the reaction gas) through the meter; the source of this error is discussed below.

[11] CO_2 and CO dissolved in the condensed H_2O within the reactor was considered insignificant, since the ~25 g of calcine contained <0.8% of H_2O.

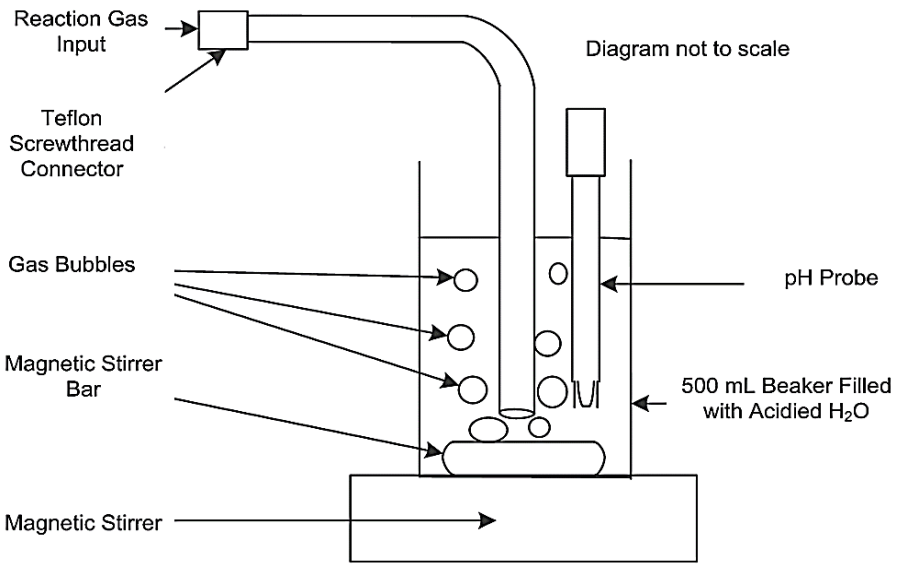

Figure 3.7 Apparatus for Determination of Chlorides in the Off-Gas

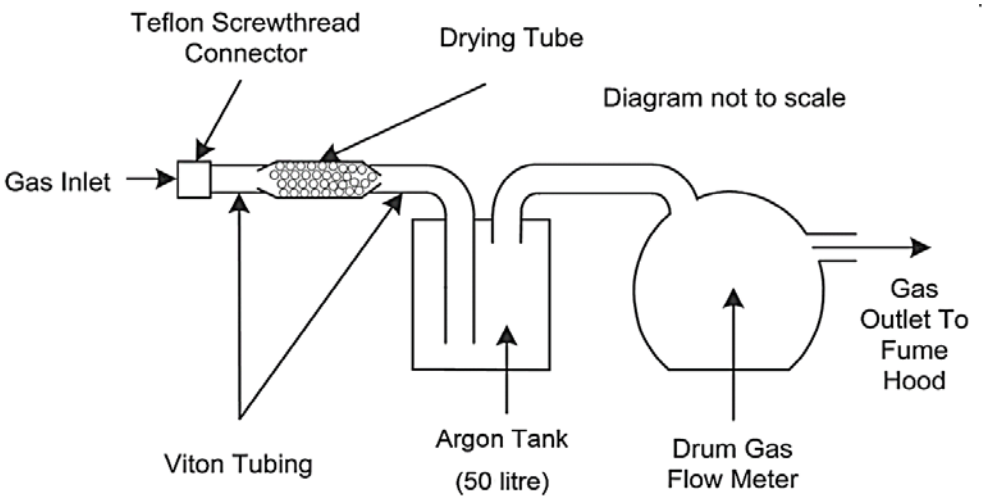

Figure 3.8 Apparatus for Carbonaceous Gas Flow Measurement in the Off-Gas

The Ritter flow meter measures volume by displacement of a 'packing liquid', with the mineral oil Odina 909, supplied by Ritter, used in this study because of its low volatility. It is standard procedure to pre-saturate the liquid with the gas that will pass through it, to ensure that gas does not dissolve into, or evolve out of the liquid during the measurement. This procedure is only effective if the gas passing through the liquid remains uniform in composition over the course of the measurement. However, CO_2 and CO in the off-gas are soluble to some extent in Odina 909 and during segregation the composition changes from an initially high ratio of CO_2 to CO, to a lower ratio as the system becomes more reducing (Table 2.8).

Any potential measurement error from the changing gas composition was minimised by using argon to both pre-saturate the packing liquid and to dilute the reaction gas, as explained above. Since the total carbonaceous off-gas volume was <1.5 litre for a segregation test, the dilution ratio of argon/carbonaceous gas was >33/1; thus minimising any error arising from the exchange of gas with the packing liquid. At times, up to five experiments were conducted in sequence without refreshing the argon saturation. At the end of these tests, a mass flow meter was used to pass a known volume of argon through the Ritter meter and the volume exiting the meter was measured using a gas bubble burette. The volume remained unchanged, which confirmed that the measurement error was negligible even after multiple experiments.

The accuracy of the gas flow measurement was limited by the number of electronic pulses that the Ritter meter generated with each milliliter (ml) increase in gas volume. The TG05 meter had the highest pulse/ml rate available at the time of this work, and according to the manufacturer's calibration, the meter measured flow rate to an accuracy of ± 0.1% at its lowest calibration limit of 16.67 ml/min.

The flow rate of gas exiting the segregation reactor was relatively high initially but declined significantly over the reaction period, for example, from ~30 ml/min during the first 5-10 minutes, decreasing to ~1 ml/min after 90 minutes (Appendix B.4). The flow rate over the initial period was high enough to be measured accurately by the meter, and these data were used to determine the initial carbon gasification rates (Section 5.6). The flow rate data towards the end of segregation were less accurate; however, the measurement of total cumulative gas volume versus time was considered reasonable over the entire time since all of the gas still passed through the meter, even if the rate was uncertain. These cumulative gas volume data were used to calculate the total carbon consumption during segregation (Section 3.4.2), and the oxygen removed by carbon reduction (Section 3.4.3).

When segregation was carried out under the most reducing conditions tested, specifically for the segregation of garnierite with activated carbon at 1223 K, a thin black deposit of carbon precipitated on the oxygen probe, above the hot zone and on the reactor wall. This deposit likely occurred due to a reversal of the Boudouard reaction (Equation 2.6) as the temperature decreased within the reactor; this would have caused the gas volume to decrease, but the error could not be determined.

3.2.4 Apparatus for Measurement of HCl in the Off-Gas

A custom made apparatus was designed for the continuous absorption of HCl from the off-gas into initially deionised water, that as previously described, had been acidified to a pH of ~2 to buffer the acidification effect from the dissolution of CO_2 (Appendix A.1). Under these conditions, the HCl content of the gas could be continuously measured by monitoring the change in pH, as described in Section 3.4.4 However, accurate carbonaceous gas flow measurements could not be carried out simultaneously, since some CO_2 and CO will dissolve into the analysis solution along with the HCl.

Allirra Glass Blowing (Perth) made the HCl analysis apparatus, which is illustrated in Figure 3.9. The apparatus consisted of a one litre Pyrex bottle capped via a 24/40 ground glass joint with a Quickfit® Dreschel head that terminated with a size 1 filter candle. The filter candle was used to disperse the reaction gas into the solution as fine bubbles. A magnetic stirrer was also used in the presence of four vertical wall baffles to promote gas/liquid contact and turbulent mixing. Using this set-up, the error associated with incomplete HCl dissolution was insignificant, as confirmed by passing the exit gas from the absorption bottle through a second solution in which no pH change was detected.

Accurate measurement of the gaseous HCl required that the off-gas be passed from the reactor and into the acidified solution without any condensation of moisture; otherwise the HCl would be absorbed into the condensate. This was in most part achieved by minimising the distance from the reactor gas outlet to the acidified solution, and by maintaining the gas line at 473 K (200°C) using heating cord. However, some condensation occurred within the internal tube of the Dreschel head. This tube was washed with the analysis solution using a pipette after each test, and the HCl data were scaled based on the resulting pH change, which generally represented 5-10% of the total H^+ change.

The gas exiting the reactor travelled along ~0.3 metres of Viton® tube before reaching the Dreschel head. The tube was connected to the reactor gas outlet and the Dreschel head inlet via Teflon® Quickfit® screw thread connectors. The reaction cap, tubing, screw thread connectors and top of the Dreschel head were all bound with heating cord whilst HCl measurements were taking place. Oxygen pressure measurements were not taken during the HCl measurements, since the weight of the oxygen probe combined with the heating cord tended to suppress the

vibration used to fluidise the reaction bed; thus the oxygen probe was removed from the reactor cap and the glass joint was instead sealed with a rubber stopper.

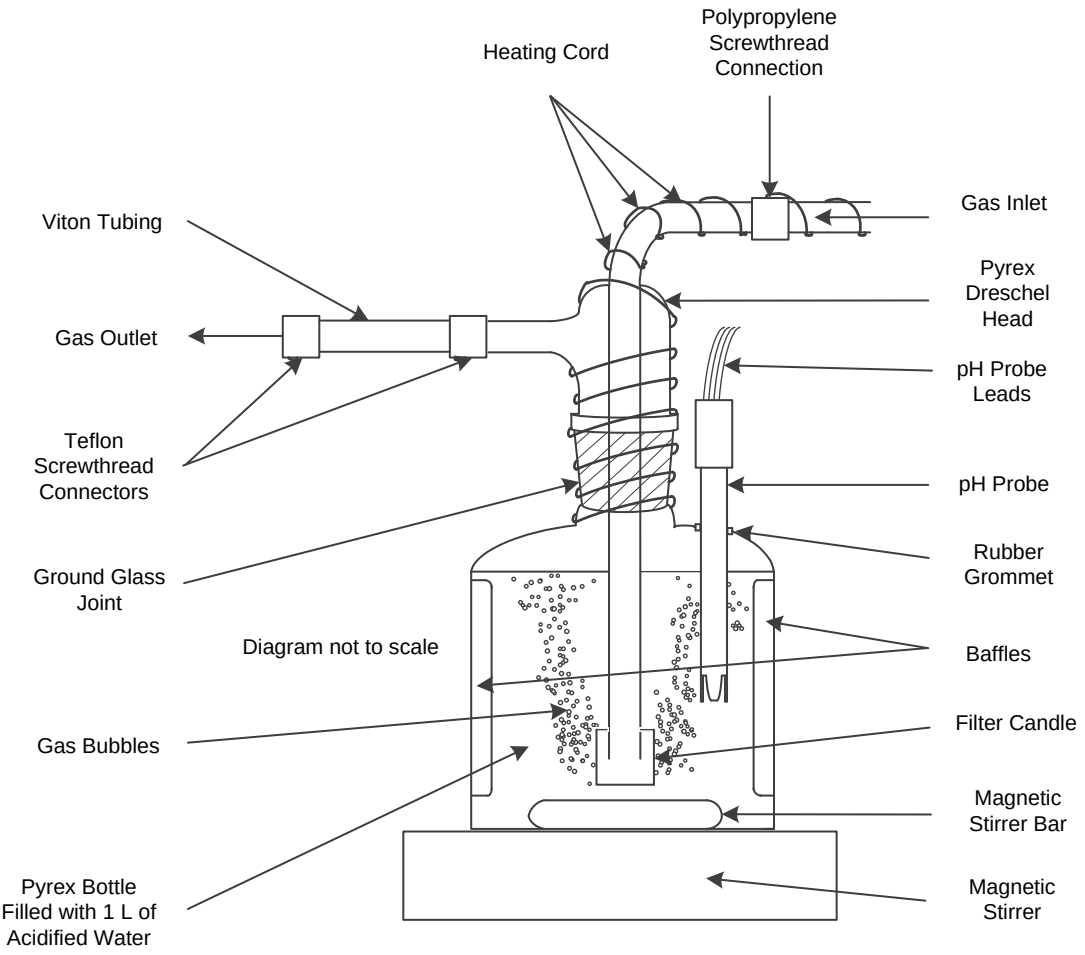

Figure 3.9 Apparatus for Measurement of HCl in the Off-Gas

The heating cord was wrapped around the Dreschel head, the Viton® tubing leading back to the reactor and the reactor cap (not shown in diagram).

The pH change resulting from the absorption of HCl in the solution was measured by a pH probe protruding through a hole in the top of the bottle. The probe, custom made by Ionode Electrodes (Queensland), included a IJ-40 pH probe coupled with a PT-1000 resistance thermometer, and was secured into the bottle with a gas tight seal using a rubber grommet. The pH probe was calibrated using pH 1.68, 4 and 7 buffer solutions at three temperatures within the range 288-313 K (15-40^{o}C), as set with a hot water bath. The PT-1000 resistance thermometer was calibrated between 273 K (0^{o}C) and 373 K (100^{o}C) using an ice bath and boiling water.

A minor temperature compensation for the pH measurement was necessary because the bubbling of hot gas through the 1 litre solution increased the

temperature by ~2 K over a 120 minute test. The temperature increase was as high as 15 K in the first tests, but this large increase was eliminated by pre-heating the solution to ~308-313 K (35-40^{o}C), and by placing a reflective heat shield coupled with a small fan between the furnace and the absorption bottle.

3.2.5 Data Logging System

An important aspect of the experimental design was the establishment of a reliable data logging system for the analogue voltages continuously outputted from the sensor devices, specifically: the DS oxygen probe sensor and thermocouple, the IJ-40 pH probe, the PT-1000 resistance thermometer and the Ritter TG05 gas flow meter.

Three steps were taken to ensure the electrical measurements were free from any electrical noise or interference: a Powershield Centurion 2000VA uninterrupted power supply (UPS) was used to provide constant voltage power to all instrumentation and to ensure the equipment remained powered during power outages; shield to earth wiring was used for all electrical connections; and custom made low-pass RC filters were used to filter alternating current (AC) interference from signals received from the oxygen sensor and pH probe.

The low-pass RC filters, while being simple circuits, were critical for obtaining noise-free data. These filters consisted of a 10 kΩ resistor in series, with a 100 µF capacitor in parallel (Figure 3.10). The variable reactance of the capacitor forced frequencies below 1.6 Hz to pass to the data logger[12], while short circuiting higher frequency signals, effectively eliminating any interference from the 50 Hz AC main power (Storr, 2013).

An inexpensive but high utility data logger, the Labjack U6, was used to process and convert the analogue voltage signals from the oxygen sensor, thermocouples, the resistance thermometer and the pH probe. The converted digital signals were sent to a laboratory computer where they were logged to Excel compatible CSV files using DAQFactory Express software. This software also allowed for manipulation of the signals to provide live tracking of user-specified output values and formats, enabling convenient monitoring of the segregation experiment.

[12] The low-pass cut-off frequency is equal to $1/2\pi RC$, where R = resistance in Ohms, and C is capacitance in Farads.

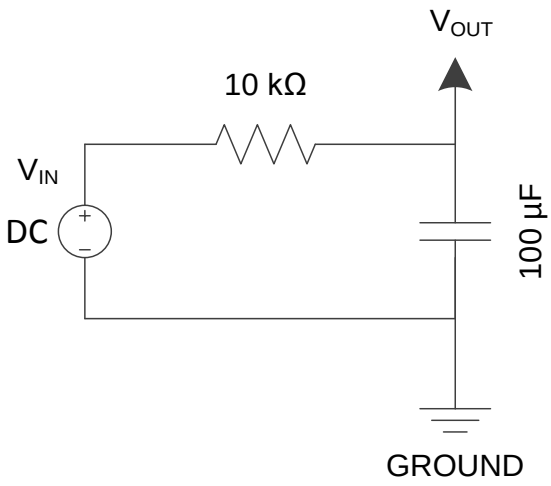

Figure 3.10 Low Pass RC Filter

In addition to being an analogue to digital converter (ADC), the Labjack provided other useful features, such as those used when logging the signals from the thermocouples and the PT-1000 resistance thermometer. The Labjack continuously measured the ambient temperature and used this to apply a zero temperature compensation to the analogue thermocouple voltages. The Labjack also provided a 200 uA continuous current output that was fed into the PT-1000 resistance thermometer inside the pH probe, with the resulting analogue voltage fed back to the Labjack to log the temperature.

The analogue voltage from the pH probe could not be sent directly to the Labjack because the probe impedance was too high. The pH signal was therefore pre-conditioned using a PHAMP-1 Battery Powered Preamplifier (supplied by Newport) to reduce the impedance before it was sent through the Labjack to the computer.

The Labjack was not used to convert the analogue signal from the Ritter drum flow meter. It was more convenient to use the Ritter Digital Input Module supplied with the meter for this purpose. These data were also logged onto the laboratory computer using Rigamo software supplied by Ritter.

3.3 Procedures

The sequence of experimental procedures is illustrated in Figure 3.11; all were carried out by this researcher unless otherwise noted. Each procedure will now be described, although some relevant detail may have already been included within the previous descriptions of equipment.

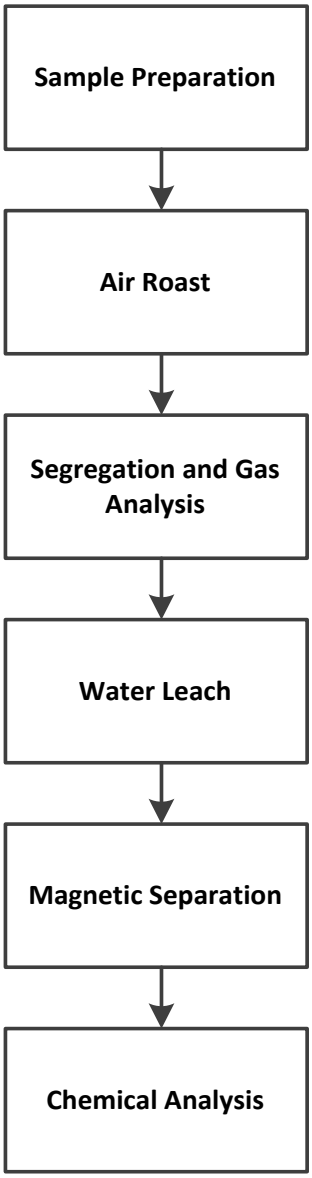

Figure 3.11 Sequence of Experimental Procedures

3.3.1 Sample Preparation

Laterite ore was received as drill core, dried under heating lights, crushed and pulverisered to pass a 212 µm screen, riffle split into 20-25 gram representative samples and then stored in sample containers.

3.3.2 The Roast and Segregation

A two-step segregation procedure used for most experiments (Section 3.2.1) and is described here. A 20-25 gram laterite sample was weighed and then subjected to a 30 minute air roast in an open crucible at the segregation temperature. This roast could not be carried out in the segregation reactor, as the closely packed reaction

bed and rapid evolution of steam caused much of the sample to be ejected from the reactor.

After roasting, the laterite was allowed to cool to room temperature, re-weighed and transferred to the Pyrex® tubing used for ore insertion (Figure 3.4). When the segregation reactor was at the required temperature, the Vibromixer was switched on and the ore was inserted into the reactor. The reactor temperature dropped ~50 K after insertion of the room temperature ore and 10-12 minutes were required for the segregation temperature to be re-established. This period allowed any residual freely bound water to be removed from the ore.

The segregation reactor was not washed between tests (Section 3.2.1) and any residual chlorides had to be removed by volatilisation. The reactor was checked to ensure no visible chloride fume was emitting from the hot reactor. If a fume was visible, the hot reactor was flushed with argon gas using the gas injection cap (Figure 3.5) until it disappeared, after which the reactor was ready for use, and the support rod was secured into the Vibromixer in preparation for the addition of the ore.

The carbon and $CaCl_2$, which were stored in an oven at 383 K (110^{o}C), were weighed and mixed in a sample boat and then transferred to a P_2O_5 desiccator. Just prior to the ore reaching the reaction temperature, the segregation reagents were secured onto the tip of the oxygen probe using Glad Wrap® in preparation for insertion into the reactor (Figure 3.4). Both procedures were done as quickly as practical to minimise the amount of atmospheric H_2O absorbed by the $CaCl_2$.

Segregation was then initiated by placing the cap housing the oxygen probe (Figure 3.2) into the reactor, which caused the Glad Wrap® to melt and the reagents to drop into the reaction bed, where they were mixed with the mechanically fluidised ore by the vibration. The reactor gas outlet was then connected to the gas analysis apparatus (Figure 3.8) and the stopper was secured by wrapping a spring over the gas outlet and onto an external hook near the top of the reactor Figure 3.1).

Segregation was allowed to proceed until 30 seconds before completion of the reaction time, at which point the gas outlet of the reactor was disconnected from the gas analysis apparatus and capped. The gas inlet of the reactor was uncapped and connected to the inlet argon gas train (Figure 3.6), the Vibromixer was switched off and the reactor support rod was unclamped from it. When the reaction time was

completed, the reactor was raised above the furnace and the segregate[13] was allowed to cool under argon to room temperature, which took ~30 minutes.

After the segregate was cool, the argon gas train was disconnected and the reactor cap removed. The reactor tube was inverted and gently tapped on the bottom to dislodge the majority of the segregate. The reactor was then turned upright and the sides and bottom scraped with a wooden pole; this process repeated until the segregate was completely removed. The segregate was transferred into a sample container and weighed. The uncapped sample container was then placed into an argon flushed $CaCl_2$ desiccator where it was kept overnight before being capped and sealed using Teflon® tape for temporary storage.

If variations to this two-step segregation procedure were used in specific tests, these will be described where appropriate in the text.

3.3.3 Carbonaceous Gas Analysis

The Ritter gas meter packing liquid was pre-saturated with argon by passing approximately 100 litres through the meter overnight. Saturation was confirmed by passing a constant flow of argon through the meter and checking that the gas flow into the meter equalled the gas flow out of the meter using a gas bubble burette. A similar check was performed after the tests to ensure the flow rate remained accurate. Other details of the carbonaceous gas analysis procedure are included in Section 3.3.3.

There was a relatively large, instantaneous evolution of gas when the carbon and $CaCl_2$ were added to initiate segregation. This evolution persisted for approximately 0.5-1 minutes and represented 1-3 ml per gram of ore. This volume was discounted from the total carbon consumption analysis as the gas was not considered to be CO_2 or CO generated from the normal reduction of oxides with carbon. It was considered more likely to result from moisture and other volatiles being released from the $CaCl_2$ and carbon. These volatiles likely absorbed during reagent preparation, since both reagents had been previously stored at 283 K (110^{o}C).

3.3.4 HCl Gas Analysis

The HCl analysis solution was prepared by adding 0.5 ml of 70% HNO_3 to a 1 litre volumetric flask, filling the flask with de-ionised water, sealing it and placing the flask next to the HCl analysis bottle to allow the solution temperature to increase to ~308-

[13] The segregate refers to all of the material treated by segregation.

313 K (35-40^{o}C) before the next test (as required to improve the accuracy of pH measurements, Section 3.2.4).

Preparations for the HCl analysis were completed within the 10-12 minute period it took for the reactor to re-establish the reaction temperature after the addition of the calcine. During this period, the following sequence of steps were carried out: the HCl analysis solution was poured into the analysis bottle; the magnetic stirrer bar was dropped into the solution; the Dreschel head was placed in the bottle; the pH probe was secured into the bottle using a rubber grommet; the magnetic stirrer was turned on; the gas inlet of the Dreschel head was attached to the gas line coming from the reactor; the heating cord from the reactor gas outlet was wrapped around the top of the Dreschel head and secured using heat resistant tape; the gas outlet of the Dreschel head was attached to a gas line that went to a fume hood; the analysis solution for the next test was prepared and the segregation reagents were prepared for addition to the reactor.

Since the oxygen probe was not used with the HCl analysis apparatus (Section 3.2.4), an alumina tube tipped with Glad Wrap® film was used to insert the carbon and $CaCl_2$. After removal of the alumina tube, the reactor cap was sealed with a rubber stopper and the reactor gas outlet was connected to the HCl analysis apparatus using a Teflon® screw connector. There was typically a lag time of 10-20 seconds between the addition of the reagents and the connection of the reaction gas outlet to the HCl analysis apparatus.

A control thermocouple was placed under a section of the heating cord to control the temperature at 473 K (200^{o}C). In some cases, liquid condensed at the top of the reactor before the heating cord reached the control temperature. When this occurred, a heat gun was used to vaporise the liquid.

During the 30 seconds before the desired segregation reaction time was complete, the heating cord was unwrapped from the top of the reactor to allow it to be removed from the furnace. Once the reactor was removed, the Dreschel head was raised above the HCl analysis bottle, and the internal surface was washed with solution from the bottle using a pipette, to capture any HCl dissolved in condensate on the walls. The pH then stabilised after 1-2 minutes to give the final reading. Once the test was complete, the analysis solution was discarded and the Dreschel head was washed with distilled water and blown through with compressed air to ensure the filter candle did not become blocked.

3.3.5 Water Leach

After most segregation tests, the segregate was ground in de-ionised water with a mortar and pestle for ~2 minutes in order to dissolve any residual chlorides, specifically any $CaCl_2$, $FeCl_2$, $NiCl_2$ and $CoCl_2$. The slurry was then filtered into a one litre volumetric flask containing 29 ml of concentrated HNO_3 to suppress hydroxide precipitation. Once filtration was complete, the solution was stored for Ca, Fe, Ni and Co analysis by ICP-MS, while the solids were transferred to an argon flushed desiccator cabinet.

The determination of residual soluble chlorides was used to confirm the extent of consumption of $CaCl_2$ and to ensure that some remained in excess at the end of segregation, as required for the production of HCl (Section 2.4.1). The analysis also provided an indication of the relative partial pressures of the respective metal chlorides within the gas at the end of segregation, and the proportion of nickel lost in the process as a $NiCl_2$. The soluble chloride data, while useful, were not quantitative, since it was not possible to leach residue from within the reactor tube after each test without greatly increasing the risk of cracking of the tube due to devitrification (Section 3.2.1).

3.3.6 Magnetic Separation

The water-leached segregate from the segregation of the nontronite and garnierite ores was subjected to magnetic separation to produce a concentrate containing the segregated ferronickel alloy. This was done using a standard Davis Tube Tester, manufactured by Sepor, for which full details and operating procedures are readily available (Sepor, 2015). Essentially, the sample is gradually washed into an inclined cylindrical glass tube that oscillates at 60 strokes per minute. As the sample progresses down the tube, the magnetic particles are captured by the magnetic field. Wash water flushes the non-magnetic fraction out of the tube until only the magnetic fraction remains.

An initial series of tests were performed using 10 gram samples of magnetite/sand mixtures which were of similar size to the segregate (-212 µm), to determine appropriate conditions for 100% separation of magnetite from the sand. The results were initially erratic because of inconsistent mains water flow. The problem was solved by installing a header feed tank above the unit. After a series of tests, it was determined that ~100% of magnetite could be recovered using the settings shown in Table 3.1, which were adopted for all magnetic separation of segregate carried out

in this work. The resulting magnetic concentrate and tailings were filtered and transferred to a desiccator cabinet to dry before analysis.

Table 3.1 Davis Tube Magnetic Separator Settings

Sample Mass	10 grams
Time	10 minutes
Wash Water Rate	450 ml/min
Magnetic Field Strength	4000 Gauss
Tube Angle	20 Degrees

3.3.7 Chemical Analysis for Metallic Nickel, Iron and Cobalt

A selective bromine-methanol leach was carried out to determine the amounts of Ni, Fe and Co within the segregation product. Details of the procedure used are given in Appendix A.2. In summary, dried samples of concentrate or segregate were leached in a solution of anhydrous bromine/methanol to selectively convert all metallic Ni, Fe and Co into soluble bromides while leaving oxides and silicates unaffected. After filtration, the leachate was heated to dryness leaving a bromide residue which was then heated to decomposition in the presence of a decomposing acid ($HCl:HNO_3:HClO_4$) to leave a Ni, Fe, Co chloride residue. The chlorides were dissolved in nitric acid and the metal content of the solution analysed by ICP.

During this procedure, the presence of any H_2O within the bromine/methanol leach solution will form HBr, which introduces analytical error through the dissolution of oxides. To avoid this, the samples were exhaustively dried by storing overnight within an argon purged $CaCl_2$ desiccator cabinet, before being placed within a desiccator containing phosphorus pentoxide (P_2O_5) until no weight change was registered.

Tests were also carried out with three grades of methanol to determine the effect of retained moisture on the leaching of iron oxides, specifically: AR grade distilled to contain 0.01% H_2O; AR grade distilled and dried using 3A molecular sieve to 0.007% H_2O; and commercial anhydrous methanol (0.005% H_2O). These tests were carried out by leaching 2.67 g of -212 µm Fe_3O_4. The commercially supplied anhydrous methanol dissolved the least amount of iron oxide (<0.4%, compared to <0.7% for the molecular sieve dried methanol and <1.2% for AR distilled methanol), and was thus selected for all analysis carried out in this work.

It appears that a small amount of iron oxide will always unavoidably leach during this chemical analysis. As such, the analysis for metallic Fe in the presence of iron

oxides will slightly overestimate the amount present. The error will be minimal for nontronite and garnierite as they contain relatively small amounts of iron oxides in the magnetic concentrate that is leached. The error will be more significant for limonite, which is mainly iron oxide as it cannot be concentrated before leaching. The analysis for metallic Ni and Co, however, should be relatively unaffected for all three ores.

3.4 Calculations

Basic calculations relevant to this work are described in this section, specifically, the calculation for (1) the oxygen pressure and CO_2/CO ratio of the gas, (2) the total carbon consumption, (3) the total oxygen removed by carbon reduction and (4) the HCl in the off-gas.

3.4.1 Oxygen Pressure and CO_2/CO in the Off-Gas

The DS oxygen probe with a $SIRO_2$ C700 oxygen sensor (Badwal et al., 1987) measures the electromotive force generated by the potential transfer of oxygen ions from a high to low oxygen pressure, across a 7% yttria stabilised zirconia (YSZ) electrode, as shown in Figure 3.12 (Ramamoorthy et al., 2003).

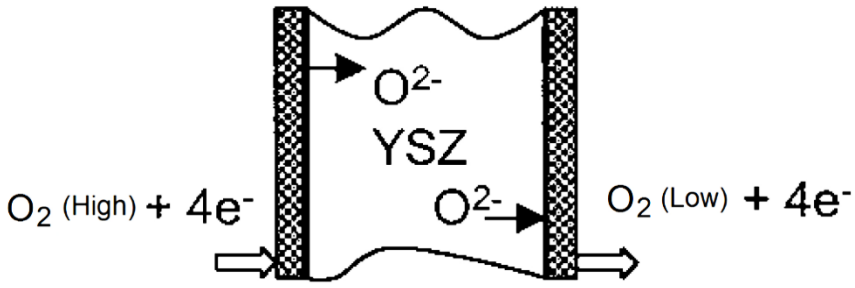

Figure 3.12 ZrO_2 Solid Electrolyte Oxygen Sensor

Oxygen ions are potentially transferred from a high oxygen pressure to a low oxygen pressure across a zirconia electrode (Ramamoorthy et al., 2003).

The oxygen concentration gradient across the sensor can be represented by:

$$O_2(high) \rightarrow O_2(low) \qquad 3.1$$

for which the Gibbs free energy is given by:

$$\Delta G = \Delta G^{\circ} + RT \ln\left(\frac{p_{O_2,low}}{p_{O_2,high}}\right) \qquad 3.2$$

G is the Gibbs free energy of the reaction (J); G° is the standard Gibbs free energy of the reaction (since O_2 is both product and reactant, $\Delta G^{\circ} = 0$); R is the universal gas constant (8.314 J/K mol); T is the temperature of the oxygen sensor (K). The $p_{O_2,high}$ is referenced to air. The average atmospheric pressure in Kalgoorlie, Western Australia where this work was carried out is 0.962 atm; since air contains 20.9 vol% O_2, the $p_{O_2,high}$ used in the calculation was 0.202 atm.

The Gibbs free energy and electromotive force across the sensor are related by:

$$\Delta G = -zFE \qquad 3.3$$

E is electromotive force (V), z is the moles of electrons transferred per mole of O_2 (4) and F is Faraday's constant (96485 C/mol electron).

Substitution of the known values and the electromotive force relationship (Equation 3.3) into the ΔG expression (Equation 3.2), with re-arrangement, gives the expression for the oxygen pressure p_{O_2} measured by the sensor as:

$$p_{O_2} = 0.202e^{\frac{-46421E}{T}} \qquad 3.4$$

$p_{O_2} = p_{O_2,low}$ which is the oxygen pressure in atmospheres ~10 mm above the reaction bed, where the sensor was located.

The p_{CO_2}/p_{CO} at the oxygen sensor was calculated assuming the oxidation of CO with O_2 to form CO_2 is at equilibrium, according to:

$$2CO(g) + O_2(g) \leftrightarrow 2CO_2(g) \qquad 2.31$$

Rearrangement of the equilibrium constant expression for Equation 2.31 gives the expression for the p_{CO_2}/p_{CO} at the oxygen sensor as:

$$\frac{p_{CO_2}}{p_{CO}} = \left(K_{2.31}p_{O_2}\right)^{0.5} \qquad 3.5$$

The p_{CO_2}/p_{CO} at the oxygen sensor was taken as the best estimate of the p_{CO_2}/p_{CO} within the segregation bed during the segregation reaction. The oxygen pressure in the reaction bed ($p_{O_{2,Bed}}$) was then calculated according to:

$$p_{O_{2,Bed}} = \frac{1}{K_{2.31,Bed}}\left(\frac{p_{CO_2}}{p_{CO}}\right)^2 \qquad 3.6$$

$K_{2.31,Bed}$ is the equilibrium constant at the temperature of the reaction bed (~10-15 K higher than at the sensor) and $p_{CO_2}/p_{CO} = \left(p_{CO_2}/p_{CO}\right)_{sensor} \approx \left(p_{CO_2}/p_{CO}\right)_{bed}$

3.4.2 Total Carbon Consumption

Total carbon consumption was calculated from the measured reaction off-gas volume, reported at 273 K and 1 atm (STP). The gas consisted of CO and CO_2; thus each mole of gas contained one mole of carbon, where:

$$n_c = n_{gas} = \frac{V_{gas}}{2.241 \times 10^4} \quad 3.7$$

n_c is the moles of carbon consumed; n_{gas} is the moles of off-gas and V_{gas} is the volume of off-gas in millilitres ($1\ mL\ =\ 1 \times 10^{-6}\ m^3$) at 273 K and 1 atm.

The fraction of carbon consumed is given by:

$$X_C = \frac{n_C}{n_C^\circ} = \frac{m_C/M_C}{m_C^\circ/M_C} = \frac{m_C}{m_C^\circ} \quad 3.8$$

n_C° is the number of moles of carbon initially added to the segregation bed; m_C is the mass of carbon consumed; m_C° is the mass of carbon initially added to the segregation bed and M_C is molar mass of carbon.

3.4.3 Total Oxygen Removed by Carbon Reduction

The segregation reaction involves the net reduction of oxides with carbon, which results in the removal of oxygen from the bed as CO and CO_2. An amount of oxygen is also removed from the bed as H_2O, but this largely enters as H_2O.

In order to calculate the moles of oxygen removed by carbon, the logged continuous carbonaceous off-gas volumes and p_{CO_2}/p_{CO} measurements from the oxygen sensor were time-aligned with Excel and the values averaged for each (nominal) 5 second time interval. The average mole fractions of CO and CO_2 in the off-gas over each time interval are given by:

$$X_{CO_2} = \frac{p_{CO_2}}{p_{total}} \quad 3.9$$

and

$$X_{CO} = \frac{p_{CO}}{p_{total}} \quad 3.10$$

p_{CO_2} and p_{CO} are the average partial pressures of CO_2 and CO in reaction carbonaceous off-gas (atm), for which $p_{total} = p_{CO_2} + p_{CO} = 0.962\ atm$ (in Kalgoorlie) since the off-gas was vented to atmosphere with only a minor pressure head. The total moles of oxygen $n_{O,total}$ within a carbonaceous off-gas containing n_{gas} total moles of CO and CO_2, is given by:

$$n_{O,total} = 2X_{CO_2}n_{gas} + X_{CO}n_{gas} \quad 3.11$$

Both the rate and the cumulative total of O removed by carbon were calculated in Excel using this approach.

3.4.4 Measurement of HCl in the Off-Gas

The amount of HCl in the off-gas is equivalent to the number of moles of H^+ which enter the solution above that already present from the addition of HNO_3. This is calculated from the measured pH on the assumption that each mole of H^+ that dissolves into the solution originated from HCl. The H^+ concentration is related to pH as shown below:

$$pH = -\log a_{H^+} = -\log \gamma_{H^+}[H^+] \quad 3.12$$

thus $$10^{-pH} = \gamma_{H^+}[H^+] \quad 3.13$$

$a_{H^+}$is the activity of H^+ in the solution relative to an ideal 1 molar solution; γ_{H^+} is the H^+ activity co-efficient and $[H^+]$ is the concentration of H^+ in the solution (mol/l). γ_{H^+} has been fitted to a linear expression over the pH range used in this work (2-2.3) using data from Sakaida and Kakiuchi (2011):

$$\gamma_{H^+} = -3.784[H^+] + 0.9415 \quad 3.14$$

Substitution into the expression for 10^{-pH} with re-arrangement gives:

$$-3.784[H^+]^2 + 0.9415[H^+] - 10^{-pH} = 0 \quad 3.15$$

where $$[H]^+ = \frac{-(0.9415) + \sqrt{(0.9415)^2 - 4(10^{pH})(-3.784)}}{2(-3.784)} \quad 3.16$$

The total moles of HCl delivered to a litre ($1\ l\ =\ 10^{-3}\ m^3$) of solution is given by:

$$n_{HCl} = [H^+]_{final} - [H^+]_{initial} \quad 3.17$$

The percent Cl from the $CaCl_2$ added to the segregation bed that reports as HCl to the analysis solution, is given by:

$$\%Cl = 100\left(\frac{n_{HCl}}{2n^{o}_{CaCl_2}}\right) \quad 3.18$$

$n^{o}_{CaCl_2}$ is the number of moles of $CaCl_2$ added to the segregation bed and n_{HCl} is the number of moles of HCl reporting to the analysis solution.

3.5 Materials and Reagents

The materials and reagents used in this work are summarised in Table 3.2.

Table 3.2 Summary of Materials and Reagents

Material	Supplier	Product	Product/Catalog Number
Laterite Ore	Heron Resources Ltd	Details: Section 4.1	
Metallurgical Coke	One Steel (now Arrium)	Details: Section 4.2	
Activated Carbon	Haycarb Holdings	Details: Section 4.2	
Calcium Chloride	Scharlau	Extra, pure granulated	CA01900500, CAS 10043-52-4
Phosphorous Pentoxide	Merck Millipore		1005401000, CAS 1314-56-3
Argon	Air Liquide	High purity	GAS-BLUA50SMART, CAS 7440-37-1
Nitrogen	Air Liquide	Industrial Grade	GAS-NIT50, CAS 7727-37-9
Nitric Acid	LabServ	AR Grade 70% Nitric Acid	BSPSL733.2.5, CAS 7697-37-2
Buffer Solutions	Australian Chemical Reagents	pH 1.68, 4.0 and 7.0	0881, 0114 and 0113
Bromine	Acros Organics	Extra pure 99%,	402845000, CAS 7726-95-6
Methanol	Scharlau	Dried (≤0.005% H_2O)	ME03042500, CAS 67-56-1
Hydrochloric Acid	Rowe Scientific	AR Grade, 32%	CH1680, CAS 7647-01-0
Perchloric Acid	Merck Millipore	AR Grade, 70-72%	1005192501, CAS 7601-90-3
Fe, Ni, Co, Ca Std. Solutions	Australian Chemical Reagents	1000 mg/L, 2% HNO_3	0701, 0721, 0678, NR
Magnetite	Savage River	-212 µm	Ground, Sieved, Separated in Lab

Chapter 4

Ore, Calcine and Carbon Characterisation

The key characteristics of the nickel laterite ores, roasted ores (calcines) and carbons used in this work are presented and discussed in this chapter.

4.1 Ore and Calcine Characteristics

Nickel laterite ores (limonite, nontronite and garnierite) were provided as drill core samples by Heron Resources Limited from deposits associated with their Kalgoorlie Nickel Project in Western Australia.

The drill core samples were dried under heating lights to remove free moisture and then split into representative 20-25 gram samples passing -212 µm. Wet chemical analyses of the representative dried nickel laterite samples were carried out by CSIRO in Perth; these results are presented in Table 4.1.

Table 4.1 Chemical Analyses of Dried Nickel Laterite Samples

wt%	Ni	Co	Fe(tot)	SiO_2	MgO	Al_2O_3	CaO	Cr	Mn	Na	S
Limonite Ore	0.934	0.035	51.2	3.11	0.41	4.47	<0.01	1.40	0.100	0.710	0.26
Nontronite Ore	1.21	0.056	24.4	40.7	2.02	3.96	<0.01	4.15	0.132	0.065	0.21
Garnierite Ore	1.27	0.033	11.7	53.3	14.8	2.58	1.97	0.62	0.170	0.220	0.06

All three ores were roasted in air to produce a calcine prior to segregation (Section 3.3.2). The sintering temperature of each calcine was estimated so that the maximum segregation temperature could be set below it, to avoid sticking of ore within the vibrated segregation bed. The estimation was done by roasting the ore at 1173 K for 30 minutes, and then increasing the temperature in ~20 K increments until sintering was visible. The temperature was monitored by a K-type thermocouple immersed into the calcine. The estimated sintering temperature for each calcine is presented in the first column of Table 4.2.

Roasting tests were also conducted to determine the bonded water retained after the laterites had been dried. This was taken as the total weight loss from dried ore after a 3 hour roast in air at 10 K below the sintering temperature, for both limonite and nontronite; for garnierite, the weight loss was discounted by 2.8% to account for the estimated CO_2 released from the 6.5% carbonate contained within it (Table 4.9).

The roasting time to achieve ~95% removal of bonded water at 10 K below the sintering temperature was also determined as a guide for future roasting tests.

Table 4.2 Sintering Temperature and Bound Water Loss during Laterite Roasting

Ore	Sintering Temperature (K)	Roasting Temperature (K)	Total Bonded Water (wt%)	Roasting Time for 95% Bonded Water Removal (minutes)
Limonite	1193	1183	12.7	12
Nontronite	1233	1223	13.1	8
Garnierite	1283	1273	9.5	15

The roasting temperatures and estimates for the bonded water contents of the dried ores are shown in Table 4.2. The removal of bonded water with roasting time, as a percent total in the dried ore, is shown in Figure 4.1. The percent of residual bonded water retained within each calcine after roasting in air for 30 minutes at 850°C (1123 K), 900°C (1173 K) and 950°C (1223 K) was also determined for later reference; these amounts are summarised in Table 4.3.

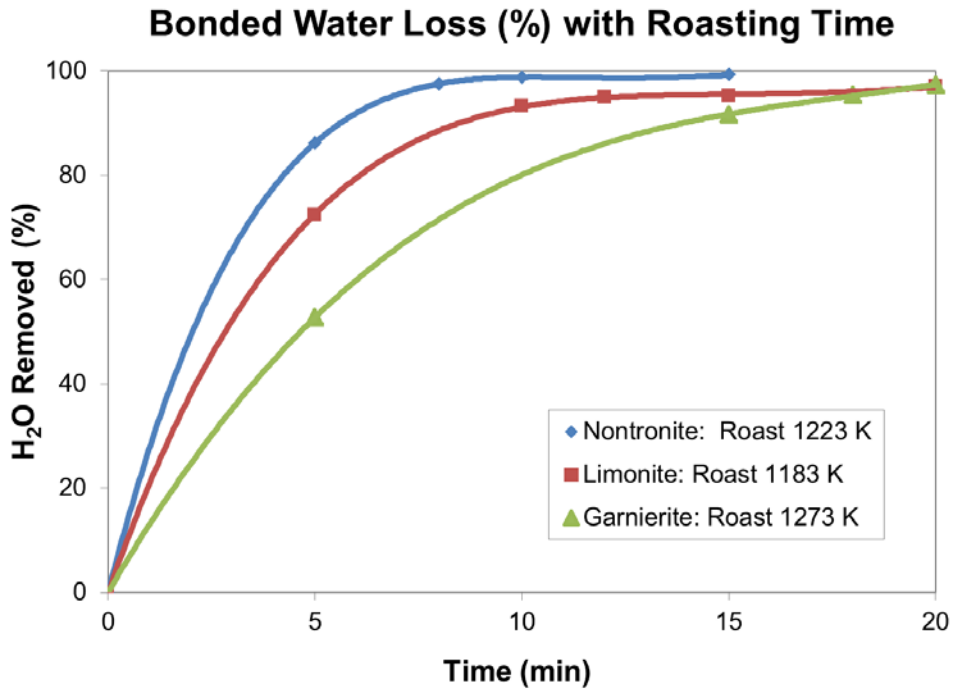

Figure 4.1 Bonded Water Removal from Laterites by Roasting

Mineralogical and size analyses of the dried, -212 µm limonite and garnierite ore samples were carried out by CSIRO in Perth using Quantitative Evaluation of

Minerals by Scanning Electron Microscopy (QEMSCAN); Amdel in Perth carried out similar analyses for nontronite.

Table 4.3 Retained Water in Laterites after Calcining

Ore was roasted in air for 30 minutes at the specified temperatures.

Temperature (K)	Retained Water (%)		
	Limonite	Nontronite	Garnierite
1123	0.75	0.70	-
1173	0.69	0.52	0.80
1223	-	0.44	0.63

Representative calcines were obtained by roasting each ore in air for 30 minutes at 900^{o}C (1173 K), with the temperature chosen since it represented the mid-point of the temperatures used for segregation.

The limonite, nontronite and garnierite calcines were characterised using Thermogravimetric-Differential Scanning Calorimetry (TGA-DSC) and Mass Spectrometry Analysis (carried out by CSIRO, Perth), Quantitative Mineralogical X-ray Diffraction (XRD) (carried out by Sietronics, Canberra), Brunauer, Emmet and Teller (BET) surface area analysis (carried out by CSIRO, Perth), and by laser size and EDS-SEM analyses (carried out by this researcher at Curtin University).

Characterisation of the ores and calcines based on these analyses will now be presented.

4.1.1 Limonite Ore

The limonite ore mineralogy analysis is shown in Table 4.4 and the mineral size distribution is shown in Figure 4.2. The material presents as a typical limonite consisting of finely grained (mostly < 32µm) iron oxides, distributed as 60% goethite, 26% limonite and 7% hematite, in addition to minor amounts of other oxides. It should be noted that limonite is not a true mineral; the name is generic for hydrated iron(III) oxide-hydroxides with varying compositions.

The distribution of Ni between the minerals in the limonite ore was not studied in this work. However, the distribution of Ni within Western Australian limonite ores (Kalgoorlie and Ravensthorpe) and others (Weda Bay and Goro) has been extensively studied (Landers et al., 2011) using high resolution synchrotron X-ray diffraction (SXRD) and a nanoscale energy filtered transition electron microscope

(EFTEM). Individual goethite crystals were mapped and Ni was found to be uniformly distributed throughout the iron oxide lattice, with Fe, O and Ni being present in approximately constant proportions; no evidence of discrete nickel minerals was found.

Table 4.4 Mineralogy of Limonite Ore

QEMSCAN analysis by CSIRO (Perth).

Mineral	Mineral Formula	wt%
Goethite	FeO(OH)	60.2
Limonite	$FeO(OH).nH_2O$	26.1
Hematite	Fe_2O_3	7.15
Spinel	$MgAl_2O_4$	4.31
Kaolinite (clay)	$Al_2Si_2O_5(OH)_4$	0.34
Magnetite	Fe_3O_4	0.23
Others	-	1.66

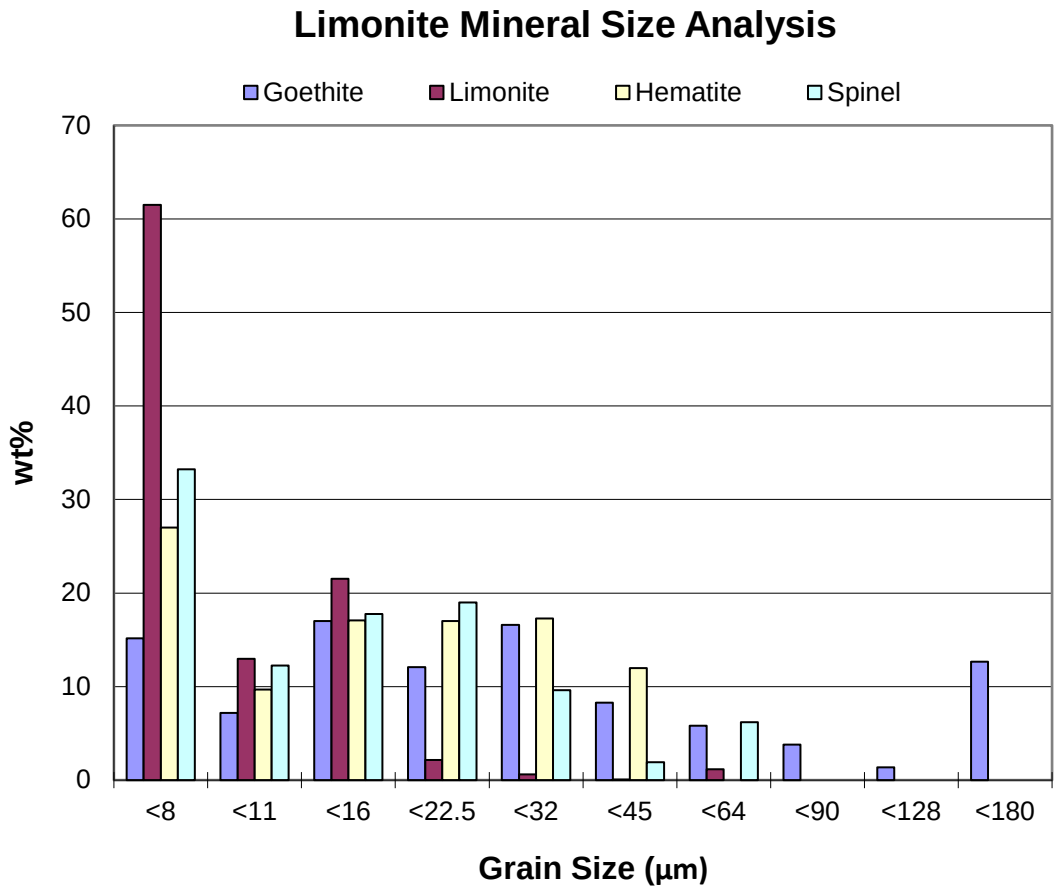

Figure 4.2 Mineral Size Distribution of Limonite Ore

QEMSCAN analysis by CSIRO (Perth).

4.1.2 Limonite Calcine

The XRD analysis of the laboratory roasted limonite ore showed that the calcine was predominantly hematite (92%) with a minor amorphous (7%) and brucite (1%) phases, as shown in Table 4.5.

Table 4.5 Mineralogy of Limonite Calcine

Ore roasted for 30 minutes in air at 1173 K; quantitative XRD[14] by Sietronics, Canberra (detection limit ~1-2% of sample)

Mineral	Formula	wt%
Hematite	Fe_2O_3	92
Amorphous	-	7
Brucite	$Mg(OH)_2$	1

The laser size analysis of the sample showed that 50% passed ~12 µm and 80% passed ~60 µm; the complete size analysis is shown in Figure 4.3. The BET analysis showed that the limonite calcine had a specific surface area of 7.68 m^2/g.

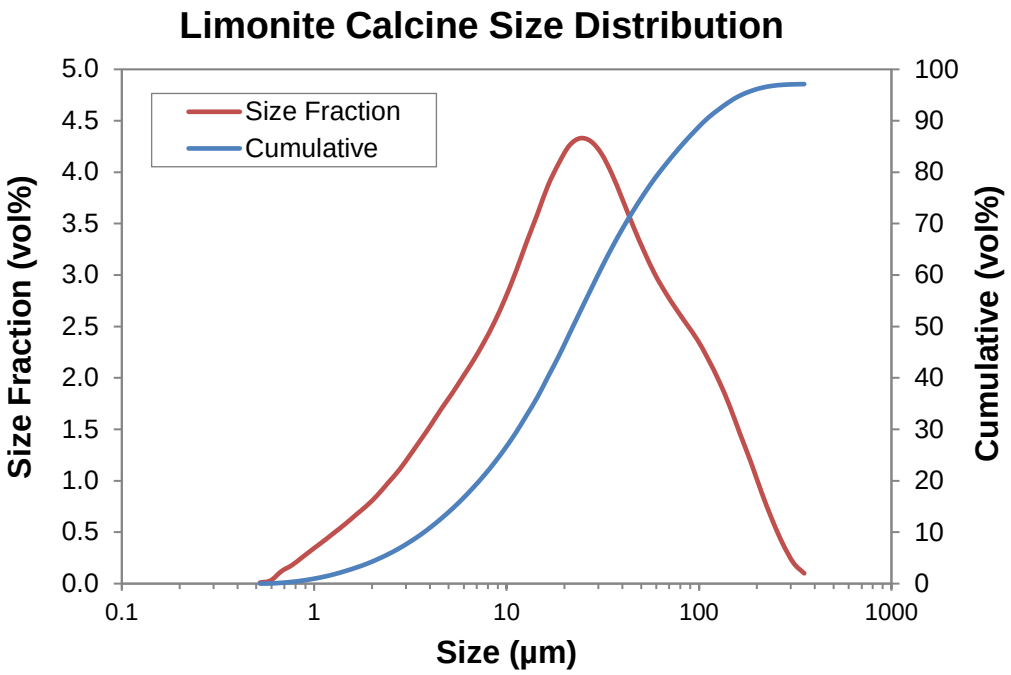

Figure 4.3 Laser Size Analysis of Limonite Calcine

Ore roasted 30 minutes in air at 1173 K.

[14] Results from quantitative XRD are quoted throughout this work; this method has a detection limit of ~2%

The mineralogy of the limonite calcine is consistent with previous studies on the dehydroxylation of goethite by heating in air, which has been extensively studied (Wolska, 1988; Wolska and Schwertmann, 1989; Gualtieri and Venturelli, 1999; Ruan et al., 2002a; Ruan et al., 2002b; Wells et al., 2006). Initial dehydroxylation begins at ~325^{o}C (598 K) and continues until ~425^{o}C (698 K), and results in the formation of an OH containing hematite-like phase called OH-hematite. The release of water during this low temperature transformation results in a significant increase in surface area through the formation of micro-pores and crystal structure defects.

As the temperature is increased, the micro-pores close and the crystal structure defects are removed; this results in a halving of the specific surface area when the temperature reaches ~900^{o}C (1173 K) (Landers et al., 2009a; Landers et al., 2009b). At this temperature, the dehydroxylation of hematite is complete and crystalline hematite becomes the stable phase. The TGA-DSC/mass spectrometry curves produced by heating the limonite ore from this work in air can be interpreted in terms of these reported mineralogical changes; the details are presented in Appendix A3.1

Based on the extensive previous work on the mineralogy of Western Australian and other limonite ores, it was accepted that Ni would be evenly dispersed throughout the hematite within the calcine produced in this work.

However, the reactivity of Ni within a roasted limonite may depend on the temperature of roasting and the crystallinity of the resulting hematite. Ni associated with OH-hematite, which forms around the limonite dehydroxylation temperature of ~325^{o}C (598 K), may be more reactive than Ni associated with crystalline hematite, which forms after roasting at 800^{o}C (1073 K). Ambient temperature leaching studies have shown that Ni leaches 9 to 34 times faster from the lower temperature OH-hematite compared to the higher temperature crystalline hematite (Landers et al., 2009a; Landers et al., 2009b).

4.1.3 Nontronite Ore

The nontronite ore mineralogy and equivalent average spherical diameter (ESD) size analyses are presented in Table 4.6. The minerals in the ore are dominantly nontronite (46%) and quartz (37%) along with lesser chromite (15%) and other minor oxides. The ESD of all minerals is 15 µm or less, except for the larger chromite which has an ESD of 47 µm.

The nontronite mineral is an Fe rich ferric smectite clay with a 2:1 clay structure consisting of tetrahedral-octahedral-tetrahedral (TOT) layers. The octahedral sheet is sandwiched between two tetrahedral silicate sheets and is rich in ferric ions. Each TOT layer has a net negative charge and is separated by a positively charged interlayer consisting of water and exchangeable cations, dominantly Mg^{2+} in WA nontronite, along with lesser Ca^{2+}, K^{+} and Na^{+} (Gaudin et al., 2004a; Gaudin et al., 2004b).

Table 4.6 Mineralogy and ESD Size of Nontronite Ore

ESD is equivalent average spherical diameter; QEMSCAN analysis by Amdel (Perth).

Mineral	Mineral Formula	wt%	ESD (μm)
Nontronite	$Fe_2Si_4O_{10}(OH)_2.M^{+}.nH_2O$	46.1	15
Quartz	SiO_2	36.8	9.4
Chromite	$FeCrO_4$	15.0	37
Fe Oxides	Fe_xO_x	1.44	8.6
Ni Bearing Smectite	$(Al,Mg,Ni,Fe)_2Si_4O_{10}(OH)_2.M^{+}.nH_2O$	0.30	8.9
Kaolinite	$Al_2Si_2O_5(OH)_4$	0.21	9.0
Minor Phases	-	0.13	8.8

Wells and Chia (2011) used the CSIRO HyChips automated scanning system to conduct a detailed study of the laterite mineralogy and composition of ores from the Kalgoorlie Nickel Deposit in Western Australia, the source of ores used in this work. It was reported that Ni in the nontronite ore was essentially all within the nontronite and iron oxide minerals, and that no Ni was contained within the free silica in the ore.

The crystal chemistry and Ni distribution of nontronite minerals (ferric smectites) from the Murrin Murrin nickel laterite deposit in Western Australia have been studied using a range of advanced techniques, specifically: Induction Coupled Plasma-Atomic Emission Spectroscopy (ICP-AES); Energy Dispersive Spectroscopy-Scanning Electron Microscopy (EDS-SEM); Transmission Electron Microscopy (TEM-EDX); and Mössbauer Spectroscopy (Gaudin et al., 2004a; Gaudin et al., 2004b). The only Ni rich phase identified in the ore was nontronite. This mineral had Fe as the dominant cation and virtually all of the Ni was substituted within the octahedral sheets of the nontronite mineral.

After roasting in air, the significant quartz (37%) and chromite (15%) in the nontronite ore (Table 4.6) were found by EDS-SEM analysis to have dense

unreacted crystalline cores that contained no Ni (Figure 4.8). This confirmed that Ni was only associated with the 46% nontronite and the 1.4% iron oxide minerals (Table 4.6) within the nontronite ore, in agreement with the work of Wells and Chia (2011).

4.1.4 Nontronite Calcine

The XRD analysis of the laboratory roasted nontronite ore confirmed that the calcine contained iron oxide as hematite (45%) with minor maghemite (5%), along with silica as cristobalite (20%) and an amorphous phase (30%), as shown in Table 4.7.

Table 4.7 Mineralogy of Nontronite Calcine

Ore roasted for 30 minutes in air at 1173 K; XRD by Sietronics, Canberra (detection limit ~1-2% of sample)

Roasted Nontronite Ore		
Mineral	Formula	wt%
Hematite	Fe_2O_3	45
Amorphous	-	30
Cristobalite	SiO_2	20
Maghemite	Fe_2O_3	5

The laser size analysis of the sample showed that 50% passed ~30 µm and 80% passed ~100 µm; the complete size analysis is shown in Figure 4.4. The BET analysis showed that the nontronite calcine had a specific surface area of 22.1 m^2/g.

The dehydration and dehydroxylation of the nontronite mineral by heating in air has been extensively studied (Grim and Kulbicki, 1961; MacKenzie and Rogers, 1977; Ding and Frost, 2002; Frost et al., 2002). It has been reported that dehydration occurs up to ~125ºC (398 K) and dehydroxylation from ~250-400ºC (523-673 K) in multiple steps, with the temperatures being dependent on the composition of the nontronite.

MacKenzie and Rogers (1977) observed that the nontronite mineral maintains its structure after dehydroxylation, with the structure only being destroyed at higher temperatures through the crystalisation of a spinel resembling maghemite (γ-Fe_2O_3). This spinel ultimately transforms to hematite from ~900ºC (1173 K), and to hematite and cristobalite from ~1150°C (1373 K), as shown in Figure 4.5.

The TGA-DSC/mass spectrometry curves produced by heating the nontronite ore from this work in air can be interpreted in terms of these reported mineralogical changes; the details are presented in Appendix A.3.2.

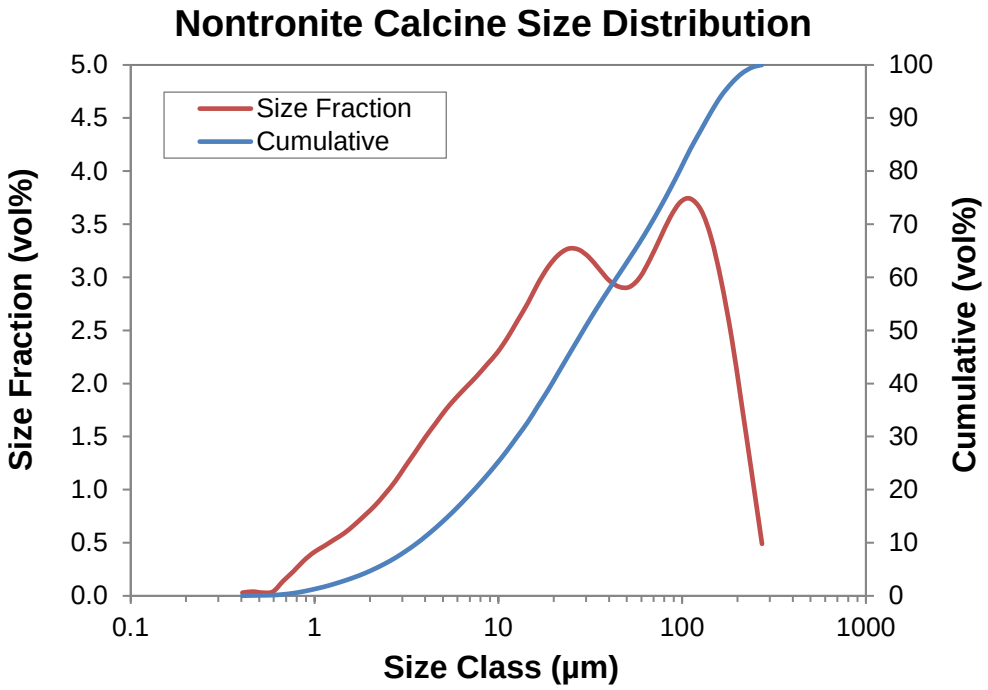

Figure 4.4 Laser Size Analysis of Nontronite Calcine

Ore roasted in air for 30 minutes at 1173 K..

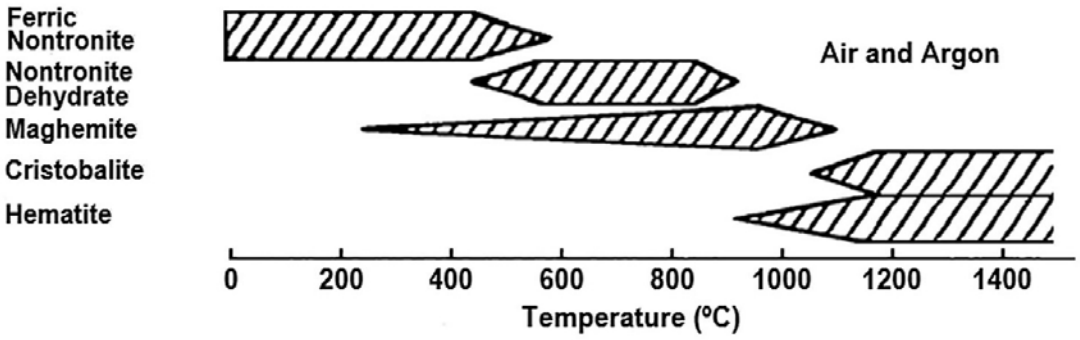

Figure 4.5 Mineralogy of the Nontronite Mineral Heated in Air

Phases observed by MacKenzie and Rogers (1977) from 0 to 1773 K through XRD analysis of the roast product.

A sample of nontronite calcine was resin-mounted, polished and carbon-coated for EDS-SEM analysis. The Ni was found to be located within nontronite dehydroxylate consisting of finely grained/amorphous conglomerates of intimately mixed iron oxide and silica, as illustrated by a backscattered electron image in Figure 4.6, and in

Figure 4.7 by an element intensity map, with Ni shown in green, Fe in red and Si in blue. Comparison of these figures indicates that the iron oxide ranges in size from very fine (< 5 μm) to amorphous, while at least part of the silica makes up the coarser particles. The Ni is dispersed throughout the dehydroxylate but most likely is associated with the iron oxide.

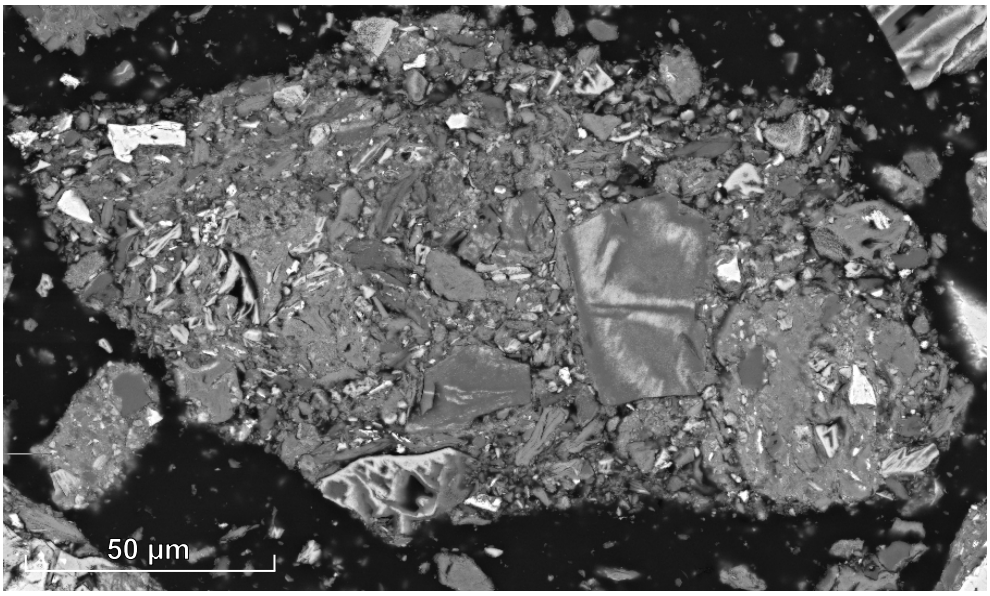

Figure 4.6 Section through a Nontronite Dehydroxylate
SEM image through a fine to amorphous mixture of iron oxide and slightly larger silica; image is of Particle 1 in Figure 4.8.

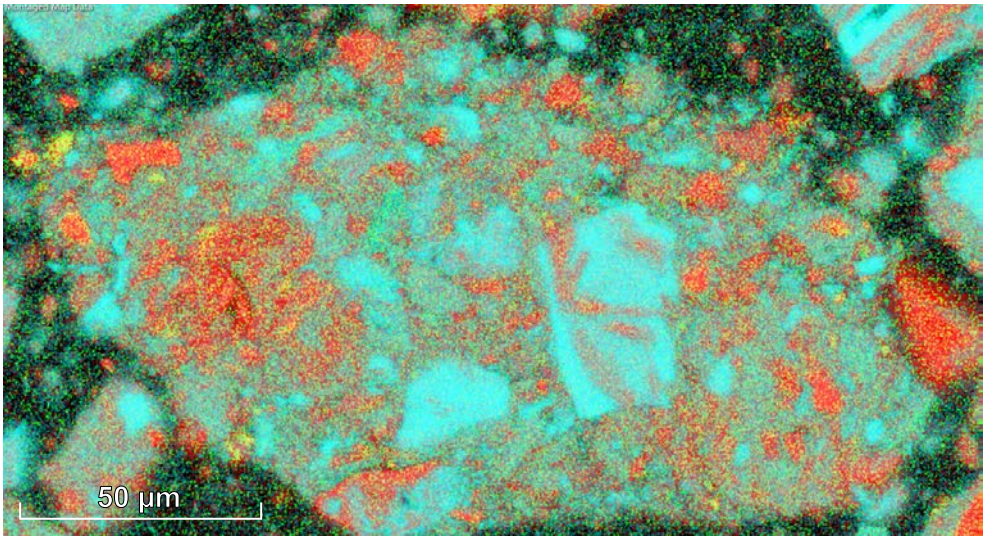

Figure 4.7 Element Map of a Nontronite Dehydroxylate
EDS map of Ni (green), Fe (red), Si (blue) for Particle 1, Figure 4.8

These conglomerate particles were found throughout the calcine, as illustrated by particles 1 through 4 in Figure 4.8. This figure shows a backscattered electron image of a 1 mm x 1 mm (1000 µm x 1000 µm) cross section of calcine, for which detailed Al, Ca, Cr, Fe, Mg, Ni and Si element maps were generated; these are provided in Appendix B.13 for reference.

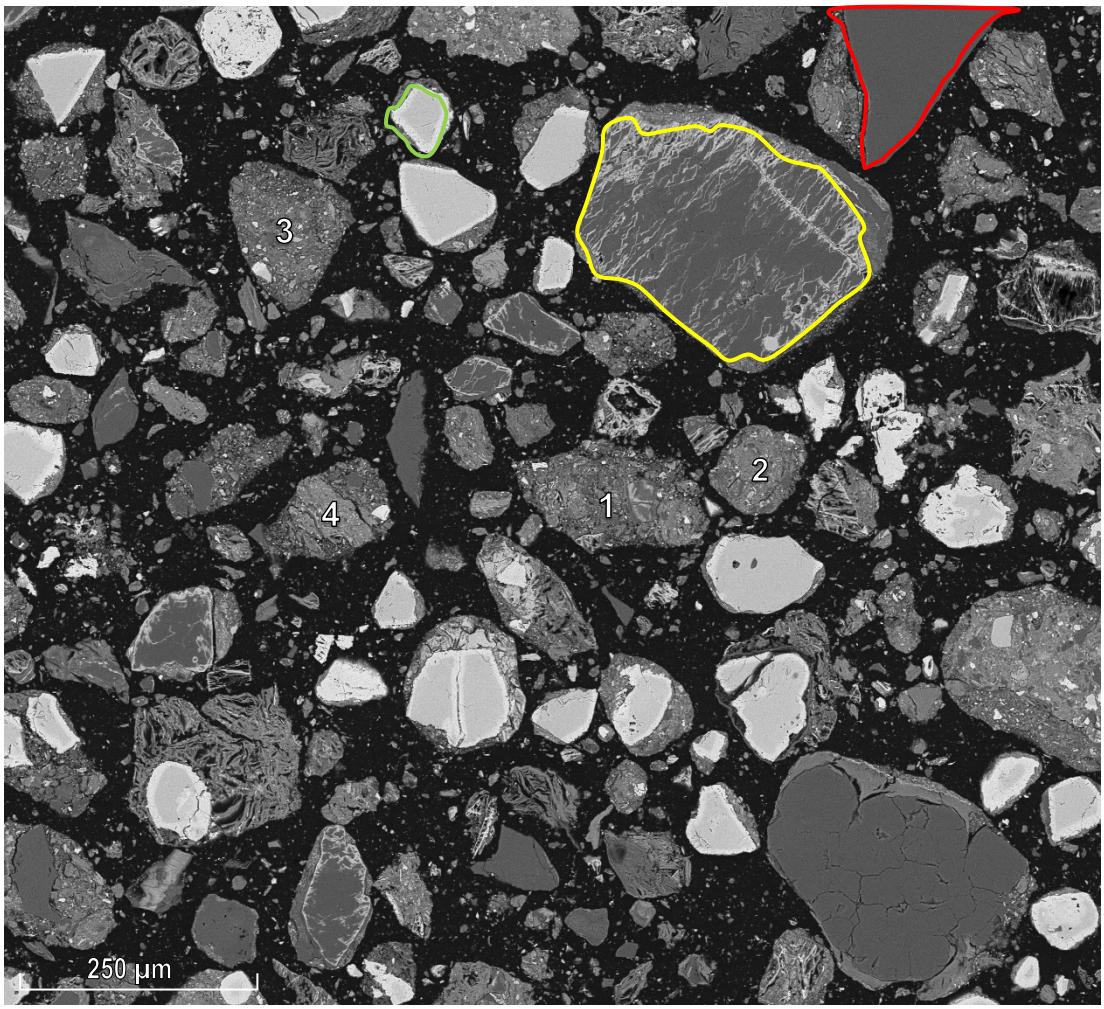

Figure 4.8 Section through a Nontronite Calcine

SEM image showing examples of particles formed after roasting nontronite in air for 30 minutes at 1173 K, specifically: nontronite dehydroxylate conglomerate particles (numbered 1 to 4), large grained primary and partly weathered silica (respectively outlined in red and yellow) and surface weathered Cr rich spinels (outlined in green).

Area compositions for each of the four dehydroxylate conglomerate particles identified in Figure 4.8 are summarised in Table 4.8. The table shows that all particles contained on average 1.6% Ni with a Fe/Si mole ratio of 0.51, very close to that of 0.5 for the mineral nontronite (Table 4.6). There is little doubt these particles

represent the dehydroxylation product of the mineral. Based on the average molar formula of these particles ($Fe_{0.51}SiO_{2.7}$), they likely are a mixture of 20% Fe_2O_3 and 80% SiO_2.

Table 4.8 Composition of Nontronite Dehydroxylate

Particle numbers refer to Figure 4.8; chemical analysis via EDS-SEM.

Particle Figure 4.8	Ni (wt%)	Average Composition (moles)
1	1.5	$Fe_{0.53}SiO_{2.8}$
2	1.5	$Fe_{0.45}SiO_{2.6}$
3	1.6	$Fe_{0.57}SiO_{2.9}$
4	1.7	$Fe_{0.51}SiO_{2.7}$
Average	1.6	$Fe_{0.51}SiO_{2.7}$

It is possible that Ni enrichment occurs on the surface of the nontronite dehydroxylate. Sidhu et al. (1980) found that up to 60% of the Ni and Co may be ejected from the maghemite structure as it transforms to hematite, possibly resulting from a 3-4 fold decrease in surface area. Some areas within Figure 4.7 appear more concentrated in Ni than others, but it was not possible to confirm whether this type of enrichment took place during dehydroxylation.

In addition to the dehydroxylate conglomerate particles containing Ni, three other types of particles were identified, but none contained Ni. One example of each is highlighted in Figure 4.8, specifically: large grained primary silica (outlined in red), large grained partially weathered silica (outlined in yellow), and relatively large Cr rich spinel (outlined in green).

The primary silica grains likely represent the 30% cristobalite detected by X-ray analysis (Table 4.7). The Cr rich spinels were reported as 15% chromite (Table 4.6) in the X-ray analysis of the nontronite ore, but were not detected in the X-ray analysis of the calcine (Table 4.7). Tathavakar et al. (2005) studied the thermal decomposition of chromite in air and found that oxidation of Fe^{2+} in chromite promotes the formation of an intermediate metastable maghemite-type spinel phase. The Cr rich spinels in the calcine had a spinel core (~$Fe_{0.8}Mg_{0.2}AlCrO_4$) surrounded by a noticeably lighter coloured phase (Figure 4.8), with the maghemite-like formula of $FeCrO_3$. It seems that the formation of this oxidation layer on the Cr rich spinel masked the detection of these particles by XRD.

4.1.5 Garnierite Ore

The garnierite ore mineralogy is summarised in Table 4.9. The hydrous magnesium silicates typical of garnierite ores are chlorite (16%, clinochlore and nimite) and serpentine (7.3% lizardite). These were present along with significant quartz (49%), iron oxides (7.6% limonite + goethite, 1% hematite), carbonate (5.4% dolomite and 1% ankerite), chromite (1.9%), kaolinite clay (1.2%) and other minor minerals.

Table 4.9 Mineralogy of Garnierite Ore
QEMSCAN analysis by CSIRO (Perth).

Mineral	Mineral Formula	wt%
Quartz	SiO_2	49.3
Clinochlore	$(Mg_5Al)(AlSi_3)O_{10}(OH)_8$	12.0
Lizardite	$(Mg,Fe)_3Si_2O_5(OH)_4$	7.25
Dolomite	$CaMg(CO_3)_2$	5.42
Nimite	$(Ni,Mg,Fe^{2+})_5Al(Si_3Al)O_{10}(OH)_8$	4.33
Limonite	$FeO(OH).nH_2O$	4.26
Goethite	$FeO(OH)$	3.37
Diopside	$MgCaSi_2O_6$	2.42
Chromite	$FeCr_2O4$	1.86
Ti-mineral	-	1.31
Kaolinite (clay)	$Al_2Si_2O_5(OH)_4$	1.15
Ankerite	$Ca(Fe,Mg,Mn)(CO_3)_2$	0.93
Hematite	Fe_2O_3	0.90

The mineral size distribution is shown in Figure 4.9. The majority of the material is <50 µm; larger sizes up to 212 µm are mainly quartz, dolomite and diopside.

In common with the nontronite mineral, the chlorite minerals are 2:1 clays which have a silicate structure consisting of negatively charged TOT layers; unlike nontronite, the positively charged interlayer separating the TOT layers is composed of magnesium and iron hydroxide $(Mg^{2+},Fe^{3+})_3(OH)_6$, commonly referred to as brucite (Brindley and Chang, 1974).

The serpentine mineral lizardite is a 1:1 clay with a tetrahedral-octahedral (TO) structure consisting of stacks of tetrahedral silicate layers connected to octahedral magnesium hydroxide $Mg(OH)_2$ (brucite) layers, held together by van der waals forces. Lizardite has a flat TO structure, whereas the other serpentine minerals, chrysotile and antigorite, have rolled and modulated TO layers respectively (Viti, 2010).

The distribution of Ni between the minerals in the garnierite ore was not studied in this work. Bunjaku et al. (2011) studied garnierite ores using EDS-SEM and found

that Ni was present mainly within the hydrous magnesium silicates with lesser amounts within goethite. The Ni is most likely substituted for Mg in the brucite interlayer of nimite and clinochlore, for Mg in the brucite layer of lizardite, or for Fe within limonite and goethite (Brand et al., 1998). An EDS-SEM analysis of the roasted garnierite (Figure 4.14) indicated that the silica and Cr spinels were unreacted during roasting and contained no Ni.

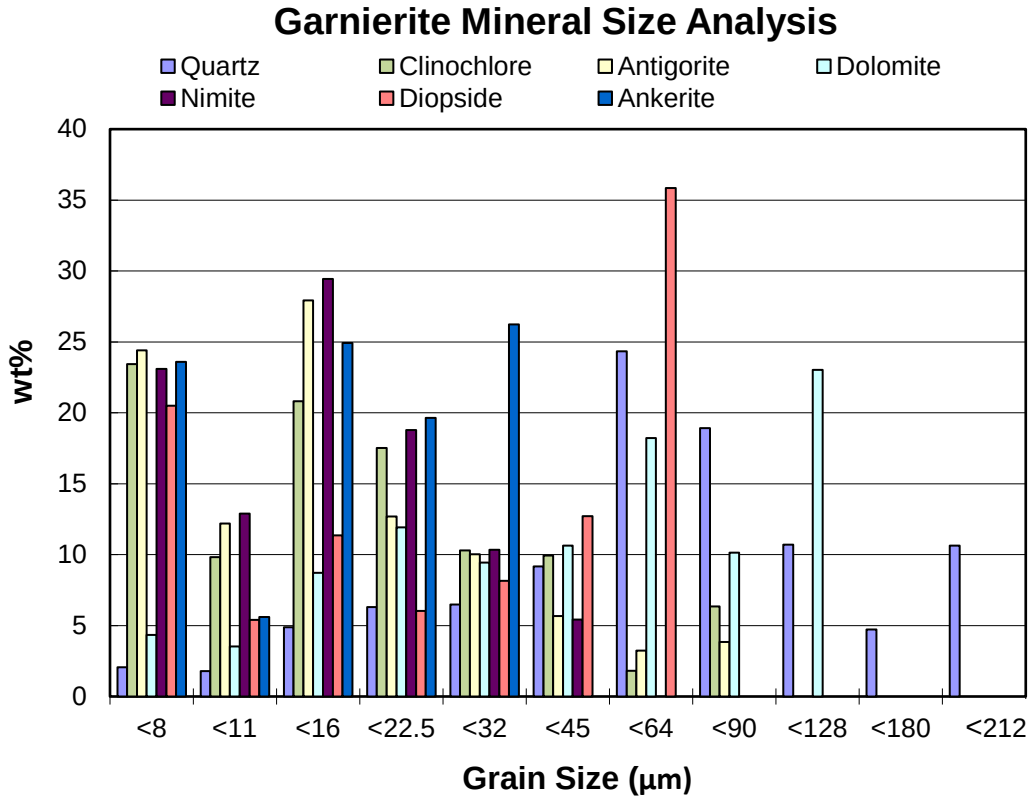

Figure 4.9 Mineral Size Distribution of Garnierite Ore

QEMSCAN analysis by CSIRO (Perth).

4.1.6 Garnierite Calcine

The XRD analysis of the laboratory-roasted garnierite showed that the calcine was predominantly quartz (33%), hematite (32%) and forsterite (23%) with a minor amorphous phase (5%), magnesia (4%) and remnant dolomite (3%), as shown in Table 4.10. The identification of remnant carbonate (dolomite) was considered atypical as none could be identified via EDS-SEM analysis of the calcine (Figure 4.14) and there did not appear to be any excess CO_2 during subsequent carbonaceous gas evolution measurements (Section 8.2.2). The 32% hematite also appeared excessive since the dried ore contained only 11.7% Fe (Table 4.1), which represents 16.7% Fe_2O_3.

Table 4.10 Mineralogy of Garnierite Calcine

Ore roasted for 30 minutes in air at 1173 K; XRD by Sietronics, Canberra

(detection limit ~1-2% of sample)

Roasted Garnierite Ore		
Mineral	Formula	wt%
Quartz	SiO_2	33
Hematite[1]	Fe_2O_3	32
Forsterite	Mg_2SiO_4	23
Amorphous	-	5
Magnesia	MgO	4
Dolomite[2]	$CaMg(CO_3)_2$	3

[1]The maximum Fe_2O_3 is 16.7% based on Fe in dried ore (Table 4.1);
[2]Dolomite was not found in the EDS-SEM analysis of the calcine.

The laser size analysis of the sample showed that 50% passed ~18 µm and 80% passed ~120 µm; the complete size analysis is shown in Figure 4.10. The BET analysis showed that the garnierite calcine had a specific surface area of 9.35 m^2/g, less than half that of the roasted nontronite (22.1 m^2/g); the lower specific surface area for garnierite is likely associated with the relatively high portion of crystalline material, as will be evident in Figure 4.14.]

The ore contained ~16% chlorite as clinochlore (12%) and nimite (4%). The dehydroxylation of clinochlore heated in air has been extensively studied (Brindley and Chang, 1974; Martin, 1977; Prieto et al., 1991; Lazarenkov et al., 2011), while one study has been conducted on the dehydroxylation of nimite (De Waal, 1970). The dehydroxylation of both clinochlore and nimite show the same characteristics.

There is a strong endothermic loss of ~75% of the water of crystallisation from ~500-750^{o}C (773-1023 K), commonly peaking at ~600^{o}C (873 K) due to dehydroxylation of the Mg or Fe-rich hydroxide sheets which separate the TOT clay layers. This results in the formation of a 'modified chlorite'.

An endothermic loss of ~25% of the water of crystallisation occurs from ~750-850^{o}C (1023-1123 K) due to dehydroxylation of the TOT clay layers, with a resulting breakdown in the chlorite structure, from which olivine and spinel crystallise exothermically from ~800-860^{o}C (1073-1133 K). In air, any Fe present in the mineral is converted to hematite. At ~1000^{o}C (1273 K) and above, olivine (dominantly forsterite Mg_2SiO_4) reacts with free silica to form pyroxene (dominantly enstatite $MgSiO_3$) according to:

$$Mg_2SiO_4(s) + SiO_2(s) \rightarrow 2MgSiO_3(s) \quad 4.1$$

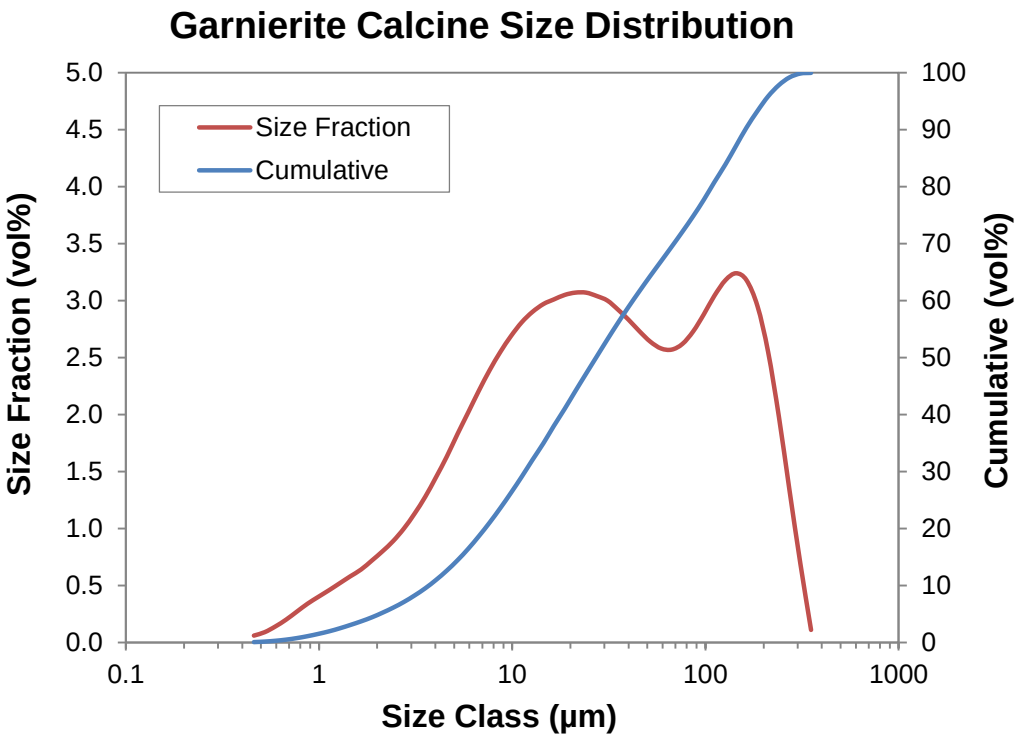

Figure 4.10 Laser Size Analysis of Garnierite Calcine

Ore roasted in air for 30 minutes at 1173 K.

The ore contained 7.3% serpentine as lizardite. The dehydroxylation of serpentine (lizardite, chrysotile and antigorite) has been extensively studied (Ball and Taylor, 1963; Brindley and Hayami, 1965; Martin, 1977; MacKenzie and Meinhold, 1994; Viti, 2010)

It is agreed that dehydroxylation occurs between ~600-800°C (873-1073 K) with the formation of porous, highly reactive and separate amorphous regions. One region is rich in Mg relative to Si, from which Mg-olivine (forsterite, Mg_2SiO_4) begins to crystallise during dehydroxylation and continues to crystallise and grow as the temperature is increased.

The other amorphous region is rich in Si relative to Mg from which Mg-pyroxene (enstatite, $MgSiO_3$) crystallises as the temperature is increased between ~800-1000°C (1073-1273 K). A reaction of residual silica with forsterite follows at ~1150°C (1423 K) to form additional enstatite.

Ultimately, the amorphous phase is entirely replaced by crystalline forsterite and enstatite such that the thermal decomposition of serpentine can be summarised stoichiometrically by the equation:

$$Mg_3Si_2O_5(OH)_4 \rightarrow Mg_2SiO_4 + MgSiO_3 + 2H_2O \quad 4.2$$

The ore contained 6.4% carbonate as dolomite (5.4%) and ankerite (1%). The dehydroxylation of dolomite in air occurs over two steps, with endothermic peaks at ~817ºC (1090 K) and ~927ºC (1200 K) (Robert and Heystek, 1951; Haul and Markus, 1952; Rowland, 1955). According to McIntosh et al. (1990), calcium carbonate is formed in the first step and then decomposed in the second step, as represented by:

$$CaMg(CO_3)_2(s) \rightarrow CaCO_3(s) + MgO(s) + CO_2(g) \quad 4.3$$

$$CaCO_3(s) \rightarrow CaO(s) + CO_2(g) \quad 4.4$$

The thermal decomposition of ankerite $Ca(Fe,Mg,Mn)(CO_3)_2$ in air occurs over three distinct endothermic steps (Kulp et al., 1951) within the temperature range ~670-930ºC (943-1203 K), with an exotherm associated with the oxidation of Fe^{2+} apparent after the initial decomposition endotherm. For calcite, the temperature of dissociation may be decreased in the presence of free silica through the formation of calcium silicate.

The TGA-DSC/mass spectrometry curves produced by heating the garnierite ore from this work in air can be interpreted in terms of these reported mineralogical changes; the details are presented in Appendix A3.3.

A sample of garnierite calcine was resin-mounted, polished and carbon-coated for EDS-SEM analysis. Ni was found within crystalline Mg-Al silicates, likely the dehydroxylation product of the chlorite minerals; and within fine to amorphous conglomerates of Mg-Fe silicate material, likely the dehydroxylation product of the serpentine mineral lizardite. Bunjaku et al. (2011) also studied air roasted garnierite ores and found Ni within Mg-Fe-Al silicates and Mg-Fe silicates.

The Mg-Al silicates found in this work were a mixture of pyroxene and olivine, indicative of the dehydroxylation product of the 16% chlorites in the dried ore (Table 4.9). These silicates were crystalline and generally located within crystalline silica particles as outlined in red in Figure 4.11. The Ni rich veins are clearly visible in blue within the EDS-SEM element map of the particle shown in Figure 4.12.

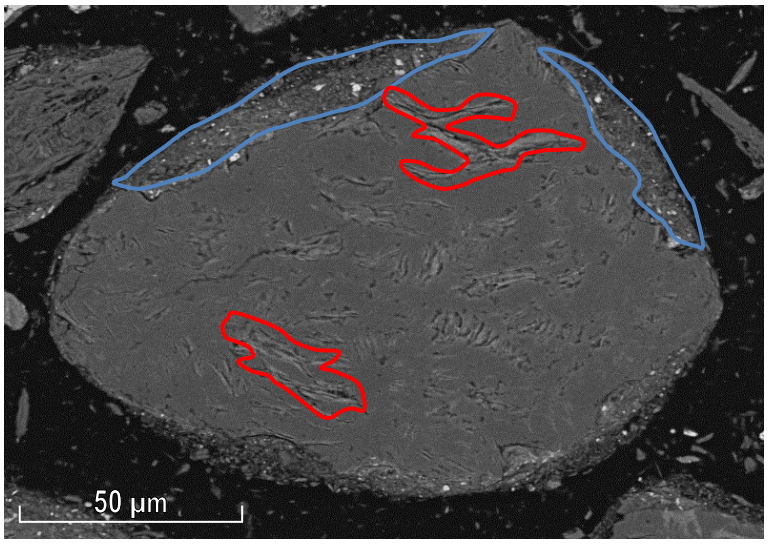

Figure 4.11 Section through a Garnierite Calcine Particle

SEM image through a silica particle with veins of pyroxene (e.g. ~11% Ni, area 5, Table 4.11) originating from chlorite (examples outlined in red), bordered by fine to amorphous serpentine dehydroxylate (~2% Ni, examples outlined in blue); particle is from Figure 4.14 (labelled Fig. 5.11,12).

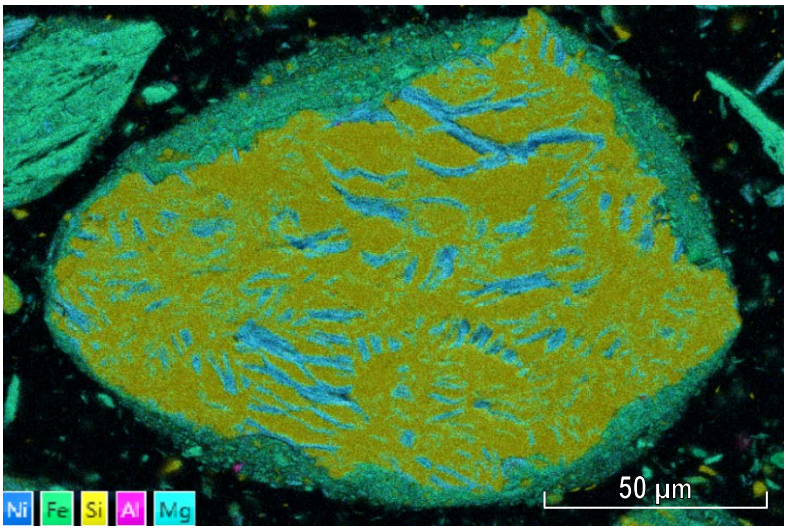

Figure 4.12 Element Map of a Garnierite Calcine Particle

Ni (blue), Fe (green), Si (yellow), Al (pink), Mg (teal); particle labelled Fig 4.11 & 4.12 in Figure 4.14.

Five areas of Mg-Al silicates within separate dehydroxylates were chemically analysed using EDS-SEM and found to have an average composition of $Mg_{0.97}Al_{0.44}Ni_{0.16}Fe_{0.11}SiO_{3.5}$, with 3-11 Ni%, as summarised in Table 4.11. The higher Ni particles may originate from nimite since this chlorite mineral is normally richer in Ni than clinochlore.

Table 4.11 Composition of Chlorite Dehydroxylation Products

Chemical analysis via EDS-SEM.

Area	Ni (wt%)	Average Composition (moles)
1	3.2	$Mg_{1.03}Al_{0.35}Ni_{0.07}Fe_{0.08}SiO_{3.4}$
2	8.3	$Mg_{1.00}Al_{0.41}Ni_{0.21}Fe_{0.12}SiO_{3.8}$
3	8.9	$Mg_{0.91}Al_{0.38}Ni_{0.20}Fe_{0.10}SiO_{3.4}$
4	7.2	$Mg_{0.96}Al_{0.62}Ni_{0.17}Fe_{0.12}SiO_{3.6}$
5	11	$Mg_{0.82}Al_{0.35}Ni_{0.22}Fe_{0.08}SiO_{2.9}$
Average	7.7	$Mg_{0.94}Al_{0.42}Ni_{0.17}Fe_{0.10}SiO_{3.4}$

Based on Fe content, and its amorphous nature, the Mg-Fe silicate material was most likely the dehydroxylation product from the 7.25% serpentine in the dried ore (Table 4.9). The material consisted of intimate mixtures of hematite, silica and Mg silicates, found on the borders of crystalline particles of silica, hematite and Cr spinel. For example, the silica rich particle shown in Figure 4.11 contains areas of serpentine dehydroxylate conglomerate particles (outlined in blue); the hematite particle shown in Figure 4.13 is also bordered by the dehydroxylate.

Four separate regions of these dehydroxylates were analysed via EDS-SEM and found to have an average composition of $Mg_{0.88}Fe_{0.41}Al_{0.10}Ni_{0.05}Ca_{0.04}SiO_{2.7}$, with 1.9-2.4% Ni, as summarised in Table 4.12.

Table 4.12 Composition of Serpentine Dehydroxylate

Areas from particles shown in Figure 4.11; chemical analysis via EDS-SEM.

Area	Ni (wt%)	Average Composition (moles)
1	1.9	$Mg_{0.88}Fe_{0.42}Al_{0.09}Ni_{0.04}Ca_{0.04}SiO_{2.7}$
2	2.4	$Mg_{0.89}Fe_{0.40}Al_{0.10}Ni_{0.05}Ca_{0.05}SiO_{2.7}$
3	2.2	$Mg_{0.87}Fe_{0.45}Al_{0.10}Ni_{0.05}Ca_{0.04}SiO_{2.6}$
4	2.3	$Mg_{0.89}Fe_{0.37}Al_{0.10}Ni_{0.05}Ca_{0.05}SiO_{2.7}$
Average	2.2	$Mg_{0.88}Fe_{0.41}Al_{0.10}Ni_{0.05}Ca_{0.04}SiO_{2.7}$

The amorphous nature of the serpentine dehydroxylate was similar to that identified for the nontronite dehydroxylate (Figure 4.6). This structure most likely arose due to oxidation of Fe^{2+} to Fe^{3+} during calcination, with Fe^{3+} being forced out of the original structure to crystallise as hematite, with the remaining material crystallising as Mg silicates (forsterite and enstatite) and silica. Due to the intimately mixed nature of

these particles, it was difficult to determine by EDS-SEM whether the Ni was associated with the Mg silicates or the hematite.

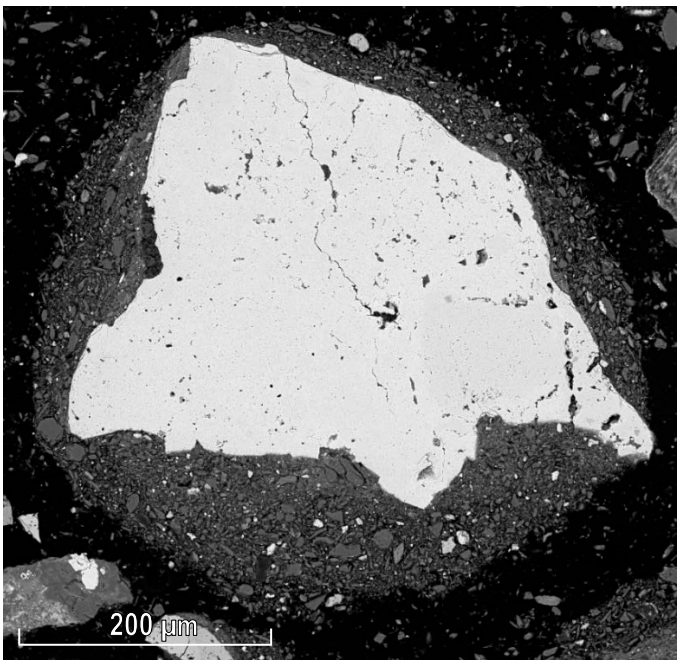

Figure 4.13 Serpentine Dehydroxylate bordering Hematite

SEM image through a hematite particle bordered by fine to amorphous serpentine dehydroxylate; hematite particle labelled Fig. 4.13 in Figure 4.14.

One rare manganese oxide rich particle of ~25 µm in size, containing 15% Ni and 7.5% Co with an average formula of $Mn_{0.42}Mg_{0.18}Ni_{0.2}Co_{0.1}O$ was also identified and has been outlined in purple on Figure 4.14. This particle would have originated from manganese wad, not identified within the unroasted ore (Table 4.9), but known to be present in the garnierite layer of nickel laterite deposits (Golightly, 1979).

Figure 4.14 shows a backscattered electron image of a 1.5 mm x 1.5 mm (1500 µm x 1500 µm) cross section of garnierite calcine that contains the particles shown in Figure 4.11, Figure 4.12 and Figure 4.13. Element maps for Al, Ca, Cr, Fe, Mg, Ni and Si for the section are provided in Appendix B.14.

Figure 4.14 shows the large crystalline silica particles that were dominant throughout the calcine, consistent with the 30% quartz identified in the calcine by XRD (Table 4.10); two examples are outlined in dark blue. Large crystalline hematite particles were also present; two examples are outlined in red. Neither the crystalline quartz nor the crystalline hematite contained any Ni.

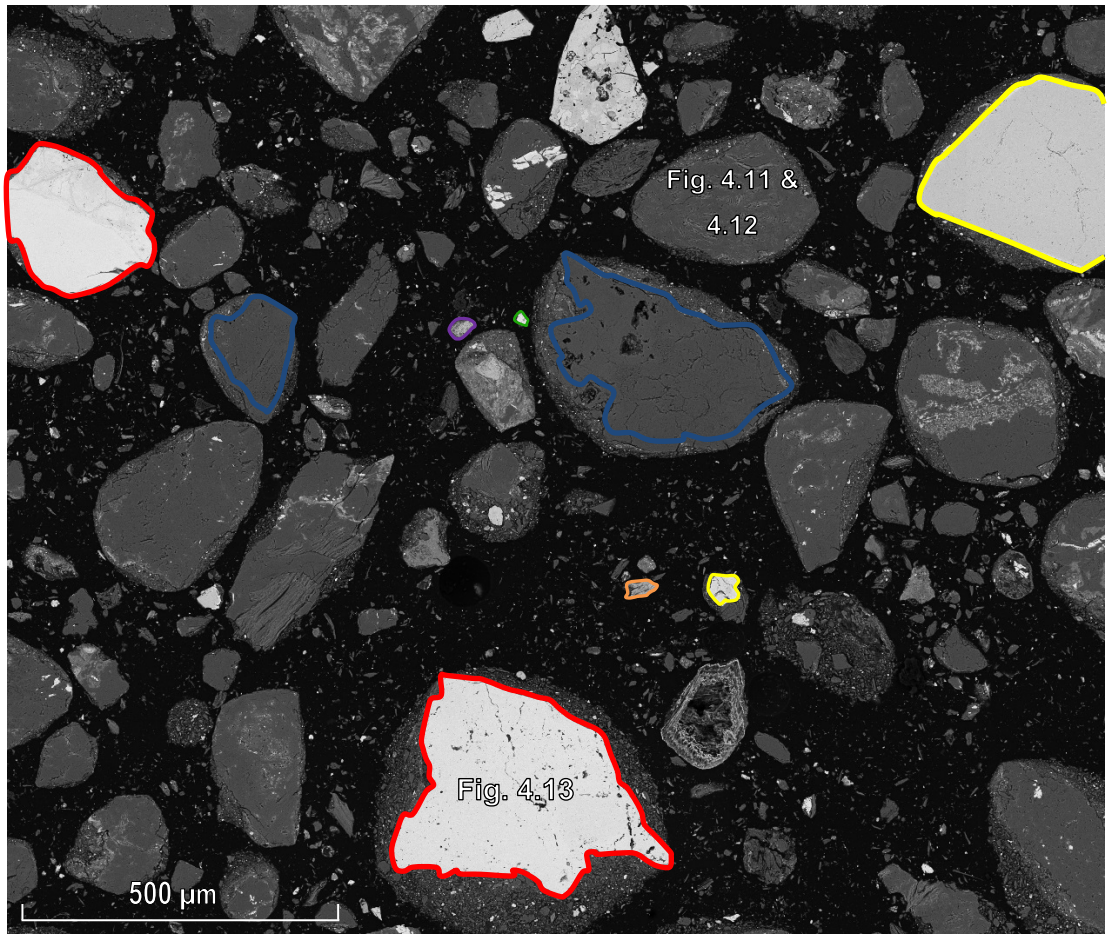

Figure 4.14 Section through a Garnierite Calcine

SEM image showing examples of particles formed after roasting garnierite in air for 30 minutes at 1173 K, specifically: crystalline hematite (red), quartz (dark blue), chromite (yellow), primary forsterite (orange) and monoxides (green); manganese oxide (purple). Examples of chlorite and serpentine dehydroxylates are shown in Figure 4.11, Figure 4.12 and Figure 4.13.

Other Ni free particles within the garnierite calcine section shown in Figure 4.14 include: minor Cr rich spinels (examples outlined in yellow), also identified within the nontronite calcine (Figure 4.8), with a core of $Fe_{0.7}Mg_{0.3}Al_{0.6}Cr_{1.4}O_4$ and an oxidised boundary of maghemite-like $FeCrO_3$; primary Mg silicates (~10-30 µm in size, example outlined in orange) with an average formula of $\sim Mg_{1.4}Fe_{0.04}SiO_3$; and monoxide particles (~10-30 µm in size, example outlined in green) originating from carbonates, some were pure MgO, but in general had the formula $Mg_xCa_yFe_zO_{x+y+z}$.

4.2 Carbon Characteristics

Metallurgical coke (mainly referred to as coke in this work) was obtained as lump material from One Steel Limited. Coconut activated carbon was obtained from Haycarb Holdings Ltd. Both carbons were ground and sized to 125-300 µm for use in subsequent reduction and segregation tests. Representative samples were analysed by CSIRO (Perth) for carbon, sulphur, ash content, absolute density and specific surface area. The results are presented in Table 4.13.

Table 4.13 Analyses of Solid Carbon Reductants

Carbon	C (wt%)	S (wt%)	Ash (wt%)	Density g/mL	Specific Surface Area m^2/g
Metallurgical Coke	78.3	0.406	11.5	1.9	1160
Activated Carbon	88.7	0.062	1.77	2.3	4.3

The laser size analysis of representative samples showed that for coke, 50% passed ~190 µm and 80% passed ~280 µm; for activated carbon, 50% passed ~225 µm and 80% passed ~300 µm. The full analyses are shown in Figure 4.15 for coke and Figure 4.16 for activated carbon.

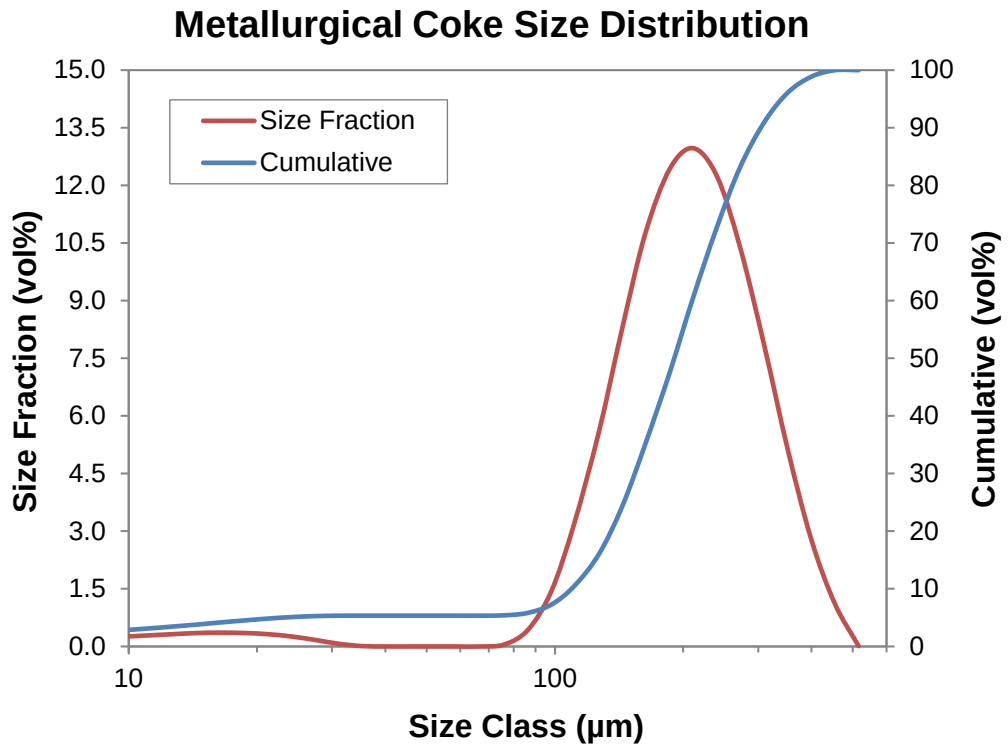

Figure 4.15 Laser Size Analysis of Metallurgical Coke

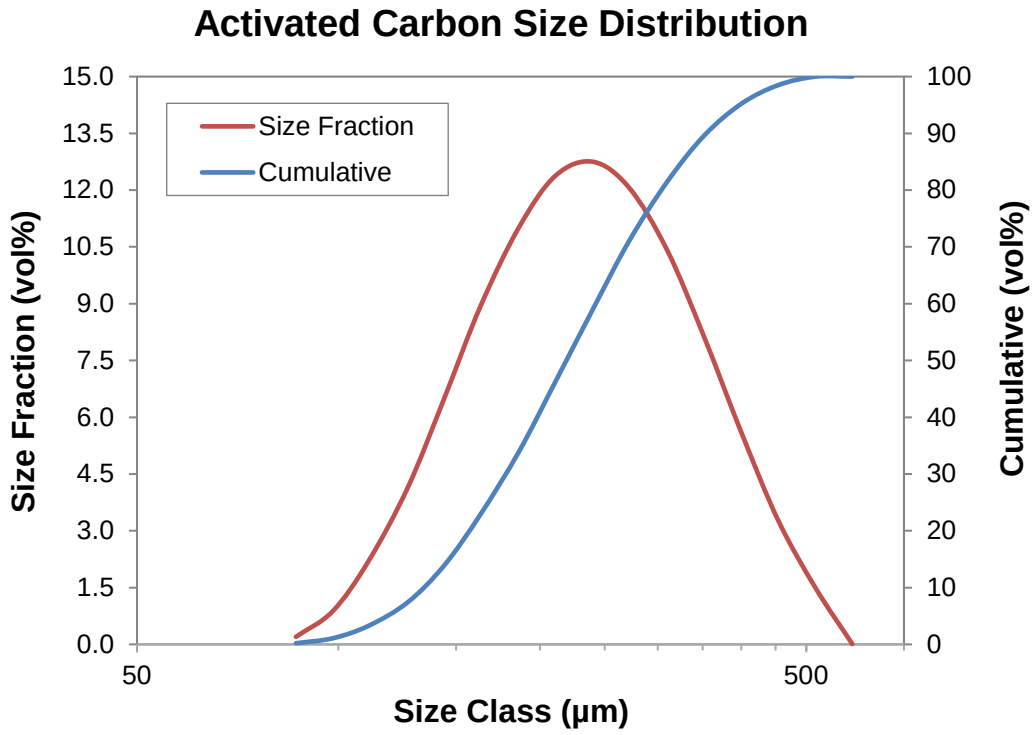

Figure 4.16 Laser Size Analysis of Activated Carbon

4.3 Discussion

Knowledge of the sintering temperature of each ore was used to determine the range of segregation temperatures; with a few exceptions, all tests were carried out below the sintering temperature so that the segregation bed would remain mechanically fluidised throughout the reaction. Knowledge of the bound water retained within the calcine after roasting at a particular temperature was a valuable reference for later assessing the potential effects of moisture on the segregation process.

Analysis of the laterite calcines confirmed that Ni was dominantly contained within fine particles. These particles were likely to be accessible by gas for chemical reaction at segregation temperatures, provided significant recrystallisation and grain growth did not occur.

Knowledge of the location of Ni within each calcine provided an important reference for the later analysis of Ni recoveries after carbon reduction or segregation. For limonite, Ni was likely present at a concentration of ~1% Ni, evenly distributed throughout finely grained to amorphous hematite; 80% of these particles passed 60 µm. For nontronite, Ni was associated with fine to amorphous mixtures of hematite

and silica at a concentration of ~1.6%; 80% of the particles in the calcine passed 100 µm, with some larger crystalline particles of silica and Cr spinel. For garnierite, Ni was associated with fine crystalline veins of Mg-Al silicate at a concentration of 3-11%, and with relatively amorphous mixtures of hematite, silica and Mg silicates at a concentration of ~2% Ni; 80% of the particles within the calcine passed 120 µm, with a significant portion of large crystalline silica and hematite particles.

Knowledge of the physical nature of the solid phases within each calcine provided a useful guide to potential surface contact kinetic limitations that may hinder the formation of solid solution products during reduction or segregation.

Chapter 5

Nickel Laterite Reduction with Solid Carbon

There are few published works on the role of solid carbon during the reduction of nickel laterite ores (Harris et al., 2009). Experimental reduction is generally carried out by passing reducing gases (CO and H_2) through the ore, rather than by generating these gases in-situ via carbon gasification. Given the limited information on nickel laterite solid carbon reduction systems, a study was carried out to investigate the changes in mineralogy during reduction, and the conditions under which metal oxides are reduced in-situ to ferronickel. The results from this study are presented in this chapter, and later compared with those from the more complex segregation process (Sections 6.2.4, 7.2.4, 8.2.4), in which the chloridisation of metal oxides, rather than their reduction to metal, is the first step in the process.

The three WA nickel laterite ores (limonite, nontronite and garnierite) were roasted in air before being reduced with either metallurgical coke (hereafter referred to as coke), or activated carbon (also referred to as Act C). The carbons were sized to 125-300 µm and added at 5 wt% of the dried ore. Experiments were conducted using the standard segregation method without $CaCl_2$ addition (Section 3.3.2), and with no attempt to concentrate the ferronickel product. The extent of metal reduction was determined by leaching the reduction product using a bromine/methanol solution to selectively solubilise the reduced metal content (Section 3.3.7).

The results of each carbon reduction test were compared to those from an idealised reduction system, as predicted by equilibrium simulation. The basis of this simulation will be discussed prior to considering the experimental results.

5.1 The Equilibrium Simulation

The reduction of Ni laterite ores dominantly involves the reduction of iron oxides. When iron oxides are reduced with solid carbon at the temperatures used in this work (1123-1223 K), the majority of reduction occurs via CO originating from the gasification of carbon with CO_2 according to the Boudouard reaction (Equation 2.6).

At temperatures less than 1273 K, the Boudouard reaction usually has a higher kinetic resistance than the reduction of powdered iron oxides with CO, and is thus

likely to be the dominant rate control in the reduction process (Section 5.6). Under this scenario, the oxide/gas reduction reactions operate close to equilibrium, and thus dominantly determines the bulk gas composition (Rao, 1971; Fruehan, 1977; Fortini and Fruehan, 2005). It was therefore considered that an equilibrium simulation in which the gas composition is set by the oxide/gas equilibria might reasonably approximate the reduction system studied in this work. These simulations were carried out using the 'Equilib' program within FactSage v6.4 software (Bale et al., 2009).

Solid carbon and iron oxides were present in the experimental reduction system at all times. Since these species cannot thermodynamically coexist at the temperatures (1123-1223 K) and pressure (1 atm) used in this work, the experimental system was not at equilibrium. As a result, when carbon was added to the ore during the simulation, it was always completely consumed by the excess of iron oxides. In order to simulate the progressive consumption of carbon within the experimental system, it was necessary to deliver the carbon to the simulation in a series of equilibrium steps. This was done using the 'open system' option in the FACTSage V6.4 'Equilib' program, which simulates off-gas production by automatically removing the equilibrated gas from the system before the next carbon addition step.

The calcine was added to the simulation in the first step. The input species were calculated per 100 grams of dried ore (Table 4.1) on the assumption that all metals report as oxides after roasting in air; these inputs are summarised in Table 5.1. Since a portion of bonded H_2O is removed from the dried ore during the roast, the total mass for each ore in Table 5.1 does not sum to 100 grams. Ultimately, the amount of bonded H_2O in the ore had little effect on the simulation, since the majority was removed in the first step; thus an average representative amount of 0.7 g was used as an input for all simulations.

The experimental carbon consumption was calculated from a representative fit of the volume of CO and CO_2 evolved over the reduction period. The mass of carbon added in each step (Table 5.1) was varied to give at least 40 steps before the total carbon added equalled the total measured carbon consumption. This number of steps was necessary to reasonably predict the start and end times for phase transformations.

Table 5.1 Equilibrium Simulation Inputs for Laterite Reduction with Carbon

Simulations are for the reduction of limonite, nontronite and garnierite calcines using coke or activated carbon. The carbon inputs are taken from representative fits of the carbon consumption data for each reduction test series (Figure 5.1, Figure 5.6 and Figure 5.14).

Calcine	Initial Simulation Inputs (g)												g/step
	NiO	Fe_2O_3	CoO	SiO_2	Mg_2SiO_4	MgO	Al_2O_3	CaO	Cr_2O_3	Na_2O	MnO	H_2O	C
Limonite	1.19	73.1	0.045	3.11	-	0.48	4.47		2.05	0.96	0.13	0.7	0.05
Nontronite	1.54	34.9	0.071	40.7	-	2.02	3.96		6.07	0.09	-	0.7	0.0125
Garnierite	1.62	16.7	0.042	44.8	19.8	3.45	2.58	1.97	0.91	0.3	0.22	0.7	0.025

The FACTSage 'Equilib' program requires the selection of solution models to predict the thermodynamic activity values of possible solid solution species. Trial simulations were conducted to determine the most appropriate solution models and the selected models are summarised in Table 5.2. The thermodynamic data for the possible pure solids were selected from the FToxid and FactPS databases, while the possible gaseous species were defined as O_2, CO, CO_2, H_2 and H_2O.

Table 5.2 Selected FACTSage Solution Activity Models

Phase	Activity Model	Solid Solution Species
ALLOY	FTmisc-FCCS	f.c.c Ni-Fe-Co-Me alloys
SPINEL	FToxid-SPINA	Complex species equivalent to Fe_3O_4, $NiFe_2O_4$, $CoFe_2O_4$, $MeFe_2O_4$, $FeMe_2O_4$ (Me: Al, Mg, Cr)
MONOXIDE	FToxid-MeO_A	FeO, NiO, CoO, MgO, MnO, Fe_2O_3, Al_2O_3, Cr_2O_3
OLIVINE	FToxid-OlivA	Fe_2SiO_4, Mg_2SiO_4, Ni_2SiO_4, Co_2SiO_4, Mn_2SiO_4, $MeFeSiO_4$ etc
PYROXENE (Clino)	FToxid-cPyrA	$Fe_2Si_2O_6$, $Mg_2Si_2O_6$, $Ca_2Si_2O_6$, $FeMgSi_2O_6$, $CaFeSi_2O_6$, $CaMgSi_2O_6$, $MgAl_2SiO_6$, $CaAlSi_2O_6$ etc.
PYROXENE (Ortho)	FToxid-oPyr	As above.

The FACTSage solid solution models for pyroxene (Table 5.2) do not include Ni within any species. However, Ni was identified within pyroxene for both nontronite (Section 5.4.4) and garnierite (Section 5.5.4). Ericson et al. (1987) also identified ~0.2% nickel in ortho-pyroxene from the MINPRO-PAMCO segregation tailings. The exclusion of Ni from the pyroxene solid solution models appears to be a limitation with the FACTSage database, since if pyroxene is a stable phase, the simulation may overestimate the amount of Ni reduced.

5.2 Equilibrium Phase Transformations

Examination of the simulation results revealed and clarified the sequence of iron oxide reduction reactions that set the oxygen pressure when the rate of reduction is controlled by the Boudouard reaction. These iron oxide reduction reactions will now be discussed.

After roasting in air, all three calcines contained iron as hematite (Fe_2O_3), with the amounts decreasing in the order limonite (73%) > nontronite (35%) > garnierite (17%) (Table 5.1); thus the first stage of reduction for all calcines is the complete reduction of hematite to magnetite (Fe_3O_4).

The calcines also contained free silica (SiO_2), although limonite contained a relatively small amount (3.1%, Table 5.1). When free silica is present, the next stage of reduction is the transformation of magnetite to fayalite (Fe_2SiO_4) through the simultaneous combination of ferrous oxide (FeO) with silica. When sufficient free silica is present, magnetite will also be reduced to form ferrosilite ($FeSiO_3$). However, if the free silica is completely consumed, excess magnetite will be reduced to form ferrous oxide.

The equilibrium oxygen pressure will fall as the calcine becomes more reduced, and if the oxygen pressure becomes low enough, simultaneous reduction of FeO (from within fayalite, ferrosilite and/or wustite) and NiO (within oxides or silicates) will produce a ferronickel alloy. The minor Co present in the ore will also be reduced into the ferronickel, but will be neglected for the purpose of this discussion.

The reduction of hematite to magnetite in the presence of solid carbon mainly occurs via a CO intermediate (Rao, 1971; Fruehan, 1977; Fortini and Fruehan, 2005) according to the reaction:

$$3Fe_2O_3(s) + CO(g) \rightarrow 2Fe_3O_4(s) + CO_2(g) \qquad 5.1$$

The CO is generated from the gasification of carbon with CO_2 according to the Boudouard reaction:

$$CO_2(g) + C(s) \rightarrow 2CO(g) \qquad 2.6$$

When the Boudouard reaction controls the rate, the oxide/gas reduction reaction (e.g. Equation 5.1) operates close to equilibrium and dominantly determines the

p_{CO_2}/p_{CO} ratio in the gas. For the reduction of hematite to magnetite, the value of the ratio is obtained by rearrangement of the equilibrium constant $K_{5.1}$ according to:

$$\frac{p_{CO_2}}{p_{CO}} = K_{5.1}\,\frac{a^3_{Fe_2O_3}}{a^2_{Fe_3O_4}} \qquad 5.2$$

$a_{Fe_2O_3}$ and $a_{Fe_3O_4}$ represent activities relative to the pure solid standard state.

The oxygen pressure is related to the p_{CO_2}/p_{CO} through the reaction:

$$2CO(g) + O_2(g) \rightarrow 2CO_2(g) \qquad 2.31$$

where

$$p_{O_2} = \frac{1}{K_{2.31}}\left(\frac{p_{CO_2}}{p_{CO}}\right)^2 \qquad 2.32$$

The oxygen pressure can also be expressed in terms of the iron oxide reduction, where 2(Equation 5.1) – (Equation 2.31) gives:

$$6Fe_2O_3(s) \rightarrow 4Fe_3O_4(s) + O_2(g) \qquad 5.3$$

and

$$p_{O_2} = K_{5.3}\,\frac{a^6_{Fe_2O_3}}{a^4_{Fe_3O_4}} \qquad 5.4$$

The reduction of hematite to magnetite is the first in a series of iron and nickel oxide reduction reactions that occur during the reduction of the laterite calcine with solid carbon. This series is presented in Table 5.3, in order of decreasing equilibrium oxygen pressure, that is, with the easiest reduction first. The rearranged equilibrium constant expressions, from which the equilibrium oxygen pressures at 1173 K can be calculated, are also presented. The equilibrium constant values at 1173 K are the numbers shown in the 3rd column of Table 5.3, and are from the FACTSage 'Reaction' program.

If the solids shown in Table 5.3 were pure with thermodynamic activities of one, each reaction would go to completion in sequence at a fixed oxygen pressure; for example, hematite would be completely reduced to magnetite at an oxygen pressure of 3.6×10^{-8} atm before the next easiest reduction would begin, and so on. However, the simulations show that within a fully equilibrated system, the reactants and products form solid solutions where the individual species have activities of less than one; thus the equilibrium oxygen pressure for each reaction will be affected according to the activity ratios shown in Table 5.3.

Table 5.3 Sequence of Laterite Reduction Reactions

Numbers in the 3rd column are equilibrium constant values at 1173 K, from the FACTSage 'Reaction' program. All activities are relative to the pure solid standard state. The reactions are simplified and do not show the CO reductant.

Oxygen Pressure Control Reactions		Equilibrium Oxygen Pressure at 1173 K (atm)
Hematite to Magnetite	$6Fe_2O_3(s) \rightarrow 4Fe_3O_4(s) + O_2(g)$	$3.6 \times 10^{-8} \frac{a_{Fe_2O_3}^6}{a_{Fe_3O_4}^4}$
Nickel Oxide to Nickel	$2NiO(s) \rightarrow 2Ni(s) + O_2(g)$	$1.0 \times 10^{-12} \frac{a_{NiO}^2}{a_{Ni}^2}$
Nickel Silicate to Nickel	$Ni_2SiO_4(s) \rightarrow 2Ni(s) + SiO_2(s) + O_2(g)$	$5.6 \times 10^{-13} \frac{a_{Ni_2SiO_4}}{a_{Ni}^2 a_{SiO_2}}$
Magnetite to Fayalite	$2Fe_3O_4(s) + 3SiO_2(s) \rightarrow 3Fe_2SiO_4(s) + O_2(g)$	$4.7 \times 10^{-13} \frac{a_{Fe_3O_4}^2 a_{SiO_2}^3}{a_{Fe_2SiO_4}^3}$
Magnetite to Ferrosilite	$2Fe_3O_4(s) + 6SiO_2(s) \rightarrow 6FeSiO_3(s) + O_2(g)$	$1.3 \times 10^{-13} \frac{a_{Fe_3O_4}^2 a_{SiO_2}^6}{a_{FeSiO_3}^6}$
Magnetite to Wustite	$2Fe_3O_4(s) \rightarrow 6FeO(s) + O_2(g)$	$4.0 \times 10^{-16} \frac{a_{Fe_3O_4}^2}{a_{FeO}^6}$
Wustite to Iron	$2FeO(s) \rightarrow 2Fe(s) + O_2(g)$	$1.6 \times 10^{-17} \frac{a_{FeO}^2}{a_{Fe}^2}$
Ferrosilite to Iron	$2FeSiO_3(s) \rightarrow 2Fe(s) + 2SiO_2(s) + O_2(g)$	$2.3 \times 10^{-18} \frac{a_{FeSiO_3}^2}{a_{Fe}^2 a_{SiO_2}^2}$
Fayalite to Iron	$Fe_2SiO_4(s) \rightarrow 2Fe(s) + SiO_2(s) + O_2(g)$	$1.5 \times 10^{-18} \frac{a_{Fe_2SiO_4}}{a_{Fe}^2 a_{SiO_2}}$

The activity of a reduction product lies on the denominator of the oxygen pressure expression (Table 5.3); thus when a product can form within a solid solution, the oxygen pressure at which reduction can occur will increase. The activity of a reactant lies on the numerator of the expression; thus when a reactant must be reduced from within a solid solution, the oxygen pressure at which reduction can occur will decrease. As a result, when solid solutions can form, the equilibrium oxygen pressure for a reduction reaction can begin either above or below the value for the pure system. If both the product and reactant form solid solutions, once reduction begins, the activity of the product will increase; thus the activity of the reactant will decrease, and the oxygen pressure will decrease progressively until reduction is complete.

The solid solutions identified within the simulated equilibrium laterite reduction systems were: (1) spinel, containing mainly magnetite (Fe_3O_4) and chromite ($FeCr_2O_4$); (2) olivine, containing mainly fayalite (Fe_2SiO_4) and forsterite (Mg_2SiO_4); (3) pyroxene, containing mainly ferrosilite ($FeSiO_3$) and enstatite ($MgSiO_3$); (4) monoxide, containing mainly ferrous oxide (FeO) with other minor oxides including NiO; and (5) alloy, containing mainly Fe and Ni with minor Co.

As the oxygen pressure within the simulated reduction system falls, the a_{Fe} and the a_{Ni} increase according to the values set by the metal reduction equilibria in Table 5.3. Once a critical combination of Ni and Fe activities is reached, a ferronickel alloy is stable and forms through the reduction of NiO (from within monoxide or silicate) and FeO (from within monoxide, fayalite or ferrosilite). The oxygen pressure (p_{O_2}) at which alloy forms will depend on the activities of NiO (a_{NiO}) and FeO (a_{FeO}) within the reduction system; for example, at 1173 K this critical pressure will lie somewhere between 1.0×10^{-12} atm (as required to reduce pure NiO), and 1.5×10^{-18} atm (as required to reduce pure $FeSiO_3$) (Table 5.3). Since NiO is less stable than FeO, the ferronickel will initially be richer in Ni than Fe.

During the equilibrium simulation, the reduction equilibria described above occur in a system free from kinetic restrictions; in reality if solid-solid contact is minimal and solid state diffusion is slow, solid solutions may only partly form or may not form at all. This is an important consideration when comparing the simulated data with the experimental results.

5.3 Limonite Reduction

Eleven limonite calcine reduction tests were performed with 5% coke for up to 180 minutes at 1123 K and 120 minutes at 1173 K, and with 5% activated carbon for up to 80 minutes at 1173 K. The metal reductions and ferronickel grades recorded after selective leaching of the product using bromine/methanol are summarised in Table 5.4, along with ferronickel grades from the equilibrium simulation.

5.3.1 Carbon Consumption

The fraction of carbon consumed during reduction is presented in Figure 5.1, as calculated from representative fits of the averaged carbonaceous off-gas volume data (Appendix B.4). As expected, carbon consumption increases with time, temperature (cf. coke at 1123 and 1173 K) and carbon surface area (cf. coke and

activated carbon at 1173 K); these trends are similar for the reduction of nontronite (Figure 5.6) and garnierite (Figure 5.14) calcines.

Table 5.4 Results from Reduction of Limonite Calcine with Solid Carbon

Ore was roasted for 30 minutes in air at the reduction temperature. Reductant addition was 5 g per 100 g of dried ore, as either coke (78.3% C) or activated carbon (88.7% C). 'FeNi Exp' is the measured ferronickel grade; 'FeNi Equil' is the simulated equilibrium ferronickel grade.

Test Code	Carbon	Temp (K)	Time (min)	Reduction (%)			FeNi Exp Ni(%)	FeNi Equil Ni(%)
				$Ni_{(\%)}$	$Fe_{(\%)}$	$Co_{(\%)}$		
LR850C1	Coke	1123	120	46	0.35	8.3	71	75
LR850C2	Coke	1123	180	62	0.63	16	64	74
LR850C3	Coke	1123	180	63	0.65	16	64	74
LR900C1	Coke	1173	40	14	0.15	-	64	78
LR900C2	Coke	1173	60	59	0.73	9.2	60	77
LR900C3	Coke	1173	120	63	0.69	14	62	75
LR900C4	Coke	1173	120	61	0.64	14	63	75
LR900C5	Coke	1173	120	45	0.48	9.6	63	75
LR900AC1	Act C	1173	60	33	0.65	8.3	48	64
LR900AC2	Act C	1173	80	21	0.99	9.0	27	39
LR900AC3	Act C	1173	80	30	1.2	15	31	39

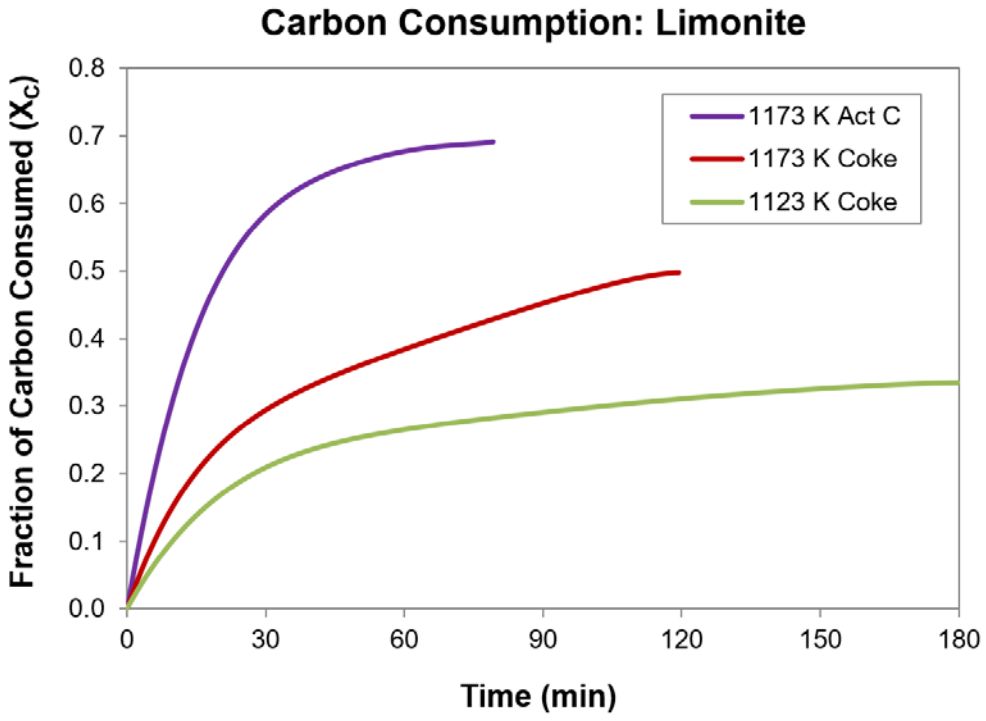

Figure 5.1 Carbon Consumed during Limonite Reduction

Reductant added at 5% of dried ore, as either coke (78.3% C) or activated carbon (88.7% C). Curves are best fits from experimental data (Appendix B.4).

5.3.2 Metal Reduction

The percents of Ni, Co and Fe reduced to metal versus time are shown in Figure 5.2 for coke at 1123 K, in Figure 5.3 for coke at 1173 K, and in Figure 5.4 for activated carbon at 1173 K. In each figure, the percents of metal reduced are compared with those predicted from an equilibrium simulation (Section 5.1), for which the carbon consumption was taken from the fitted data shown in Figure 5.1.

When coke was the reductant, the measured and simulated metal reductions were in reasonable agreement (Figure 5.2 and Figure 5.3), although the measured Ni reduction was lower than simulated for some points. Figure 5.4 shows that when activated carbon was used as the reductant, the metal reductions were well below the simulated values. The metal reductions were also lower than achieved with coke at the same temperature after an equivalent reduction time (cf. 64% Ni with activated carbon and 77% Ni with coke after 60 minutes at 1173 K, Table 5.4).

Activated carbon has a significantly larger surface area per gram than coke (Table 4.13), and a greater fraction is consumed during reduction (Figure 5.1). It was therefore surprising that the metal reductions achieved with activated carbon were below those achieved with coke; also in contrast to coke, the metal reductions with activated carbon were well below those predicted by the equilibrium simulation.

The ferronickel grades achieved during reduction (FeNi Exp) and those predicted by simulation (FeNi Equil) are shown in the last two columns of Table 5.4. For reduction with coke and activated carbon, the ferronickel grades (Ni%) were consistently lower than those predicted by the simulation. This may result from additional Fe being reduced through direct contact with solid carbon, as this type of reduction is not accounted for in the simulation. The bromine/methanol leach can also overestimate Fe when used to leach alloy from the limonite reduction product (Section 3.3.7). It is therefore likely that the actual differences between the measured and predicted ferronickel grades are less than shown in the table.

A reasonable agreement between the measured and predicted ferronickel grades and metal reductions achieved when using coke, indicates that the experimental bulk gas was close to equilibrium with the alloy. This agrees with the work of Rhamdhani et al. (2009) who found that reduction of limonite is thermodynamically controlled by the gas composition. Under this scenario, Figure 5.2 and Figure 5.3 indicate that, when coke is used, the maximum achievable nickel reduction is ~65%, with an associated ~13% of the Co and ~0.4% of the Fe co-reduced.

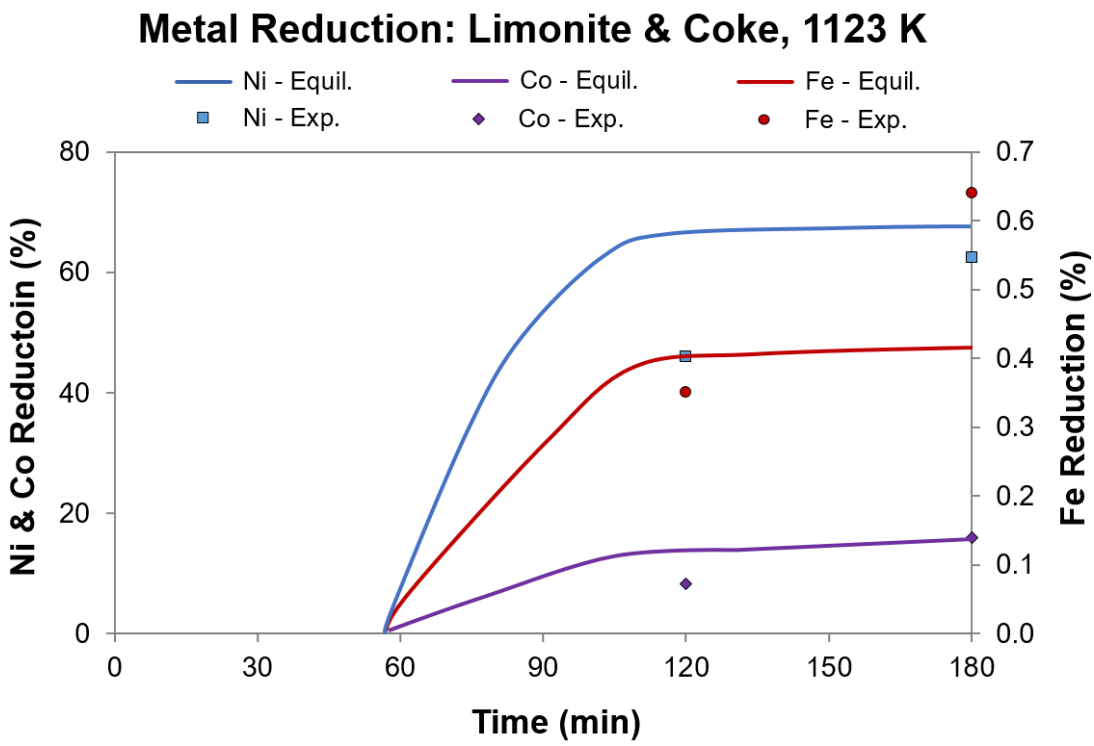

Figure 5.2 Simulated & Measured Metal Reduction, Limonite & Coke, 1123 K

Lines are equilibrium; points represent averaged experimental data (Table 5.4).

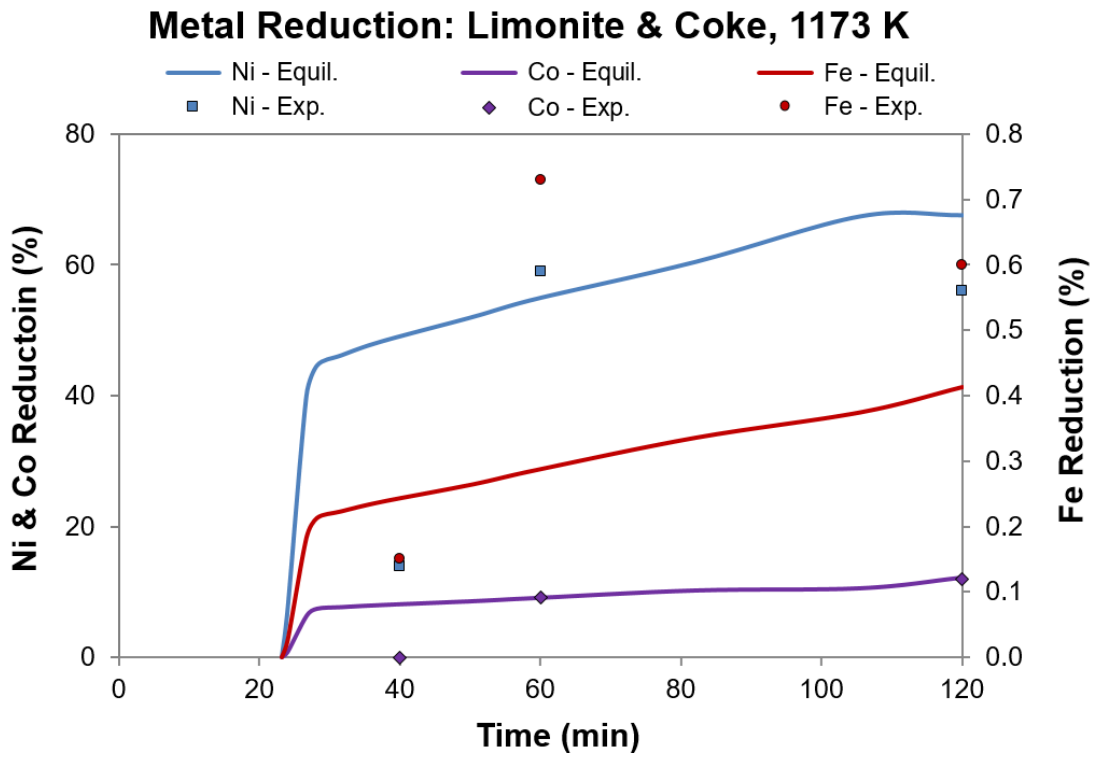

Figure 5.3 Simulated & Measured Metal Reduction, Limonite & Coke, 1173 K

Lines are equilibrium; points represent averaged experimental data (Table 5.4).

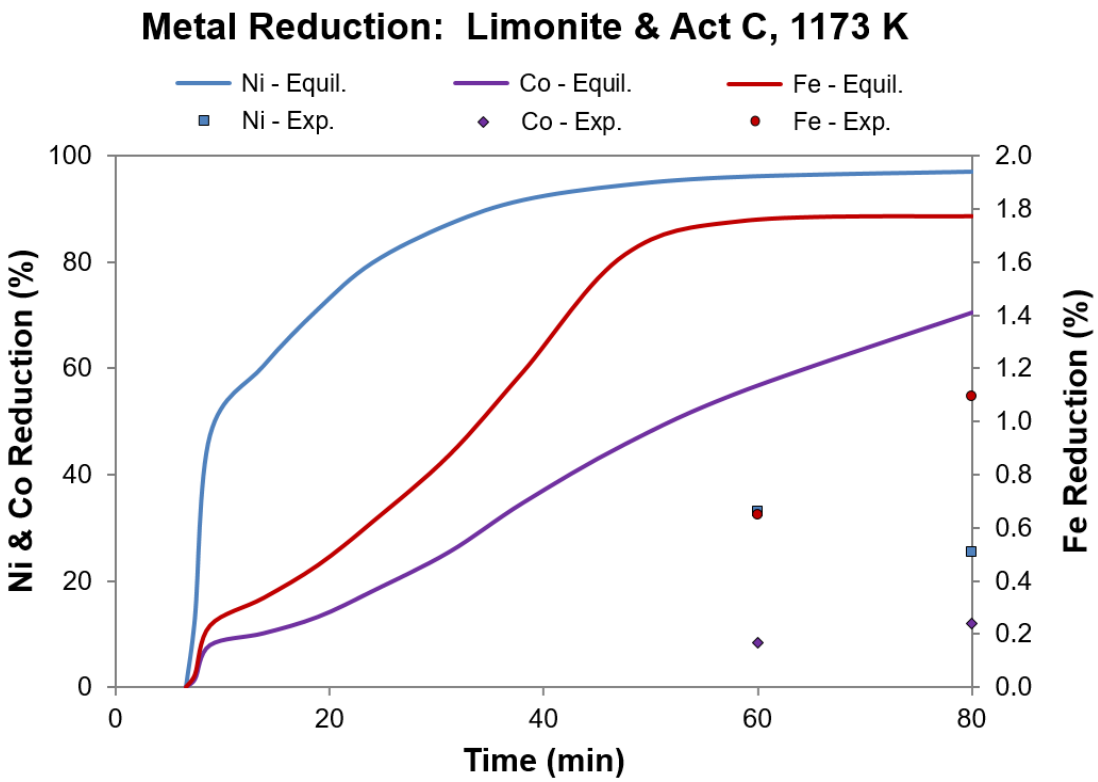

Figure 5.4 Simulated & Measured Metal Reduction, Limonite & Act C, 1173 K

Lines are equilibrium; points represent averaged experimental data (Table 5.4).

The metal reductions achieved using activated carbon were much lower than predicted, most likely due to the alloy being finely dispersed within the calcine and inaccessible to the leach solution. This became apparent after EDS-SEM analysis of a limonite calcine segregated in the presence of activated carbon (Figure 7.7).

The segregation product contained small, widely dispersed ferronickel nuclei, formed due to the strong reducing conditions promoted by the high surface area of reductant. These fine metallic particles were likely entrapped within the remnant iron oxides through grain coarsening, rendering them inaccessible to the bromine/methanol leach solution. This aspect needs further investigation, however, the presence of entrapped leach resistant ferronickel has been recently observed within reduced saprolite ore (Chen et al., 2013). The formation of inaccessible alloy may also explain why Utigard and Bergman (1992) used a hydrogen evolution method[15] for the analysis of in-situ ferronickel rather than a bromine/methanol leach, which they found to be less reliable.

[15] This involves dissolving the reduction product in concentrated HCl.

Given the apparent limitations of analysing for reduced metal after reduction with activated carbon, it is not possible to confirm that the extent of reduction is controlled by the gas-solid equilibrium, as is likely when using coke. However, if equilibrium could be achieved, Figure 5.4 indicates that a maximum reduction of ~95% of Ni is possible at 1173 K with the activated carbon addition used in this work, along with a maximum ~15% co-reduction of Co and ~7% of Fe.

5.3.3 Equilibrium Simulation and Oxygen Pressure

The results of the equilibrium simulation for the reduction of limonite calcine with coke at 1173 K are summarised in Figure 5.5. The figure shows the mass (grams) of each solid phase which forms over time from a calcine which initially contains 73.1 grams of Fe_2O_3 (Table 5.1). The simulated oxygen pressure of the bulk gas is also included in the figure along with the representative (averaged) measured oxygen pressure (labelled LR900C). The full set of measured oxygen pressure data are provided in Appendix B.5.

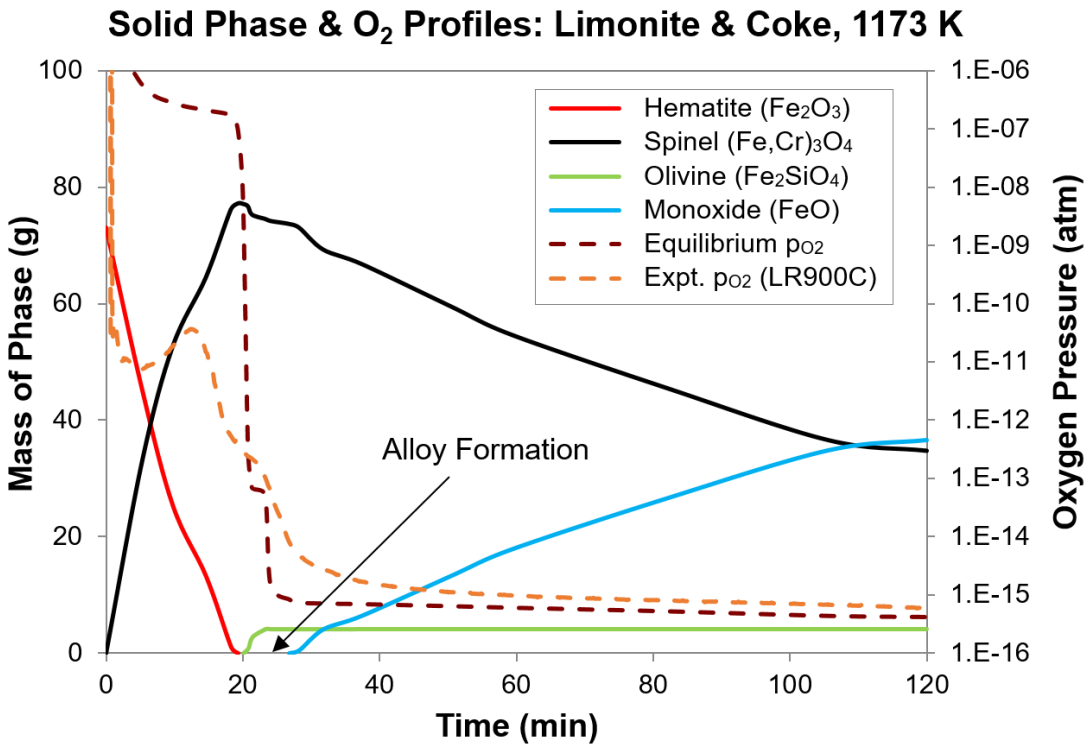

Figure 5.5 Equilibrium Simulation of Limonite Reduction with Coke, 1173 K

Phase profiles are for 100 grams of dried ore. The dashed brown line represents the simulated p_{O_2}; the dashed orange line represents the measured p_{O_2}.

Figure 5.5 shows that the equilibrium reduction of limonite calcine results in the following progression of phase transformations as the oxygen pressure decreases

with time: hematite →[16] magnetite (in spinel) → fayalite (in olivine). There is insufficient free silica for the formation of ferrosilite; rather once the formation of fayalite is complete, the transformation of magnetite (in spinel) → ferrous oxide (in monoxide) continues for the remainder of the time.

The simulated phase transformations at 1123 K with coke and at 1173 K with activated carbon are similar to those at 1173 K with coke; all are summarised in Table 5.5. The transformations occur earlier and over shorter periods if the temperature is increased (cf. coke at 1123 K and 1173 K) or if the carbon surface area is increased (cf. coke at 1173 K and activated carbon at 1173 K). Figures showing the phase transformation and oxygen pressure profiles at 1123 K with coke and at 1173 K with activated carbon are provided in Appendix B.7.

Table 5.5 Solid Phase Transformations during Limonite Calcine Reduction

Equilibrium phase transformations during the simulated equilibrium reduction of limonite calcine with coke and activated carbon. Alloy forms initially through reduction of spinel, then through the reduction of both spinel and monoxide.

Simulated Phase Transformation Times (minutes)			
Phase Change	Coke 1123 K 180 min total	Coke 1173 K 120 min total	Act C 1173 K 80 min total
Hematite → Spinel	0 → 40.2	0 → 19.2	0 → 6.3
Spinel → Olivine	40.2 → 60	20.8 → 24	6.3 → 7.4
Spinel → Monoxide	100 → End	28.2 → End	8.8 → 47
Alloy Formation Initiating p_{O_2} (atm)	60 → End 1.3×10^{-16}	24.0 → End 1.4×10^{-15}	7.4→ End 1.4×10^{-15}

The arrow implies that the mass of phase increases over the time.

The simulated p_{O_2} (Figure 5.5) is maintained above ~10^{-7} atm while controlled by the reduction of hematite → magnetite (in spinel) (Table 5.3). The p_{O_2} then falls to ~5×10^{-14} atm where it is briefly held while magnetite (in spinel) is reduced to fayalite (in olivine). Once all the free silica is combined with ferrous oxide into fayalite, the p_{O_2} again falls rapidly before being controlled to ~10^{-15} atm by the reduction of magnetite (in spinel) → ferrous oxide (in monoxide). The rapid fall in p_{O_2} after the formation of fayalite is complete initiates the formation of ferronickel after ~24 minutes (Figure 5.5). Ultimately, the unreduced Ni remains dissolved within the monoxide, spinel and olivine phases in equilibrium with the alloy.

[16] The arrow (→) is included to simplify reading of the text. It should be read as "to".

The rapid initial fall in the measured p_{O_2} (Figure 5.5) is a result of the oxygen sensor having to heat to the reaction temperature before taking reliable measurements (Section 3.2.1) although the experimental value is clearly lower than the simulated p_{O_2} while hematite is being reduced to magnetite over the first 19.2 minutes of the reduction. This is due to the Boudouard reaction having some effect on the gas composition; however, as shown in Figure 5.19, the effect results in only a small change in the mole fraction of CO_2 in the gas.

Once hematite reduction is complete, the measured p_{O_2} follows the same pattern as the simulated value, but decreases less rapidly. This is likely because the fayalite takes more time to form and enter a solid solution than assumed by the equilibrium simulation.

The measured and simulated p_{O_2} for coke at 1123 K and activated carbon at 1173 K follow similar patterns to coke at 1173 K (Appendix B.7). The solid phases in the reduction test product were not examined; however, the solid phases within a similarly reduced limonite segregation product were studied. The XRD (Table 7.10) and EDS-SEM (Figure 7.5) analyses confirmed that magnetite, wustite and fayalite were present, as predicted by the equilibrium simulation (Figure 5.5).

5.3.4 Summary

The simulated and experimental reductions of limonite calcine, at least with coke, appear similar. This confirms that reduction of calcine by the bulk gas operates close to equilibrium and dominantly controls the oxygen pressure, while the gasification of carbon through the Boudouard reaction dominantly controls the rate. As control of the oxygen pressure shifts from the magnetite/fayalite reduction to the magnetite/ferrous oxide reduction (Table 5.3), the simulated and experimental oxygen pressures fall and initiate the formation of alloy. Hence, it appears that the formation of alloy when reducing limonite calcine is mainly delayed by the period required to reduce all hematite to magnetite.

When activated carbon is used instead of coke, the conditions are more reducing, such that at 1173 K, the oxygen pressure to initiate alloy formation is achieved after 7.4 minutes, compared to 24 minutes with coke (Table 5.5). These more reducing conditions almost certainly result in the formation of very fine ferronickel that is likely encapsulated in gangue and difficult to leach selectively.

When using coke as the reductant, there appear to be few kinetic restrictions in the reduction system. The calcine is dominantly hematite that can transform directly to magnetite through to ferrous oxide and ferronickel without the need for contact with any external solid surface. Under this scenario, the reduction is limited by the extent to which the oxygen pressure can be lowered by the gas/calcine equilibrium. In this work, a maximum of ~65% of the Ni was reduced along with ~0.7% of the Fe when using a coke addition of 5% of the dried ore.

A gas-solid equilibrium may also be approached when using activated carbon as the reductant, but this could not be confirmed because the likely formation of fine ferronickel prevented a reliable analysis of the extent of reduction. If a gas-solid equilibrium was achieved when using activated carbon, the simulation shows that ~95% of the Ni could be reduced along with only ~1.8 of the Fe (Figure 5.4).

5.4 Nontronite Reduction

Fifteen nontronite calcine reduction tests were performed with 5% coke for up to 210 minutes at 1123 K, and for up to 120 minutes at both 1173 K and 1223 K. Experiments with 5% activated carbon were performed for 60 minutes at 1223 K. The metal reductions and ferronickel grades achieved after selective leaching of the product using bromine/methanol are summarised Table 5.6, along with ferronickel grades from the equilibrium simulation.

5.4.1 Carbon Consumption

The fraction of carbon consumed during reduction is presented in Figure 5.6, as calculated from representative fits of the averaged carbonaceous off-gas volume data (Appendix B.4).

5.4.2 Metal Reduction

Table 5.6 shows that the maximum Ni reductions achieved with coke are only 4.4%, 6.6% and 29% respectively at 1123, 1173 and 1223 K, and only 8.7% with activated carbon at 1233 K. The reductions of Fe and Co are also relatively low.

The low reductions at 1123 and 1173 K with coke are not unexpected; the equilibrium simulation (Section 5.4.3) predicts that no alloy should form at either of these temperatures. The metal reductions that were recorded are most likely the result of direct solid-solid contact of carbon with the ore, rather than gaseous reduction with carbon monoxide.

Table 5.6 Results from Reduction of Nontronite Calcine with Solid Carbon

Ore was roasted for 30 minutes in air at the reduction temperature. Reductant addition was 5 g per 100 g of dried ore, as either coke (78.3% C), or activated carbon (88.7% C). 'FeNi Exp' is the measured ferronickel grade; 'FeNi Equil' is the simulated equilibrium ferronickel grade.

Test Code	Carbon	Temp (K)	Time (min)	Reduction (%)			FeNi Exp Ni(%)	FeNi Equil Ni(%)
				$Ni_{(\%)}$	$Fe_{(\%)}$	$Co_{(\%)}$		
NR850C1	Coke	1123	120	3.4	0.17	0.28	50	NP
NR850C2	Coke	1123	210	3.8	0.22	0.16	46	NP
NR850C3	Coke	1123	210	4.4	0.16	0.18	59	NP
NR900C4	Coke	1173	90	2.3	0.094	0.074	55	NP
NR900C1	Coke	1173	120	3.5	0.16	0.038	52	NP
NR900C2	Coke	1173	120	6.6	0.13	0.30	71	NP
NR900C3	Coke	1173	120	4.9	0.10	0.16	71	NP
NR950C4	Coke	1223	60	2.9	0.23	-	39	NP
NR950C1	Coke	1223	120	26	0.79	5.5	62	74
NR950C2	Coke	1223	120	23	0.57	4.9	67	74
NR950C3	Coke	1223	120	29	0.78	8.2	64	74
NR950AC1	Act C	1223	60	4.9	0.84	3.5	22	31
NR950AC2	Act C	1223	60	4.6	0.69	3.5	25	31
NR950AC3	Act C	1223	60	5.1	0.88	4.0	23	31
NR950AC4	Act C	1223	60	8.7	1.1	5.1	29	31

NP = No Alloy Present

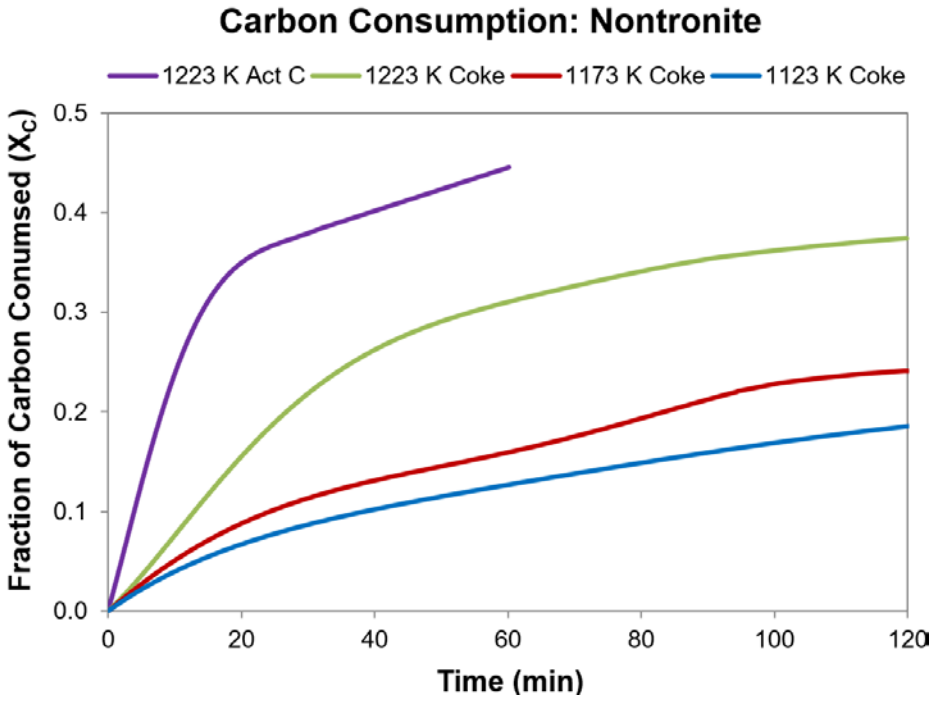

Figure 5.6 Carbon Consumed during Nontronite Reduction

Reductant added at 5% of dried ore, as either coke (78.3% C) or activated carbon (88.7% C). Curves are best fits from experimental data (Appendix B.4).

The simulation predicts alloy formation when coke or activated carbon is used at 1223 K. The percents of Ni, Co and Fe reduced versus time are shown in Figure 5.7 for coke at 1223 K, and in Figure 5.8 for activated carbon at 1223 K. In each figure, the percents of metal reduced are compared with those predicted from the equilibrium simulation using the carbon consumption data shown in Figure 5.6. Both figures show that the measured metal reductions are much lower than the simulated values, especially for activated carbon.

The simulation will slightly overestimate Ni reduction, since a significant amount of Ni containing pyroxene was identified within the reduced nontronite (Figure 5.12), yet Ni is not included in the FACTSage pyroxene solid solution models (Section 5.1). However, this cannot fully account for the difference between the measured and simulated Ni reductions[17].

Figure 5.9 shows the presence of very fine (<1 μm), bright ferronickel particles throughout a sectioned nontronite dehydroxylate (Table 4.8) after reduction with activated carbon for 30 minutes at 1223 K. It therefore seems likely, as discussed for limonite (Section 5.3.2), that the presence of this fine ferronickel results in the measured Ni reduction being significantly lower than predicted. Fine ferronickel also likely accounts for the lower than predicted Ni reductions when using coke at 1223 K, although the calcine was not examined to confirm this.

The measured ferronickel grades after reduction with coke for 120 minutes at 1223 K averaged 64% Ni compared to the prediction of 74% Ni (Table 5.6). However if the measured grades are adjusted by subtracting the background Ni and Fe likely formed through direct contact with carbon[18], the grades at 120 minutes averaged 71%, very close to the predicted value. In addition, only background amounts of Ni (<5% recovery) and Fe (<0.25% recovery) were recovered when using coke at 1123 K or 1173 K. This is in agreement with equilibrium predictions that no reduction should occur at these temperatures (Table 5.7). It therefore seems likely that the bulk gas and calcine were relatively close to equilibrium during the actual reduction, at least when using coke.

[17] The simulated gangue contained 49 grams of pyroxene after 120 minutes; if assumed to contain ~0.20% Ni, similar to the pyroxene tailings from the MINPRO-PAMCO pilot plant (Ericson et al., 1987), only 8% of the Ni would be retained in the pyroxene.

[18] The grades with coke after 120 minutes at 1223 K were adjusted by subtracting the 2.9% Ni and 0.29% Fe reduced after 60 minutes (Table 5.6); these were taken as background, since no reduction was predicted after this time (Figure 5.11).

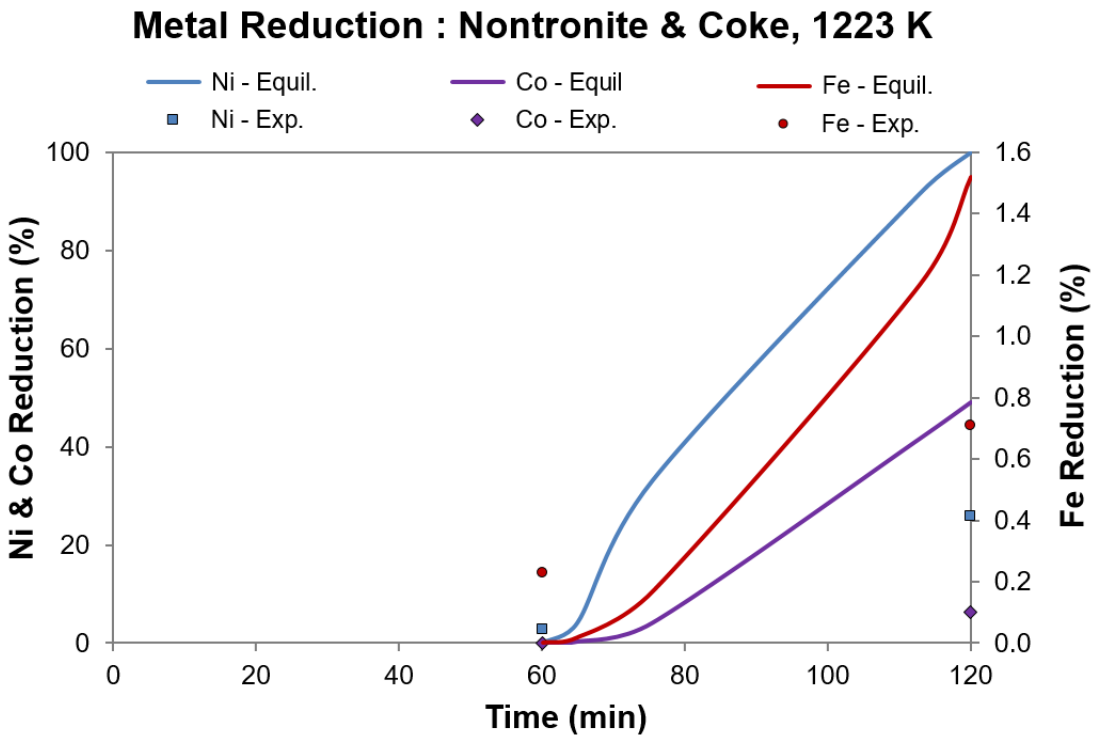

Figure 5.7 Simulated & Measured Metal Reduction, Nontronite & Coke, 1223 K

Lines are equilibrium; points represent averaged experimental data (Table 5.6).

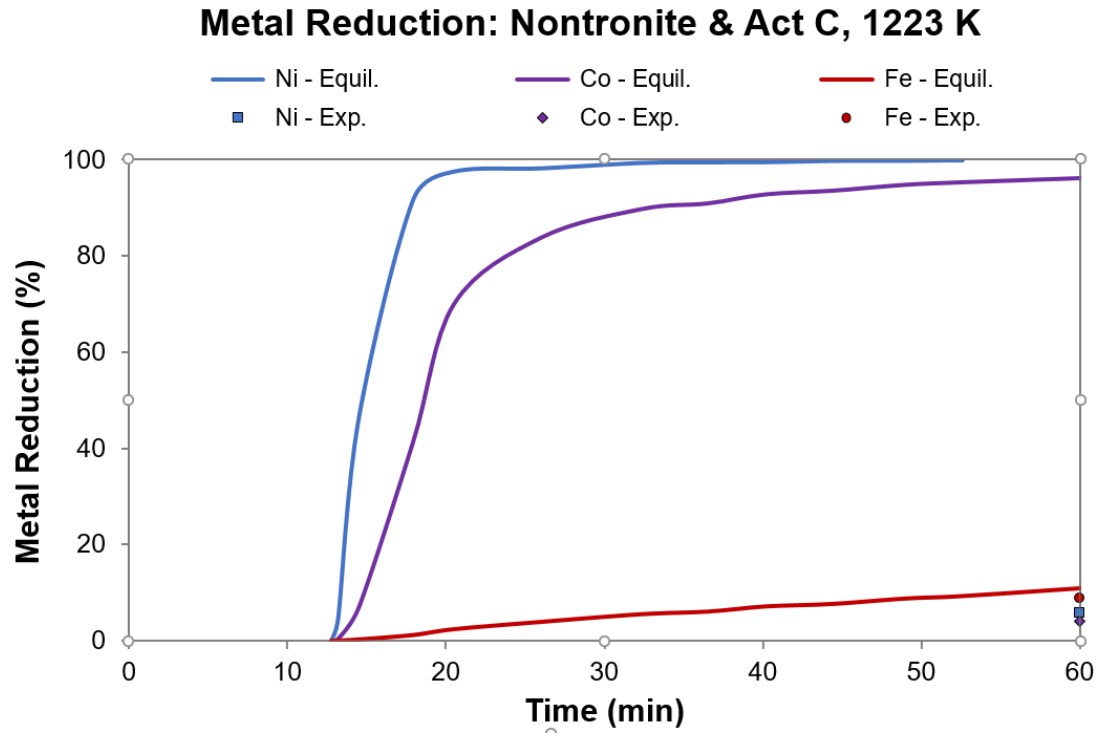

Figure 5.8 Simulated & Measured Metal Reduction, Nontronite & Act C, 1223 K

Lines are equilibrium; points represent averaged experimental data (Table 5.6).

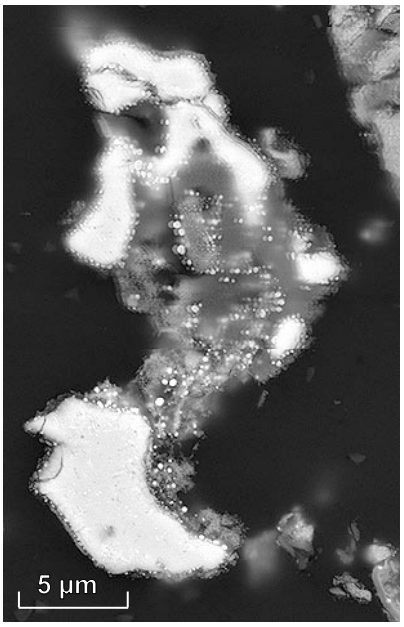

Figure 5.9 Fine Alloy within Reduced Nontronite Dehydroxylate

SEM image through a particle from a nontronite calcine after reduction for 30 minutes with activated carbon at 1223 K; the particle consists of iron oxides (the lighter coloured, non-ferronickel phase) and iron silicates (the darker phase).

If equilibrium is achieved when using coke, reduction of ~100% of the Ni is possible at 1223 K, with an associated co-reduction of ~15% of the Co and ~0.5% of the Fe (Figure 5.7). However, the reduction product would be difficult to recover via leaching due to the formation of fine ferronickel. If equilibrium is achieved when using activated carbon, virtually all the Ni and Co could be reduced (Figure 5.8), although, in comparison to coke, leaching of the reduction product appears even more limited by the formation of fine ferronickel.

5.4.3 Equilibrium Simulation and Oxygen Pressure

The results of the equilibrium simulations for the reduction of nontronite calcine with coke are summarised in Figure 5.10 for 1173 K, and in Figure 5.11 for 1223 K. The calcine initially contains mainly silica (40.7 grams) and hematite (34.9 grams), as shown in Table 5.1. The simulated oxygen pressures for the bulk gas are also included in the figures along with the representative (averaged) measured oxygen pressures (labelled NR900C at 1173 K and NR950C at 1223 K). The full set of measured oxygen pressure data are provided in Appendix B.5.

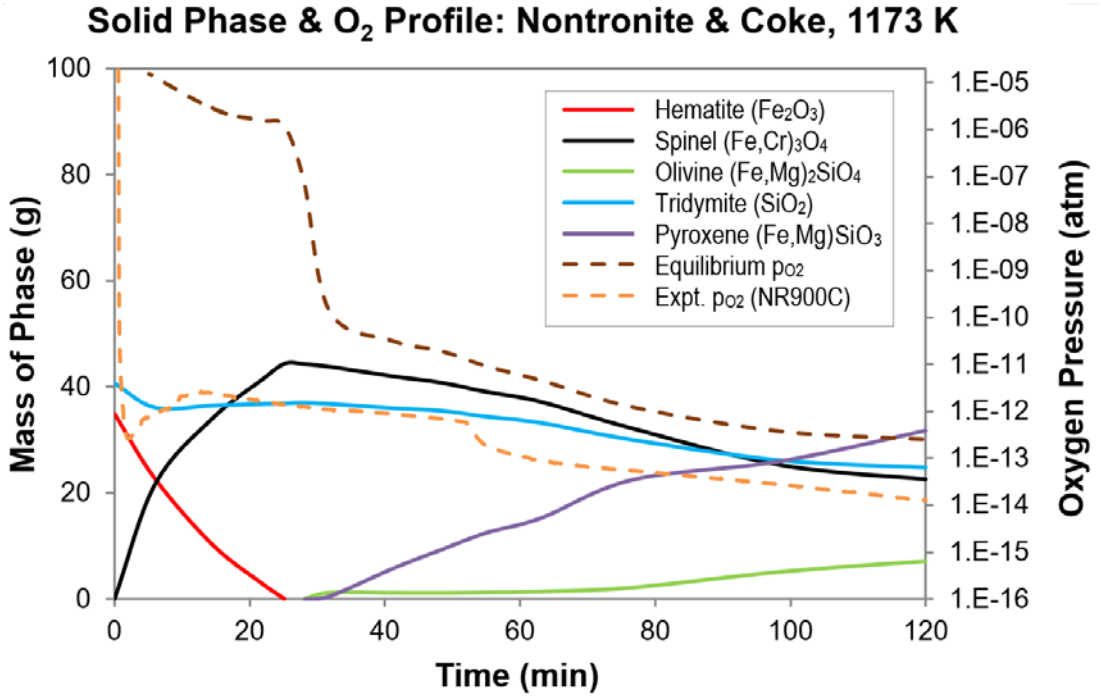

Figure 5.10 Equilibrium Simulation of Nontronite Reduction with Coke, 1173 K

Phase profiles are for 100 grams of dried ore. The dashed brown line represents the simulated p_{O_2}; the dashed orange line represents the measured p_{O_2}.

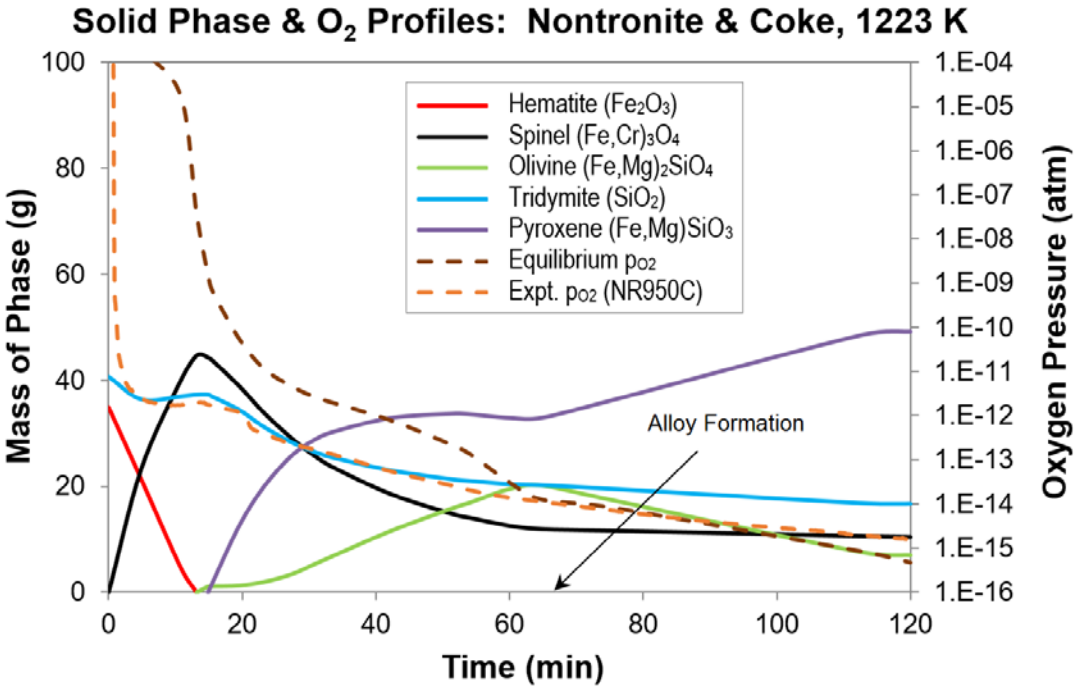

Figure 5.11 Equilibrium Simulation of Nontronite Reduction with Coke, 1223 K

Phase profiles are for 100 grams of dried ore. The dashed brown line represents the simulated p_{O_2}; the dashed orange line represents the measured p_{O_2}.

Figure 5.10 and Figure 5.11 show that the equilibrium reduction of nontronite calcine results in the following progression of transformations as the oxygen pressure decreases with time: hematite → magnetite (in spinel) → fayalite (in olivine). Unlike limonite, nontronite contains sufficient free silica such that ferrosilite (in pyroxene) begins to form through the reduction of magnetite soon after fayalite formation initiates, and the formation of pyroxene and fayalite continue for the remainder of the reduction period. No reduction to ferronickel is predicted at 1173 K; at 1223 K, ferronickel is predicted to form after 65 minutes.

The simulated phase transformations at 1123 K with coke and at 1223 K with activated carbon are similar to those at 1173 and 1223 K with coke; all are summarised in Table 5.7. As observed for limonite, the transformations occur earlier and over shorter periods if the temperature or the carbon surface area is increased. Figures illustrating these data and oxygen pressure profiles are provided in Appendix B.7.

Table 5.7 Solid Phase Transformations during Nontronite Calcine Reduction

Equilibrium phase transformations during the simulated equilibrium reduction of nontronite calcine with coke and activated carbon. Alloy forms initially through reduction of spinel and olivine, then (with activated carbon only) through the reduction of pyroxene.

Simulated Phase Transformation Times (minutes)				
Phase Change	Coke 1123 K 210 min total	Coke 1173 K 120 min total	Coke 1223 K 120 min total	Act C 1223 K 60 min total
Hematite → Spinel	0 → 46	0 → 25	0 → 13	0 → 3.4
Spinel → Olivine	54 → End	31.8 → End	14.9 → 65	4.1 → 13.1
Spinel → Pyroxene	54 → End	31.8 → End	15.6 → 65	4.3 → 13.1
Olivine → Pyroxene	Doesn't occur	Doesn't occur	65 → End	13.1 → 20.5
Alloy Formation Initiating p_{O_2} (atm)	No Alloy (2.5×10^{-16})*	No Alloy (1.7×10^{-15})*	65 → End 1.4×10^{-14}	13.2→ End 1.4×10^{-14}
Silica	Reacts throughout	Reacts throughout	Reacts throughout	Reacts throughout

*Not achieved
The arrow implies that the mass of phase increases over the time.

The simulated p_{O_2} for coke at 1173 K (Figure 5.10) is maintained above ~10^{-6} atm while being controlled by the reduction of hematite → magnetite (in spinel) (Table 5.3). The p_{O_2} then falls rapidly until arrested at ~10^{-10} atm by the reduction of magnetite (in spinel) to both fayalite (in olivine) and ferrosilite (in pyroxene). The

simulated p_{O_2} continues to fall for the remainder of the reduction under the control of these reactions.

The measured p_{O_2} lies below the simulated value for the entire experiment, probably because of some influence from the Boudouard reaction on the gas composition in this range (Figure 5.19); however, neither the simulated nor experimental values were ever low enough for alloy formation.

For reduction at 1223 K (Figure 5.11), the simulated p_{O_2} drops to the critical level for alloy formation after 65 minutes with coke, and after 13.2 minutes with activated carbon (Table 5.7). In both cases, the measured p_{O_2} crosses above the simulated value just after alloy formation, and remains above it for the remainder of the reduction period.

5.4.4 Nickel in Partially Reduced Calcine

A sample of nontronite calcine was subjected to a mild reduction (reduction with coke at 1173 K for 30 minutes) before being resin-mounted, polished and carbon coated for EDS-SEM analysis. The mild reducing conditions were selected so that the deportment of Ni could be studied in a partially reduced calcine prior to alloy formation. Figure 5.12 shows a backscattered electron image of a ~1 mm x 1 mm (1000 µm x 1000 µm) cross section through the partially reduced nontronite calcine. Detailed Al, Ca, Fe, Mg, Ni and Si element maps through this cross section are provided in Appendix B.15.

The majority of the Ni was found within conglomerates of silica, olivine and pyroxene, as identified by EDS-SEM chemical analysis. Six examples, numbered 1 to 6, are marked within Figure 5.12; their average molar formulae and Ni percents are shown in Table 5.8. The particles contained between 2.4-3.5% Ni, an upgrade from the ~1.5% Ni contained within the nontronite dehydroxylate from the original unreduced calcine (Table 4.8). The partly reduced dehydroxylate also contained variable amounts of Mg, Al, Na and Cr in addition to the Fe and Si found in the original dehydroxylate particles (Table 4.8), presumably due to interaction with other minerals during reduction.

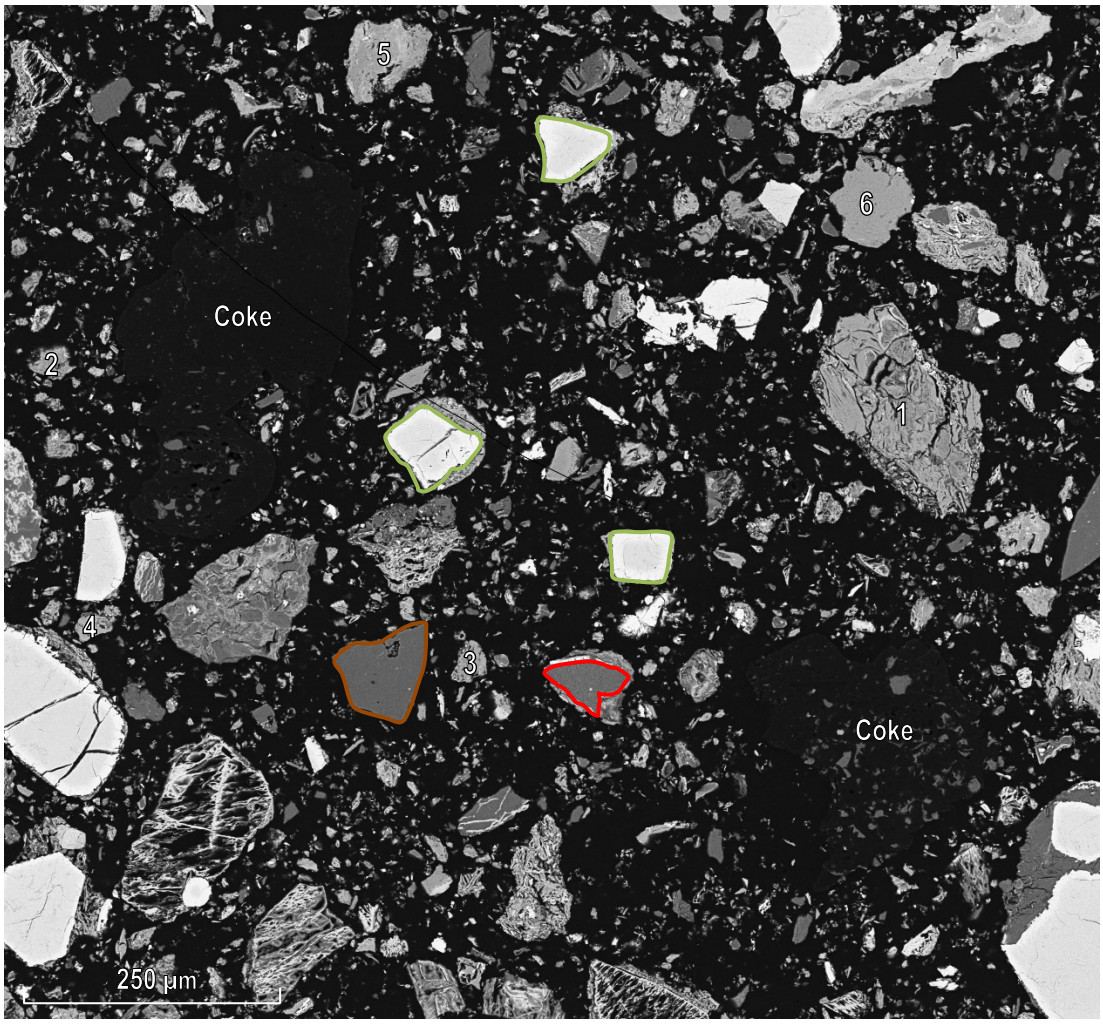

Figure 5.12 Section through Partially Reduced Nontronite Calcine

SEM image through a nontronite calcined reduction with coke at 1173 K for 30 minutes with no alloy formation. The particles shown are: complex silica, olivine and pyroxene conglomerates with 2.4-3.5% Ni (numbered 1 to 6); large primary Cr rich spinels with rims enriched to 1-1.5% Ni (outlined in green); a large Ni free Al silicate (outlined in brown); and primary crystalline silica (outlined in red).

Large Cr rich spinels with unreacted cores and altered maghemite-like ($FeCrO_3$) rims were identified in the original nontronite calcine (Figure 4.8). These were still present in the partially reduced calcine, but with the rims reduced to chromite ($FeCr_2O_3$) and enriched with 1-1.5% Ni; this enrichment could account for ~5% of the total Ni content[19]. It is unclear how the chromite became Ni enriched during reduction. Several Cr rich spinels are identified (outlined in green) in Figure 5.12,

[19] 100 g of dried nontronite ore contained ~15 g of chromite with an average spherical diameter of 37 µm (Table 4.6) and a density of 4.65 g/cm^3. The total contained Ni was estimated from the (average) total number of particles, assuming a ~5 µm thick surface layer (Figure 5.13) containing 1.25%Ni.

and a single particle is shown in Figure 5.13. The lighter chromite rim is surrounding a darker, unreacted ($Fe_{0.7}Mg_{0.3}Al_{0.6}Cr_{1.4}O_4$) spinel core (Figure 5.13).

Table 5.8 Partially Reduced Nontronite Dehydroxylate

Particles numbers refer to Figure 5.12; chemical analysis via EDS-SEM.

Particle Figure 5.12	Ni (wt%)	Average Composition (moles)
1	2.0	$Fe_{0.37}Al_{0.08}Mg_{0.1}SiO_{2.4}$
2	2.4	$Fe_{0.32}Al_{0.12}Mg_{0.12}SiO_{2.5}$
3	2.5	$Fe_{0.40}Al_{0.17}Mg_{0.08}SiO_{2.7}$
4	2.5	$Fe_{0.63}Al_{0.13}Mg_{0.13}SiO_{2.7}$
Average	2.4	$Fe_{0.43}Al_{0.13}Mg_{0.11}SiO_{2.6}$
5	3.5	$Fe_{0.35}Al_{0.15}Mg_{0.10}Na_{0.10}Cr_{0.07}SiO_{2.6}$
6	3.5	$Fe_{0.26}Al_{0.16}Mg_{0.07}Na_{0.06}Cr_{0.06}SiO_{2.7}$
Average	3.5	$Fe_{0.31}Al_{0.16}Mg_{0.09}Na_{0.08}Cr_{0.07}SiO_{2.7}$

Other particles identified in Figure 5.12 are primary silica (an example is outlined in red) which was also present in the nontronite calcine, and a single aluminium silicate particle (outlined in brown); neither contained Ni.

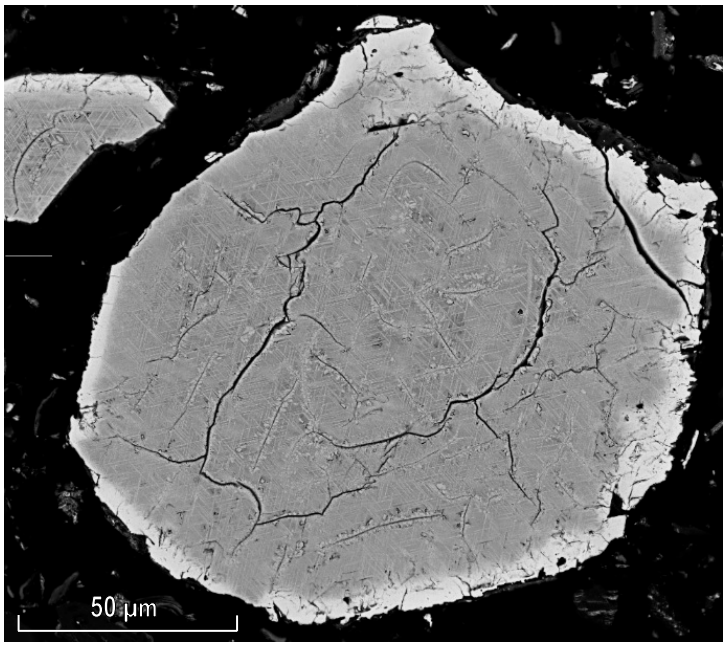

Figure 5.13 Section through a Partially Reduced Cr Rich Spinel Particle

SEM image through a Cr rich spinel formed after nontronite reduction with coke at 1173 K for 30 minutes. The particle has an unreacted core and a chromite rim enriched with 1-1.5% Ni.

5.4.5 Summary

The measured metal reductions for nontronite were much lower than predicted from the equilibrium simulations. However, the measured and simulated ferronickel grades were comparable and it is likely, at least when using coke, that the reduction of nontronite calcine by the bulk gas operates close to equilibrium, with the Boudouard reaction mainly controlling the rate. The lower than predicted metal reductions were attributed to a lack of accessibility of the bromine/methanol leach solution to very fine ferronickel encapsulated within the calcine.

In contrast to limonite, nontronite ore contains significant free silica that combines with ferrous oxide to form olivine and pyroxene. This silicate formation controls the oxygen pressure at a higher level compared to when ferrous oxide is the reduction product (Table 5.3) and suppresses the formation of alloy during reduction with coke at 1123 and 1173 K, but not at 1223 K.

The formation of silicates during reduction requires surface contact between ferrous oxide and silica. This contact is facilitated within the nontronite calcine, since iron oxide and silica are intimately mixed within the very finely grained to amorphous nontronite dehydroxylate (Table 4.8). This dehydroxylate also contain the majority of Ni, and was enriched to ~2.4-3.5% Ni after partial reduction (Table 5.8).

5.5 Garnierite Reduction

Twelve garnierite calcine reduction tests were performed with 5% coke for up to 120 minutes at 1173 K and 1223 K; and with 5% activated carbon for up to 80 minutes at 1223 K. The metal reductions and ferronickel grades recorded after selective leaching of the product using bromine/methanol are summarised in Table 5.9, along with ferronickel grades from the equilibrium simulation.

5.5.1 Carbon Consumption

The fraction of carbon consumed during reduction is presented in Figure 5.14. The arrest in carbon consumption at ~20 minutes during reduction with coke at 1223 K was atypical but evident in all three experiments under these conditions, and occurs approximately after Fe_3O_4 is completely reduced to FeO. The arrest did not occur when using coke at 1123 K but the reason is unclear; this aspect requires further investigation.

Table 5.9 Results from Reduction of Garnierite Calcine with Solid Carbon

Ore was roasted for 30 minutes in air at the reduction temperature. Reductant addition was 5 g per 100 g of dried ore, as either coke containing 78.3% C, or activated carbon containing 88.7% C. 'FeNi Exp' is the measured ferronickel grade; 'FeNi Equil' is the simulated equilibrium ferronickel grade.

Test Code	Carbon	Temp (K)	Time (min)	Reduction (%)			FeNi Exp Ni(%)	FeNi Equil Ni(%)
				$Ni_{(\%)}$	$Fe_{(\%)}$	$Co_{(\%)}$		
GR900C4	Coke	1173	60	35	1.7	8.2	69	77
GR900C1	Coke	1173	120	57	7.3	33	46	43
GR900C2	Coke	1173	120	29	2.3	15	58	43
GR900C3	Coke	1173	120	24	1.6	11	61	43
GR950C1	Coke	1223	60	49	3.0	21	64	41
GR950C3	Coke	1223	80	16	1.6	8.4	53	37
GR950C4	Coke	1223	92	14	0.87	5.9	64	37
GR950C2	Coke	1223	120	65	4.3	30	62	37
GR950AC2	Act C	1223	20	16	2.8	11	38	39
GR950AC1	Act C	1223	60	28	7.1	20	30	26
GR950AC3	Act C	1223	80	8.2	2.5	6.1	26	24
GR950AC4	Act C	1223	80	14	3.6	8.9	30	24

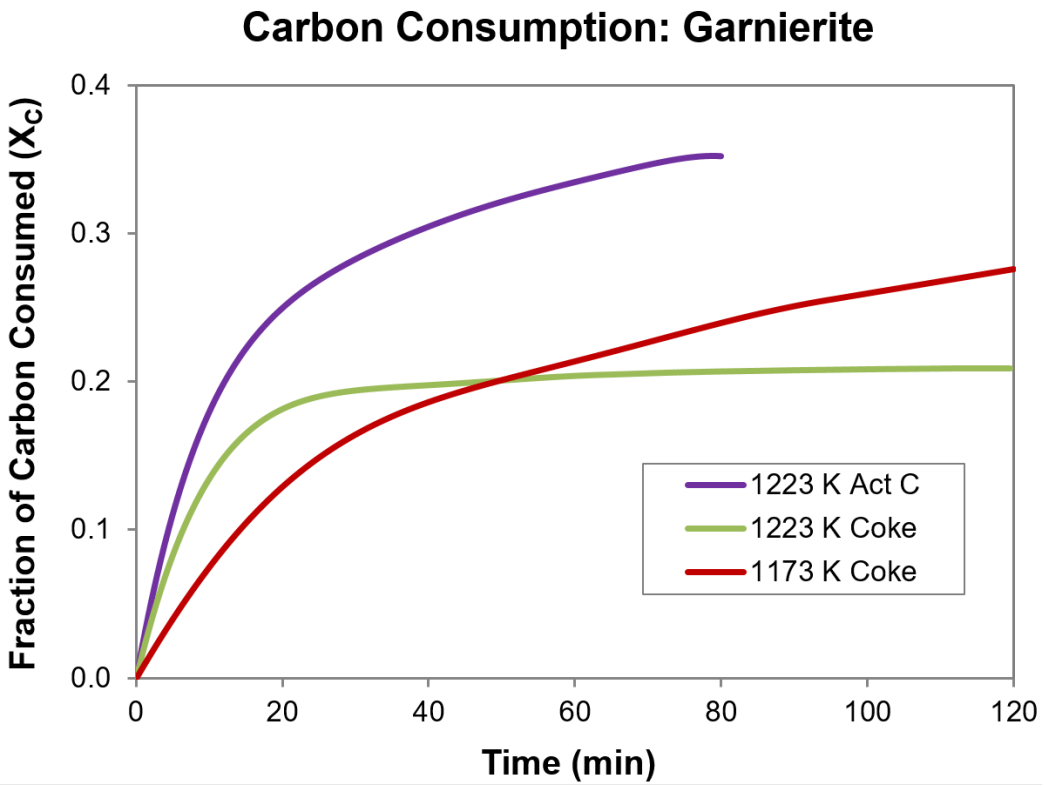

Figure 5.14 Carbon Consumed during Garnierite Reduction

Reductant added at 5% of dried ore, as either coke (78.3% C) or activated carbon (88.7% C). Curves are best fits from experimental data (Appendix B.4).

5.5.2 Metal Reduction

The measured metal reduction percents (Table 5.9) are variable and the trend of increasing reduction with increasing time, noted for limonite (Table 5.4) and nontronite (Table 5.6), is not clearly evident for garnierite. The maximum Ni reductions achieved with coke after 120 minutes were 37% (averaged) at 1123 K and 65% at 1173 K; a maximum of 28% was achieved with activated carbon after 60 minutes, falling to 11% (averaged) after 80 minutes.

The percents of Ni, Co and Fe reduced versus time are shown in Figure 5.15 for coke at 1173 K. Metal reductions are compared with those predicted from the equilibrium simulation (Section 5.5.3) using the carbon consumption data shown in Figure 5.14. It can be seen that the measured reductions lie well below those predicted by the simulation; when using coke at 1173 K, for example (Figure 5.15), the simulation predicts that reduction of ~100% of Ni and Co is possible, with an associated co-reduction of ~15% of the Fe. The same is true for reduction with coke at 1223 K, and especially for reduction with activated carbon at 1223 K.

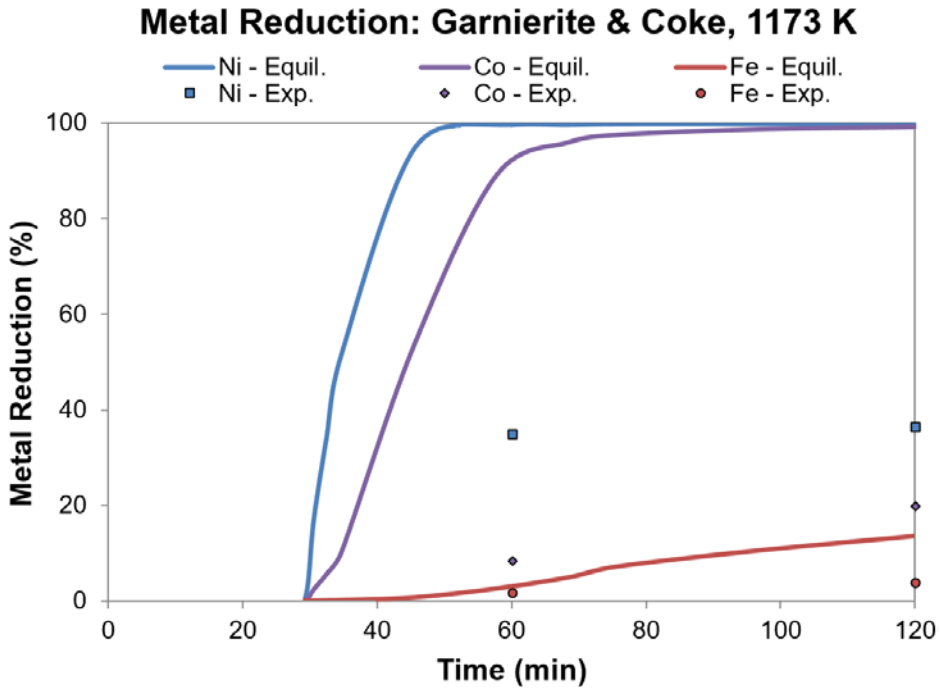

Figure 5.15 Simulated & Measured Metal Reduction, Garnierite & Coke, 1173 K
Lines are equilibrium; points represent averaged experimental data (Table 5.9).

Since garnierite contains a relatively small amount of reducible iron oxides compared to nontronite or limonite, the oxygen pressure reached during reduction was lower than for either the nontronite or the limonite calcine. For reduction with

coke at 1173 K, for example, the measured oxygen pressure after 120 minutes was ~10^{-14} atm for nontronite (Figure 5.10), ~10^{-15} atm for limonite (Figure 5.5) and ~$3x10^{-17}$ atm for garnierite (Figure 5.16).

The stronger reducing conditions facilitate the formation of fine in-situ ferronickel deposits, which likely explains the low and variable Ni reductions achieved during the garnierite reduction tests (Table 5.9). The reduction of garnierite calcine with carbon was not the focus of this study and the presence of fine ferronickel in the reduction product requires further confirmation. However, the presence of in-situ ferronickel was confirmed within a garnierite calcine after segregation with coke (Figure 8.2).

5.5.3 Equilibrium Simulation and Oxygen Pressure

The results of the equilibrium simulation for the reduction of garnierite calcine with coke at 1173 K are summarised in Figure 5.16. The calcine initially contains mainly SiO_2 (44.8 grams), Mg_2SiO_4 (19.8 grams) and Fe_2O_3 (16.7 grams) as shown in Table 5.1. The simulated oxygen pressure of the bulk gas is also included in the figure along with the representative (averaged) measured oxygen pressure (labelled GR900C). The full set of measured oxygen pressure data are provided in Appendix B.5.

According to the simulation, enstatite ($MgSiO_3$) is stable within the unreduced calcine, and iron oxide reduction begins with the transformation of hematite → magnetite (in spinel), followed by the reduction of magnetite (in spinel) → fayalite (which dissolves into newly formed Mg-rich olivine) and simultaneously, magnetite (in spinel) → ferrosilite (which dissolves into the existing Mg-rich pyroxene). Alloy formation begins after 30.6 minutes.

The wide divergence between the measured and simulated oxygen pressures during the last half of the test indicates that the simulation is not particularly representative of the experimental system. This is probably because hematite and silica are dominantly present in the unreduced calcine as discrete coarse particles (Section 4.1.6). Once hematite is reduced to magnetite, the subsequent ferrous oxide reduction product cannot readily combine with silica to form Fe silicates, and the silicates cannot readily form solid solutions.

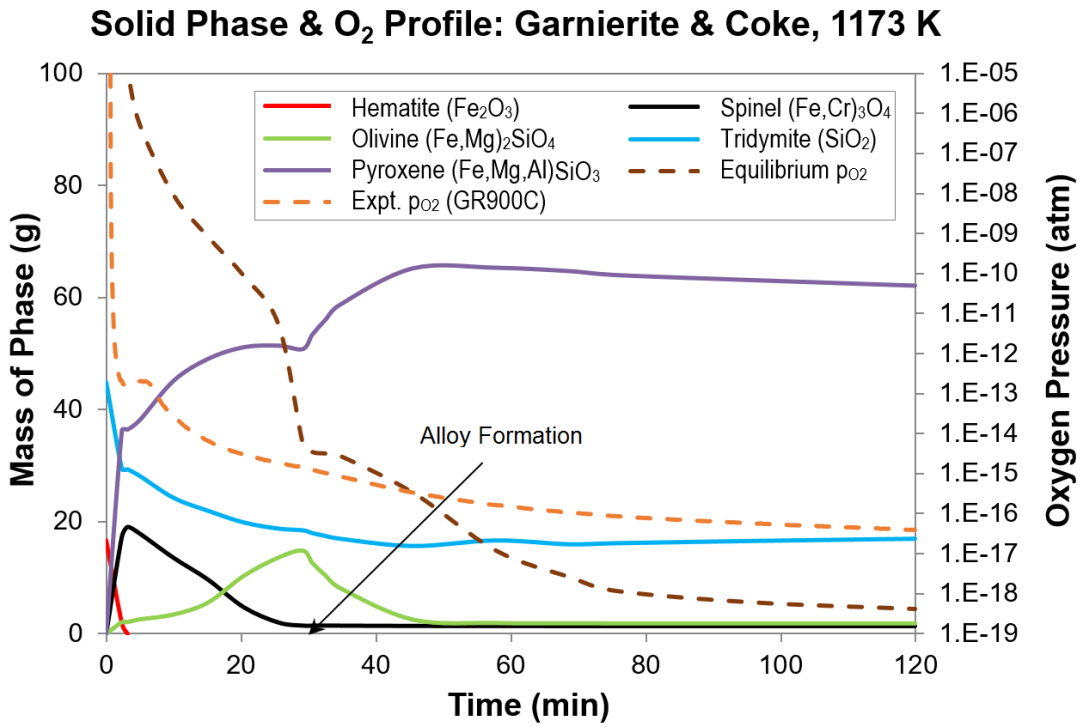

Figure 5.16 Equilibrium Simulation of Garnierie Reduction with Coke, 1173 K

Phase profiles are for a 100g dried ore. Dashed brown line represents the simulated p_{O_2}; dashed orange line represents the experimental p_{O_2}.

Without the buffering effect of Fe silicate formation, the p_{O_2} would fall rapidly, and in the presence of metastable ferrous oxide, be initially controlled by the Fe_3O_4/FeO equilibrium and then subsequently by the FeO/Fe equilibrium. This may be the reason why the experimental p_{O_2} reaches only ~3x10^{-17} atm (cf. Table 5.3), significantly higher than the ~4x10^{-19} atm predicted by the simulation at the end of the test. The higher experimental p_{O_2} is also consistent with the experimental ferronickel grades being higher than the simulated values (Table 5.9).

The presence of metastable iron oxides during reduction of garnierite calcine is supported by results from an EDS-SEM analysis of a reduction product (Section 5.5.4), which shows a significant number of coarse iron oxide and silica particles still present after reduction with coke at 1173 K for 30 minutes. The simulated phase transformations with coke and activated carbon at 1223 K show the same trends as those at 1173 K with coke; all are summarised in Table 5.10. Figures illustrating these data and oxygen pressure profiles are provided in Appendix B.7.

The relatively high p_{O_2} within the experimental system (compared to the equilibrium system), however, would not suppress the formation of ferronickel, since as shown in Table 5.10, this can form when the p_{O_2} is ~4x10^{-15} atm at 1173 K and ~3x10^{-14} atm at 1223 K.

A comparison of the oxygen pressures at which ferronickel can initially form within all the three calcines is informative. The simulated oxygen pressure required to initiate alloy formation at 1173 K, for example, decreases in the order; garnierite (3.9x10^{-15} atm, Table 5.10) > nontronite (1.7x10^{-15} atm, Table 5.7) > limonite (1.4x10^{-15}, Table 5.5). In comparison, the FACTSage simulations show that the a_{FeO} within the calcine increases in the order: garnierite ($a_{FeO} \leq 0.1$), nontronite ($a_{FeO} \leq 0.3$) and limonite ($a_{FeO} \leq 0.8$). If the a_{FeO} dominantly determined the p_{O_2} at which alloy formed, the value should be lowest for garnierite[20]. However, the p_{O_2} is highest for garnierite calcine which contains the most NiO (1.62%, Table 5.1) and lowest for limonite calcine which contains the least NiO (1.19%, Table 5.1). This indicates that the critical p_{O_2} required to initiate in-situ ferronickel reduction depends dominantly on the a_{NiO} in the calcine rather than the a_{FeO}. This is an important observation in relation to later consideration of the suppression of in-situ reduction to alloy during the segregation process.

Table 5.10 Solid Phase Transformations during Garnierite Calcine Reduction

Equilibrium phase transformations during the simulated equilibrium reduction of garnierite with coke and activated carbon. Alloy forms initially through the reduction of olivine, and then through the reduction of pyroxene.

Simulated Phase Transformation Times (minutes)			
Phase Change	Coke 1173 K 120 min. total	Coke 1223 K 120 min. total	Act C 1223 K 80 min. total
Hematite → Spinel	0 → 3.1	0 → 1.1	0 → 0.7
Spinel → Olivine	0 → 31	0 → 10	0 → 6.9
Spinel → Pyroxene	0 → 31	0 → 10	0 → 6.9
Olivine → Pyroxene	31 → 58	10 →16	6.9 → 10
Alloy Formation Initiating p_{O_2} (atm)	31 → End 3.9x10^{-15}	10 → End 3.1x10^{-14}	6.9→ End 3.1x10^{-14}
Silica	Falls 0 → 58 Increases 58 →	Falls 0→ 15 Increases 15 →	Falls 0 →10 Increases 10 →

The arrow implies that the mass of phase increases over the time, unless otherwise noted.

[20] This follows from the equilibrium constant for the reaction $2FeO(s) \rightarrow 2Fe(s) + O_2(g)$ from which the p_{O_2} required to achieve a given a_{Fe} at a particular temperature decreases as the a_{FeO} decreases.

5.5.4 Nickel in Partially Reduced Calcine

A sample of garnierite calcine was subjected to a mild reduction (reduction with coke at 1173 K for 30 minutes) before being resin-mounted, polished and carbon coated for EDS-SEM analysis. The mildly reducing conditions were selected so that the deportment of Ni could be studied in a partially reduced calcine prior to alloy formation. Figure 5.17 shows a backscattered electron image of a ~1 mm x 1.2 mm (1000 µm x 1200 µm) cross section through the partially reduced calcine. Detailed Al, Ca, Fe, Mg, Ni and Si element maps through this cross section are provided in Appendix B.16.

The majority of the Ni was found within the partially reduced chlorite and serpentine dehydroxylates, originally identified within the unreduced calcine (Figure 4.14). These materials appeared similar to when present in the unreduced calcine (Section 4.1.6). The residual chlorite dehydroxylate was present within relatively crystalline veins through silica (Figure 4.11), while the serpentine dehydroxylate conglomerates, now more crystalline, bordered iron oxide, silica and Cr spinel particles (Figure 5.18).

Four regions of the partially reduced chlorite dehydroxylate from Figure 5.17 were analysed via EDS-SEM, as summarised in Table 5.11. This material consisted of Mg and Fe silicates (pyroxene and olivine) containing 5-10% Ni, with an average molar composition ($Mg_{0.78}Fe_{0.35}Al_{0.27}Ni_{0.17}SiO_{3.1}$) a little higher in Fe and Si than the original material (Table 4.11).

Four regions of the partially reduced serpentine dehydroxylate conglomerate particles were analysed via EDS-SEM, as summarised in Table 5.12. This material contained 1.9-2.3% Ni, and had an average molar composition of $Mg_{0.78}Fe_{0.51}Al_{0.09}Ni_{0.04}Ca_{0.04}SiO_{2.7}$, very similar to the unreduced material (Table 4.12).

The partially reduced material appeared as fine crystalline mixtures of pyroxene and olivine, with the Fe_2O_3 in the originally fine to amorphous material now reduced to FeO and combined with SiO_2 and Mg silicates. An example of a partially reduced serpentine dehydroxylate surrounding a Cr spinel is shown in Figure 5.18.

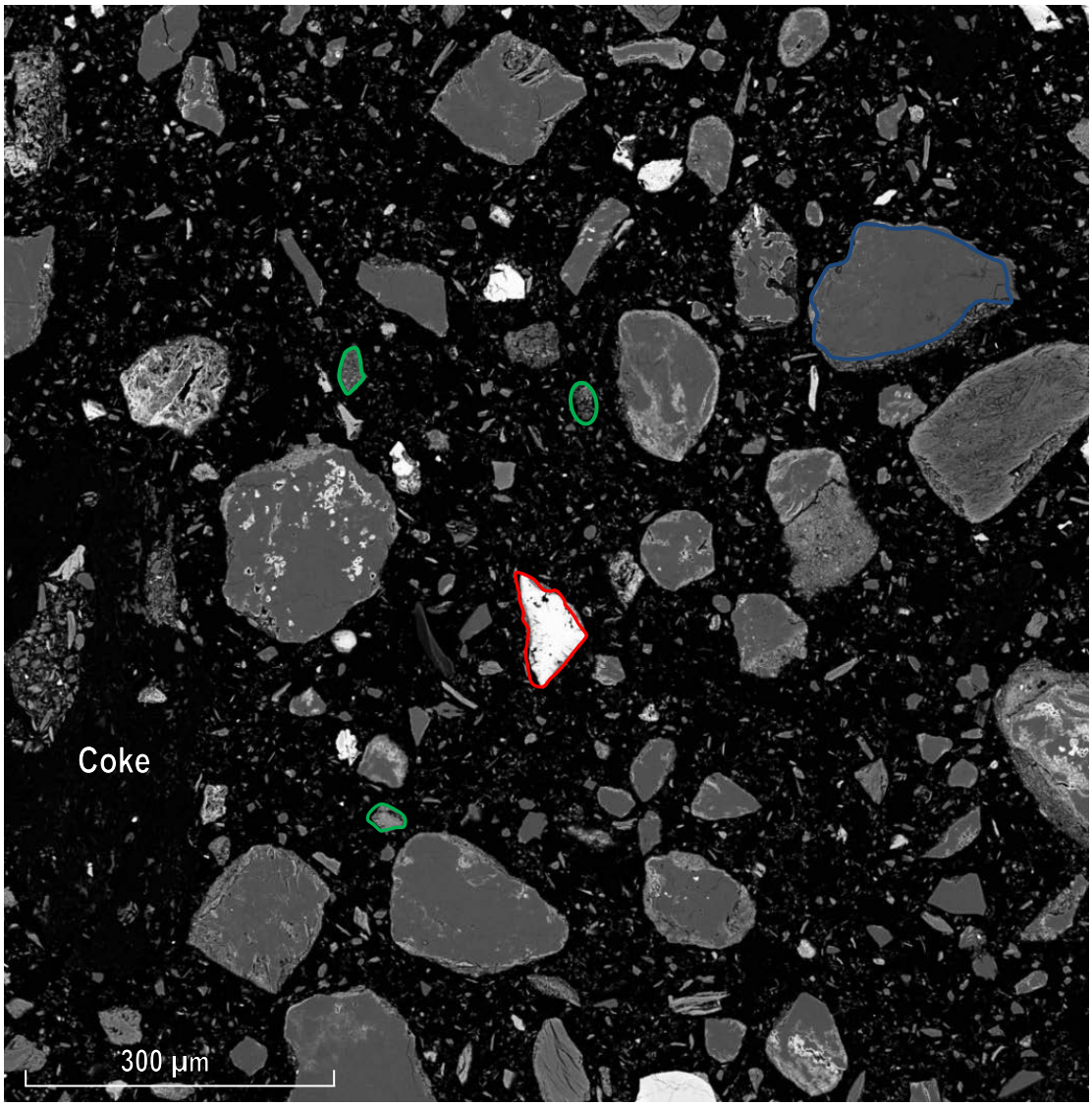

Figure 5.17 Section through Partially Reduced Garnierite Calcine

SEM image through a garnierite calcine reduced with coke at 1173 K for 30 minutes with no alloy formation. The particles shown are: monoxide with 4.5-5% Ni (outlined in green); primary quartz (outlined in dark blue); partially reduced iron oxide (magnetite/wustite, outlined in red). Cr spinels are not shown, but an example can be seen in Figure 5.18. Residual chlorite dehydroxylates (containing 5-10% Ni) are generally present throughout the crystalline silica (Figure 4.11), whilst residual serpentine dehydroxylates (containing 1.9-2.3% Ni) border the larger particles (Figure 5.18).

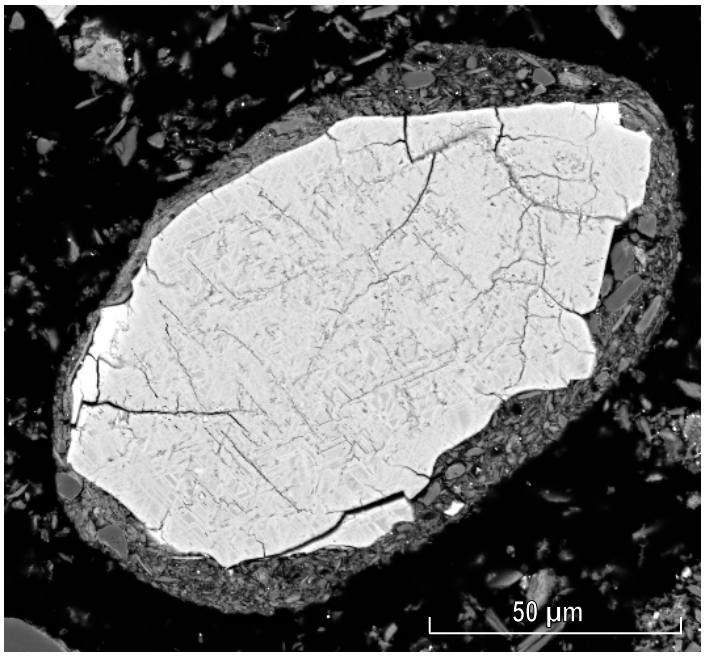

Figure 5.18 Section through a Cr Spinel with Serpentine Dehydroxylate Border

SEM image through a Cr spinel bordered by partially reduced serpentine dehydroxylate conglomerate particles.

Table 5.11 Partially Reduced Chlorite Dehydroxylate

Areas from Figure 5.17; chemical analysis via EDS-SEM

Area	Ni (wt%)	Average Composition (moles)
1	6.4	$Mg_{0.78}Fe_{0.39}Al_{0.32}Ni_{0.15}SiO_{3.3}$
2	8.3	$Mg_{0.76}Fe_{0.31}Al_{0.24}Ni_{0.18}SiO_{2.9}$
3	5.3	$Mg_{1.03}Fe_{0.54}Al_{0.37}Ni_{0.16}SiO_{3.9}$
4	10	$Mg_{0.53}Fe_{0.15}Al_{0.15}Ni_{0.18}SiO_{2.5}$
Average	7.5	$Mg_{0.78}Fe_{0.35}Al_{0.27}Ni_{0.17}SiO_{3.1}$

Table 5.12 Partially Reduced Serpentine Dehydroxylate

Area from Figure 5.17; chemical analysis via EDS-SEM.

Area	Ni (wt%)	Average Composition (moles)
1	1.9	$Mg_{0.69}Fe_{0.44}Al_{0.07}Ni_{0.04}Ca0_{.04}SiO_{2.5}$
2	1.9	$Mg_{0.77}Fe_{0.55}Al_{0.08}Ni_{0.04}Ca_{0.03}SiO_{2.7}$
3	2.1	$Mg_{0.73}Fe_{0.49}Al_{0.09}Ni_{0.04}Ca_{0.02}SiO_{2.8}$
4	2.4	$Mg_{0.94}Fe_{0.51}Al_{0.10}Ni_{0.05}Ca_{0.05}SiO_{2.9}$
Average	2.1	$Mg_{0.78}Fe_{0.51}Al_{0.09}Ni_{0.04}Ca_{0.04}SiO_{2.7}$

Ni was also identified in monoxide particles of ~10-30 µm in size; three examples are outlined in green in Figure 5.17. These particles contained 4.5-5.5% Ni, with an average composition of $Fe_{0.3}Mg_{0.95}Ni_{0.05}O$, and likely originated from the Ni free carbonate decomposition products within the garnierite calcine (Figure 4.14). It is unclear how the Ni transported to the monoxide during reduction.

Other particles identified in Figure 5.17 are the dominant crystalline quartz (an example outlined in dark blue) and crystalline iron oxide particles (example outlined in red), both found in the original calcine (Figure 4.14); neither the quartz nor the iron oxides contained Ni. Minor Cr rich spinels from the original calcine (Figure 4.14) were still present, some with reduced chromite ($FeCr_2O_4$) boundaries similar to those found in the partially reduced nontronite calcine (Figure 5.13) but without the 1-1.5% Ni enrichment.

5.5.5 Summary

In garnierite, significant silica and hematite exist as discrete coarse particles such that when iron oxide is reduced to FeO, it cannot readily combine with silica to form iron silicates and subsequent silicate solid solutions. As a result, the Fe_3O_4/FeO and subsequent FeO/Fe equilibria likely control the oxygen pressure, rather than equilibria involving iron silicates within both pyroxene and olivine solid solutions, as predicted by the equilibrium simulation.

Since the amount of iron oxide in garnierite is smaller than for either limonite or nontronite, and the amount of carbon added per gram of ore was kept constant, the reduction with garnierite reaches a lower final oxygen pressure compared to the other calcines. The oxygen pressure also falls relatively quickly during garnierite reduction since there is very limited buffering by iron silicate formation, as happens during nontronite reduction.

Only low and variable levels of metal reduction were detected through bromine/methanol leaching of the reduction product, most likely due to a lack of accessibility of the leach solution to very fine ferronickel encapsulated within the residual gangue. Most of the Ni prior to reduction was located at a concentration of ~7.5% within partially reduced chlorite dehydroxylate containing Mg-Fe-Al silicates, and at ~2.1% within partially reduced serpentine dehydroxylate containing Mg-Fe silicates.

5.6 The Rate of Carbon Gasification

When iron oxides are reduced with solid carbon under the conditions used in this work, the gas composition is mainly set by the iron oxide reduction equilibria, while the rate is mainly set by the rate of carbon gasification via the Boudouard reaction.

The rate of the Boudouard reaction is known to be sensitive to the presence of impurities adsorbed onto the carbon surface (Turkdogan and Vinters, 1972). However, no Boudouard rate measurements have been reported in the presence of laterite ores. In this work, it was possible to obtain a measurement of the rate of carbon gasification in the presence of limonite, nontronite and garnierite calcines during the initial period of reduction when hematite is converted to magnetite.

These measurements were considered valuable, not only to quantity the influence of the different laterite ore types on the carbon gasification rate, but also to provide for a comparison of rates when chloride salt was present during segregation.

At the initial stage of reduction, the p_{CO_2}/p_{CO} in the gas is mainly set by the equilibrium for the reduction of hematite to magnetite, as previously discussed (Section 5.2) according to:

$$\frac{p_{CO_2}}{p_{CO}} = K_{5.1}\frac{a_{Fe_2O_3}^3}{a_{Fe_3O_4}^2} \qquad 5.2$$

Since $K_{5.1}$ is large for all three temperatures used in this study: 2.6x10^4 (1123 K), 2.1x10^4 (1173 K), 1.8x10^4 (1223 K), p_{CO_2}/p_{CO} is also very large during the reduction of hematite to magnetite. It follows that $X_{CO_2} \cong 1$ for all three temperatures, where X_{CO_2} is the mole fraction of CO_2 within the CO+CO_2 portion of the gas.

Figure 5.19 shows the experimental and simulated X_{CO_2} values within the carbonaceous off-gas for the first 30 minutes of reduction with coke at 1173 K for each of the calcines.

It can be seen from Figure 5.19 that the value of X_{CO_2} is very close to one during the hematite to magnetite reduction period for all calcines types. This confirms that the Boudouard reaction is the dominant rate control during this initial period, and that the rate of carbon consumption is a measure of the rate of the Boudouard reaction.

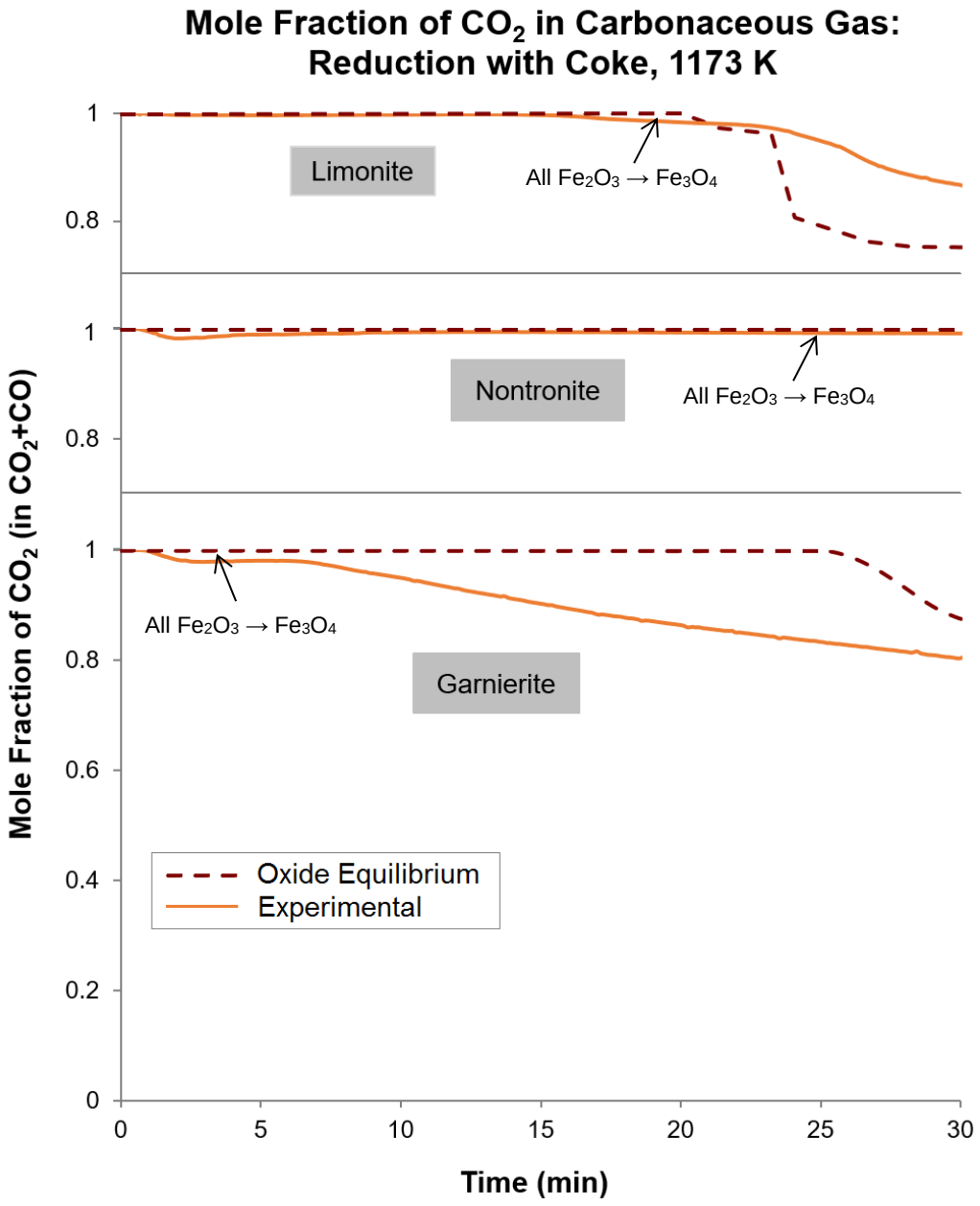

Figure 5.19 Mole Fraction of CO_2 within Carbonaceous Off-Gas

Dashed line shows X_{CO_2} when iron oxide reduction equilibria completely determine the carbonaceous gas composition. Solid line shows X_{CO_2} experimental value. Arrow shows end of hematite reduction to magnetite.

The rate of the Boudouard reaction is known to be chemically controlled by the surface reaction rather than by diffusion when the temperatures is <1373 K and when the carbon particle diameter is < 0.2 cm (2000 µm) (Turkdogan et al., 1968). This confirms that the rate will be controlled by the surface reaction for the temperatures (1123-1223 K) and carbon size (80% passing 280 µm and 320 µm) used in this work.

The surface reaction is accepted to be a two-step process in which a low resistance equilibrium adsorption of CO_2 onto the surface is followed by a high resistance rate-limiting desorption of the activated complex (Roberts and Harris, 2006). This process is most accurately described by the Langmuir-Hinshelwood (LH) rate equation (Appendix A.4.1). However, the LH equation cannot be meaningfully applied to the current experimental data, as it is complex and would require a rigorous experimental programme to evaluate the multiple rate constants.

For the present work, it was convenient to approximate the Boudouard rate equation by a simpler power function equation (Fortini and Fruehan, 2005) in which the rate of change in the mass of carbon (dm_c/dt) is related to the mass of carbon (m_c) present at time t and the partial pressures of CO_2 and CO in the gas, according to:

$$-\frac{dm_C}{dt} = m_c k_{BR}\left(p_{CO_2} - \frac{p_{CO}^2}{K_{BR}}\right) \qquad 5.5$$

k_{BR} is the Boudouard rate constant and K_{BR} is the Boudouard reaction equilibrium constant with values of 16.0 at 1123 K, 34.5 at 1173 K and 71.8 at 1223 K.

The equation is valid provided the specific surface area (area/mass) of carbon remains constant. This applies during the first 20% of carbon gasification with CO_2, as determined by Turkdogan et al. (1968). It was found that during this initial gasification period, oxidation occurs uniformly over the entire available carbon surface. The surface area increases as the mass of carbon decreases such that the area/mass remains approximately constant. A more detailed development of Equation 5.5 is given in Appendix A.4.2.

In the current experiments, Equation 5.5 essentially applies over the hematite to magnetite reduction range for all three calcines. Since the value of p_{CO} is small within this range and K_{BR} is relatively large at the temperatures used in this work, the p_{CO}^2/K_{BR} term in Equation 5.5 is negligible, and with $p_{CO_2} \approx 1$ atm, Equation 5.5 can be simplified to:

$$-\frac{dm_C}{dt} = m_c k_{BR} \qquad 5.6$$

If $m_{c,o}$ represents the mass of carbon at time $t = 0$, rearrangement and integration between 0 and t, gives:

Rearrange

$$-\int_{m_{c,o}}^{m_c} \frac{dm_C}{m_C} = k_{BR}\int_o^t dt \qquad 5.7$$

Integrate $$\ln\frac{m_c}{m_{c,o}} = -k_{BR}t \quad (5.8)$$

Since the fractional conversion of carbon X_c is given as:

$$X_c = 1 - \frac{m_c}{m_{C,o}} \quad (5.9)$$

Substitution of Equation 5.9 into Equation 5.8 gives the integrated rate equation expressed in terms of fractional conversion:

$$-\ln(1 - X_C) = k_{BR}t \quad (5.10)$$

The Boudouard rate constant can thus be determined from Equation 5.10 as the slope from a plot of $-\ln(1 - X_C)$ versus time t. Others (Turkdogan and Vinters, 1969; Turkdogan and Vinters, 1970; Rao, 1971; Fruehan, 1977) have used this equation (or a closely related equation) to determine the rate constant for the Boudouard reaction within relatively concentrated CO_2 gas.

The plots of Equation 5.10 for the reduction of nontronite calcine are shown in Figure 5.20, as calculated from the carbon consumption (Figure 5.6) over the first 4 minutes of reduction, where the rate of carbon gasification was approximately constant and the $p_{CO_2} \approx 1$ atm. Similar plots for nontronite and garnierite calcines are presented in Appendix B.1.

The calculated Boudouard rate constants are summarised in Table 5.13. Values from the work of Turkdogan and Vinters (1970) and Fruehan (1977) are presented for comparison. Turkdogan and Vinters (1970) reacted CO_2 with coke and activated carbon in the absence of ore, whereas Fruehan (1977) reduced FeO with coke and measured the Boudouard reaction rate based on carbon gasification being the rate control. The data from Fruehan (1977) were read from Figure 9 of the paper.

The data in Table 5.13 indicate that, in all cases, the Boudouard reaction rate was significantly enhanced when the specific surface area (area/mass) of the reductant was increased by replacing coke with activated carbon. For the present work, the rate was increased by 3.8x for nontronite, 1.4x for limonite and 1.9x for garnierite when activated carbon replaced coke under otherwise similar conditions; in contrast, the data from Turkdogan and Vinters (1970) and Fruehan (1977) both show a 10x increase.

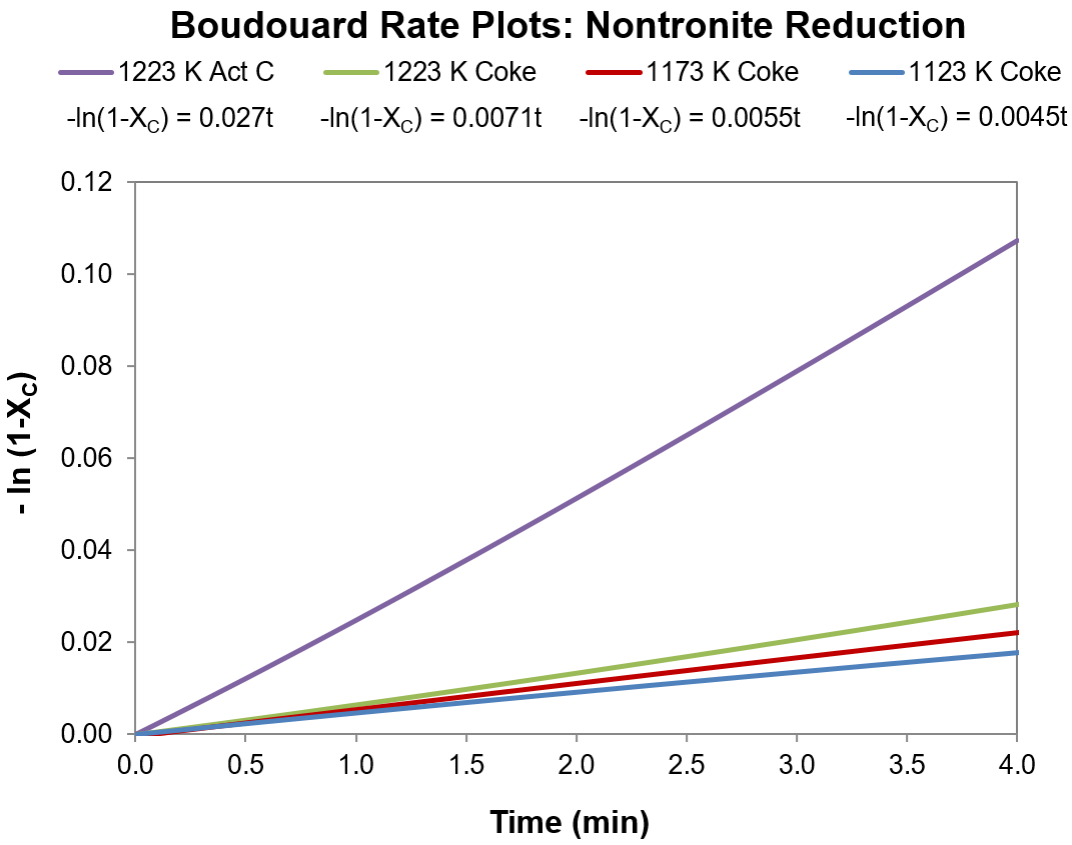

Figure 5.20 Integrated Boudouard Rate Equation Plots, Nontronite Reduction

Plots apply to the first 4 minutes of the hematite to magnetite reduction period for which p_{CO_2}~ 1 atm and the specific surface area of carbon is relatively constant.

Table 5.13 Boudouard Rate Constants for Reduction with Carbon

Carbon	Temperature (K)	k_{BR} (/min)			C/CO_2 only	C/CO_2 FeO/Fe
		Nontronite	Garnierite	Limonite	T & V* 1970	F* 1977
Coke	1123	$4.5x10^{-3}$	-	$1.2x10^{-2}$	$4.2x10^{-4}$	-
Coke	1173	$5.5x10^{-3}$	$8.3x10^{-3}$	$1.9x10^{-2}$	$1.6x10^{-3}$	$3.25x10^{-3}$
Coke	1223	$7.1x10^{-3}$	$1.9x10^{-2}$	-	$5.2x10^{-3}$	$1.09x10^{-2}$
Act C	1173	-	-	$3.6x10^{-2}$	$1.6x10^{-2}$	$3.25x10^{-2}$
Act C	1223	$2.7x10^{-2}$	$2.7x10^{-2}$	-	$5.4x10^{-2}$	$1.09x10^{-1}$

*T&V is Turkdogan and Vinters (1970); F is Fruehan (1977), as taken from his figure 9 and adjusted for ~30% CO_2 in equilibrium with FeO/Fe.

Table 5.13 also shows that the rate in the presence of laterite was generally larger than that measured by either Turkdogan and Vinters (1970) or Fruehan (1977), consistent with the Boudouard reaction being catalysed by the fine material present in the calcine (Turkdogan and Vinters, 1972). The specific increase in rate, however, appears dependent on the type of laterite present, with the rate being

fastest for limonite, and slowest for nontronite. This difference may be due to limonite calcine having the highest portion of Fe_2O_3, which is known to catalyse the Boudouard reaction, while the nontronite calcine had the highest portion of amorphous material, which may affect the carbon surface and slow its gasification relative to limonite or garnierite.

The activation energies for the Boudouard reaction were calculated using the log form of the well-known Arrhenius equation:

$$\ln k_{BR} = \ln k_0 - \frac{E}{RT} \qquad 5.11$$

k is the rate constant, k_0 is the pre-exponent/collision frequency factor, T is the temperature (K), R is the universal gas constant (J/Kmol) and E is the activation energy (J/mol). A plot of $\ln k$ versus $1/T$ was used to determine the collision frequency factor (k_0) from the zero intercept and the activation energy (E) from the slope.

These plots are shown in Figure 5.21 using the measured rate constants from Table 5.13. Plots using the data of Turkdogan and Vinters (1970) and Fruehan (1977) are included for comparison. The fitted equations and calculated k_0 and E values are summarised in Figure 5.21. Activation energies recorded by other researchers within ore free systems are summarised in Table 5.15.

Figure 5.21 highlights the variable catalytic influence of the laterites on the Boudouard reaction. The catalytic effect appears to increase the rate more at lower temperatures, especially for limonite and nontronite, as shown in the figure. As a result, the activation energies, specifically 46 kJ/mol for limonite and 96 kJ/mol for nontronite (Table 5.14), are much lower than the 287 kJ/mol recorded by Turkdogan and Vinters (1970), and the values reported for most other ore free systems (Table 5.15).

Coke gasification in the presence of roasted garnierite was also enhanced relative to the measurements of Turkdogan and Vinters (1970) and Fruehan (1977), but the reaction exhibited a more substantial decrease in rate as the temperature fell, as shown in Figure 5.21. This results in the higher activation energy of 207 kJ/mol (Table 5.14). The data from Fruehan (1977), who reduced pure FeO to Fe, lie above those of Turkdogan and Vinters (1970), indicating that the presence of FeO enhanced the rate.

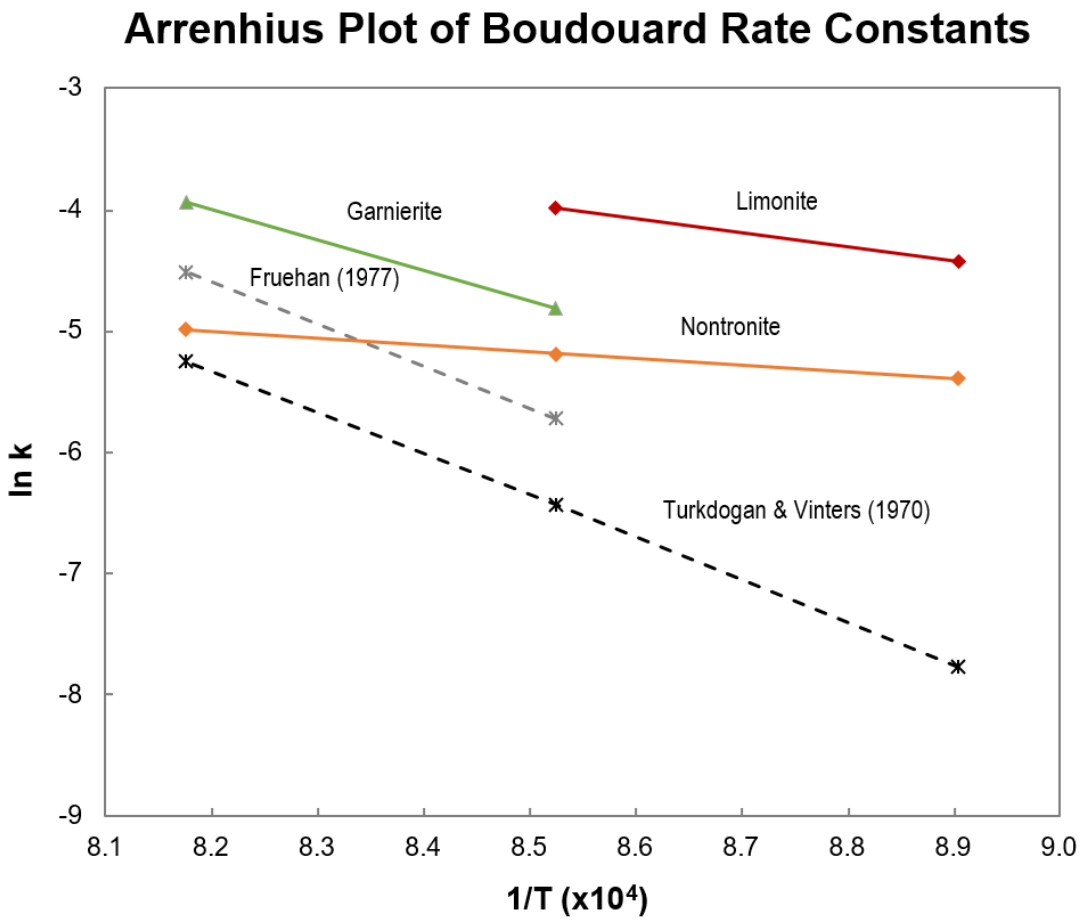

Figure 5.21 Arrhenius Plots of Boudouard Rate Constants

Data are for reduction with coke, taken from Table 5.13.

Table 5.14 Boudouard Reaction Activation Energies, Reduction with Carbon

Values calculated using the Boudouard rate constants for the reduction of limonite, nontronite and garnierite with coke.

Ore	Temperature (K)	Arrhenius Expression	k_0 (/min)	E (kJ/mol)
Limonite	1123–1173	$\ln k_{BR} = 0.433 - \frac{5580}{T}$	372	96
Nontronite	1123–1223	$\ln k_{BR} = 16.4 - \frac{24900}{T}$	1.54	46
Garnierite	1173-1223	$\ln k_{BR} = 5.92 - \frac{11600}{T}$	1.35×10^7	207

Table 5.15 Summary of Boudouard Reaction Kinetic Data

Reported kinetic data for the Boudouard reaction, showing the carbon type, temperature, partial pressure of CO_2 and activation energy.

Carbon	Temperature (K)	Partial Pressure of CO_2 (atm)	Activation Energy (kJ/mol)	Reference
Met Coke	973-1573	0.9–1.0	287	Turkdogan and Vinters (1970)
Coconut Charcoal	973-1573	0.9–1.0	287	Turkdogan and Vinters (1970)
Pure Carbon	1180-1220	0.6-0.7	301	Rao (1971)
Pet Coke	NS	up to 1.0	214	Harris and Smith (1990)
Coke	1173-1123	0.3	289	Fruehan (1977)*
Brown Coal Char	NS	0.1–1.0	230	Harris and Smith (1990)
Coal	987-1165	10.1–1.0	131	Ye et al. (1998)

*Calculated from estimated k values given in Table 5.13; NS = not specified.

5.7 Discussion

For all laterite ores studied, it appears that the oxygen pressure profile during reduction is mainly controlled by the iron oxide reduction equilibria and hence is dependent on the mineralogy of the ore. The profile especially depends on the amounts of hematite and free silica contained within the calcine, and whether these are in intimate contact such that silicates can both form and diffuse into solid solutions during reduction. As such, the oxygen pressure profile that develops during a reduction with solid carbon is a unique characteristic of the calcine being reduced.

An indicative equilibrium profile can be obtained by thermodynamic simulation, but in reality, metastable phases can exist during reduction due to surface contact limitations. The actual oxygen profile may thus depend on the relative rates of a number of reduction reactions that include metastable phases, and to a lesser extent, it may depend on the influence of the Boudouard reaction. For the ores studied, the simulated oxygen profile was a good predictor of the experimental oxygen pressure for limonite, reasonable for nontronite and poor for garnierite.

For each laterite ore, the time it takes to move through the unique oxygen pressure profile during reduction depends on the rate at which carbon can reduce CO_2 to CO via the Boudouard reaction. This rate increases with increases in both temperature and the surface area of carbon. The rate is enhanced in the presence of laterite, and is catalysed to different extents by the specific impurities present in each ore, with the rate being the highest for limonite and the lowest for nontronite.

For the different laterite ores, the rate at which the oxygen pressure falls depends on the amount of reducible iron oxides present relative to amount of added carbon; for example, garnierite contains the least amount of iron oxide and shows a relatively fast decline in oxygen pressure. However, the rate of reduction is also dependant on the effect of impurities on the carbon gasification rate. Nontronite contains half the iron oxide present in limonite, but takes longer for hematite to be completely converted to magnetite (cf. Table 5.7 and Table 5.5). This is because of the much slower rate of the Boudouard reaction in the presence of nontronite compared to limonite (Figure 5.21).

Ferronickel will form if the oxygen pressure is reduced to a critical value. This value depends mainly on the activity of NiO in the ore and hence on the Ni content and mineralogy. It appears likely that the greater the rate at which the oxygen pressure falls through the critical value, the greater the number of small ferronickel nuclei that form, and the finer and more widely these ferronickel are dispersed, although this must also depend on the mineralogy. Once fine alloy forms within the calcine, it may be encapsulated and difficult to detect with a bromine/methanol selective leach, although more work is needed to clarify this. Any fine ferronickel which forms would also be difficult to separate from the gangue by any conventional physical concentration process.

For limonite, the relatively high iron oxide/carbon ratio slows the reduction rate such that fine ferronickel appeared to form only when coke was replaced by activated carbon. This resulted in Ni reductions close to the equilibrium predictions, except when using activated carbon.

For nontronite, the relatively slow carbon gasification rate and the formation of Fe silicates inhibited the decrease in oxygen pressure such that ferronickel was predicted to form, and did form, only at the highest reduction temperature when using coke, or when using activated carbon. In both cases, and especially when using activated carbon, the Ni reduction detected by the bromine/methanol leach was much less than predicted.

For garnierite, the relatively low iron oxide/carbon ratio combined with insufficient iron silicate formation to buffer the fall in oxygen pressure, appears to have resulted in the formation of fine alloy under all conditions tested. Overall, this led to variable and much lower than predicted reductions of Ni, as detected by a bromine/methanol leach.

For nontronite calcine, after partial reduction, but prior to alloy formation, the Ni was present at ~3.5% within nontronite dehydroxylate containing Fe silicates. For garnierite calcine, the Ni was present at ~7.5% within chlorite dehydroxylate containing Mg-Fe-Al silicates and at ~2.1% within serpentine dehydroxylate containing Mg-Fe silicates.

For both limonite and nontronite, and probably for garnierite, reduction in the presence of carbon is likely chemically controlled by the equilibrium between the bulk gas and the calcine, at least with the fine laterite calcines and coke used in this work. Under equilibrium conditions, it is predicted that the majority of Ni can be reduced along with a relatively small amount of Fe; however, the reduction product would likely be difficult to recover unless the reducing conditions were controlled to inhibit the formation of fine ferronickel. In this work, the maximum reductions detected using a bromine/methanol leaching method were 63% Ni and 1.2% Fe for limonite, 29% Ni and 1.1% Fe for nontronite, and 65% Ni and 7.3% Fe for garnierite.

Chapter 6

Nontronite Segregation

A study of the segregation process applied to a nontronite nickel laterite ore from Heron Resource's Kalgoorlie Nickel Project is presented throughout this chapter. Similar studies for limonite and garnierite ores from the same deposit are presented in subsequent chapters.

The segregation of laterite first involves roasting the ore in air to produce a calcine, which is then reduced in the presence of solid carbon and a $CaCl_2$ salt, with oxygen removed mainly as CO_2 and CO. The process occurs by a series of intermediate steps, specifically: chloridisation of Ni and Fe oxides with HCl, transport of the gaseous metal chlorides to the carbon surface, and reduction of the metal chlorides to ferronickel by H_2. The reductant is supplied through gasification of carbon with steam, while HCl is initially supplied through hydrolysis of $CaCl_2$ and then recycled along with H_2O through a coupling of the reaction steps (Section 2.2).

The segregation process operates in parallel with another reduction process, in which CO reduces Fe and Ni oxides in-situ within the calcine; this enhances the chloridisation of Fe, since the vapour pressure of ferrous chloride is much greater than ferric chloride (Figure 2.4). The CO_2 produced by this in-situ reduction process then reacts with solid carbon to regenerate CO via the Boudouard reaction. If segregation is to be successful, it must largely occur before the in-situ reduction of Fe and Ni oxides to form ferronickel.

The response of nontronite calcine to the segregation process has been examined through consideration of: the recoverable Ni, Fe and Co as a function of temperature, time and carbon surface area; the changes in mineralogy, oxygen pressure, carbon consumption and extent of oxygen removal during segregation; the grade and nature of the ferronickel product; the HCl recycle, including HCl lost in the off-gas; the residual chloride within the segregation bed; the effects of varying the roasting times and temperatures; and the nature of the magnetic concentrate.

6.1 Recovery of Metals

Sixty three tests were performed using a two-step segregation method (Section 3.3.2) which enabled the determination of a reaction 'zero' time for kinetic analysis. The metal recoveries and ferronickel grades were determined by a selective

bromine/methanol leach (Section 3.3.7) of the magnetic concentrate produced using a Davis Tube Tester (Section 3.3.6). The ferronickel formed during segregation is relatively large (~10-200 µm) and accessible to the leach solution (Section 6.3.3).

The solid carbon was sized between 125-300 µm and added at 5% of the dried ore as either metallurgical coke or activated carbon; the $CaCl_2$ salt was also added at 5% of the dried ore. Reagent addition was standardised for all three laterite ores studied, rather than optimised, so that the effects of ore mineralogy could be compared more readily.

Multiple tests were conducted for up to 210 minutes with coke at 1173 K, up to 120 minutes with coke at both 1173 K and 1223 K, and up to 80 minutes with activated carbon at 1223 K. Two single tests were conducted for 60 minutes with coke at 1248 K and 1278 K, both above the 1233 K sintering temperature of the calcine. The results of all tests are summarised in Table 6.1.

Table 6.1 Metal Recoveries and Ferronickel Grades, Nontronite Segregation
Ore was roasted for 30 minutes in air at the segregation temperature.
Reagent addition per 100 g of dried ore was 5 g of either coke (78.3% C), or activated carbon (88.7% C) and 5 g of $CaCl_2$.

Test Code	Carbon	Temp (K)	Time (minutes)	Recovery (%)			FeNi Ni(%)
				$R_{Ni(\%)}$	$R_{Fe(\%)}$	$R_{Co(\%)}$	
N850C4	Coke	1123	10	11	0.10	1.5	84
N850C3	Coke	1123	20	17	0.11	1.3	88
N850C1	Coke	1123	30	16	0.10	1.0	89
N850C6	Coke	1123	45	22	0.14	1.7	88
N850C7	Coke	1123	70	27	0.25	2.9	84
N850C5	Coke	1123	80	35	0.37	4.6	82
N850C9	Coke	1123	90	39	0.51	6.7	79
N850C2	Coke	1123	100	25	0.19	2.2	87
N850C11	Coke	1123	110	23	0.17	2.1	87
N850C8	Coke	1123	120	41	0.74	9.1	73
N850C10	Coke	1123	120	29	0.31	3.8	82
N850C19	Coke	1123	180	41	0.57	5.5	78
N900C24	Coke	1173	9	17	0.19	1.7	81
N900C10	Coke	1173	19	34	0.34	2.9	83
N900C11	Coke	1173	34	40	0.53	6.1	79
N900C12	Coke	1173	49	57	1.1	13	72
N900C13	Coke	1173	64	64	1.4	16	70
N900C14	Coke	1173	64	55	1.2	17	69
N900C20	Coke	1173	79	61	1.7	22	64
N900C7	Coke	1173	90	58	2.0	23	59
N900C15	Coke	1173	94	61	1.6	19	66
N900C22	Coke	1173	94	54	1.2	16	68
N900C16	Coke	1173	109	62	1.7	21	64
N900C21	Coke	1173	109	62	1.9	25	61

Table 6.1 Metal Recoveries and Ferronickel Grades (cont'd)

Test Code	Carbon	Temp (K)	Time (minutes)	Recovery (%)			FeNi Ni(%)
				$R_{Ni(\%)}$	$R_{Fe(\%)}$	$R_{Co(\%)}$	
N900C3	Coke	1173	110	60	1.9	24	61
N900C1	Coke	1173	120	59	2.0	24	59
N900C2	Coke	1173	120	59	1.9	23	60
N900C4	Coke	1173	120	61	1.9	24	61
N900C5	Coke	1173	120	54	1.5	18	64
N900C8	Coke	1173	120	62	2.0	24	61
N900C9	Coke	1173	120	59	2.1	25	58
N900C17	Coke	1173	124	66	2.8	29	54
N900C18	Coke	1173	124	69	2.4	29	59
N900C19	Coke	1173	124	74	2.3	27	61
N950C11	Coke	1223	9	38	0.40	5.2	82
N950C12	Coke	1223	19	63	1.0	11	76
N950C13	Coke	1223	34	70	3.5	33	49
N950C6	Coke	1223	40	65	2.5	27	57
N950C14	Coke	1223	49	67	3.3	34	50
N950C5	Coke	1223	50	64	2.5	27	56
N950C15	Coke	1223	64	79	4.9	31	44
N950C4	Coke	1223	70	71	4.1	37	46
N950C2	Coke	1223	80	68	4.4	35	44
N950C16	Coke	1223	94	67	5.9	36	36
N950C11	Coke	1223	96	73	5.1	39	42
N950C17	Coke	1223	109	82	8.9	44	32
N950C8	Coke	1223	110	73	6.2	40	37
N950C1	Coke	1223	120	70	4.8	37	42
N950C3	Coke	1223	120	72	6.8	39	34
N950C7	Coke	1223	120	67	5.0	37	40
N950C10	Coke	1223	120	69	5.3	37	39
N950C18	Coke	1223	124	75	14	38	21
N950C19	Coke	1223	124	67	4.9	35	41
N975C*	Coke	1248	60	74	14	24	21
N1000C*	Coke	1273	60	79	29	31	12
N950AC1	Act C	1223	5	33	1.6	17	51
N950AC2	Act C	1223	10	56	10	31	21
N950AC3	Act C	1223	15	51	10	25	19
N950AC7	Act C	1223	20	59	18	33	14
N950AC8	Act C	1223	25	67	22	37	13
N950AC9	Act C	1223	42	65	30	34	10
N950AC10	Act C	1223	50	69	33	35	9.4
N950AC11	Act C	1223	60	68	29	35	11

*Tests carried out above the calcine sintering temperature

The data in Table 6.1 generally show that the recoveries of Ni, Fe and Co increase with both time and temperature. However, there are relatively large variations between tests conducted under equivalent conditions. For example, for the six 120 minute tests at 1173 K with coke, the Ni, Fe and Co recoveries ranged from 54-62%, 1.5-2.1% and 18-25% respectively. Given the small sample size (~25 g) and cumulative error associated with the multi-step experimental procedure (Section 3.3), this variation is not unexpected, although it made it necessary to carry out a relatively large number of tests to clearly establish trends.

6.1.1 Nickel

Previous work indicates that multiple factors, such as the activity of NiO and the partial pressures of HCl and H_2O, may affect the Ni segregation rate (Section 2.4); however, due to the variation in the data, it was not possible to account for all of these factors within a fundamental rate equation. An alternative empirical equation, analogous to the 'first order to a limit' rate equation usually applied to flotation data, was found suitable to describe the rate of change of segregated nickel recovery with time.

6.1.1.1 First Order to a Limit Rate Equation

The 'first order to a limit' rate equation is used to describe flotation kinetics when recovery is limited by a portion of the valuable metal being within a mineral that will not float (Kelly and Spottiswood, 1982). In this work, it similarly appears that recovery is limited by a portion of the Ni within the ore that will not segregate. The 'first order to a limit' equation, as it relates to Ni segregation, is developed below.

Consider that $m_{Ni,o}$ is the initial mass of Ni in the ore, from which $R_{Ni,\max}$ is the maximum possible fractional recovery of Ni via segregation, and m_{Ni} is the mass of Ni already segregated to form ferronickel at any time during the process. If the rate of Ni segregation is first order with respect to the reactive mass of Ni remaining in the ore, the 'first order to a limit' rate equation may be expressed as:

$$\frac{dm_{Ni}}{dt} = k_{Ni}(R_{Ni,max}m_{Ni,o} - m_{Ni}) \qquad 6.1$$

dm_{Ni} is the mass of nickel segregated in time dt, k is a first order rate constant and $(R_{Ni,max}m_{Ni,o} - m_{Ni})$ is the amount of reactive Ni remaining in the ore at any time t.

The fractional recovery of Ni (R_{Ni}) may be expressed as:

$$R_{Ni} = \frac{m_{Ni}}{m_{Ni,o}} \qquad 6.2$$

Division of Equation 6.1 throughout by $m_{Ni,o}$ and substitution for R_{Ni} gives the rate in terms of the fractional recovery of Ni:

Divide by $m_{Ni,o}$

$$\frac{d(m_{Ni}/m_{Ni,o})}{dt} = k_{Ni}\left(R_{Ni,max}\frac{m_{Ni,o}}{m_{Ni,o}} - \frac{m_{Ni}}{m_{Ni,o}}\right) \qquad 6.3$$

Substitute for R_{Ni}

$$\frac{dR_{Ni}}{dt} = k_{Ni}(R_{Ni,max} - R_{Ni}) \quad 6.4$$

Re-arrangement and integration of Equation 6.4 between the limits $t = 0, t$ and $R_{Ni} = 0, R_{Ni}$ (Appendix A.4.3) gives the expression for the fractional recovery of Ni after a specific reaction time, t:

$$R_{Ni} = R_{Ni,max}(1 - e^{-k_{Ni}t}) \quad 6.5$$

6.1.1.2 Recovery and Rate Equations

The parameters ($R_{Ni,max}$, k_{Ni}) for the integrated rate equations were fitted from the Ni recovery data (Table 6.1) using the Solver add-in within Microsoft Excel, to determine the fit of least squared deviations (Brown, 2001). The fitted parameters are presented in Table 6.2, and the integrated rate equations are plotted in Figure 6.1 along with the experimental data.

Table 6.2 Integrated Rate Equations, Recovery of Nickel from Nontronite

Fitted parameters for 'first order to a limit' integrated rate equations. R_{Ni} is the fractional Ni recovery; $R_{Ni,max}$ is the maximum fractional nickel recovery; k_{Ni} is a first order rate constant ($/min$); t is reaction time.

Series	Carbon	Temp (K)	Time (max) (minutes)	Integrated Rate Equation $R_{Ni} = R_{Ni,max}(1 - e^{-k_{Ni}t})$	Fit r^2
N850C	Coke	1123	210	$R_{Ni} = 0.43(1 - e^{-0.019t})$	0.96
N900C	Coke	1173	120	$R_{Ni} = 0.63(1 - e^{-0.038t})$	0.93
N950C	Coke	1223	120	$R_{Ni} = 0.71(1 - e^{-0.093t})$	0.93
N950AC	Act C	1223	60	$R_{Ni} = 0.67(1 - e^{-0.136t})$	0.97

The Ni recovery increases over time while approaching a limit (Figure 6.1), with an increase in temperature raising both the recovery limit and the rate at which the limit is approached. When coke was replaced by activated carbon at 1223 K, the rate remained relatively unchanged, although the recovery limit decreased slightly from 71 to 67%[21]. The only other available data on nontronite segregation was produced by Chermak et al. (1973), who reported a Ni recovery of 70% after 60 minutes at 1273 K, similar to the maximum of 71% reported here for 1223 K (Table 6.2).

[21] For convenience, fractional recovery used in the rate equations will often be expressed as a percent recovery in the text.

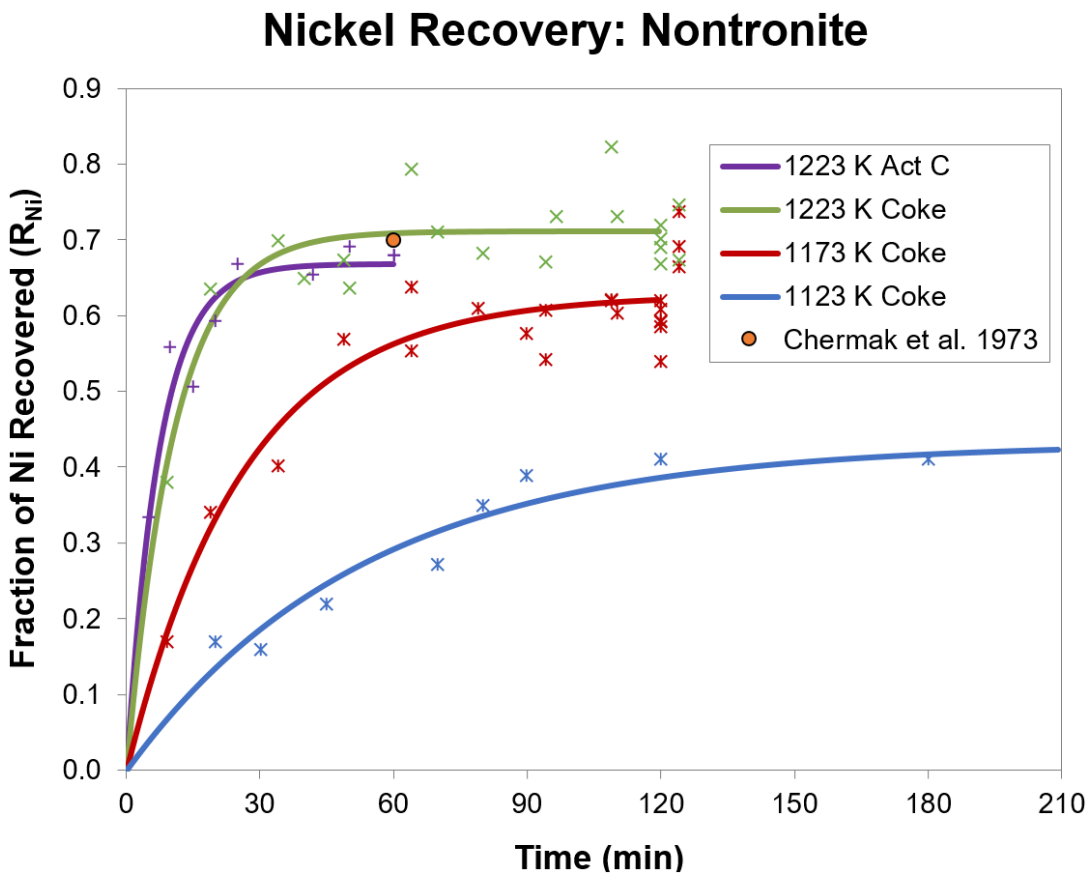

Figure 6.1 Nickel Recovery, Nontronite

Fitted curves are of the form $R_{Ni} = R_{Ni,max}(1 - e^{-k_{Ni}t})$, see Table 6.2. Chermak et al. (1973) used coke at 1273 K (Table 2.6). For this graph, and all others for metal recovery in this Chapter, dot points represent data from Table 6.1.

6.1.1.3 Rate Control

The rate of Ni segregation will only be significantly increased through promotion of the rate-limiting step, which can be either chloridisation of NiO, reduction of $NiCl_2$, generation of the H_2 reductant, or a diffusion transport pathway.

The reduction of $NiCl_2$ is known to be a fast reaction with low kinetic resistance under segregation conditions (Section 2.4.3) and thus is unlikely to be the rate control. The H_2 reductant is generated by gasification of carbon with H_2O which can be a relatively high resistance reaction under segregation conditions (Section 2.4.5). However, if this reaction was the rate control, increasing the surface area of carbon would increase the Ni segregation rate, but it appears not to do so (cf. coke and activated carbon at 1223 K, Figure 6.1). A diffusion rate control is also unlikely, given the fine size of the calcine (Figure 4.4) and carbon particles (Figure 4.15 &

Figure 4.16) and the vibration applied to the reacting bed (Section 3.2.1). It therefore appears that, by elimination, the chloridisation of NiO is the likely rate control for Ni segregation under the conditions used here.

Brittan and Liebenberg (1972), after their study on the segregation of garnierite ores, also concluded that chloridisation of NiO was the rate control. However, their experiments were very different from a genuine segregation system and the conclusion appears speculative. In their work, chloridisation was carried out by passing moisturised gas with a high concentration of HCl (up to 40%) through a fluidised calcine, and then reducing the metal chlorides by passing the off-gas through a separate carbon plug.

The rate of chloridisation was rapid under these conditions and equilibrium between solid and gas was achieved within the fluidised bed; thus the rate of chloridisation was dependent on the flow of the gas containing the HCl. The rate of chloride reduction onto carbon was also rapid for both Ni and Fe. The alloy deposited on the leading edge of the carbon plug, with the H_2O required for the generation of the H_2 reductant simultaneously delivered to the carbon surface along with the metal chlorides in the gas.

Brittan and Liebenberg (1972) considered that, in a genuine segregation system where chloridisation and reduction occur together, NiO chloridisation would be slower than the generation of H_2 and reduction of $NiCl_2$ at the carbon surface, and thus chloridisation would be rate controlling. This conclusion is aligned with their earlier findings for the segregation of Cu from a siliceous ore (Brittan, 1970).

The work presented here for nontronite agrees with the Brittan and Liebenberg (1972) assessment of the likely Ni segregation rate control for a garnierite ore, but through study of a genuine segregation system.

The chloridisation of NiO during segregation with HCl occurs according to the reverse hydrolysis equation:

$$NiO(s) + 2HCl(g) \rightarrow NiCl_2(g) + H_2O(g) \qquad 2.15$$

As noted by Brittan and Liebenberg (1972), the fast and thermodynamically favourable reduction of $NiCl_2$ with H_2 should provide the main driving force for Ni segregation by maintaining p_{NiCl_2} at a low level, below that of the equilibrium value for the chloridising reaction.

NiO can also be chloridised with $FeCl_2$, according to the exchange reaction:

$$NiO(s) + FeCl_2(g) \rightarrow NiCl_2(g) + FeO(s) \qquad 2.23$$

Equation 2.23 represents a combination of the chloridising reactions of FeO and NiO with HCl. The HCl chloridisation of FeO operates near equilibrium (Section 2.4.2), but the NiO chloridisation with HCl (Equation 2.15) does not. Thus the p_{NiCl_2} in the segregation gas will be less than the equilibrium value for Equation 2.23, driving the chloridisation of NiO by $FeCl_2$. Thus $FeCl_2$, in addition to HCl, should be an effective chloridising agent for NiO, especially since reaction 2.23 has a higher equilibrium constant than reaction 2.15, as pointed out by Brittan and Liebenberg (1972) and others (Section 2.4.2).

When both HCl and $FeCl_2$ contribute to the chloridisation of NiO, a fundamental equation for the isothermal rate of NiO chloridisation (and thus Ni segregation) can be approximated by a rate expression using a power function. The development of this equation for Ni segregation is shown in Appendix A.4.4, with the resulting expression of the form:

$$\frac{-dm_{NiO}}{dt} = Aa_{NiO}\left(k_{2.15}p_{HCl}^2 + k_{2.23}p_{FeCl_2}\right) \qquad 6.6$$

dm_{NiO} is the mass of NiO chloridised in time dt; A is the surface area of NiO; a_{NiO} is the activity of NiO relative to a pure solid standard state[22]; p_{HCl} and p_{FeCl_2} are the partial pressures of the denoted gases in contact with the ore; $k_{2.15}$ and $k_{2.23}$ are rate constants for the respective NiO chloridisation reactions given by Equations 2.15 and 2.23.

Since $\frac{dm_{Ni}}{dt} \propto \frac{-dm_{NiO}}{dt}$, comparison of Equation 6.1 with Equation 6.6 gives:

$$k_{Ni}(R_{Ni,max}m_{Ni,o} - m_{Ni}) \propto Aa_{NiO}\left(k_{2.15}p_{HCl}^2 + k_{2.23}p_{FeCl_2}\right) \qquad 6.7$$

If the area/mass of the Ni is approximately constant, then 'the area of NiO available for the reaction' (Aa_{NiO})[23] will be proportional to the 'mass of reactive nickel' ($R_{Ni,max}m_{Ni,o} - m_{Ni}$), thus:

$$k_{Ni} \propto (k_{2.15}p_{HCl}^2 + k_{2.23}p_{FeCl_2}) \qquad 6.8$$

[22] Activity is used in preference to concentration since NiO can be combined within various mineral species, i.e. silicates or monoxide solutions

[23] If NiO is pure, $a_{NiO} = 1$ and thus all of the area A is available for reaction etc.

This equation shows the relationship between the 'first order to a limit' rate constant k_{Ni} and the power function rate constants $k_{2.15}$ and $k_{2.23}$. It can be seen that k_{Ni} is not a true rate constant since its value depends on p_{HCl} and p_{FeCl_2}.

In this work, the amount of HCl within the gas was measured as a function of time, which enabled isothermal profiles of the maximum possible HCl pressure in the gas to be generated (Figure 6.26). The maximum p_{HCl} profiles varied with temperature, with the p_{HCl} being initially higher at the lower segregation temperature, but eventually higher at the higher segregation temperature. The $FeCl_2$ in gas was not measured, but the p_{FeCl_2} is expected to change with both the p_{HCl} and a_{FeO} in the ore, and probably increases over time as the a_{FeO} increases during reduction, as observed by Rey et al. (1972a). The influences of p_{HCl} and p_{FeCl_2} could not be incorporated into the rate equation using the data generated in this work.

Although k_{Ni} is not a genuine rate constant, it is still a useful parameter through which segregation rates can be quantified and compared, and from which apparent activation energies can be calculated for different ores under standard conditions, as used in this work.

6.1.1.4 Recovery Limit

Nickel recovery approached an upper limit, within experimental error, under all conditions tested. The maximum fractional Ni recoveries achieved ($R_{Ni,max}$) are shown as a function of temperature in Figure 6.2. The data at 1123, 1173 and 1223 K were taken from the fitted rate equations (Table 6.2). The data at 1248 and 1273 K were generated from single tests using a reaction time in excess of that required to approach the maximum recovery at these temperatures (Table 6.1); both of these tests were above the calcine sintering temperature but this did not impact on the trend shown in the figure.

A sample of nontronite calcine which had been segregated with coke for 70 minutes at 1173 K was resin-mounted, polished and carbon coated, with a 1.7 x 1.5 mm (1700 µm x 1500 µm) section subject to EDS-SEM analysis to determine the location of unsegregated Ni. A backscattered electron image of this section and accompanying EDS chemical maps are presented in Appendix B.17.

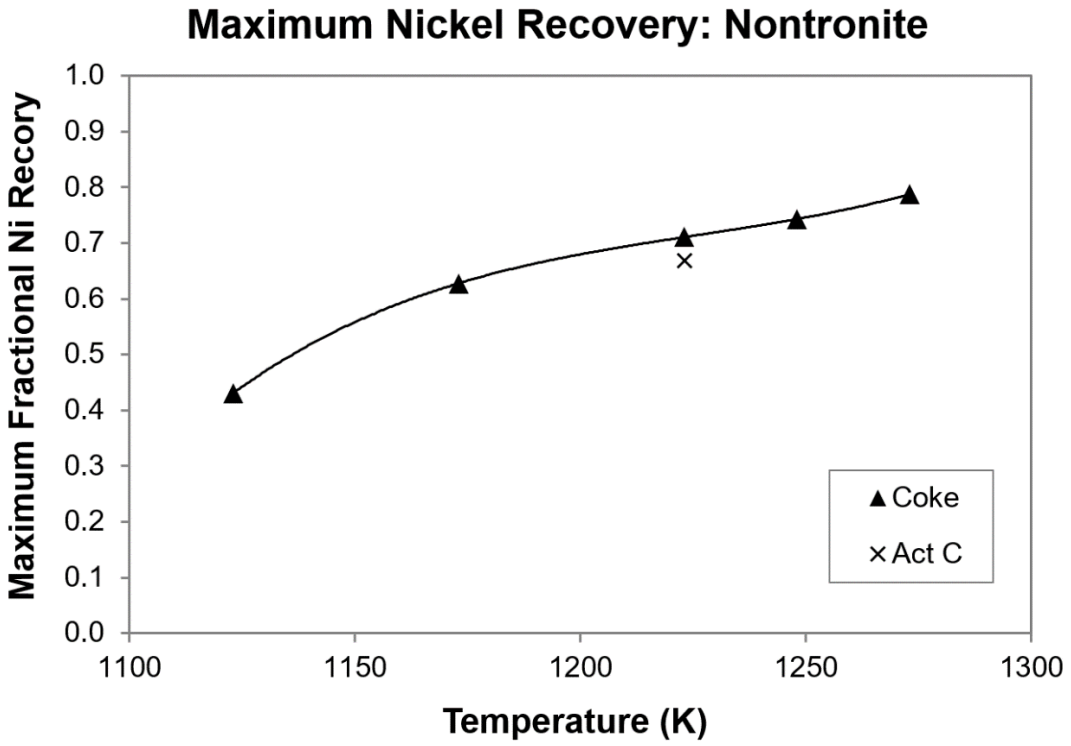

Figure 6.2 Maximum Nickel Recovery, Nontronite

The Ni recovery predicted for the segregation product examined by EDS-SEM was 58%, as calculated from the integrated rate equation (Table 6.2). The majority of the unsegregated Ni was located within remnant nontronite dehydroxylate conglomerate particles. A typical example is shown as a backscattered electron image in Figure 6.3, and in Figure 6.4 as an element intensity map, with Fe in red and Si in blue.

Chemical analysis of areas within the remnant dehydroxylate particles showed they were mixtures of silica, ferrosilite ($FeSiO_3$) and minor fayalite (Fe_2SiO_4). These particles likely formed from the fine grained to amorphous conglomerates of silica and iron oxides present after the initial calcination of the ore (Figure 4.6); Ni was distributed throughout these conglomerates, likely associated mainly with iron oxides. Recrystallisation and grain growth within the initially amorphous to fine grained silica appears to have left voids within the structure, as shown in Figure 6.3.

The compositions of four typical remnant dehydroxylate conglomerate particles found within the analysed section of segregated nontronite (Appendix B.17) are shown in Table 6.3. These were Fe rich silicates containing minor Mg and Al, with an average silicate composition close to pyroxene. The particles contained between 0.3-0.8% Ni (average 0.6%) and were significantly enriched in Fe, as indicated by

the average Fe/Si mole ratio. The ratio was 1.0 for the segregated particles, compared to 0.51 for the unsegregated particles within the calcine (Table 4.8), and 0.43 for the partially reduced particles (Table 5.8). The Fe enrichment during segregation is evidence that NiO is at least partly chloridised by $FeCl_2$ through reaction 2.23, after adsorption of $FeCl_2$ onto the particle surface.

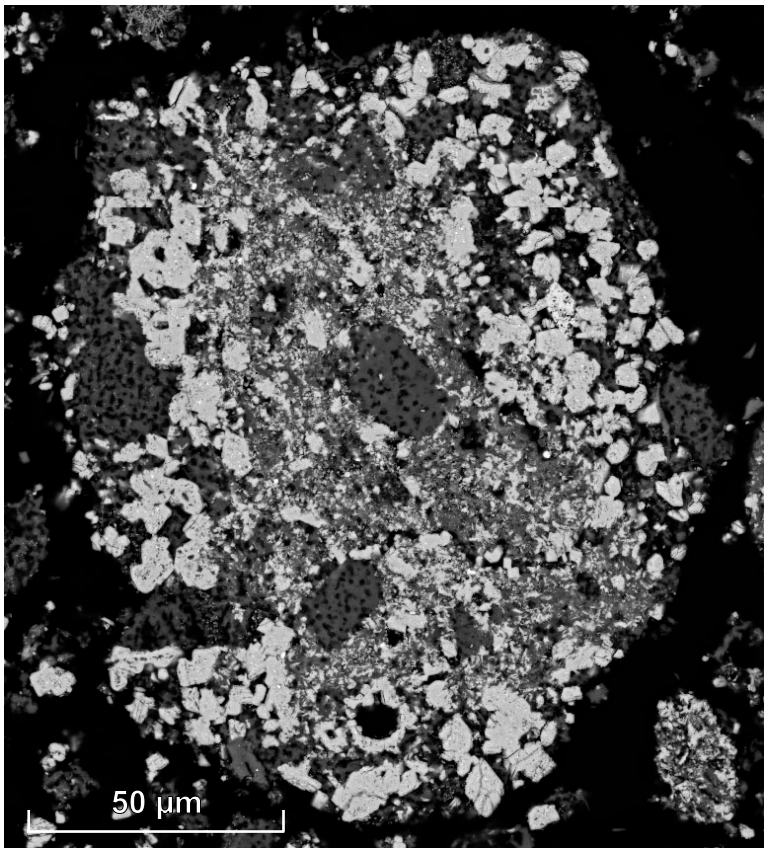

Figure 6.3 Section through a Remnant Nontronite Dehydroxylate Particle

SEM image through a remnant nontronite dehydroxylate particle after segregation with coke for 70 minutes at 1173 K showing: silica (darkest phase), ferrosilite (lighter phase) and fayalite (lightest coloured phase).

Table 6.3 Compositions of Remnant Nontronite Dehydroxylate Particles

Chemical analysis via EDS-SEM.

Particle Number	Ni (wt%)	Average Composition (moles)
1	0.3	$Fe_{0.60}Mg_{0.05}Al_{0.11}SiO_{2.65}$
2	0.5	$Fe_{0.65}Mg_{0.05}Al_{0.07}SiO_{2.50}$
3	0.7	$Fe_{1.20}Mg_{0.15}Al_{0.08}SiO_{3.10}$
4	0.8	$Fe_{1.50}Mg_{0.17}Al_{0.04}SiO_{3.30}$
Average	0.6	$Fe_{1.0}Mg_{0.11}Al_{0.08}SiO_{2.89}$

Minor Ni was located within Ca rich silicate rims found on some silica particles, presumably formed through $CaCl_2$ hydrolysis during segregation. An example of a rimmed particle is shown in Figure 6.5; it had an average composition of ~$Ca_{0.4}Fe_{0.4}Al_{0.1}Mg_{0.1}SiO_3$ and contained up to 0.7% Ni. All Cr rich spinels were found to be Ni free in the segregated material; in contrast, after reduction with carbon in the absence of chloride, these spinels contained Ni within a chromite boundary (Figure 5.13).

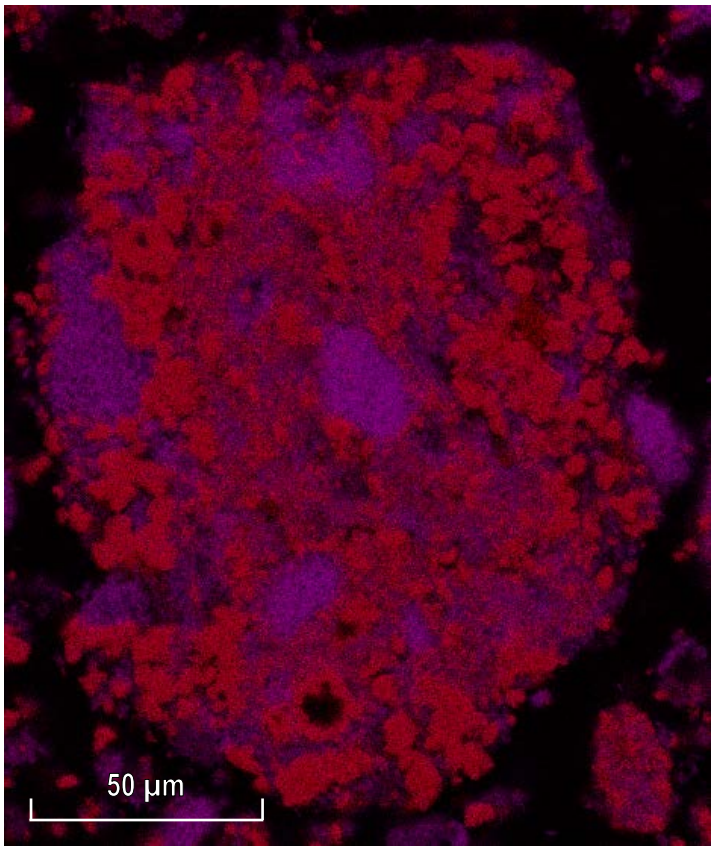

Figure 6.4 Fe and Si Distribution, Remnant Nontronite Dehydroxylate Particle
Chemical map for particle shown in Figure 6.3; Fe (red) and Si (purple). Ni was associated with Fe, but omitted due to its low concentration (~0.6%)

When segregating with coke, an average of ~4% Ni was typically lost in the segregation tails from ferronickel not collected during magnetic separation (Table 6.4) and ~0.2-2.5% Ni was lost from the sample as soluble chloride (Table 6.14). Handling and volatilisation losses were estimated from a mass balance (Appendix B.2) at 1.5% and 2.0% respectively. These losses collectively account for ~10% of the Ni; the remaining ~32% of the projected 42% Ni loss from the segregated nontronite shown in Figure 6.3 is likely from Ni remaining in iron silicates within the remnant nontronite dehydroxylate particles.

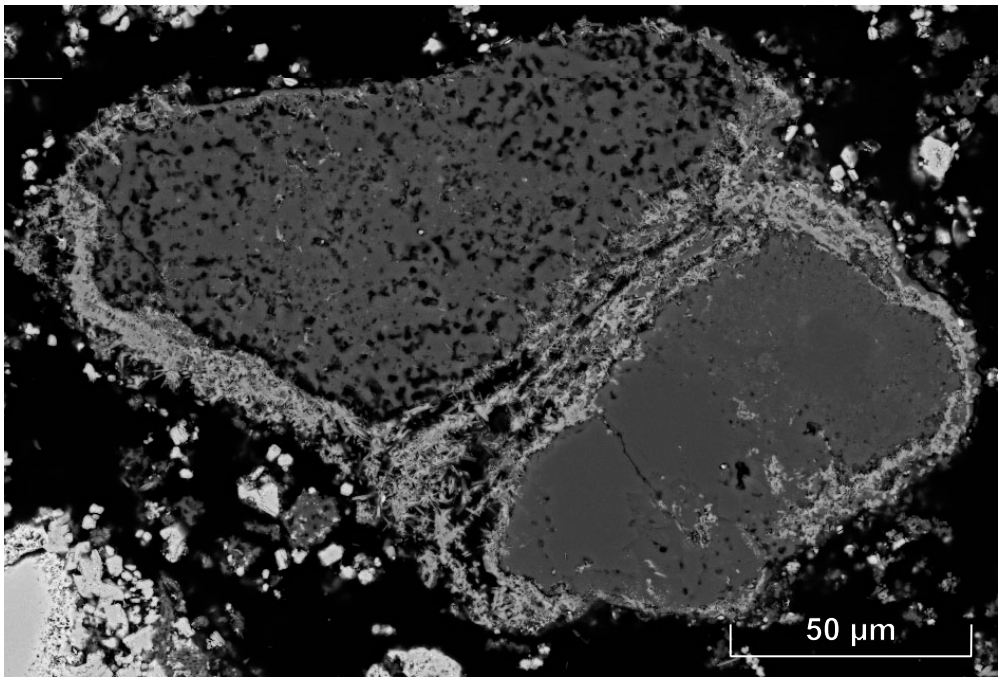

Figure 6.5 Section through a Silica particle bordered with Calcium Silicate

SEM image through a Ca silicate rimmed silica particle formed after segregation with coke for 70 minutes at 1173 K; the rim contains ~0.7% Ni.

Table 6.4 Metallic Nickel in Tails, Segregation of Nontronite with Coke

Metallic Ni recovered by a bromine/methanol leach of tails containing minimal in-situ alloy, after separation of magnetic concentrate. Test conditions as specified.

Test Code	Carbon	Temp (K)	Time (minutes)	Recovery of Ni from Tails (%)
N900C24	Coke	1173	9	2.2
N900C10	Coke	1173	19	2.5
N900C11	Coke	1173	34	4.1
N900C12	Coke	1173	49	5.8
N900C15	Coke	1173	94	3.5
N900C16	Coke	1173	109	6.9
N900C17	Coke	1173	124	5.2
N900C18	Coke	1173	124	1.9
N900C19	Coke	1173	124	3.8
Average	Coke	1173	76	4.0
N950C11	Coke	1223	9	2.2
N950C12	Coke	1223	19	2.5
N950C15	Coke	1223	64	4.1
N950C19	Coke	1223	124	5.8
Average	Coke	1223	54	3.6

When activated carbon was used at 1223 K, much of the unsegregated Ni remaining within the nontronite dehydroxylate particles was present as in-situ ferronickel. A typical particle with bright spots of in-situ reduced alloy throughout is shown in Figure 6.6. It appears that the in-situ reduction to ferronickel contributed to a slight decrease in the segregation recovery limit when using activated carbon compared to coke, as shown in Figure 6.2.

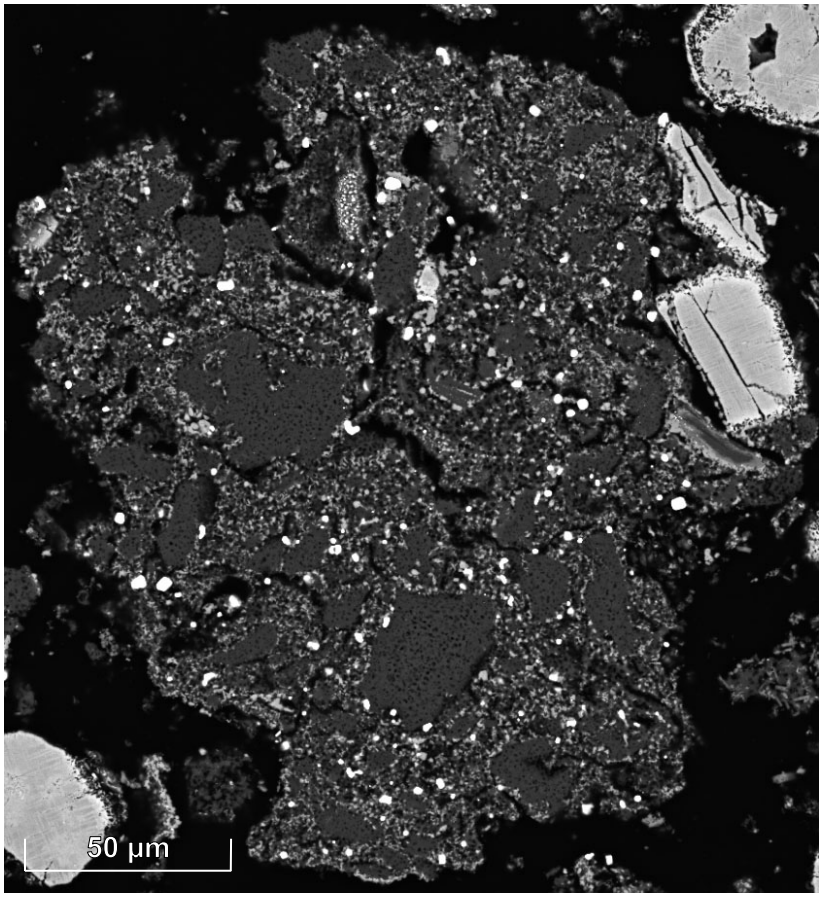

Figure 6.6 Remnant Nontronite Dehydroxylate Particle with In-situ Alloy

SEM image through a remnant nontronite dehydroxylate particle containing bright spots of in-situ ferronickel after segregation with activated carbon for 60 minutes at 1223 K. Silica is the darker phase, surrounded by a lighter Fe silicate; the dense lighter particles are Cr rich spinels.

The presence of in-situ reduced alloy rendered many of the gangue particles sufficiently ferromagnetic such that they reported along with segregated alloy to the concentrate (Figure 6.17). However, as already described (Chapter 5), the fine in-situ alloy remained largely undissolved by the bromine/methanol leach.

Figure 6.1 shows that at any temperature, the rate of Ni segregation was initially rapid and then slowed to a limit. Since the recovery of Ni by segregation appears to be kinetically controlled by the chloridisation of NiO, both the a_{NiO} and the chloridising environment (p_{HCl}, p_{FeCl_2}) will affect the rate, as shown by Equation 6.6. The NiO in the nontronite calcine is initially contained within fine to amorphous conglomerates of iron oxides and silica, from which iron silicates precipitate and grow during the segregation process, and in which the majority of unsegregated Ni remains at the end of the process.

As segregation progresses, the a_{NiO} within the conglomerates likely decreases; thus the segregation rate decreases. Eventually, the rate becomes negligible, with the residual NiO remaining within the iron silicates at a relatively low activity; thus recovery appears to reach a limit. A decrease in the a_{NiO} has also been proposed by Brittan and Liebenberg (1972) and Seaborn (1976) to explain why the segregation rate of Ni slows significantly with time.

Table 6.1 shows that as the temperature is increased, the Ni recovery reaches a higher limit within a shorter time. This is consistent with the segregation rate increasing with temperature, since it is chemically controlled. A greater amount of NiO also can be removed from the iron silicates at higher temperatures, possibly because more is removed earlier before becoming fully incorporated within the silicates.

It appears that the nontronite segregation process should be conducted at higher temperatures to maximise Ni recovery. Ultimately, the temperature will be limited by sintering of the ore. In this work, a maximum recovery of 79% Ni was achieved after segregation for 60 minutes at 1273 K, some 40 K above the sintering temperature (Table 4.2).

6.1.2 Iron

Iron is unavoidably segregated along with Ni to form a ferronickel alloy (Section 2.4.4). However, the fractional recoveries of Fe (Table 6.1) are significantly lower than for Ni, in agreement with the higher thermodynamic stability of FeO compared to NiO (Figure 2.2).

6.1.2.1 Zero Order Rate Equation

The isothermal rate of recovery of Fe was found to be constant within experimental error under all conditions, and could be described in terms of fractional recovery by a zero order rate equation:

$$\frac{dR_{Fe}}{dt} = k_{Fe} \qquad 6.9$$

$R_{Fe} = m_{Fe}/m_{Fe,o}$ is the fractional recovery of Fe, where m_{Fe} is the mass of Fe recovered from the original mass $m_{Fe,o}$; dR_{Fe} is the fractional recovery of Fe in time dt; and k_{Fe} is the zero order rate constant.

Integration between the limits $t = 0, t$ and $R_{Fe} = 0, R_{Fe}$ gives the expression for fractional recovery of Fe at any time t:

$$R_{Fe} = k_{Fe}t \qquad 6.10$$

6.1.2.2 Recovery and Rate Equations

The integrated rate equations, as determined from least square linear fits of the Fe recovery data (Table 6.1), are presented in Table 6.5 and plotted in Figure 6.7 along with the experimental data. The rate of recovery, which is constant with time at a specific temperature and carbon addition, increases when the temperature and carbon surface area (cf. activated carbon and coke at 1223 K) are increased. Few previous Ni laterite segregation studies report on the recovery of Fe, and no comparable data are available for nontronite.

Table 6.5 Integrated Rate Equations, Recovery of Iron from Nontronite

Fitted parameters for zero order integrated rate equations. R_{Fe} is the fractional Fe recovery; k_{Fe} is a zero order rate constant (/min); t is reaction time.

Series	Carbon	Temp (K)	Time (max) (minutes)	Integrated Rate Equation $R_{Fe} = k_{Fe}t$	Fit r^2
N850C	Coke	1123	210	$R_{Fe} = 4.3 \times 10^{-5}t$	0.87
N900C	Coke	1173	120	$R_{Fe} = 1.8 \times 10^{-4}t$	0.84
N950C	Coke	1223	120	$R_{Fe} = 5.3 \times 10^{-4}t$	0.71
N950AC	Act C	1223	60	$R_{Fe} = 8.5 \times 10^{-3}t$	0.95

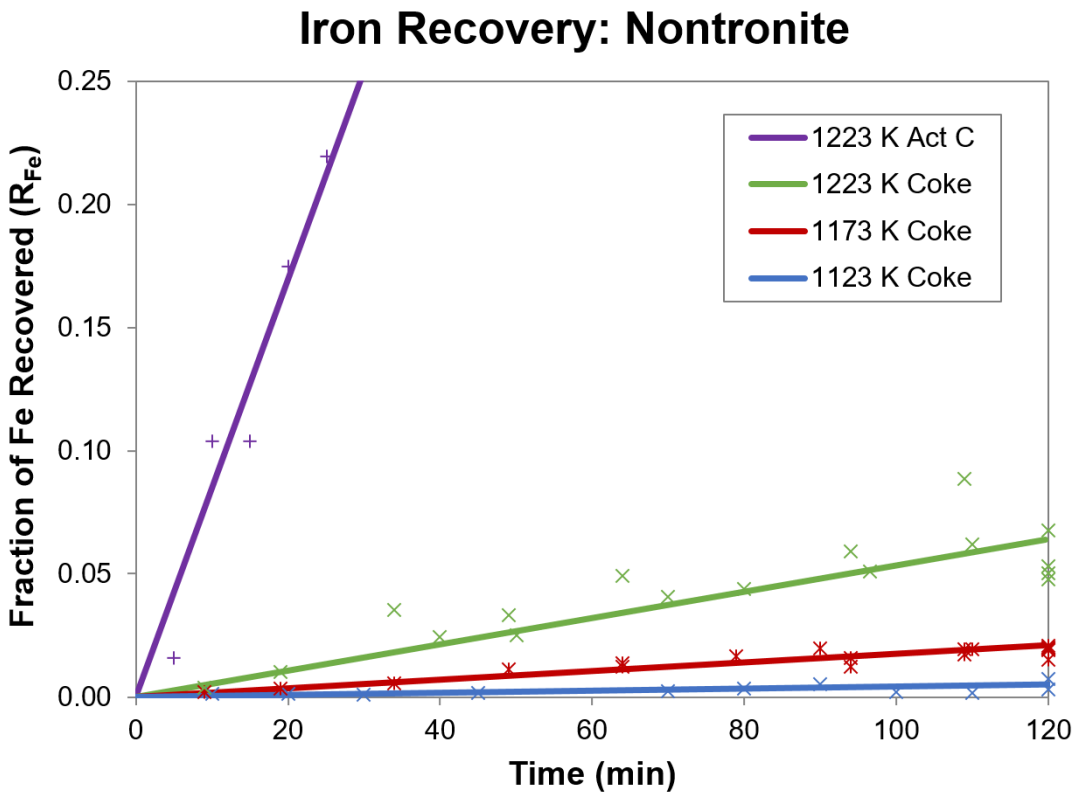

Figure 6.7 Iron Recovery, Nontronite

Fitted curves are of the form $R_{Fe} = k_{Fe}t$, see Table 6.5.

6.1.2.3 Rate Control

Increasing the carbon surface area at 1223 K (by replacing coke with activated carbon) increased the Fe segregation rate by ~16x (Table 6.5). This indicated that the rate was controlled either by the supply of H_2 from the gasification of carbon with H_2O (the water gas reaction) or by the reduction of $FeCl_2$ with H_2.

The gaseous reduction of $FeCl_2$ by H_2 has a relatively low kinetic resistance and a low activation energy of 54 kJ/mol (Young Lee and Gyu Kim, 2005) and it is known to be rapid under Ni segregation conditions (Brittan and Liebenberg, 1972). The rate control was almost certainly the supply of H_2 via the water gas reaction, which has a high activation energy of 160-240 kJ/mol (Harris and Smith, 1990) and, like the Boudouard reaction, has a relatively high kinetic resistance at Ni segregation temperatures.

The water gas reaction is represented by:

$$H_2O(g) + C(s) \rightarrow H_2(g) + CO(g) \qquad 2.5$$

for which the isothermal rate of H_2 generation can be approximated (Appendix A.4.5) by a power rate equation in the form:

$$\frac{dm_{H_2}}{dt} = A_C k_{2.5} p_{H_2O} \qquad 6.11$$

dm_{H_2} is the mass of H_2 generated in time dt; A_C is the surface area of the carbon; $k_{2.5}$ is the rate constant for the water gas reaction; and p_{H_2O} is the partial pressure of water vapour.

Since $NiCl_2$ is also reduced by H_2 in a fast, thermodynamically favourable reaction, the amount of H_2 available for $FeCl_2$ reduction must be discounted accordingly; thus the rate of H_2 generation that controls the segregation of Fe, as shown in Appendix A.4.6, is given by:

$$\frac{dm_{H_2}}{dt} = A_C k_{2.5} p_{H_2O} - 2.68 \times 10^{-2} A_{NiO} a_{NiO} \left(k_{2.15} p_{HCl}^2 + k_{2.23} p_{FeCl_2} \right) \qquad 6.12$$

Since[24] $\frac{dR_{Fe}}{dt} \propto \frac{dm_{H_2}}{dt}$, then comparison of Equations 6.9 with Equation 6.12 gives:

$$k_{Fe} \propto A_C k_{2.5} p_{H_2O} - 2.68 \times 10^{-2} A_{NiO} a_{NiO} \left(k_{2.15} p_{HCl}^2 + k_{2.23} p_{FeCl_2} \right) \qquad 6.13$$

Thus the zero order rate constant k_{Fe} is not a true rate constant, since it is affected by the p_{H_2O} and the available carbon surface area A. The effect of surface area is evident through comparison of the k_{Fe} values at 1223 K for coke (5.34×10^{-4}) and activated carbon (8.47×10^{-3}), as shown in Table 6.5. It may also be expected that the rate of Fe segregation would change as the p_{H_2O} within the system changes over time.

The rate of Fe segregation would be expected to decrease as carbon is consumed, and as the p_{H_2O} falls as H_2O leaves the system; thus the term $A_C k_{2.5} p_{H_2O}$ would decrease with time. However, the rate at which H_2 is consumed by Ni segregation falls with time, such that the second term in Equation 6.12 also decreases. This may explain why no decline in Fe segregation rate over time is observable within the accuracy of the present data (Figure 6.7).

[24] $R_{Fe} = m_{Fe}/m_{Fe}^o$ where m_{Fe}^o is a constant; thus $dR_{Fe}/dt \propto dm_{Fe}/dt$. Since $FeCl_2$ is reduced by H_2 to produce Fe, then $dm_{Fe}/dt \propto dm_{H_2}/dt$ and thus $dR_{Fe}/dt \propto dm_{H_2}/dt$.

6.1.3 Co-recovery of Nickel and Iron

Figure 6.8 shows a plot of Ni recovery versus Fe recovery for segregation of nontronite in the presence of coke and activated carbon. All lines were fitted using the segregation rate equations for Ni (Table 6.2) and Fe (Table 6.5).

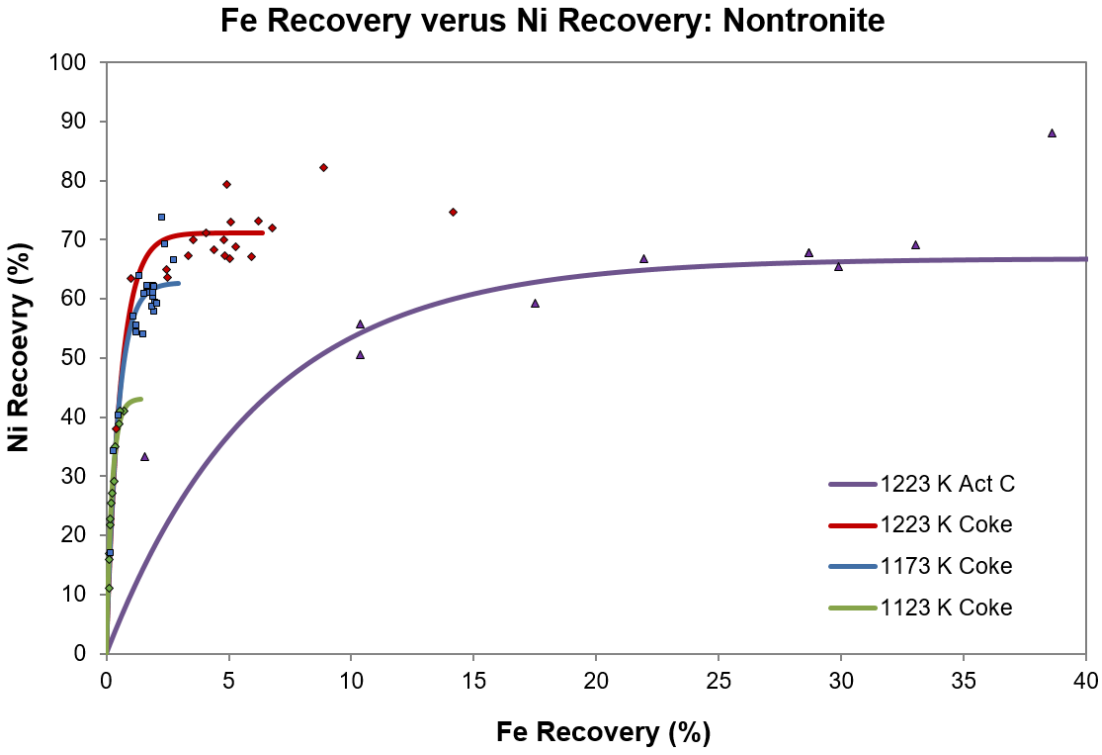

Figure 6.8 Fe Recovery versus Ni Recovery, Nontronite Segregation

The Ni and Fe recovery data (from Table 6.1, shown as dot points on the figure) are presented along with the predicted recoveries using the nickel and iron rate equations developed in Sections 6.1.1.3 and 6.1.2.2 respectively; rate equation data are shown as continuous lines on the figure.

Examination of the co-recovery curves for coke (Figure 6.8) illustrates that as the temperature is increased (from 1123 to 1173 K), co-reduction of Ni and Fe remain essentially the same (the curves overlap) until Ni reduction begins to approach the limiting maximum recovery at each temperature. The amount of Ni segregated decreases as the approach occurs, but Fe segregation continues which results in a flattening of the co-recovery curves, as shown in the figure. The extensive overlap of the co-reduction curves when using coke at three different temperature implies that the rate of the Fe segregation control reaction (the Boudouard reaction) and the rate of the Ni segregation control reaction (NiO chloridisation) change to a similar extent with change in temperature.

Figure 6.8 also shows that for a given recovery of Ni, the co-segregation of Fe increases with increase in the available area of the carbon reductant (cf. coke and Act C at 1223 K). The increase is significant because, as already discussed, increasing the carbon surface area enhances the rate of Fe segregation (Sections 6.1.1.3) but not the rate of Ni segregation (Section 6.1.2.2).

6.1.4 Cobalt

Cobalt segregated along with Ni and Fe and dissolved within the ferronickel. Co recoveries are reported here, but the data are considered the least reliable, given the small amount of Co (0.056%) in the ore (Table 4.1).

6.1.4.1 Recovery and Rate Equations

The rate of Co recovery at the lower segregation temperatures of 1123 and 1173 K was adequately described by a zero order rate equation (Section 6.1.2.1), while at the higher temperature (1223 K), the rate was better described by a 'first order to a limit' rate equation (Section 6.1.1.1). The integrated rate equations, as fitted from the Co recovery data (Table 6.1), are presented in Table 6.6 and plotted in Figure 6.9 along with the experimental data.

Table 6.6 Integrated Rate Equations, Recovery of Cobalt from Nontronite

Equations are zero order, $R_{Co} = k_{Co}t$, or 'first order to a limit', $R_{Co} = R_{Co,max}(1 - e^{-k_{Co}t})$. R_{Co} is the fractional Co recovery; k_{Co} is the rate constant; t is time.

Series	Carbon	Temp (K)	Time (max) (minutes)	Integrated Rate Equation	Fit r^2
N850C	Coke	1123	210	$R_{Co} = 4.7 \times 10^{-4}t$	0.72
N900C	Coke	1173	120	$R_{Co} = 2.2 \times 10^{-3}t$	0.90
N950C	Coke	1223	120	$R_{Co} = 0.40(1 - e^{-0.030t})$	0.93
N950AC	Act C	1223	60	$R_{Co} = 0.34(1 - e^{-0.148t})$	0.97

Figure 6.9 shows that Co recovery increased with both time and temperature. At 1123 and 1173 K, recovery increased at a constant rate, while at 1223 K, recovery increased and approached an upper limit. The recovery at the lower temperatures only reached 26%; for longer times and higher recoveries, the data would most likely follow first order to a limit behaviour. The rate increased when the surface area of carbon was increased by replacing coke with activated carbon, but the maximum recovery decreased from 40 to 34%, consistent with the formation of in-situ reduced alloy (Section 6.1.1.4).

The Co recovery is intermediate between the recoveries reported for Ni and Fe, in agreement with the relative thermodynamic stabilities of the oxides (Figure 2.2). Few previous studies have reported on Co recoveries from segregation and no comparable data were available for the segregation of nontronite ores. Co recoveries which lie between those for Ni and Fe have been reported by Takahashi et al. (1966) and Rey et al. (1972a) for limonite and garnierite ores respectively, in agreement with the present data.

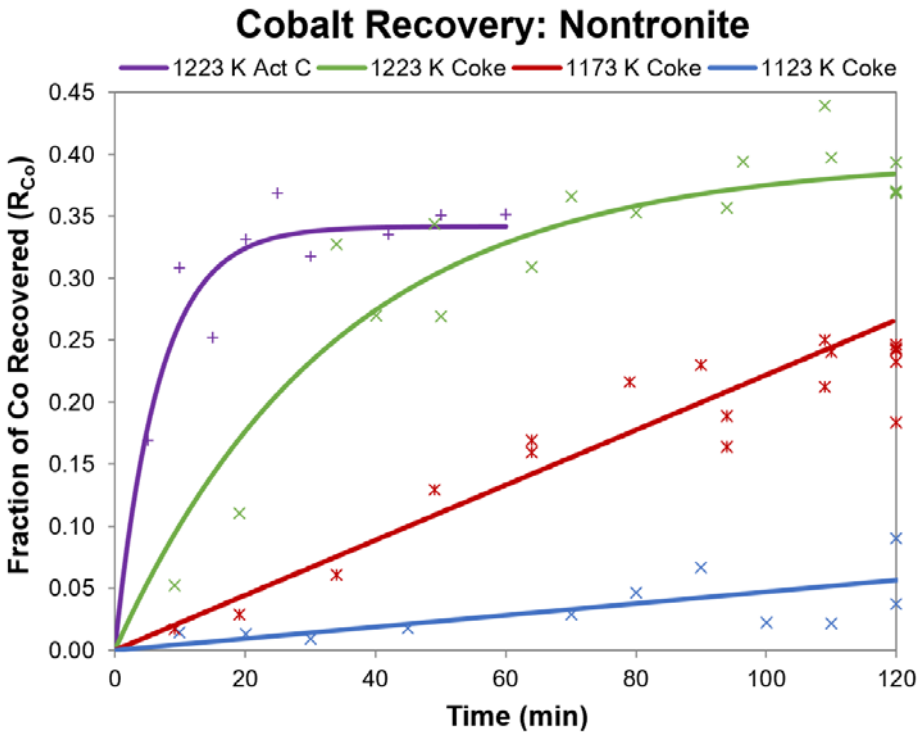

Figure 6.9 Cobalt Recovery, Nontronite

Parameters for fitted curves are summarised in Table 6.6.

6.1.4.2 Rate Control

In common with Fe, the rate of Co segregation is promoted by increasing the carbon surface area. This indicates that both the Fe and Co segregation rates are controlled by the water gas reaction (Section 6.1.2.3). However, when coke is replaced by activated carbon at 1223 K, the segregation rate is increased by ~16x for Fe (Table 6.5) and only ~5x for Co (Table 6.6). The lesser enhancement of the Co segregation rate compared to the Fe segregation rate implies that Co segregation is controlled to a lesser extent by the water gas reaction; it is more likely subject to mixed control by both the water gas reaction and chloridisation. The kinetic resistance of CoO chloridisation is likely higher than for FeO chloridisation, since the concentration of CoO is much lower than FeO within nontronite.

6.1.5 Activation Energies

The apparent activation energies for the recoveries of Ni, Co and Fe during segregation with coke were estimated from Arrhenius plots of the fitted rate constants (Table 6.2, Table 6.5 and Table 6.6) versus temperature. The plots are presented in Appendix B.3 and the values are shown Table 6.7.

Table 6.7 Activation Energies for Metal Recoveries, Nontronite Segregation

Activation energy (E) and collision frequency factor (k_0) are calculated from a plot of ln k versus 1/T. R is the universal gas constant; T is the temperature (K). Data are for segregation with coke.

Metal	Activation Energy (kJ/mol)	Arrhenius Equation $k = k_0 e^{\frac{-E}{RT}}$
Nickel	180	$k_{Ni} = 5.44 \times 10^{6} e^{\frac{-21900}{T}}$
Iron	290	$k_{Fe} = 1.10 \times 10^{11} e^{\frac{-34600}{T}}$
Cobalt	300	$k_{Co} = 7.71 \times 10^{10} e^{\frac{-36500}{T}}$

There are also no published data for the activation energies of Ni, Co or Fe recoveries within a segregation system. The respective apparent activation energies of 180 and 300 kJ/mol, as reported in this work for Ni and Co (Table 6.7), are relatively high values, consistent with the proposed chemical rate controls for these processes, namely: chloridisation for Ni segregation, and a mixed chloridisation/water gas reaction control for Co segregation.

The water gas reaction is likely the dominant control for Fe segregation. There are no published rate data for the water gas reaction on coke within a segregation system. However, activation energies for chloride free systems on various petroleum cokes and chars are available and range from 160-240 kJ/mol, (Harris and Smith, 1990), somewhat lower than the 290 kJ/mol (Table 6.7) reported here for Fe segregation.

6.2 Segregation versus Carbon Reduction

Since segregation is a form of carbon reduction that uses chloride as an intermediate, it is informative to compare the experimental results from the segregation system with those from an equivalent reduction system to which $CaCl_2$ was not added (Section 5.4).

6.2.1 Oxygen Pressure

The oxygen pressure (p_{O_2}) measurements from the segregation of nontronite with coke at 1123, 1173 and 1223 K were combined to provide representative average profiles at each temperature (Appendix B.5). The average p_{O_2} profile for segregation with coke at 1173 K (N900C) is shown in Figure 6.10, along with the average profile from the equivalent chloride free system (NR900C). The equilibrium oxygen pressures for the reduction of iron oxides, including non-stoichiometric wustite ('FeO')[25], are referenced by lines across the diagram.

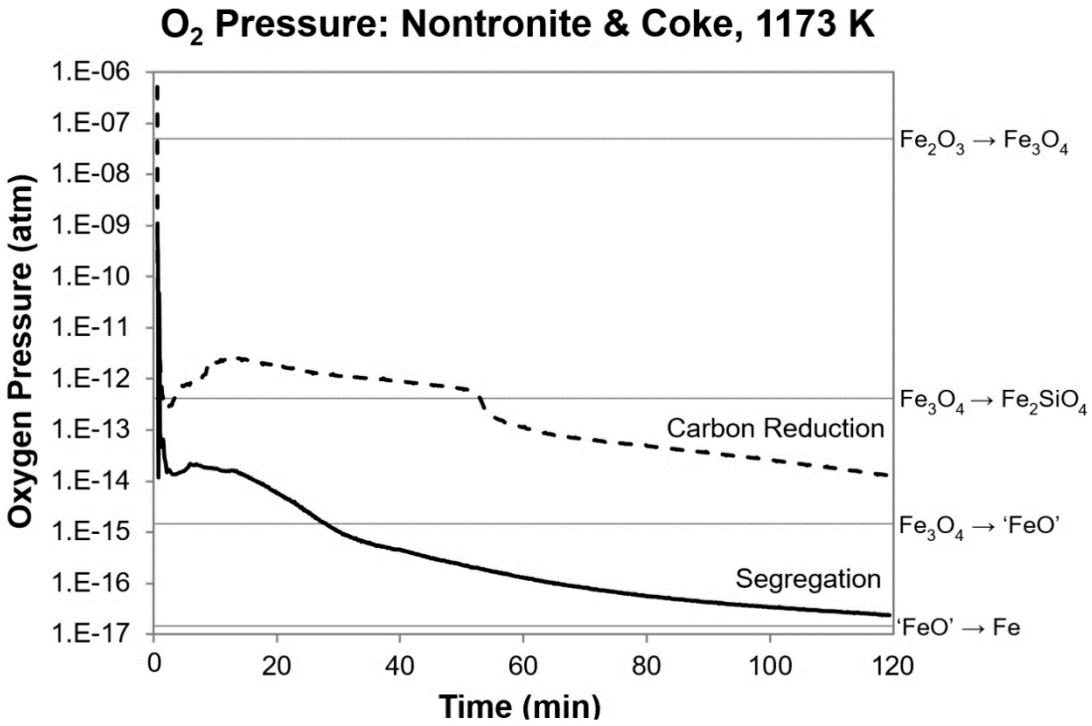

Figure 6.10 Oxygen Pressure Profile Comparison, Nontronite with Coke, 1173 K

Details for the representative oxygen profiles, N900C for segregation and NR900C for reduction, are in Appendix B.5.

Figure 6.10 shows that the oxygen pressure is significantly lower for segregation compared to reduction with carbon. As can be seen, the p_{O_2} for carbon reduction reaches ~1.3x10^{-14} atm after 120 minutes, just above the Fe_3O_4/'FeO' line. In contrast, the p_{O_2} for segregation falls below the Fe_3O_4/'FeO' line after 30 minutes and reaches ~2.4x10^{-17} atm after 120 minutes, just above the 'FeO'/Fe line. Similar

[25] The equilibrium oxygen pressures for the wustite reactions are from the FACTSage 'Equilib' program and differ slightly form those for stoichiometric ferrous oxide (FeO) in Table 5.3.

trends are apparent with coke at 1123 and 1223 K, and the corresponding figures for these temperatures are presented in Appendix B.5. No oxygen pressure measurements were made for segregation with activated carbon, and no comparable oxygen pressure measurements for segregation are available in the literature.

6.2.2 Carbon Consumption

Profiles of fractional carbon consumption during segregation with coke were calculated from representative best fits of the cumulative carbonaceous off-gas volume (Appendix B.4); these are presented in Figure 6.11 (solid lines) along with similar best fits (dashed lines) for reduction without chloride (previously shown in Figure 5.6). The corresponding carbonaceous off-gas volumes, standardised at 1 atm and 273 K, are included on the secondary y-axis of Figure 6.11.

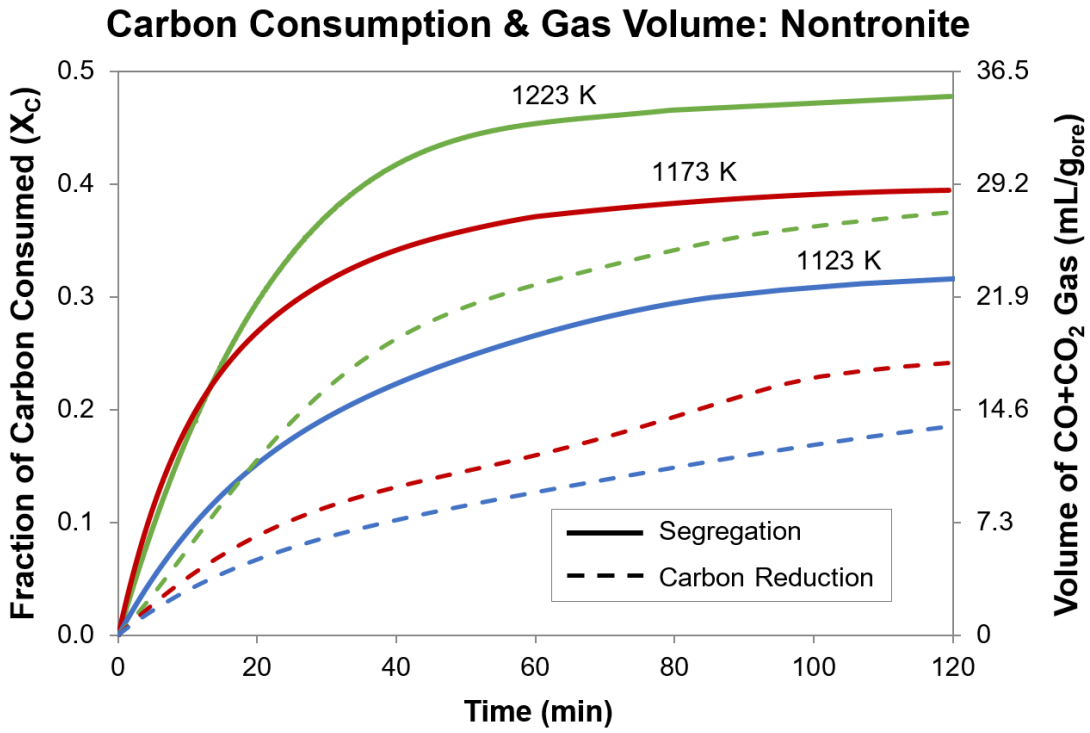

Figure 6.11 Carbon Consumption and Carbonaceous Gas Volume Comparison
Curves are best fits from experimental data (Appendix B.4). Coke (78.3% C) added at 5% of dried ore. Volume is ml/gram ($1\ ml = 1x10^{-6}m^3$) of dried ore at STP (1 atm, 273 K), where each mole of C consumed yields one mole of gas.

Figure 6.11 shows that for segregation, the rate of carbon consumption is initially rapid and slows dramatically over time; in contrast, for carbon reduction, the rate of carbon consumption begins less rapidly and does not plateau to the same extent as for segregation. Most significantly, the carbon consumption for segregation is greater than for carbon reduction in the absence of chloride at all temperatures.

A comparison of the carbon consumption and oxygen pressures achieved after 120 minutes by reduction or segregation with coke is given in Table 6.8. From the table, it is evident that the use of chloride in the segregation process increases the carbon consumption by 1.3-1.7x, and deceases the oxygen pressure by up to three orders of magnitude.

Table 6.8 Carbon Consumption and Oxygen Pressure Comparison, Nontronite
Carbon consumption X_C is expressed as a fraction of the 3.92 g (within 5 g coke) added per 100 g of dried ore.

Carbon	Temp (K)	Time (minutes)	Reduction		Segregation	
			X_C	pO_2 (atm)	X_C	pO_2 (atm)
Coke	1123	120	0.19	2.4×10^{-14}	0.32	5.0×10^{-17}
Coke	1173	120	0.24	1.3×10^{-14}	0.40	2.4×10^{-17}
Coke	1223	120	0.38	1.6×10^{-15}	0.49	9.6×10^{-17}

The rate of carbon consumption during segregation can be quantified by the value of the Boudouard rate constant for the gasification of carbon with CO_2, as previously calculated for the chloride free carbon reduction system (Section 5.6). The rate constant was calculated from plots of $-\ln(1 - X_C)$ versus time over an initial period when the area/mass of carbon remains approximately constant and the gas is rich in CO_2[26]. Details are given in Appendix B.1, and the calculated rate constants are presented and compared with those for carbon reduction in Table 6.9.

The data in Table 6.9 confirms that the Boudouard reaction rate is enhanced during segregation compared to reduction with coke, specifically by ~2.4x at 1123 K, ~4.7x at 1173 K and ~3x at 1223 K. As noted in the table, the rate constant for segregation at 1223 K appears to in error, but this does not change the comparison between the segregation and reduction systems. The rate during segregation at 1223 K was based on only two tests (Appendix B.1); both showed initial carbon

[26] The initial gas from segregation is rich in CO_2, but unlike reduction with coke alone, it also contains HCl and H_2O (Table 2.8); since the Boudouard rate is proportional to p_{CO_2}, the rate constants calculated for segregation will be slightly underestimated.

consumptions similar to those at 1173 K (cf. averaged curves at 1173 and 1223 K, Figure 6.11), but significantly higher final carbon consumptions than at the lower temperature. Poor initial mixing of reagents and ore may have resulted in this experimental variation.

Table 6.9 Boudouard Rate Constant Comparison, Nontronite

Reduction rate constants are from Table 5.13. Calculations Appendix B.1.

Carbon	Temp (K)	k_{BR} (/min)	
		Reduction	Segregation
Coke	1123	4.5×10^{-3}	1.1×10^{-2}
Coke	1173	5.5×10^{-3}	2.6×10^{-2}
Coke	1223	7.1×10^{-3}	2.1×10^{-2}*

*This value is lower than at 1173 K and appears to be in error; otherwise the activation energy would be negative.

The Boudouard carbon gasification rates for nontronite reduction in the absence of chloride were lower than for either garnierite or limonite reduction (Figure 5.21). It may be that the larger portion of amorphous material within the nontronite calcine (30%, Table 4.7) compared to limonite (7%, Table 4.5) and garnierite (5%, Table 4.10) affected the carbon surface and slowed the gasification during the carbon reduction of nontronite. It appears that presence of chloride nullified effects of the amorphous material; however, whatever the reason, the presence of chloride during segregation resulted in a very significant enhancement in the carbon gasification rate in the presence of nontronite.

The average Boudouard reaction activation energy for segregation was 189 kJ/mol, compared to 46 kJ/mol for reduction (Table 6.10). The carbon gasification rate was thus not only faster, but also enhanced more by an increase in temperature during segregation compared to reduction.

Table 6.10 Boudouard Activation Energy Comparison, Nontronite

Activation energy (E) and collision frequency factor (k_0) calculated from a plot of ln k_{BR} versus 1/T (Appendix B.1). R is the universal gas constant, T is the temperature (K). Data for reduction are from Table 5.14.

System	Temperature Range (K)	Activation Energy (kJ/mol)	Arrhenius Expression $k_{BR} = k_0 e^{\frac{-E}{RT}}$
Segregation	1123-1173	189	$k_{BR} = 6.72 \times 10^6 e^{\frac{-22700}{T}}$
Reduction	1123-1223	46	$k_{BR} = 1.54 e^{\frac{-5580}{T}}$

6.2.3 Equilibrium Simulation and Oxygen Removal

Equilibrium simulations were performed as described in Section 5.1, using the carbon consumption data from Figure 6.11 but without taking into account the addition of $CaCl_2$ or any reactions involving chloride. The results for the segregation with coke at 1173 K are summarised in Figure 6.12. The figure shows the phase and oxygen pressure changes that are predicted from interaction of the calcine with the bulk gas in the absence of chloride, on the assumption that the Boudouard reaction controls the reduction rate. The simulated p_{O_2} of the bulk gas is included in the figure along with the measured p_{O_2} (N900C).

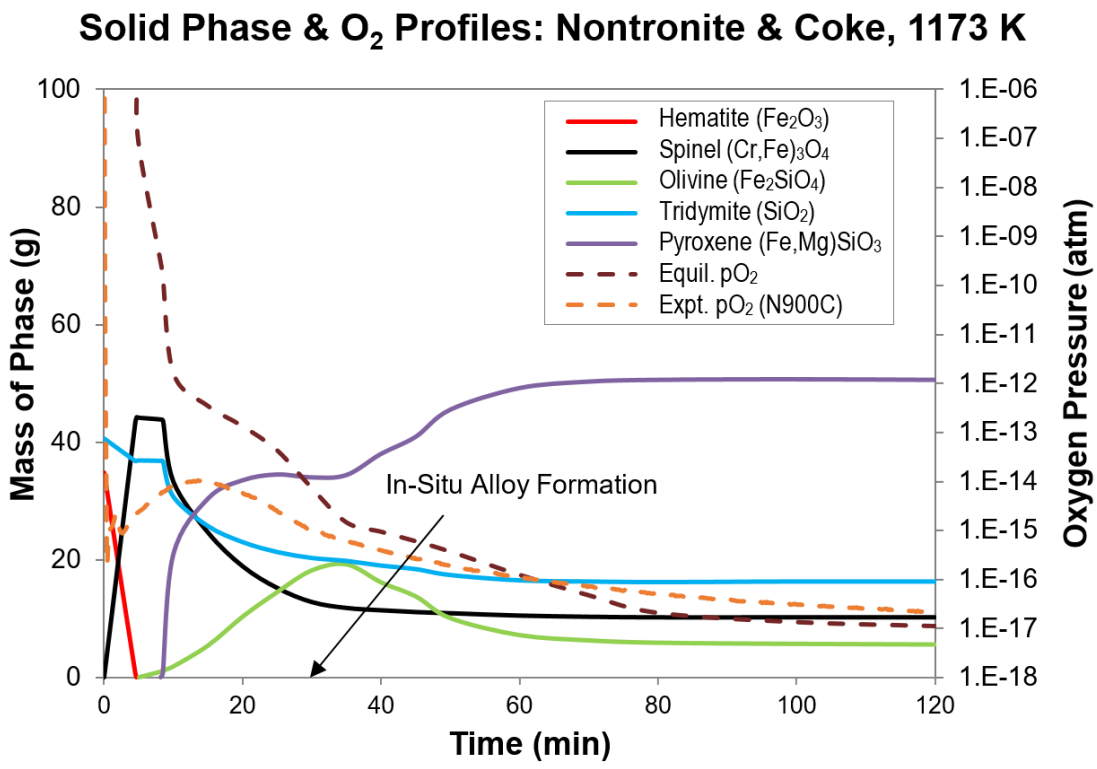

Figure 6.12 Equilibrium Simulation of Nontronite Segregation with Coke, 1173 K

Phase profiles are for 100 g of dried ore. The dashed brown line represents the simulated p_{O_2}; the dashed orange line represents experimental p_{O_2}.

The progression of phase changes shown in Figure 6.12 occur more rapidly than similar changes noted for the reduction with coke at 1173 K (Figure 5.10), in response to the increased carbon usage and lower p_{O_2} encountered with segregation. A comparison of the equilibrium and experimental p_{O_2} indicates that the p_{O_2} is still dominantly controlled by the oxide reduction equilibria, even when the rate of carbon gasification is significantly enhanced within the segregation process compared to the reduction process.

The simulated phase transformations and oxygen pressure profiles for segregation with coke at 1123 and 1223 K show comparable characteristic to those in Figure 6.12 and are presented in Appendix B.8.

The total oxygen progressively removed from the calcine during segregation can be calculated using the representative carbon consumption profiles (Figure 6.11) and the CO_2 and CO content of the off-gas, as calculated from the representative oxygen pressure profiles (e.g. N900C in Figure 6.12). The time necessary for the reduction of iron oxides by the bulk gas can be estimated from the total oxygen removed, discounted by that released by the oxide reduced by segregation. Details are provided in Appendix A.5.

Figure 6.13 shows the cumulative oxygen removed through in-situ reduction of iron oxides by CO, expressed on the y-axis as a percent, where 100% represents complete removal of O from all of the available Fe_2O_3 from the original calcine (i.e. the iron oxide not reduced by segregation). Horizontal lines are drawn for 11.1% O removal, which represents complete conversion of Fe_2O_3 to Fe_3O_4, and 33.3% O removal, which represents complete conversion of Fe_3O_4 to FeO. For nontronite, the FeO was likely contained within olivine and pyroxene which are dominant oxide phases formed during segregation (Figure 6.12).

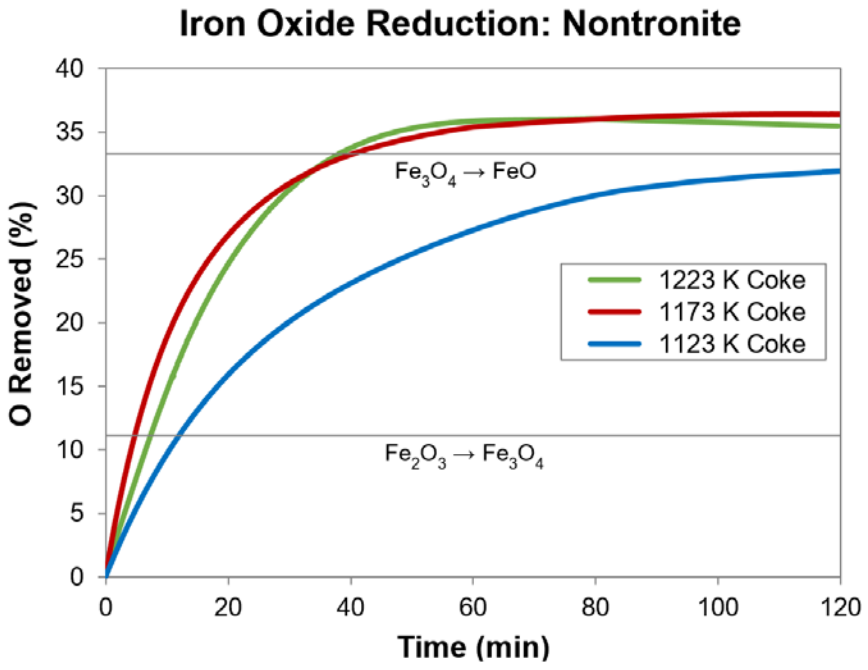

Figure 6.13 Removal of O from Iron Oxides, Nontronite Segregation

O removed in carbonaceous gas during segregation (Appendix A.5): 11.1% O removal represents $Fe_2O_3 \rightarrow Fe_3O_4$; 33.3% represents $Fe_3O_4 \rightarrow FeO$.

The predicted iron oxide conversions times, from both the equilibrium simulation (e.g. Figure 6.12) and experimental oxygen removal data (Figure 6.13), are summarised and compared in Table 6.11. The predictions for 1123 and 1173 K are similar, although at 1223 K, where the initial experimental carbon consumption appeared too low, some differences are evident. Overall, the experimental and simulated predictions are in reasonable agreement.

Table 6.11 Iron Oxide Conversion Times, Nontronite

Temp (K)	$Fe_2O_3 \rightarrow \mathbf{Fe_3O_4}$ (minutes)		$Fe_3O_4 \rightarrow \mathbf{FeO}$ (minutes)	
	Experimental	Simulated	Experimental	Simulated
1123	12.1	12.3	-	-
1173	4.8	4.7	40.7	~40
1223	7.3	4.6	38.2	~35

Figure 6.13 shows that once all Fe_3O_4 is converted to FeO, as occurs only at 1173 and 1223 K, the rate of oxygen removal drops substantially and then virtually stops. Since oxygen removal is controlled by the Boudouard reaction, the rate will depend on the pressure of CO_2 in contact with the carbon, as well as the total carbon surface area (Section 5.6).

While Fe_3O_4 is being reduced to FeO, the p_{CO_2} at 1173 K, for example, is maintained at ~0.7 atm by the oxide reduction equilibrium; however once this conversion is complete, the p_{CO_2} falls rapidly to ~0.3 atm or lower, to where reduction of FeO to Fe begins. The fall in the p_{CO_2}, combined with the cumulative loss of carbon surface area through gasification and potential graphitisation over time (Rey et al., 1972b), dramatically slows the Boudouard reaction rate. In addition, as the CO_2/CO in the gas decreases, the removal of oxygen per mole of carbon becomes less efficient.

The major phases within a nontronite product after 70 minutes of segregation with coke at 1173 K, as determined by XRD, are listed in Table 6.12 along with the simulated equilibrium phases identified under equivalent chloride free conditions (Figure 6.12).

The phases identified by XRD show good agreement with predictions from the equilibrium simulation, with confirmation of the presence of olivine (as fayalite), silica (as cristobalite), spinel (as chromite) and pyroxene (as diopside). However, the proportion of simulated pyroxene (59%) was significantly higher than actual (12%), with the simulated olivine (6%) being significant lower than actual (31%).

Table 6.12 Solid Phases in the Nontronite Segregation Product

Experimental composition determined by quantitative XRD analysis.

Phase	Experimental		Simulated	
	wt%	Major Component	wt%	Major Component
Olivine	30	Fe_2SiO_4	6	Fe_2SiO_4
Silica	23	Cristobalite	21	Tridymite
Spinel	13	$FeCr_2O_4$	12	$FeCr_2O_4$
Pyroxene	11	$CaMgSi_2O_6$	58	$Fe_2Si_2O_6$
Feldspar	8	$CaAl_2Si_3O_8$	1	$CaAl_2Si_2O_8$

The formation of pyroxene requires a solid-solid reaction between silica and olivine, and thus may be kinetically restricted by inadequate surface contact. The XRD analysis indicated that pyroxene contained Mg and not Fe; however, Fe was identified throughout the silicate phases during EDS-SEM examination in much higher concentrations than Mg (Figure 6.3, Table 6.3).

6.2.4 Comparison of Nickel Recovery

The maximum Ni recoveries from segregation (Table 6.2) and reduction (Table 5.6) are compared in Table 6.13. The maximum recovery in the reduction system was much lower under all conditions (4.4-29%) in comparison to segregation recoveries (43-71%). This comparison shows that segregation is a superior reduction process compared to carbon reduction under all circumstances. This is not only because fine alloy from in-situ reduction may be inaccessible to a leach solution and hence suppresses recovery (Section 5.7), it is also because reduction by segregation is possible when in-situ reduction to alloy cannot occur at all, as is evident when using coke at 1123 K. The equilibrium simulations at this temperature for both reduction (Figure 5.10) and for segregation (Appendix B.8) predict that the oxygen pressure within the bulk gas does not fall below the critical value necessary for in-situ alloy formation; however 43% Ni was recovered by segregation at this temperature (Figure 6.14).

Overall segregation is a fundamentally superior reduction system, since the oxygen pressure needs to be sufficiently low only at the carbon surface for reduction to take place. In the absence of chloride, the oxygen pressure throughout the entire system (i.e. within the bulk gas) must be sufficiently low for reduction to take place.

Table 6.13 Comparison of Maximum Nickel Recovery, Nontronite

Recovery from selective bromine/methanol leach of segregation/reduction product. Maximum segregation recoveries from Table 6.2; Maximum reduction recoveries from Table 5.6.

Carbon	Temperature (K)	Maximum Ni Recovery (%)	
		Segregation	Reduction*
Coke	1123	43	4.1
Coke	1173	63	5.0
Coke	1223	71	26
Act C	1223	67	5.8

*Averaged: 2 pts (1123K), 3 pts (1173 K), 3 pts (1223 K), 4 pts (Act C, 1223 K)

6.3 Ferronickel

The ferronickel alloy contained minor Co in addition to Ni and Fe, however, this minor amount is ignored for the purpose of the following discussion.

6.3.1 Ferronickel Grade

The Ni grade (Ni%) of the ferronickel, as listed in Table 6.1, is shown in Figure 6.14 as a function of segregation time, with the trend lines drawn rather than fitted. The figure shows that the ferronickel becomes leaner in Ni (and richer in Fe) as the reaction time, temperature and carbon surface area increase.

The trends are more dramatically illustrated by changes in the instantaneous ferronickel grades, shown in Figure 6.15, compared to changes in the cumulative grades, shown in Figure 6.14. The instantaneous grades were estimated over five second intervals using the integrated rate equations for metal recovery (Table 6.2 and Table 6.5). The trends observed can all be explained by changes in the relative rates of Ni and Fe segregation.

At constant temperature, the rate of Fe segregation remains essentially constant over the entire reaction period (Section 6.1.2.2); however, the rate of Ni segregation decreases with time as less NiO becomes available for chloridisation (Section 6.1.1.2). The ferronickel grade is thus maximised at the start of the reaction and decreases over time as the rate of Ni segregation decreases relative to the rate of Fe segregation.

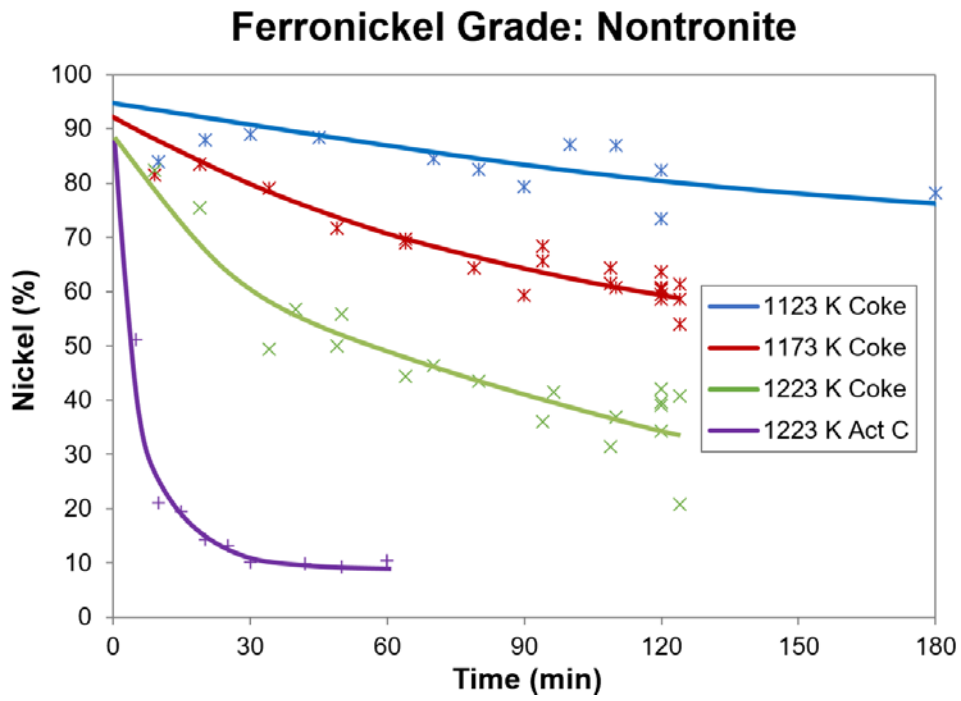

Figure 6.14 Ferronickel Grade, Nontronite Segregation

Cumulative ferronickel grades for nontronite segregation; data from Table 6.1.

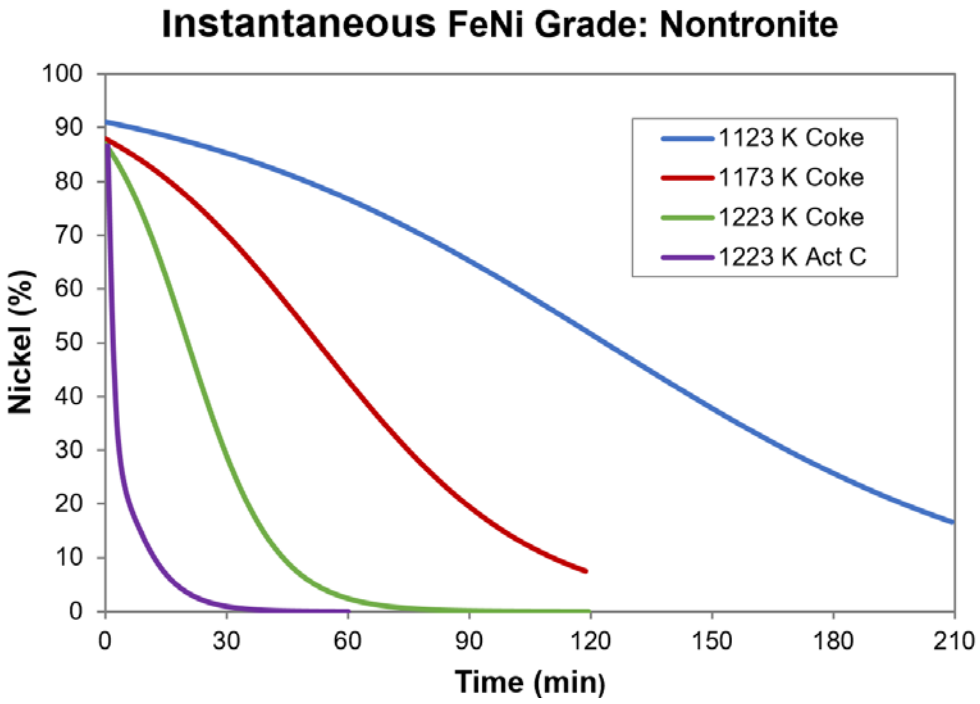

Figure 6.15 Instantaneous Ferronickel Grade, Nontronite Segregation

Data are calculated from the integrated rate equations for Ni (Table 6.2) and Fe (Table 6.5) recovery, averaged over 5 second intervals.

As temperature is increased, the recovery of Fe increases more than the recovery of Ni, thus the ferronickel grade decreases with increase in temperature at any given reaction time. The recovery of Fe is also significantly enhanced relative to the recovery of Ni when the surface area of carbon is increased (Figure 6.14), resulting in a considerably lower grade ferronickel when activated carbon is used instead of coke.

This work shows, in agreement with the literature (Section 2.4.4), that the grade of segregated ferronickel decreases as the bulk gas becomes more reducing, consistent with FeO being thermodynamically more stable than NiO. However, the grade of ferronickel appears to be kinetically controlled rather than thermodynamically controlled. The two appear almost co-incidental because the same factors which decrease the CO_2/CO ratio within the bulk gas by enhancing the Boudouard reaction, also selectively promote the kinetics of Fe segregation over Ni segregation, specifically: increases in reaction time, temperature or carbon surface area.

Hudyma (1993b) studied the relationship between the reducing strength of the bulk gas and the resulting segregated ferronickel through sampling the off-gas from laboratory segregation tests. It was concluded that the ferronickel grade depended directly on the CO_2/CO ratio of the gas, with a lower ratio resulting in a lower grade. While the grade of ferronickel does decrease as the CO_2/CO of the bulk gas decreases (and hence the p_{O_2}, Equation 2.32), the direct dependency is only true for in-situ reduced ferronickel.

While the overall segregation process and ferronickel compositions are kinetically controlled, the reductions of $NiCl_2$ and $FeCl_2$ with H_2 at the carbon surface are near equilibrium. This agrees with the literature (Section 2.4.3), and also with this work, since the Ni and Fe segregation rates are respectively controlled by chloridisation and the water gas reaction, and thus all other segregation steps should operate close to equilibrium.

As a consequence, the composition of ferronickel formed at the carbon surface at any time will be related to the chloride gas composition at the surface according to the equilibrium relationship (Section 2.4.3):

$$\frac{p_{FeCl_2}}{p_{NiCl_2}} = K_{2.26}\frac{a_{Fe}}{a_{Ni}} \qquad 2.28$$

p_{NiCl_2} and p_{FeCl_2} are the partial pressures of the denoted gases; $K_{2.26}$ is the equilibrium constant for the metal-chloride exchange reaction (Equation 2.26); a_{Fe} and a_{Ni} are the activities of the denoted metals (relative to the pure solid standard states); and $a_{Fe}/a_{Ni} \approx X_{Fe}/X_{Ni}$, where X represents mole fraction.

Figure 6.15 shows that the instantaneous grade of the segregated ferronickel decreases with time; thus the p_{FeCl_2}/p_{NiCl_2} at the carbon surface must also increases with time, in accord with Equation 2.28. This increase is likely due to the FeO chloridisation reaction operating near equilibrium (Section 2.4.2), while the NiO chloridisation reaction does not (Section 6.1.1.3). Under this scenario, any $FeCl_2$ consumed through reduction with H_2 at the carbon surface is replaced rapidly by the FeO chloridisation reaction, which buffers the p_{FeCl_2} near its equilibrium value[27]. In contrast, the $NiCl_2$ consumed by H_2 at the carbon surface cannot be replaced at the same rate by the slower NiO chloridisation reaction; thus the p_{NiCl_2} declines as the rate of chloridisation declines. As a result, p_{FeCl_2}/p_{NiCl_2} increases with time, corresponding to an increase in a_{Fe}/a_{Ni} (Equation 2.28) and a decrease in the grade of alloy.

6.3.2 Suppression of In-Situ Reduction to Ferronickel

Only minor in-situ alloy was observed for all segregations carried out with coke, even though the equilibrium simulations based on carbon usage predicted that alloy should form at both 1173 K (Figure 6.12) and 1223 K (Appendix B.8).

Since the simulated p_{O_2} was different to the value measured during segregation (Figure 6.12), the simulation methodology was modified to align the simulated and measured oxygen pressures, in order to better predict the ability of the bulk gas to form in-situ alloy while segregation was in progress. This was done using FACTSage to progressively add the actual amount of carbon consumed by segregation in a given time, but also setting the system to have the same p_{O_2} as the measured value at that time. This was achieved within FACTSage by enforcing the target oxygen pressure by a minor automatic adjustment to the oxygen balance. The predicted compositions of in-situ alloys which can form at the measured oxygen pressure during segregation are shown in Figure 6.16 (dashed lines) along with the compositions of the segregated alloy (solid lines) that formed during the experiment.

[27] The equilibrium pressure of $FeCl_2$ may also increase over time as the activity of FeO increases through reduction of iron oxide, but this also depends on the pressure of HCl.

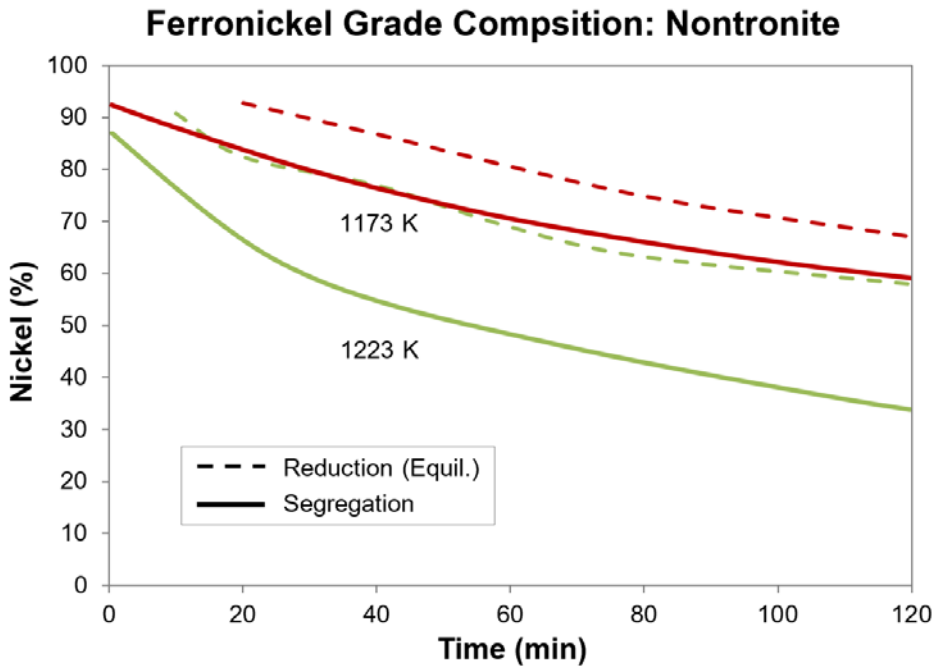

Figure 6.16 Equilibrium and Experimental Ferronickel Grades, Nontronite
Data at 1123 K are not shown, since in-situ alloy was unstable at this temperature over the entire segregation period.

Figure 6.16 shows that in-situ alloy becomes stable during segregation with coke after 25 minutes at 1173 K, and after 10 minutes at 1223 K, as indicated by the beginning of the dashed lines at each temperature. However, only minor amounts of in-situ ferronickel were observed in the segregated calcine, indicating that in-situ reduction was suppressed.

The suppression of in-situ alloy most likely occurred because a significant portion of NiO was rapidly removed from the calcine early in the process when the Ni segregation rate was highest (Figure 6.1). As previously discussed (Section 5.2), in-situ ferronickel formation will be initiated when the p_{O_2} is lowered to a critical value, which depends mainly on the activity of NiO, and which decreases as the activity of NiO decreases. When NiO is rapidly removed by segregation, the critical p_{O_2} is likely lowered and maintained below the p_{O_2} prevailing in bulk gas such that no in-situ alloy forms.

Noticeable in-situ alloy did form when nontronite was segregated with activated carbon at 1223 K, presumably since the p_{O_2} was able to be reduced below the critical value under these more reducing conditions. However, this likely occurred late in the process since the effect on Ni recovery was minor (Figure 6.1).

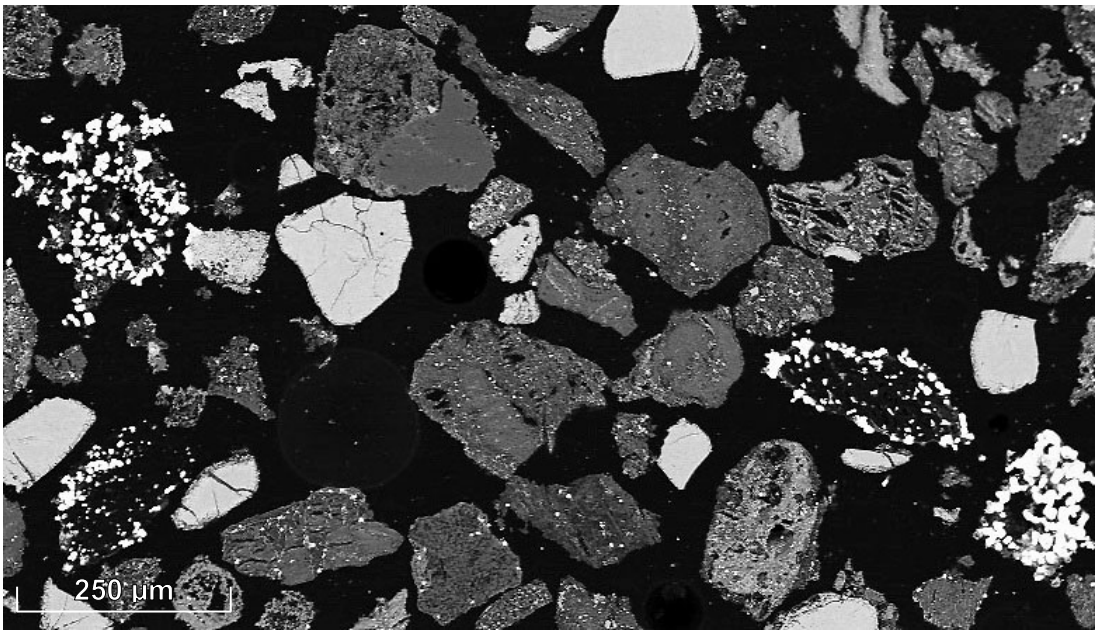

Figure 6.17 Sectioned Concentrate after Segregation with Activated Carbon
SEM image through a magnetic concentrate produced after segregation with activated carbon for 60 minutes at 1223 K. Bright alloy clusters (5-20 µm) are located throughout the activated carbon particles. Remnant dehydroxylate particles (silica/iron silicates) contain bright points of in-situ alloy (<5 µm); the lighter dense particles are Ni free chromite.

Figure 6.17 shows particles within a magnetic concentrate after segregation for 60 minutes with activated carbon at 1223 K. Most of the Ni is segregated and contained within Fe rich, bright clusters of 5-20 µm ferronickel particles located throughout the activated carbon. Remnant nontronite dehydroxylate particles are present and show bright spots of in-situ reduced Fe rich ferronickel of <5 µm (see also Figure 6.6). The presence of this alloy renders the gangue ferromagnetic such that many of the particles report to the concentrate along with segregated ferronickel.

EDS-SEM point analysis of the alloy in Figure 6.17 showed that the segregated alloy was of lower grade (~10% Ni) than the in-situ alloy (~15% Ni), consistent with the oxygen pressure at the carbon surface being lower than in the bulk gas; otherwise the segregated alloy would be oxidised.

6.3.3 The Ferronickel Deposit

Segregated ferronickel mainly formed on coke particles as complete or partial coatings, as shown in Figure 6.18, while for activated carbon, it was located

throughout the carbon particles, as shown in Figure 6.17. The distribution of ferronickel throughout activated carbon is consistent with a higher rate of H_2 being supplied by the water gas reaction due to the increased carbon surface area.

The ferronickel appeared to nucleate on the surface of coke particles as spherical (Figure 6.19) grains and cubic crystals (Figure 6.20). After nucleation, further alloy grew as cubic crystals on the existing alloy nuclei, with the cubic crystals eventually meshing together through grain growth, resulting in a dense metal coating on the coke surface (Figure 6.20). Others have observed initial growth as cubic crystals (Section 2.4.4), although Hudyma (1981) observed both cubic and spherical grain growth on coal. Ferronickel particles found in the segregation concentrate typically ranged in size from 20-250 µm, with characteristic branch-like structures, as shown by the inset in Figure 6.20.

Sections through some coke particles revealed the presence of Al rich silicates (yellow outline, Figure 6.21), thought to be remnants of the 11.5% ash contained within the coke (Table 4.13). Further, EDS-SEM analysis of the surface of the unwashed particles revealed the presence of Fe-Ni chloride[28] (blue outline, Figure 6.21); however the analysis could not be quantitatively determined due to the proximity of the underlying alloy. These chlorides were most likely adsorbed onto the surface prior to reduction, as also observed by Hudyma (1981), who considered adsorption fundamental to the reduction mechanism.

Figure 6.22 shows a polished section through a discrete ferronickel particle. This ferronickel may have been released from a coke particle by carbon gasification, or detached during light grinding of the segregation product prior to magnetic separation. The EDS-SEM surface analysis (point 1, Figure 6.22) showed the presence of a sulphide containing 50% Fe, 47% S and 3% Ni. Sulphides of varying compositions were found on the surface of other ferronickel particles formed on coke, with compositions ranging from Fe sulphide (point 1, Figure 6.22), through Ni-Fe sulphide, to Ni-Fe alloy containing minor sulphur (point 1, Figure 6.20). The EDS spot analyses varied within the range Ni (21-50%), Fe (39-64%) and S (0.5-47%). Sulphides are readily soluble within the bromine/methanol leach, and so any surface coatings would not inhibit the analysis for reduced alloy.

[28] The chloride appeared as an oxychloride to EDS-SEM, probably due to oxidation after segregation.

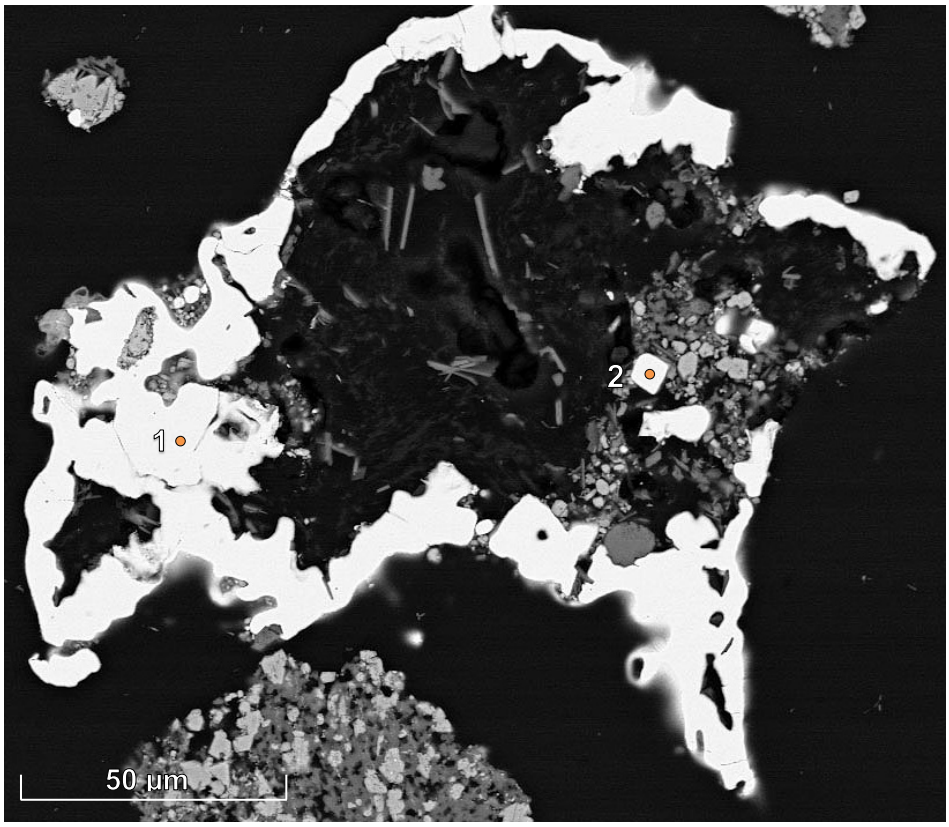

Figure 6.18 Section through a Coke Particle coated with Ferronickel

SEM image through a coke particle partly coated in ferronickel; gaps in the coating allow gas to the carbon surface. Point (**1**) is 57% Ni; Point (**2**) is 60% Ni.

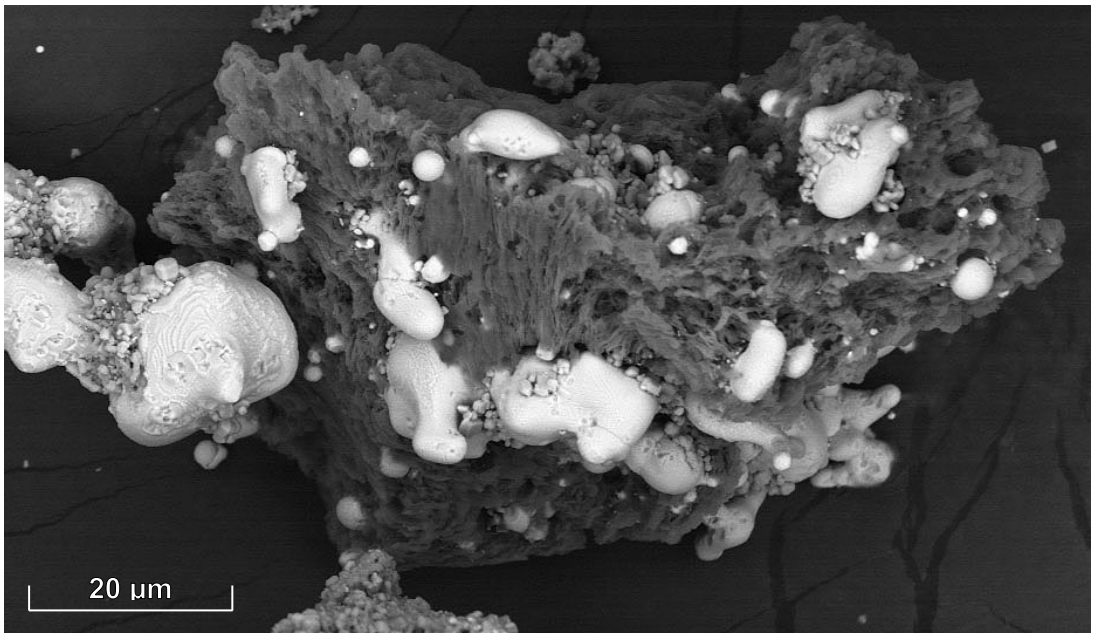

Figure 6.19 Coke Particle showing Initial Ferronickel Growth

SEM image of coke particle coated with spherical and cubic grains of ferronickel.

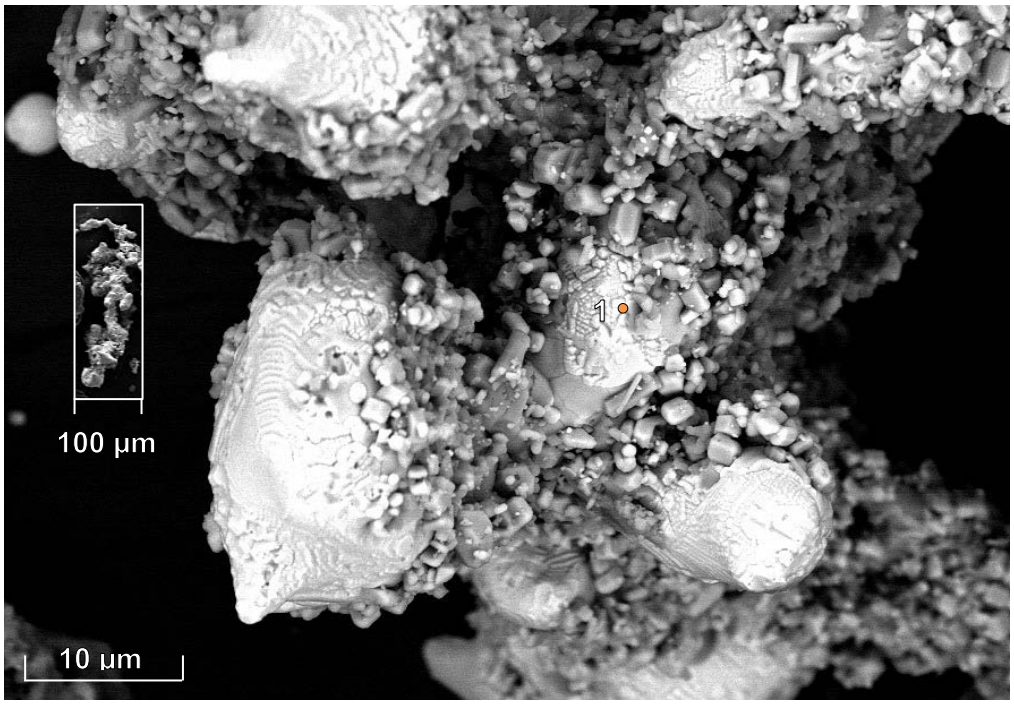

Figure 6.20 Ferronickel Coating over Coke Particle

SEM image showing initial crystalline cubic ferronickel structure with regions of meshing and consolidation from additional deposition and grain growth, formed on coke after segregation for 70 minutes at 1173 K. Point (**1**) is 35.7% Ni, 63.8% Fe and 0.5%S.

A similar low melting point sulphide phase was found by Rey et al. (1972b) on the surface of segregated ferronickel. The sulphur almost certainly originated from the coke, which contained 0.41% S (Table 4.13); no sulphide phase was observed when using activated carbon which contained 0.06% S (Table 4.13). It has been reported by others (Section 2.4.4) that the presence of sulphur can be beneficial to the growth of ferronickel particles, and to the recovery of Ni in the segregation process.

All ferronickel particles shown in Figure 6.18 and Figure 6.20 to Figure 6.22 resulted from the segregation of nontronite with coke for 70 minutes at 1173 K, for which the cumulative ferronickel grade (Figure 6.14) and the instantaneous grade (Figure 6.15) are predicted to be ~70% and ~40% respectively. EDS spot analysis of selected ferronickel grains showed their composition were not uniform, with the proportion of Ni higher in the centre of the grain compared to the edge. Analysis of numerous spots across the ferronickel grain (outlined in red) in Figure 6.21 showed a variation in grade from 60-80% Ni, but the area composition was 70% Ni, as predicted from Figure 6.14. Cobalt was also found in the alloy at a concentration of ~0.5%.

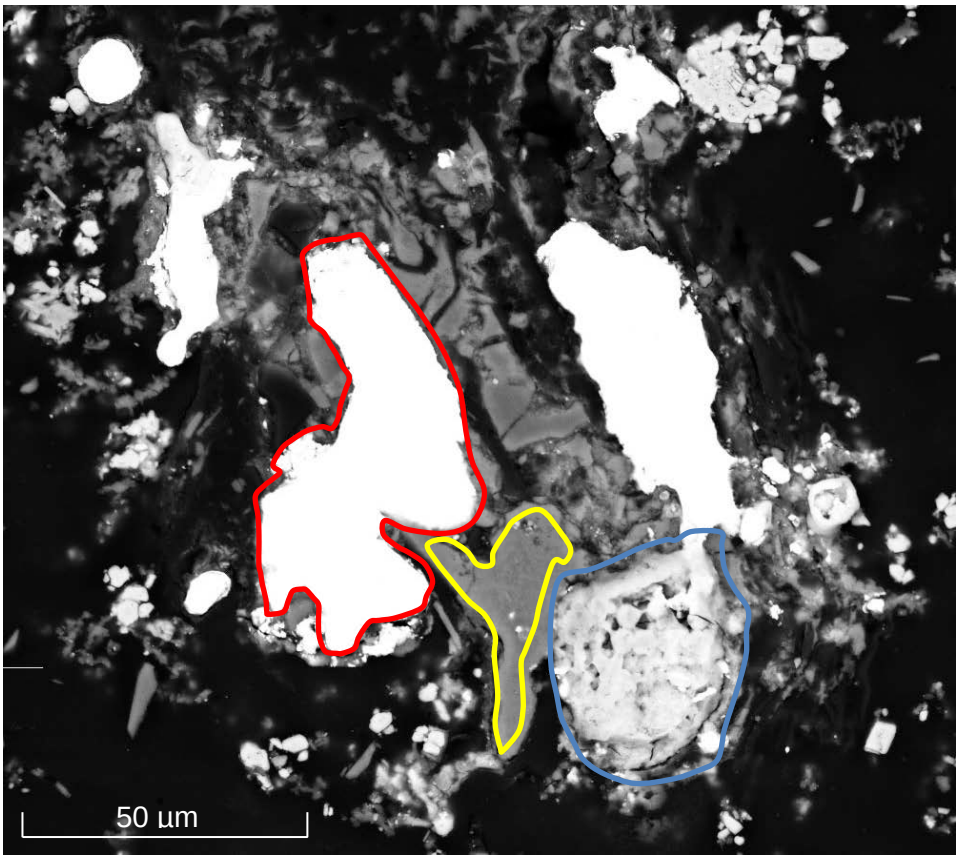

Figure 6.21 Unpolished Section through Ferronickel and Coke Particles

SEM image through ferronickel (outlined in red) with an average grade 70% Ni, formed after segregation at 1173 K for 70 minutes, remnant Al silicate ash from coke (outlined in yellow) and unwashed ferronickel surface coated in chloride (blue) are also shown.

In Figure 6.22, the EDS spot analysis of two points (3,4) showed the grade at the centre of the particle to be 65% Ni. The average analysis of three points (2,5,6) showed the grade to be ~47% Ni near the surface of the particle. This variation in composition across the ferronickel is relatively small given that the instantaneous ferronickel grade is predicted to decrease from ~90-40% Ni over the reaction period (Figure 6.15). Equalisation of the composition must occur by diffusion as the reaction proceeds, as also reported by Rey et al. (1972b).

6.4 Chloride

Chloride enters the experimental system as $CaCl_2$ and leaves as either HCl gas or metal chloride vapour, with the remainder being present as water soluble chlorides within the solid segregation product. The deportment of chloride during the segregation process is examined in this section.

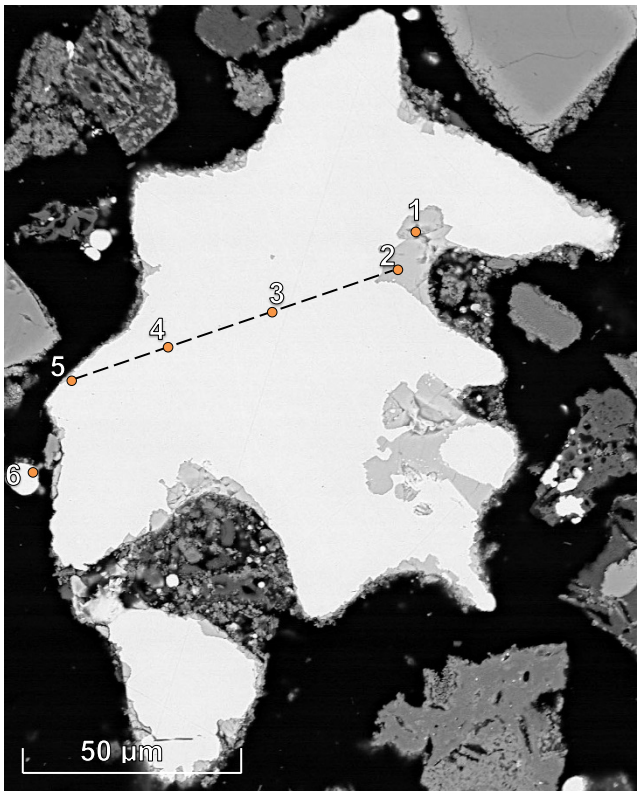

Figure 6.22 Section through a Discrete Ferronickel Particle

SEM image through a discrete ferronickel particle, formed after segregation with coke for 70 minutes at 1173 K. Point (**1**) 3% Ni, 47% S, rest Fe; (**2**): 41% Ni; (**3**, **4**) 65% Ni; (**5**) 59% Ni; (**6**) 40% Ni.

6.4.1 Residual Chloride

The amounts of Ni, Fe, and Ca present as chlorides within the solid segregation product were determined by a water leach (Section 3.3.5). The respective recoveries are summarised Table 6.14, along with the recovery of total Cl and the $FeCl_2/NiCl_2$ mole ratio. The full set of data is presented in Appendix B.10.

Table 6.14 Residual Soluble Chlorides, Nontronite Segregation

Carbon	Temp (K)	Recovery (%) as Soluble Chloride				$FeCl_2/NiCl_2$ (mole ratio)
		Ni	Fe	$CaCl_2$	Total Cl	
Coke	1123	1.0-2.0	2.0-3.0	6.0-24	27-58	15-70
Coke	1173	0.5-2.5	2.0-3.0	6.0-15	26-43	15-80
Coke	1223	0.2-1.7	1.5-3.0	4.0-17	20-46	20-400
Act C	1223	0.3-2.0	1.0-2.5	5.0-11	15-35	20-200

Recoveries of Co and Mg as chlorides were negligible.

Table 6.14 shows that 4-24% of the original $CaCl_2$ remained after segregation. along with up to 3.0% of Fe as $FeCl_2$ and 2.5% of Ni as $NiCl_2$. The $FeCl_2/NiCl_2$ values may be indicative of the final partial pressure ratio in the gas; however, the data are too scattered to provide any trends.

The residual $CaCl_2$ during segregation with coke at 1173 K is shown in Figure 6.23. The residual drops rapidly to 14% over the first 20 minutes, and then declines slowly for the remainder of segregation. The data with coke at 1123 and 1223 K show similar trends and are presented in Appendix B.10. Importantly, these data confirm that sufficient $CaCl_2$ was present to provide for the regeneration of HCl throughout the entire process.

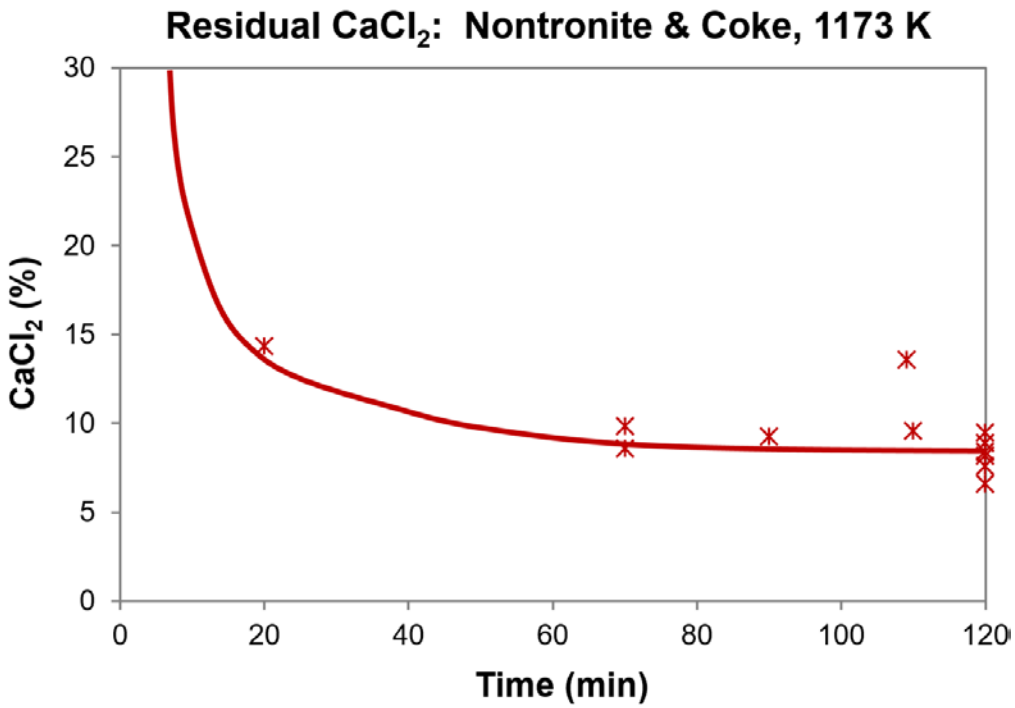

Figure 6.23 Residual $CaCl_2$, Nontronite with Coke at 1173 K

Residual $CaCl_2$ is relative to the initial 5 g of $CaCl_2$/100 g of dried ore.

The trend line has been drawn rather than fitted.

The total residual soluble chloride, calculated as the sum of the residual $CaCl_2$, $NiCl_2$ and $FeCl_2$ (Table 6.14), is shown during segregation at 1173 K with coke in Figure 6.24 as a percent of the initial chloride added as $CaCl_2$. The figure indicates that, after 120 minutes, ~30% of the original chloride added as $CaCl_2$ can be accounted for by the residual chlorides, with ~10% as $CaCl_2$ (Figure 6.23) and ~20% as residual $FeCl_2$ and $NiCl_2$.

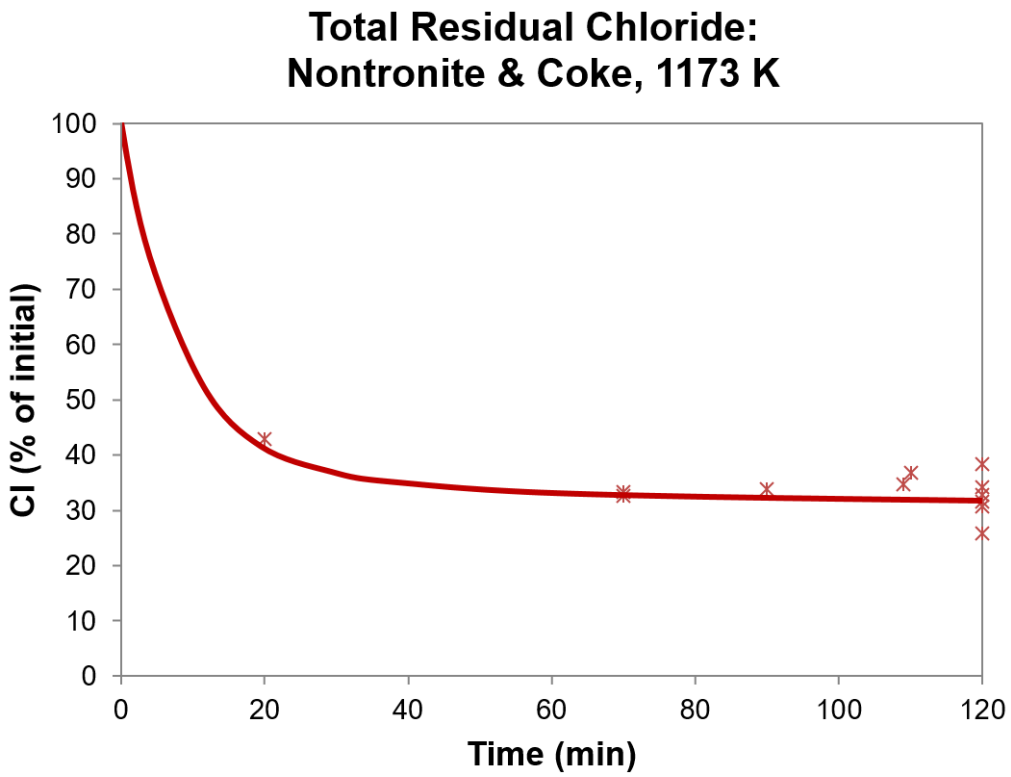

Figure 6.24 Total Residual Soluble Chloride, Nontronite with Coke at 1173 K

Residual $CaCl_2$ is relative to the initial 5 g of $CaCl_2$/100 g of dried ore.

The trend line has been drawn rather than fitted.

6.4.2 HCl in the Off-Gas

The amount of HCl in the segregation off-gas was measured using dedicated experiments in which the off-gas line was heated to prevent the condensation of HCl prior to continuous absorption within acidified water (Sections 3.2.4). The cumulative amount of HCl was calculated through monitoring of the pH of the solution (Section 3.3.4). There was an initial lag time of ~2 minutes before the reaction gases reached the HCl analysis solution and this was discounted from the time scale.

The HCl measurements were performed over 120 minutes with coke at 1123, 1173 and 1223 K. The data from two experiments at both 1173 and 1223 K were combined using Microsoft Excel to provide a single profile for each temperature; the data at 1123 K were from one test (Appendix B.9). The curves showing the cumulative HCl within the gas at each temperature are presented in Figure 6.25, with HCl represented as a percent of the original chloride added as $CaCl_2$.

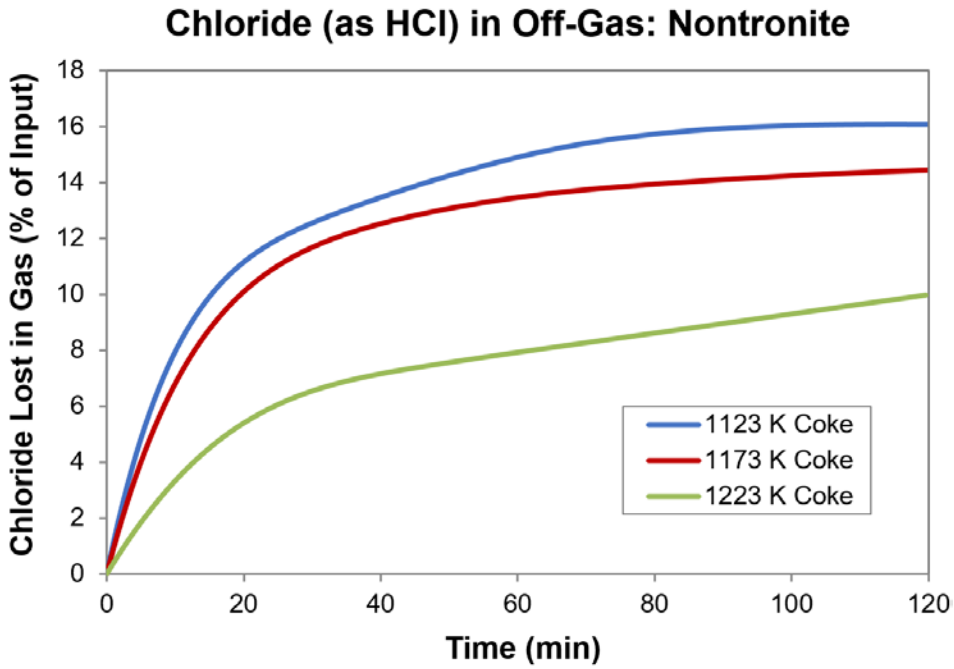

Figure 6.25 Chloride as HCl in Off-Gas, Nontronite with Coke

Chloride input as $CaCl_2$, with 5 g/100 g of dried ore.

The loss of HCl in the off-gas results from the hydrolysis of $CaCl_2$ through reaction with H_2O from the calcine (Equation 2.10), and thus is likely to depend on the rate at which moisture is released from the calcine and the accompanying volume of evolved gases. Figure 6.25 confirms that at constant temperature, the loss was highest at the start of segregation when the release of moisture from the calcine and reagents was highest, and when the evolution of off-gas was highest; the rate then decreased significantly after ~20 minutes at all temperatures.

Figure 6.25 also confirms that the total loss of chloride as HCl in the off-gas was highest at the lowest temperature where the amount of water available for release from the calcine was also the highest, as shown in Table 4.3. After 120 minutes, the total chloride lost in the gas was 16.1% at 1123 K, 14.4% at 1173 K and 10.0% at 1223 K.

These losses are small compared to those expected based on the total chloride remaining in the segregation product (Figure 6.24). After 120 minutes at 1173 K for example, ~60% of the chloride was lost from the reaction bed within the first 20 minutes. This required the off-gas to contain an average of ~65% HCl over this time, well above the measured values. Discrepancies of similar magnitude exist for all other segregation tests, including those conducted with limonite (Section 7.4.2) and garnierite (Section 8.4.2).

Additional chloride could be lost as Fe chlorides, but the amount should be small early in the reaction, since the activity of FeO is low in the presence of hematite and the moisture content of gas is relatively high, which should minimise $FeCl_2$ formation. There may have been an instantaneous non-equilibrium release of HCl through the reaction of hygroscopic $CaCl_2$ with self-absorbed moisture as soon as the chloride dropped into the bed, which was able to escape before the reactor cap was fully sealed. The system was sealed as quickly as possible and once sealed, it was ~2 minutes before the first HCl was detected in the absorption bottle. If there was an instantaneous release of HCl it was not was detected and the loss of chloride remains unexplained.

The pressure of HCl in the off-gas was estimated using the data for the cumulative volume of HCl and carbonaceous (CO & CO_2) components within the off-gas. The moles of HCl reporting to the off-gas over 5 second intervals were calculated from the fitted curves shown in Figure 6.25, and combined with the moles of CO and CO_2 reporting to the gas over the same time, calculated from the fitted curves in Figure 6.11. The ratio of the moles of HCl over the total moles of HCl, CO and CO_2 gave an estimate for the maximum possible p_{HCl} at 1 atm total pressure. The gas also contained H_2O and $FeCl_2$ but these were not measured. These calculated pressures are presented in Figure 6.26 versus time for segregation with coke at 1123, 1173 and 1223 K.

Figure 6.26 shows that p_{HCl} had the highest initial value of ~0.23 atm at 1123 K, where the highest loss of HCl (Figure 6.25) coincided with the lowest initial evolution of carbonaceous off-gas (Figure 6.11). Conversely, the smallest initial p_{HCl} value was ~0.05 atm at 1223 K. The p_{HCl} was relatively constant at both 1173 and 1223 K for the first 40 minutes, but fell rapidly for the first 20 minutes at 1123 K before leveling out. When the time exceeded 60 minutes, the prediction of p_{HCl} became less reliable because the accompanying volume of carbonaceous gases became small and variable, as indicated by the dashed lines on Figure 6.26.

The relatively constant p_{HCl} values at the higher temperatures of 1173 and 1223 K are consistent with rapid attainment and maintenance of the $CaCl_2$ hydrolysis equilibrium, accompanied by a consistent release of moisture from the calcine; the initial fall in pressure at 1123 K is consistent with a decreasing release of the initially relatively high moisture retained within the calcine.

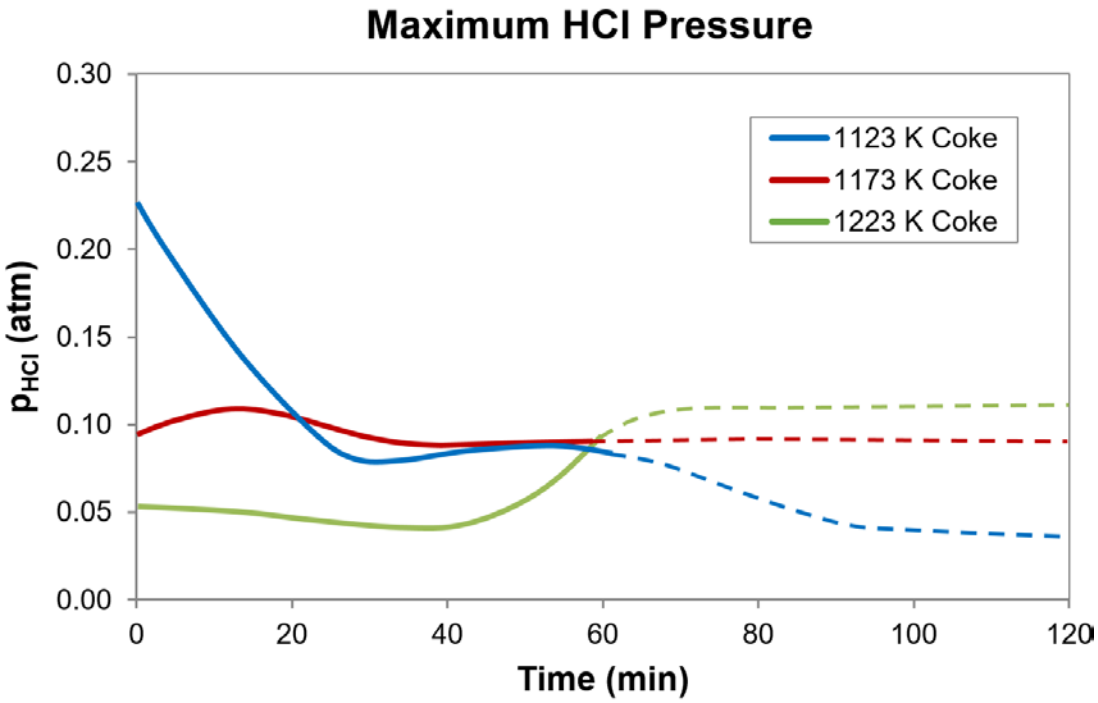

Figure 6.26 Maximum Possible HCl Pressure in Off-Gas, Nontronite

Pressure of HCl is calculated assuming only CO, CO_2 and HCl are in the gas at 1 atm (excludes H_2O and $FeCl_2$ which were not measured). The data become less reliable after 60 minutes due to relatively low and variable gas evolution.

An amount of H_2O would accompany the HCl in the off-gas, as largely determined by the equilibrium for the hydrolysis of $CaCl_2$ in the presence of SiO_2 (Equation 2.10, Section 2.4.1). The equilibrium dictates that the amount of H_2O should be significantly less than HCl content, as indicated in Table 6.15. This demonstrates the capacity of the $CaCl_2$ hydrolysis reaction to efficiently capture the H_2O as it is released from the ore by conversion into HCl, which minimises the H_2O loss in the gas.

Table 6.15 Maximum HCl and H_2O Pressures in Off-Gas, Nontronite

p_{HCl} values are from Figure 6.26; p_{H_2O} values are estimated from $CaCl_2$ hydrolysis forming $CaSiO_3$, for which $p_{H_2O} = p_{HCl}^2 / K_{2.10}$ for pure phases.

Time (minutes)	1123 K Max. Pressure (atm)		1173 K Max. Pressure (atm)		1223 K Max. Pressure (atm)	
	HCl	H_2O	HCl	H_2O	HCl	H_2O
0	0.23	0.071	0.08	0.006	0.05	0.002
40	0.08	0.009	0.08	0.006	0.04	0.001
80	0.05	0.003	0.08	0.006	0.12	0.009

6.4.3 HCl Recycle

An important characteristic of the segregation process is the recycle of HCl between the carbon and the ore. Within this recycle, HCl is regenerated near the carbon surface from the reduction of Ni and Fe chlorides with H_2 according to the reactions:

$$NiCl_2(s) + H_2(g) \rightarrow Ni(s) + 2HCl(g) \quad 2.24$$

$$FeCl_2(s) + H_2(g) \rightarrow Fe(s) + 2HCl(g) \quad 2.25$$

The rate of HCl regeneration ($\mathcal{R}_{HCl,regen}$) is equal to twice the combined rates of reactions 2.24 and 2.25, according to:

$$\mathcal{R}_{HCl,regen} = 2(v_{2.24} + v_{2.25}) \quad mol/min\, g_{ore} \quad 6.14$$

$v_{2.24}$ and $v_{2.25}$ are the respective rates of $NiCl_2$ and $FeCl_2$ reduction, as estimated over 5 second intervals using the respective integrated rate equations for Ni recovery (Table 6.2) and Fe recovery (Table 6.5). All rates are presented in moles per minute per gram of dried ore (mol/min g_{ore}). A relatively small portion of $CoCl_2$ is also reduced but is ignored for the purpose of this discussion.

A portion of the regenerated HCl is lost in the off-gas, while the remainder is recycled back to the ore to participate in further chloridisation of metal oxides; thus for any small segment of time, the rate at which HCl recycles ($\mathcal{R}_{HCl,recyc}$) is approximately[29] equal to the rate at which it is regenerated, minus the rate at which it is lost in the off-gas ($\mathcal{R}_{HCl,loss}$), according to:

$$\mathcal{R}_{HCl,recyc} = \mathcal{R}_{HCl,regen} - \mathcal{R}_{HCl,loss} \quad 6.15$$

The rate at which HCl is lost in the gas was also calculated over 5 second intervals using the fitted chloride gas data (Figure 6.25).

The calculated rates are presented in Figure 6.27 for 1123 K, Figure 6.28 for 1173 K and Figure 6.29 for 1223 K. The HCl regeneration rates from $NiCl_2$ and $FeCl_2$ reduction respectively are shown in blue and green; the rate of HCl loss in the gas is shown in red and the rate of recycle in purple. The dashed black line shows the percent of HCl recycled.

[29] Since $\mathcal{R}_{HCl,recyc}$ changes with time, Equation 6.15 is approximately true for any small segment of time.

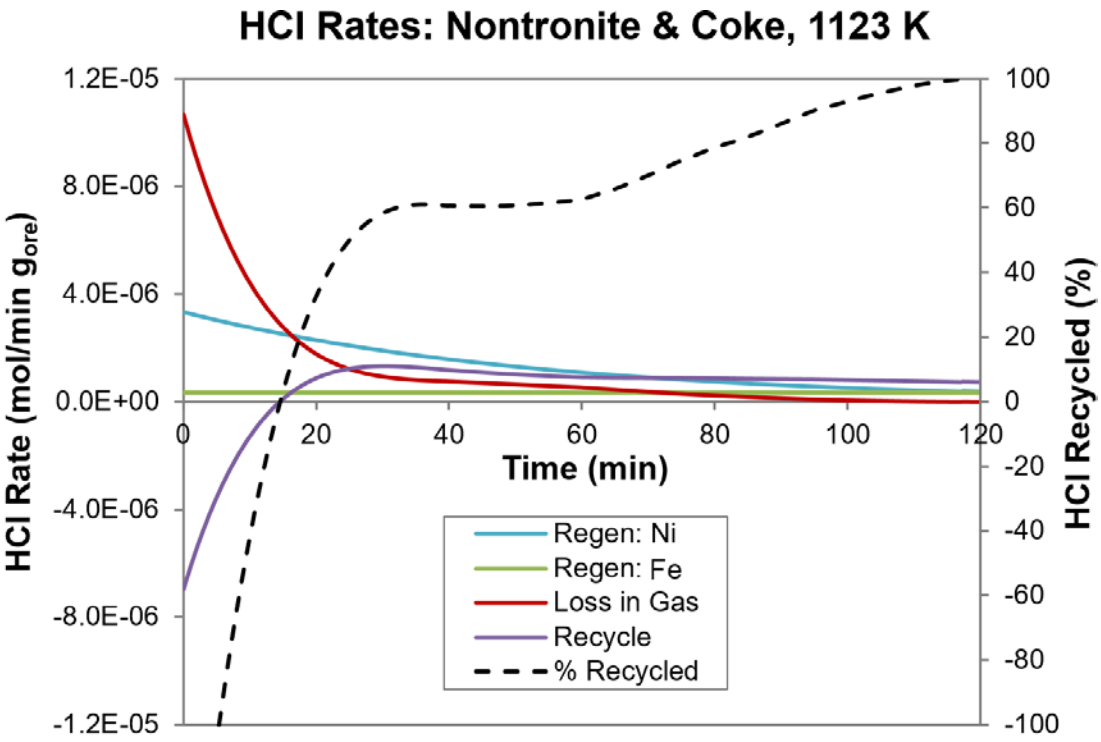

Figure 6.27 HCl Regen, Loss and Recycle Rates, Nontronite with Coke, 1123 K

Regen: Ni and Regen: Fe are the rates at which HCl is regenerated by chloride reduction through Equations 2.24 and 2.25 respectively.

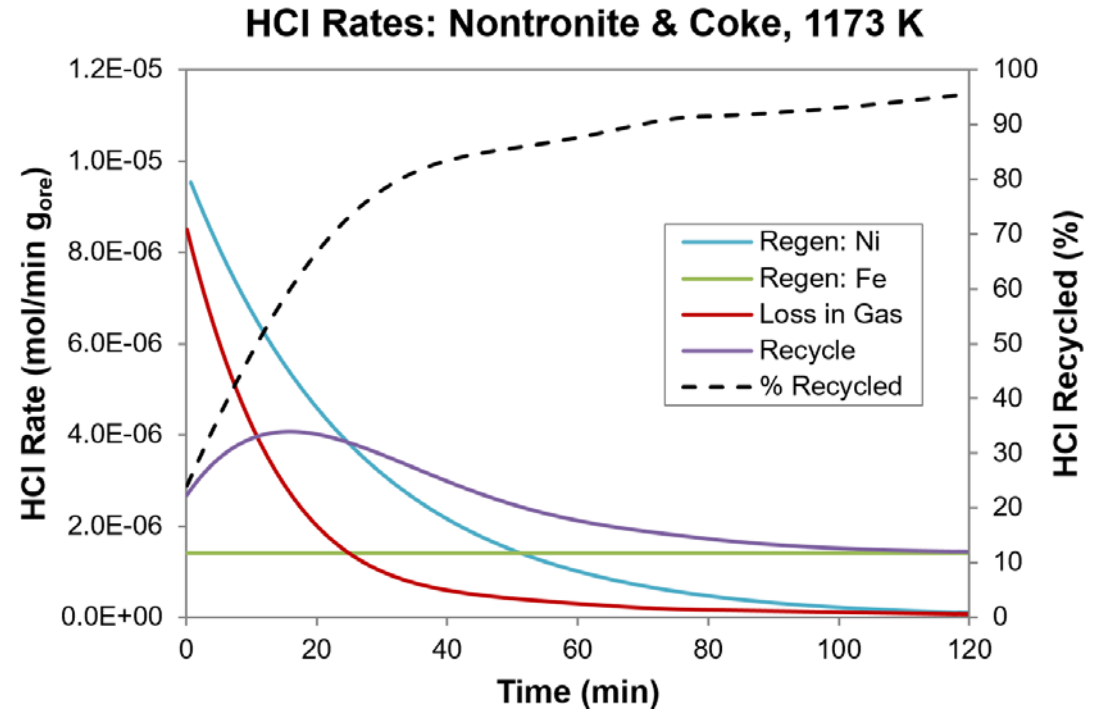

Figure 6.28 HCl Regen, Loss and Recycle Rates, Nontronite with Coke, 1173 K

Regen: Ni and Regen: Fe are the rates at which HCl is regenerated by chloride reduction through Equations 2.24 and 2.25 respectively.

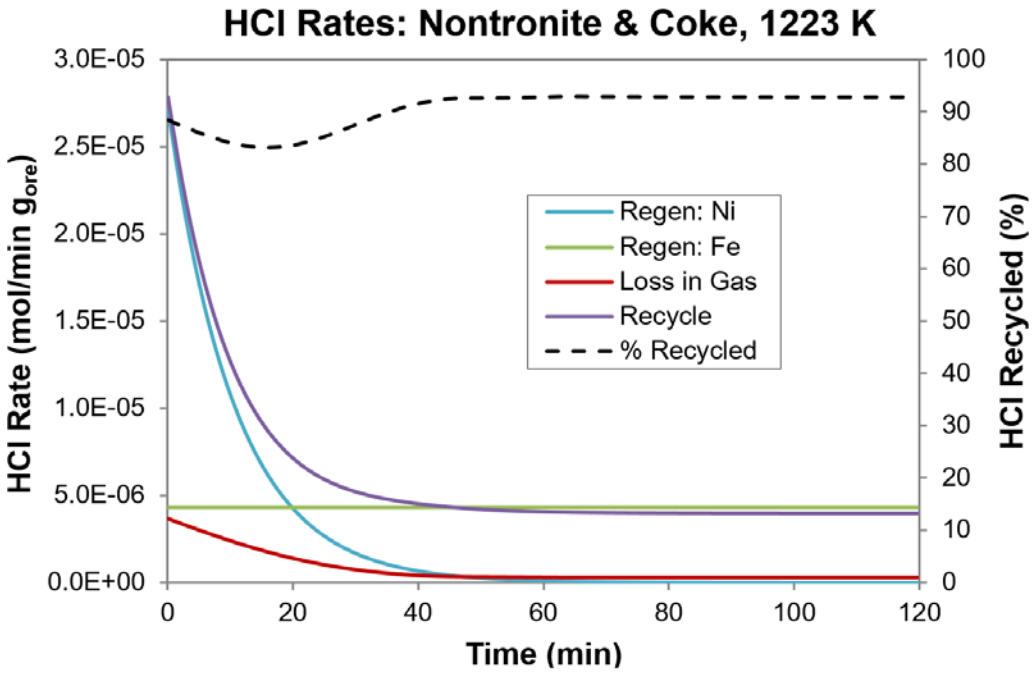

Figure 6.29 HCl Regen, Loss and Recycle Rates, Nontronite with Coke, 1223 K

Regen: Ni and Regen: Fe are the rates at which HCl is regenerated by chloride reduction through Equations 2.24 and 2.25 respectively.

All figures show that at fixed temperature, the recycle efficiency, as described by the percent of HCl recycled, is lowest during the initial stages of segregation while the evolution of carbonaceous gases is greatest, but approaches 100% as the evolution of gas (Figure 6.11) decreases over time. As the temperature increases, the efficiency of the recycle also increases because the rate of HCl regeneration is enhanced relative to that lost in the gas due to increases in both the Ni and especially the Fe segregation rates.

When the HCl recycle is not 100% efficient, most[30] of the lost HCl must be replenished through hydrolysis of $CaCl_2$. When the percent recycle is negative, as occurs for the first 15 minutes of segregation at 1123 K (Figure 6.27), the HCl from hydrolysis must exceed that regenerated by reduction to replenish the HCl.

Rey et al. (1972a) suggested that the HCl and H_2O contents of the gas are likely so small towards the end of segregation that the process cannot continue to operate in the normal way, and that chloridisation may occur via direct contact between $CaCl_2$ and metal oxide (Section 2.4.2). Examination of the segregation product (Appendix

[30] All of the HCl is not necessarily replaced since the p_{HCl} can fall over time if the p_{H_2O} available for hydrolysis falls over time due to a decreasing release of bound moisture from the calcine.

B.17) indicates this mechanism is possible, since Ca and Cl were widely associated with particle surfaces, and no discrete $CaCl_2$ could be identified. However, while HCl may not be required for chloridisation during the later stage of segregation, the process cannot be sustained without a source of hydrogen, since metal chloride reduction is not possible without it (Section 2.4.3).

This work has shown that, even though the evolution of gas decreases significantly with time, the process has the capacity to continue since: (1) excess $CaCl_2$ is present to maintain an atmosphere containing HCl; (2) the thermodynamically favourable hydrolysis equilibrium minimises the loss of H_2O by efficiently capturing it as HCl and; (3) as the gas evolution decreases, the increase in the efficiency of the HCl recycle can adequately account for the segregation rates obtained in the present experiments, as demonstrated by the viable recycle profiles shown at all three temperatures.

6.5 Effect of Roasting Conditions

The mineralogical changes, which occur when nontronite ores are roasted in air, have been described in detail in Section 4.1.4. It is well understood that the heating profile and final temperature of the roast will affect the amount of moisture retained in the calcine, as well as the final mineral phases present and their crystallinity. All of these factors have the potential to impact on the recovery of Ni and the ferronickel grade (Sections 2.4.6 & 2.4.8).

The majority of segregation tests in this study included a standardised roast for all three ores, to enable a more efficient comparison of other factors affecting the process. The standard roast involved heating the ore in air for 30 minutes at the segregation temperature, after which the calcine was cooled and stored. The segregation was then conducted using a two-step method (Section 3.3.2). The first step was to rapidly heat the calcine to the segregation temperature under argon; the second step was to add the $CaCl_2$ and carbon at the segregation temperature to initiate the reaction at a defined zero time.

A modified procedure was used to assess the effects of roasting on the segregation process. The ore was roasted using non-standard conditions and the calcine stored as before. The segregation was then conducted using a one-step method in which the calcine was mixed with $CaCl_2$ and carbon at room temperature and then rapidly heated under argon to the reaction temperature. This one step was used to

minimise the ore heating period prior to segregation, so as to emphasise the effect of the non-standard roast.

All one-step segregation tests were conducted at 1173 K using 5% coke and 5% $CaCl_2$ with respect to the mass of dried ore. An 80 minute time period was selected so that the final Ni recovery would approach the upper limit predicted for the segregation using the standard roast (Figure 6.1). Three to five segregation tests were conducted with each of three non-standard roasts, described here as 'low temperature', 'rapid' and 'high temperature' roasts.

The 'low temperature' roast was carried out for three days, just below the main dehydroxylation temperature of the ore (~570 K for nontronite, Section 4.1.4). These conditions were selected to remove most of the chemically bound water at a temperature low enough to minimise crystallinity of the minerals formed, so as to produce a relatively amorphous, reactive mineralogy.

The 'rapid' roast was carried out just below the ore sintering temperature (1223 K for nontronite, 10 K below sintering, Table 4.2) for a time long enough to remove the majority of combined water (8 min for nontronite, Figure 4.1). This was a 'shock' roast, designed to rapidly remove the chemically bound water so as to produce numerous micro-pores, while minimising the time for the crystallisation and densification of the resulting minerals.

The 'high temperature' roast was carried out just below the ore sintering temperature (1223 K for nontronite) for a period of three hours. The purpose was to form well-developed crystalline minerals to contrast with the minerals formed during the low temperature and rapid roasts. A summary of the three non-standard roast conditions is given in Table 6.16.

Table 6.16 Non-Standard Conditions for Air Roast, Nontronite

Roast	Time	Temperature Set Point	Temp (K)
Low Temp	3 days	Just below ore dehydroxylation	~570
Rapid	8 min	Just below ore sintering	~1223
High Temp	3 hrs		

6.5.1 Recovery of Metals

The averaged values for metal recoveries and ferronickel grades are presented in Table 6.17, for one step segregation preceded by the non-standard roasts. The mole fractions of moisture retained in the calcines after each roast and the percent residual $CaCl_2$ after segregation are also presented. Equivalent data from the standard roast and segregation are included for comparison. Data for the individual non-standard roast/modified segregation tests are presented in Appendix B.11.

Table 6.17 Effect of Roast Type on Nontronite Segregation

Mass fraction of retained water is calculated from weight change relative to the maximum possible change (Table 4.2); segregation for 80 minutes at 1173 K with 5% coke and 5% $CaCl_2$, based on dried ore.

Roast	Retained Water (mass fraction)	Recovery (%)			FeNi	Residual $CaCl_2$ (%)
		Ni	Fe	Co	Ni(%)	
Low Temp	$2.1x10^{-2}$	49	1.1	14	70	6.6
Rapid Heat	$3.3x10^{-3}$	61	1.6	20	66	11
High Temp	$2.0x10^{-4}$	60	1.4	18	68	13
Standard*	$5.2x10^{-3}$	60	1.4	18	67	8.0

*Standard values taken from fitted equations: Ni (Table 6.2), Fe (Table 6.5), Co (Table 6.6)

Table 6.17 shows that variation of the roasting conditions, which changed the crystallinity of the minerals and the amounts of water retained in the calcines, had little impact on either the Ni, Fe and Co recoveries by segregation or the ferronickel grade. The slightly lower metal recovery from the 'low temperature' roast was likely due to mechanical loss; the relatively high level of retained moisture in the calcine resulted in a more rapid evolution of H_2O in the early period of segregation, which caused material to be ejected from the reaction zone and stick to the walls of the reactor. As expected, the residual $CaCl_2$ generally decreased as the amount of retained moisture increased, due to enhanced hydrolysis.

Rey et al. (1972a) and Rey et al. (1972b), as discussed in Section 2.4.6, also reported that Ni segregation can be insensitive to the amount of moisture retained in the calcine, provided sufficient $CaCl_2$ was present to 'absorb the excess moisture'; in other words, provided sufficient $CaCl_2$ was present to establish the p_{HCl}^2/p_{H2O} ratio in the gas by the hydrolysis equilibrium. This appears to be the case for all of the segregation work conducted in this study, since residual $CaCl_2$ was present after every test.

Multiple other researchers have reported that moisture has a significant impact on Ni segregation (Section 2.4.7), but they reached this conclusion after passing H_2O through the segregation bed in a carrier gas. This reduces the partial pressures of Ni and Fe chlorides by disturbing the p_{HCl}^2/p_{H2O} ratio created by the $CaCl_2$ hydrolysis equilibrium, which both decreases the Ni recovery and increases ferronickel grade, since $FeCl_2$ is more sensitive to hydrolysis than $NiCl_2$.

Rey et al. (1972a) (Section 2.4.8) reported that increasing the roasting time at high temperature decreased Ni recovery by allowing the NiO to become entrapped within olivine. However, the 'high temperature' roast carried out in this work, in which the calcine was held for 3 hours just below the ore sintering temperature (1223 K, Table 6.16), yielded the same segregation recovery as for the 'rapid roast', in which the ore was held for only 8 minutes at this temperature.

Rey et al. (1972a) conducted their roasting tests under mildly reducing conditions in which the reduction of iron oxides to Fe_3O_4 and FeO occurred, thus providing for the formation fayalite (Fe_2SiO_4) which can readily form solid solutions with forsterite (Mg_2SiO_4) and capture NiO as silicate. In addition, Ni could also dissolve as trevorite ($NiO.Fe_2O_3$) within a spinel solid solution with magnetite. When roasting in air, as carried out in this work, iron oxide remains as hematite. This appears to prevent NiO from entering spinels or silicates during the roast and the Ni recovery by segregation appears unaffected.

6.5.2 HCl in the Off-Gas

The cumulative HCl reporting to the off-gas was measured in a single experiment during each of the non-standard roast/modified segregation tests; these data are shown in Figure 6.30 as a percent of the total chloride added. A lag time of ~3-4 minutes from when the system was sealed to the first change in pH was discounted from the time scale.

Figure 6.30 shows that the rate of chloride loss is greatest over the initial 20 minutes and strongly dependent on the roast conditions. The 'low temperature' calcine, which contained the highest residual H_2O, showed the highest loss; the 'high temperature' calcine, which contained the lowest residual H_2O, showed the lowest loss. This is expected from the impact of released moisture on the hydrolysis of $CaCl_2$. If amorphous silicate phases form as expected during the rapid and low temperature roasts, then the presence of this material may also promote the loss of HCl relative to the 'high temperature' roast, since the $CaCl_2$ hydrolysis equilibrium may be enhanced by the increased surface area of silica (Equation 2.10).

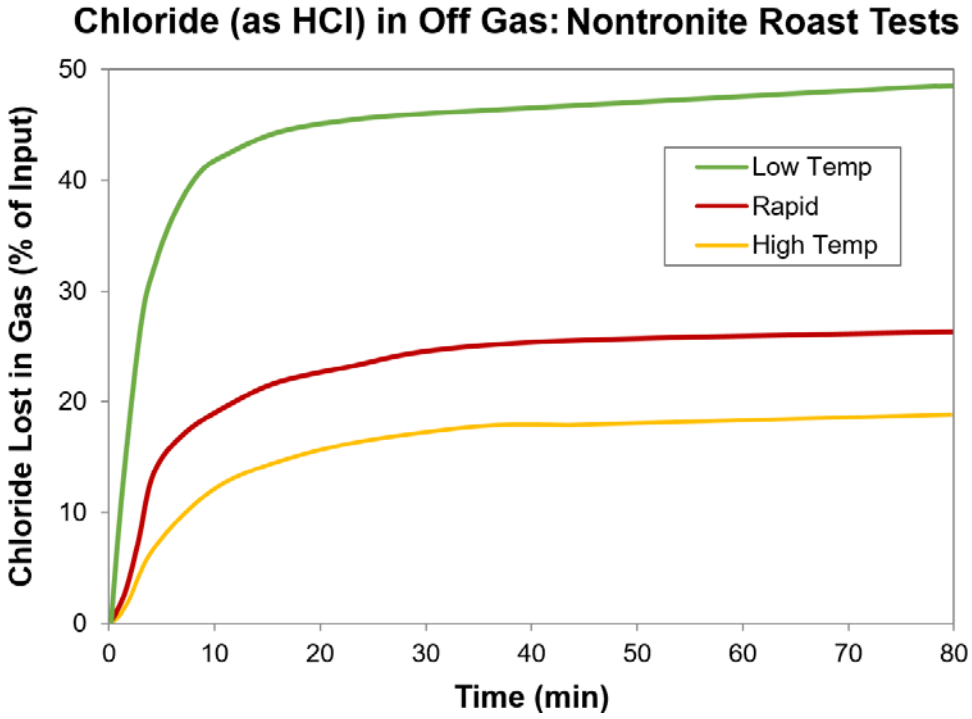

Figure 6.30 Chloride as HCl in Off-Gas, Nontronite Non-Standard Roasts

$CaCl_2$ addition was 5 g/100 g of dried ore.

Figure 6.30 shows that the p_{HCl} would be relatively high within the first 10 minutes of segregation after the 'low temperature' roast but as shown in Table 6.17, the Ni segregation recovery is not changed. The Ni segregation rate is controlled by the chloridisation of NiO and should be enhanced if the p_{HCl} is relatively high. However, as observed by others (Section 2.4.1), the hydrolysis of $CaCl_2$ during the initial release of significant H_2O is not necessarily an equilibrium process, and a high partial pressure of H_2O may supress $NiCl_2$ formation during the early stages of segregation.

6.6 Magnetic Concentrate

The grade (Ni%) of the magnetic concentrate obtained from the segregation product using the Davis Tube Tester (Section 3.3.6) provides a measure of the potential to upgrade the segregation product prior to recovery of the ferronickel.

Detailed data for the Ni grade of the magnetic concentrate from the nontronite segregation tests are presented in Appendix B.6. The change in concentrate grade versus time of segregation is shown in Figure 6.31, for coke at 1123, 1173 and 1223 K, and for activated carbon at 1223 K.

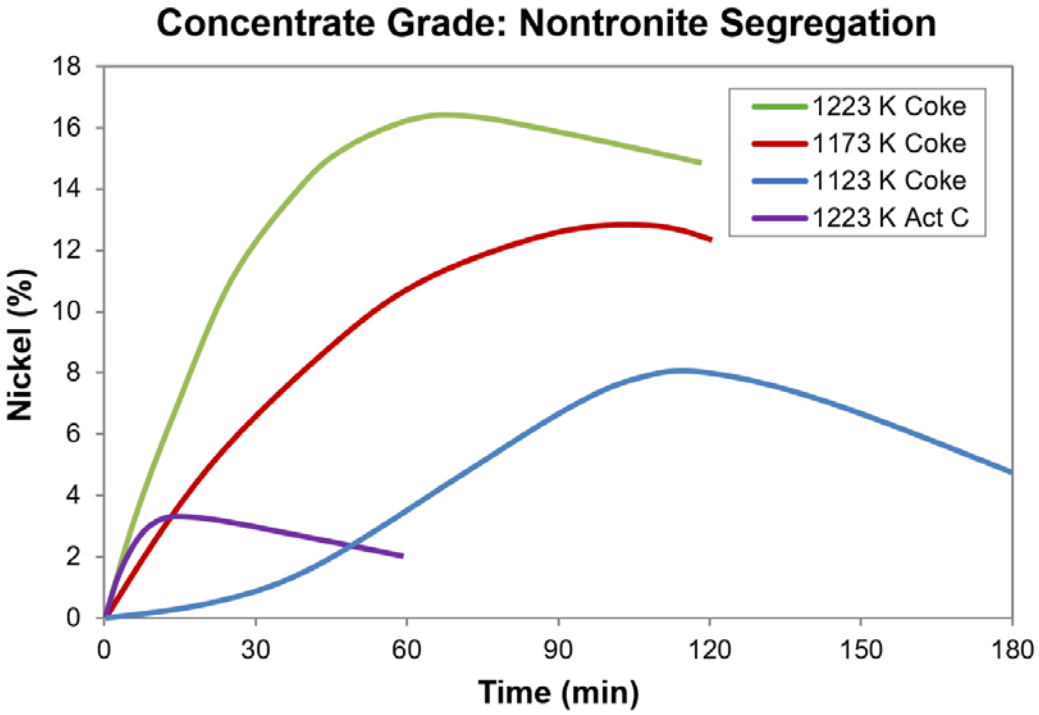

Figure 6.31 Magnetic Concentrate Grade, Nontronite Segregation
Trends are drawn rather than fitted, see Appendix B.6.

It can be seen that for all temperatures the concentrate grade increased to a maximum, which varied from 3-16% Ni depending on temperature and carbon type, before it decreased again. The maximum occurs when FeO is the dominant iron oxide in the gangue, either as monoxide or within silicate. This is because FeO is the least magnetic iron oxide, and forms later in the reduction when most of the Ni is already segregated.

Initially, Fe_2O_3 reduces to Fe_3O_4, which all reports to the magnetic concentrate. As Fe_3O_4 reduces to FeO the mass of the concentrate decreases as the Ni continues to segregate. The grade reaches a maximum as reduction of FeO to Fe begins, and

then falls due to dilution of the ferronickel with Fe. At constant temperature, the maximum grade with activated carbon (3%) was much lower than with coke (16%), since in-situ reduction to alloy renders much of the gangue magnetic (Figure 6.17). As the temperature increases, the grade increases in response to the increased Ni recovery, for example, the maximum grade when using coke increases from 8% at 1123 K to 16% at 1223 K.

The Ni upgrade ratio, calculated as the percent of Ni in the concentrate divided by the percent of Ni in the ore ($\frac{\%Ni_{Con}}{\%Ni_{Ore}}$), increased for coke from 6.6 at 1123 K, to 10.4 at 1173 K and 13.3 at 1223 K, compared to only 2.6 at 1223 K when using activated carbon.

6.7 Discussion

The segregation of nontronite calcine appears to be kinetically controlled. The rates of segregation of Ni, Fe and Co from a roasted nontronitic Ni laterite ore were measured and fitted to a series of empirical 'first order to a limit' or zero order rate equations. It was concluded that chloridisation of NiO from within the calcine is the rate control for Ni segregation, whereas the generation of the H_2 reductant at the carbon surface by the water gas reaction is the rate control for Fe segregation; the rate for Co segregation is likely controlled by both. The overall percent metal recovery by segregation was highest for Ni, intermediate for Co and lowest for Fe, in parallel with the increasing stabilities of the respective metal oxides.

The rate of Ni segregation was considered to be fundamentally related to the activity of NiO in the calcine and the pressures of HCl and $FeCl_2$ in the bulk gas. The rate of Ni segregation was initially rapid but slowed with time and approached a limit, which along with the initial rate, increased with increase in temperature. Prior to segregation, the majority of Ni was present in the calcine within fine grained to amorphous intimate mixtures of silica and iron oxides within nontronite dehydroxylate particles which contained at ~1.6% Ni. Iron silicates (ferrosilite and minor fayalite) crystallised from within these mixtures during segregation and contained the majority of unsegregated Ni.

The activity of NiO within the calcine was not measured, but the Ni segregation rate was consistent with the activity being high initially and then decreasing with time as NiO was removed from the calcine and the remainder became dissolved within the iron silicates. The initially rapid rate of NiO chloridisation and hence segregation

appeared fundamental to the success of the process. This was because the early removal of NiO lowered and maintained the critical oxygen pressure required for in-situ reduction to alloy below that within the bulk gas; otherwise in-situ rather than segregated ferronickel will form and Ni recovery will decrease.

The segregation limit was found to increase with temperature and a maximum recovery of 79% was obtained using coke at the 1273 K, likely close to the practical upper temperature limit, since it was 40 K above the sintering temperature of the calcine.

The rate of Fe segregation at constant temperature was considered to be fundamentally related to the surface area of carbon and the pressure of H_2O in the gas, discounted by the rate at which Ni segregation consumed H_2. These factors appeared to compensate each other since the rate of Fe segregation was found to be constant within experimental error for the duration of the segregation process.

The grade of ferronickel produced was kinetically controlled by the Ni and Fe segregation rates. The grade decreased with time as the Ni segregation rate decreased while the Fe segregation rate stayed constant. The grade also decreased with increase in temperature and carbon surface area since both factors increased the rate of Fe segregation compared to Ni segregation. The reduction of Ni and Fe chlorides by H_2 was likely near equilibrium, with the instantaneous grade of ferronickel related to the $FeCl_2/NiCl_2$ ratio of the gas at the carbon surface.

The ferronickel deposits were typical of those observed by others. They appeared to nucleate as spherical grains or cubic crystals on the carbon surface, and afterwards as cubic crystals on existing alloy. These grains/crystals eventually meshed together to form coarse 20-250 µm conglomerates, partially or completely covering carbon particles. The reduction likely involved an adsorption mechanism since chlorides were observed on the carbon and alloy surfaces. Sulphur from coke presented as minor sulphides on the surface of some ferronickel particles. The average ferronickel grades measured by EDS-SEM were in good agreement with those determined by dissolution, with some variation between Ni rich centres and Fe rich edges, in keeping with the changing grade of the instantaneously reduced alloy.

In common with reduction in the absence of chloride, the CO_2/CO ratio and the oxygen pressure within the bulk gas were dominantly controlled by the iron oxide reduction equilibria, while the rate of change of the CO_2/CO ratio was controlled by the gasification of CO_2 at the carbon surface by the Boudouard reaction. All factors

which decreased the ferronickel grade also decreased the CO_2/CO ratio, such that the oxygen pressure within the bulk gas decreased as the ferronickel grade decreased. However, the ferronickel grade was not controlled by the oxygen pressure, as has been suggested by others.

The rate of the Boudouard reaction fundamentally depends on the pressure of CO_2 in the gas and the carbon surface area. This rate slowed dramatically along with the production of carbonaceous off-gas once all Fe_3O_4 had been reduced to FeO because this dramatically reduced the CO_2 within the gas at a time when much of the carbon surface area had already been consumed.

The rate of the Boudouard reaction was increased significantly within the segregation system relative to the chloride free carbon reduction system, resulting in higher carbon consumption and lower oxygen pressures. This was presumably because the surface reaction on the carbon was catalysed by the presence of chloride. Even with the lower oxygen pressures encountered during segregation, no in-situ reduction to ferronickel was observed, except when coke was replaced by activated carbon. The increased carbon surface area reduced the oxygen pressure such that in-situ ferronickel was able to form within the iron silicates of the dehydroxylate particles. However, superior Ni recoveries were achieved with segregation compared to carbon reduction under all conditions tested.

The initial amount of HCl within the gas increased with the amount of bound water available for release from the calcine, consistent with the HCl being controlled by the hydrolysis of $CaCl_2$. The presence of free silica in the ore enhanced the hydrolysis and likely ensured that any moisture released by the calcine was rapidly captured by hydrolysis, thus maintaining a very low pressure of H_2O within the gas.

HCl consumed in the chloridisation was regenerated during the reduction, but an amount was lost in the gas which decreased the efficiency of the recycle. However, the amount of added $CaCl_2$ was sufficient to ensure that as HCl was lost in the off-gas, it was largely replaced by hydrolysis to maintain a recycle to the chloridisation process.

The amount of HCl regenerated by chloride reduction increased as the temperature increased such that the recycle efficiency increased with temperature. The recycle efficiency also increased towards 100% as the volume of off-gas decreased during the segregation. Although only small amounts of HCl and H_2O would have remained within the gas towards the end of segregation, the efficiency of recycle,

the very rapid reduction reactions involving hydrogen, and the favourable thermodynamics for the production of $FeCl_2$, probably explain why the segregation of Fe can continue at the same rate towards the end of the process.

An investigation of a range of roasting conditions designed to vary both the retained moisture content and the crystallinity of the calcine prior to segregation had little ultimate effect on the segregation recovery of Ni. An increase in the retained moisture also increased the initial release of HCl into the gas from $CaCl_2$ hydrolysis, but the effect was transient, presumably because sufficient $CaCl_2$ was available to control the chloridising atmosphere for the duration of segregation, through maintenance of the hydrolysis equilibrium.

Extended roasting time also had little effect on Ni recovery likely because the iron oxides which are closely associated with Ni, were isolated and stabilised as hematite while being roasted in air, thus preventing the formation of iron silicates and spinels, into which NiO is readily dissolved. In contrast, when roasting was conducted by others for extended times under mildly reducing conditions, iron silicates and spinels were able to form and Ni recoveries were reduced.

The segregated ferronickel was magnetically separated into a concentrate prior to leaching to determine metal recoveries. The concentrate grade doubled from 8 to 16% Ni as the temperature of segregation with coke was increased from 1173 to 1223 K and the Ni upgrade ratio increased from 6.6 to 13.3; the grade and upgrade ratio with activated carbon were much lower.

Overall, it seems that segregation has potential for the recovery of Ni from nontronite because the mineralogy of the ore is conducive to segregation occurring when using a coke reductant, without the formation of in-situ alloy. The maximum recoveries achieved by segregation of nontronite were ~80% Ni along with ~30% of both Co and Fe when using coke at 1273 K from a single test, and ~70% Ni along with ~40% of the Co and ~5% of the Fe from multiple tests when using coke at 1223 K.

However, the segregation conditions were not optimised to maximise the Ni recovery. Since Ni segregation is controlled by the chloridisation reaction, a strategy to maximise recovery might be to accelerate this rate to remove as much Ni as possible from the calcine before it can dissolve within iron silicates at a significantly reduced a_{NiO}. This would need to be done by increasing the initial p_{HCl}

while still controlling the p_{H_2O} by hydrolysis since the introduction of an external gas would disturb the segregation reaction.

$MgCl_2$ has a much more favourable hydrolysis reaction than $CaCl_2$ and would be consumed too quickly if used as a chloridising agent on its own (Section 2.4.1). However, if used in solution with $CaCl_2$, it may accelerate the initial chloridisation of NiO by boosting the p_{HCl}, before being consumed and leaving $CaCl_2$ to sustain the hydrolysis for the remainder of the reaction. Increasing the chloride addition beyond 5% may also be advantageous since with the nontronite tests, the residual $CaCl_2$ was quite low. If these strategies were adopted it might be possible to increase the recovery above the 79% achieved in this work, possibly up to 85%. A higher temperature might increase the recovery further but this would be limited by sintering.

Chapter 7

Limonite Segregation

A study of the segregation process applied to a limonite nickel laterite ore from Heron Resource's Kalgoorlie Nickel Project is presented throughout this chapter. This study was performed to provide a comparison with the main study on nontronite ore from the same deposit (Chapter 6). This presentation will be identically structured, with the discussion focused on differences between the ores; the description of common aspects will be dealt with briefly.

7.1 Recovery of Metals

Forty two segregation tests were performed using a two-step segregation method (Section 3.3.2), with multiple tests conducted for up to 150 minutes with coke at 1123 K, up to 120 minutes with coke at 1173 K, and up to 80 minutes with activated carbon at 1173 K. These test results are summarised in Table 7.1.

The limonite segregation product could not be concentrated by magnetic separation since it contained too much magnetite; flotation has been used as an alternative (Iwasaki et al., 1966; Wright and Gooden, 1973) but could not be applied in this work because the sample size was too small.

The metal recoveries and ferronickel grades are therefore only indicative since the entire segregation product had to be leached with bromine/methanol to determine the metallic content; thus in-situ ferronickel could have leached along with segregated alloy. The small amount of iron oxides known to dissolve within the leach (Section 3.3.7) may also exaggerate the metallic Fe analysis, given the substantial amount of iron oxides within the segregation product (Table 7.10).

7.1.1 Nickel

As with nontronite, it appears Ni recovery was limited by a portion of Ni within the ore that would not segregate. However, unique to limonite, the data showed a distinct 'induction period' before Ni recovery began. A 'first order to a limit' rate equation (Section 6.1.1.1) was used to describe the rate of segregated Ni recovery, but the time scale within the equation was discounted by the induction period.

Table 7.1 Metal Recoveries and Ferronickel Grades, Limonite Segregation

Ore was roasted for 30 minutes in air at the segregation temperature. Reagent addition per 100 g of dried ore was 5 g of either coke (78.3% C) or activated carbon (88.7% C), and 5 g of $CaCl_2$.

Test Code	Carbon	Temp (K)	Time (minutes)	Recovery (%)			FeNi
				$R_{Ni(\%)}$	$R_{Fe(\%)}$	$R_{Co(\%)}$	Ni(%)
L850C3	Coke	1123	10	0.49	0.18	0.06	4.8
L850C2	Coke	1123	20	3.3	0.18	1.0	25
L850C4	Coke	1123	30	0.20	0.05	ND	6.3
L850C5	Coke	1123	45	32	0.18	4.9	76
L850C1	Coke	1123	57	43	0.31	6.9	72
L850C9	Coke	1123	90	51	0.47	13	67
L850C11	Coke	1123	110	54	0.37	11	73
L850C10	Coke	1123	120	50	0.38	9.4	71
L850C12	Coke	1123	120	60	0.51	14	68
L850C18	Coke	1123	150	64	0.63	16	65
L900C4	Coke	1173	5	0.33	0.10	0.1	5.7
L900C25	Coke	1173	5	0.23	0.05	ND	8.6
L900C5	Coke	1173	10	2.7	0.30	1.3	14
L900C26	Coke	1173	10	1.3	0.04	ND	38
L900C6	Coke	1173	15	6.7	0.06	1.1	66
L900C27	Coke	1173	15	1.2	0.03	ND	46
L900C7	Coke	1173	20	46	0.28	8.3	75
L900C8	Coke	1173	25	55	0.44	11	69
L900C9	Coke	1173	30	64	0.50	16	70
L900C28	Coke	1173	30	66	0.66	17	65
L900C23	Coke	1173	45	70	0.79	18	62
L900C29	Coke	1173	60	70	0.77	18	62
L900C24	Coke	1173	70	72	1.1	18	54
L900C10	Coke	1173	80	73	0.88	22	60
L900C16	Coke	1173	90	80	1.1	24	57
L900C2	Coke	1173	100	77	0.93	22	60
L900C18	Coke	1173	105	80	1.1	24	57
L900C12	Coke	1173	110	79	1.1	25	58
L900C1	Coke	1173	120	77	1.1	23	57
L900C15	Coke	1173	120	79	1.1	25	57
L900C17	Coke	1173	120	81	1.3	19	52
L900AC5	Act C	1173	5	11	0.23	2.8	47
L900AC8	Act C	1173	10	23	0.44	6.9	49
L900AC12	Act C	1173	15	29	0.64	8.4	45
L900AC11	Act C	1173	20	28	0.69	10	42
L900AC10	Act C	1173	25	33	0.82	12	42
L900AC13	Act C	1173	30	54	2.7	25	27
L900AC9	Act C	1173	35	20	0.89	10	29
L900AC6	Act C	1173	40	60	4.0	29	22
L900AC14	Act C	1173	50	57	4.3	32	19
L900AC7	Act C	1173	60	63	3.5	29	25
L900AC15	Act C	1173	70	69	4.1	33	24
L900AC4	Act C	1173	80	61	6.4	30	15

ND = Not Detected

7.1.1.1 Recovery and Rate Equations

The parameters ($R_{Ni,max}$, k_{Ni}) for the integrated rate equations were fitted from the Ni recovery data (Table 7.1). The values for the induction period I and the fitted parameters are presented in Table 7.2, and the equations are plotted in Figure 7.1 along with the experimental data.

Table 7.2 Integrated Rate Equations, Recovery of Nickel from Limonite

Induction-discounted 'first order to a limit' integrated rate equations. R_{Ni} is fractional Ni recovery; $R_{Ni,max}$ is the maximum fractional Ni recovery; k_{Ni} is a first order rate constant ($/min$); t is time; I is induction period (min).

Series	Carbon	Temp (K)	Time maximum (minutes)	Induction Period (minutes)	Integrated Rate Equation $R_{Ni} = R_{Ni,max}(1 - e^{-k_{Ni}(t-I)})$	Fit r^2
L850C	Coke	1123	150	25	$R_{Ni} = 0.60(1 - e^{-0.034(t-25)})$	0.96
L900C	Coke	1173	120	10	$R_{Ni} = 0.80(1 - e^{-0.049(t-10)})$	0.93
L900AC	Act C	1173	80	4.5	$R_{Ni} = 0.67(1 - e^{-0.048(t-4.5)})$	0.93

The maximum recovery under all conditions was 80% (Table 7.2), close to the 78% and 83% reported by Iwasaki et al. (1966), who segregated limonite with a similar composition at a higher temperature (1223 K, Table 2.6); these data are included in Figure 7.1. The data from Wright and Gooden (1973) were not included since their recoveries seemed too low (17-60%, Table 2.6) because only 2% coke was used[31].

Figure 7.2 shows that, for the period of induction, the residual $NiCl_2$ within the solid product from segregation with coke at 1123 and 1173 was negligible, as was the residual $FeCl_2$ (Appendix B.10). It therefore seems that Ni and Fe oxides are not chloridised during the induction period.

The chloridisation of NiO with HCl (Section 2.4.2) is given by the reaction:

$$NiO(s) + 2HCl(g) \rightarrow NiCl_2(g) + H_2O(g) \qquad 2.15$$

from which the maximum (equilibrium) pressure of $NiCl_2$ can be calculated as:

$$p_{NiCl_2} = K_{2.15}\frac{p_{HCl}^2}{p_{H_2O}}a_{NiO} \qquad 7.1$$

[31] Based on the carbon consumption measured in this work, the carbon within the 2-3% coke would be likely totally consumed during segregation, leaving the segregated alloy unprotected from oxidation.

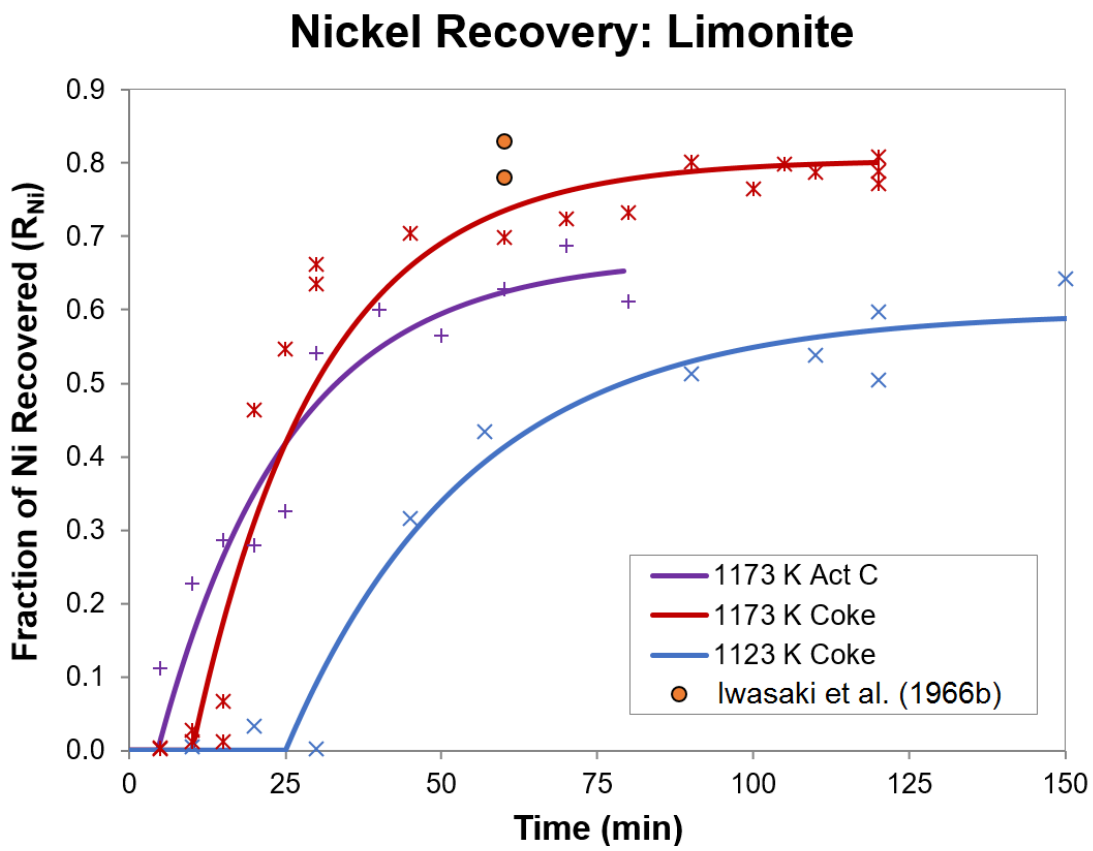

Figure 7.1 Nickel Recovery, Limonite

Fitted curves are summarised in Table 7.2. Other data are from Iwasaki et al. (1966) who used 5.8% coke and 4.6% $CaCl_2$ at 1223 K (Table 2.6). For this graph, and all others for metal recovery in this Chapter, dot points represent data from Table 7.1.

The amount of HCl in the off-gas was measured in this work (Figure 7.18) and the maximum possible HCl pressure has been calculated (Figure 7.19), with the values presented in Table 7.13. The highest HCl pressure occurs at the start of segregation, which for segregation with coke at 1173 K is 0.08 atm. Since $K_{2.15} = 9.6\times10^{-2}$ at this temperature, the maximum initial pressure of $NiCl_2$ in the off-gas for segregation with coke at 1173 K is given by Equation 7.1 as:

$$p_{NiCl_2} = 6.1\times10^{-4}\frac{a_{NiO}}{p_{H_2O}} \quad atm \qquad 7.2$$

The hydrolysis of $CaCl_2$ during hematite reduction most likely involves the reaction of CaO with Fe_2O_3 to form calcium ferrite ($CaFe_2O_4$), as given by Equation 2.11. There will also be some hydrolysis with the formation of calcium silicate ($CaSiO_3$), as given by Equation 2.10, because of the 3.11% SiO_2 within the limonite ore (Table

4.1)[32]. Table 7.13 shows that the p_{H_2O} in equilibrium with 0.08 atm of HCl at 1173 K is 1.5 atm for the $CaFe_2O_4$ hydrolysis equilibrium, and $5.8x10^{-3}$ atm for the $CaSiO_3$ equilibrium.

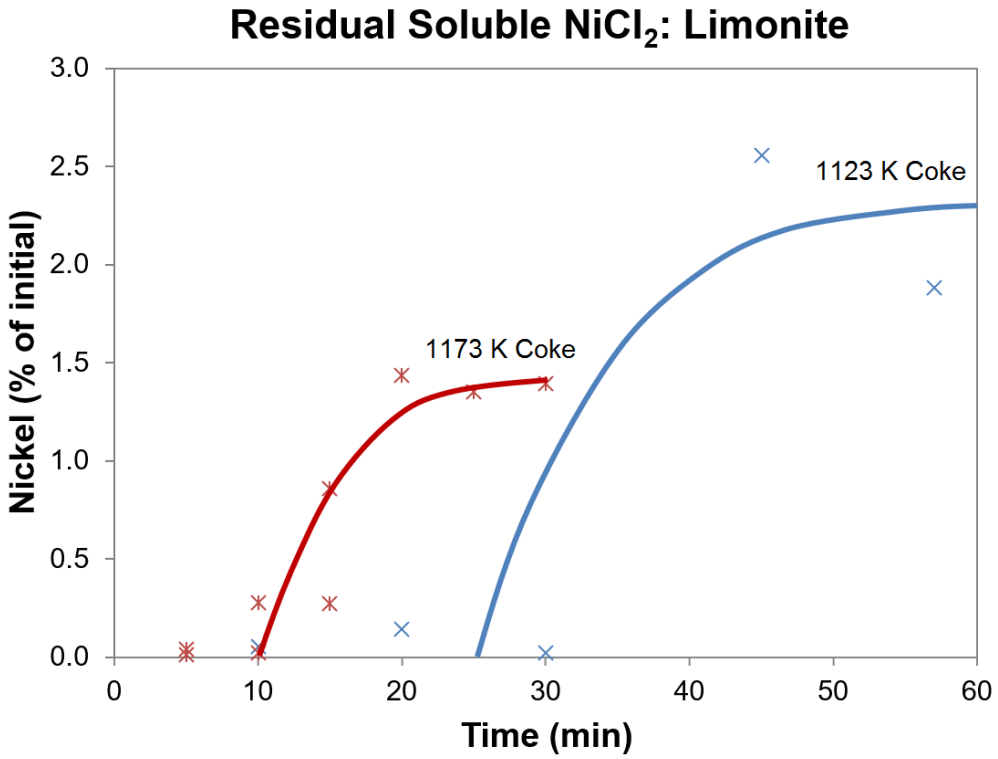

Figure 7.2 Residual Soluble $NiCl_2$, Limonite

Soluble $NiCl_2$ determined by water leach of the segregation product (Section 7.4.1); full set of data available in Appendix B.10.

Since no residual $NiCl_2$ was detected during the induction period (Figure 7.2), and no segregation takes place, it seems that the $CaCl_2$ hydrolysis is not capable of reducing the p_{H_2O} to a low enough level during this period for a significant amount of $NiCl_2$ to exist in the gas, according to Equation 7.2. A similar calculation for iron oxide based on Equation 2.17, provides the following relationship for the maximum (equilibrium) pressure of $FeCl_2$ in the gas:

$$p_{FeCl_2} = 5.4x10^{-3}\frac{a_{FeO}}{p_{H_2O}} \quad atm \qquad 7.3$$

The a_{FeO} will be low during the hematite to magnetite conversion (FactSage v6.4), and it seems that the p_{FeCl_2} is also negligible during the induction period.

[32] The reactor is made from silica, but contact of $CaCl_2$ with fresh silica on the reactor walls was unlikely, since these were pre-coated with silicate to protect them from direct attack by $CaCl_2$ (Section 3.2.1).

The p_{CO_2}/p_{CO} within the bulk gas (Figure 7.3), is significantly higher for limonite[33] (~800-100, for the induction period) compared to garnierite (~210-64) and nontronite (~35-15), as shown in the figure for segregation with coke at 1173 K. In addition to poor chloridisation during the induction period, the relatively high p_{CO_2}/p_{CO} within the bulk gas may inhibit the reduction of chlorides, by keeping the conditions too oxidising at the carbon surface.

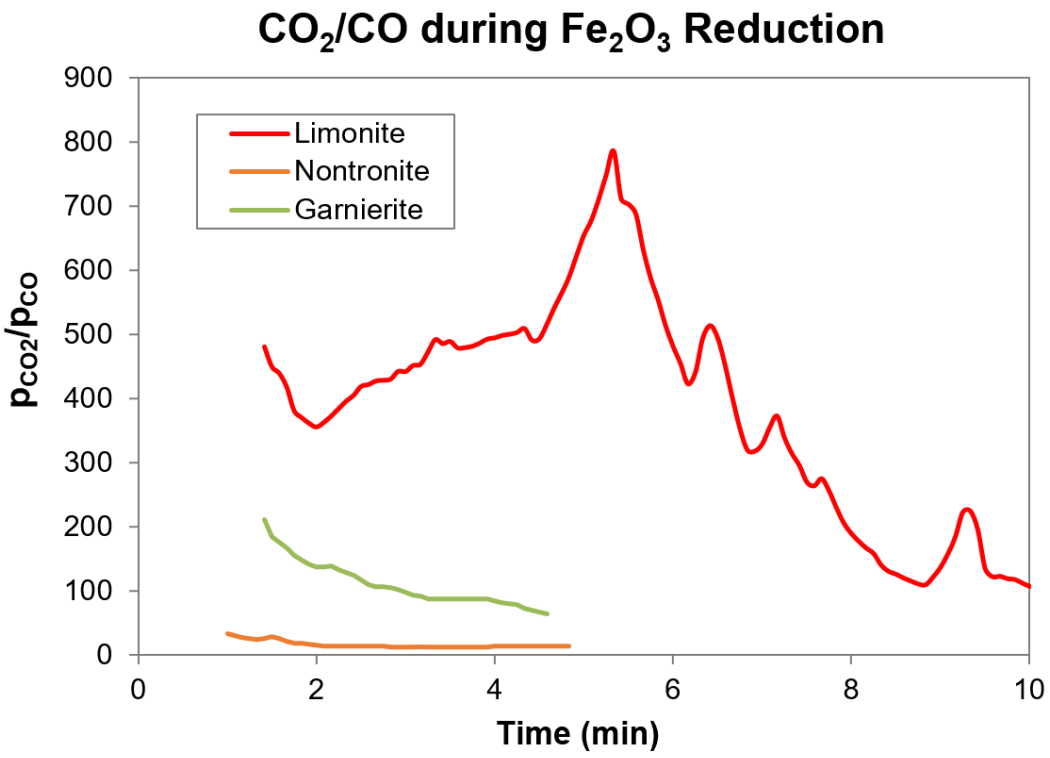

Figure 7.3 CO_2/CO during Fe_2O_3 Reduction, Segregation with Coke at 1173 K

The p_{CO_2}/p_{CO} values were calculated from the measured oxygen pressure (Section 3.4.1). For limonite, only the 10 minute induction period is shown rather than the total 14 minute Fe_2O_3 reduction time (Table 7.9). The first ~1 minute of data is missing since the p_{O_2} was unstable while the probe heated to temperature.

Once hematite reduction is mostly complete and the evolved volume of moisture and carbonaceous gases decrease, it seems that formation of $CaSiO_3$ can provide the p_{HCl}^2/p_{H_2O} needed for chloridisation of Ni and Fe oxides so that segregation occurs. The SEM-EDS analysis of the segregation product verifies that all of the non-chloride calcium observed was present within silicates, including the Al silicate residue ash associated with coke particles.

[33] Limonite contains the greatest amount of Fe_2O_3 (Table 4.5); thus the p_{CO_2}/p_{CO} remains the highest for limonite during hematite reduction, since the Boudouard reaction has the least influence on the gas composition.

7.1.1.2 Rate Control

In common with nontronite, there was no significant change in the Ni segregation rate when coke was replaced by activated carbon at 1173 K (Table 7.2); thus NiO chloridisation is likely the dominant rate control (Section 6.1.1.3).

7.1.1.3 Recovery Limit

Nickel recovery approached an upper limit, within experimental error, under all conditions tested. This limit (cf. $R_{Ni,max}$, Table 7.2) increased from 60 to 80% as the temperature increased from 1123 to 1173 K in the presence of coke, but decreased from 80 to 67% when coke was replaced by activated carbon at 1173 K.

The fractional Ni recovery limits are shown in Figure 7.4 as a function of temperature; comparable data (Table 2.6) from Iwasaki et al. (1966) and Warner et al. (1972) at higher temperatures up to 1273 K, are also included. It appears from Figure 7.4, that the Ni recovery limit may reach a maximum at ~1180 K, which is close to the sintering temperature of the limonite ore (1193 K, Table 4.2).

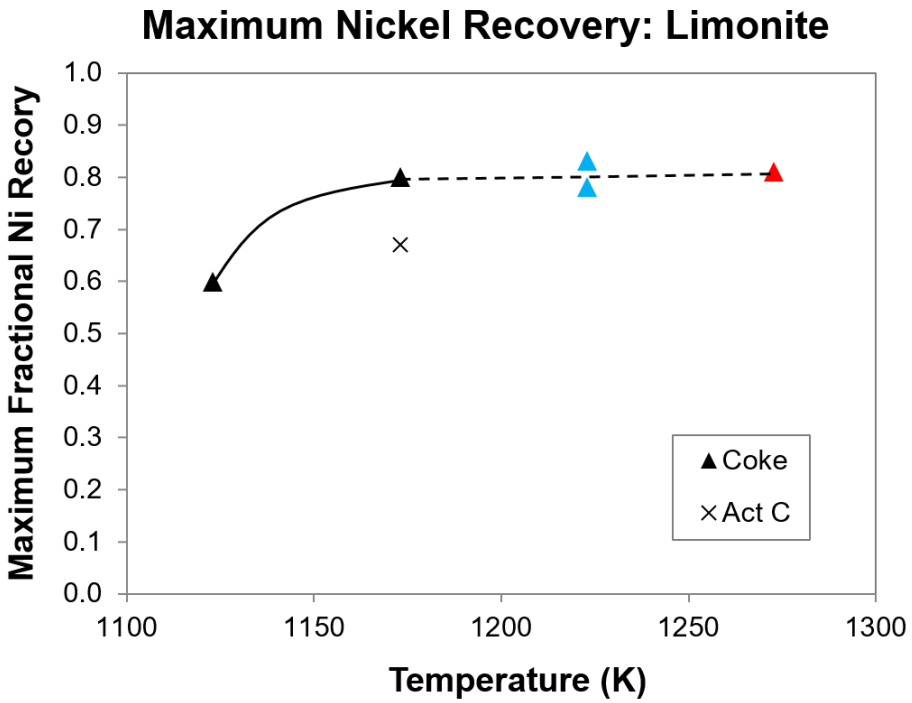

Figure 7.4 Maximum Nickel Recovery, Limonite

Blue values from Iwasaki et al. (1966) as per Figure 7.1; red value from Warner et al. (1972), who used 5% $CaCl_2$ and 7% coke (Table 2.6). The trend line is drawn, with interpolation to other data indicated by a dotted line.

A sample of limonite calcine, which had been segregated with coke for 80 minutes at 1173 K, was resin-mounted, polished and carbon coated. A 1.3 x 0.8 mm (1300 µm x 800 µm) section was subjected to EDS-SEM analysis to determine the location of the unsegregated Ni. A backscattered electron image of this section and accompanying EDS chemical maps are presented in Appendix B.18.

The majority of segregated material was a mixture of wustite ('FeO') and magnetite (Fe_3O_4) formed from the reduction of the 92% hematite contained in the calcine (Table 4.5), in which Ni was assumed to be widely distributed (Section 4.1.2). Most particles were <50 µm across; a larger example is shown in Figure 7.5. Nickel was not detected within any of these particles when analysed using EDS.

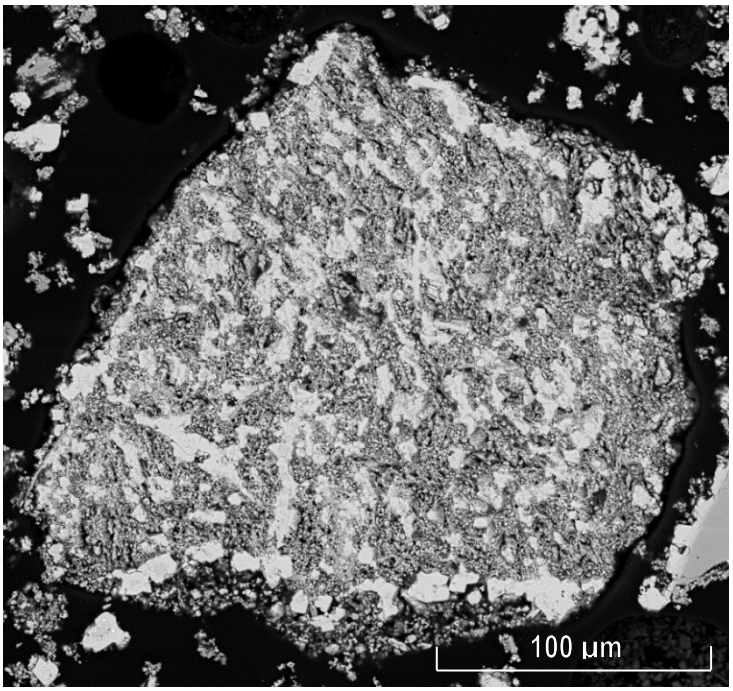

Figure 7.5 Section through a Remnant Hematite Particle

SEM image through a remnant hematite particle after segregation for 80 minutes at 1173 K with coke; wustite is the lighter phase, magnetite is the darker phase.

The integrated rate equation (Table 7.2) predicts that 22% of Ni would not be recovered from the segregation product examined with the SEM ($R_{Ni(\%)} = 78\%$ after segregation with coke for 80 minutes at 1173 K). The only gangue particles found to contain Ni were minor Cr spinels with edges enriched with 2-5% Ni. One typical particle, with an average composition of $Fe_{0.9}Cr_{1.3}Al_{0.6}Mg_{0.2}O_4$, is shown in Figure 7.6; an inset shows a Ni map of the same particle highlighting the Ni enriched boundary, shown in purple.

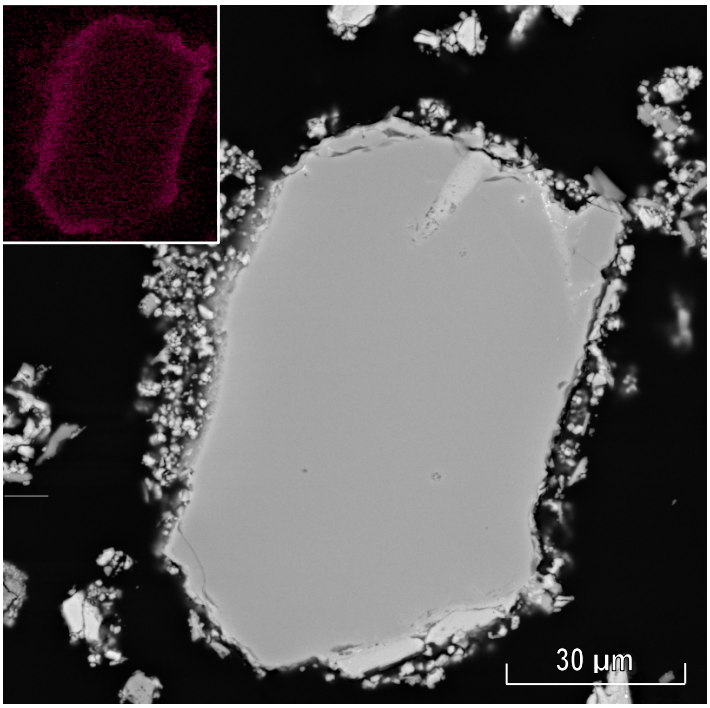

Figure 7.6 Section through a Cr Spinel with Ni Enriched Boundary

SEM image through a Cr spinel with a composition of $Fe_{0.9}Cr_{1.3}Al_{0.6}Mg_{0.2}O_4$ and a boundary containing ~2-5% Ni. The inset (top left) shows a Ni map (Ni in purple) highlighting the boundary; segregation was for 80 minutes at 1173 K with coke.

The limonite calcine was not examined with the SEM prior to segregation. However, it is likely the boundary enrichment occurred during segregation, since the Cr spinels found in the nontronite and garnierite calcines did not contain Ni. However, the associated Ni loss was likely to be minor since few spinel particles were present within the limonite calcine (none were detected by X-ray analysis, Table 4.4) and not all of the spinels observed had Ni enriched boundaries.

Nickel loss through volatilisation was minimal and a non-selective leach of a segregation product limonite (Appendix B.2) showed that virtually all of the Ni remained in the product. It therefore seems likely that most of the ~22% unrecovered Ni remained within the remnant hematite particles at a level below the EDS detection limit of ~0.3% Ni, which could adequately account for the loss[34].

In-situ ferronickel was identified throughout the iron oxide gangue after segregation with activated carbon for 60 minutes at 1173 K, as shown in Figure 7.7 (alloy

[34] The dried limonite contained 0.934% Ni (Table 4.1); it loses ~13% bound moisture (Table 4.2) and a further ~10% of mass if all Fe_2O_3 is converted to FeO; thus if all of the Ni remained in the gangue, it would assay 1.15% Ni; if only 78% is recovered, the iron oxide residue would contain ~0.25% Ni, which is below the EDS-SEM detection limit.

outlined in yellow). Very little in-situ ferronickel was observed after segregation with coke (Appendix B18); thus the decreased recovery with activated carbon compared to coke at 1173 K (cf. 67% and 80%, Table 7.2) is likely due to fine, leach resistant in-situ ferronickel.

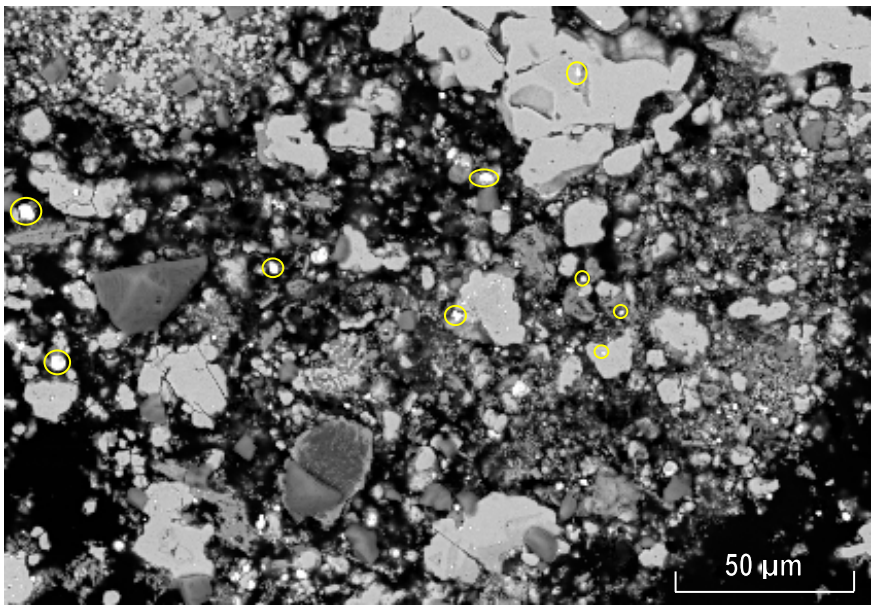

Figure 7.7 Section through Remnant Iron Oxides showing In-Situ Ferronickel
SEM image through remnant iron oxides formed after segregation with activated carbon for 60 minutes at 1173 K; in-situ ferronickel is outlined in yellow and contained an average of 25% Ni, compared to 20% Ni expected from segregated Ni under these conditions (Figure 7.15).

The in-situ ferronickel shown in Figure 7.7 had an average grade of 25% Ni, as analysed by EDS, and consisted of fine (<5 µm), relatively light coloured particles; these were hard to distinguish from the similarly light coloured iron oxide phases.

7.1.2 Iron

The Fe recovery data did not appear to show an induction period, likely because of the unavoidable non-selective dissolution of a small amount of iron oxide within the bromine/methanol analytical solution (Section 3.3.7) when leaching the limonite segregation product. However, since no residual $FeCl_2$ was detected during the induction period for Ni segregation (Appendix B.10), the same induction periods used for Ni were discounted from the time scale of the Fe segregation equations.

The Fe recovery appeared to increase at a constant rate under all conditions within experimental error, as also observed for nontronite; thus a zero order rate equation was used to describe the rate of segregated Fe recovery (Section 6.1.2.1).

7.1.2.1 Recovery and Rate Equations

The induction time discounted integrated rate equations, as fitted from the Fe recovery data (Table 7.1), are presented in Table 7.3 and plotted in Figure 7.9 along with the experimental data. The rate of recovery, which was constant at a specific temperature and carbon addition, increased when the temperature and carbon surface area were increased. No comparable Fe recovery data were found in the literature.

Table 7.3 Integrated Rate Equations, Recovery of Iron from Limonite

Fitted parameters for induction-discounted zero order integrated rate equations. R_{Fe} is fractional Fe recovery; k_{Fe} is a zero order rate constant (/min); t is reaction time; I is the induction period (min).

Series	Carbon	Temp (K)	Time maximum (minutes)	Induction Period (minutes)	Integrated Rate Equation $R_{Fe} = k_{Fe}(t - I)$	Fit r^2
L850C	Coke	1123	150	4.5	$R_{Fe} = 5.1 \times 10^{-5}(t - 4.5)$	0.82
L900C	Coke	1173	120	10	$R_{Fe} = 1.2 \times 10^{-4}(t - 10)$	0.71
L900AC	Act C	1173	80	25	$R_{Fe} = 7.5 \times 10^{-4}(t - 25)$	0.84

7.1.2.2 Rate Control

The rate constant for segregated Fe recovery increased ~6x when coke was replaced by activated carbon at 1173 K (Table 7.3); thus the rate is likely controlled by the water gas reaction (Section 6.1.2.3). For nontronite, the rate was increased 16x by activated carbon (Table 6.5), which represented a very similar change in terms of the mass of Fe, since limonite contained twice as much Fe as nontronite (Table 4.1).

7.1.3 Co-recovery of Nickel and Iron

Figure 7.8 shows a plot of Ni recovery versus Fe recovery for segregation of limonite. All lines are fitted using the segregation rate equations for Ni (Table 7.2) and Fe (Table 7.3).

The figure shows that for a given recovery of Ni, the co-recovery of Fe increases significantly with an increase in the available area of carbon reductant (cf. coke and Act C at 1173 K). While Ni approaches its maximum recovery (Section 7.1.1.3), for a given recovery of Ni, the co-recovery of Fe is relatively similar with an increase in temperature (cf. coke at 1123 and 1173 K). When Ni recovery is close to maximum, significantly more Fe is co-reduced per unit Ni recovered, as illustrated by the change in slope of each curve.

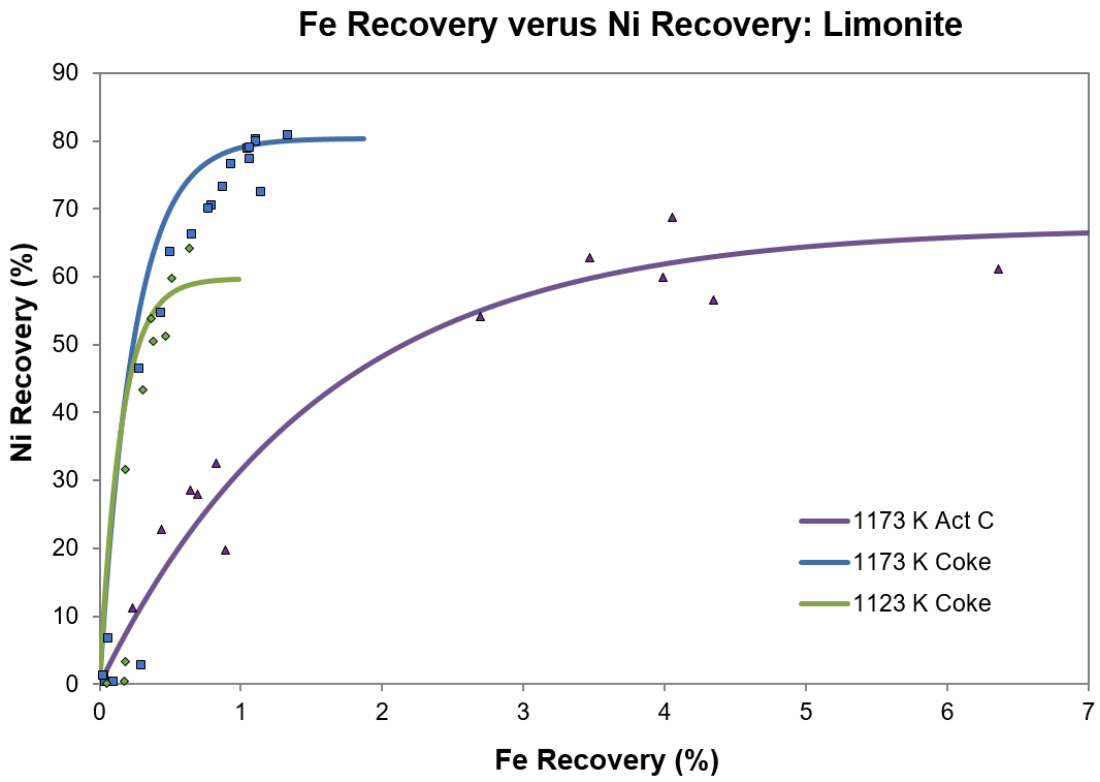

Figure 7.8 Fe Recovery versus Ni Recovery, Limonite Segregation

The Ni and Fe recovery data (from Table 7.1, shown as dot points on the figure) are presented along with the predicted recoveries using the nickel and iron rate equations developed in Sections 7.1.1.1 and 7.1.2.1 respectively; rate equation data are shown as continuous lines on the figure.

7.1.4 Cobalt

The limonite ore contained only 0.035% Co (Table 4.1) and so the Co recovery data are less reliable than those for Ni (Table 7.1). However, in common with Ni, it appeared there was an induction period over which recovery was initially suppressed. After this period, the rate was suitably characterised by a zero order rate equation (Section 6.1.2.1) at 1123 K, while at 1173 K it was better characterised by a 'first order to a limit' rate equation (Section 6.1.1.1).

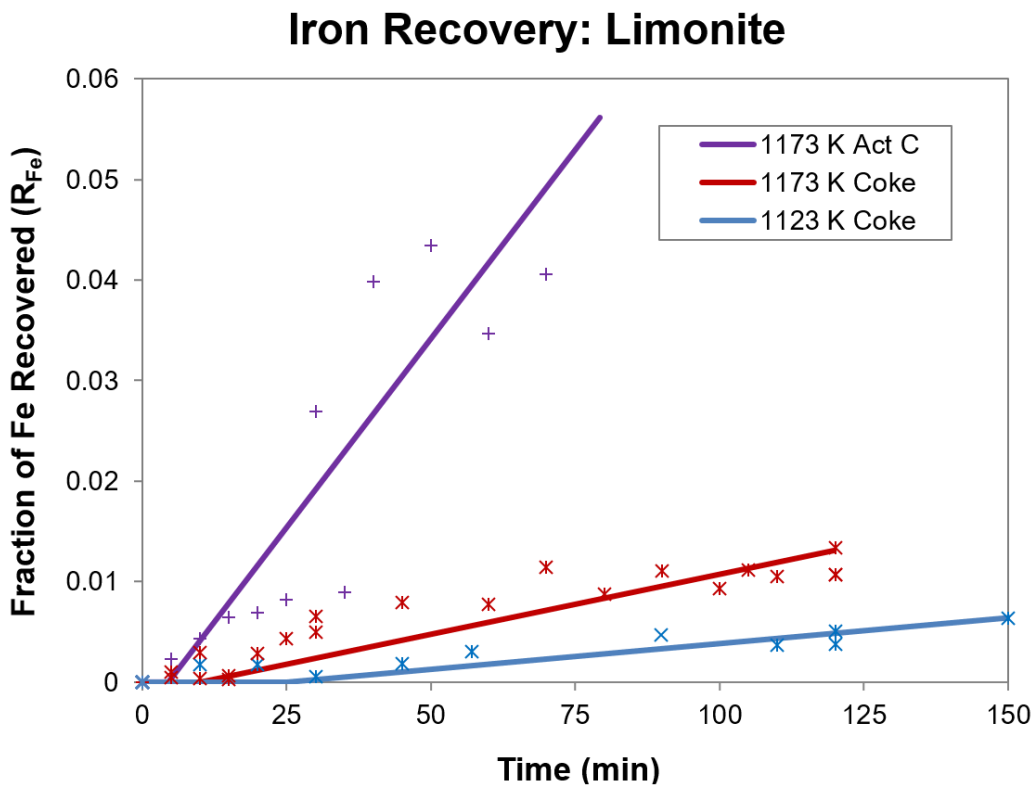

Figure 7.9 Iron Recovery, Limonite

Parameters for fitted equations are summarised in Table 7.3.

7.1.4.1 Recovery and Rate Equations

The integrated rate equations, as fitted from the Co recovery data (Table 7.1), are presented in Table 7.4 and plotted in Figure 7.10 along with the experimental data. The recovery at 1123 K increased at a constant rate but only reached 16%; for longer times and higher recoveries, the data would likely approach a limit.

Table 7.4 Integrated Rate Equations, Recovery of Cobalt from Limonite

Rate equations discounted for induction time are zero order, $R_{Co} = k_{Co}(t - I)$ and 'first order to a limit', $R_{Co} = R_{Co,max}(1 - e^{-k_{Co}(t-I)})$; R_{Co} is fractional Co recovery; k is a rate constant with units ($/min$); I is induction period (min); t is time.

Series	Carbon	Temp (K)	Time maximum (minutes)	Induction Period (minutes)	Integrated Rate Equation	Fit r^2
L850C	Coke	1123	150	25	$R_{Co} = 1.4 \times 10^{-3}(t - 25)$	0.80
L900C	Coke	1173	120	10	$R_{Co} = 0.23(1 - e^{-0.043(t-10)})$	0.90
L900AC	Act C	1173	80	4.5	$R_{Co} = 0.40(1 - e^{-0.033(t-4.5)})$	0.90

The maximum Co recovery with coke (23%, Table 7.4) was slightly lower than the 28 and 33% reported by Iwasaki et al. (1966) after segregation of limonite at a higher temperature (1223 K, Table 2.6); no other comparable data for Co recovery were found in the literature.

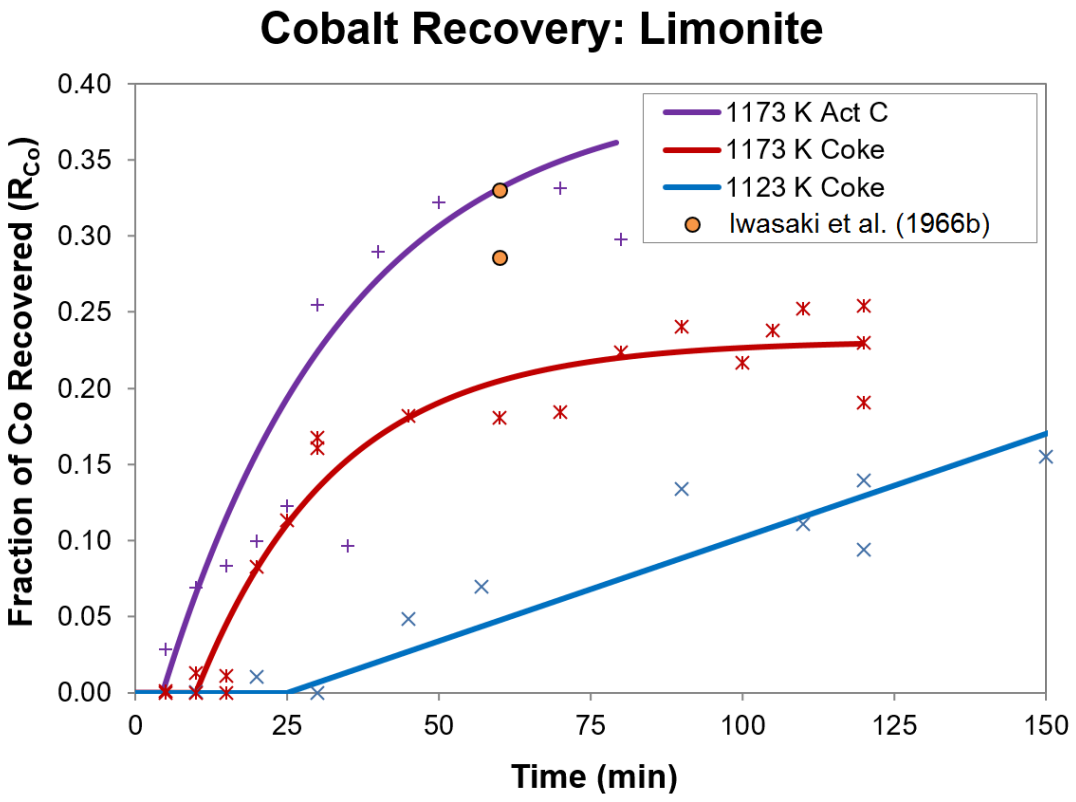

Figure 7.10 Cobalt Recovery, Limonite

Fitted curves are summarised in Table 7.4. Other data are from Iwasaki et al. (1966), who used 5.8% coke and 4.6% $CaCl_2$ at 1223 K (Table 2.6).

7.1.4.2 Rate Control

The rate appeared to increase when coke was replaced by activated carbon (Figure 7.10); however, the fitted rate constant for activated carbon (0.033, Table 7.4) at 1173 K is lower than that for coke (0.043, Table 7.4). Within the experimental error, the rates were similar when activated carbon was used, and it could not be concluded that the water gas reaction was the rate control.

With CoO at such a low concentration within limonite, chloridisation is likely the dominant rate control. The maximum Co recovery was enhanced when activated carbon was used (from 23 to 40%, Table 7.4), although the reason is unclear. Since more Fe is segregated using activated carbon, it could be that more Co becomes accessible to chloridisation because it is closely associated with Fe in calcine.

7.1.5 Activation Energies

The apparent activation energies for the recoveries of Ni, Co and Fe during segregation with coke were estimated from Arrhenius plots of the fitted rate constants (Table 7.2, Table 7.3 and Table 7.4) versus temperature. The plots are presented in Appendix B.3 and the values are shown Table 7.5.

Table 7.5 Activation Energies for Metal Recoveries, Limonite Segregation

Activation energy (E) and collision frequency factor (k_0) calculated from a plot of ln k versus 1/T (Appendix B.3). R is the universal gas constant; T is the temperature (K). Data are specific to segregation with coke.

Metal	Activation Energy (kJ/mol)	Arrhenius Expression $k = k_0 e^{\frac{-E}{RT}}$
Nickel	83	$k_{R_{Ni}} = 2.35 \times 10^2 e^{\frac{-9900}{T}}$
Iron	190	$k_{R_{Fe}} = 2.25 \times 10^4 e^{\frac{-23000}{T}}$
Cobalt	380	$k_{R_{Co}} = 8.00 \times 10^{14} e^{\frac{-46000}{T}}$

The apparent activation energy for Ni segregation of 83 kJ/mol (Table 7.5) is significantly lower than for nontronite (180 kJ/mol, Table 6.7) but still consistent with chemical control through chloridisation, as proposed for both. The apparent activation energy for Fe segregation is 190 kJ/mol (Table 7.5), lower than for nontronite (290 kJ/mol, Table 6.7), but close to the published values of 160-240 kJ/mol for the water gas reaction (Harris and Smith, 1990), which is believed to be the dominant rate control. The apparent activation energy for Co segregation (380 kJ/mol, Table 7.5) is higher than for nontronite (300 kJ/mol, Table 6.7) and consistent with a chemical rate control; however the rate control is undetermined.

7.2 Segregation versus Carbon Reduction

Throughout this section, the results from segregation are compared with those from an equivalent reduction system to which $CaCl_2$ was not added (Section 5.3).

7.2.1 Oxygen Pressure

The average p_{O_2} profile for segregation with coke at 1173 K (L900C) is shown in Figure 7.11, along with the average profile from the equivalent chloride free reduction system (LR900C). The equilibrium p_{O_2} values for the transformation of iron oxides are referenced by lines across the diagram.

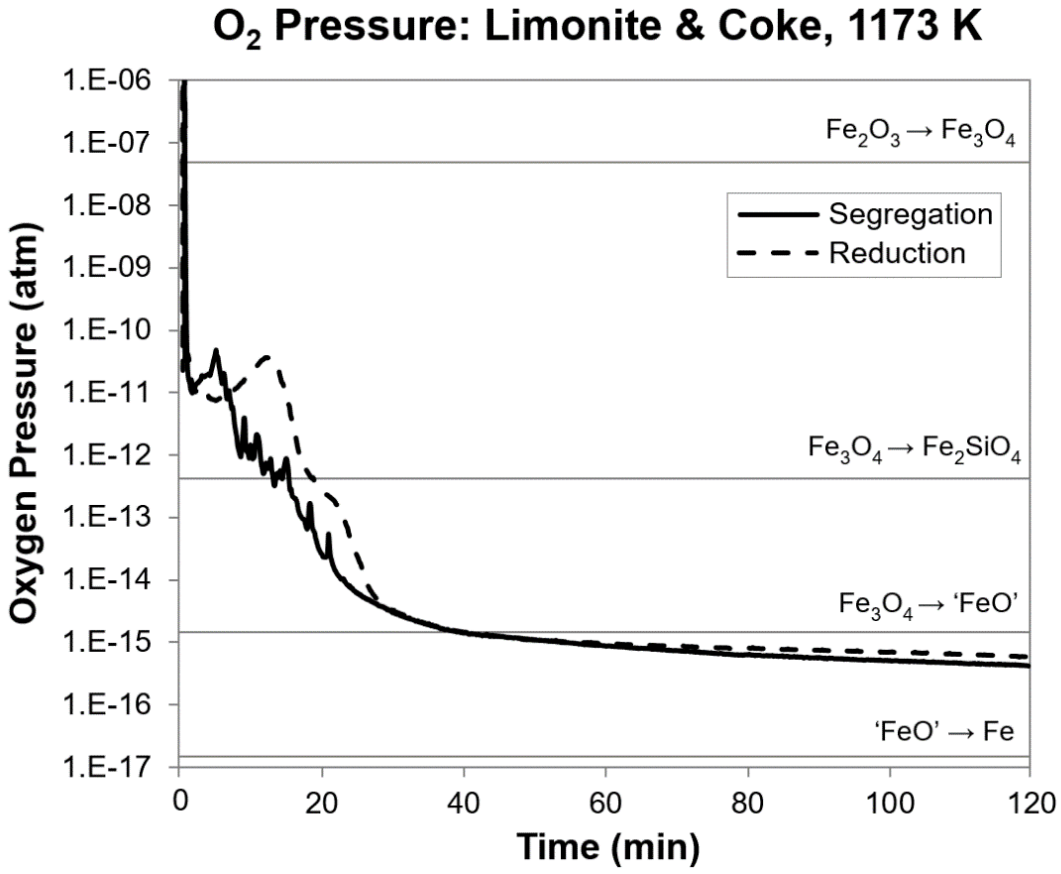

Figure 7.11 Oxygen Pressure Profile Comparison, Limonite with Coke, 1173 K

Details for the representative oxygen profiles, L900C for segregation and LR900C for reduction, are given Appendix B.5.

Figure 7.11 shows that the segregation and chloride free reduction systems have very similar p_{O_2} profiles; thus in contrast to nontronite (Section 6.2.1), the presence of chloride had little impact on the oxygen pressure. The p_{O_2} profiles for segregation and reduction at 1123 K with coke, and at 1173 K with activated carbon showed similar relationships (Appendix B.5).

7.2.2 Carbon Consumption

Profiles of carbon consumption during segregation and chloride free reduction are shown in Figure 7.12; the supporting data used to develop these curves are presented in Appendix B.4.

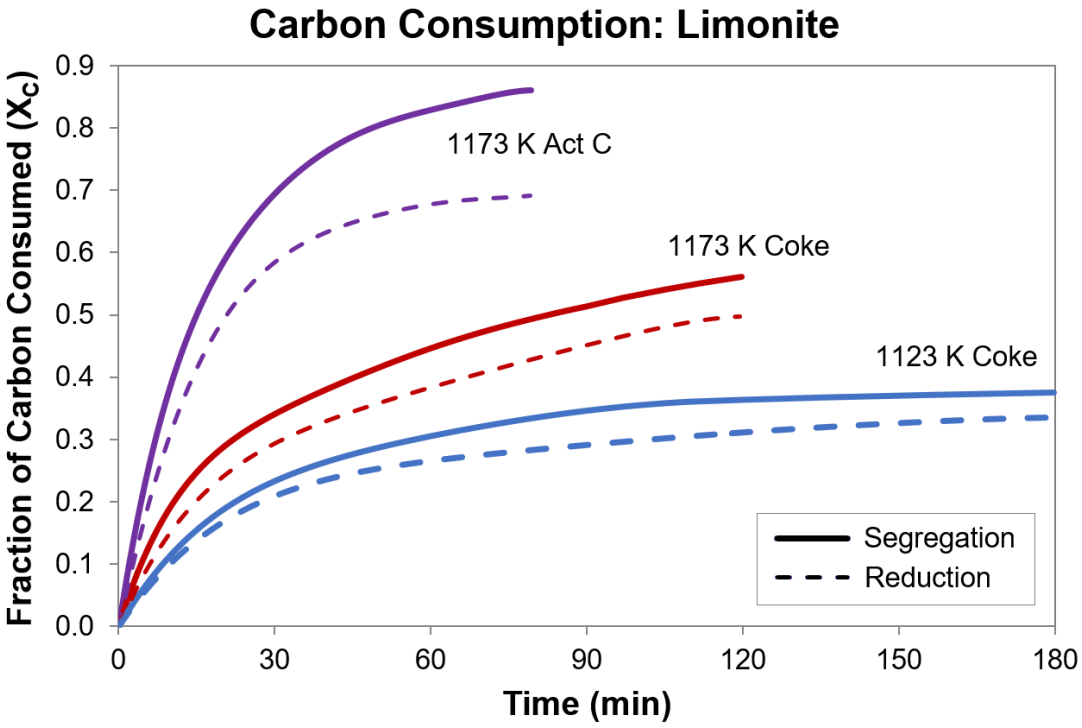

Figure 7.12 Carbon Consumption, Limonite

Reductant added at 5% of dried ore, either as coke (78.3% C) or activated carbon (88.7% C). Curves are best fits from experimental data (Appendix B.4).

Figure 7.12 shows that carbon consumption was increased during segregation relative to reduction. A comparison of the final carbon consumptions and oxygen pressures is given in Table 7.6. The table shows that total carbon consumption for segregation was 12% higher than reduction when using coke, and 24% higher when using activated carbon; however the p_{O_2} difference in both cases was relatively small.

Table 7.6 Carbon Consumption and Oxygen Pressure Comparison, Limonite

Carbon consumption X_C is expressed as a fraction of the 3.92 g (within 5 g coke) or 4.44 g (within 5 g Act C) added per 100 g of dried ore.

Carbon	Temp (K)	Time (minutes)	Reduction		Segregation	
			X_C	pO_2 (atm)	X_C	pO_2 (atm)
Coke	1123	180	0.33	5.6×10^{-17}	0.37	1.2×10^{-16}
Coke	1173	120	0.50	5.9×10^{-16}	0.56	4.3×10^{-16}
Act C	1173	80	0.69	6.6×10^{-17}	0.86	2.0×10^{-16}

Table 7.7 presents a comparison of the Boudouard rate constants for the initial carbon gasification during segregation (Appendix B.1) with those previously calculated for reduction (Section 5.6). The Boudouard reaction rate was enhanced 1.2-1.4x during segregation compared to reduction.

Table 7.7 Boudouard Rate Constant Comparison, Limonite

Reduction rate constants are from Table 5.13. Calculations are in Appendix B.1.

Carbon	Temp (K)	k_{BR} (/min)	
		Reduction	Segregation
Coke	1123	1.2×10^{-2}	1.4×10^{-2}
Coke	1173	1.9×10^{-2}	2.5×10^{-2}
Act C	1173	3.6×10^{-2}	5.2×10^{-2}

The apparent activation energy for the Boudouard reaction on coke during segregation was 97 kJ/mol, compared to 136 kJ/mol for reduction (Table 7.8); consistent with the presence of chloride catalysing the Boudouard reaction.

Table 7.8 Boudouard Activation Energy Comparison, Limonite

Activation energy (E) and collision frequency factor (k_0) as calculated from a plot of ln k_{BR} versus 1/T (Appendix B.3); R is the universal gas constant; T is the temperature (K); reduction data from Table 5.14.

System	Temperature Range (K)	Activation Energy (kJ/mol)	Arrhenius Expression $k_{BR} = k_0 e^{\frac{-E}{RT}}$
Segregation	1123-1173	97	$ln\, k_{BR_{Seg}} = 5.92 - \frac{11600}{T}$
Reduction	1123-1173	136	$ln\, k_{BR_{Red}} = 10.26 - \frac{16400}{T}$

7.2.3 Equilibrium Simulation and Oxygen Removal

Equilibrium simulations were performed using the method described in Section 5.1 with the carbon consumption data from Figure 7.12. The results during segregation with coke at 1173 K are summarised in Figure 7.13, with the simulated and measured p_{O_2} of the bulk gas included for comparison; the measured p_{O_2} is labelled L900C.

Figure 7.13 shows the same progression of equilibrium solid phase transformations that are predicted during reduction (Figure 5.3). The calcine consists almost entirely of hematite and the oxygen pressure is dominantly controlled by the reduction of relatively pure iron oxide species, with few kinetic restrictions, i.e. hematite to

magnetite followed by magnetite to wustite. As a result, the oxygen pressure profiles for segregation and reduction are very similar (Figure 7.11), even though the phase changes begin earlier for segregation because the carbon consumption is greater. The simulated solid phase transformations and p_{O_2} profiles for segregation with coke at 1123 K and activated carbon at 1173 K (Appendix B.8) present a similar picture.

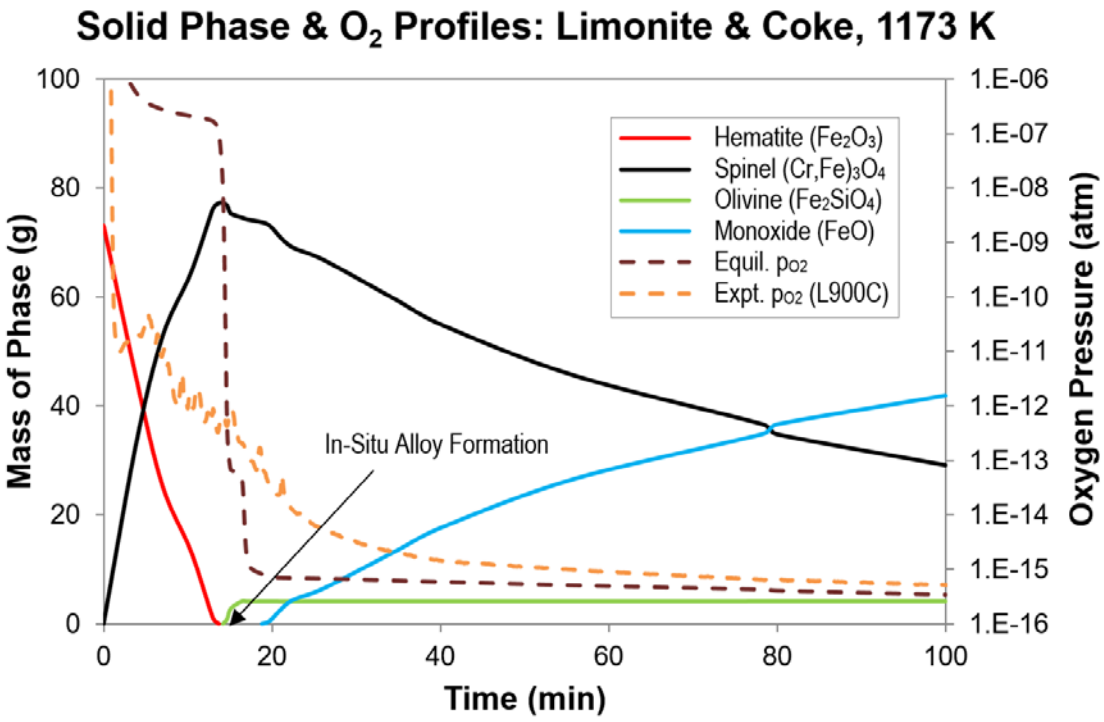

Figure 7.13 Equilibrium Simulation of Limonite Segregation with Coke, 1173 K

Phase profiles are for 100 g of dried ore. The dashed brown line represents simulated p_{O_2}, the dashed orange line represents experimental p_{O_2}.

The progressive total oxygen removed from iron oxides by in-situ reduction during segregation was calculated as described for nontronite (Section 6.2.3), using the carbon consumption profiles (Figure 7.12) and the CO_2 and CO content of the off-gas, as calculated from the representative oxygen pressure profiles (e.g. L900C in Figure 6.12). Figure 7.14 shows the times at which the total oxygen removed coincides with that required to convert all Fe_2O_3 to Fe_3O_4 (11.1% O removal from Fe_2O_3) and all Fe_3O_4 to FeO (33.3% O removal from Fe_2O_3), as explained previously. A comparison of these measured times and those predicted from the equilibrium simulations is given in Table 7.9. They are very similar.

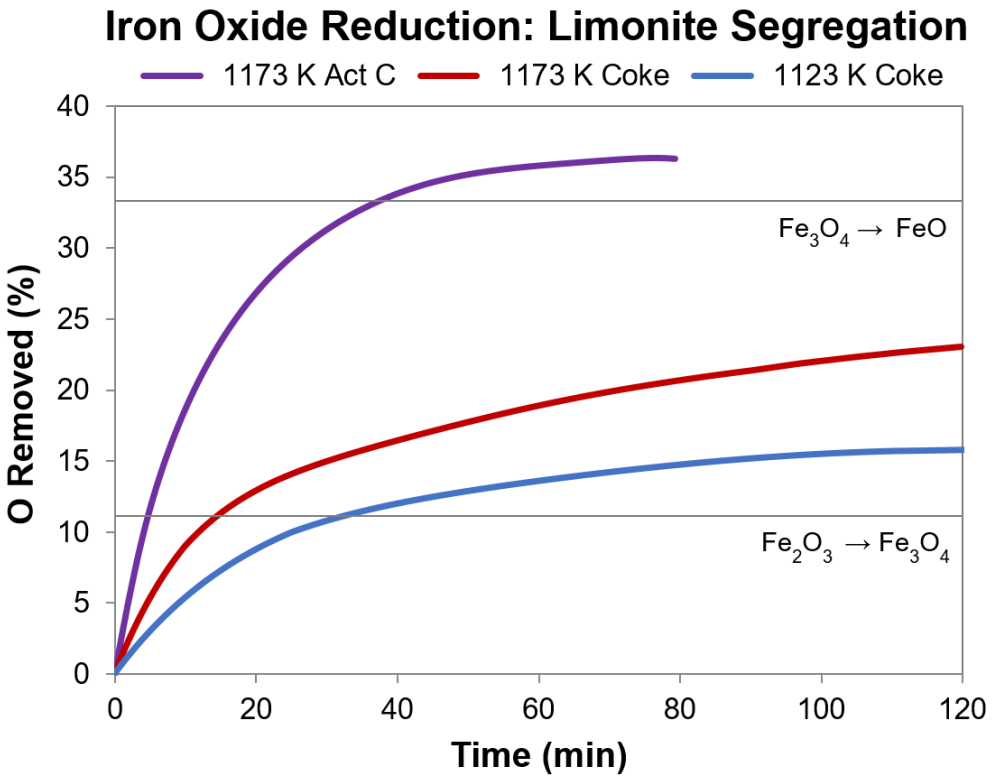

Figure 7.14 Removal of O from Iron Oxides, Limonite Segregation

O removed in carbonaceous gas during segregation (Appendix A.5): 11.1% O removal represents $Fe_2O_3 \rightarrow Fe_3O_4$; 33.3% represents $Fe_3O_4 \rightarrow FeO$.

Table 7.9 Iron Oxide Conversion Times, Limonite Segregation

Carbon	Temperature (K)	$Fe_2O_3 \rightarrow \mathbf{Fe_3O_4}$ (minutes)		$Fe_3O_4 \rightarrow \mathbf{FeO}$ (minutes)	
		Experimental	Simulated	Experimental	Simulated
Coke	1123	31	31	-	-
Coke	1173	14	13.7	-	-
Act C	1173	4.5	5.2	37	35

The major phases within a limonite segregation product after an 80 minute segregation with coke at 1173 K were identified by XRD and are listed in Table 7.10, alongside the phases identified under equivalent equilibrium simulation conditions (Figure 7.13).

The XRD analysis and equilibrium simulation are in good agreement; both confirmed the presence of spinel (as magnetite), monoxide (as wustite) and olivine (as fayalite). However, it appears that much of the monoxide was very finely grained since it was detected as an amorphous phase with the XRD.

Table 7.10 Solid Phases in Limonite Segregation Product

Experimental composition determined by quantitative XRD after segregation for 80 minutes with coke at 1173 K; the simulated values are for these conditions.

Phase	Experimental		Simulated	
	wt%	Major Component	wt%	Major Component
Spinel	48	Fe_3O_4	44	Fe_3O_4
Amorphous	28	-	0%	-
Monoxide	15	FeO	46	FeO
Olivine	7	Fe_2SiO_4	5	Fe_2SiO_4

All of the above illustrates that the equilibrium phase changes as predicted by the simulation are an accurate reflection of the changes occurring within the segregation process and are similar to those for the chloride free reduction system.

7.2.4 Comparison of Nickel Recovery

The maximum Ni recoveries from segregation (Table 7.2) and reduction (Table 5.4) are compared in Table 7.11. The recoveries were similar at 1123 K and higher with segregation at 1173 K when using coke, and more than double with segregation when using activated carbon at 1173 K.

Table 7.11 Comparison of Maximum Nickel Recovery, Limonite

Recovery from selective bromine/methanol leach of segregation/reduction product. Maximum segregation recoveries from Table 7.2; maximum reduction recoveries from Table 5.4.

Carbon	Temperature (K)	Maximum Ni Recovery (%)	
		Segregation	Reduction*
Coke	1123	60	63
Coke	1173	80	56
Act C	1173	67	26

*Averaged: 2 pts (1123 K), 3 pts (1173 K), 2 pts (Act C, 1173 K)

The results show that segregation is at least as good as chloride free carbon reduction when using coke at 1123 K, and is superior at higher temperatures and when using activated carbon. Since the entire segregation product was leached to assess the metal recovery, the superior performance of segregation with limonite is likely because the ferronickel is coarser and more readily accessible to the leach solution compared to the in-situ reduced alloy.

7.2.5 In-Situ Reduction to Ferronickel

Reduction of the calcine by the bulk gas to form ferronickel was predicted to occur for all three equilibrium simulations, for example, after 17 minutes with coke at 1173 K (Figure 7.13), 36 minutes with coke at 1123 K and 6 minutes at 1173 K with activated carbon (Appendix B.8). When the measured rather than equilibrium p_{O_2} values were used in the simulation (method described in Section 6.3.2), in-situ ferronickel was predicted to form after 40 minutes with coke at 1173 K and 11 minutes with activated carbon.

As for nontronite (Section 6.3.2), it appears that chloridisation was able to lower the NiO level in the calcine, and largely maintain it below that required for in-situ reduction to ferronickel when using coke. An amount of in-situ alloy still formed when coke was replaced with activated carbon (Figure 7.7); however, the Ni recovered under these conditions (67%), was still more than double that recovered when using carbon reduction (26%) alone, as shown in Table 7.11.

7.3 Ferronickel

The segregated ferronickel deposits were similar to those already discussed in detail for nontronite (Section 6.3.3). The cumulative grade of the ferronickel (Ni%), as listed in Table 7.1, is shown in Figure 7.15 as a function of segregation time, with the trend lines drawn rather than fitted; the instantaneous grade is shown in Figure 7.16.

As for nontronite segregation, the ferronickel grade appears to be kinetically controlled. The grade becomes leaner in Ni (and richer in Fe) over time as the Ni segregation rate (Table 7.2) decreases relative to the Fe segregation rate (Table 7.3). The grade also decreases when the temperature or carbon surface area is increased, since both promote the segregation of Fe over Ni.

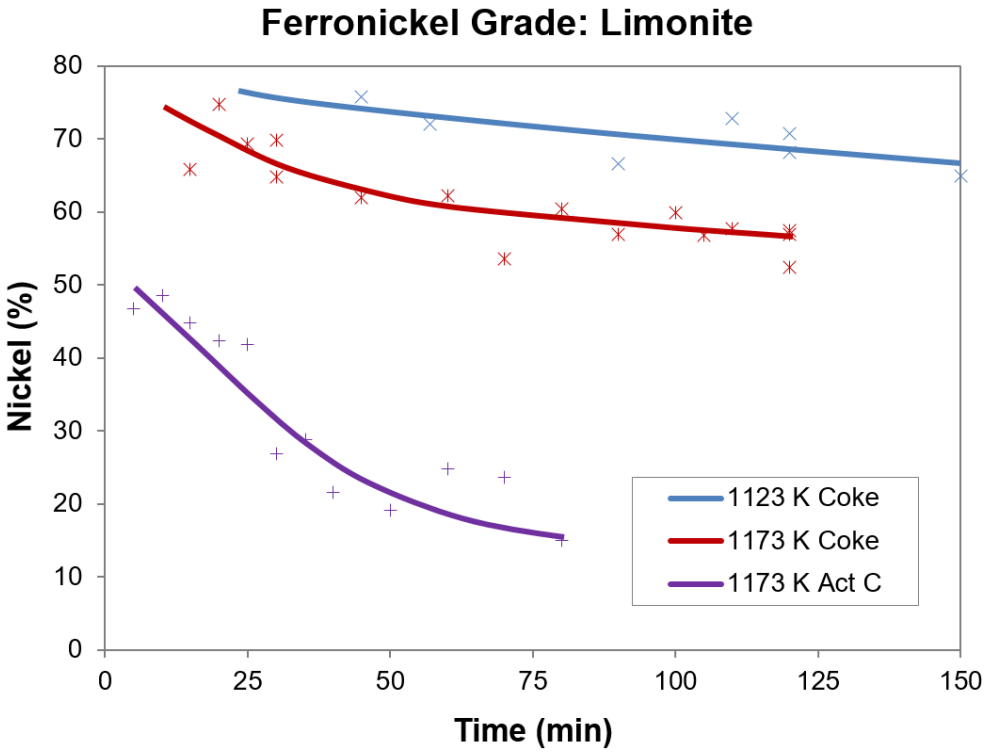

Figure 7.15 Ferronickel Grade, Limonite

Cumulative ferronickel grade for limonite segregation; data from Table 7.1.

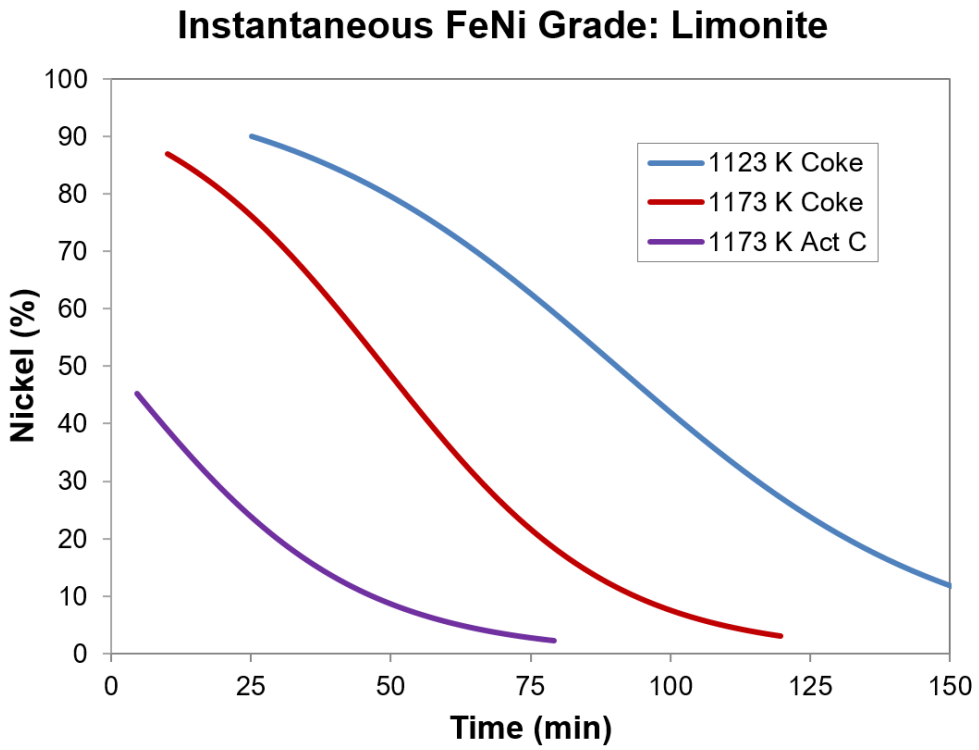

Figure 7.16 Instantaneous Ferronickel Grade, Limonite

Data are calculated from the integrated rate equations for Ni (Table 7.2) and Fe (Table 7.3) recoveries, averaged over 5 seconds.

7.4 Chloride

The deportment of chloride during the segregation process is examined in this section.

7.4.1 Residual Chloride

The amounts of Ni, Fe, and Ca present as chlorides within the solid segregation product, as determined by a water leach (Section 3.3.5) are summarised in Table 7.12, along with the recovery of total Cl and the $FeCl_2/NiCl_2$ mole ratio. The full set of data is presented in Appendix B.10. The residual $CaCl_2$ during segregation with coke at 1173 K is shown in Figure 7.17.

Table 7.12 Residual Soluble Chlorides, Limonite Segregation

Carbon	Temp (K)	Recovery (%) as Soluble Chloride				$FeCl_2/NiCl_2$ (mole ratio)
		Ni	Fe	$CaCl_2$	Total Cl	
Coke	1123	0.1-2.5	0.3-0.6	33-58	42-63	8-770
Coke	1173	0.1-1.8	0.1-0.7	35-51	45-64	16-1200
Act C	1173	0.1-4.5	0.5-0.9	37-58	49-70	4-1470

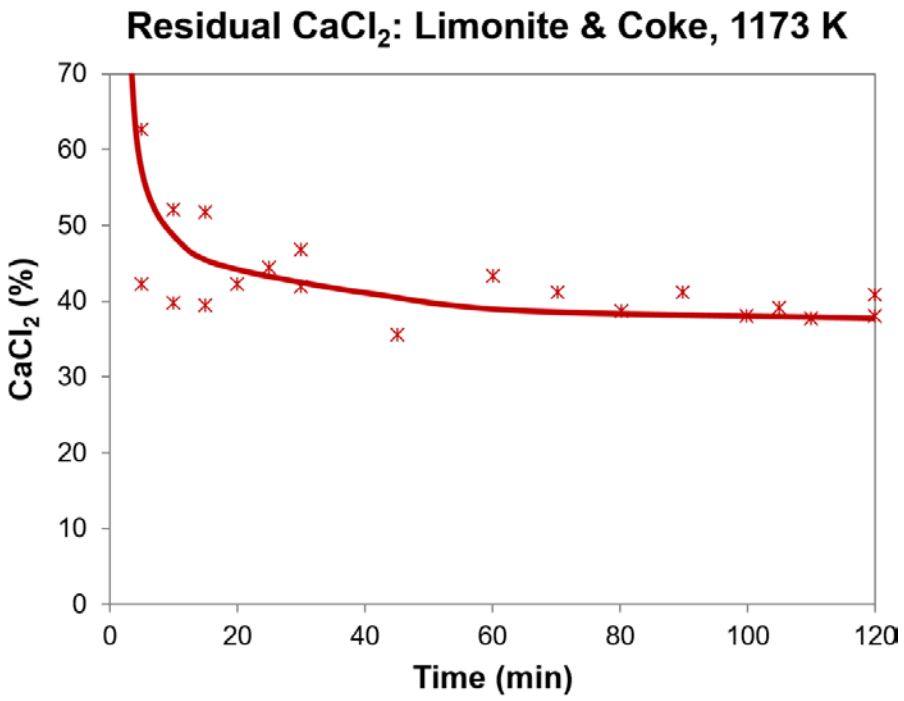

Figure 7.17 Residual $CaCl_2$, Limonite with Coke at 1173 K

Residual $CaCl_2$ is relative to the initial 5 g $CaCl_2$/100 g of dried ore.

The trend line is drawn and not fitted.

Table 7.12 shows that 33-58% of the original $CaCl_2$ remained after segregation, which confirmed sufficient $CaCl_2$ was present for hydrolysis to form HCl. The chloride residue also contained minor $FeCl_2$ and $NiCl_2$, although up to 4.5% Ni was retained as chloride when using activated carbon; the reason for this is unclear.

Figure 7.17 shows that the residual $CaCl_2$ drops rapidly over the first 20 minutes to ~43%, a significantly higher level than the ~13% present after 20 minutes (Figure 6.23Figure 6.25) when also segregating nontronite with coke at 1173 K. The higher chloride loss for nontronite compared to limonite is consistent with the more thermodynamically favourable hydrolysis of $CaCl_2$ that occurs with nontronite because of the much higher free silica content in the calcine. The residual chloride data for limonite segregation with coke at 1123 K and activated carbon at 1173 K (Appendix B.10) show early losses of chloride consistent with those in Figure 7.17.

7.4.2 HCl in the Off Gas

Figure 7.18 shows the cumulative chloride lost in the off-gas as HCl (Section 3.3.4), as a percent of the input as $CaCl_2$, during 120 minutes of segregation with coke at 1123 and 1173 K. Data from two experiments were combined to give each profile (Appendix B.9), with an initial detection lag time of ~2 minutes discounted from the time scale for each. The maximum possible pressure of HCl in the off-gas (p_{HCl}) was estimated using the data for the cumulative volume of HCl (Figure 7.18) and carbon consumption (Figure 7.12) on the assumption that the gas contained only HCl, CO and CO_2. These pressures are shown in Figure 7.19 as a function of segregation time.

The profiles for HCl loss shown in Figure 7.18 are similar to those for nontronite (Figure 6.25). The rate of loss was highest at the start of segregation when release of moisture from the calcine and evolution of carbonaceous gases were the highest; the rate of loss then decreased significantly after 20 minutes.

The total chloride loss was 9.6% at 1123 K and 10.6% at 1173 K after 120 minutes, consistent with the similar amounts of bound water in the calcines (0.75% at 1123 K and 0.69% at 1173 K, Table 4.3). As noted for nontronite (Section 6.4.2), the Cl losses in the gas were relatively small compared to those expected based on the total residual soluble chloride.

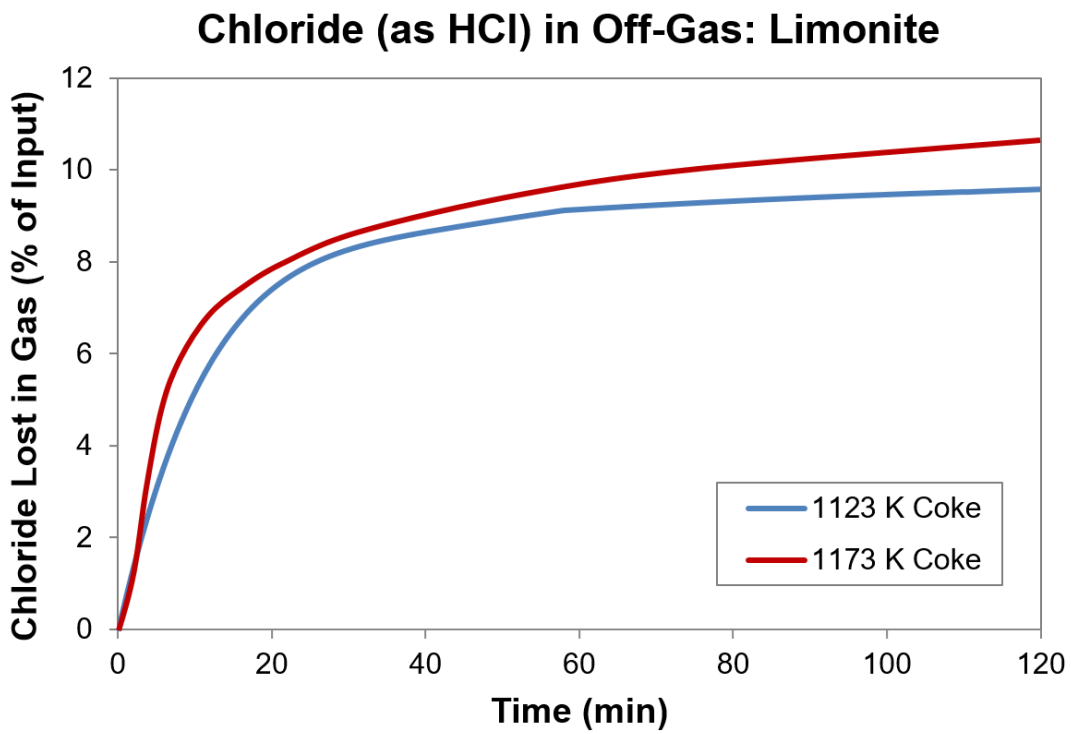

Figure 7.18 Chloride as HCl in the Off-Gas, Limonite with Coke

$CaCl_2$ addition was 5 g per 100 g of dried ore.

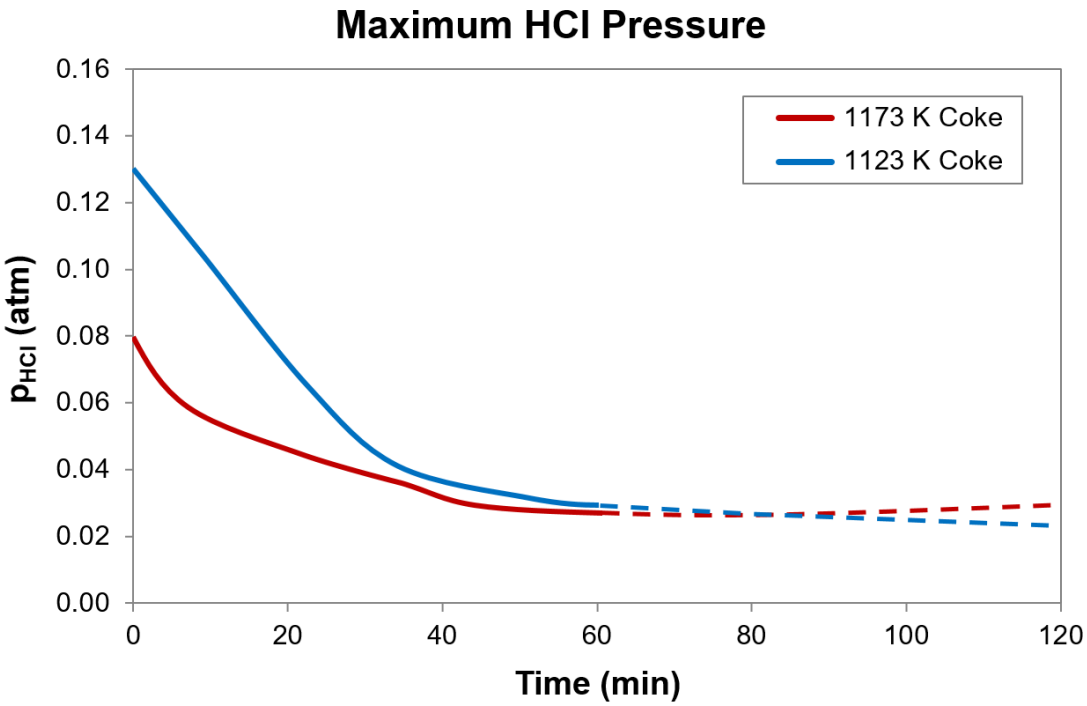

Figure 7.19 Maximum Possible HCl Pressure in Off-Gas, Limonite

Pressure of HCl is calculated assuming only CO, CO_2 and HCl are in the gas at 1 atm (excludes H_2O and $FeCl_2$ which were not measured). The data become less reliable after 60 minutes due to relatively low gas evolution.

Figure 7.19 shows that the maximum p_{HCl} had the highest initial value at 1123 K (~0.13 atm), and the lowest at 1173 K (~0.08 atm), because at the lower temperature the volume of carbonaceous gas was lower (Figure 7.12). The p_{HCl} decreased over the first 40 minutes at both 1123 and 1173 K, consistent with a decreasing release of moisture from the calcine.

As discussed (Section 7.1.1.1), the generation of HCl by hydrolysis of $CaCl_2$, likely dominantly occurs through the formation of calcium ferrite $CaFe_2O_4$ during hematite reduction, and later through the formation of $CaSiO_3$. The p_{H_2O} values in equilibrium with the estimated p_{HCl} according to these hydrolysis reactions, as calculated from the respective equilibrium constants, are shown in Table 7.13. It is clear from the high values of p_{H_2O} required for the $CaFe_2O_4$ equilibrium that the hydrolysis of $CaCl_2$ in the presence of hematite could not control the p_{H_2O} in the gas. The level of H_2O would thus more likely depend on the rate of release of bound water from the calcine during the early period of segregation.

Table 7.13 Maximum HCl and H_2O Pressures in Off-Gas, Limonite

p_{HCl} values are from Figure 7.19; p_{H_2O} values are estimated from the $CaCl_2$ hydrolysis reactions, forming either $CaFe_2O_4$ (Equation 2.11) or $CaSiO_3$ (Equation 2.10), for which $p_{H_2O} = p_{HCl}^2/K$ for pure phases.

Time (minutes)	1123 K Max. Pressure (atm)			1173 K Max. Pressure (atm)		
	HCl	H_2O ($CaFe_2O_4$)	H_2O ($CaSiO_3$)	HCl	H_2O ($CaFe_2O_4$)	H_2O ($CaSiO_3$)
0	0.14	9.2	$2.7x10^{-2}$	0.08	1.5	$5.8x10^{-3}$
40	0.04	0.75	$2.2x10^{-3}$	0.03	0.21	$8.1x10^{-4}$
80	0.02	0.19	$5.4x10^{-4}$	0.03	0.21	$8.1x10^{-4}$

7.4.3 HCl Recycle

The amount of HCl recycled during segregation was calculated as before (Section 6.4.3) as the rate of HCl produced by reduction $FeCl_2$ and $NiCl_2$, minus the rate at which HCl lost in the gas. Figure 7.20 and Figure 7.21 show the recycle profiles at 1123 K and 1173 K respectively. All rates are presented in moles per minute per gram of dried ore (mol/min g_{ore}), and the percent of HCl recycled is shown in each figure by the dashed line.

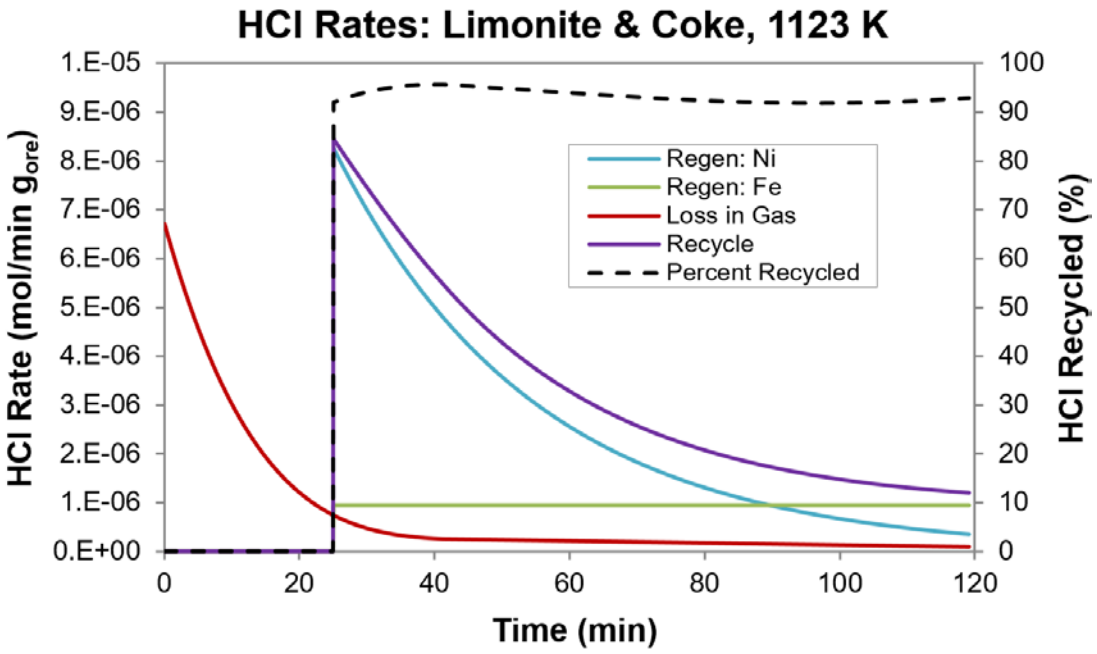

Figure 7.20 HCl Regen, Loss and Recycle Rates, Limonite with Coke at 1123 K

Regen: Ni and Regen: Fe are the rates at which HCl is regenerated by chloride reduction through Equations 2.24 and 2.25 respectively.

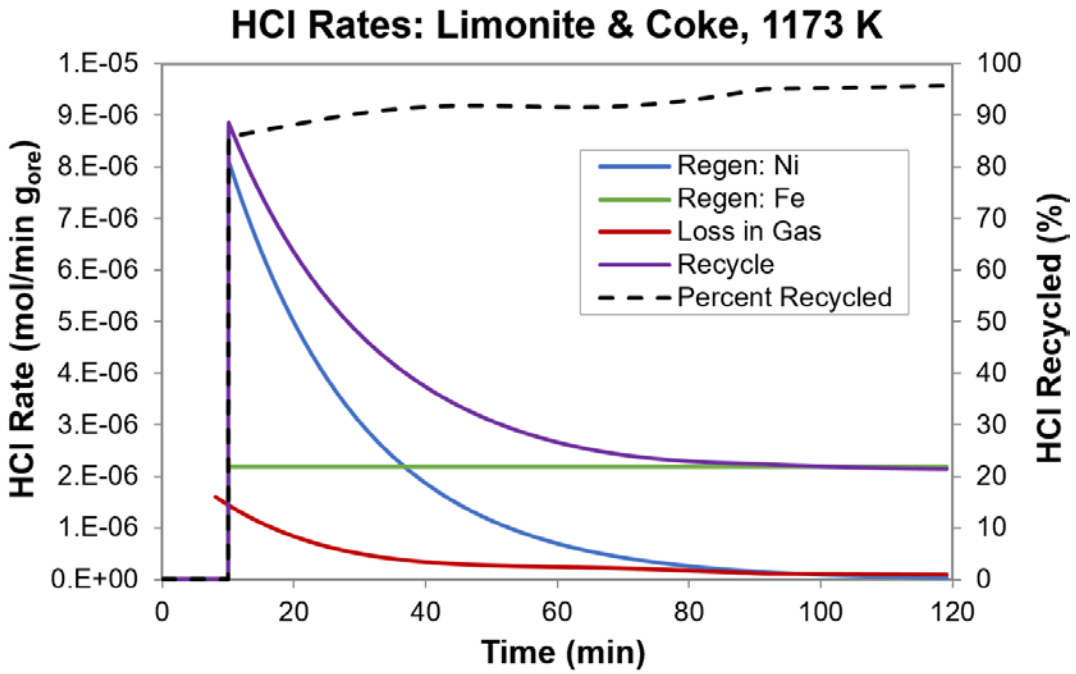

Figure 7.21 HCl Regen, Loss and Recycle Rates, Limonite with Coke at 1173 K

Regen: Ni and Regen: Fe are the rates at which HCl is regenerated by chloride reduction through Equations 2.24 and 2.25 respectively.

During the induction period, there is no segregation and hence no recycle as shown in the figures; however significant HCl is lost in the gas during this period. Once the induction period ends, the evolution of carbonaceous gas has decreased significantly, the p_{HCl} in the gas is relatively low (~0.03 atm compared to 0.05-0.10 atm for nontronite after 40 minutes), and the rate of HCl loss in the gas has also decreased (Figure 7.18); thus the recycle is highly efficient.

7.5 Effect of Roasting Conditions

The three non-standard roasting conditions used in these tests were described in Section 6.5, and are summarised for limonite in Table 7.14.

Table 7.14 Non-Standard Conditions for Air Roast, Limonite
Limonite dehydroxylation begins at ~600 K (Section 4.1.2);
sintering temperature is 1193 K (Table 4.2).

Roast	Time	Temperature Set Point	Temperature (K)
Low Temp	3 days	Just below ore dehydroxylation	~570
Rapid	12 min	Just below ore sintering	~1183
High Temp	3 hrs		

The averaged values for metal recoveries and ferronickel grades from segregation using the non-standard roasts are summarised in Table 7.15, along with comparative data using the standard roast. Data for the individual non-standard roasting tests are presented in Appendix B.11.

Table 7.15 Effect of Roast Type on Limonite Segregation
Mass fraction of retained water is calculated from weight change relative to the maximum possible change (Table 4.2); segregation for 80 minutes at 1173 K with 5% coke and 5% $CaCl_2$, based on dried ore.

Roast	Retained Water (mass fraction)	Recovery (%)			FeNi Ni(%)
		Ni	Fe	Co	
Low Temp	2.0×10^{-2}	77	0.84	23	63
Rapid Heat	3.9×10^{-3}	80	0.97	23	60
High Temp	4.0×10^{-4}	77	0.98	21	59
Standard*	6.9×10^{-3}	78	0.85	22	62

*Standard values taken from fitted equations: Ni (Table 7.2), Fe (Table 7.3), Co (Table 7.4)

Table 7.15 shows that variation of roasting conditions had little impact on the segregation metal recoveries (77-80%) and ferronickel grade (59-63%). It seems likely that most of the excess moisture is released during the induction period before segregation begins, thus nullifying the effect of retained moisture in the calcine. As for nontronite, any differences in crystallinity of the minerals due to non-standard roasting also appear to have little effect on the segregation outcome.

The cumulative HCl reporting to the off-gas was measured in a single experiment during each of the non-standard roast/modified segregation tests. The chloride in the gas is shown in Figure 7.22 as a percent of the total chloride added, with a lag time of ~3-4 minutes discounted from the time scale.

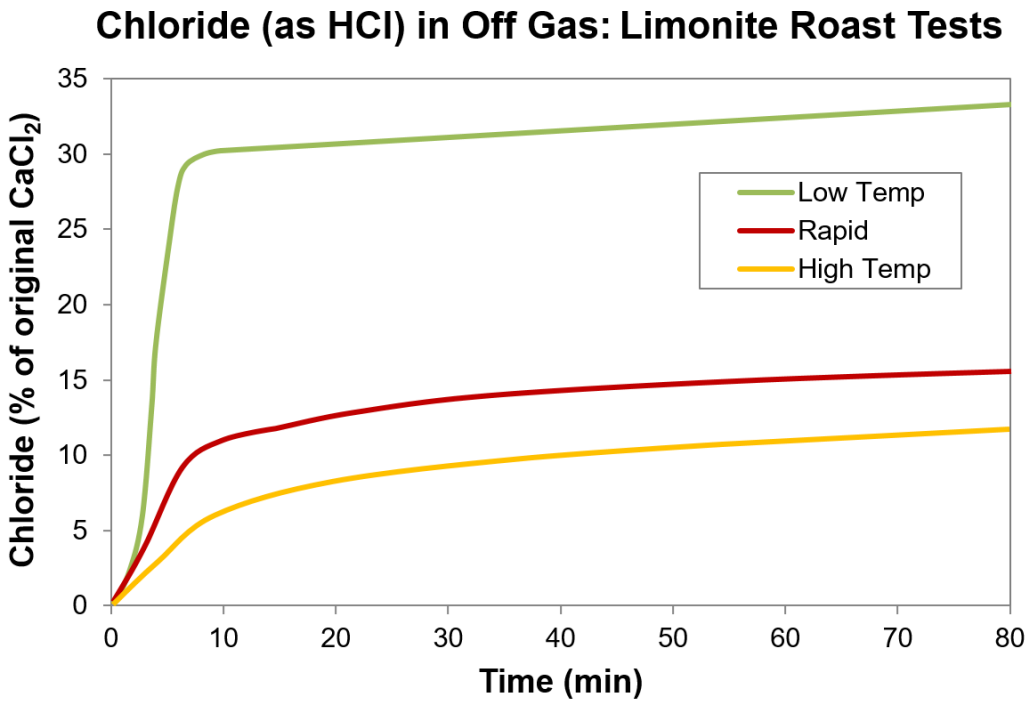

Figure 7.22 Chloride as HCl in the Off-Gas, Limonite Non-Standard Roasts

$CaCl_2$ addition was 5 g/100 g dried ore.

The trends shown in Figure 7.22 were also observed with nontronite (Section 6.5.2). The rate of chloride loss was greatest over the initial 10 minutes and was strongly dependent on the roast conditions since the 'low temp' calcine with the highest residual water (Table 7.15) has the highest HCl evolution. The results confirm that most of the excess moisture was released from the calcine during the induction period when non-equilibrium release of HCl occurred.

7.6 Discussion

Many of the observations regarding segregation made through the study of nontronite, also apply to limonite; some aspects will not be discussed here.

The segregation metal recoveries from limonite were potentially indicative only, because unlike nontronite, the segregation product could not be concentrated prior to leaching by magnetic separation. This likely resulted in a minor enhancement of the Fe recovery due to unavoidable dissolution of minor iron oxides, and possible enhancement of all metal recoveries due to dissolution of some in-situ ferronickel along with segregated alloy; however, in-situ alloy was only apparent when using activated carbon.

Unique to limonite, segregation began after an induction period, in which little or no chloridisation occurred because the hydrolysis reaction of $CaCl_2$ was unfavourable. This likely occurred because, with a large amount of hematite initially present in the calcine and only a small amount of free silica, the hydrolysis product was calcium ferrite rather than calcium silicate. The CO_2/CO within the bulk gas was also exceptionally high during this period, due to the large amount of hematite being reduced; this may also have inhibited potential reduction of chloride at the carbon surface.

As with nontronite, the rates of Ni, Fe and Co recoveries by segregation were described by 'first order to a limit' or zero order rate equations, but with the time scales discounted by the induction period. Chloridisation of NiO was the likely rate control for Ni and Co segregation, while Fe segregation was likely controlled by the water gas reaction.

In common with nontronite, the rate of Ni segregation was initially rapid but slowed with time and approached a limit, which increased with temperature. Prior to segregation, the Ni was distributed at ~1% throughout the fine to amorphous hematite that made up the majority of the calcine. After segregation with coke, most of the remaining Ni was likely present below the EDS-SEM detection limit of 0.3% within wustite and magnetite. In-situ reduced alloy was noticeable within the calcine segregated with activated carbon and this reduced the overall Ni recovery detected by the leach; no in-situ ferronickel was noticeable after using coke.

As for nontronite, the CO_2/CO and oxygen pressure in the bulk gas appeared to be controlled mainly by the iron oxide reduction reactions, with the rate controlled by

the Boudouard reaction. The presence of chloride enhanced the rate of carbon gasification when using coke, but only marginally compared to the significant enhancement noted for nontronite. This made little difference to the oxygen pressure profile, which appeared buffered at similar values by the uncomplicated reduction of large amounts of relatively pure iron oxides. Overall, the Ni recovery from segregation was at least as good as for reduction using coke at 1123 K, and superior when using coke at 1173 K and when using activated carbon.

The residual chloride after limonite segregation was greater than for nontronite, since the $CaCl_2$ hydrolysis was not as effective due to the relatively small amount of silica present in the calcine. The HCl recycle is also very efficient after the induction period, because the HCl pressure and the evolution of gas are both low. Variations within the retained moisture or the crystallinity of the hematite within the calcine during roasting had no impact on the Ni segregation recovery.

The maximum recoveries achieved by segregation of limonite were ~80% Ni along with ~23% of the Co and ~1% of the Fe when using coke at 1173 K. Although the mineralogy of limonite is conducive to segregation occurring without the formation of in-situ alloy when using coke, it is unlikely that Ni recovery could be improved much beyond the 80% achieved here. This appears close to the maximum for limonite based on published Ni recoveries that were similar for temperatures up to 1273 K. It might be possible to reduce the induction period by the addition of fine silica to promote hydrolysis, but this would result in more residual NiO dissolved within iron silicates. Ultimately, the recovery appears limited by the large mass of iron oxides available for dissolution of residual NiO at a low activity.

Chapter 8

Garnierite Segregation

A study of the segregation process applied to a garnierite nickel laterite ore from Heron Resource's Kalgoorlie Nickel Project is presented throughout this chapter. This study was performed to provide a comparison with the main study on nontronite ore from the same deposit (Chapter 6). This presentation will be identically structured, with the discussion focused on differences between the ores; the description of common aspects will be dealt with briefly.

8.1 Recovery of Metals

Fifty one tests were performed using a two-step segregation method (Section 3.3.2), with multiple tests conducted for up to 120 minutes with coke at both 1173 K and 1223 K, and up to 80 minutes with activated carbon at 1223 K. The results are summarised in Table 8.1.

Table 8.1 Metal Recoveries and Ferronickel Grades, Garnierite Segregation
Ore was roasted for 30 minutes in air at the segregation temperature.
Reagent addition per 100 g of dried ore was 5 g of either coke (78.3% C), or activated carbon (88.7% C) and 5 g of $CaCl_2$.

Test Code	Carbon	Temp (K)	Time (minutes)	Recovery (%)			FeNi Ni(%)
				$R_{Ni(\%)}$	$R_{Fe(\%)}$	$R_{Co(\%)}$	
G900C22	Coke	1173	5	4.3	0.08	ND	85
G900C23	Coke	1173	5	0.6	0.04	ND	59
G900C24	Coke	1173	10	14	0.23	1.5	87
G900C25	Coke	1173	15	6.7	0.21	1.0	77
G900C26	Coke	1173	15	2.9	0.10	0.24	76
G900C4	Coke	1173	20	25	0.50	4.5	84
G900C27	Coke	1173	30	36	0.91	8.3	81
G900C28	Coke	1173	45	38	1.1	10	79
G900C29	Coke	1173	60	49	2.2	19	71
G900C21	Coke	1173	73	47	2.2	17	70
G900C12	Coke	1173	90	48	3.0	25	63
G900C6	Coke	1173	100	42	2.0	17	69
G900C14	Coke	1173	105	51	3.5	26	61
G900C15	Coke	1173	105	46	2.4	20	68
G900C8	Coke	1173	110	41	2.3	18	66
G900C7	Coke	1173	120	48	2.9	22	64
G900C9	Coke	1173	120	37	2.0	16	66
G900C11	Coke	1173	120	47	2.9	22	63
G900C13	Coke	1173	120	54	4.0	28	60
G900C1	Coke	1173	120	45	2.6	20	65
G900C3	Coke	1173	120	43	2.3	19	67
G900C30	Coke	1173	157	56	3.8	27	62

Table 8.1 Metal Recoveries and Ferronickel Grades (cont'd)

Test Code	Carbon	Temp (K)	Time (minutes)	Recovery (%)			FeNi Ni(%)
				$R_{Ni(\%)}$	$R_{Fe(\%)}$	$R_{Co(\%)}$	
G950C8	Coke	1223	5	18	0.37	3.7	84
G950C9	Coke	1223	10	24	0.63	6.4	81
G950C11	Coke	1223	15	29	0.93	9.1	77
G950C10	Coke	1223	20	36	1.5	13	72
G950C12	Coke	1223	25	31	1.2	11	74
G950C7	Coke	1223	30	39	1.7	15	71
G950C6	Coke	1223	45	58	4.6	30	58
G950C4	Coke	1223	60	51	4.0	29	58
G950C22	Coke	1223	60	62	5.4	31	55
G950C23	Coke	1223	70	66	6.4	35	53
G950C3	Coke	1223	80	47	4.2	27	55
G950C24	Coke	1223	80	61	7.1	33	48
G950C13	Coke	1223	90	62	7.1	39	49
G950C18	Coke	1223	97	63	7.2	37	49
G950C1	Coke	1223	100	68	7.8	40	49
G950C14	Coke	1223	110	63	8.0	40	46
G950C2	Coke	1223	120	58	7.7	33	45
G950C5	Coke	1223	120	57	6.7	34	48
G950C15	Coke	1223	120	68	9.1	42	45
G950C17	Coke	1223	120	61	7.2	36	48
G950C19	Coke	1223	120	71	10	44	43
G950AC5	Act C	1223	5	23	3.8	12	40
G950AC7	Act C	1223	10	34	8.7	17	30
G950AC9	Act C	1223	15	39	11	19	28
G950AC11	Act C	1223	20	45	15	23	24
G950AC10	Act C	1223	31	42	16	21	22
G950AC8	Act C	1223	60	49	26	25	17
G950AC6	Act C	1223	80	50	34	26	14
G950AC12	Act C	1223	80	48	19	24	22

ND = Not Detected

8.1.1 Nickel

As with nontronite and limonite, it appears Ni recovery was limited by a portion of Ni within the ore that would not segregate; thus the 'first order to a limit' rate equation was used to describe the rate of segregated Ni recovery with time (Section 6.1.1.1).

8.1.1.1 Recovery and Rate Equations

The parameters ($R_{Ni,max}$, k_{Ni}) for the integrated rate equations were fitted from the Ni recovery data (Table 8.1). These parameters are presented in Table 8.2, and the equations are plotted in Figure 8.1 along with the experimental data. The data show that, in contrast to limonite and nontronite, the rate of Ni recovery increased with increase in the carbon surface area (cf. coke and activated carbon at 1223 K).

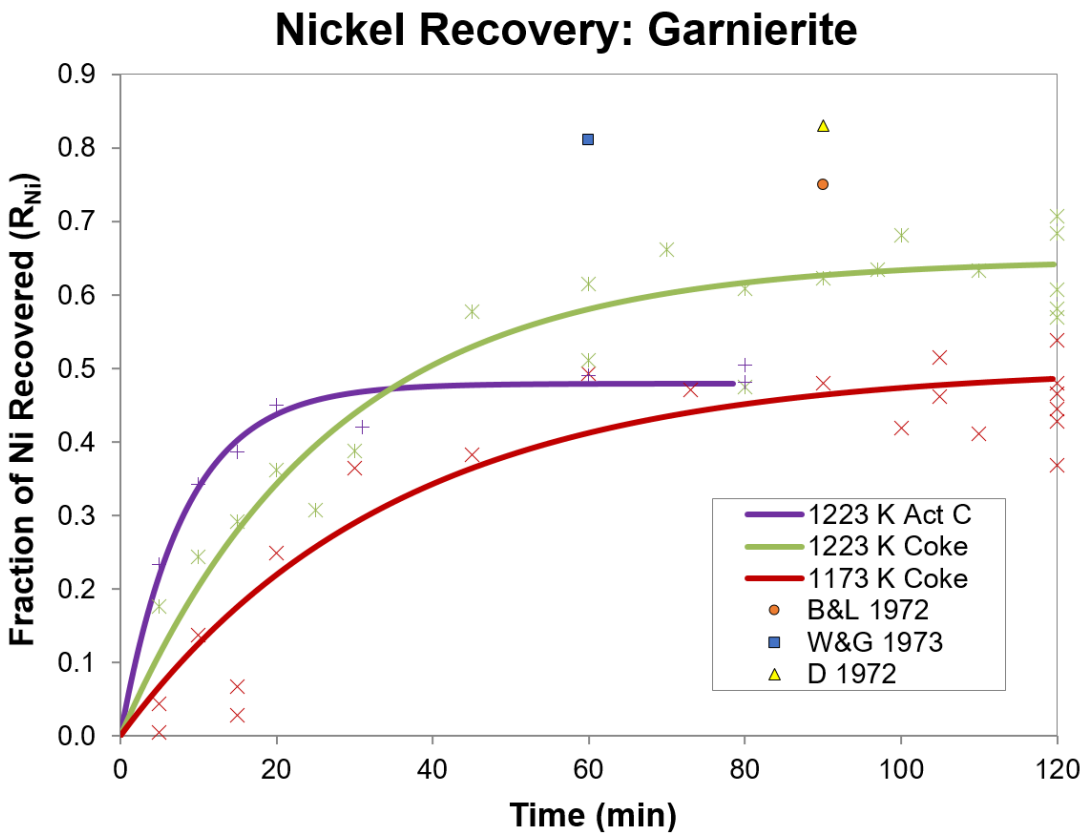

Figure 8.1 Nickel Recovery, Garnierite

Fitted curves are summarised in Table 8.2. Other data are from: Brittan and Liebenberg (1972), Davidson (1972) & Wright and Gooden (1973), see Table 2.6. For this graph, and all others for metal recovery in this Chapter, dot points represent data from Table 8.1.

Table 8.2 Integrated Rate Equations, Recovery of Nickel from Garnierite

Fitted parameters for 'first order to a limit' integrated rate equations. R_{Ni} is fractional Ni recovery; $R_{Ni,max}$ is the maximum fractional Ni recovery; k_{Ni} is a first order rate constant ($/min$); t is reaction time.

Series	Carbon	Temp (K)	Time maximum (minutes)	Integrated Rate Equation $R_{Ni} = R_{Ni,max}(1 - e^{-k_{Ni}t})$	Fit r^2
G900C	Coke	1173	120	$R_{Ni} = 0.50(1 - e^{-0.029t})$	0.85
G950C	Coke	1223	120	$R_{Ni} = 0.65(1 - e^{-0.038t})$	0.91
G950AC	Act C	1223	80	$R_{Ni} = 0.48(1 - e^{-0.122t})$	0.94

The maximum recovery obtained under all conditions was 65% (Table 8.2), which is 12-22% lower than reported by others who segregated garnierite of similar chemical composition (Table 2.6). This relatively low recovery was likely due to a comparatively high Ni loss through in-situ ferronickel, since the standardised 5% carbon addition appears excessive for garnierite; other workers added 2-3.5% C.

8.1.1.2 Rate Control

The rate of Ni recovery increased ~3.2x when coke was replaced by activated carbon at 1223 K (Table 8.2), indicating the rate is likely controlled by the water gas reaction (Section 6.1.2.3). However, since the rate of Fe segregation, which is also believed to be controlled by the water gas reaction (Section 8.1.2.2), increased to a greater extent (~6.4x), it is more likely that the Ni recovery rate is jointly controlled by chloridisation and the water gas reaction, as also noted for Co segregation from nontronite (Section 6.1.4.2).

Since chloridisation was the dominant rate control for both limonite and nontronite, it appears that NiO in garnierite calcine is more readily chloridised than in the other calcines. NiO is more accessible within garnierite since it is largely present at higher concentrations within fewer particles, some containing up to 11% Ni (Table 4.11).

8.1.1.3 Recovery Limit

Nickel recovery approached an upper limit, within experimental error, under all conditions tested. This limit ($R_{Ni,max}$, Table 8.2) increased from 50 to 65% as the temperature increased from 1173 to 1223 K with coke, but decreased from 65 to 48% with activated carbon at 1223 K.

A sample of garnierite calcine, which had been segregated with coke for 70 minutes at 1173 K, was resin-mounted, polished and carbon coated. A 1.0 x 1.0 mm (1000 µm x 1000 µm) section was subjected to EDS-SEM analysis to determine the location of the unsegregated Ni. A backscattered electron image of this section and accompanying EDS chemical maps are presented in Appendix B.19. The unsegregated Ni was located within chlorite and serpentine dehydroxylates, either dissolved within silicates or as in-situ ferronickel.

Prior to segregation, the chlorite dehydroxylates presented as Mg-Al crystalline silicates (pyroxene and olivine) located as sections/veins within large crystalline silica particles (Figure 4.11). After segregation, the remnant chlorite dehydroxylates, as shown in Figure 8.2, remained as silicates (grey striated areas, example outlined

in red) within a segregated garnierite particle consisting mainly of silica (dense, darker areas).

The unsegregated dehydroxylate contained an average of 7.7% Ni, with an average molar composition of $Mg_{0.94}Al_{0.42}Ni_{0.17}Fe_{0.10}SiO_{3.4}$, based on 5 separate areas (Table 4.11), compared to 0.6% Ni for the segregated dehydroxylate, with an average molar composition of $Mg_{0.59}Al_{0.55}Fe_{0.37}Ca_{0.21}Ni_{0.01}SiO_{3.6}$, based on 4 separate areas (Table 8.3).

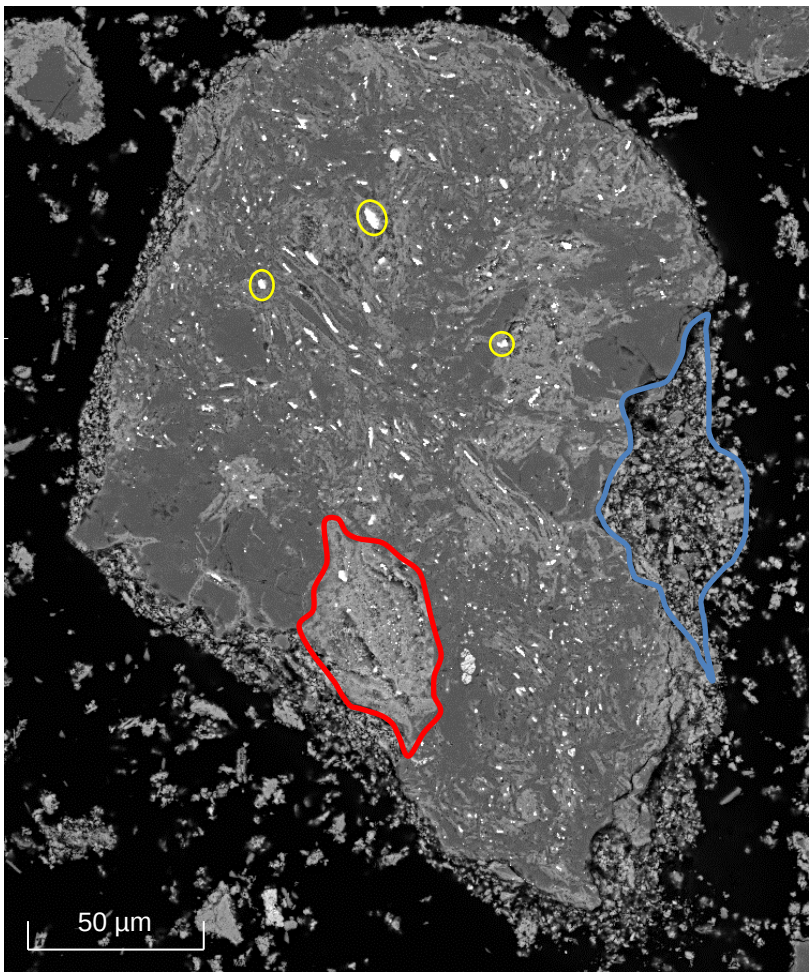

Figure 8.2 Section through a Segregated Garnierite Particle

SEM image through a segregated garnierite particle consisting mainly of silica (dense, darker areas) and containing remnant chlorite dehydroxylate (grey striated areas, example outlined in red), remnant serpentine dehydroxylate (fine grained material, example outlined in blue) and in-situ ferronickel within chlorite (examples outlined in yellow, average grade 80% Ni); segregation for 70 minutes with coke at 1173 K.

The chlorite dehydroxylate contained a Fe/Si mole ratio of 0.1, initially but this increased to 0.37 as segregation took place. As for nontronite (Section 6.1.1.4), it appears that $FeCl_2$ likely absorbed onto the dehydroxylate during segregation and chloridised the NiO from the calcine via the exchange reaction (Equation 2.23):

$$NiO(s) + FeCl_2(g) \rightarrow NiCl_2(g) + FeO(s) \qquad 2.23$$

This mechanism is supported by Matsumori (1999), who found that during the reduction of garnierite, FeO can substitute for NiO during the recrystallisation of silicates. It was not possible to calculate the extraction of Ni from the dehydroxylate without knowing the change in mass during segregation. However, the extraction was 92% from the chlorite dehydroxylate on the assumption of no mass change.

Table 8.3 Composition of Remnant Chlorite Dehydroxylate

Four areas of remnant chlorite dehydroxylate, free from in-situ alloy, as selected from segregated garnierite (Appendix B.19); analysis via EDS-SEM.

Area Number	Ni (wt%)	Average Composition (moles)
1	0.6	$Mg_{0.68}Al_{0.66}Fe_{0.43}Ca_{0.14}Ni_{0.02}SiO_{3.7}$
2	0.4	$Mg_{0.49}Al_{0.61}Fe_{0.32}Ca_{0.28}Ni_{0.01}SiO_{3.7}$
3	0.6	$Mg_{0.46}Al_{0.52}Fe_{0.32}Ca_{0.22}Ni_{0.01}SiO_{3.5}$
4	0.7	$Mg_{0.71}Al_{0.42}Fe_{0.41}Ca_{0.19}Ni_{0.02}SiO_{3.6}$
Average	0.6	$Mg_{0.59}Al_{0.55}Fe_{0.37}Ca_{0.21}Ni_{0.01}SiO_{3.6}$

Prior to segregation, the serpentine dehydroxylate presented as fine to amorphous conglomerates of Mg-Fe silicate material bordering large crystalline particles such as silica, hematite or spinel (Figure 4.11, Figure 4.13). After segregation, the remnant serpentine dehydroxylates remained as fine grained material, as shown in Figure 8.2 (example outlined in blue), bordering larger particles dominantly containing silica.

The unsegregated serpentine dehydroxylate contained an average of 2.2% Ni with an average molar composition of $Mg_{0.88}Fe_{0.41}Al_{0.10}Ni_{0.05}Ca_{0.04}SiO_{2.7}$, based on 4 separate areas (Table 4.12), compared to 1.0% Ni for the segregated dehydroxylate, with an average composition of $Mg_{0.83}Fe_{0.58}Al_{0.17}Ca_{0.10}Ni_{0.02}SiO_{3.1}$, based on 4 separate areas (Table 8.4).

The initial Fe/Si mole ratio within serpentine dehydroxylate was much higher than for the chlorite dehydroxylate, and only increased from 0.41 to 0.58 during segregation.

It seems that the driving force for Fe exchange via reaction 2.23 was less for the serpentine dehydroxylate, and hence less Ni was removed during segregation. The extraction of Ni was 55% from serpentine assuming no mass change during segregation.

An estimate of the maximum Ni recovery from garnierite during segregation was obtained on the assumption that the 16.33% chlorite in the ore (Table 4.9) contained 7.7% Ni (Table 4.11) and the 7.25% serpentine in the ore (Table 4.9) contained 2.2% Ni (Table 4.12). This estimates 1.41% Ni in the dried ore, compared to the assay of 1.27% (Table 4.1). With 92% extraction from the chlorite and 55% from the serpentine, the extraction of Ni from the ore could be as high as 88%, with the remainder dissolved within silicates.

Table 8.4 Composition of Remnant Serpentine Dehydroxylate

Four areas of remnant serpentine dehydroxylate, free from in-situ alloy, as selected from segregated garnierite (Appendix B.19); analysis via EDS-SEM.

Area Number	Ni (wt%)	Average Composition (moles)
1	1.1	$Mg_{0.82}Fe_{0.49}Al_{0.27}Ca_{0.13}Ni_{0.03}SiO_{3.3}$
2	0.9	$Mg_{0.84}Fe_{0.77}Al_{0.14}Ca_{0.06}Ni_{0.02}SiO_{3.1}$
3	0.8	$Mg_{0.73}Fe_{0.45}Al_{0.14}Ca_{0.11}Ni_{0.02}SiO_{3.0}$
4	1.1	$Mg_{0.91}Fe_{0.61}Al_{0.15}Ca_{0.08}Ni_{0.03}SiO_{3.1}$
Average	1.0	$Mg_{0.83}Fe_{0.58}Al_{0.17}Ca_{0.10}Ni_{0.02}SiO_{3.1}$

However, the maximum Ni recovery predicted from the integrated rate equation (Table 8.2) was only 43%, for segregation after 70 minutes with coke at 1173 K. Up to 5% Ni can be lost as a soluble chloride (Table 8.14) and 5% through handling during the multi-step experimental procedure, as estimated by a mass balance check (Appendix B.2). The remaining 35% of the 88% of Ni not dissolved within silicates was likely present as in-situ ferronickel, which noticeably formed within chlorite dehydroxylate when segregation was carried out using coke; examples are outlined in yellow in Figure 8.2.

The formation of in-situ ferronickel can also explain why Ni recovery was significantly lower at 1223 K with activated carbon ($R_{Ni,max} = 0.46$) compared to coke ($R_{Ni,max} = 0.65$) at 1223 K (Table 8.2), since activated carbon will generate a lower p_{O_2} in the bulk gas and thus promote further in-situ reduction to alloy.

8.1.2 Iron

The Fe recovery appeared to increase at a constant rate under all conditions within experimental error, as also observed for nontronite and limonite; thus a zero order rate equation was used to describe the rate of segregated Fe recovery (Section 6.1.2.1).

8.1.2.1 Recovery and Rate Equations

The integrated rate equations, as fitted from the Fe recovery data (Table 8.1), are presented in Table 8.5 and plotted in Figure 8.3. The experimental data are also included. The rate of recovery, which was constant with time at a specific temperature and carbon addition, increased when the temperature and carbon surface area were increased.

Table 8.5 Integrated Rate Equations, Recovery of Iron from Garnierite

Fitted parameters for zero order integrated rate equations. R_{Fe} is fractional Fe recovery; k_{Fe} is a zero order rate constant (/min); t is reaction time.

Series	Carbon	Temp (K)	Time maximum minutes	Integrated Rate Equation $R_{Fe} = k_{Fe}\, t$	Fit r^2
G900C	Coke	1173	120	$R_{Fe} = 2.4 \times 10^{-4} t$	0.85
G950C	Coke	1223	120	$R_{Fe} = 7.2 \times 10^{-4} t$	0.91
G950AC	Act C	1223	80	$R_{Fe} = 4.6 \times 10^{-3} t$	0.91

8.1.2.2 Rate Control

The rate of segregated Fe recovery increased ~6.4x when coke was replaced by activated carbon at 1223 K (Table 8.5); thus the rate is likely controlled by the water gas reaction (Section 6.1.2.3).

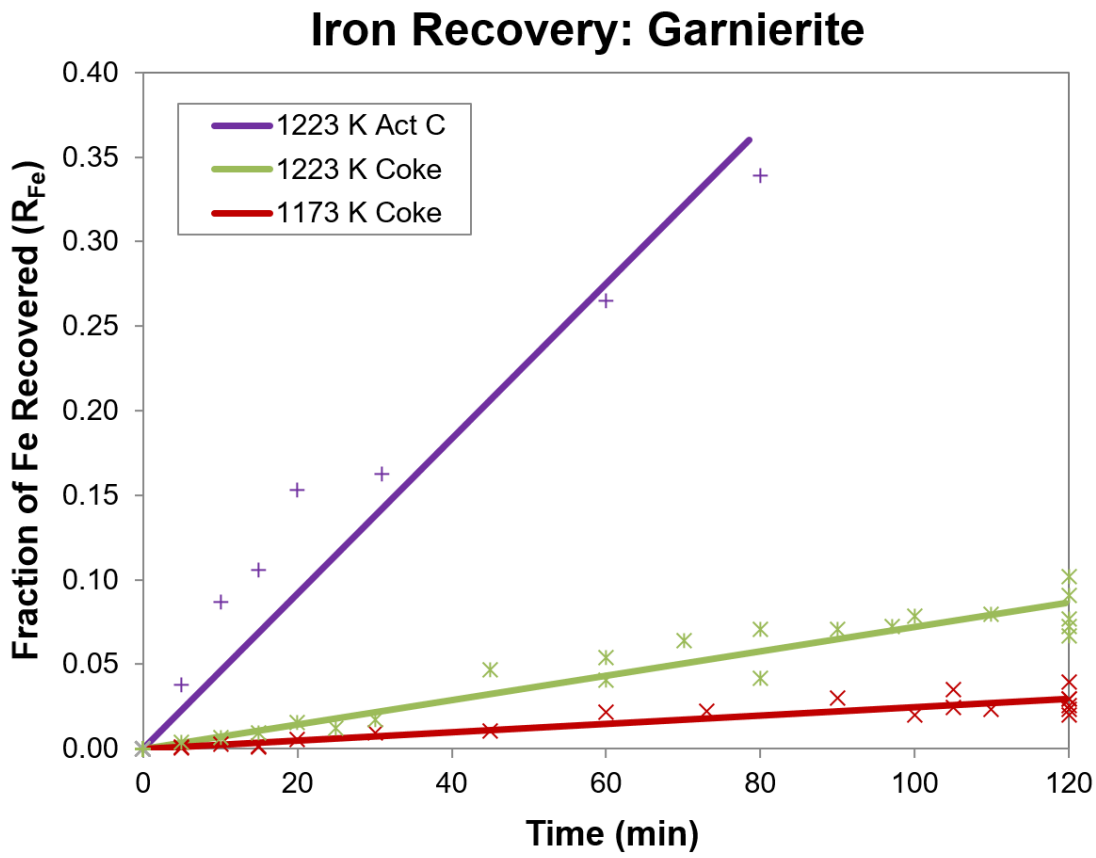

Figure 8.3 Iron Recovery, Garnierite

Fitted rate equations take the form $R_{Fe} = k_{Fe}t$, see Table 8.5.

8.1.3 Co-recovery of Nickel and Iron

Figure 8.4 shows a plot of Ni recovery versus Fe recovery for segregation of garnierite. All lines are fitted using the segregation rate equations for Ni (Table 8.2) and Fe (Table 8.5).

The figure shows that for a given recovery of Ni, the co-recovery of Fe increases significantly with an increase in the available area of the carbon reductant (cf. coke and Act C at 1223 K). While Ni approaches its maximum recovery (Section 8.1.1.3), for a given recovery of Ni, the co-recovery of Fe is slightly higher with an increase in temperature (cf. coke at 1173 and 1223 K). This implies the rate of the Fe segregation control reaction (the Boudouard reaction) increases to a greater extent compared to the Ni segregation control reactions (mixed control: NiO chloridisation and the water-gas reaction). When Ni recovery is close to maximum, significantly more Fe is co-reduced per unit Ni recovered, as illustrated by the change in slope of each curve.

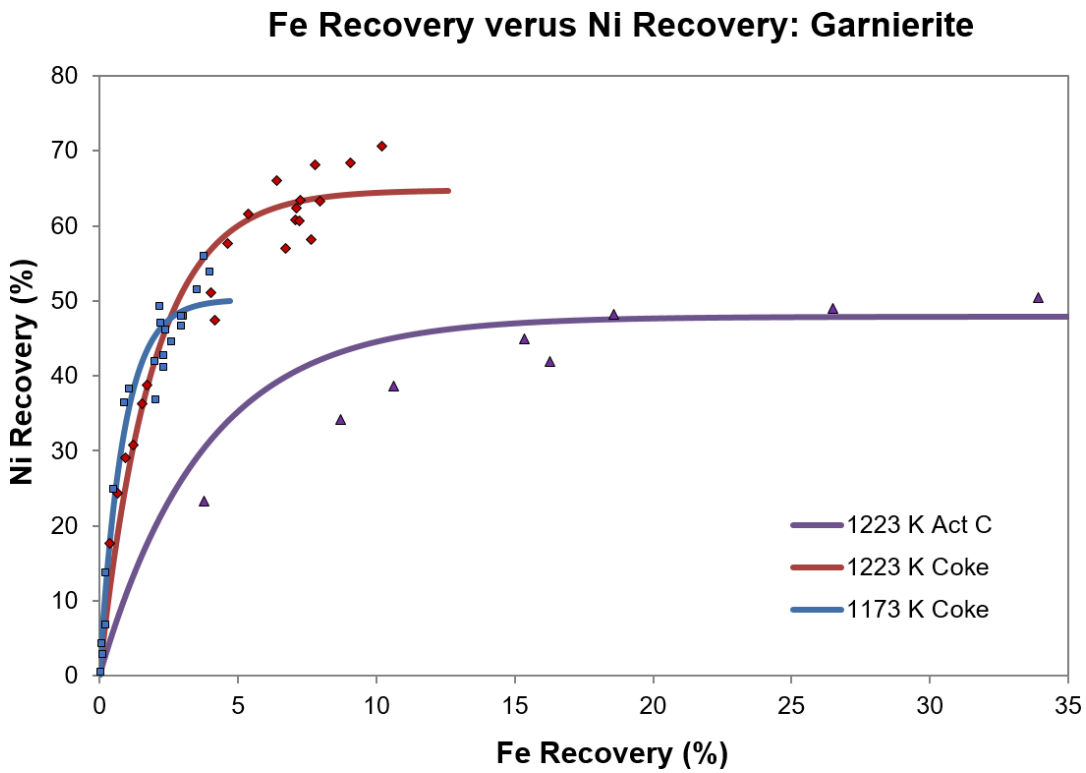

Figure 8.4 Fe Recovery versus Ni Recovery, Garnierite Segregation

The Ni and Fe recovery data (from Table 8.1, shown as dot points on the figure) are presented along with the predicted recoveries using the nickel and iron rate equations developed in Sections 8.1.1.1 and 8.1.2.1 respectively; rate equation data are shown as continuous lines on the figure.

8.1.4 Cobalt

The rate of segregated Co recovery over time was suitably characterised by the zero order rate equation (Section 6.1.2.1) at the lower temperature (1173 K), while at 1223 K it was better characterised by the 'first order to a limit' rate equation (Section 6.1.2.1).

8.1.4.1 Recovery and Rate Equations

The integrated rate equations, as fitted from the Co recovery data (Table 8.1), are presented in Table 8.6 and plotted in Figure 8.5 along with the experimental data. The recovery increased with both time and temperature. Rey et al. (1972a) reported a single recovery for Co of 51%, along with 88% Ni and 6.3% Fe from garnierite when using 2% coke and 6% $CaCl_2$ at 1253 K. The Co recovery is slightly higher than the maximum of 44% obtained in this work (Table 8.6), but the lower coke likely favours higher recoveries (Section 8.1.1.1).

Table 8.6 Integrated Rate Equations, Recovery of Cobalt from Garnierite

Equations are zero order, $R_{Co} = k_{Co}t$, or 'first order to a limit', $R_{Co} = R_{Co,max}(1 - e^{-k_{Co}t})$. R_{Co} is the fractional Co recovery; k_{Co} is the rate constant; t is time.

Series	Carbon	Temp (K)	Time maximum (minutes)	Integrated Rate Equation	Fit r^2
G900C	Coke	1173	120	$R_{Co} = 1.9 \times 10^{-3}t$	0.84
G950C	Coke	1223	120	$R_{Co} = 0.44(1 - e^{-0.018t})$	0.91
G950AC	Act C	1223	80	$R_{Co} = 0.24(1 - e^{-0.118t})$	0.94

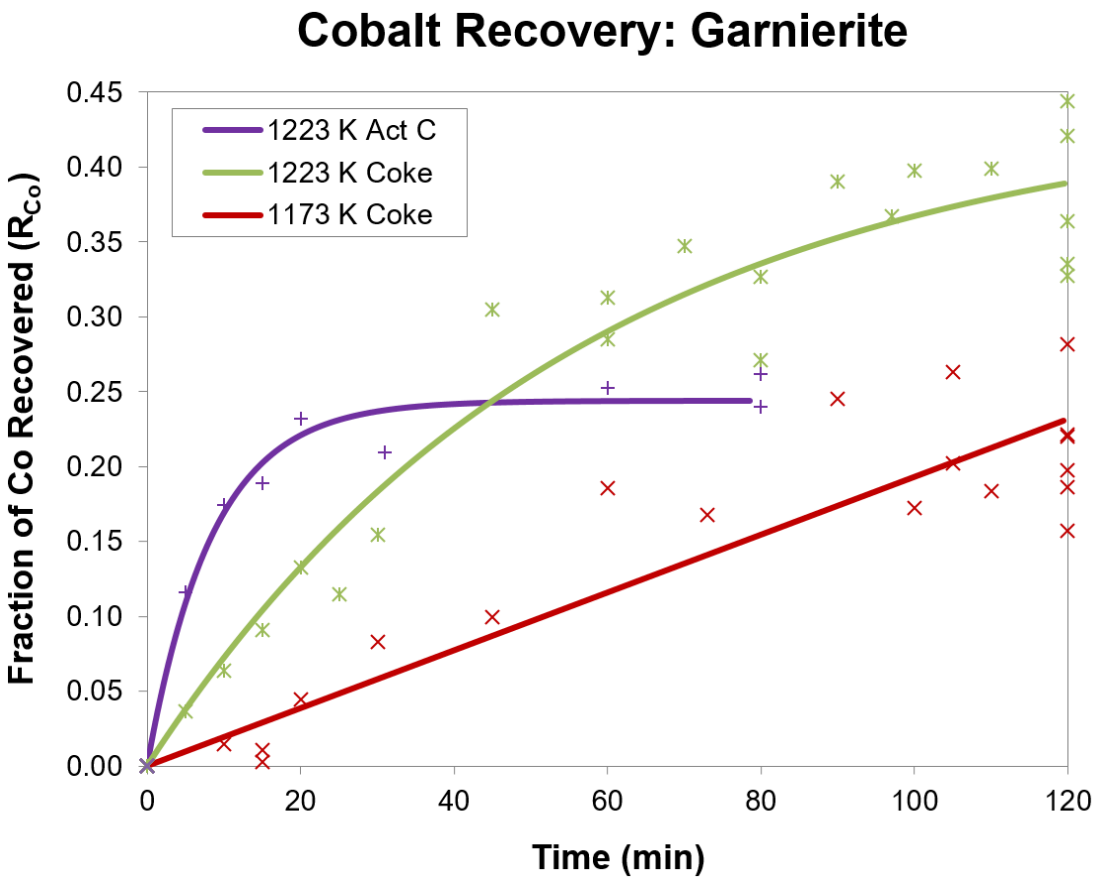

Figure 8.5 Cobalt Recovery, Garnierite

Parameters for fitted equations are summarised in Table 8.6.

8.1.4.2 Rate Control

The rate of segregated Co recovery increased ~6.6x when coke was replaced by activated carbon at 1223 K, virtually the same increase as for Fe recovery (~6.4x); thus the rate was likely controlled by the water gas reaction (Section 6.1.2.3).

8.1.5 Activation Energies

The apparent activation energies for the recoveries of Ni, Fe and Co during segregation with coke were estimated from Arrhenius plots of the fitted rate constants (Table 8.2, Table 8.5 and Table 8.6) versus temperature. The plots are presented in Appendix B.3 and the values are shown Table 8.7.

The apparent activation energy for Ni segregation of 65 kJ/mol is lower than the value of 83 kJ/mol found for limonite; it was expected to be higher since the water gas reaction appears to partly control the reaction rate. The respective activation energies for Fe and Co segregation of 260 and 190 kJ/mol are compatible with chemical control through the water gas reaction, and comparable to the values reported for limonite (190 and 380 kJ/mol) and nontronite (290 and 300 kJ/mol).

Table 8.7 Activation Energies for Metal Recoveries, Garnierite Segregation

Activation energy (E) and collision frequency factor (k_0) are calculated from a plot of ln k versus 1/T (Appendix B.3). R is the universal gas constant, T is the temperature (K). Data are specific to segregation with coke.

Metal	Activation Energy (kJ/mol)	Arrhenius Expression $k = k_0 e^{\frac{-E}{RT}}$
Nickel	65	$k_{R_{Ni}} = 21.6e^{\frac{-7800}{T}}$
Iron	260	$k_{R_{Fe}} = 6.29 \times 10^{7} e^{\frac{-31000}{T}}$
Cobalt	190	$k_{R_{Co}} = 1.30 \times 10^{14} e^{\frac{-23000}{T}}$

8.2 Segregation versus Carbon Reduction

Throughout this section, the results from segregation are compared with those from an equivalent reduction system to which $CaCl_2$ was not added (Section 5.5).

8.2.1 Oxygen Pressure

The average p_{O_2} profile for segregation with coke at 1173 K (G900C) is shown in Figure 8.6, along with the average profile from the equivalent chloride free reduction system (GR900C). The equilibrium p_{O_2} values for the transformation of iron oxides are referenced by lines across the diagram.

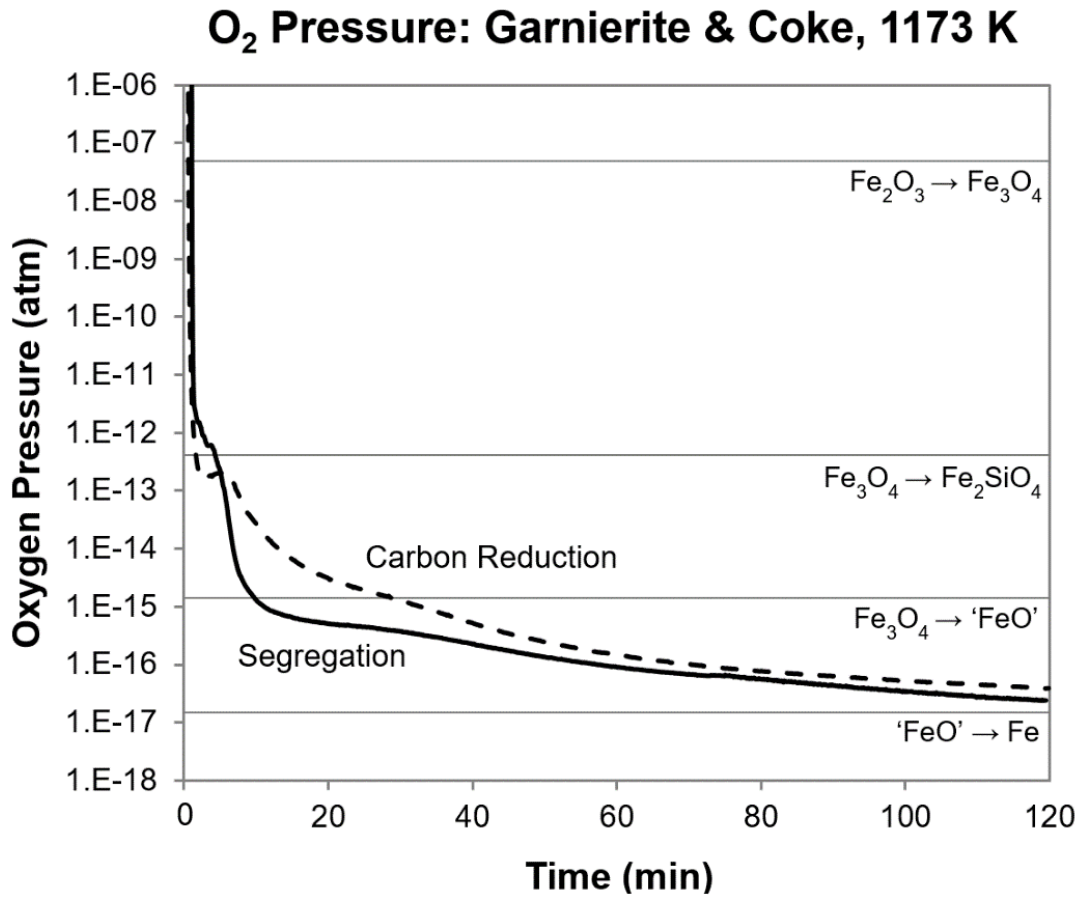

Figure 8.6 Oxygen Pressure Profiles, Garnierite with Coke at 1173 K

Details for the representative oxygen profiles are given in Appendix B.5.

Figure 8.6 shows that the p_{O_2} for segregation fell faster and to a lower value than for the chloride free reduction systems and ultimately lay just below the reduction system value, close to the p_{O_2} for the reduction of 'FeO' (wustite) to Fe. The p_{O_2} profiles for garnierite segregation and reduction at 1223 K with coke and activated carbon showed similar relationships, with some minor variations (Appendix B.5).

8.2.2 Carbon Consumption

The profiles for carbon consumption during segregation and reduction are shown in Figure 8.7; the supporting data used to develop these curves are presented in Appendix B.4.

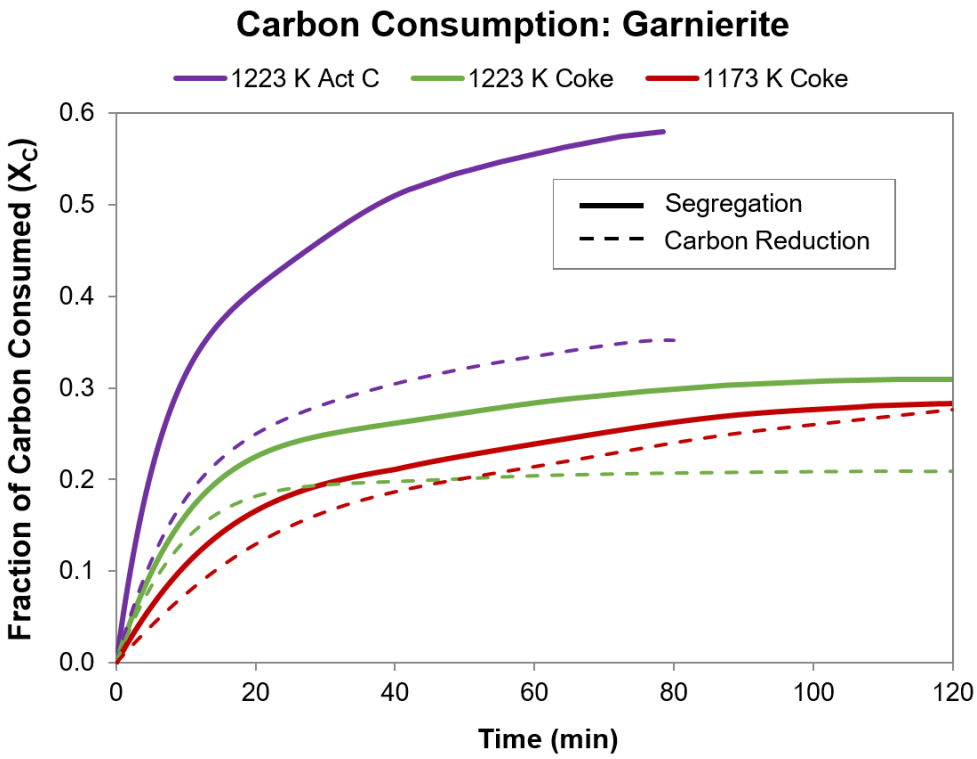

Figure 8.7 Carbon Consumption, Garnierite

Reductant added at 5% of dried ore, as either coke (78.3% C) or activated carbon (88.7% C). Curves are best fits from experimental data (Appendix B.4).

Figure 8.7 shows that carbon consumption was increased during segregation relative to reduction, but by variable amounts. Table 8.8 shows that total carbon consumption was the same for coke at 1173 K, but 50% higher at 1223 K; total C consumption was 65% higher for activated carbon at 1223 K. As a result, the final p_{O_2} values (Table 8.8) were very similar for coke at 1173 K, but lower for segregation when using both coke and activated carbon at 1223 K.

The Boudouard rate constants (Appendix B.1) for the initial gasification of carbon during segregation were slightly higher for segregation compared to reduction under all conditions (Table 8.9). The values for segregation were ~1.6x higher with coke at 1173 K, ~1.2x higher at 1223 K, and ~2x higher with activated carbon at 1223 K.

Table 8.8 Carbon Consumption and Oxygen Pressure Comparison, Garnierite

Carbon consumption X_C is expressed as a fraction of the 3.92 g (within 5 g coke) or 4.44 g (within 5 g Act C) added per 100 g of dried ore.

Carbon	Temp (K)	Time (minutes)	Reduction		Segregation	
			X_C	pO_2 (atm)	X_C	pO_2 (atm)
Coke	1173	120	0.28	4.0×10^{-17}	0.28	2.4×10^{-17}
Coke	1223	120	0.21	1.5×10^{-16}	0.31	3.0×10^{-17}
Act C	1223	80	0.35	3.0×10^{-17}	0.58	6.2×10^{-17}

Table 8.9 Boudouard Rate Constant Comparison, Garnierite

Reduction rate constants are from Table 5.13. Calculations are in Appendix B.1.

Carbon	Temp (K)	k_{BR} (/min)	
		Reduction	Segregation
Coke	1173	8.1×10^{-3}	1.3×10^{-2}
Coke	1223	1.9×10^{-2}	2.3×10^{-2}
Act C	1223	2.6×10^{-2}	5.3×10^{-2}

The apparent activation energy for the Boudouard reaction on coke during segregation was 130 kJ/mol compared to 207 kJ/mol for reduction (Table 8.10); the lower value being consistent with chloride catalysing the Boudouard reaction.

Table 8.10 Boudouard Activation Energy Comparison, Garnierite

Activation energy (E) and collision frequency factor (k_0) are calculated from a plot of ln k_{BR} versus 1/T (Appendix B.3). R is the universal gas constant; T is the temperature (K); reduction data from Table 5.14.

System	Temperature Range (K)	Activation Energy (kJ/mol)	Arrhenius Expression $k = k_0 e^{\frac{-E}{RT}}$
Segregation	1173–1223	130	$k_{BR_{Seg}} = 8.10 \times 10^3 e^{\frac{-15600}{T}}$
Reduction	1173-1223	207	$k_{BR_{Red}} = 1.35 \times 10^7 e^{\frac{-24900}{T}}$

8.2.3 Equilibrium Simulation and Oxygen Removal

Equilibrium simulations were performed using the method described in Section 5.1 and the carbon consumption data from Figure 8.7. The results during segregation with coke at 1173 K are summarised in Figure 8.8, with the simulated and measured p_{O_2} of the bulk gas included for comparison; the measured p_{O_2} is labelled G900C.

Figure 8.8 shows the same progression of equilibrium solid phase transformations that were predicted during reduction (Figure 5.15). As before, the simulation does not closely represent the experimental system, and the measured p_{O_2} does not achieve the very low values predicted by the simulation. This discrepancy likely results from lack of surface contact between the relatively large crystalline iron oxide and silica particles within the calcine (Section 4.1.6). Their presence likely created kinetic restrictions for the formation of silicates and silicate solid solutions that were not accounted for within the simulation.

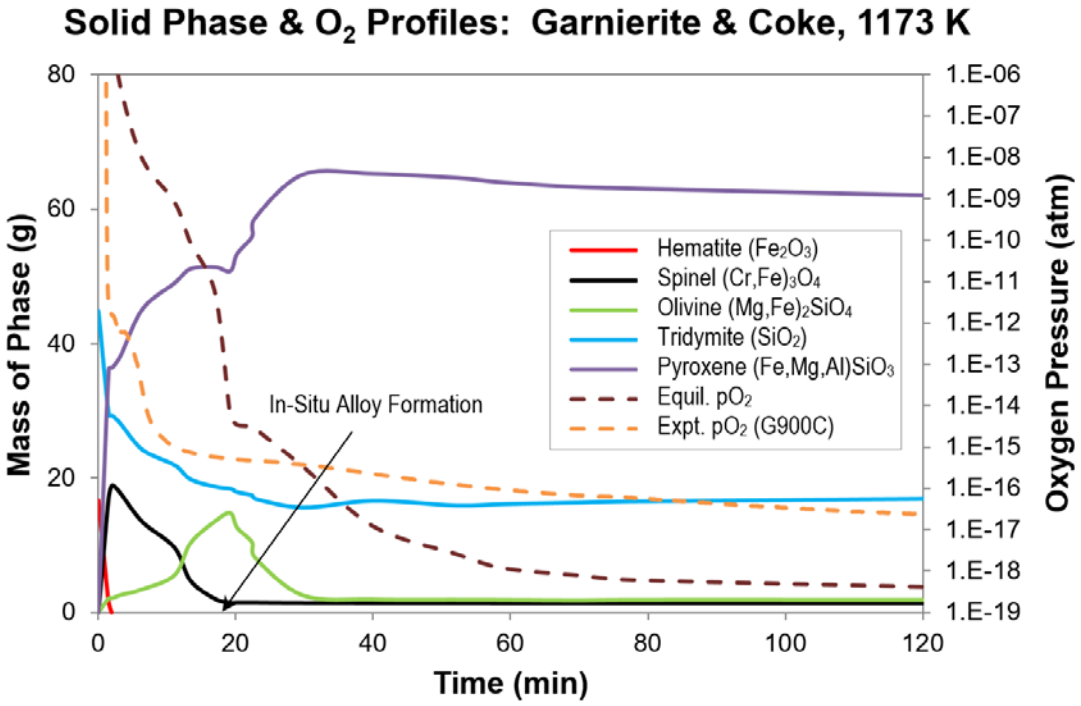

Figure 8.8 Equilibrium Simulation of Garnierite Segregation with Coke, 1173 K

Phase profiles are for 100 g of dried ore. The dashed brown line represents simulated p_{O_2}; the dashed orange line represents experimental p_{O_2}

An XRD analysis of the segregation production (Table 8.12) supported this view. The analysis showed that the experimental product contained significantly more free silica (29% compared to 19%) and metastable olivine (25% compared to 2%), and far less stable pyroxene (29% compared to 72%) than predicted by the simulation.

The simulated solid phase transformations and p_{O_2} profiles for segregation with coke and activated carbon at 1223 K (Appendix B.8) show similar patterns as for coke at 1173 K (Figure 8.8).

The poor agreement between the simulation and experimental system was reinforced by the measured times for the conversion of iron oxides (assessed from Figure 8.9) which were longer than predicted by the simulation (Table 8.11).

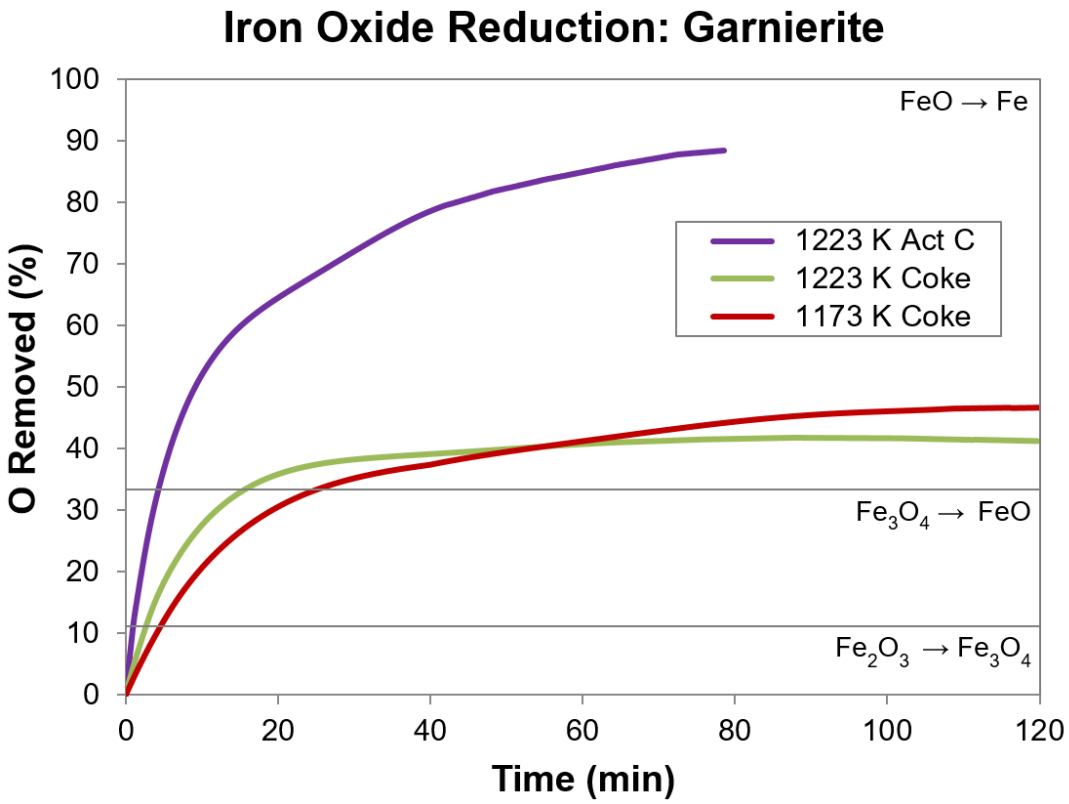

Figure 8.9 Removal of O from Iron Oxides, Garnierite Segregation

O removed in carbonaceous gas (Appendix A.4): 11.1% O removal represents $Fe_2O_3 \rightarrow Fe_3O_4$; 33.3% represents $Fe_3O_4 \rightarrow FeO$; 100% represents $FeO \rightarrow Fe$.

Table 8.11 Iron Oxide Conversion Times, Garnierite Segregation

Carbon	Temp (K)	$Fe_2O_3 \rightarrow \mathbf{Fe_3O_4}$ (minutes)		$Fe_3O_4 \rightarrow \mathbf{FeO}$ (minutes)	
		Experimental	Simulated	Experimental	Simulated
Coke	1173	4.5	2	24.9	19
Coke	1223	2.7	1.1	15.5	10
Act C	1223	1.0	0.4	4.3	3

Table 8.12 Solid Phases in the Garnierite Segregation Product

Experimental composition determined by quantitative XRD after segregation for 70 minutes with coke at 1173 K; the simulated values are for these conditions.

Phase	Experimental		Simulated	
	wt%	Major Component	wt%	Major Component
Pyroxene	29	NS	72	$(Fe,Mg,Al)_2Si_2O_6$
Silica	29	Quartz	19	Tridymite
Olivine	25	Mg_2SiO_4	2	$(Fe,Mg)_2SiO_4$
Feldspar	9	$CaAl_2Si_2O_8$	5	$CaAl_2Si_2O_8$ & $NaAlSi_3O_8$
Amorphous	9	-	NP	NP
Spinel	N	NP	2	$(Cr,Fe)_3O_4$
NP = Not Present, NS = not specified				

8.2.4 Comparison of Nickel Recovery

The maximum Ni recoveries from segregation (Table 8.2) and reduction (Table 5.9) are compared in Table 8.13. The recoveries were similar at 1223 K with coke, but higher for segregation at 1173 K, and also for segregation at 1223 K with activated carbon. These differences were attributed to in-situ reduction to ferronickel during segregation.

Table 8.13 Comparison of Maximum Nickel Recovery, Garnierite

Recovery from selective bromine/methanol leach of segregation/reduction product. Maximum segregation recoveries from Table 8.2; maximum reduction recoveries from Table 5.9.

Carbon	Temperature (K)	Maximum Ni Recovery (%)	
		Segregation	Reduction
Coke	1173	50	37[1]
Coke	1223	65	65
Act C	1223	48	28[2]

[1]Averaged: 3 pts; [2]28% at 60 minutes, 11% (2pts) at 80 minutes

8.2.5 In-Situ Reduction to Ferronickel

Noticeable in-situ reduction to ferronickel occurred when segregation of garnierite was carried out with coke at 1173 K (Figure 8.2). More in-situ ferronickel would be expected to form when segregation was carried out using coke or activated carbon at 1223K. This likely explains why the Ni recovery by segregation was greater than

for reduction at 1173 K (where in-situ reduction to alloy relative to segregation was less) but similar at 1223 K (where in-situ reduction relative to segregation was greater). The recovery from segregation with activated carbon at 1223 K was only 48% but still 1.7x better than achieved from reduction alone.

When the experimental p_{O_2} values were used in the equilibrium simulation (method described in Section 6.3.2), ferronickel was predicted to form under all experimental conditions after ~10 minutes, and ferronickel did form in all segregation tests.

There was clearly a greater tendency for in-situ ferronickel formation when segregating garnierite compared to nontronite or limonite, since when segregating these calcines, ferronickel did not form when using coke, even when it was predicted to form.

This likely can be explained by the relativity high initial concentration of NiO within the chlorite dehydroxylate of the garnierite calcine (Table 4.11), and the stronger reducing conditions since only a relatively small amount of iron oxide was present (Table 5.1) to buffer the fall in oxygen pressure. It appeared that, under all conditions, chloridisation was unable to reduce the a_{NiO} quickly enough to prevent the p_{O_2} in the bulk gas falling below the critical value for in-situ ferronickel formation. Less in-situ ferronickel would be expected if 2-3% rather than 5% coke was used, as in other segregation studies on garnierite ore (Table 2.6).

8.3 Ferronickel

The cumulative grade of the ferronickel (Ni%) as listed in Table 8.1, is shown in Figure 8.10 as a function of segregation time, with the trend lines drawn rather than fitted; the instantaneous grade is shown in Figure 8.11.

As for nontronite and limonite segregation, the ferronickel grade appears to be kinetically controlled. The grade became leaner in Ni (and richer in Fe) over time as the Ni segregation rate (Table 8.2) decreased relative to the Fe segregation rate (Table 8.5). The grade also decreased with increasing temperature and carbon surface area, since these changes promote the segregation of Fe over Ni.

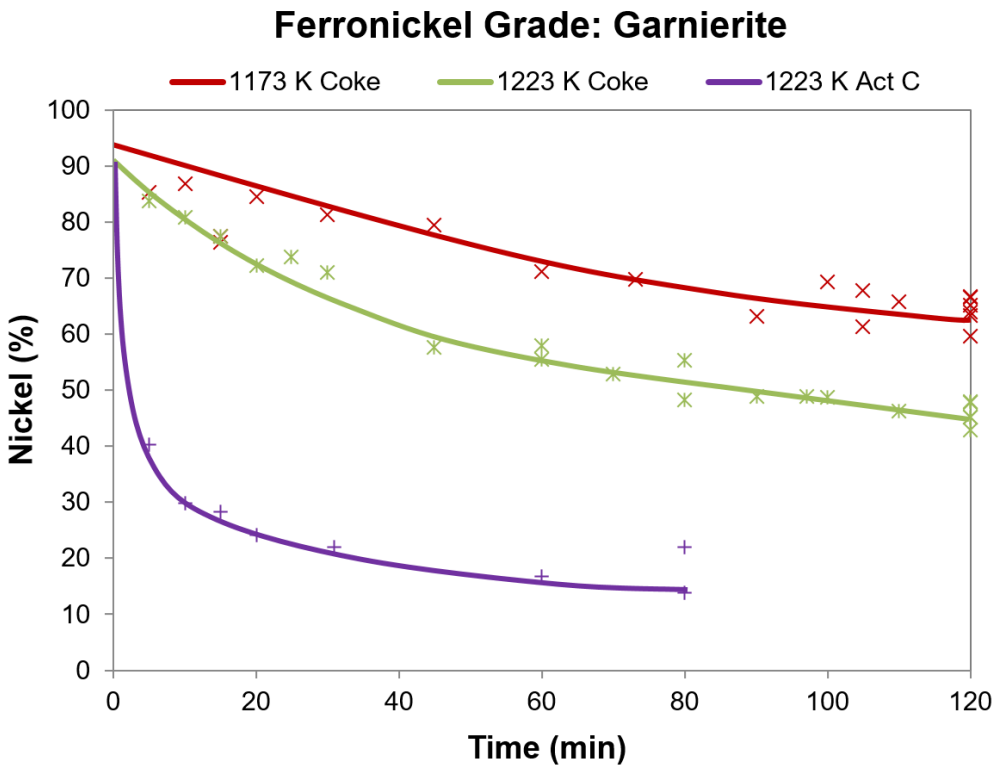

Figure 8.10 Ferronickel Grade, Garnierite Segregation

Cumulative ferronickel grade for garnierite segregation; data from Table 8.1.

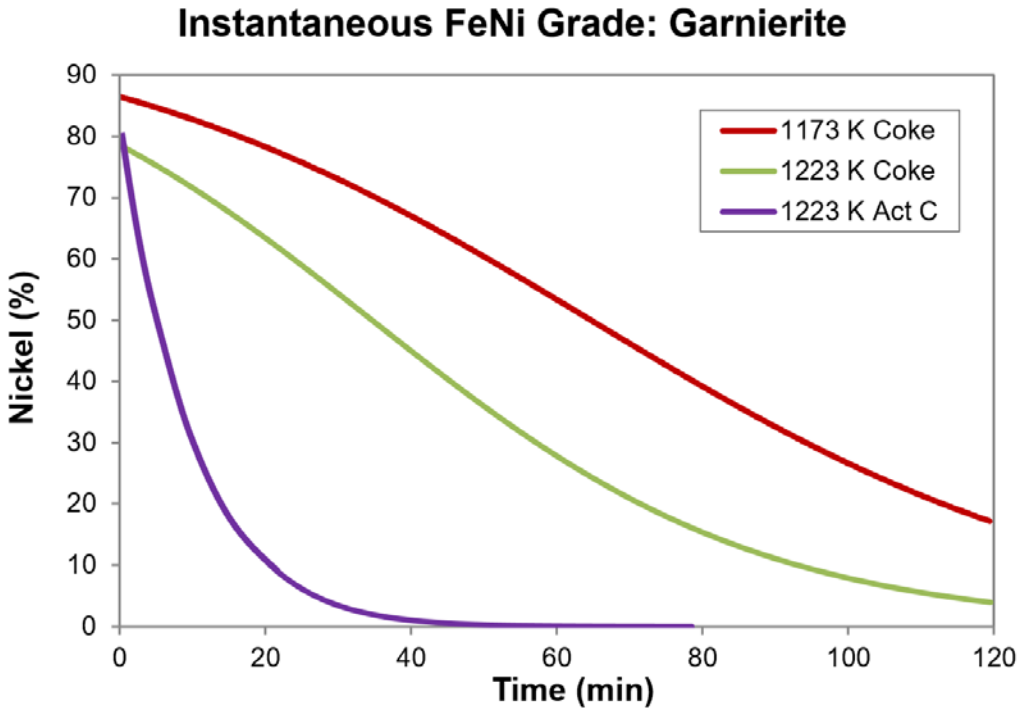

Figure 8.11 Instantaneous Ferronickel Grade, Garnierite

Data are calculated from the integrated rate equations for Ni (Table 8.2) and Fe recoveries (Table 8.5), averaged over 5 second intervals.

8.4 Chloride

The deportment of chloride during the segregation process is examined in this section.

8.4.1 Residual Chloride

The amounts of Ni, Fe, and Ca present as chlorides within the solid segregation product as determined by a water leach (Section 3.3.5) are summarised in Table 8.14, along with the recovery of total Cl and the $FeCl_2/NiCl_2$ mole ratio. The full set of data is presented in Appendix B.10. The residual $CaCl_2$ during segregation with coke at 1173 K is shown in Figure 8.12.

Table 8.14 Residual Soluble Chlorides, Garnierite Segregation

Carbon	Temp (K)	Recovery (%) as Soluble Chloride				$FeCl_2/NiCl_2$ (Mole Ratio)
		Ni	Fe	$CaCl_2$	Total Cl	
Coke	1173	0.5-4.0	3.0-6.0	18-58	42-63	5-90
Coke	1223	1.1-3.5	2.3-6.0	9.0-44	21-72	10-45
Act C	1223	1.0-5.0	4.0-8.0	17-40	39-76	15-35

Recoveries of Co and Mg as chlorides were negligible.

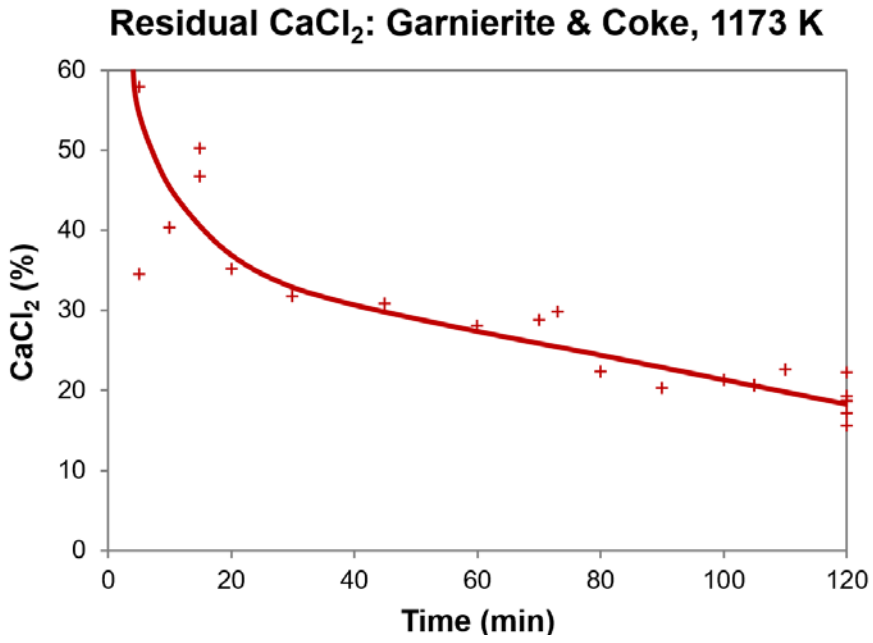

Figure 8.12 Residual $CaCl_2$, Garnierite with Coke at 1173 K

Residual $CaCl_2$ is relative to the initial 5 g $CaCl_2$/100 g of dried ore.

The trend line is drawn and not fitted.

Table 8.14 shows that 9-58% of the original $CaCl_2$ remained after segregation. The chloride residue also contained up to 8.0% of Fe as $FeCl_2$ and 5% of Ni as $NiCl_2$. Figure 8.12 shows that 35% of the $CaCl_2$ is retained after 20 minutes, compared to 43% retained for limonite (Figure 7.17) and 13% for nontronite (Figure 6.23).

The chloride loss for limonite calcine was relatively small since it contained only a small amount of silica to promote the $CaCl_2$ hydrolysis. The loss for nontronite was relatively large since it contained a significant amount of very fine silica (<10 µm, Table 4.6). Garnierite contained at least as much free silica a nontronite, but of a larger size (45-250 µm, Figure 4.9), and the loss of chloride was less than for nontronite. Garnierite may also release moisture relatively slowly, as noted by Rey et al. (1972b), who found that garnierite released measurable water for up to 84 minutes during segregation (Section 2.4.3).

8.4.2 HCl in the Off-Gas

The amount of HCl in the off-gas (Section 3.3.4) as a percent of the original chloride added as $CaCl_2$ is shown in Figure 8.13. The loss was greater at 1173 K compared to 1223 K, because the calcine retained a greater amount of moisture for release at the lower temperature (Table 4.3). The total chloride loss recorded as HCl in the off-gas was 12.5% at 1173 K and 7.0% at 1223 K after 120 minute segregation with coke.

The estimated maximum pressure of HCl in the off-gas versus time is shown Figure 8.14. The p_{HCl} at 1173 K fell from 0.20 to 0.04 atm during the first 20 minutes before becoming steady, consistent with a decreasing and then steady release of moisture from the ore; at 1223 K, the p_{HCl} stayed relatively constant at ~0.05 atm. Table 8.15 shows the equilibrium p_{HCl} and p_{H_2O} values based on the formation of $CaSiO_3$ during $CaCl_2$ hydrolysis.

8.4.3 HCl Recycle

The amount of HCl recycled during segregation was calculated as before (Section 6.4.3) as the rate of HCl produced by reduction of $FeCl_2$ and $NiCl_2$, minus the rate at which HCl lost in the gas. Figure 8.15 and Figure 8.16 show the recycle profiles at 1173 K and 1223 K respectively. All rates are presented in moles per minute per gram of dried ore (mol/min g_{ore}), and the percent of HCl recycled is shown in each figure by the dashed line.

After the initial period of high gas loss, the recycle efficiency increased above 80%, since the p_{HCl} in the gas was relatively low at both temperatures (0.04-0.06 atm), and approached 100% as gas evolution slowed over time.

Table 8.15 Maximum HCl and H_2O Pressures in Off-Gas, Garnierite

p_{HCl} values are from Figure 8.14; p_{H_2O} values are estimated from $CaCl_2$ hydrolysis in presence of silica, for which $p_{H_2O} = p_{HCl}^2 / K_{2.10}$ for pure phases.

Time (minutes)	1173 K Max. Pressure (atm)		1223 K Max. Pressure (atm)	
	HCl	H_2O	HCl	H_2O
0	0.20	0.037	0.05	0.002
40	0.04	0.001	0.06	0.002
80	0.04	0.001	0.05	0.002

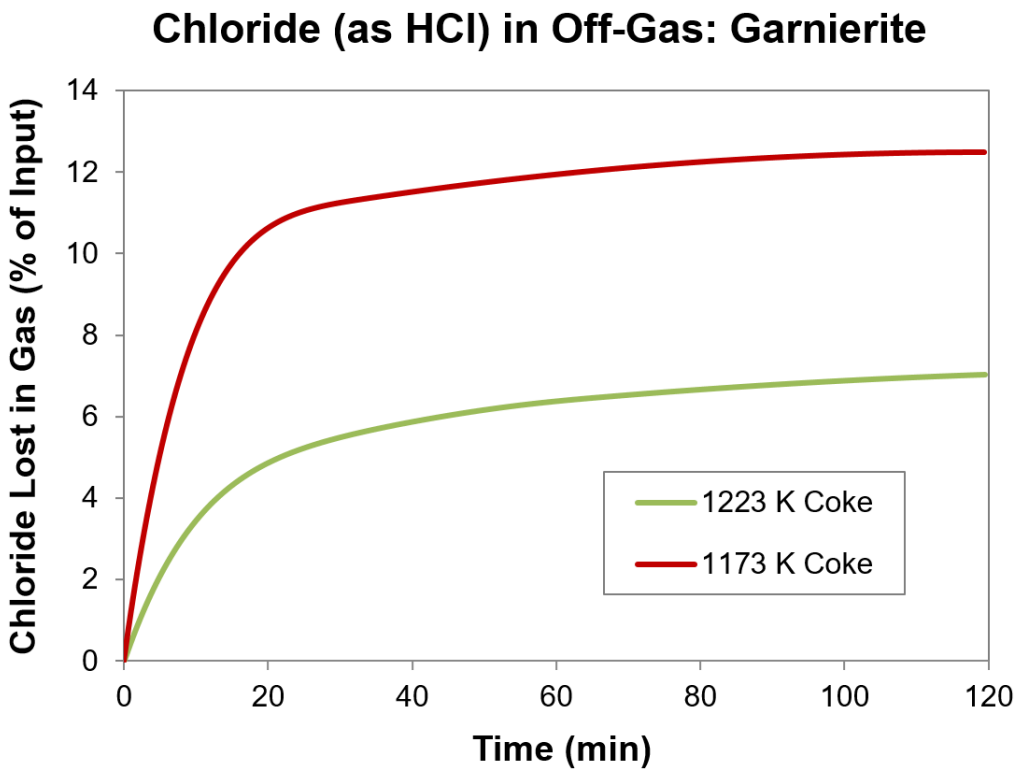

Figure 8.13 Chloride as HCl in the Off-Gas, Garnierite with Coke

Chloride input as $CaCl_2$, with 5 g/100 g of dried ore. Each profile averaged from two tests with ~2 minute lag time discounted from the time scale (Appendix B.9).

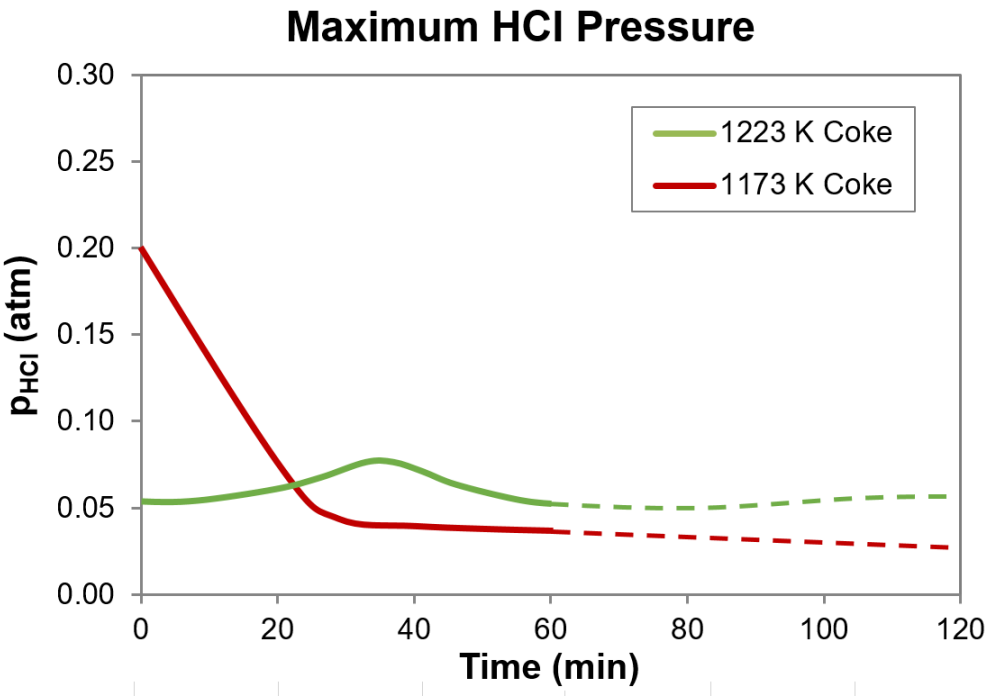

Figure 8.14 Maximum Possible HCl Pressure in Off-Gas, Garnierite

Calculated at a total pressure of 1 atm from the cumulative HCl and $CO+CO_2$ in the off-gas (Figure 8.13 and Appendix B.4 respectively), excluding H_2O and $FeCl_2$; the data are less reliable after 60 minutes due to low gas evolution.

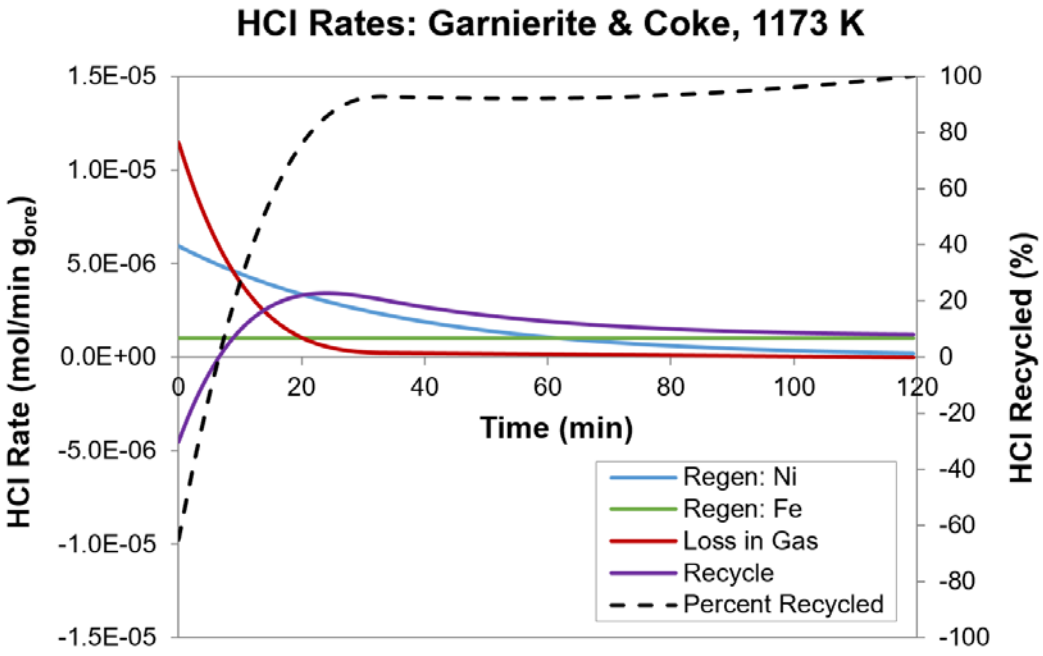

Figure 8.15 HCl Regen, Loss and Recycle Rates, Garnierite with Coke, 1173 K

Regen: Ni and Regen: Fe are the rates at which HCl is regenerated by chloride reduction through Equations 2.24 and 2.25 respectively.

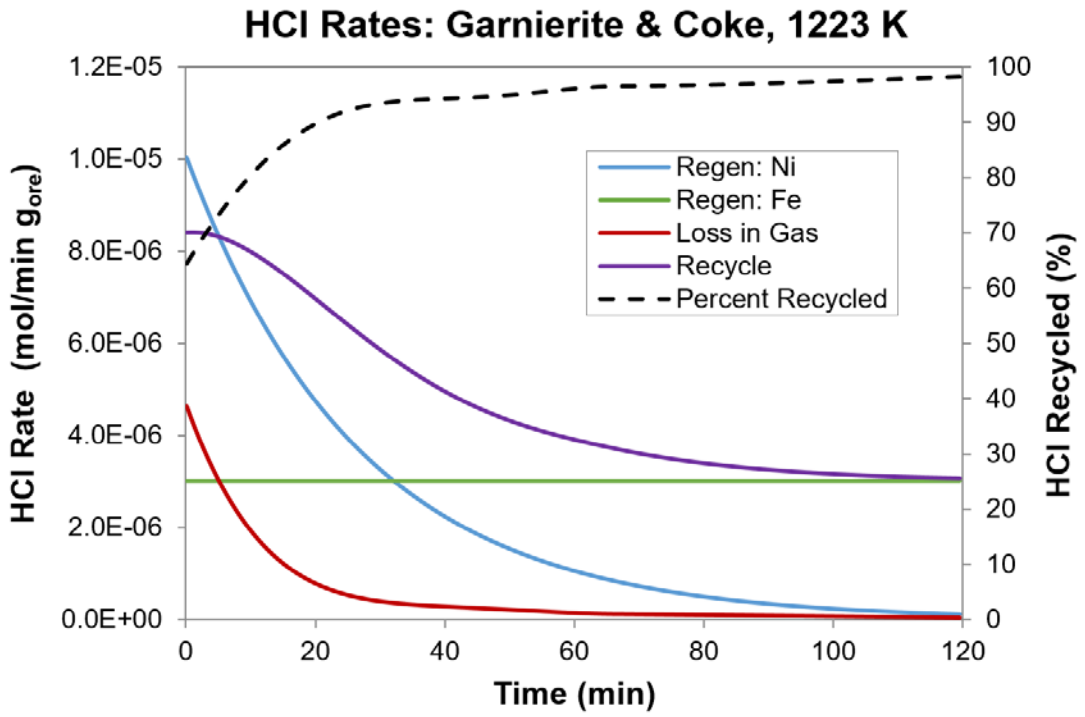

Figure 8.16 HCl Regen, Loss and Recycle Rates, Garnierite with Coke, 1223 K

Regen: Ni and Regen: Fe are the rates at which HCl is regenerated by chloride reduction through Equations 2.24 and 2.25 respectively

8.5 Effect of Roasting Conditions

The three non-standard roasting conditions used in these tests are summarised in Table 8.16, and described in Section 6.5. The averaged values for metal recoveries and ferronickel grades from segregation after using the non-standard roasts are summarised in Table 8.17, along with the comparative data using the standard roast. Data for the individual non-standard tests are presented in Appendix B.11.

Table 8.16 Non-Standard Conditions for Air Roast, Garnierite

Garnierite dehydroxylation (2nd stage) begins at 1023 K (Section 4.1.6); sintering temperature is 1283 K (Table 4.2).

Roast	Time	Temperature Set Point	Temperature (K)
Low Temp	3 days	Just below ore dehydroxylation	~923
Rapid	15 min	Just below ore sintering	~1273
High Temp	3 hrs		

Table 8.17 shows that metal recoveries from the non-standard roasts were higher (49-57%) than the recovery after 80 minutes using the standard roast and segregation methods. Since all of the non-standard roasts gave superior results, it is possible the improvement was related to the modified one-step segregation method rather than the roasting method.

Table 8.17 Effect of Roast Type on Garnierite Segregation

Mass fraction of retained water is calculated from weight change relative to the maximum possible change (Table 4.2); segregation for 80 minutes at 1173 K with 5% coke and 5% $CaCl_2$, based on dried ore.

Roast	Retained Water (mass fraction)	Recovery (%)			FeNi Ni(%)	Residual $CaCl_2$ (%)
		Ni	Fe	Co		
Low Temp	$1.1x10^{-2}$	49	2.6	21	67	20
Rapid Heat	$2.9x10^{-3}$	51	2.7	22	67	32
High Temp	$8.5x10^{-4}$	57	2.9	24	68	31
Standard*	$8.0x10^{-3}$	43	1.4	14	67	29

*Standard values taken from fitted equations: Ni (Table 8.2), Fe (Table 8.5), Co (Table 8.6)

In the one-step method, $CaCl_2$ and coke were added to the roasted calcine at room temperature, and hence were present during the heating to the segregation temperature. It is possible that an amount of Ni was segregated as the calcine approached the segregation temperature, thus reducing the likelihood of in-situ ferronickel by decreasing the a_{NiO} early in the reaction.

The prolonged high temperature roast gave the highest Ni recovery, in contrast to the work of Rey et al. (1972a), who found that prolonged roasting of garnierite at higher temperatures locked up the Ni in silicates and reduced recovery (Section 2.4.8). However, Rey et al. (1972a) used mildly reducing conditions in which iron oxides could potentially form silicates rather than be present as hematite during air roasting as used here.

The cumulative HCl reporting to the off-gas for each non-standard roast/modified segregation test is shown in Figure 8.17 as a percent of the total chloride added as $CaCl_2$. The trends shown are similar to those for nontronite and limonite and confirm that release of HCl was dependent on the release of moisture from the calcine, which mostly occurred in the early stages of segregation.

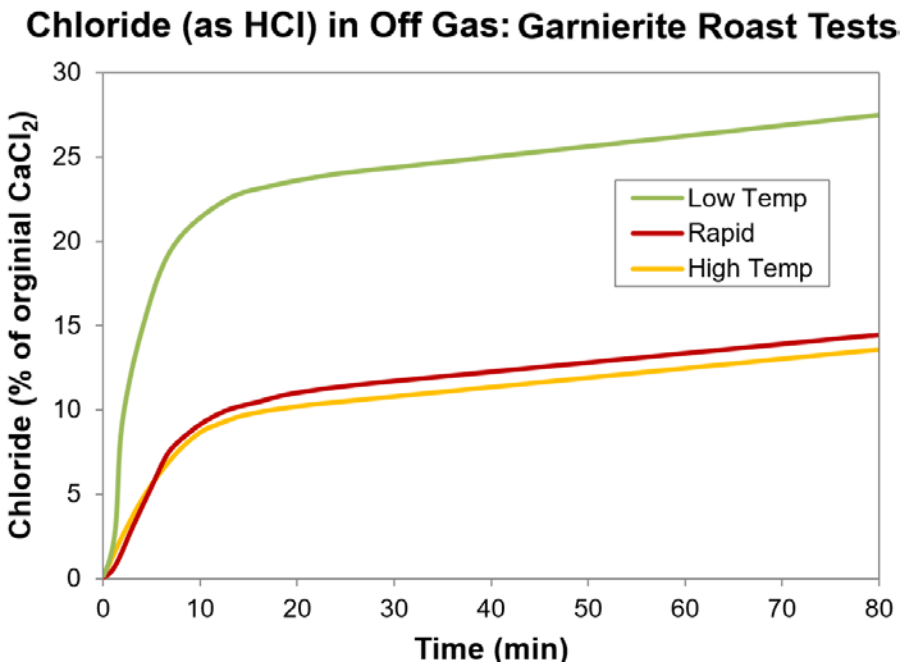

Figure 8.17 Chloride as HCl in Off-Gas, Garnierite Non-Standard Roasts

$CaCl_2$ addition was 5 g/100 g of dried ore. Each profile from a single test with ~3-4 minute lag time discounted from the time scale. (Appendix B.9).

8.6 Magnetic Concentrate

The changes in magnetic concentrate grade obtained using a Davis Tube Tester (Section 3.3.6) versus segregation time are shown in Figure 8.18; the full set of data are presented in Appendix B.6. The maximum concentrate grade was 12% and 11% with coke at 1173 and 1223 K respectively, and 6.2% at 1223 K with activated carbon; the maximum Ni upgrade ratio (Section 6.6) was 9.6 at 1173 K with coke, 8.6 at 1223 K with coke and 4.9 at 1223 K with activated carbon.

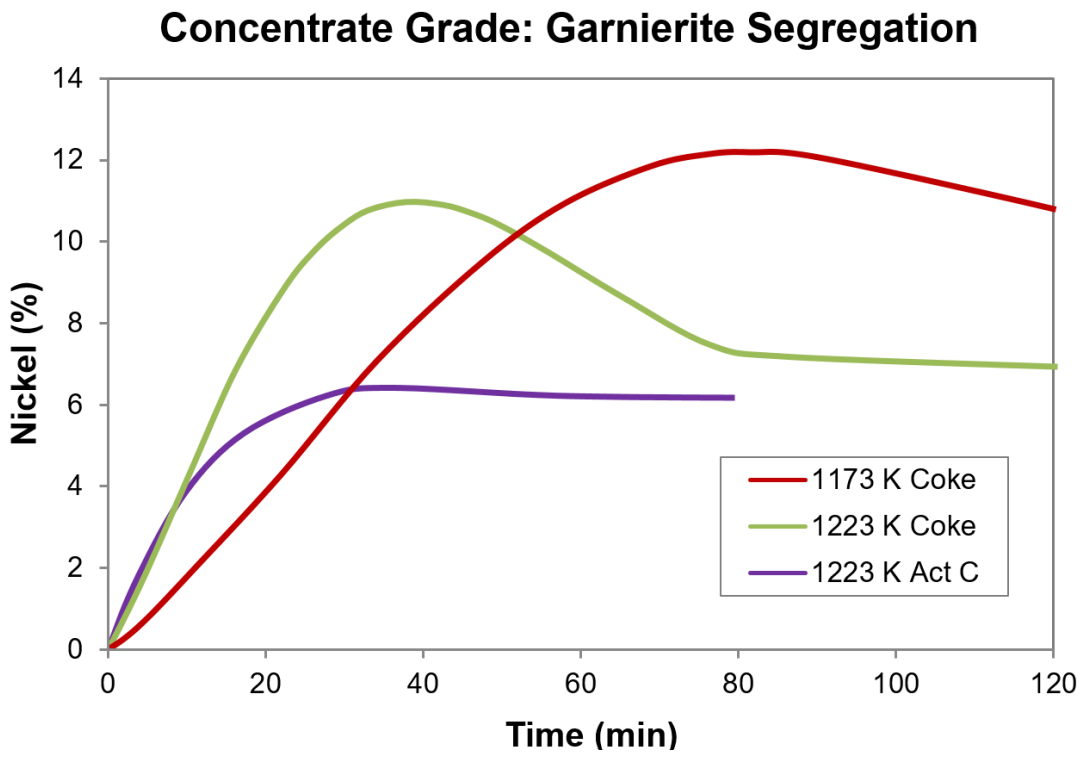

Figure 8.18 Magnetic Concentrate Grade, Garnierite Segregation

Trends are drawn rather than fitted, see Appendix B.6.

8.7 Discussion

Many of the observations regarding segregation made through the study of nontronite and limonite also apply to garnierite; some aspects will not be discussed here.

As for nontronite and limonite, the rates of Ni, Fe and Co segregation were described by 'first order to a limit' and zero order rate equations. The Fe and Co segregation rates appeared controlled by the water gas reaction, and unique to garnierite, the Ni segregation rate appeared controlled by both chloridisation and the water gas reaction.

Following a period of initially rapid Ni segregation, the rate slowed and approached a limit that increased with temperature, to a maximum of 65% Ni recovery with coke at 1223 K; the recovery with activated carbon at this temperature was only 48%. This lower recovery was indicative of the formation of in-situ ferronickel, which in contrast to both nontronite and limonite, also formed during segregation when using coke. This highlighted a greater tendency to form ferronickel when segregating garnierite, compared to either nontronite or limonite.

However, as for nontronite and limonite, Ni recoveries from segregation were at least as good as from the chloride free reduction and superior under some conditions, even with the less than ideal segregation conditions for garnierite used in this work. The presence of chloride marginally increased the rate of carbon gasification and consumption via the Boudouard reaction when using coke, but the oxygen pressure profiles were very similar. The experimental oxygen pressures were higher than the equilibrium-simulated values likely because of kinetic restrictions with the formation of silicates; however, the oxygen pressure still seemed to be controlled by metastable iron oxides and silicates in the calcine.

The amount of HCl in the off-gas and residual chloride after segregation were both consistent with the influence of moisture on the $CaCl_2$ hydrolysis reaction and the availability of silica. The HCl loss increased as the moisture released from the ore increased. The residual chloride was greater than for nontronite, which contained significant fine silica to promote calcium silicate formation, and less than for limonite, which contained only minor free silica.

Within garnierite calcine, the Ni was more concentrated within fewer particles. Most of the Ni was concentrated within a chlorite dehydroxylate, making it more difficult for the Ni concentration to be lowered by chloridisation before in-situ reduction to ferronickel occurred. In addition, the calcine contained a relatively small amount of iron oxides, while the carbon addition was relatively large (for garnierite segregation, at least), such that the oxygen pressure fell rapidly making in-situ reduction to ferronickel more likely.

Prior to segregation, the Ni was present at ~7.7% within finely crystalline Mg-Al silicates of chlorite dehydroxylate, and at ~2.2% within fine to amorphous Mg-Fe silicates of serpentine dehydroxylate. After segregation, up to 90% of Ni was removed from the remnant chlorite, with NiO chloridisation likely assisted by an exchange reaction with $FeCl_2$; the serpentine dehydroxylate was richer in Fe and the exchange appeared less effective, with only ~50% Ni being removed. However, since chlorite accounted for most of the Ni, only a small amount remained dissolved within the silicates. The recovery of Ni by segregation, however, was lowered because ferronickel reduced in-situ remained within the chlorite dehydroxylate.

In-situ ferronickel likely formed for all segregation tests with garnierite, and thus suppression of in-situ ferronickel is the key to improving the metal recovery. The segregation of Ni from garnierite was jointly controlled by the water gas reaction,

which indicates that the chloridisation reaction was fast compared to either nontronite or garnierite. However, the rate was insufficient to lower the initially high a_{NiO} enough to the prevent in-situ reduction of ferronickel when using 5% coke. Based on the experience of others (Table 2.6), lowering the coke from 5% to 2-3% would be the first step in decreasing the amount of in-situ ferronickel.

Another strategy for reducing in-situ reduction would be to control the change in oxygen pressure by adjusting the mineralogy through addition of iron oxides containing free silica. The formation of iron silicate during the reduction buffers the fall in oxygen pressure, as demonstrated for nontronite (Section 5.4.3). The addition of iron oxides to garnierite type ores has improved Ni recovery in previous work (Section 2.4.9). The effect was attributed to the release of NiO from Mg silicates through a solid-solid exchange with iron silicate.

However, if the NiO is mainly associated with fine silicate veins within crystalline silica, as in the current ore (Figure 8.2), the required solid-solid contact for such an exchange may be limited. Most likely, when previously successful, the addition of iron oxides improved Ni recovery by buffering the fall in oxygen pressure which reduced in-situ reduction. This is supported by the observations of Davidson (1972) who noted in passing that “the addition of iron oxides also greatly decreased the quantity of ferronickel present as small inclusions within the olivine particles”.

The improvement in Ni recovery found for the non-standard roasts highlights another possible strategy for reducing in-situ Ni during garnierite segregation. The results indicate that it may be advantageous to carry out segregation at a lower temperature to segregate the highly reactive NiO under less reducing conditions, before increasing the temperature to finalise the segregation of the less reactive NiO. This may explain the two-stage segregation method for garnierite proposed by Titova et al. (1975), in which segregation was initiated at a lower temperature (~1073 K) and then completed at a higher temperature (~1273 K).

The maximum recoveries by segregation of garnierite were ~65% of the Ni along with ~45% of the Co and ~9% of the Fe; this was achieved with multiple tests at 1223 K with coke. Based on the options available, it seems likely that the maximum Ni recovered by segregation from the garnierite ore may be increased well above 65%. A recovery of at least 85% seems possible given that most of the Ni had been reduced from the silicates and that recoveries up to 93% have been obtained elsewhere for garnierite ores (Table 2.6).

Chapter 9

Conclusion

A detailed fundamental study of the segregation process for the recovery of Ni from laterite ores was carried out to provide a better understanding of the process and the potential for its application to Western Australian nickel laterite ores. This work focused on nontronite, an ore uniquely dominant within the WA laterite profile, although limonite and garnierite were also studied to provide a mineralogical contrast.

Segregation was confirmed to be a non-equilibrium carbon reduction process that operates via a chloride intermediate. The process operates in parallel and in direct competition with in-situ reduction of roasted ore by the bulk gas. Ferronickel that is reduced in-situ is finely dispersed and difficult to recover; ferronickel that forms through segregation is coarse and readily accessible. For segregation to be successful, it must occur before in-situ reduction by the gas to form ferronickel.

The rate of Ni segregation appears dominantly dependant on the rate of chloridisation of NiO from the calcine. The rate is rapid at first but then slows to a limit, which increases with temperature. The initial rate must be rapid enough to reduce and maintain the NiO in the calcine at a concentration low enough to prevent in-situ reduction by the gas. For optimal Ni recovery, the rate must also be fast enough to remove as much NiO from the calcine as possible, before it forms solutions within silicates at a reduced activity.

The kinetic data provided valuable insight into the likely rate controls for Ni, Fe and Co segregation. The rate control for Ni segregation appeared to depend mainly on the chloridisation of NiO, but the rate can also depend on the water gas reaction when the resistance to NiO chloridisation is reduced. This can occur when concentrated areas of NiO exist within the calcine, as found within garnierite. Fundamentally, the Ni segregation rate depends on the activity of NiO and the partial pressures of HCl and $FeCl_2$ in the gas, and evidence was found to directly support the participation of $FeCl_2$ in the NiO chloridisation process. However, the accuracy of the kinetic data was insufficient for incorporation of these parameters into a fundamental rate equation.

The isothermal rate of recovery of Fe was found to be constant for all three ores, but increased with temperature. The rate was controlled by the water gas reaction which fundamentally depends on the partial pressure of H_2O and the available surface area of carbon. The rate control for Co segregation was likely chloridisation, with some dependence on the water gas reaction.

The grade of the segregated ferronickel was kinetically controlled by the relative rates of Ni and Fe segregation. The grade became richer in Fe with increase in time and temperature and as the CO_2/CO in the bulk gas decreased. However, unlike the grade of in-situ ferronickel, the grade of segregated ferronickel was not directly dependent on the carbonaceous gas composition. There was a correlation because the factors that reduced the CO_2/CO in the gas also increased the rate of Fe segregation relative to Ni segregation, thus reducing the grade.

The recovery of Ni from chloride free reduction and from segregation is strongly dependent on mineralogy, as demonstrated through the behaviour of three distinctly different ores. The oxygen pressure profile during reduction and segregation was uniquely dependant on the mineralogy, especially the relative amounts of hematite and free silica, with the formation of iron silicates, for example, able to buffer the oxygen pressure at higher levels during the reduction of nontronite, compared to the other ores.

In addition to the temperature and available carbon, the rate of reduction was also dependent on the effect of minerals within the calcine on the carbon surface, which can either slow or accelerate the rate of reduction. In all cases, the presence of chloride catalysed the reduction. The effect of mineralogy was well illustrated by the rate of carbon consumption with nontronite; this was dramatically less during reduction in the absence of chloride, but much more rapid and similar to the other ores during segregation.

The hydrolysis of $CaCl_2$ is critical to the process since the reaction generates HCl for chloridisation while absorbing and controlling the H_2O content in the gas so that Ni and Fe chlorides are stable. The effectiveness of hydrolysis was also dependent on mineralogy, since sufficient free silica must be present to form $CaSiO_3$ to promote the reaction. Unique to limonite, segregation began only after an induction period in which little or no chloridisation occurred because the hydrolysis was unfavourable. This was likely caused by the initial presence of a large amount of hematite; with

only minor silica in the calcine, this resulted in the unfavourable formation of calcium ferrite rather than calcium silicate as the product of hydrolysis.

Ni and Fe chlorides are susceptible to hydrolysis and the effect of retained moisture within the calcine on Ni segregation had been studied by others, with conflicting results. Non-standard roasts were used to assess this effect and the results confirmed that provided sufficient $CaCl_2$ was available for hydrolysis, the amount of retained moisture had little effect on Ni recovery. From the results of earlier studies, it was considered that extended roasting times were detrimental to Ni segregation. Those roasts were carried out under mildly reducing conditions that likely promoted the transformation of iron oxides to silicates that dissolved the NiO. No effect of extended roasting time was observed in this work, highlighting the advantage of roasting in air to stabilise the iron oxides as hematite prior to segregation.

Measurement of the HCl within the off-gas and residual chlorides confirmed that sufficient $CaCl_2$ was present for all segregation tests to maintain chloridisation, and that the recycle of HCl was relatively efficient. The impact of mineralogy was again evident with the residual chloride being least for the nontronite since it contained the most free silica to promote hydrolysis.

Examination of the location of Ni within the calcine before and after segregation using EDS-SEM showed that Ni was evenly distributed throughout the iron oxides within limonite, at 1% before and <0.03% after segregation. The Ni within nontronite was located within fine to amorphous hematite/silica mixtures at a concentration of 1.6% while the unsegregated material remained within finely crystalline iron silicates. The Ni within garnierite was mainly associated with finely crystalline Mg-Al silicates at a concentration of 7.7%, compared to 1.3% within the ore; most of the unsegregated Ni remained as in-situ reduced ferronickel within the silicate.

The three ores were roasted and segregated under standardised rather than optimised conditions to facilitate comparison of mineralogical and other factors affecting the process. Under these conditions, in-situ ferronickel was suppressed by segregation when using coke with both limonite and nontronite; it only formed when using activated carbon. In-situ ferronickel formed under all conditions when segregating garnierite. This likely occurred because the high local concentration of NiO made it susceptible to in-situ reduction, and the oxygen pressure fell too quickly because the coke addition was relatively large compared to the amount of iron oxides in the calcine.

The recovery of Ni by segregation under the adopted standardised conditions was greatest for limonite, intermediate for nontronite and least for garnierite, as illustrated at 1173 K in Figure 9.1 for segregation with 5% coke and 5% $CaCl_2$. The Ni recoveries after 120 minutes are ~80% for limonite, ~60% for nontronite and ~50% for garnierite. Higher recoveries of ~80% were achieved for nontronite when the temperature was increased to 1273 K, and ~65% for garnierite when the temperature was increased to 1223 K.

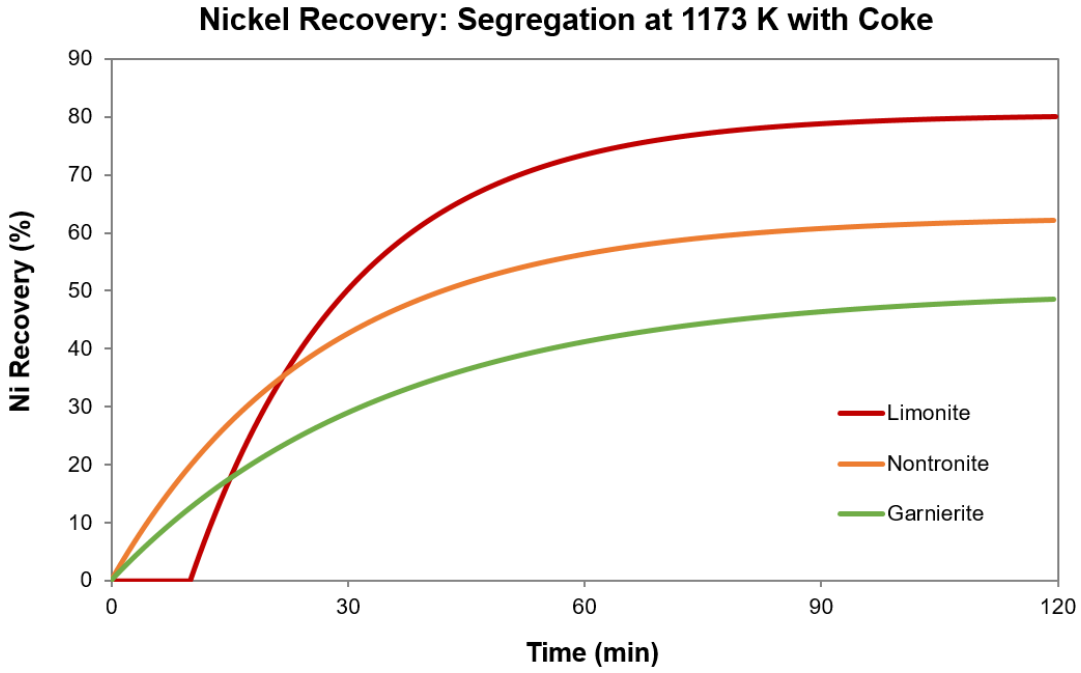

Figure 9.1 Ni Recovery from WA Laterites, Segregation at 1173 K with Coke

$CaCl_2$ and coke addition was 5 g/100 g of dried ore.

Maximum Ni recoveries of 85% seem possible for nontronite and likely for garnierite when using optimisation strategies developed from this work. These strategies focus on increasing the rate of NiO chloridisation to maximise the initial removal of NiO from the calcine, while lessening the fall in oxygen pressure to minimise the in-situ reduction of NiO in the calcine. Optimisation studies for the segregation of laterite ore would benefit from careful monitoring and minimisation of in-situ ferronickel formation as a prerequisite for the maximisation of Ni recovery by segregation.

Virtually under all conditions tested in this work, segregation proved superior to in-situ reduction with carbon, and likely would be superior to any reduction that produces in-situ reduced ferronickel. A pilot scale process using a mechanical kiln has been developed for Ni segregation (Ericson and Svensson, 1985), in an attempt

to overcome well-documented challenges concerning the need to deliver heat to the endothermic reaction without disturbance from burner gas (Warner et al. 1972). On balance, segregation seems to offer an attractive process for the reduction and upgrading of Ni laterites; however, the influence of mineralogy is such that the response of a laterite would be difficult to predict without adequate testing.

References

ALCOCK, R. A. The Character and Occurrence of Primary Resources Available to the Nickel Industry. *In:* TYROLER, G. P. & LANDOLT, C. A., eds. Extractive Metallurgy of Nickel and Cobalt, January 25-28 1988 Phoenix, Arizona. TMS, 67-89.

AVRAAMIDES, J. 1982. A Roast-Leach Method for Recovering Valuable Metals from Nickel Refinery Copper Sulphides Precipitates. *Proc. Australas. Inst. Min. Metall.,* 284**,** 55-62.

BADWAL, S., BANNISTER, M. & GARRETT, W. 1987. Oxygen Measurement with $SIRO_2$ Sensors. *J. Phys. E: Sci. Instrum.,* 20**,** 531-540.

BALE, C., BÉLISLE, E., CHARTRAND, P., DECTEROV, S., ERIKSSON, G., HACK, K., JUNG, I., KANG, Y., MELANÇON, J., PELTON, A., ROBELIN, C. & PETERSEN, S. 2009. FactSage Thermochemical Software and Databases — Recent Developments. *Calphad,* 33**,** 295-311.

BALL, M. C. & TAYLOR, H. F. W. 1963. The Dehydration of Chrysotile in Air and Under Hydrothermal Conditions. *Mineralogical Magazine,* 33**,** 467-482.

BATTLE, T., LEARY, K., REEVES, J., ERICSON, A. S. & ZANDER, B. Reduction-Segregation Of Ilmenite: Iron And Titanium Co-Products From Solid-State Processing. Extraction and Processing for the Treatment and Minimization of Wastes, 1996 Phoenix, Arizona. TMS.

BEAR, I., MERRIT, R. & TURNBULL, A. 1976. Mechanism of Segregation of Lead Sulphide from Lead Sulphate. *Trans. Inst. Min Metall. C,* 85**,** C63-C67.

BEAR, I., MORESBY, J. & CURNICK, L. 1977. The Treatment of Smelter Fume prior to Segregation Roasting. *International Journal of Mineral Processing,* 4**,** 69-81.

BEAR, I., MORESBY, J. & WOODS, G. 1983. Removal of Copper from Oxidized Nickel Matte by Segregation-Roasting. *International Journal of Mineral Processing,* 11**,** 1-17.

BEAR, I. J. & MERRIT, R. R. 1975. Treatment of Lead Sulphate Materials by the Segregation Process. *Trans. Inst. Min Metall. C,* 84**,** C92-C98.

BEAR, I. J. & MORESBY, J. F. 1978. Recovery of Copper from Refractory Furnace-Lining Bricks by Segregation Roasting. *Proc. Australas. Inst. Min. Metall.,* 266**,** 21-27.

BRAND, N., BUTT, C. & ELIAS, M. 1998. Nickel Laterites: Classifications and Features. *AGSO Journal of Australian Geology & Geophyscis,* 17**,** 81-88.

BRINDLEY, G. & HAYAMI, R. 1965. Mechanism of Formation of Forsterite and Enstatite from Serpentine. *Mineralogical Magazine,* 35**,** 189-195.

BRINDLEY, G. W. & CHANG, T. 1974. Development of Long Basal Spacings in Chlorites by Thermal Treatment. *American Mineralogist,* 59**,** 152-158.

BRITTAN, M. 1970. Kinetics of Copper Segregation by the TORCO Process. *Journal of the South African Institute of Mining and Metallurgy***,** 278-289.

BRITTAN, M. 1971. A Kinetic Model of Copper Segregation and its Application to TORCO Plant Design. *Trans. Inst. Min Metall. C,* 80**,** C262-C272.

BRITTAN, M. & LIEBENBERG, R. 1971. A Kinetic Analysis of the TORCO Copper Segregation Process. *Trans, Inst. Min Metall. C,* 80**,** C156-C169.

BRITTAN, M. & LIEBENBERG, R. 1972. Nickel Segregation Research at Anglo American Research Laboratories. Part III. Kinetics and Mechanism of Nickel Segregation. *In:* DOR, A. (ed.) *Nickel Segregation.* San Francisco, California: The AIME Metallurgical Society.

BROWN, A. M. 2001. A Step-by-Step Guide to Non-Linear Regression Analysis of Experimental Data using a Microsoft Excel Spreadsheet. *Computer Methods and Programs in Biomedicine,* 65**,** 191-200.

BUNJAKU, A., KEKKONEN, M., TASKINEN, P. & HOLAPPA, L. 2011. Thermal Behaviour of Hydrous Nickel-Magnesium Silicates when Heating up to 750°C. *Mineral Processing and Extractive Metallurgy (Trans. Inst. Min Metall. C),* 120**,** 139-146.

BUTT, C. Nickel Laterites - Characteristic, Classification and Processing Options. LEME Seminar, 28th August 2007. CRC LEME.

CANTERFORD, J. 1975. The Treatment of Nickeliferous Laterites. *Minerals Sci. Engng,* 7**,** 3-17.

CATHRO, K. 1973. Segregation and Acetonitrile Leaching Tests on Ukaparinga Copper Ore. *Proc. Australas. Inst. Min. Metall.***,** 17-21.

CHASE, C. Treatment of Manganiferous Silver Ores for Recovery of Silver in the View of Changed Precious Metals Economics. Proceedings of the 110th AIME Meeting, 22-26 February 1981 Chicago, Illinois. 23-33.

CHEN, J., JAK, E. & HAYES, C. The Recovery of Ferro-Nickel from Saprolite Ores Using Reduction Roasting. The Thirteeth International Ferroalloys Congress - Other Ferro Alloys Fundamentals, June 9 - 13 2013 Almaty, Kazakhstan. 713-722.

CHERMAK, L., ZOLKINA, M. & PRONIN, A. 1973. Liquation Roasting of Oxidized Nickel Ores. *Tsvetnye Metally/Non-Ferrous Metals,* 14**,** 16-19.

CHU, G., ZHAO, S. & YANG, T. 2012. Extraction of Nickel from Molybdenum Leaching Residue of Metalliferous Black Shale by Segregation Roasting and Acid Leaching. *Journal of Central South University,* 19**,** 340-346.

COF. 2015. *Ceramic Oxide Fabricators Australia Pty Ltd - Alumina Ceramics and Zirconia Oxygen Sensors* [Online]. Available: http://www.cof.com.au/c700sensor.shtml [Accessed 8th July 2015.

DALVI, A. D., BACON, G. & OBORNE, R. 2004. The Past and Future of Nickel Laterites. *PDAC 2004 International Convention, Trade Show & Investors Exchange.*

DATTA, P., RAY, H. & JENA, P. 1992. Segregation Reaction for Copper. *Trans. Inst. Min Metall. C,* 101**,** C171-C176.

DAVIDSON, R. 1972. Nickel Segregation Research at Anglo American Research Laboratories. Part 4. The Role of Iron Oxides in Nickel Segregation. *In:* DOR, A. (ed.) *Nickel Segregation.* San Francisco, California: The AIME Metallurgical Society.

DE WAAL, S. A. 1970. Nickel Minerals from Barberton, South Africa: II. Nimite, A Nickel-Rich Chlorite. *The American Mineralogist,* 55**,** 18-30.

DING, Z. & FROST, R. L. 2002. Controlled Rate Thermal Analysis of Nontronite. *Thermochimica Acta,* 389**,** 185-193.

DJOHARI, A., OWADA, S., HARADA, T. & GOTO, S. Application of the Segregation Process to Manganese Nodules. Proceedings of the MMIJ/IMM Joint

Symposium (Today's Technology for the Mining and Metallurgical Industry), 1989 Kyoto, Japan. 359-371.

DOR, A. 1972. The Chloro-Metallization of Lateritic Nickel Ores. *In:* DOR, A. (ed.) *Nickel Segregation.* San Francisco, California: The AIME Metallurgical Society.

ELIA, M., MCDONALD, T. & CRISP, A. 1986. Errors in Measurements of CO_2 with the Use of Drying Agents. *Clinica Chimica Acta,* 158**,** 237-244.

ELIAS, M. 2002. Nickel Laterite Deposits - Geological Overview, Resources and Exploitation. *In:* COOKE, D. R. & PONGRATZ, J. (eds.) *Giant Ore deposits - Characteristics, Genesis and Exploration.* Hobart, University of Tasmania.

ELIAS, M., DONALDSON, M. & GIORGETTA, N. 1981. Geology, Mineralogy, and Chemistry of Lateritic Nickel-Cobalt Deposits near Kalgoorlie, Western Australia. *Economic Geology,* 76**,** 1775-1783.

ERICSON, A. & SVENSSON, J. MINPRO Mechanical Kiln - A New and Efficient Tool for the Nickel Segregation Process. Extractive Metallurgy 85, 1985. IMM : London, 551-568.

ERICSON, A., SVENSSON, J. & ISHII, K. 1984. Development of the MINPRO-PAMCO Nickel Segregation Process. *JOM,* 36**,** 42-46.

ERICSON, A., SVENSSON, J. & ISHII, K. 1987. The MINPRO-PAMCO Nickel Segregation Process. *International Journal of Minerals Processing,* 19**,** 223-236.

FAZAKERLEY, V. & MONTI, R. Murrin Murrin Nickel-Cobalt Deposits. *In:* BERKMAN, D. & MACKENZIE, D., eds. Geology of Australian and Papua New Guinean Mineral Deposits, 1998 Melbourne. AusIMM, 229-334.

FENSON, D. 1981. *Processes of Iron Segregation*. United States patent application.

FERRON, C., VERMAUT, N. & SHUNGU, T. Treatment of Copper-Cobalt Oxide Ores by the Segregation Process. SME Annual General Meeting, 1992 Phoenix, Arizona.

FERRON, C., VERMAUT, N. & SHUNGU, T. Segregation Roasting of Cobalt Ores. The Paul E. Queanu International Symposium, Extractive Metallurgy of Copper, Nickel and Cobalt, Vol 1: Fundamental Aspects, 1993. 603-621.

FLORES, C. & JORDAN, T. 1993. Factors Influencing Silver Extraction from Refractory Manganiferous Silver Ores by Segregation-Cyanide Leaching. *Hydrometallurgy Fundamentals, Technology and Innovation*

FLORES, C., JORDAN, T. & TWIDWELL, L. Recovery of Silver from Manganiferous Silver Ores by Segregation Roasting-Flotation. SME Annual Meeting, Feburary 14-17 1994 Albuquerque, New Mexico.

FLORES, C., JORDAN, T. & TWIDWELL, L. 1995. Statistical Approach For The Recovery Of Silver From Manganiferous Silver Ores. *SME Transactions,* 298**,** 4-7.

FORTINI, O. M. & FRUEHAN, R. J. 2005. Rate of Reduction of Ore-Carbon Composites: Part I. Determination of Intrinsic Rate Constants. *Metallurgical and Materials Transactions B,* 36**,** 865-872.

FROST, R. L., KLOPROGGE, T. J. & DING, Z. 2002. The Garfield and Uley Nontronites - An Infrared Spectroscopic Comparison. *Spectrochimica Acta Part A,* 58**,** 1881-1894.

FRUEHAN, R. 1977. The Rate of Reduction of Iron Oxides by Carbon. *Metallurgical Transactions B,* 8**,** 279-286.

FRUEHAN, R. & MARTONIK, L. 1973a. The Rate of Chlorination of Metals and Oxide: Part II. Iron and Nickel in HCl(g). *Metallurgical Transactions,* 4**,** 2789-2792.

FRUEHAN, R. & MARTONIK, L. 1973b. The Rate of Chlorination of Metals and Oxides: Part III. The Rate of Chlorination of Fe_2O_3 and NiO in Cl_2 and HCl. *Metallurgical Transactions,* 4**,** 2793-2797.

GAUDIN, A., GRAUBY, O., NOACK, Y., DECARREAU, A. & PETIT, S. 2004a. Accurate Crystal Chemistry of Ferric Smectites from the Lateritic Nickel Ore of Murrin Murrin (Western Australia). I. XRD and Multi-Scale Chemical Approaches. *Clay Minerals,* 39**,** 301-315.

GAUDIN, A., PETIT, S., ROSE, J., MARTIN, F., DECARREAU, A., NOACK, Y. & BORSCHNECK, D. 2004b. The Accurate Crystal Chemistry of Ferric Smectites from the Lateritic Nickel Ore of Murrin Murrin (Western Australia). II. Spectroscopic (IR and EXAFS) Approaches. *Clay Minerals,* 39**,** 453-467.

GOLIGHTLY, J. Nickeliferous Laterite: A General Description. International Laterite Symposium, 1979. SME, 21.

GRIM, R. E. & KULBICKI, G. 1961. Montmorillonite: High Temperature Reactions and Classification. *The American Mineralogist,* 46**,** 1329-1369.

GROTOWSKI, A. & GROTOWSKA, M. 1990. The Mechanism of Copper (I) Sulfide Formation in the Segregation Process. *International Journal of Mineral Processing,* 30**,** 287-297.

GROTOWSKI, A. & ŻMUDZIŃSKI, K. 1987. Treatment of Sulphide-Oxide Copper Ore by Segregation. *International Journal of Mineral Processing,* 21**,** 293-305.

GUALTIERI, A. F. & VENTURELLI, P. 1999. In Situ Study of the Goethite-Hematite Phase Transformation by Real Time Synchrotron Powder Diffraction. *American Mineralogist,* 84**,** 895-904.

HADJIAT, H. 1969. *Reactions in the Segregation of Copper Ores.* PhD, University of London.

HALLET, C. J. A Thermodynamic Analysis of the Solid State Reduction of Nickel from Laterite Minerals. Proceedings of the Nickel Cobalt International Symposium, Nickel-Cobalt 97, 1997. CIM, 299-312.

HANF, N. 1972a. Nickel Segregation Research at Anglo American Research Laboratories. Part 1. Themodynamic and Kinetic Relationships in the Segregation Process. *In:* DOR, A. A. (ed.) *Nickel Segregation.* San Francisco, California: The AIME Metallurgical Society.

HANF, N. 1972b. Nickel Segregation Research at Anglo American Research Laboratories. Part 2. Hydrogen Chloride Evolution Studies in the Nickel Segregation System. *In:* DOR, A. (ed.) *Nickel Segregation.* San Francisco, California: The AIME Metallurgical Society.

HANF, N. & SOLE, M. 1970. High Temperature Hydrolysis of Sodium Chloride. *Trans. Faraday Soci.,* 66**,** 3065-3094.

HANF, N. & SOLE, M. 1972. High Temperature Hydrolysis of Sodium Chloride in the Presence of Silica. *Trans. Inst. Min Metall. C,* 81**,** C97-C103.

HARRIS, C., PEACEY, J. & PICKLES, C. Thermal Upgrading of Nickeliferous Laterite - A Review. *In:* LUI, J., PEACEY, J., BARATI, M., KASHANI-NEJAD, S. & DAVIS, B., eds. Pyrometallurgy of Nickel and Cobalt 2009 - Proceedings of the 48th Conference of Metallurgists, 2009 Sudbury, Ontario, Canada. CIM, 51-79.

HARRIS, D. J. & SMITH, I. W. 1990. Intrinsic Reactivity of Petroleum Coke and Brown Coal Char to Carbon Dioxide, Steam and Oxygen. *23rd Symposium (International) on Combustion.*

HAUL, R. A. W. & MARKUS, J. 1952. On the Thermal Decomposition of Dolomite. IV. Thermogravimetric Investigation of the Dolomite Decomposition. *Journal of Applied Chemistry,* 2**,** 298-306.

HELLSTEN, K., LEWIS, C. & DENN, S. Cawese Nickel-Cobalt Deposit. *In:* BERKMAN, D. & MACKENZIE, D., eds. Geology of Australian and Papua New Guinean Mineral Deposits, 1998 Melbourne. AusIMM, 335-338.

HOOVER, M., HAN, K. & FUERSTENAU, D. 1975. Segregation Roasting of Nickel, Copper and Cobalt from Deep-Sea Manganese Nodules. *International Journal of Mineral Processing,* 2**,** 173-185.

HUDYMA, I. 1981. Growth of Metallic Nickel Grains in the Segregation Process: 1 - Growth and Aggregation of Metallic Nickel Grains on Coal Particles. *Trans. Inst. Min Metall. C,* 90**,** C147-C151.

HUDYMA, I. 1984. Growth of Metallic Nickel Grains in the Segregation Process: 2 - Growth and Aggregation of Metallic Nickel Grains on Silica Particles. *Trans. Inst. Min Metall. C,* 93**,** C86-C91.

HUDYMA, I. 1993a. Composition of Ferro-Nickel Produced from Silicate and Magnesite Ores by Segregation Process. *Fizykochemiczne Porblemy Mineralurgii,* 27**,** 241-244.

HUDYMA, I. 1993b. Role of Segregation Process Atmosphere in Formation and Composition of Ferrornickel Grains. *Trans. Inst. Min Metall. C,* 102**,** C125-C129.

IMRIS, I. 1977. Segregation Roasting of Antimony Raw Materials. *The Institution of Mining and Metallurgy, Advances in Extractive Metallurgy***,** 161-167.

ISHII, K. & SVENSSON, J. 1980. Segregation Roasting of Nickel Oxide Ore. *Australia Japan Extractive Metallurgy Symposium.* Sydney, Australia.

IWASAKI, I. 1972a. *Process for Recovering Nickel from Nickel Ores*. United States patent application.

IWASAKI, I. 1972b. A Thermodynamic Interpretation of the Segregation Process for Copper and Nickel Ores. *Minerals Sci. Engng.,* 4**,** 14-23.

IWASAKI, I., MALICSI, A. & JAGOLINO, N. 1973. *Segregation Process for Copper and Nickel Ores,* New York, Gordon and Breach.

IWASAKI, I., TAKAHASHI, Y. & KAHATA, H. 1966. Extraction of Nickel from Iron Laterites and Oxidized Nickel Ores by a Segregation Process. *Trans. Soc. Mining Eng. AIME,* 235**,** 308-320.

JAGOLINO, N. 1970. *The Application of a Segregation Process to a Philippine Nickeliferous Laterite.* Masters, University of Minnesota.

JOHANSSON, O. & ZANDER, B. 1997. Nickel 1996 Commodities Meeting: Reduction - Segregation of Nickel: Minpro 2.0 Process. *Minerals Industry International.*

KELLY, E. & SPOTTISWOOD, D. 1982. *Introduction to Mineral Processing*, John Wiley & Sons Inc.

KIMURA, K. & KONDO, Y. 1975. A Thermodynamic Calculation on the Nickel Segregation Process. *Trans, JIM,* 16**,** 745-754.

KISON, K., DICKESON, J. & BELCHER, C. 1968. The Determination of Metallic Iron, Nickel and Cobalt in Reduced Ores and Oxides. *Analytica Chimica Acta,* 41**,** 107-112.

KOBA, K. & IDA, S. 1980. Gasification Reactivities of Metallurgical Cokes with Carbon Dioxide, Steam and their Mixtures. *Fuel,* 59**,** 59-63.

KONDO, H., ASAKI, Z. & KONDO, Y. 1978. Hydrolysis of Fused Calcium Chloride at High Temperature. *Metallurgical Transactions B,* 9**,** 477-483.

KUCK, P. H. 2014. Nickel. Mineral Commodity Summaries: U.S. Geological Survey.

KULP, L. J., KENT, P. & KERR, P. F. 1951. Thermal Study of the Ca-Mg-Fe Carbonate Minerals. *The American Mineralogist,* 36**,** 643-670.

KWATARA, M., TAYABALLY, J., PEEK, E. & SCHONEWILLE, R. Segregation Roasting of a Saprolitic Laterite Ore: An Experimental Investigation. EPD Congress 2011, 27th February - 3rd March 2011 2011 San Diego, California. John Wiley & Sons, Inc., 17.

LANDERS, M., GILKES, R. J. & WELLS, M. 2009a. Dissolution Kinetics of Dehydroxylated Nickeliferous Goethite from Limonitic Lateritic Nickel Ore. *Applied Clay Science,* 42**,** 615-624.

LANDERS, M., GILKES, R. J. & WELLS, M. 2009b. Rapid Dehydroxylation of Nickeliferous Geothite in Lateritic Nickel Ore: X-Ray Diffraction and TEM Investigations. *Clays and Clay Minerals,* 57**,** 751-770.

LANDERS, M., GRAFE, M., GILKES, R. J., SAUNDERS, M. & WELLS, M. A. 2011. Nickel Distribution and Speciation in Rapidly Dehydroxylated Geothite in Oxide-Type Lateritic Nickel Ores: XAS and TEM Spectroscopic (EELS and EFTEM) Investigation. *Australian Journal of Earth Sciences,* 58**,** 745-765.

LAZARENKOV, V. G., TALOVINA, I. V., VORONTSOVA, N. I., MEZENTSEVA, O. P. & RYZHKOVA, S. O. 2011. Nickel Chlorites in the Oxide-Silicate Nickel Deposits of the Urals. *Lithology and Mineral Resources,* 46**,** 312-320.

LU, Z., GRIMSEY, E. & PARKER, A. 1983. Copper Separation from Iron and Nickel-Iron Sulfide Concentrates by a Double-roast, Acetonitrile Leaching Process. *Proceedings of the Australasian Institute of Mining and Metallurgy,* 288**,** 19-27.

MA, J. & PICKLES, C. 2003. Microwave Segregation Proces for Nickeliferous Silicate Laterites. *Canadian Metallurgical Quarterly,* 42**,** 313-326.

MACKAY, K. & GIBSON, N. 1968. Development of the Pilot Commerical TORCO Plant at Rhokana Corporation, Ltd., Zambia. *Trans. Inst. Min Metall. C,* 77**,** C19-C31.

MACKENZIE, K. & MEINHOLD, R. 1994. Thermal Reactions of Chrysotile Revisited: A 29Si and 25Mg MAS NMR Study. *American Mineralogist,* 79**,** 43-50.

MACKENZIE, K. J. D. & ROGERS, D. E. 1977. Thermal and Mössbauer Studies of Iron-Containing Hydrous Silicates: I. Nontronite. *Thermochimica Acta,* 18**,** 177-196.

MARCUSON, S. 1977. *Studies of Segregation Treatment of Roasted Copper Concentrate.* PhD, Columbia Univeristy.

MARCUSON, S. 1978. Studies on Segregation of Roasted Copper Concentrates: Separate Na and Cl Additions and Effects of Sulphate. *Trans. Inst. Min Metall. C,* 87**,** C261-265.

MARCUSON, S. 1980. Application of the Segregation Process to Roasted Copper Concentrates. *Minerals Sci, Engng,* 12**,** 21-35.

MARCUSON, S. & KELLOGG, H. 1977. Studies on Segregation of Roasted Copper Concentrate. *Trans. Inst. Min Metall. C,* 86**,** C195-C201.

MARTIN, C. 1977. The Thermal Decomposition of Chrysotile. *Mineralogical Magazine,* 41**,** 453-459.

MARTINEZ, E. 1967. The Copper Segregation Process Studied by Thermoanalysis. *Trans. Soc. Mining Eng. AIME,* 238**,** 172-179.

MATSUMORI, T. 1999. Reduction Mechanism of Siliceous Nickel Ores - Fundamental Study on Fe-Ni Smelting (2nd Report). *Shigen-to-Sozai,* 115**,** 603-609.

MCINTOSH, R. M., SHARP, J. H. & WILBURN, F. W. 1990. The Thermal Decomposition of Dolomite. *Thermochimica Acta,* 165**,** 281-296.

MCKINNEY, W. & EVANS, L. 1963. Segregation of Copper Ores by Direct Firing Methods. *U.S Bureua of Mines,* R.I 6215.

MCKINNEY, W. & WADDLETON, P. 1962. Use of Various Salts as Copper-Volatizing Agent in the Segregation Process. *U.S Bureua of Mines Report of Investigation No. 6044***,** 1-17.

MEHROTRA, S. & SRINIVASAN, V. 1994. Extraction of Nickel from an Indian Laterite by Segregation Roasting. *Trans. Inst. Min Metall. C,* 103**,** C97-C104.

MILLER, G. W., SAMPSON, D., FLEAY, J., CONWAY-MORTIMER, J. & ROCHE, E. Ravensthorpe Nickel Project Beneficiation Prediction MLR and Interpretation of Results. International Laterite Nickel Symposium, 2004. TMS.

MONHEMIUS, A. 1987. *Treatment of Laterite Ores of Nickel to Produce Ferronickel, Matte, or Precipitated Sulphide*, John Wiley & Sons, Inc.

MOULDEN, J. & TAPLIN, B. 1924. *Improvements in or Relating to the Heat Treatment of Oxidized Copper Ores*. British Patent patent application.

NAGANO, K., KOJIMA, K. & TAKAHASHI, Y. Extraction of Nickel from Iron Laterites and Oxidized Nickel Ores by a Segregation Process. 9th International Mineral Processing Congress, 1970 Prague. 319-327.

OKAMOTO, Y., UEDA, Y. & NOGUCHI, F. 1971a. Extraction of Nickel from Garnerite Ore by the Segregation-Magnetic Seperation Process. *Memoirs of the Kyushu Institute of Technology (Engineering)***,** 41-61.

OKAMOTO, Y., UEDA, Y. & NOGUCHI, F. 1971b. Mechanism of Segregation from Garnierite Ores. *Memoirs of the Kyushu Institute of Technology (Engineering),* 1**,** 23-40.

OPIE, W. 1976. A Minimum Pollution, Low-Energy Pyrometallurgical Process for Treating Chalcopyrite Concentrates. *Extractive Metallurgy of Copper (1976) Volume I* TMS

OPIE, W., COFFIN, L., ARMANT, D. & CIMLER, O. 1979. Selective Recovery of Copper from Copper-Nickel Sulfide Concentrates by Applying Segregation Technology. *Metallurgical Transactions B,* 10**,** 27-32.

PAREKH, B., JEPSEN, L. & GOLDBERGER, W. 1988. Segregation Roasting and Beneficiation of Deep Sea Nodules. *Marine Mining,* 7**,** 417-429.

PARISER, H. & PARISER, G. Changes in the Ferro Chrome & Ferro Nickel Markets. The Twelfth International Ferroalloys Congress Proceedings, 2010 Helsinki, Finland. 641-652.

PIETSCH, H. 1972. Application of the Segregation Process on the Nickel Extracted from Laterite Ores. *In:* DOR, A. (ed.) *Nickel Segregation.* San Francisco, California: The AIME Metallurgical Society.

PINKNEY, E. & PLINT, N. 1967. Treatment of Refractory Copper Ores by the Segregation Process. *Trans. Inst. Min Metall. C,* 76**,** C114-C132.

PIPER, D. 2009. Australian Nickel Preview: Heron's New Route to Laterite Viability. *Paydirt.*

POLLANDT, F. & PEASE, M. 1960. Extraction of Copper and Silver by the Segregation Process in Peru. *Trans. Inst. Min Metall. C,* 69**,** 687-697.

PRIETO, A., LOBÓN, J., ALÍA, J., RULL, F. & MARTIN, F. 1991. Thermal and Spectroscopic Analysis of Natural Trioctahedral Chlorites. *Journal of thermal analysis,* 37**,** 969-981.

RAMAMOORTHY, R., DUTTA, P. & AKBAR, S. 2003. Oxygen Sensors: Materials, Methods, Designs and Applications. *Journal of Material Sciences,* 38**,** 4271-4282.

RAMPACEK, C., MCKINNEY, W. & WADDLETON, P. 1959. Treating Oxidised and Mixed Oxide-Sulphide Copper Ores by the Segregation Process. *U.S Bureua of Mines,* R.I. 5501.

RAO, Y. 1971. The Kinetics of Reduction of Hematite by Carbon. *Metallurgical Transactions,* 2**,** 1439-1447.

REY, M. 1980. Memoirs of Milling and Process Metallurgy: 4 - Segregation Processes. *Trans, Inst. Min Metall. C,* 79**,** C101-C107.

REY, M. 1985. The Copper Segregation Process. *SME Mineral Processing Handbook, Vol 2.*

REY, M., FORMANEK, V., BLANQUET, P. & ROUSSEAU, A. 1972a. Chemical Reactions and Kinetics of the Segregation of Oxidized Nickel Ores when using Calcium Chloride. *In:* DOR, A. (ed.) *Nickel Segregation.* San Francisco, California: The AIME Metallurgical Society.

REY, M., FORMANEK, V., ORISINI, J., LUSSIEZ, G. & PIERRE, M. 1972b. Influence of Various Factors on Segregation of Oxidized Nickel Ores. *In:* DOR, A. (ed.) *Nickel Segregation.* San Francisco, California: The AIME Metallurgical Society.

REY, M. R. W. 1967. Early Development of the Copper Segregation Process. *Trans. Inst. Min Metall. C,* 77**,** C42-C44.

REZNIK, I., KORTSENSHTEIN, N., SAMUILOV, E., LOZNITSKII, Y. & MAIOROV, A. 1998. Thermodynamic Analysis of the Segregation-Roasting Mechanism of Oxidized Nickel Ores. *Russian Journal of Non-Ferrous Metals,* 39**,** 12-19.

REZNIK, I., TARASOV, A. & MAYOROV, D. Mechanism and Technology of Segregation Roasting of Oxide Nickel Ores with Subsequent Calcine Flotation and Concentrate Leaching. *In:* SCHLESINGER, M. E., ed. EPD Congress 2003, 2003.

RHAMDHANI, M. A., HAYES, C., P, & JAK, E. 2009. Nickel Laterite Part 2 - Thermodynamic Analysis of Phase Transformations occuring during Reduction Roasting. *Trans. Inst. Min Metall. C,* 118**,** 146-155.

ROBERT, R. & HEYSTEK, H. 1951. Differential Thermal Analysis of the Dolomite Composition. *American Mineralogist,* 37**,** 166-179.

ROBERTS, D. G. & HARRIS, D. J. 2006. A Kinetic Analysis of Coal Char Gasification Reactions at High Pressures. *Energy & Fuels,* 20**,** 2314-2320.

ROWLAND, R. A. 1955. Differential Thermal Analysis of Clays and Carbonates. *CMS Bulletin***,** 151-163.

RUAN, H. D., FROST, R. L., KLOPROGGE, J. T. & DUONG, L. 2002a. Infrared Spectroscopy of Goethite Dehydroxylation. II. Effect of Aluminium Substitution on the Behaviour of Hydroxyl Units. *Spectrochimica Acta Part A: Molecular and Biomolecular Spectroscopy,* 58**,** 479-491.

RUAN, H. D., FROST, R. L., KLOPROGGE, J. T. & DUONG, L. 2002b. Infrared Spectroscopy of Goethite Dehydroxylation: III. FT-IR Microscopy of In Situ Study of the Thermal Transformation of Goethite to Hematite. *Spectrochimica Acta Part A: Molecular and Biomolecular Spectroscopy,* 58**,** 967-981.

SAKAIDA, H. & KAKIUCHI, T. 2011. Determination of Single-Ion Activities of H^+ and Cl^- in Aqueous Hydrochloric Acid Solutions by Use of an Ionic Liquid Salt Bridge. *The Journal of Physical Chemistry B,* 115**,** 13222-13226.

SALY, N. M. & ABDUL WAHAB, A. A.-A. 2006. Beneficiation of Al-Hussainyiat Low Grade Iron Ore by Segregation Roasting. *Iraqi Bulletin of Geology and Mining,* 2**,** 103-113.

SATAPATHY, B., DUTTA, P., DEY, D. & JENA, P. 1986. Recovery of Copper from Converter Slag by Segregation Roasting. *Trans, Inst. Min Metall. C,* 95**,** C79-C82.

SCHULZ, N. & LEX, H. 1968. Reduction and Magnetic Separation of Manganiferous Iron Ores by the R-N Process. *Trans. Soc. Mining Eng. AIME,* March**,** 71-76.

SEABORN, C. 1976. *A Study of the Chlorination Reactions of the Nickel Segregation Reactions.* PhD, University of New South Wales.

SEPOR. 2015. *Davis Tube Tester* [Online]. Available: http://www.sepor.com/davis-tube-tester/ [Accessed 9th July 2015.

SIDHU, P. S., GILKES, R. J. & POSNER, A. M. 1980. The Behavior of Co, Ni, Zn, Cu, Mn and Cr in Magnetite during Alteration to Maghemite and Hematite. *Soil Science Society of America Journal (SSSAJ),* 44**,** 135-138.

SIMONS, C. The Production of Nickel: Extractive Metallurgy - Past, Present and Future. *In:* TYROLER, G. & LANDOLT, C., eds. Symoposium on Metallurgy of Nickel and Cobalt, 1988 Phoenix, Arizona. TMS, 91-134.

SOLE, M. & TAYLOR, J. Nickel Segregation Research at the Anglo American Research Laboratories Part V. The Characterisation of Refractory Nickel ores and the correlation of their Mineralogical, Chemical, Thermal and Infrared Analyses with Segregation Behaviour. *In:* DOR, A., ed. Nickel Segregation, 23 February 1972 San Francisco, California. The AIME Metallurgical Society, 129-144.

STORR, W. 2013. *Low Pass Filter - Passive RC Filter Tutorial* [Online]. Available: http://www.electronics-tutorials.ws/filter/filter_2.html [Accessed 9th July 2015.

SUDOL, S. 2005. The Thunder from Down Under: Everything you wanted to know about Laterites but were afraid to ask. *Canadian Mining Journal*.

TAKAHASHI, Y., KOJIMA, K. & KAHATA, H. 1966. On Segregation Roasting Reactions of Nickel Ores. *Tetsu to Hagane (Iron and Steel Institue of Japan),* 52**,** 18-20.

TATHAVAKAR, V., ANTONY, M. P. & JHA, A. 2005. The Physical Chemistry of Thermal Decomposition of South African Chromite Minerals. *Metallurgical and Materials Transactions B,* 36**,** 75-84.

TAYLOR, A. Nickel Processing Technology 10 Years on from Cawse, Bulong and Murrin Murrin. ALTA Nickel/Cobalt, May 15-17 2007 Perth, Western Australia.

TITI-MANYAKA, R. & IWASAKI, I. 1972. Thermogravimetric Investigation of the Chlorination Behaviors of Some Common Metals and Their Oxides. *Trans. Soc. Mining Eng. AIME,* 252**,** 307-313.

TITOVA, E., KOVTUN, V., YAKOVLEVA, R. & MAIOROV, A. 1988. Nickel and Cobalt Recovery from Oxidized Nickel Ores by Segregation. *English Translation of Tsveynye Metally* 29**,** 30-33.

TITOVA, E., P, MAIOROV, A., D, REZNIK, I., D, POLOSINA, E., E, & OSIPOVA, A., S 1975. Using Segregation to Recover Nickel from Iron-Bearing Oxidized Nickel Ores. *English Translation of Tsveynye Metally,* 16**,** 10-12.

TOMÁŠEK, R., VIRČÍKOVÁ, E. & MOLNÁR, L. Segregation Roasting - An Alternative Method for Beneficiation of Nickel Oxide Ores, Copper Dump Slags and Processing of Magnesite Raw Materials. Pyrometallurgy 95, 1995 Cambridge, England. IMM: London, 53-64.

TURKDOGAN, E., KOUMP, V., VINTERS, J. & PERZAK, T. 1968. Rate of Oxidation of Graphite in Carbon Dioxide. *Carbon,* 6**,** 467-484.

TURKDOGAN, E. & VINTERS, J. 1969. Kinetics of Oxidation of Graphite and Charcoal in Carbon Dioxide. *Carbon,* 7**,** 101-117.

TURKDOGAN, E. & VINTERS, J. 1970. Effect of Carbon Monoxide on the Rate of Oxidation of Charcoal, Graphite and Coke in Carbon Dioxide. *Carbon,* 8**,** 39-53.

TURKDOGAN, E. & VINTERS, J. 1972. Catalytic Oxidation of Carbon. *Carbon,* 10**,** 97-111.

TWIDWELL, L. & BEUERMAN, K. 1984. The Segregation Process Applied to Dead Roasted Copper Concentrates: The Distribution of Impurities. *Proc. Australas. Inst. Min. Metall.,* 289**,** 295-301.

UTIGARD, T. & BERGMAN, R. A. 1992. Gaseous Reduction of Laterite Ores. *Metallurgical Trans. B*, 23B, 217-275.

VALIX, M. & CHEUNG, H. 2002. Effect of Sulfur on the Mineral Phases of Laterites ores at High Temperature Reduction. *Minerals Engineering,* 15.

VITI, C. 2010. Serpentine Minerals Discrimination by Thermal Analysis. *American Mineralogist,* 95**,** 631-638.

WARNER, S., SRIDHAR, R. & BAKKER, H. 1972. Thermal Constraints on the Segregation of Nickel from Lateritic Ores. *In:* DOR, A. (ed.) *Nickel Segregation.* San Francisco, California: The AIME Metallurgical Society.

WEBB, I. 1973. *A Study of the Segregation Process for the Extraction of Nickel from Laterites.* PhD, University of New South Wales.

WELLS, M., FITZPATRIK, R. & GILKES, R. J. 2006. Thermal and Mineral Properties of Al^{-}, Cr^{-}, Mn^{-}, Ni^{-} and Ti^{-} Substitued Goethite. *Clay and Mineral Society,* 54**,** 176-194.

WELLS, M. A. & CHIA, J. 2011. Quantification of Ni Laterite Mineralogy and Composition: A New Approach. *Australian Journal of Earth Sciences,* 58**,** 711-724.

WOLSKA, E. 1988. Relations between the Existence of Hydroxyl Ions in the Anionic Sublattice of Hematite and its Infrared and X-Ray Characteristics. *Solid State Ionics,* 28–30, Part 2**,** 1349-1351.

WOLSKA, E. & SCHWERTMANN, U. 1989. Nonstoichiometric Structures during Dehydroxylation of Goethite. *Zeitschrift fur Kristallographie,* 189**,** 223-237.

WRIGHT, J. 1973. The Segregation Process. *Minerals Sci, Engng,* 5**,** 119-134.

WRIGHT, J. 1994. Nickel Laterite Treatment by Segregation. *In:* NILMANI, M., LEHNER, T. & RANKIN, W. (eds.) *Pyrometallurgy for Complex Materials and Wastes.* University of Melbourne, Victora, Australia: The Minerals, Metal & Materials Society.

WRIGHT, J. & GOODEN, J. 1973. The Treatment of Refractory Nickel Oxide Ores by the Segregation Process - Laboratory Testing. *Amdel Bulletin,* 15**,** 49-69.

YAZAWA, A. 1979. Thermodynamic Evalulations of Extractive Metallurgical Processes. *The Metallurgical Society of AIME,* 10B**,** 307-321.

YE, D., AGNEW, J. & ZHANG, D. 1998. Gasification of a South Australian low-rank Coal with Carbon Dioxide and Steam: Kinetics and Reactivity Studies. *Fuel,* 77**,** 1209-1219.

YOUNG LEE, H. & GYU KIM, S. 2005. Kinetic Study on the Hydrogen Reduction of Ferrous Chloride Vapor for Preparation of Iron Powder. *Powder Technology,* 152**,** 16-23.

YOUNG, R. 1986. The Analysis of Ferroalloys. *Talanta,* 33**,** 561-565.

Western Australian School of Mines
Department of Mining Engineering and Metallurgical Engineering

An Investigation of the Segregation Process Applied to Western Australian Nickel Laterites

Volume 2: Appendices

David Eric Grimsey

This thesis is presented for the Degree of
Doctor of Philosophy
of
Curtin University

October 2015

Table of Contents

List of Figures

List of Tables

Appendix A Calculations and Procedures

A.1 Acidification Effect of Carbon Dioxide

An experimental objective was to continuously measure the HCl content in the off-gas by dissolving it in water and measuring the change in pH. However, the off-gas also contained a varying amount of CO_2 which will dissolve and increase the pH through carbonic acid formation. Since carbonic acid is relatively weak and poorly dissociated, the concept was to add a small amount of strong nitric acid to the de-ionised water prior to dissolution of the off-gas, to provide a background pH independent of the solubility of CO_2. Any change in pH could then be attributed to the addition of HCl from the gas.

The effect on the H+ concentration of adding HNO_3 in the presence of dissolved CO_2 was calculated using detailed information provided in the book chapter "Chemistry of Carbonic Acid in Water" (Mook, 2001), made available on the web by the International Atomic Energy Agency.

The calculations, as outlined below, showed that addition of 0.5 ml of 70% nitric acid to 1 litre of water at 293 K (20^{o}C) provided a reasonably stable H^+ compared to when it is absent, when gas containing CO_2 up to 1 atm pressure was equilibrated with the water. The comparison is illustrated in Figure B.1.

The CO_2 acidification effect could be suppressed even further using a higher nitric acid addition; however, this would also result in a decreased sensitivity the pH measurements when adding HCl. The equations in Table B.1 were taken into account in the calculation, where the symbol K represents equilibrium constant, p represents partial pressure (atm), [ ] represents ideal activity relative to 1 molar solution (mol/l).

Table A.1 Equations for CO_2 Acidification

Reaction	Chemical Equation	Equations
CO_2 dissolution	$CO_2(g) + H_2O(l) \leftrightarrow H_2CO_3(aq)$	$K_{A1} = \frac{[H_2CO_3]}{p_{CO_2}}$
H_2CO_3 dissociation	$H_2CO_3(aq) \leftrightarrow H^+(aq) + HCO_3^-(aq)$	$K_{A2} = \frac{[H^+][HCO_3^-]}{[H_2CO_3]}$
HCO_3^- dissociation	$HCO_3^-(aq) \leftrightarrow H^+(aq) + CO_3^{2-}(aq)$	$K_{A3} = \frac{[H^+][CO_3^{2-}]}{[HCO_3^-]}$
H_2O dissociation	$H_2O(l) \leftrightarrow H^+(aq) + OH^-(aq)$	$K_{A4} = [H^+][OH^-]$
HNO_3 dissociation	$HNO_3 \leftrightarrow H^+ + NO_3^-$	$[HNO_3](added) = [NO_3^-]$
Electrical neutrality	$[H^+] = [HCO_3^-] - 2[CO_3^{2-}] - [OH^-] - 3[NO_3^-]$	

Values for the equilibrium constants from Table available from the literature (Mook, 2001) as a function of temperature

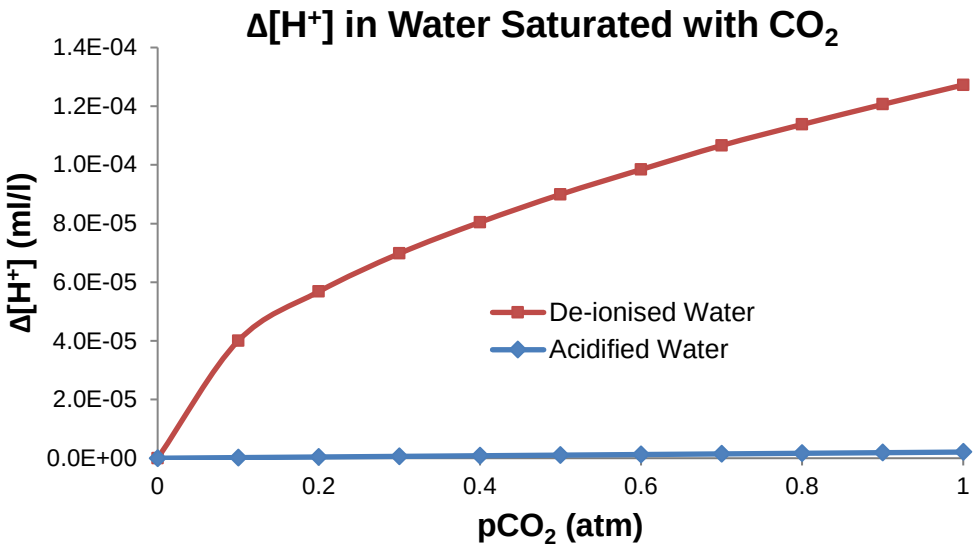

Figure A.1 Effect of CO_2 Pressure on H^+ Concentration in Water (293 K)

Acidified water contains 0.5 ml of 70% HNO_3 per litre of de-ionised water.

$$K_{A1} = -\frac{2622.38}{T} - 0.0178471T + 15.5873$$

$$K_{A2} = \frac{3404.71}{T} + 0.032786T + 14.8435$$

$$K_{A3} = \frac{2902.39}{T} + 0.02379 - 6.4980$$

$$lnK_{A4} = 148.9802 - \frac{13847.26}{T} - 23.6521 \ln T$$

In addition to the four K values, the equation set contains eight unknowns: p_{CO_2}, $[H_2CO_3]$, $[H^+]$, $[HCO_3^-]$, $[CO_3^{2-}]$, $[OH^-]$, $[NO_3^-]$ and $[HNO_3](added)$.

Once the temperature is defined (393 K), the four K values may be calculated. The $[HNO_3](added)$ is known from the acid strength (15.70 mol/l at 393 K) and volume (0.5 ml) of nitric acid added. If p_{CO_2} is specified (0-1 atm), the remaining six unknowns which includes $[H^+]$ may be calculated from the six listed equations using Excel Solver.

A.2 Bromine Methanol Leach

Fully dried 1-20 g samples of magnetic concentrate or segregate were washed into 250 ml conical flasks using 20-30 ml of anhydrous methanol and then 1 ml of bromine was added. The flasks were allowed to sit for ~30 seconds before being sealed with a rubber stopper to prevent ingress of atmospheric H_2O during the leach. The delay was necessary to allow heat from the exothermic mixing of bromine and methanol to dissipate; otherwise the stopper would be ejected due to the pressure build up. The samples were then leached for 1 hour using a shaker to solubilise the metallic Ni, Fe and Co as bromides.

The leachates were filtered into a 250 ml beakers using bromine resistant filter paper (Whatman 541) and the solid residues and filter papers were washed with methanol until the filtrates ran clear. The beakers were then placed onto a hotplate maintained at 333 K (60°C) and heated to dryness. It was important not to heat at higher temperatures since the methanol would boil so vigorously that loss of metal bromides through vapour entrainment may occur. After drying, the beakers were allowed to cool to room temperature.

The cooled bromide resides were decomposed on a hotplate at maximum heat using 20 ml of a decomposition acid (a 2:5:5 mixture of concentrated HCl:HNO_3:$HClO_4$). The beakers were kept on the hotplate until dense white fumes of perchloric acid ($HClO_4$) began to appear. After cooling, a solid greenish chloride precipitate remained.

The precipitates were dissolved in 7 ml of concentrated nitric acid and 30 ml of de-ionised water and then filtered into 250 ml volumetric flasks. De-ionised water was used for washing and filling of the volumetric flask. After filtration was complete, the solutions were analysed by ICP using a Vista-PRO CCD Simultaneous ICP-OES machine.

A.3 Thermal Analysis

A.3.1 Limonite Ore

The TGA-DSC/mass spectrometry curves produced during the heating in air of the limonite from this work are presented in Figure B.2. From the figure, the curve for the $H_2O(g)$ ion current indicates that dehydration occurs up to ~190°C (463 K), with a peak current at 145°C (418 K), an associated endothermic peak at 85.8°C (358.8 K) and a weight loss of 6.72%.

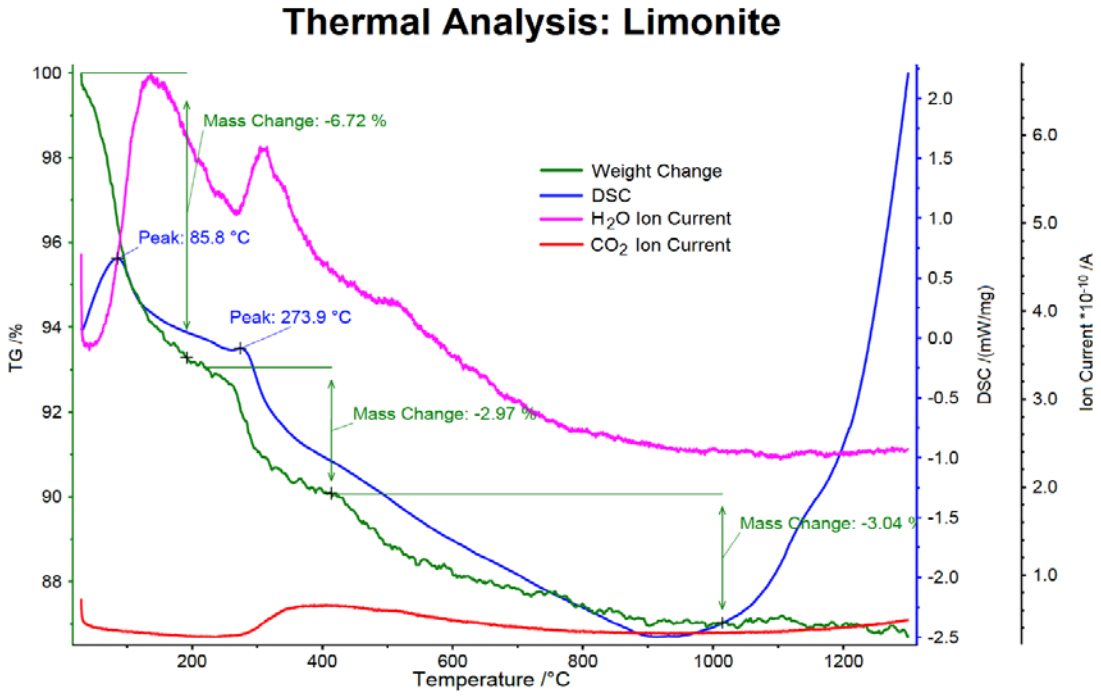

Figure A.2 TGA-DSC and Mass Spectrometric Analysis Curves for Limonite
Analysis by CSIRO (Perth): 50 mg sample heated at 10 K/min with continuous mass spectrometric analysis of evolved H_2O and CO_2 using ion current measurement.

The dehydrated goethite then dehydroxylates to form OH-hematite up to ~400°C (673 K), with significant removal of water occurring from ~280°C (553 K); as indicated by the increase in the $H_2O(g)$ ion current at this temperature and an associated DSC power input (endothermic) peak at 273.9°C (546.9 K). The $H_2O(g)$ ion current peaks at ~310°C (583 K) and the total weight loss from low temperature dehydroxylation is 2.97% at ~400°C (673 K). The OH-hematite then progressively dehydroxylates through to crystalline hematite from ~400-850°C (673-1123 K), with an associated weight loss of 3.04%. The total weight change is 12.73%, which compares well with the 12.7% determined in this work (Table 4.2).

A.3.2 Nontronite Ore

The TGA-DSC/mass spectrometry curves produced during the heating of the nontronite from this work in air are presented in Figure B.3. From the figure, the H_2O(g) ion current indicates that interlayer dehydration occurs up to ~185°C (458 K), with the peak current and an endothermic peak occurring at ~90°C (363 K) with a weight loss of 7.0%.

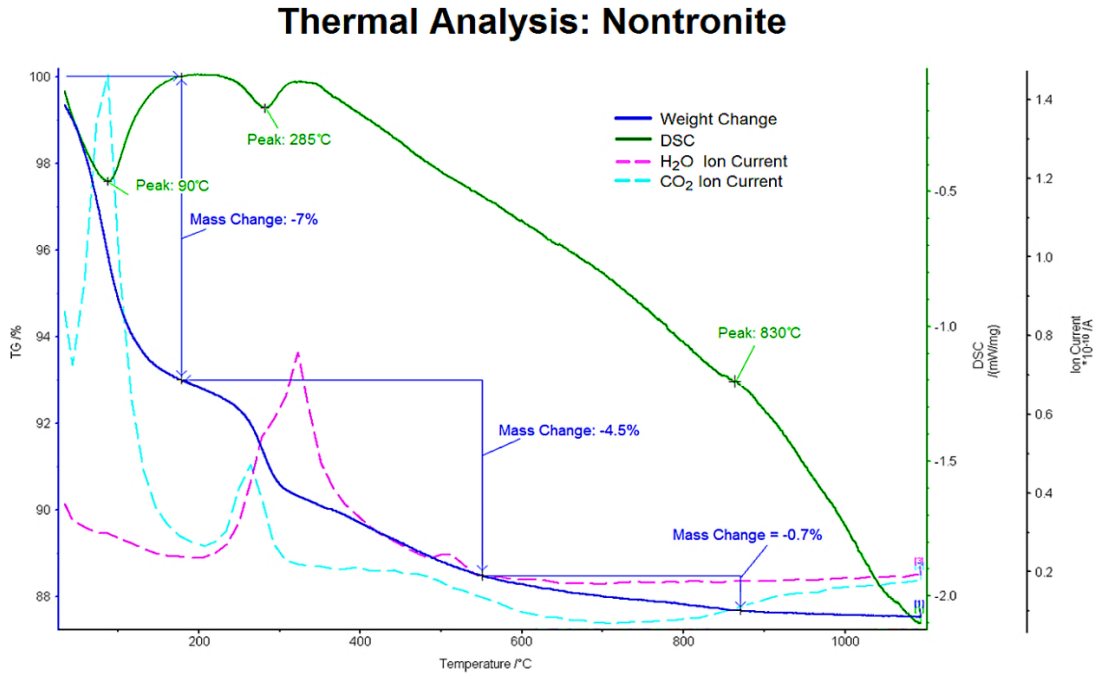

Figure A.3 TGA-DSC and Mass Spectrometric Analysis Curves for Nontronite
DSC power input is plotted on a negative scale; thus endothermic peaks are reversed compared to Figure B.2 and Figure B.4.

The nontronite then dehydroxylates to form nontronite dehydrate and maghemite (Figure 4.5) from ~200-550°C (473-823 K) with a corresponding H_2O(g) ion current peak at ~265°C (538 K), an endothermic peak at 285°C (558 K) and a weight loss of 4.5%. The hematite appears to crystallise from the nontronite dehydrate and maghemite at ~830°C (1103 K), as indicated by a small exothermic peak. The small evolution of CO_2 at ~325°C (598 K) could not be explained. The total weight loss to ~950°C (1223 K) is 12.2%, marginally lower than the 13.1% determined in this work (Table 4.2).

A.3.3 Garnierite Ore

The TGA-DSC/mass spectrometry curves produced during the heating of the garnierite from this work in air are presented in Figure B.4.

The thermal analysis curves for garnierite are complicated by the presence of overlapping mineral decompositions. However, it appears that dehydration occurs up to ~200°C (473 K) with a corresponding H_2O(g) ion current peak at ~150°C (423 K) and 1.09% weight loss. The next H_2O ion current peak at ~300°C (573 K) corresponds to the dehydroxylation of goethite which appears to occur from ~240-425°C (513-698 K) with a weight loss of 0.86%.

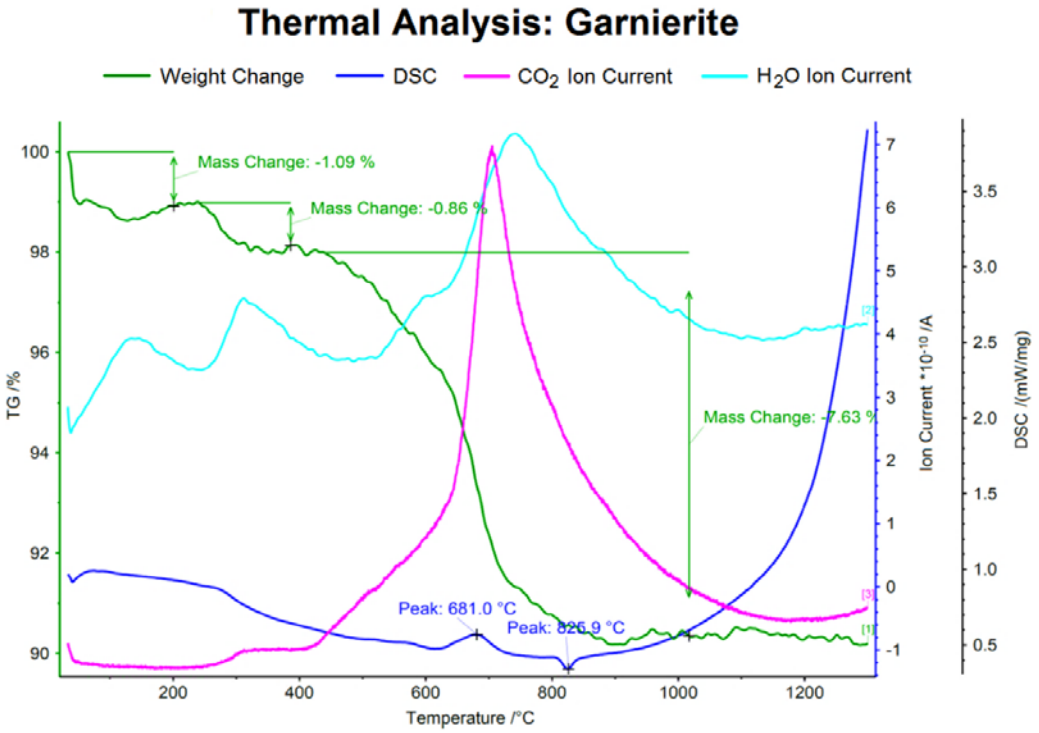

Figure A.4 TGA-DSC and Mass Spectrometric Analysis Curves for Garnierite
Further details see caption of Figure B.2.

Chlorite and lizardite likely dehydroxylate over a broad temperature range from ~425-880°C (698-1153 K) with a corresponding endothermic peak at 681°C (954 K) and two H_2O(g) ion current peaks; one at ~600°C (873 K) which is likely associated with the dehydroxylation of the chlorite interlayer cations and one at ~750°C (1023 K) which is likely associated with the dehydroxylation of the TOT brucite layers within serpentine. The exothermic (reduced power input) DSC peak at 826°C (1099 K) likely corresponds to the crystallisation of hematite or forsterite.

The ion current curve for CO_2(g) peaks at 973 K (700°C), indicating that the maximum decomposition of carbonate occurs at this temperature. The total weight loss, including CO_2 from carbonate is 9.58%; significantly less than the 12.3% determined by this researcher (Table 4.2). This may indicate that the mineralogy of the small TG/DSC sample (50 mg) was not entirely representative of the ore.

A.4 Rate Equations

A.4.1 Langmuir-Hinshelwood (LH) Equation

The generally accepted mechanism for the Boudouard reaction can be represented by an equilibrium dissociative adsorption of $CO_2(g)$ on to a free active site on the carbon surface C_f, to form an activated complex $C(O)$, followed by the slower, rate controlling desorption of the complex from the surface to give $CO(g)$, as represented by Roberts and Harris (2006):

Step 1 (Equilibrium)	$C_f + CO_2(g) \leftrightarrow C(O) + CO(g)$	$\boldsymbol{k_1, k_2}$
Step 2 (Rate Limiting)	$C(O) \rightarrow CO(g)$	$\boldsymbol{k_3}$

k_1 is rate constant for the forward reaction of step 1, k_2 is the rate constant for the back reaction of step 1 and k_3 is the rate constant for step 2. The rate may be represented by the LH equation in which $[C_t]$ is the total concentration of active sites on carbon.

$$R = \frac{[C_t]k_1 p_{CO_2}}{1 + \frac{k_2}{k_3}p_{CO} + \frac{k_1}{k_3}p_{CO_2}}$$

A.4.2 Rate Equation for the Boudouard Reaction

The power function rate equation (Grimsey, 2012) for the Boudouard reaction in the presence of pure solid carbon ($a_C = 1$), can be written as:

$$-\frac{dn_C}{dt} = A_C k_{2.6}\left(a_C p_{CO_2} - \frac{p_{CO}^2}{K_{BR}a_C}\right) mol/time$$

a_C is the activity of carbon relative to the pure solid (used instead of concentration) A_C is the area of carbon, $k_{2.6}$ is the power rate constant, K_{BR} is the Boudouard reaction equilibrium constant and p_{CO}^2/K_{BR} represents the p_{CO_2} which would be in equilibrium with the actual p_{CO_2} in the reaction. Since $a_C = 1$ for pure carbon:

$$-\frac{dn_C}{dt} = A_C k_{2.6}\left(p_{CO_2} - \frac{p_{CO}^2}{K_{BR}}\right) \quad mol/time$$

Since $n_C = m_C/12.0$ and if the constant specific surface area is given by $S = A/m_C$, then $A = Sm_C$ and substitution in the above equation gives:

$$-\frac{dm_C}{dt} = 12.0 S m_C k \left(a_C p_{CO_2} - \frac{p_{CO}^2}{K_{BR}} \right) \quad mass/time$$

$$\therefore \quad -\frac{dm_C}{dt} = m_C k_{BR} \left(p_{CO_2} - \frac{p_{CO}^2}{K_{BR}} \right) \quad mass/time$$

The equivalent equation used by Fortini and Fruehan (2005) is written as:

$$R_C = m_C k_C \left(p_{CO_2} - p_{CO_2}^C \right) \quad mass/time$$

where $R_C = -\frac{dm_C}{dt}$, $p_{CO_2}^C$ represents "the pressure of CO_2 in equilibrium with carbon at the temperature and pressure of the system at hand'. This is equal to p_{CO}^2/K_{BR} as determined by the equilibrium constant expression for the Boudouard reaction.

A.4.3 Integrated First Order to a Limit Rate Equation

$$\frac{dR_{Ni}}{dt} = k_{Ni}(R_{Ni,max} - R_{Ni})$$

Rearrange $$\frac{dR_{Ni}}{(R_{Ni,max} - R_{Ni})} = k_{Ni} dt$$

Let $$u = R_{Ni,max} - R_{Ni}$$

Then $$du = -dR_{Ni}$$

Where $$dR_{Ni} = -du$$

Substitution gives $$-\frac{du}{u} = k_{Ni} dt$$

Integrate between limits $t = 0, t$ and $R_{Ni} = 0, R_{Ni}$. Thus limits for u are $R_{Ni,max}$ and $R_{Ni,max} - R_{Ni}$.

$$-\int_{R_{Ni,max}}^{R_{Ni,max} - R_{Ni}} \frac{du}{u} = k_{Ni} \int_0^t dt$$

$$-[\ln u]_{R_{Ni,max}}^{R_{Ni,max} - R_{Ni}} = k_{Ni}[t]_0^t$$

$$-\left[\ln\left(R_{Ni,max} - R_{Ni}\right) - \ln\left(R_{Ni,max}\right)\right] = k_{Ni} t$$

$$\ln\left(R_{Ni,max} - R_{Ni}\right) - \ln\left(R_{Ni,max}\right) = -k_{Ni} t$$

$$\ln\frac{R_{Ni,max}-R_{Ni}}{R_{Ni,max}}=-k_{Ni}t$$

$$\frac{R_{Ni,max}-R_{Ni}}{R_{Ni,max}}=e^{-k_{Ni}t}$$

$$R_{Ni,max}-R_{Ni}=R_{Ni,max}e^{-k_{Ni}t}$$

$$-R_{Ni}=R_{Ni,max}e^{-k_{Ni}t}-R_{Ni,max}$$

$$R_{Ni}=R_{Ni,max}-R_{Ni,max}e^{-k_{Ni}t}$$

$$R_{Ni}=R_{Ni,max}(1-e^{-k_{Ni}t})$$

A.4.4 Rate Equation for Nickel Chloridisation

For the chloridisation of NiO with HCl according to $NiO(s)+2HCl(g)\rightarrow NiCl_2(g)+H_2O(g)$ the isothermal power function rate equation can be written as:

$$\frac{-dm_{NiO}}{dt}=A_{NiO}k_{2.15}\left(a_{NiO}p_{HCl}^2-\frac{p_{NiCl_2}p_{H_2O}}{K_{2.15}}\right)\ mass/time$$

dm_{NiO} is the mass of NiO chloridised in time dt; A_{NiO} is the surface area of NiO; a_{NiO} is the activity of NiO relative to a pure solid standard state (used in preference to concentration since NiO can be combined within silicates etc); p_{HCl}, p_{NiCl_2} and p_{FeCl_2} are the partial pressures of the denoted gases in contact with the ore; $k_{2.15}$ and $K_{2.15}$ are the respective rate constant and equilibrium constant for the NiO chloridisation reaction with HCl as represented by Equation 2.15.

Although $K_{2.15}$ is small (e.g. $K_{1173}=2.6\times10^{-2}$), p_{NiCl_2} is very small because of the rapid and thermodynamically favourable ($K_{1173}=5500$) reduction of $NiCl_2$ by H_2 taking place at the carbon surface (Section 2.4.3), thus the $p_{NiCl_2}p_{H_2O}/K_{2.15}$ in Equation 2.15 can be neglected, such that:

$$\frac{-dm_{NiO}}{dt}\approx A_{NiO}k_{2.15}a_{NiO}p_{HCl}^2$$

Similarly, the chloridisation of NiO with $FeCl_2$ through the reaction $NiO(s)+FeCl_2(g)\rightarrow NiCl_2(g)+FeO(s)$ can be expressed as:

$$\frac{-dm_{NiO}}{dt}\approx A_{NiO}k_{2.23}\left(a_{NiO}p_{FeCl_2}-\frac{p_{NiCl_2}a_{FeO}}{K_{2.23}}\right)$$

Since p_{NiCl_2} is very small, this equation reduces to:

$$\frac{-dm_{NiO}}{dt} \approx A_{NiO} k_{2.23} a_{NiO} p_{FeCl_2}$$

Combination of the above two simplified rate equations gives the total rate of NiO chloridisation according to:

$$\frac{-dm_{NiO}}{dt} = A a_{NiO} \left(k_{2.15} p_{HCl}^2 + k_{2.23} p_{FeCl_2}\right)$$

A.4.5 Rate Equation for Water Gas Reaction

For the gasification of carbon with steam according to $H_2O(g) + C(s) \rightarrow H_2(g) + CO(g)$, the isothermal power function rate equation can written as:

$$\frac{dm_{H_2}}{dt} = A_C k_{2.5} \left(a_C p_{H_2O} - \frac{p_{CO} p_{H_2}}{K_{2.5}}\right)$$

dm_{H_2} is the mass of H_2 generated within time dt; A_C is the surface area of carbon; a_C is the activity of the available carbon relative to a pure solid standard (used in preference to concentration); p_{H_2O}, p_{CO} and p_{H_2} are the partial pressures of the denoted gases in contact with the carbon; $k_{2.5}$ is the rate constant; $K_{2.5}$ is the equilibrium constant for the water gas reaction. $K_{2.5}$ is relatively large at segregation temperatures (e.g. $K_{1173} = 27.7$) and the p_{H_2} is maintained at a very low level because of the rapid and thermodynamically favourable reduction of $NiCl_2$ with H_2 ($K_{1173} = 5500$); thus with $a_C = 1$ for solid carbon, the equation reduces to:

$$\frac{dm_{H_2}}{dt} \approx A_C k_{2.5} p_{H_2O}$$

A.4.6 Rate Equation for Iron Segregation

The H_2 available for the reduction of $FeCl_2$ is discounted by the amount used for the reduction of $NiCl_2$. If mass m_{NiO} is in grams, it contains $m_{NiO}/74.7$ moles of Ni. In the chloride reduction, 1 mole of $NiCl_2$ is reduced by 1 mole of H_2; thus the segregation of $m_{NiO}/74.7$ moles of Ni requires $m_{H_2} = 2\, m_{NiO}/74.7$ grams of H_2; thus $dm_{H_2}/dt = 2.68\, x10^{-2}\, dm_{NiO}/dt$, since:

$$\frac{-dm_{NiO}}{dt} = A_{NiO} a_{NiO} \left(k_{2.15} p_{HCl}^2 + k_{2.23} p_{FeCl_2}\right)$$

The rate of H_2 consumption by Ni segregation can therefore be given by:

$$\frac{-dm_{H2}}{dt} = 2.68x10^{-2} A_{NiO} a_{NiO} \left(k_{2.15} p_{HCl}^2 + k_{2.23} p_{FeCl_2}\right)$$

The rate of H_2 production by the water gas reaction available to reduce $FeCl_2$ is thus given by:

$$\frac{dm_{H_2}}{dt} = A_C k_{2.5} p_{H_2O} - 2.68x10^{-2} A_{NiO} a_{NiO} \left(k_{2.15} p_{HCl}^2 + k_{2.23} p_{FeCl_2}\right)$$

A.5 Oxygen Removal during Segregation

A.5.1 Oxygen Removed by Segregation

The amount of oxygen removed from the system through alloy formation via segregation can be calculated from the amount of Fe and Ni that has segregated. A very small portion of oxygen is removed via Co segregation, but is neglected for the purposes of this calculation. Since Fe and Ni exist within the air-roasted laterite as Fe_2O_3 and NiO, the total moles of oxygen removed when n_{Ni} moles of Ni and n_{Fe} moles of Fe are segregated to form ferronickel is given by:

$$n_{O,seg} = n_{Ni} + 1.5 n_{Fe}$$

n_{Ni} and n_{Fe} are calculated using the integrated rate equations for nickel and iron recovery by segregation.

A.5.2 Oxygen Removed by In-Situ Reduction

As oxygen is only removed from the reaction system via segregation or in-situ reduction, the moles of oxygen removed via in-situ reduction are given by:

$$n_{O,in-situ} = n_{O,total} - n_{O,seg}$$

Iron oxides are assumed to reduce in the sequence $Fe_2O_3 \rightarrow Fe_3O_4 \rightarrow FeO \rightarrow Fe$. If Fe_2O_3 is considered to have 0% of its oxygen removed, while Fe has 100%, the sequential percentage of oxygen removed from iron oxides can be calculated from the stoichiometry of each reaction, where:

$$6Fe_2O_3 \rightarrow O_2 + 4Fe_3O_4 \qquad 11.1\%$$

$$2Fe_3O_4 \rightarrow O_2 + 6FeO \qquad 33.3\%$$

$$2FeO \rightarrow O_2 + 2Fe \qquad 100\%$$

The original moles of oxygen associated with Fe_2O_3 are calculated from the chemical composition and weight of the ore with all initial Fe as Fe_2O_3. As segregation progresses, part of the 'pool' of oxygen from the original Fe_2O_3 is removed via segregation; thus over time the total number of moles of oxygen that must be removed via in-situ reduction for 100% iron oxide reduction decreases, designated as $n_{O,required}$, decreases in accordance with:

$$n_{O,required} = n^{O}_{O_{Fe_2O_3}} - n^{seg}_{O_{Fe_2O_3}}$$

$n^{O}_{O_{Fe_2O_3}}$ is the moles of O associated with the initial Fe_2O_3 and $n^{seg}_{O_{Fe_2O_3}}$ is the moles of O from the initial Fe_2O_3 that has been removed by segregation to form alloy.

The percentage of oxygen removed from the available Fe_2O_3 can be calculated on the assumption that all oxygen removed from the system via in-situ reduction is removed from the initial Fe_2O_3, where:

$$\%O = 100\left(\frac{n_{O,in-situ}}{n_{O,required}}\right)$$

Appendix B Figures and Tables

B.1 Boudouard Rate Plots

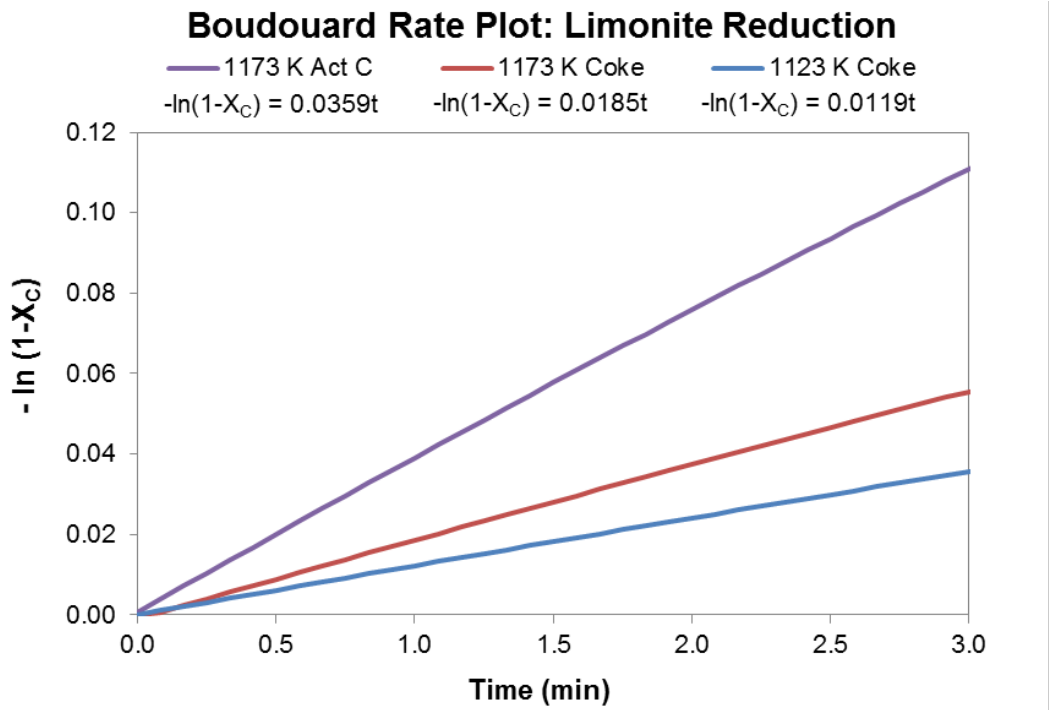

Figure B.1 Integrated Boudouard Rate Equation Plot, Limonite Reduction

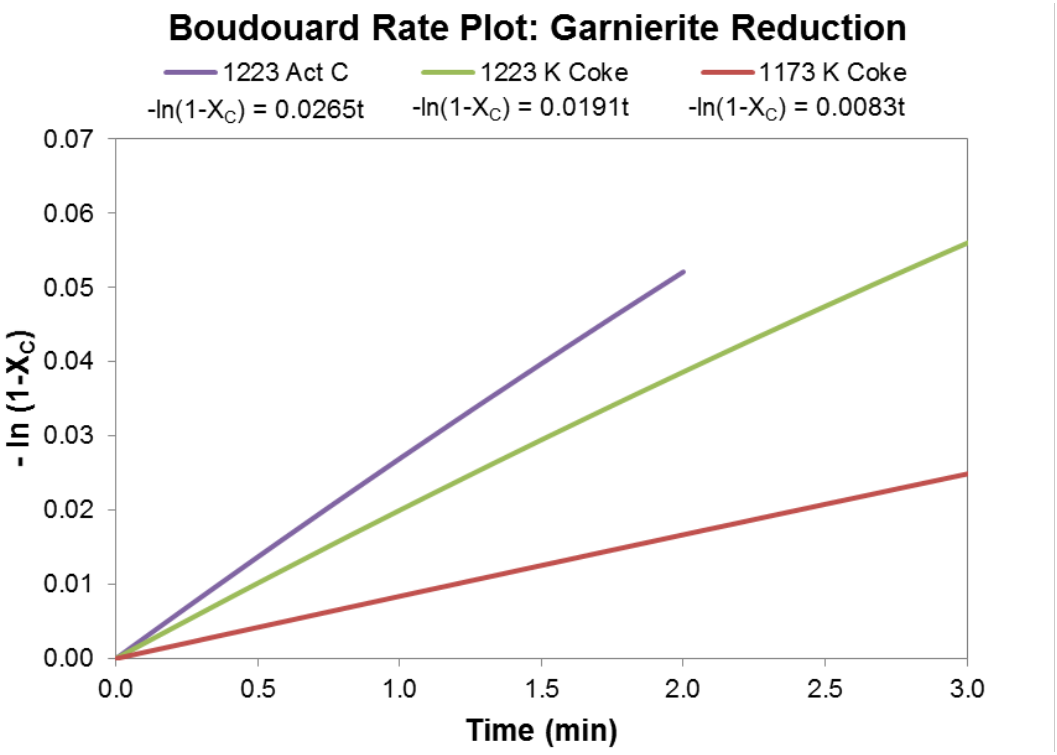

Figure B.2 Integrated Boudouard Rate Equation Plot, Garnierite Reduction

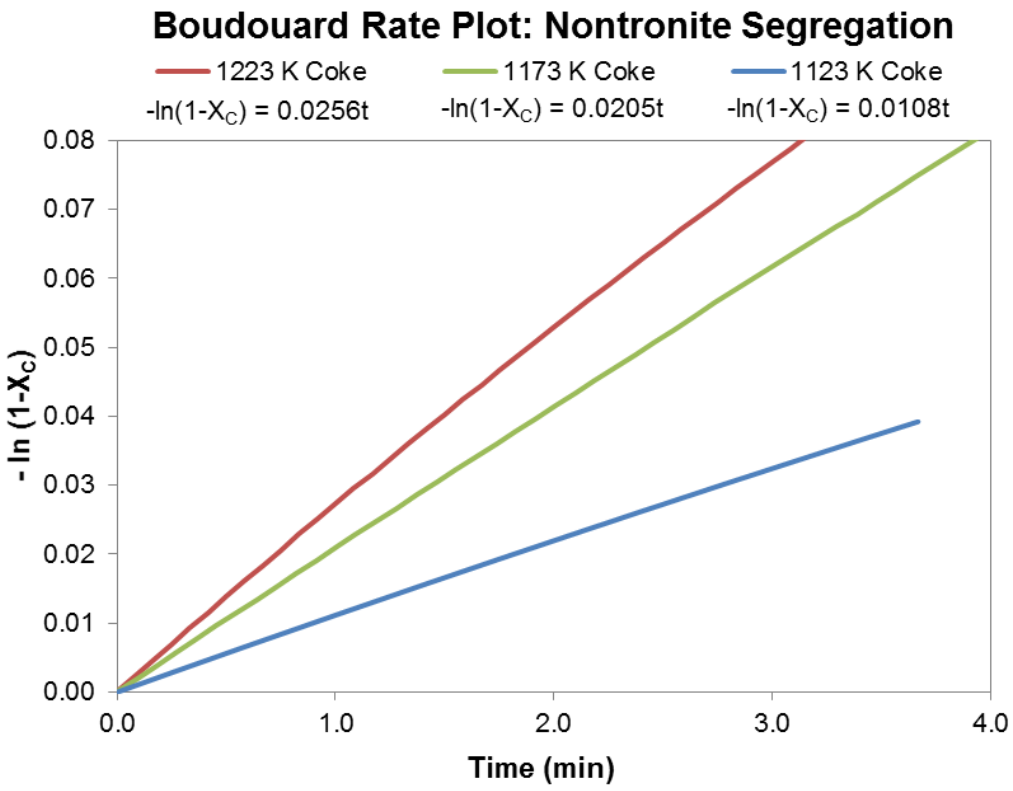

Figure B.3 Integrated Boudouard Rate Equation Plot, Nontronite Segregation

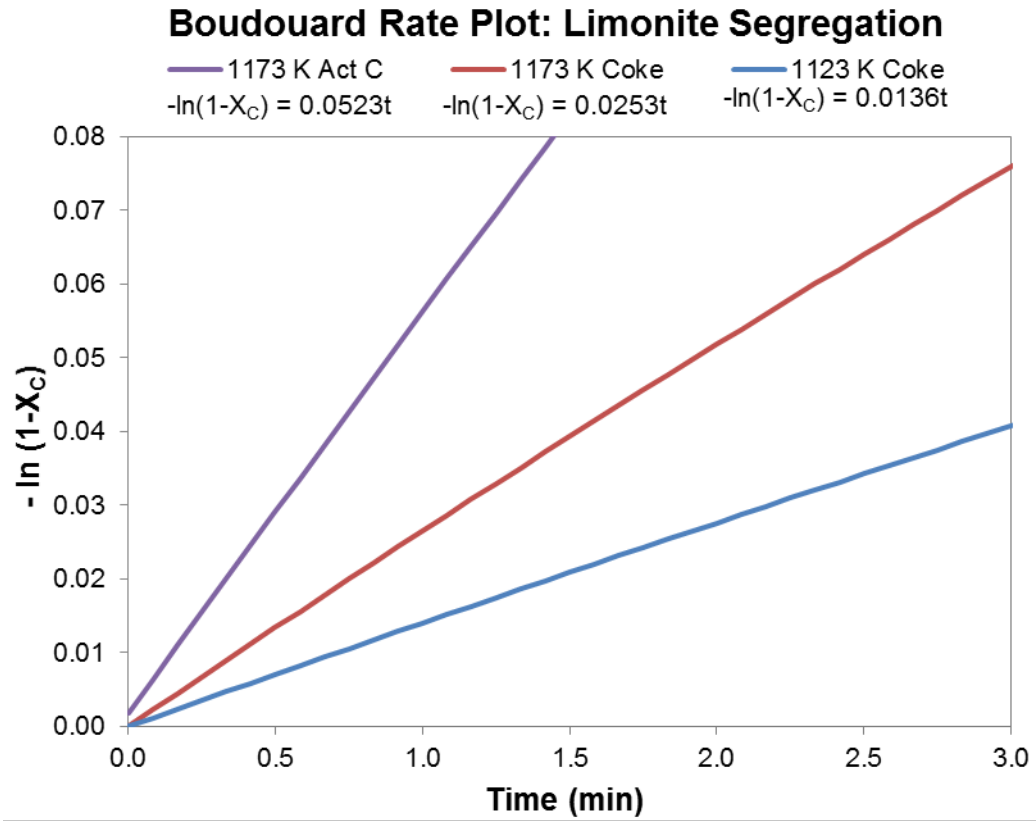

Figure B.4 Integrated Boudouard Rate Equation Plot, Limonite Segregation

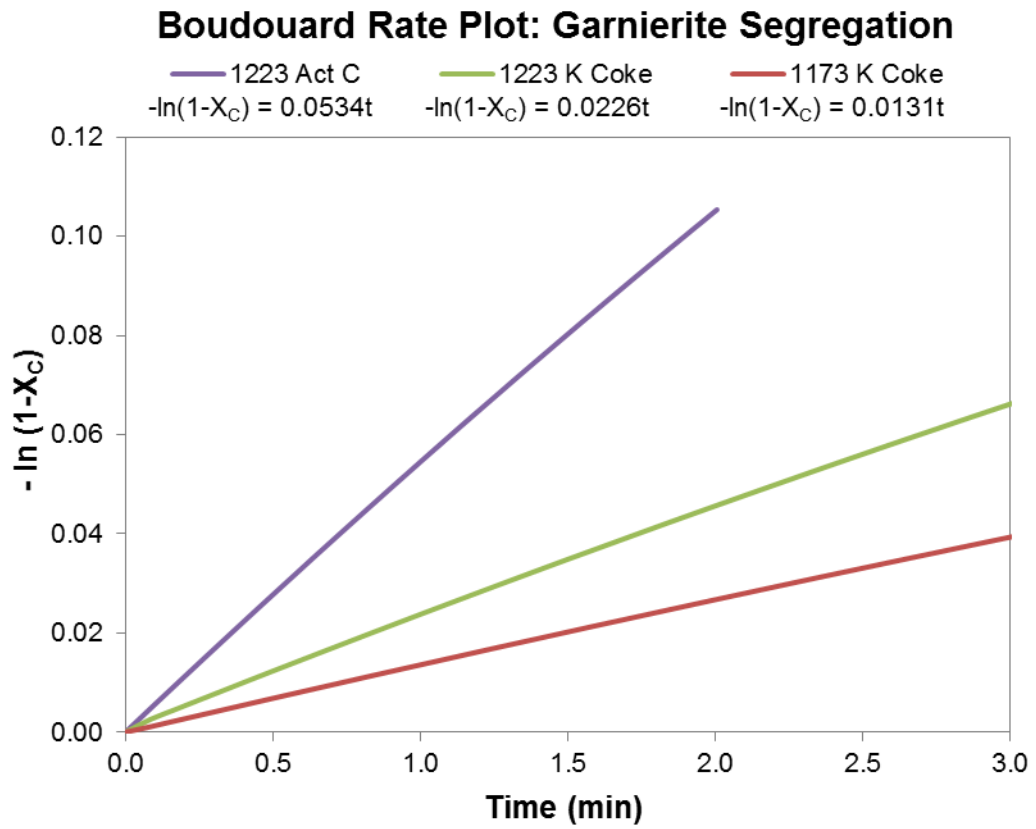

Figure B.5 Integrated Boudouard Rate Equation Plot, Garnierite Segregation

B.2 Segregation Mass Balances

Table B.1 Nickel Segregation Mass Balances

Calculated using data from segregation tests at 1173 K with coke. Segregation times were 70 minutes for nontronite and garnierite and 80 minutes for limonite. Chemical analysis was non-selective; thus nickel from all nickel containing species was accounted for.

Ore Type	Nickel Outputs (% of input)					
	Segregation Product	Magnetic Con	Non-Magnetic Tail	Residual Chloride	Handling Loss	Volatilisation Loss
Limonite	99.4	-	-	-	-	0.59
Nontronite	-	65.7	30.7	1.5	1.5	2.03
Garnierite	-	50.0	41.3	2.5	5.0	1.22

B.3 Arrhenius Plots

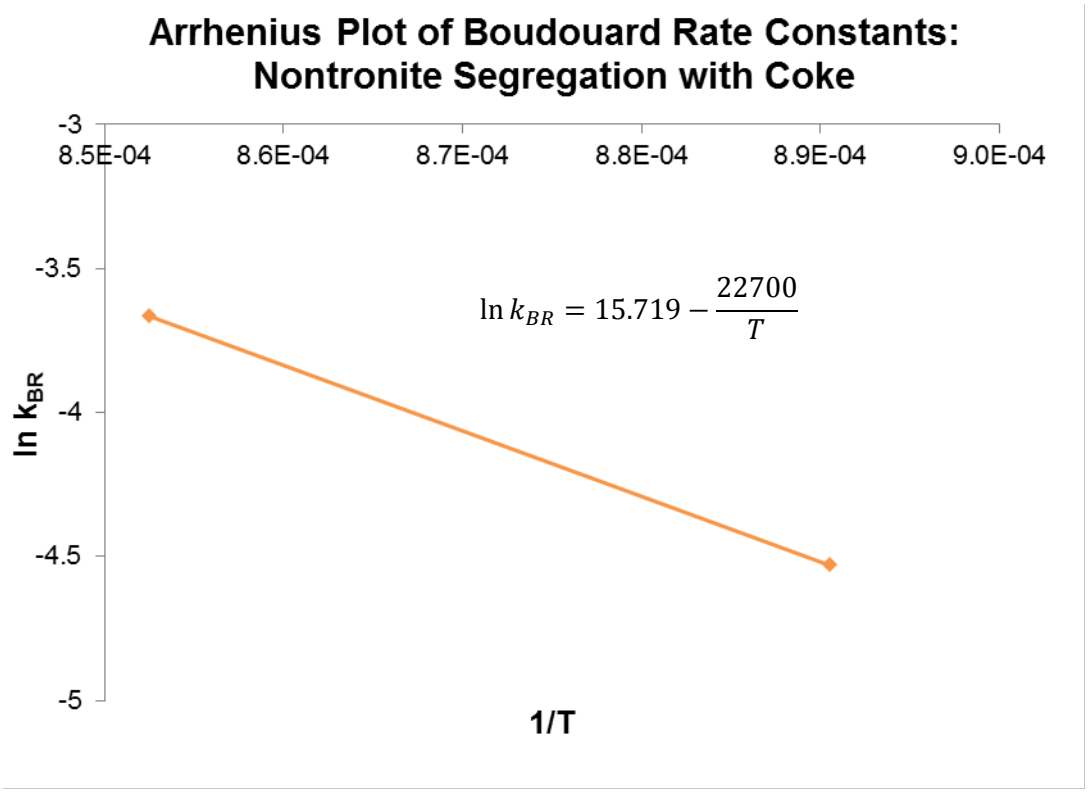

Figure B.6 Arrhenius Plot of Boudouard Rate Constants, Nontronite with Coke

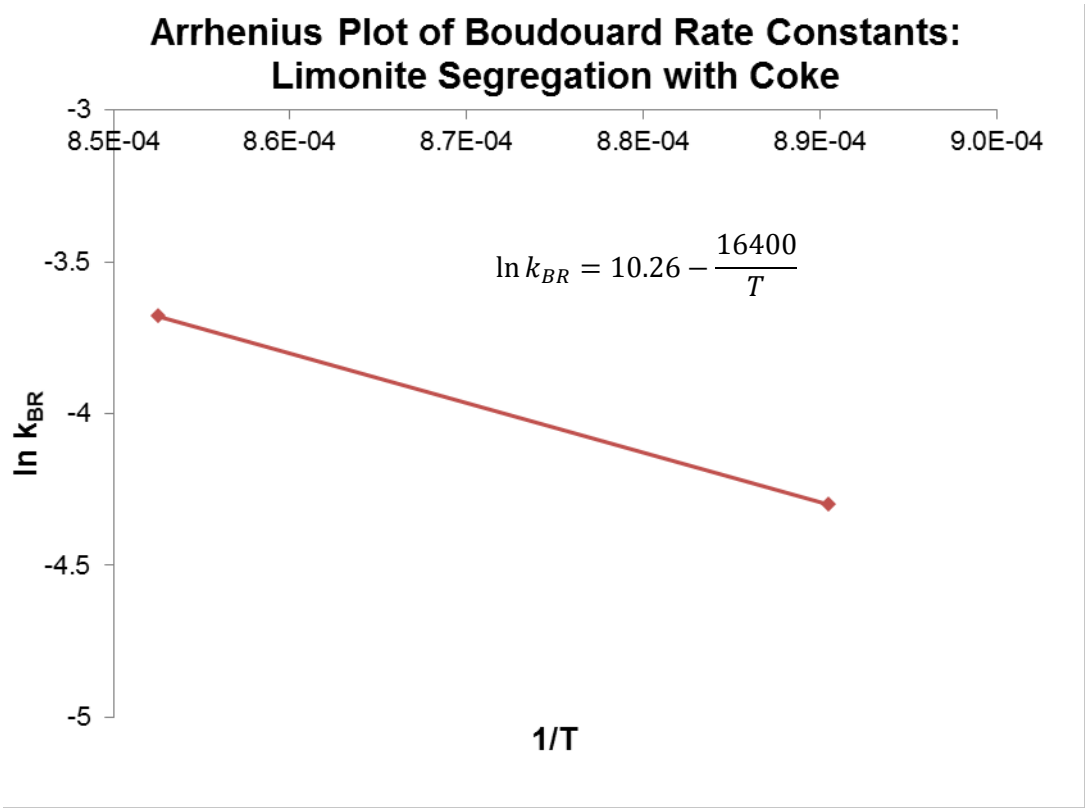

Figure B.7 Arrhenius Plot of Boudouard Rate Constants, Limonite with Coke

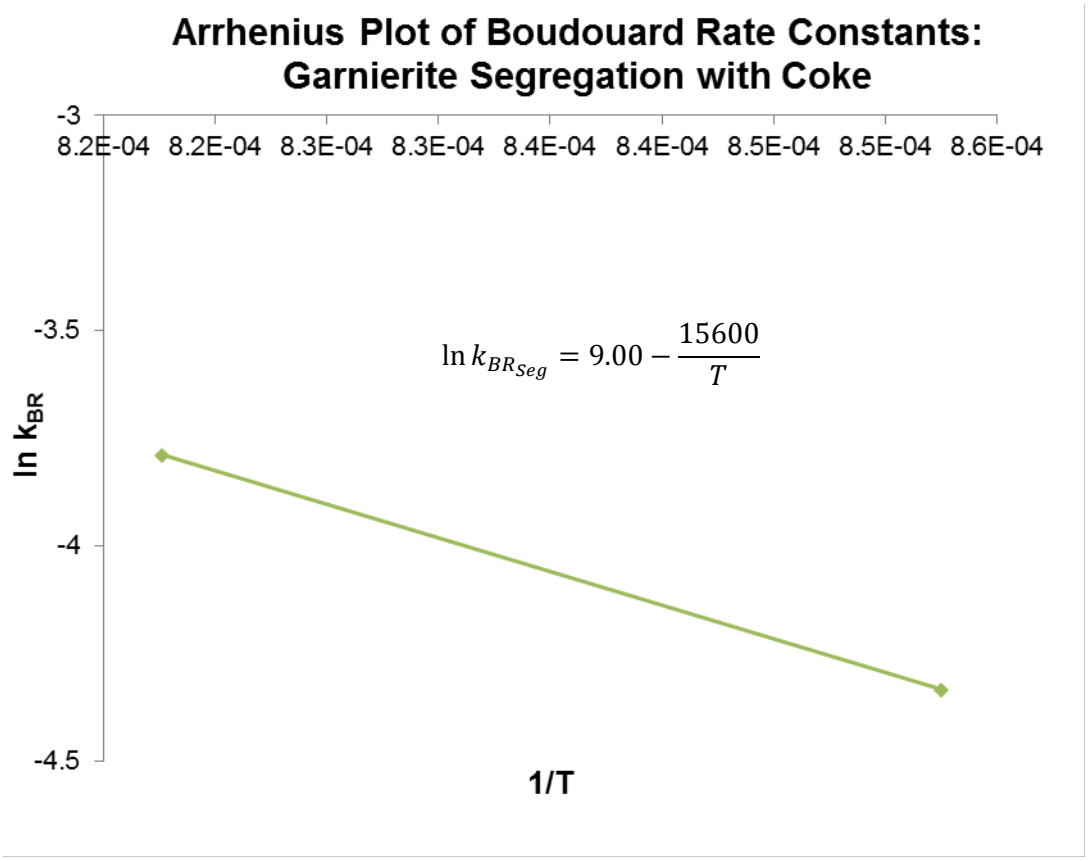

Figure B.8 Arrhenius Plot of Boudouard Rate Constants, Garnierite with Coke

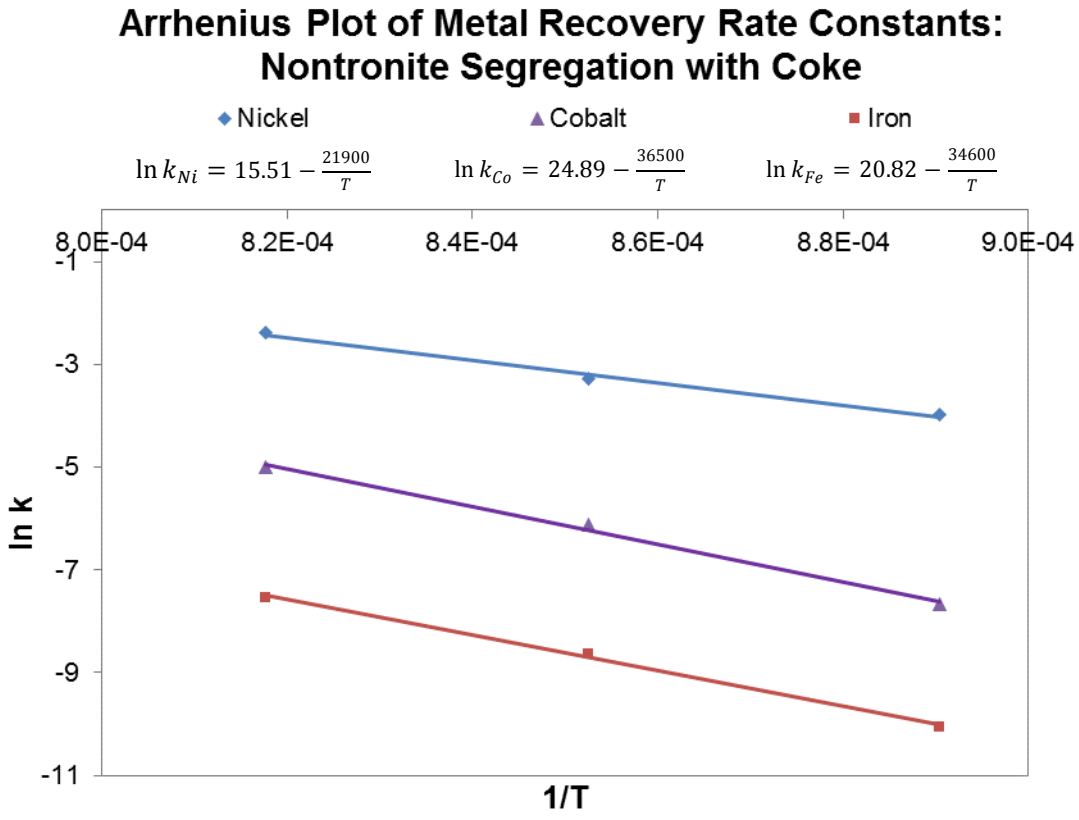

Figure B.9 Arrhenius Plot for Metal Recovery, Nontronite Segregation with Coke

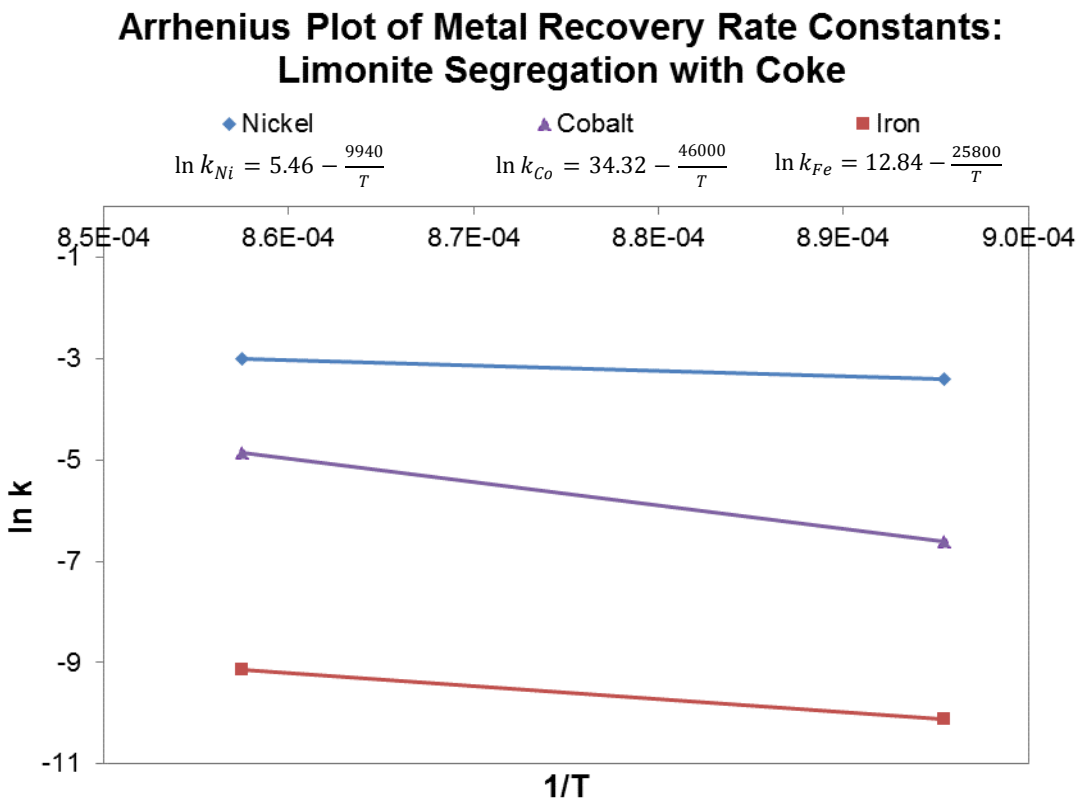

Figure B.10 Arrhenius Plot for Metal Recovery, Limonite Segregation with Coke

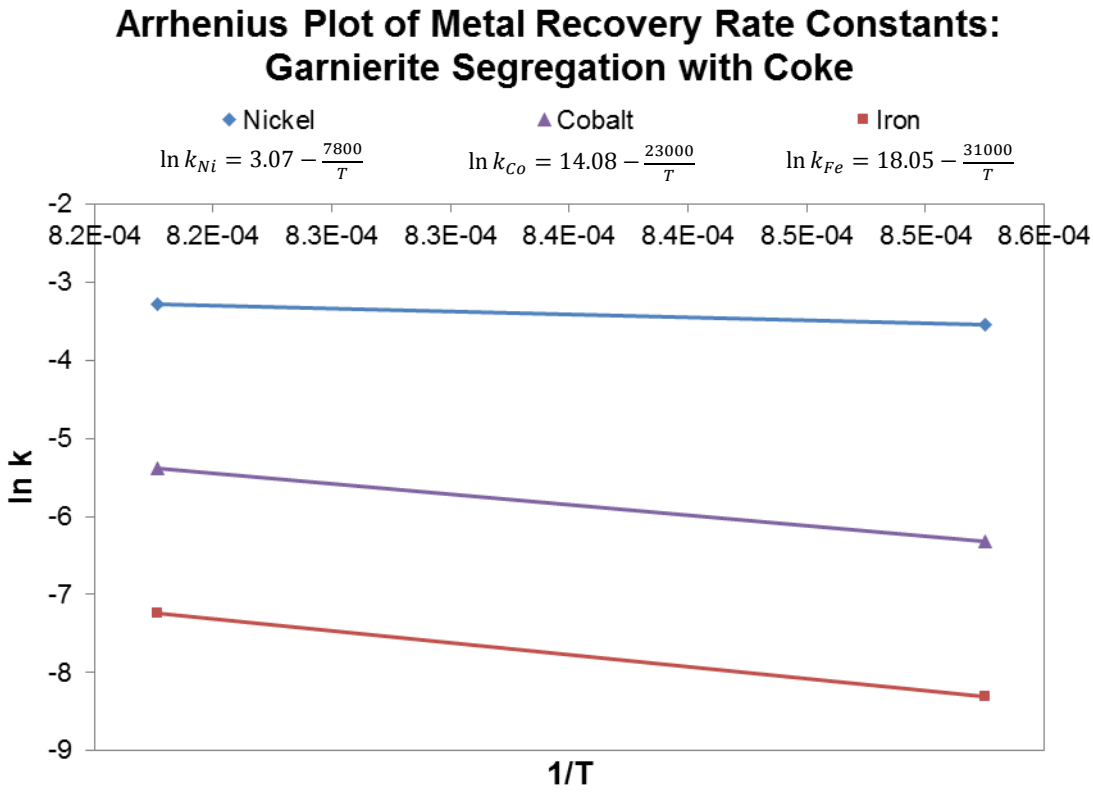

Figure B.11 Arrhenius Plot for Metal Recovery, Garnierite Segregation with Coke

B.4 Carbon Consumption & Gas Volumes

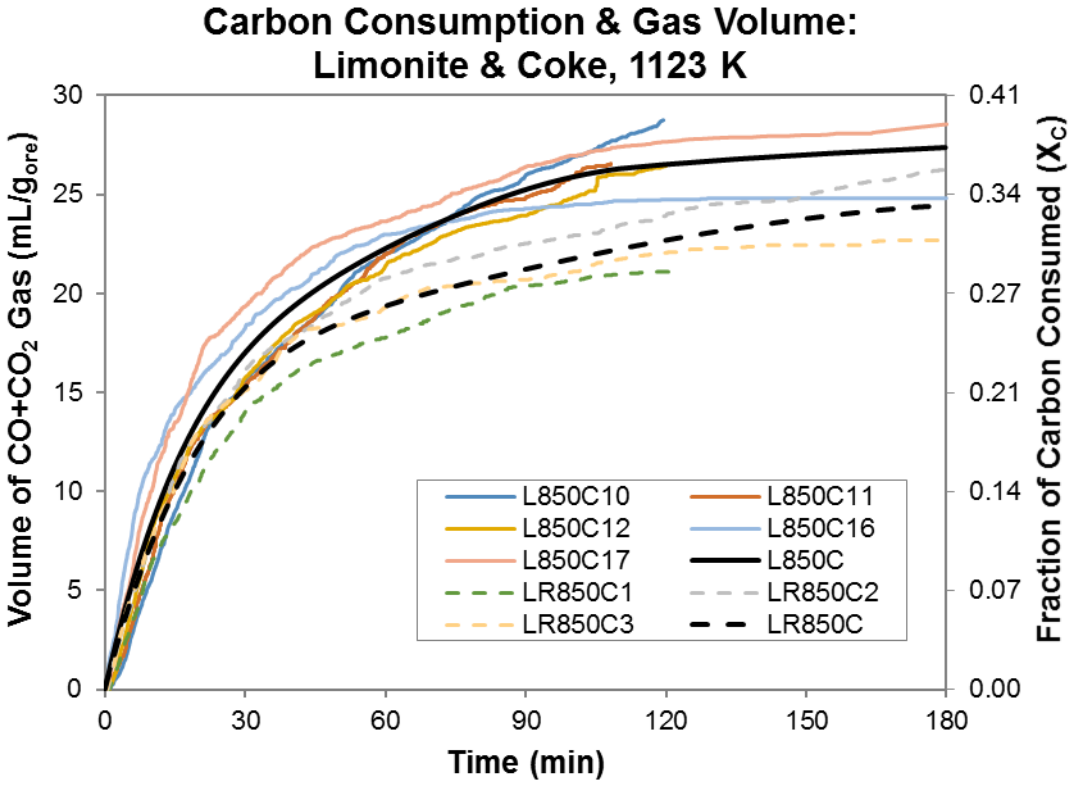

Figure B.12 Gas Volume & Carbon Consumption, Limonite & Coke at 1123 K

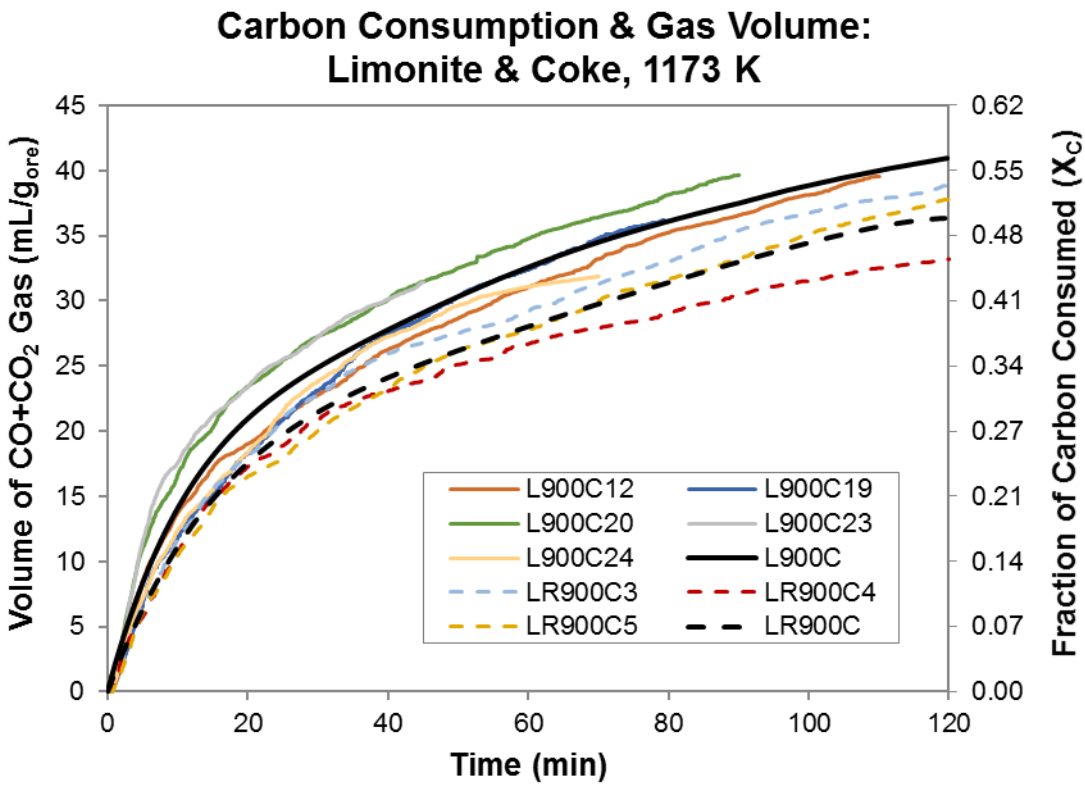

Figure B.13 Gas Volume & Carbon Consumption, Limonite & Coke at 1173 K

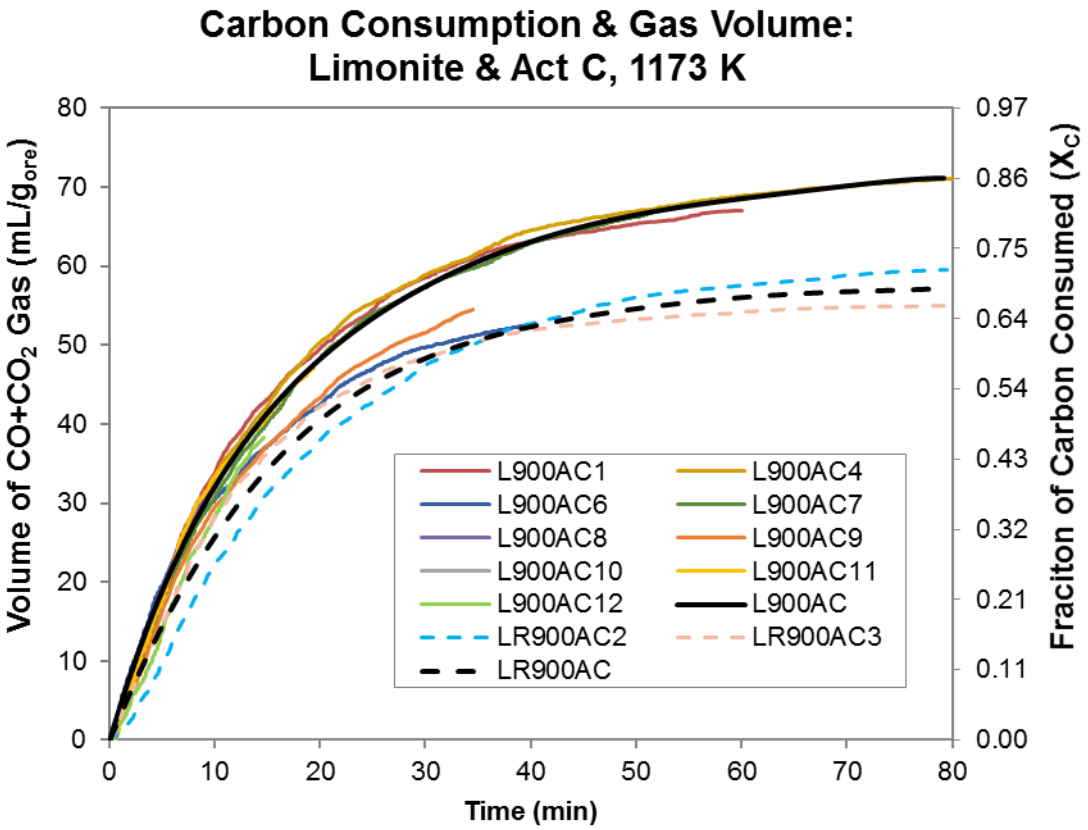

Figure B.14 Gas Volume & Carbon Consumption, Limonite & Act C at 1173 K

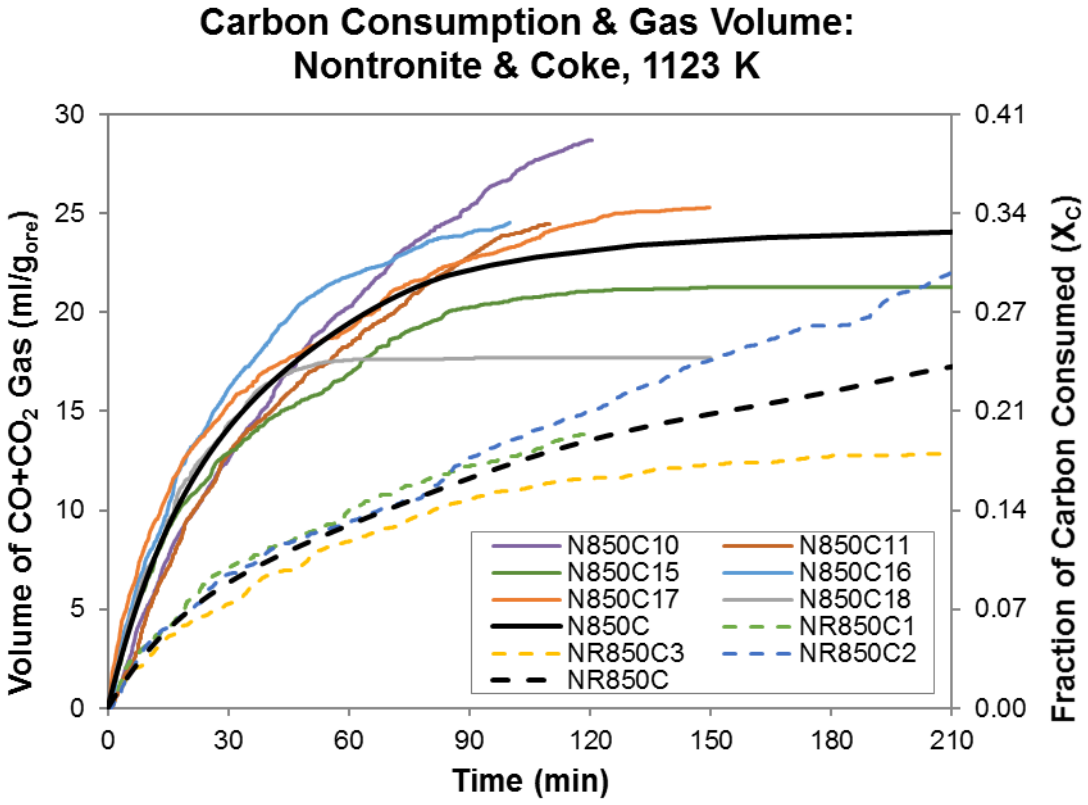

Figure B.15 Gas Volume & Carbon Consumption, Nontronite & Coke at 1123 K

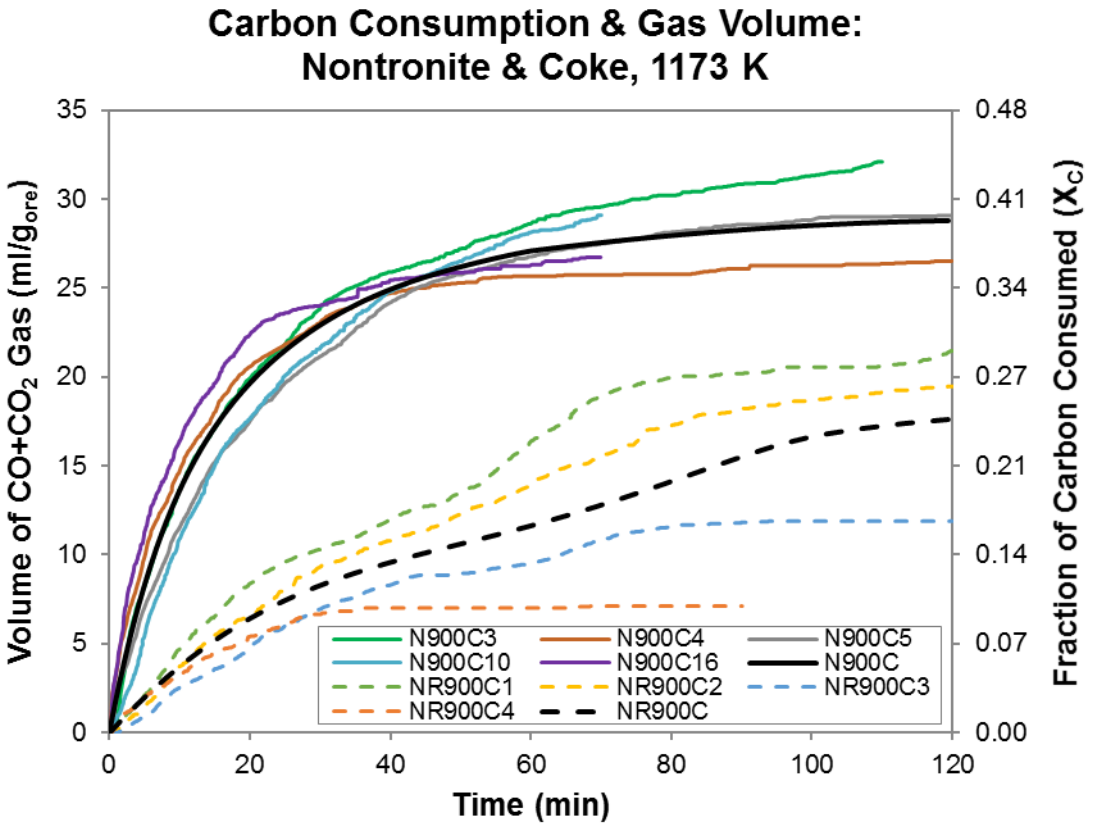

Figure B.16 Gas Volume & Carbon Consumption, Nontronite & Coke at 1173 K

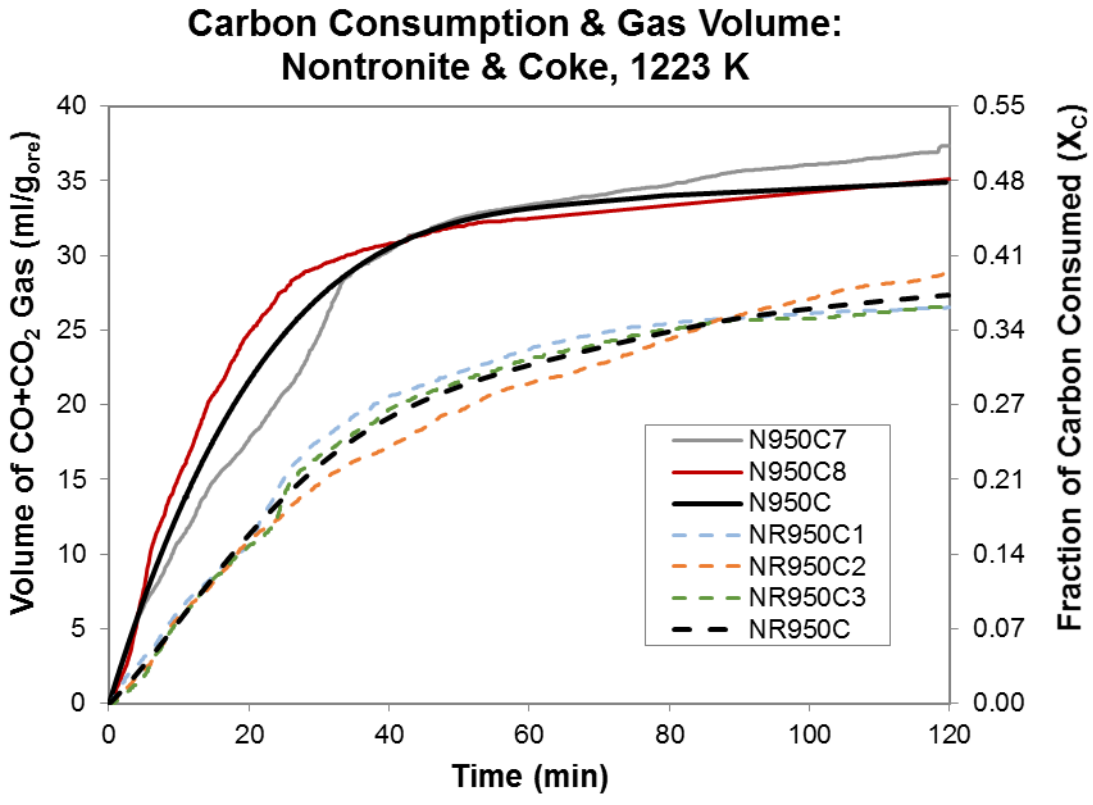

Figure B.17 Gas Volume & Carbon Consumption, Nontronite & Coke at 1223 K

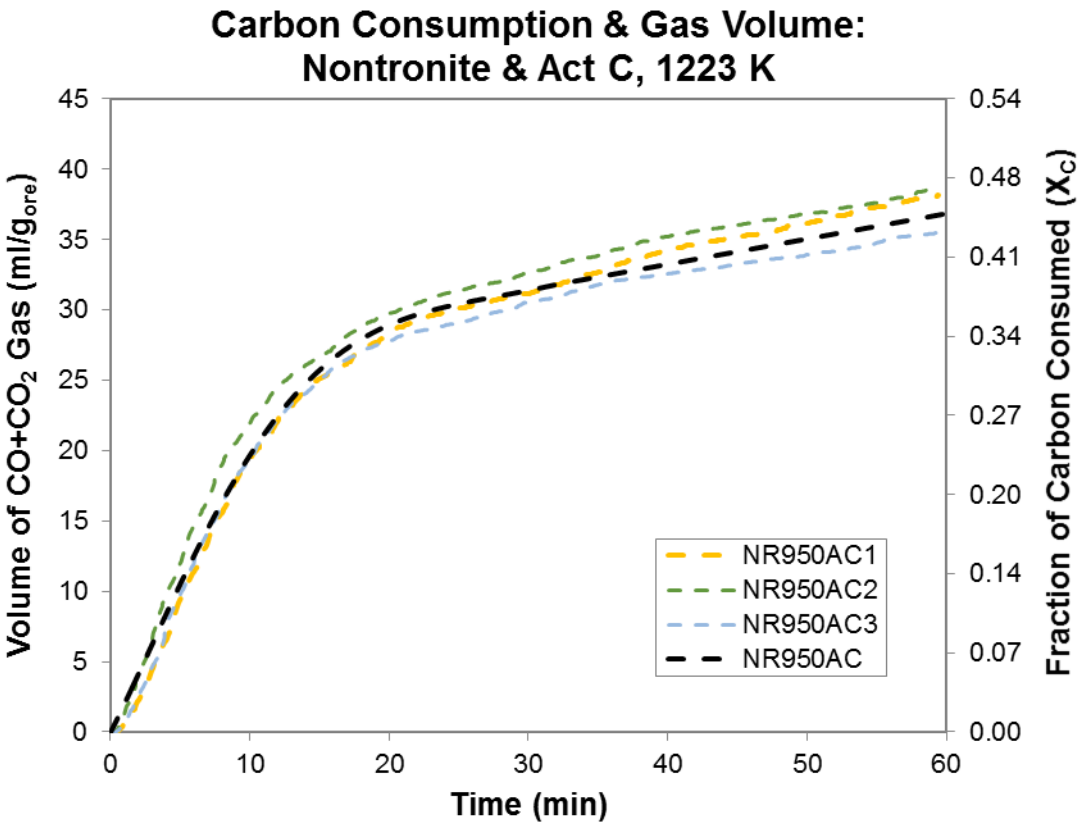

Figure B.18 Gas Volume & Carbon Consumption, Nontronite & Act C at 1223 K

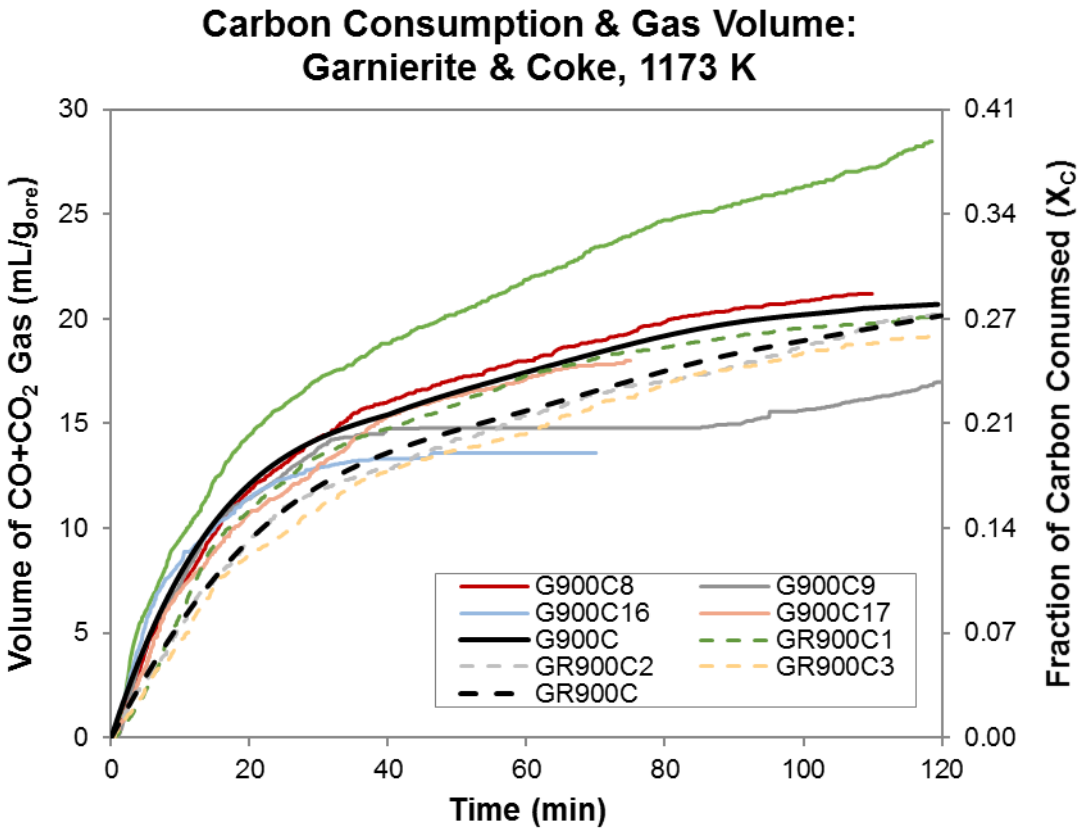

Figure B.19 Gas Volume & Carbon Consumption, Garnierite & Coke at 1173 K

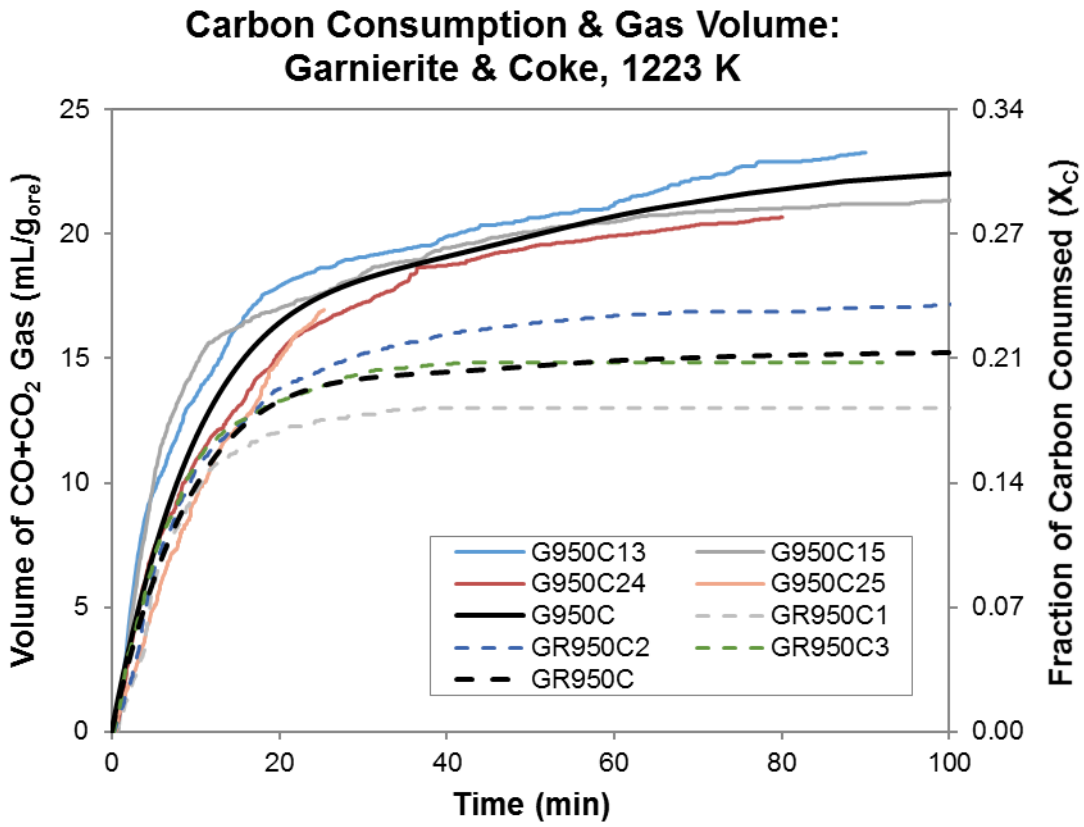

Figure B.20 Gas Volume & Carbon Consumption, Garnierite & Coke at 1223 K

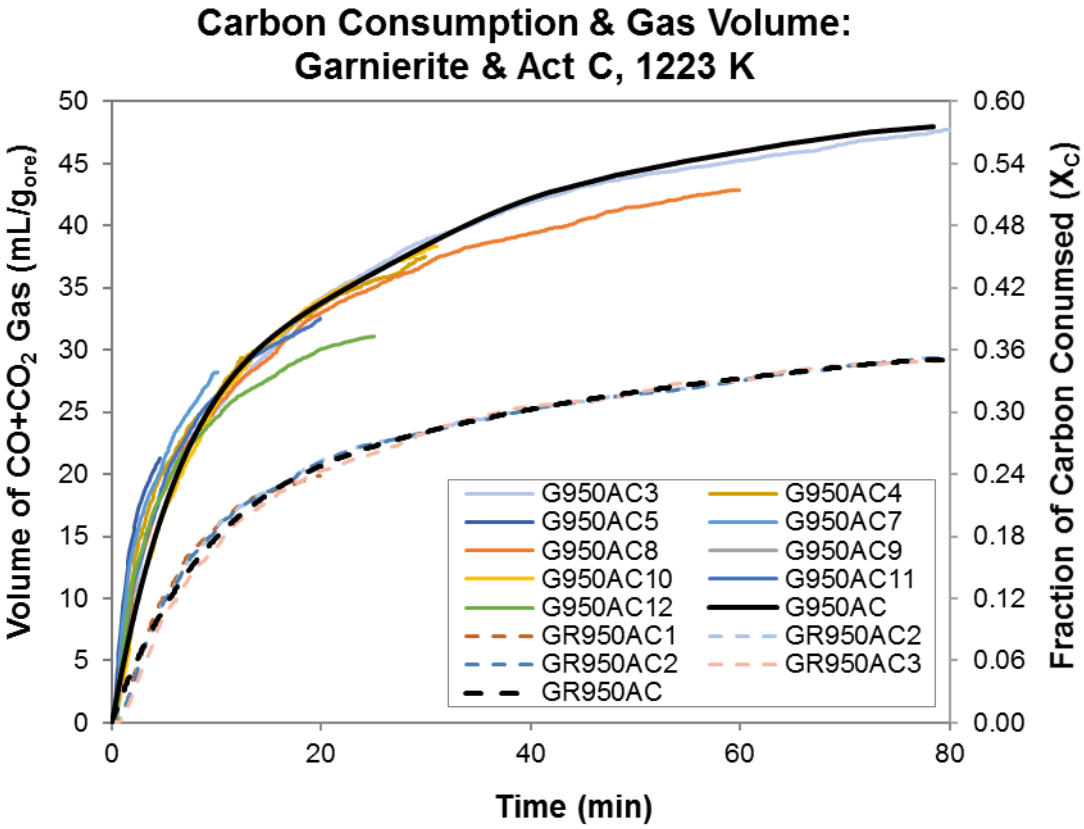

Figure B.21 Gas Volume & Carbon Consumption, Garnierite & Act C at 1223 K

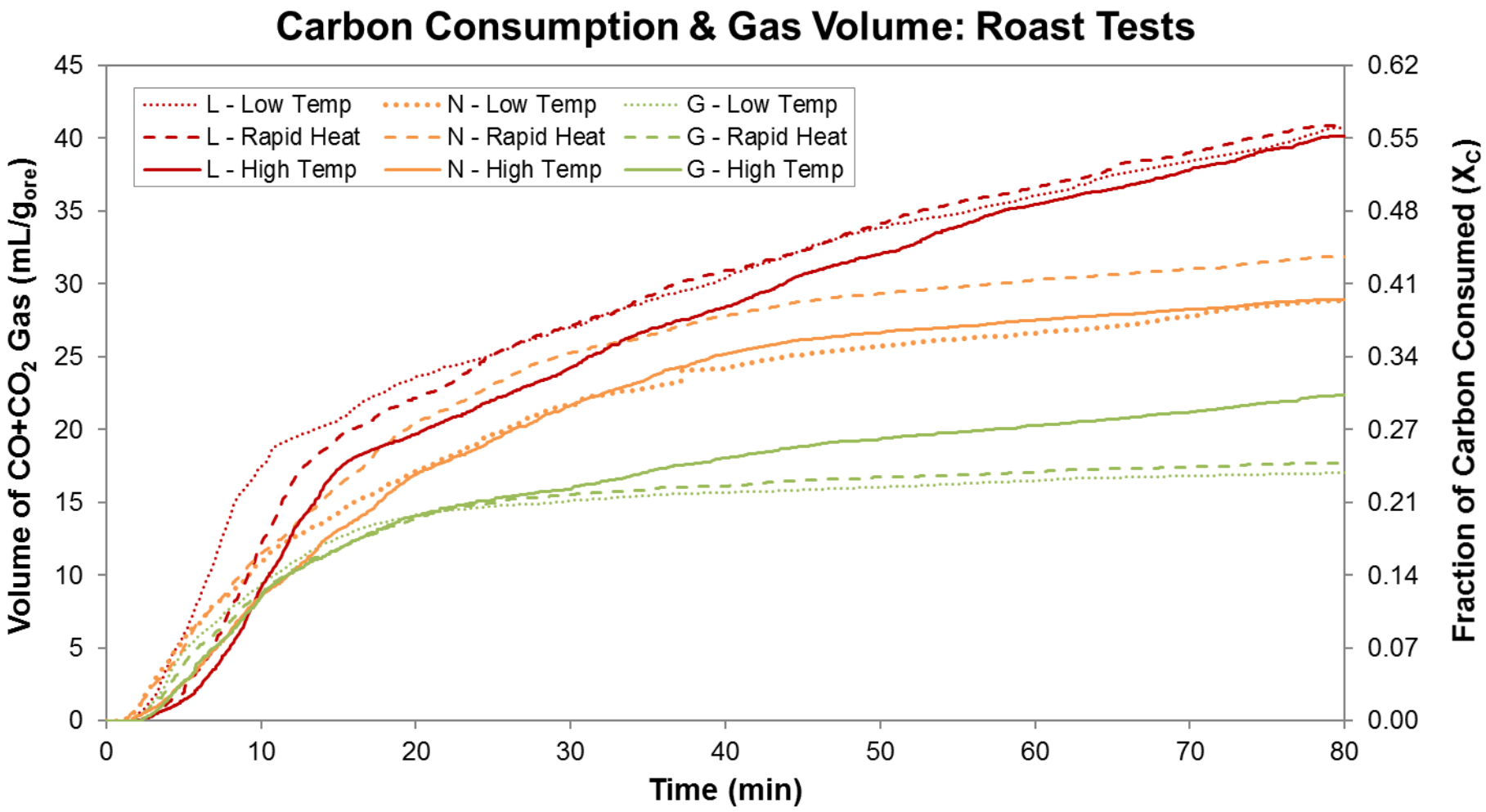

Figure B.22 Gas Volume & Carbon Consumption, Roast Tests

B.5 Oxygen Pressure

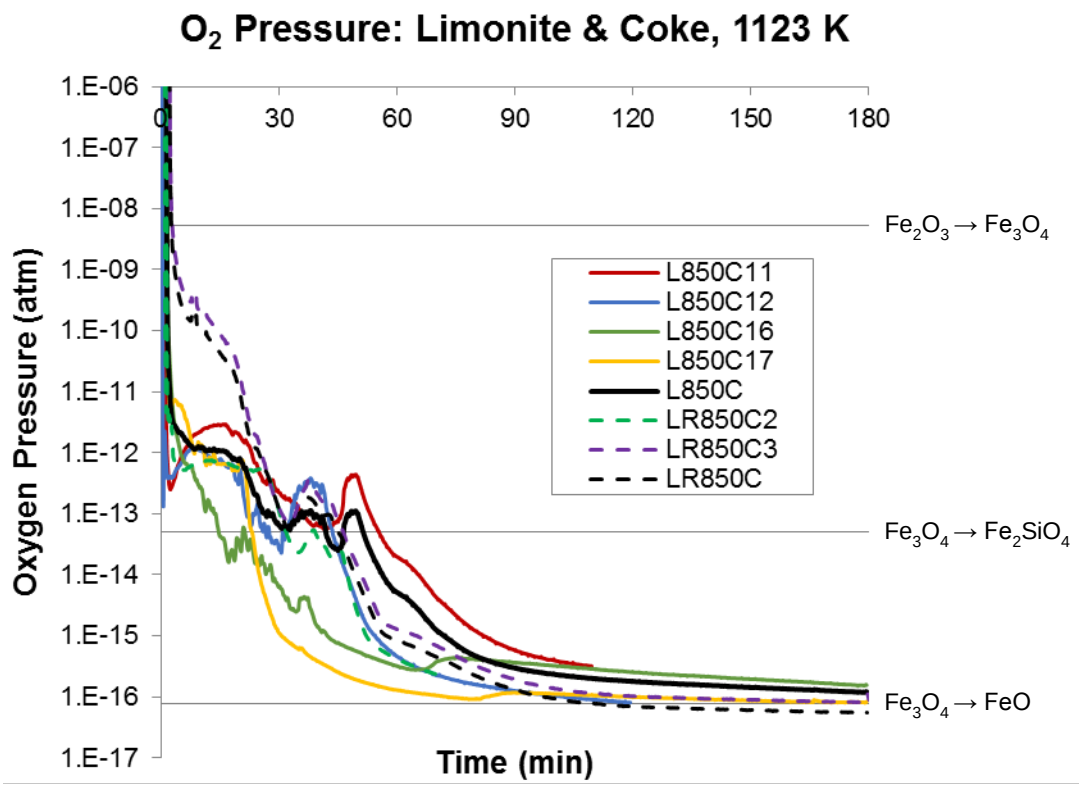

Figure B.23 O_2 Pressure Profile, Limonite & Coke at 1123 K

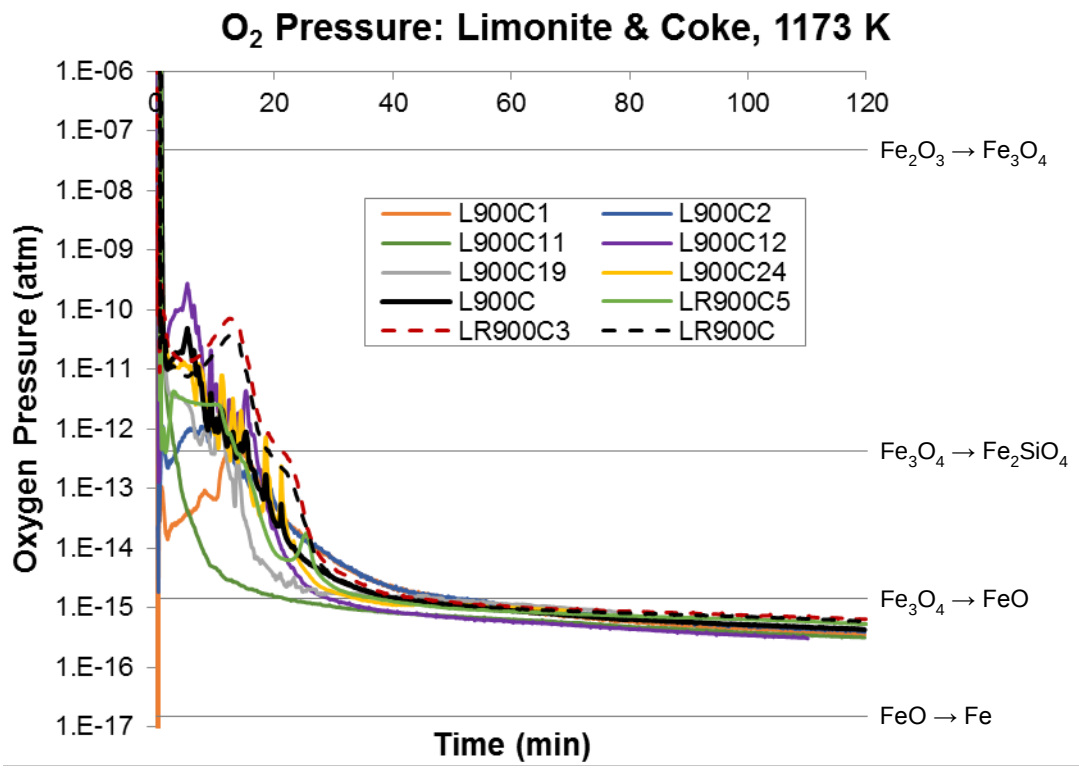

Figure B.24 O_2 Pressure Profile, Limonite & Coke at 1173 K

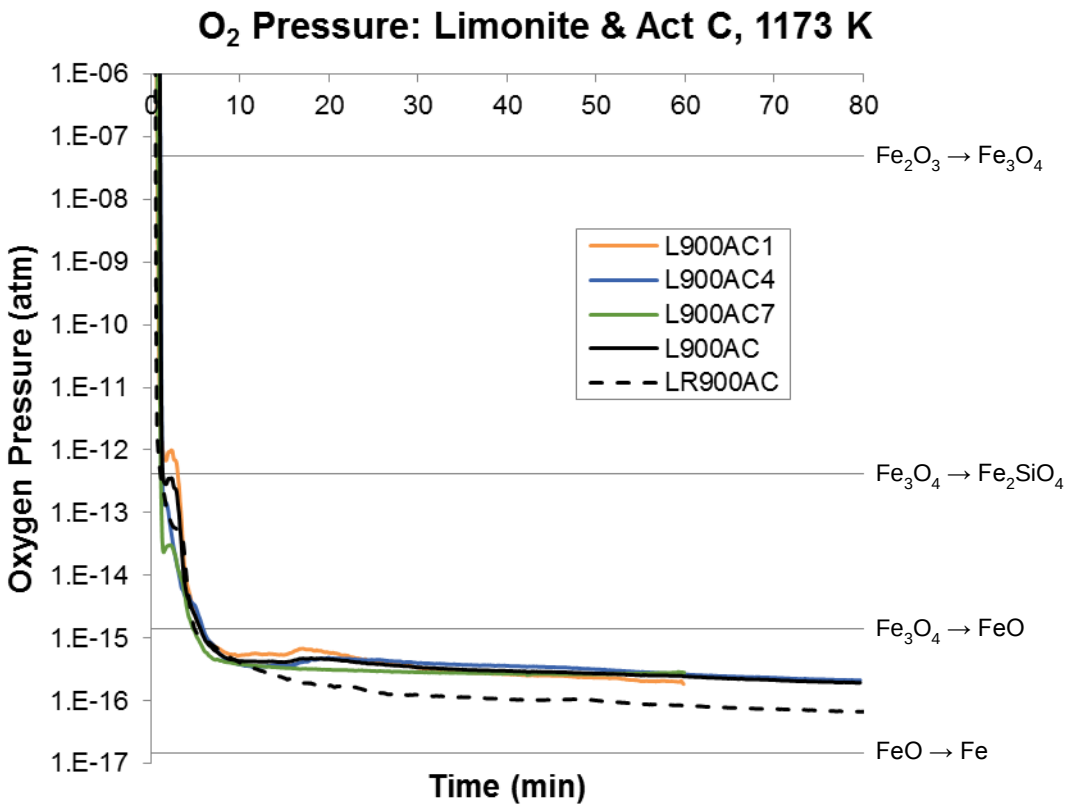

Figure B.25 O_2 Pressure Profile, Limonite & Act C at 1173 K

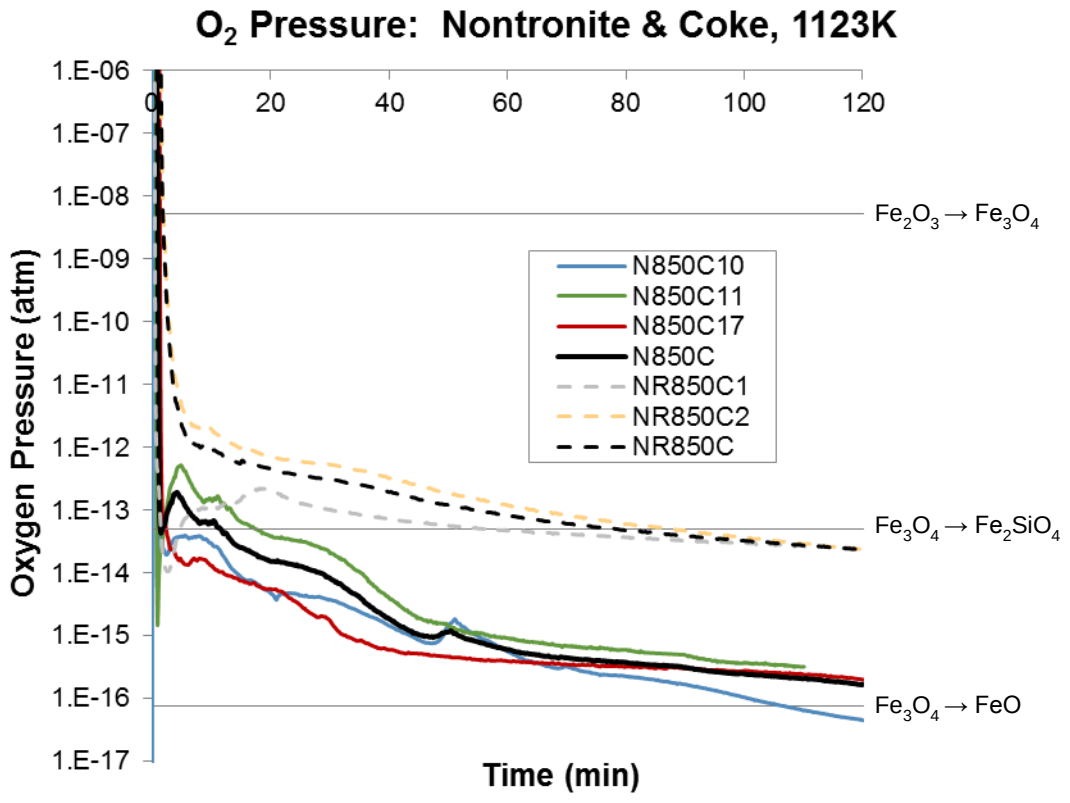

Figure B.26 O_2 Pressure Profile, Nontronite & Coke at 1123 K

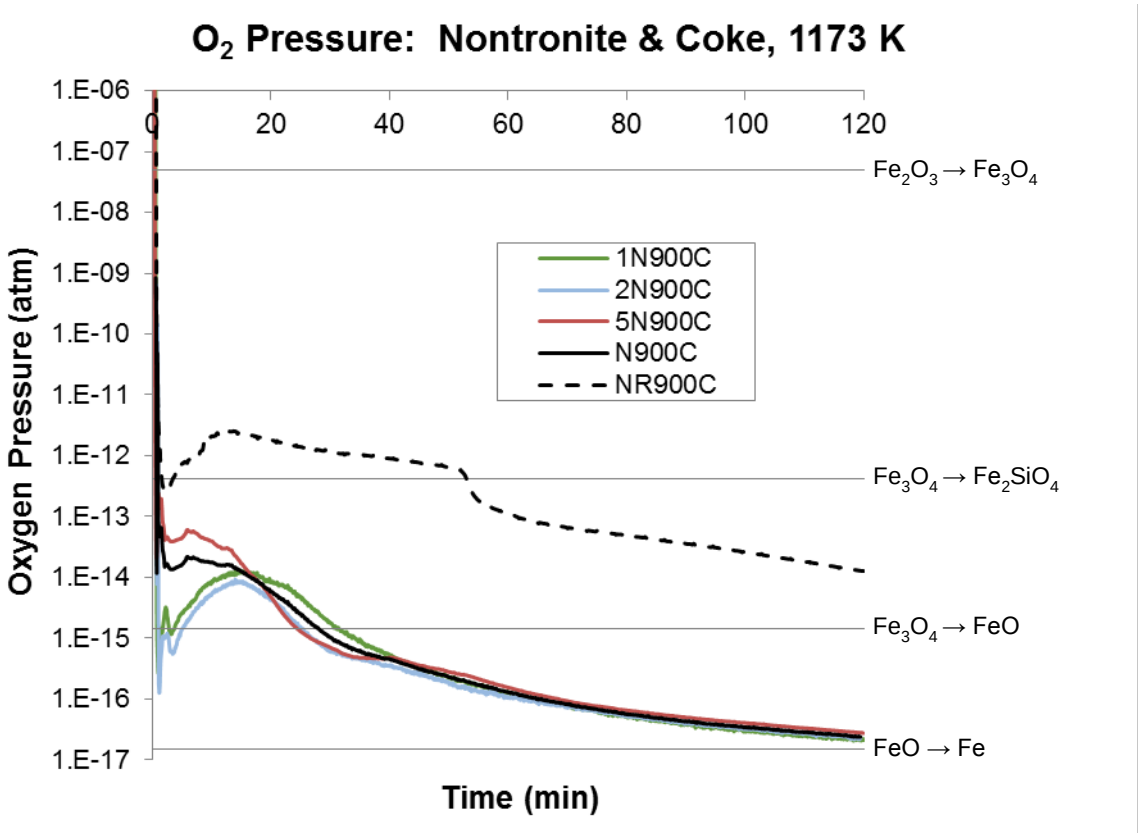

Figure B.27 O_2 Pressure Profile, Nontronite & Coke at 1173 K

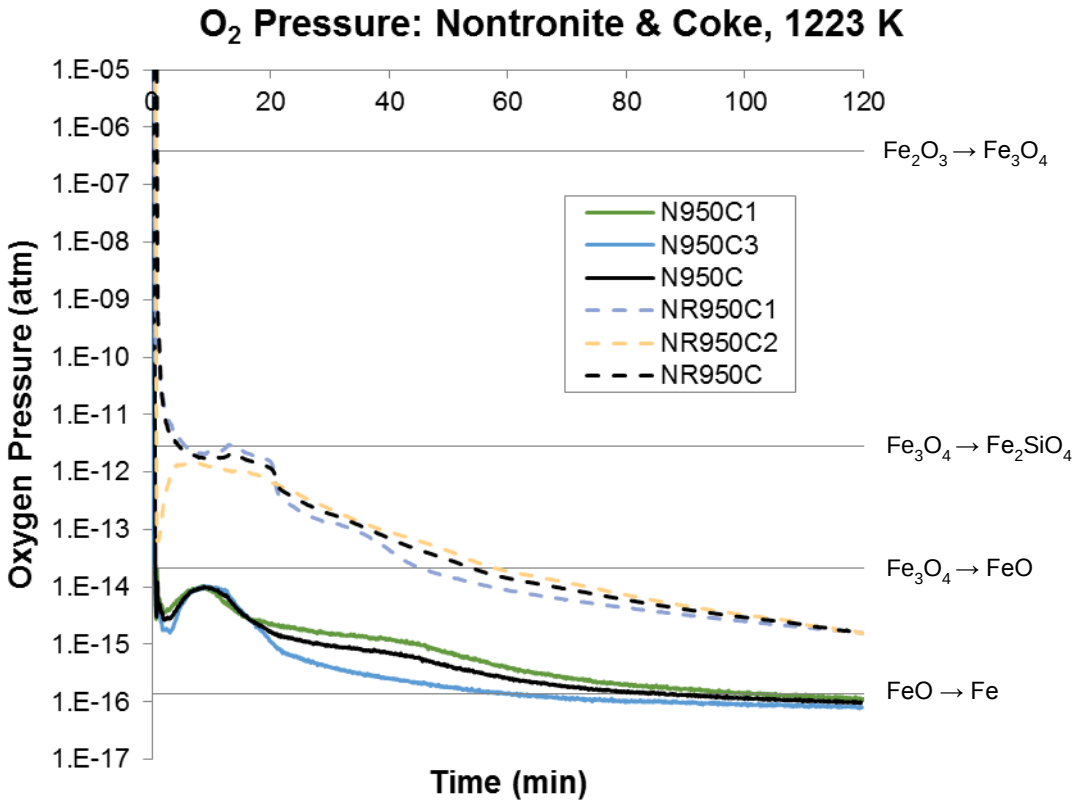

Figure B.28 O_2 Pressure Profile, Nontronite & Coke at 1223 K

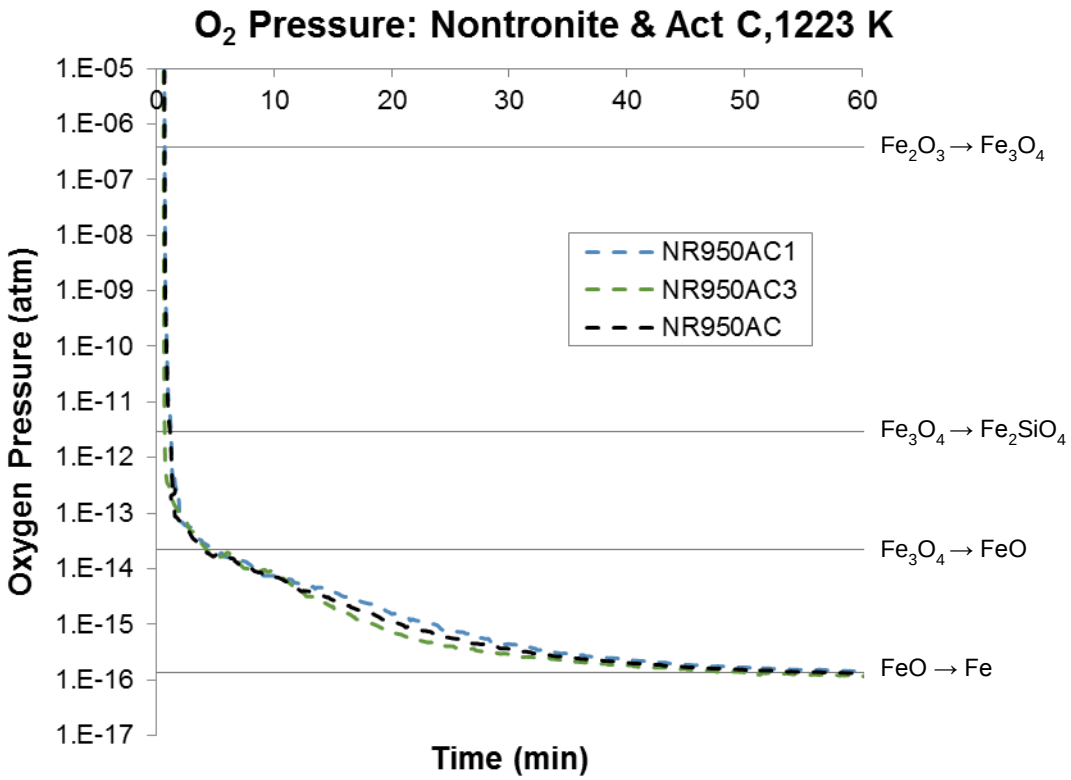

Figure B.29 O_2 Pressure Profile, Nontronite & Act C at 1223 K

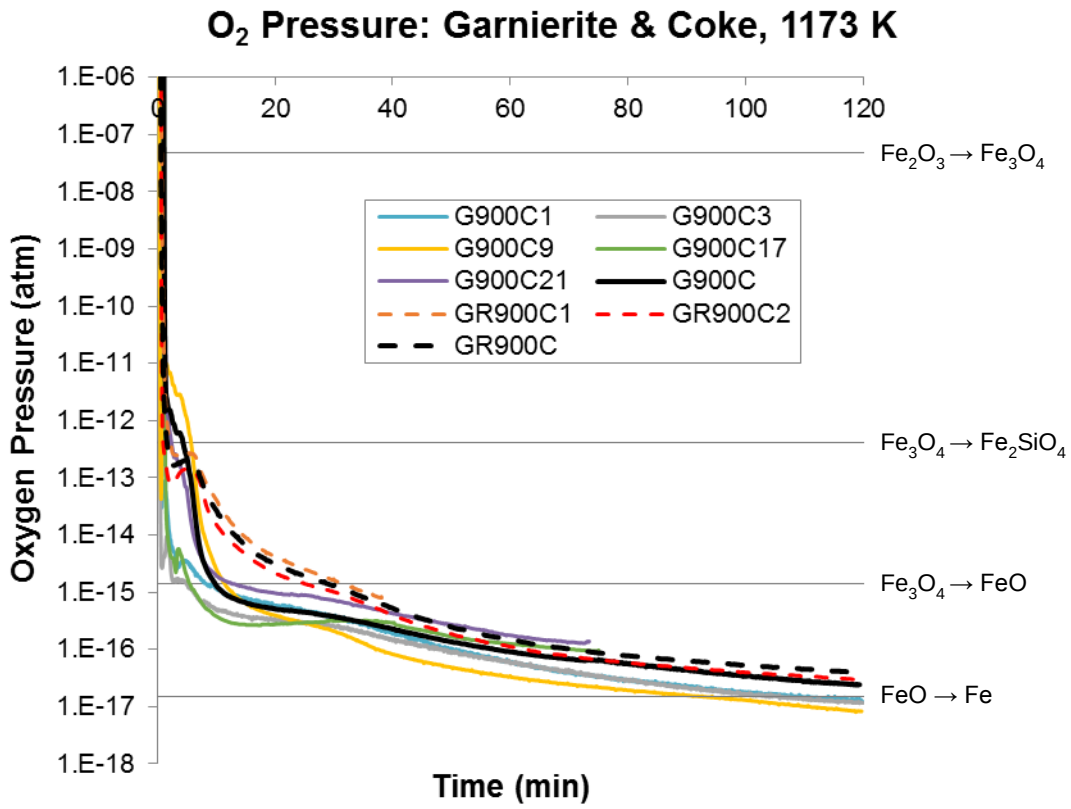

Figure B.30 O_2 Pressure Profile, Garnierite & Coke 1173 K

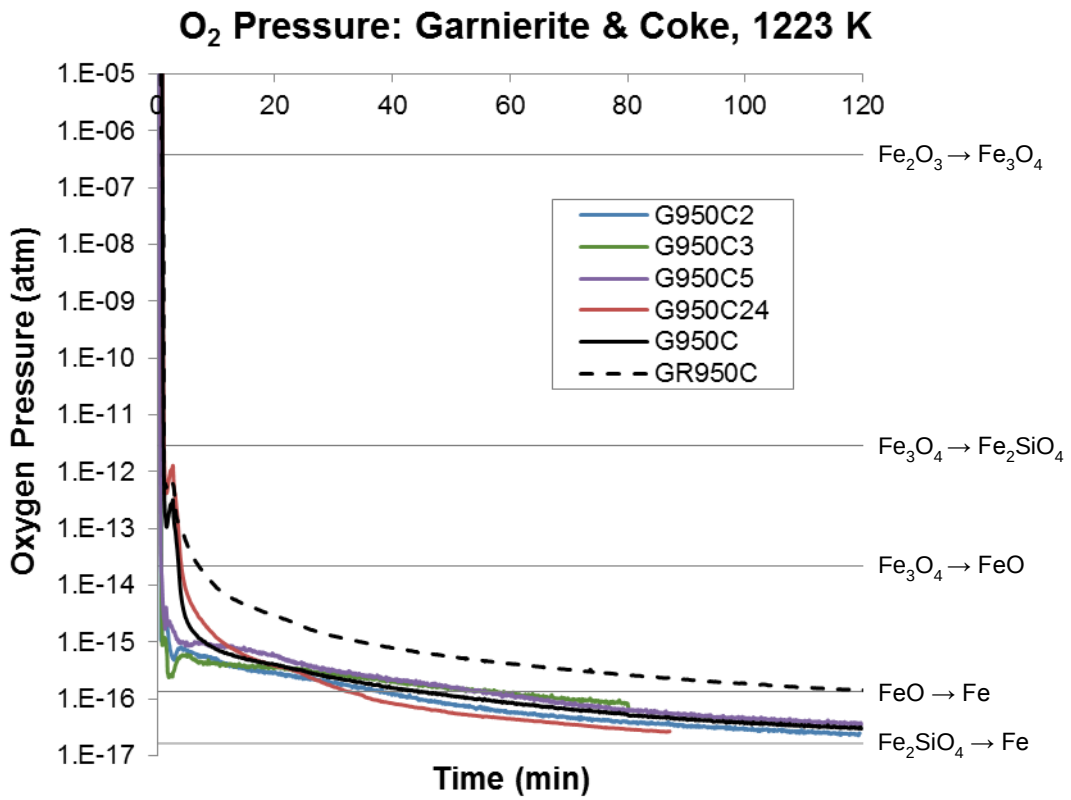

Figure B.31 O_2 Pressure Profile, Garnierite & Coke 1223 K

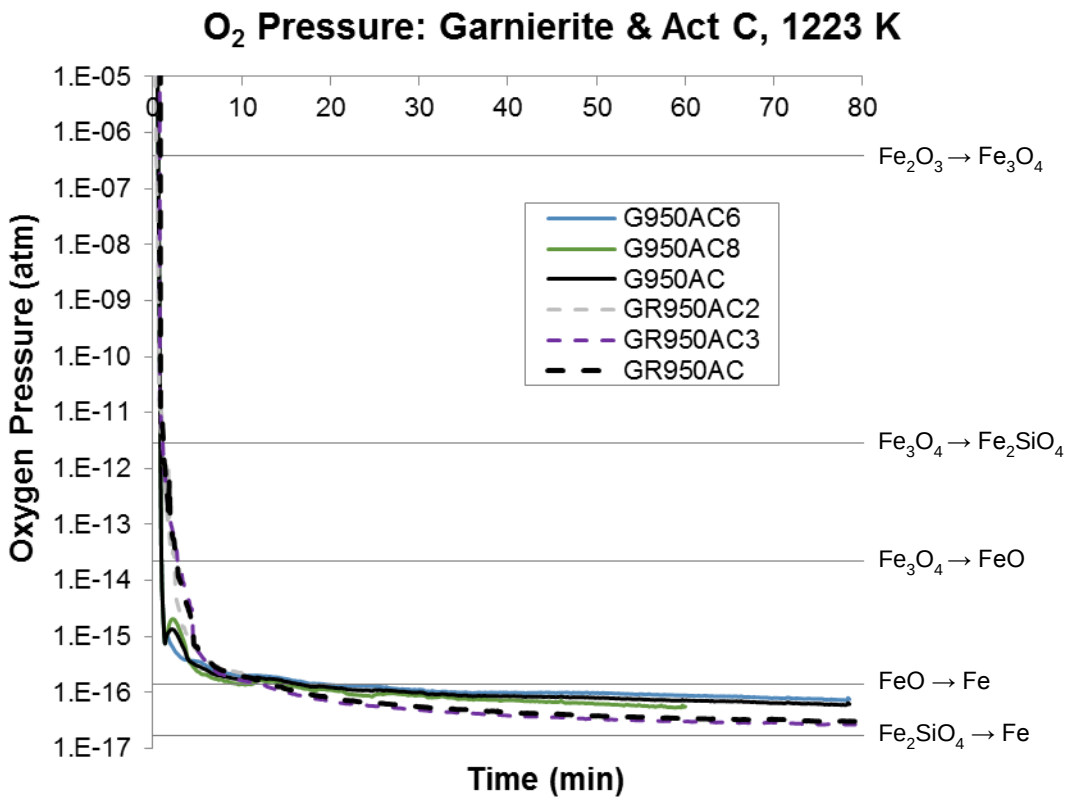

Figure B.32 O_2 Pressure Profile, Garnierite & Act C at 1223 K

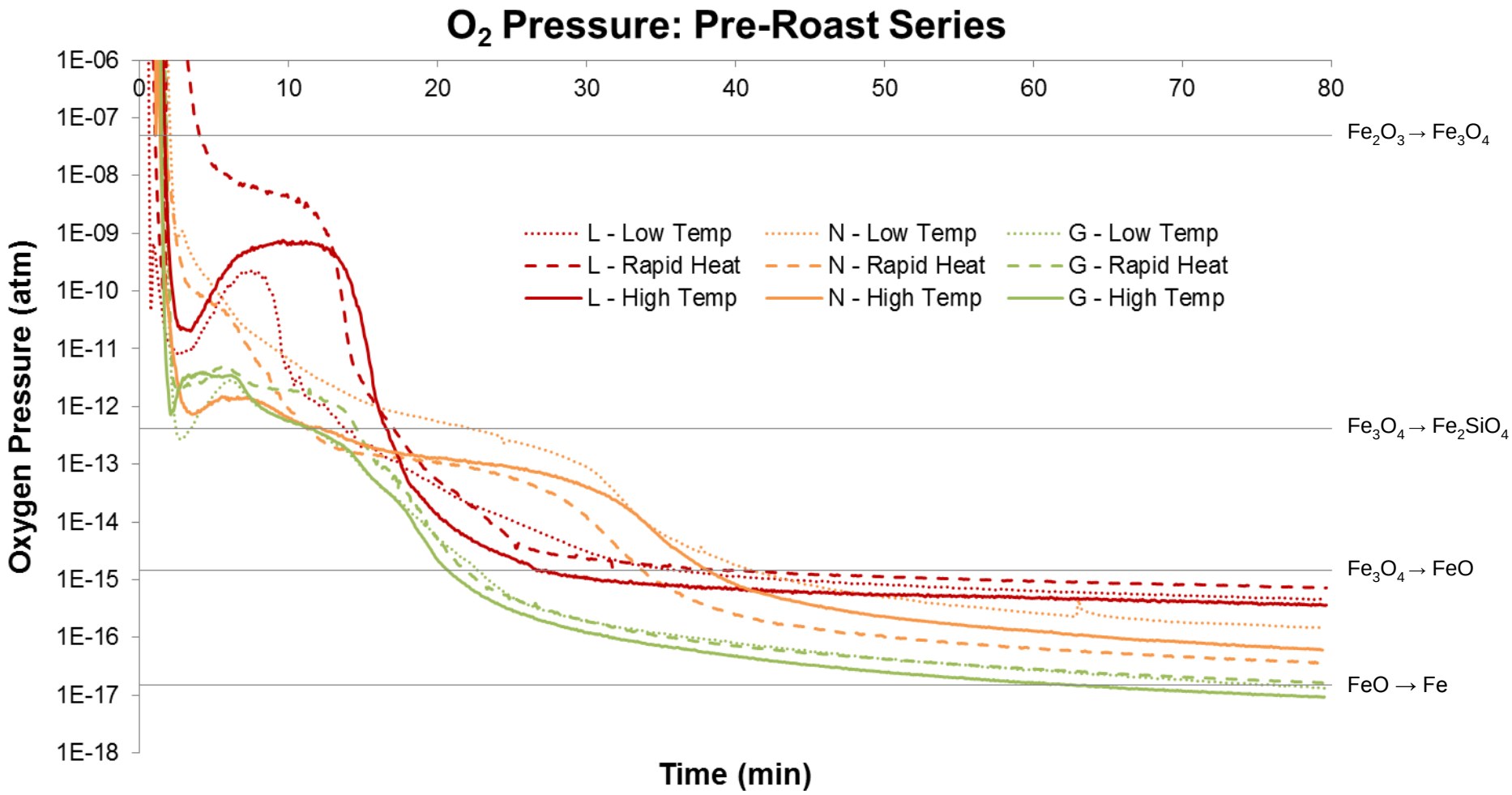

Figure B.33 O_2 Pressure Profiles, Roast Tests

B.6 Magnetic Concentrate Grade

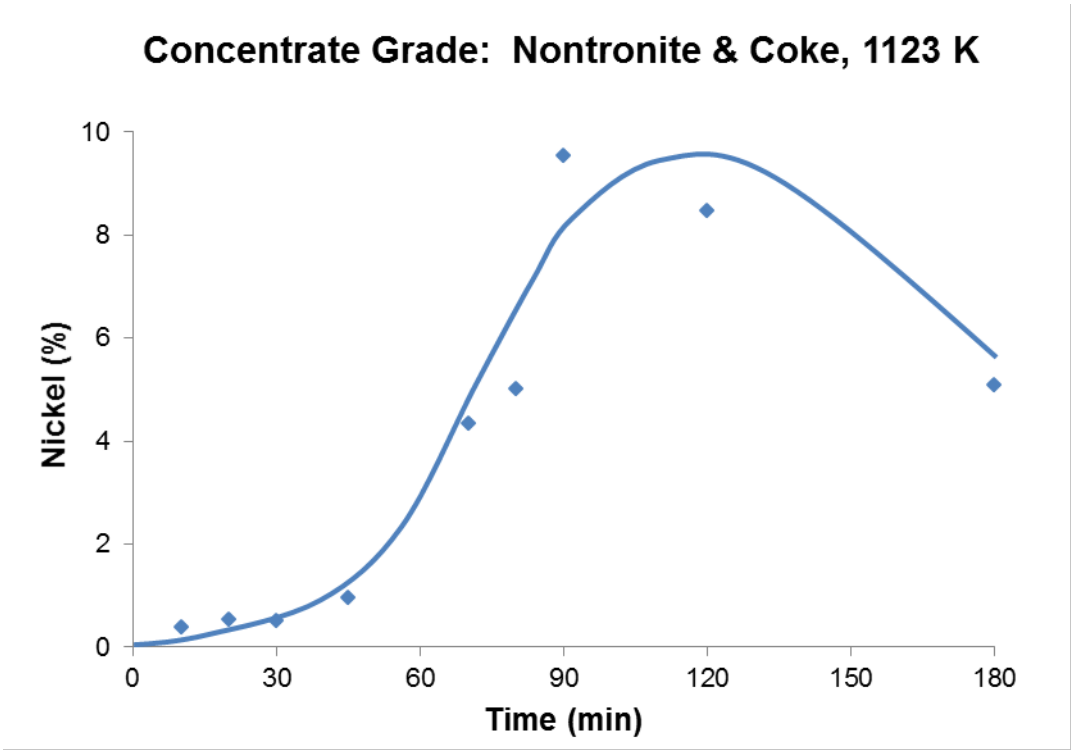

Figure B.34 Magnetic Concentrate Grade, Nontronite with Coke at 1123 K

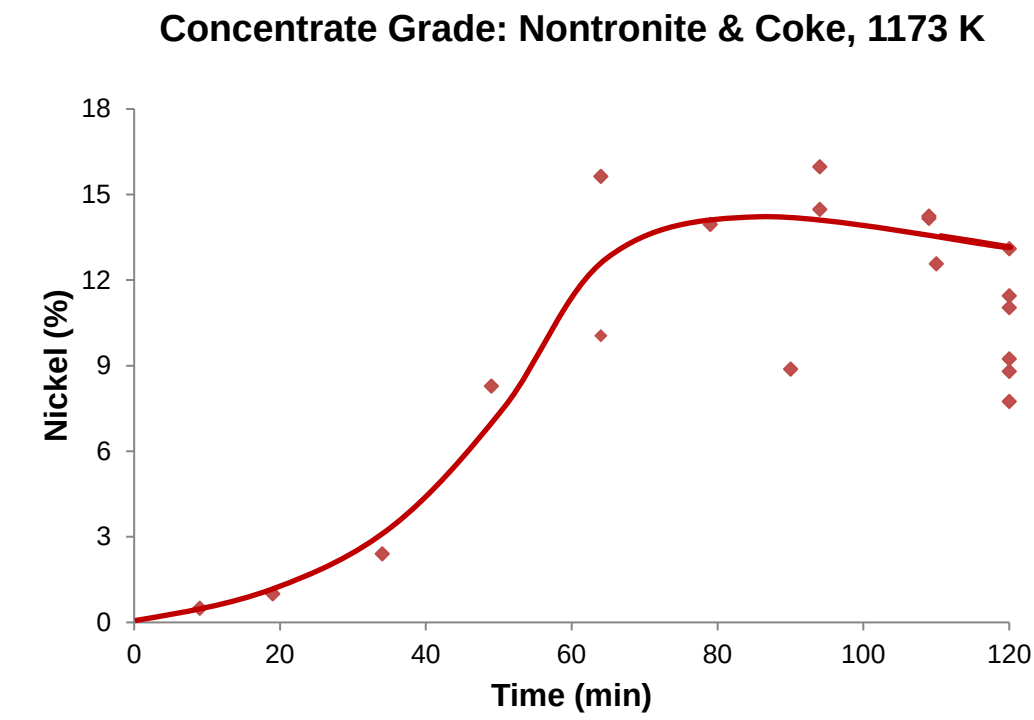

Figure B.35 Magnetic Concentrate Grade, Nontronite with Coke at 1173 K

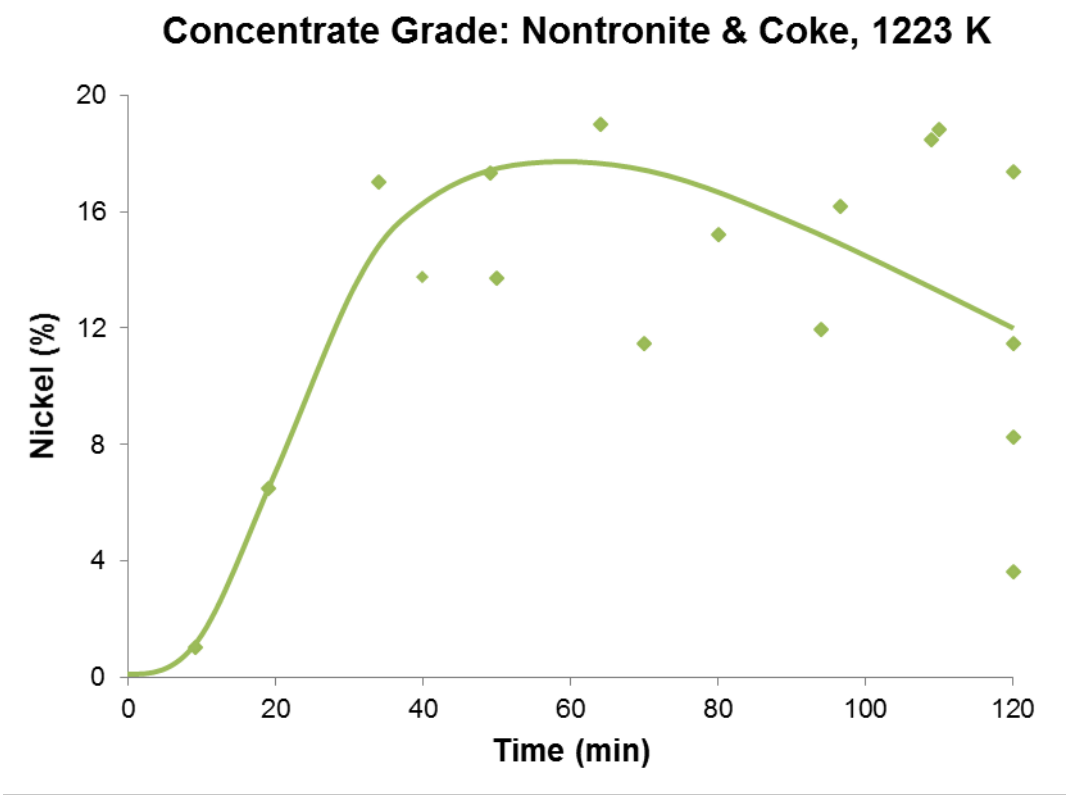

Figure B.36 Magnetic Concentrate Grade, Nontronite with Coke at 1223 K

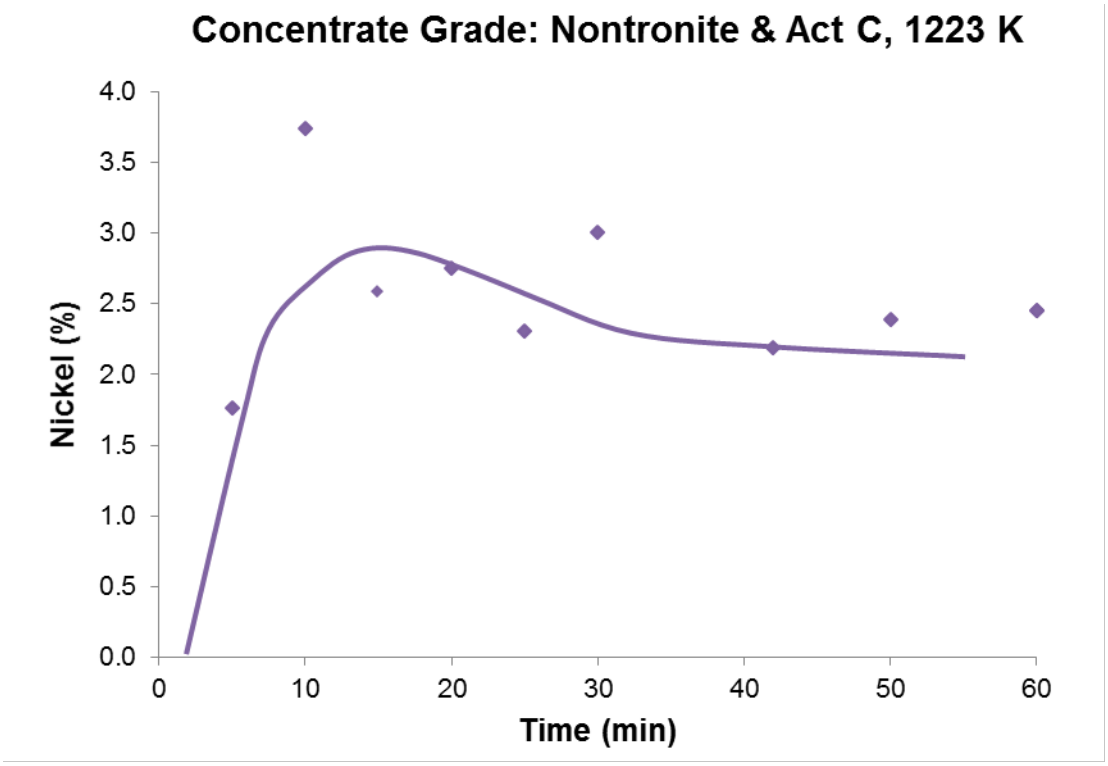

Figure B.37 Magnetic Concentrate Grade, Nontronite with Act C at 1223 K

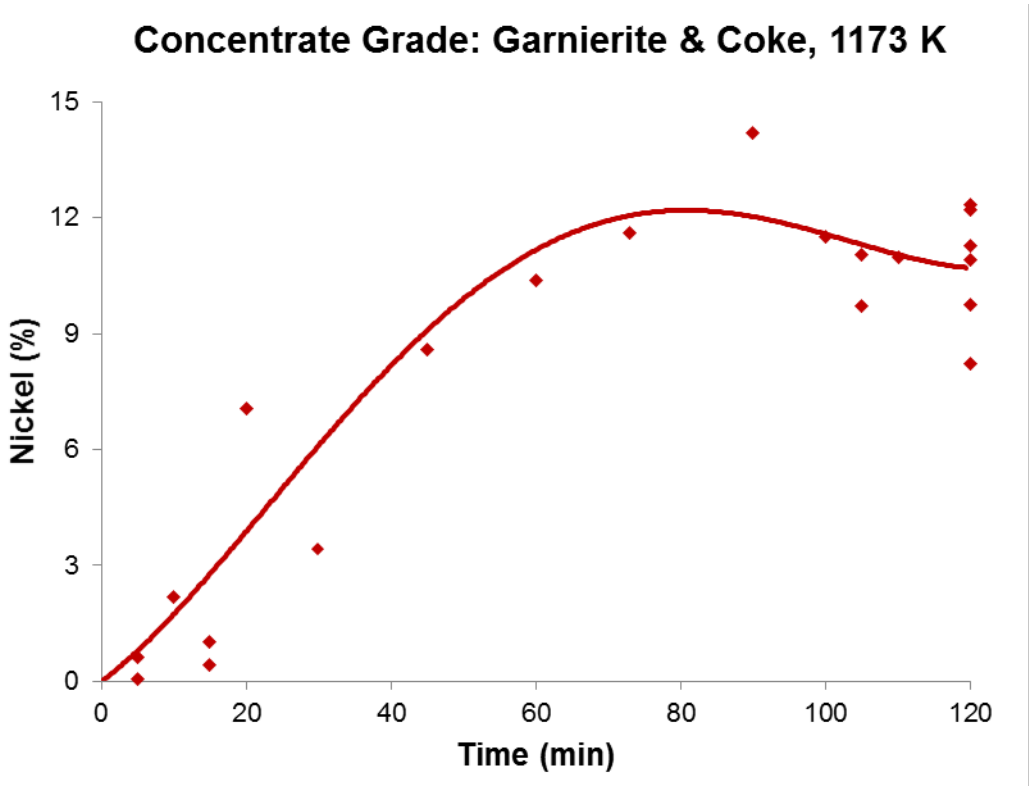

Figure B.38 Magnetic Concentrate Grade, Garnierite with Coke at 1173 K

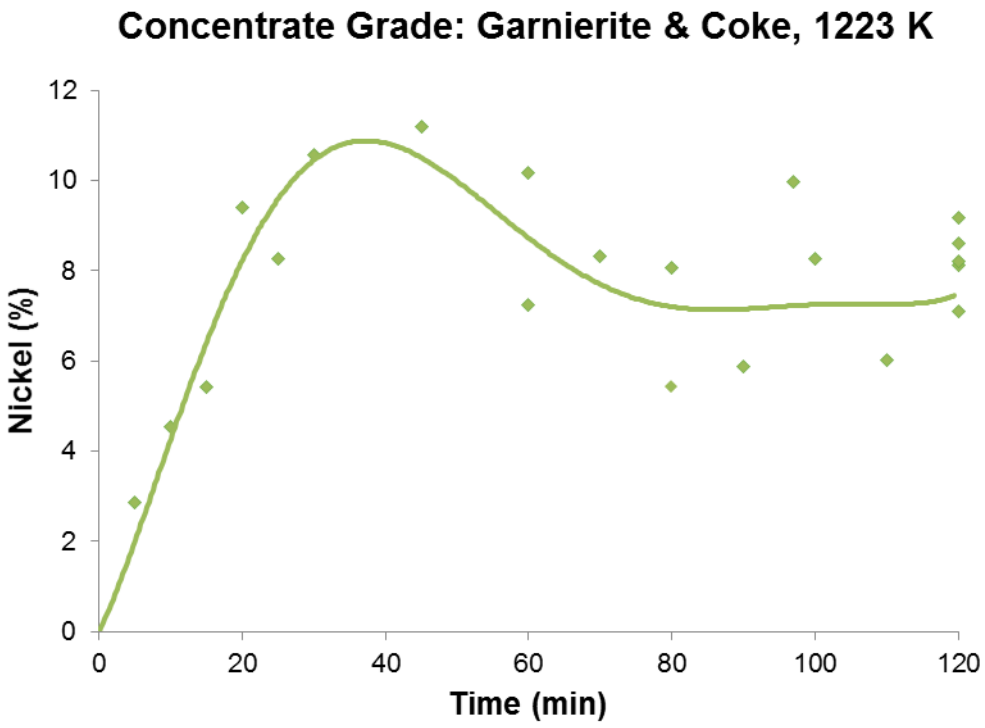

Figure B.39 Magnetic Concentrate Grade, Garnierite with Coke at 1223 K

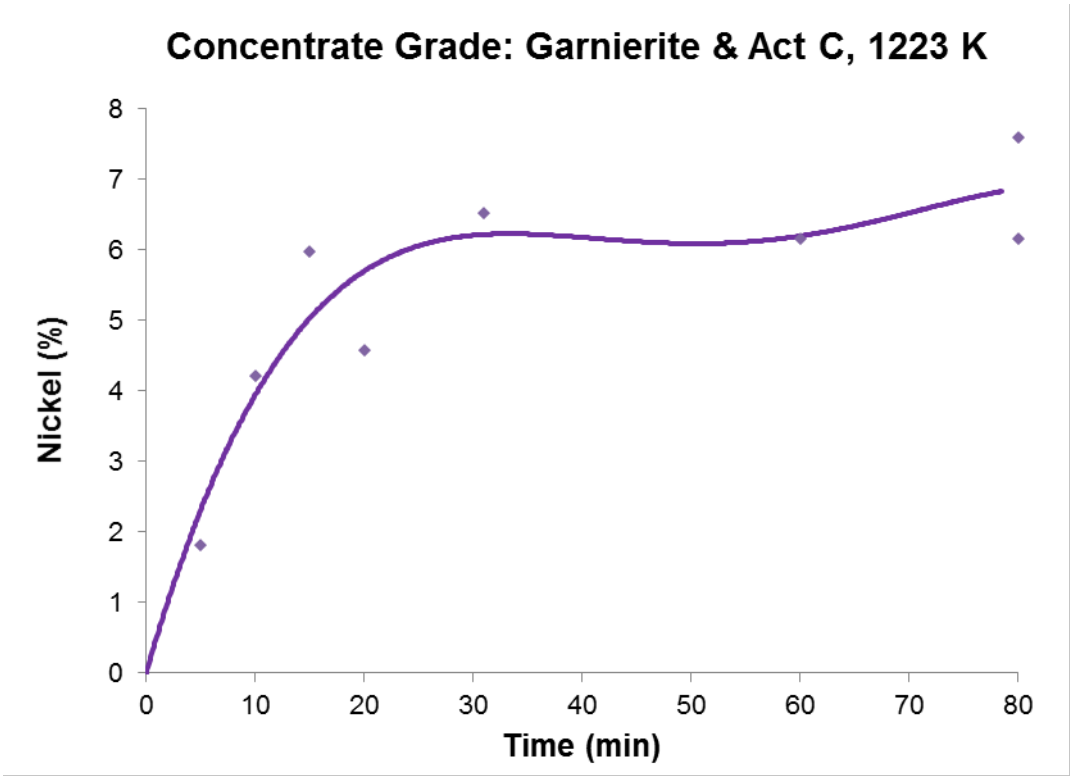

Figure B.40 Magnetic Concentrate Grade, Garnierite with Act C at 1223 K

B.7 Reduction Equilibrium Simulations

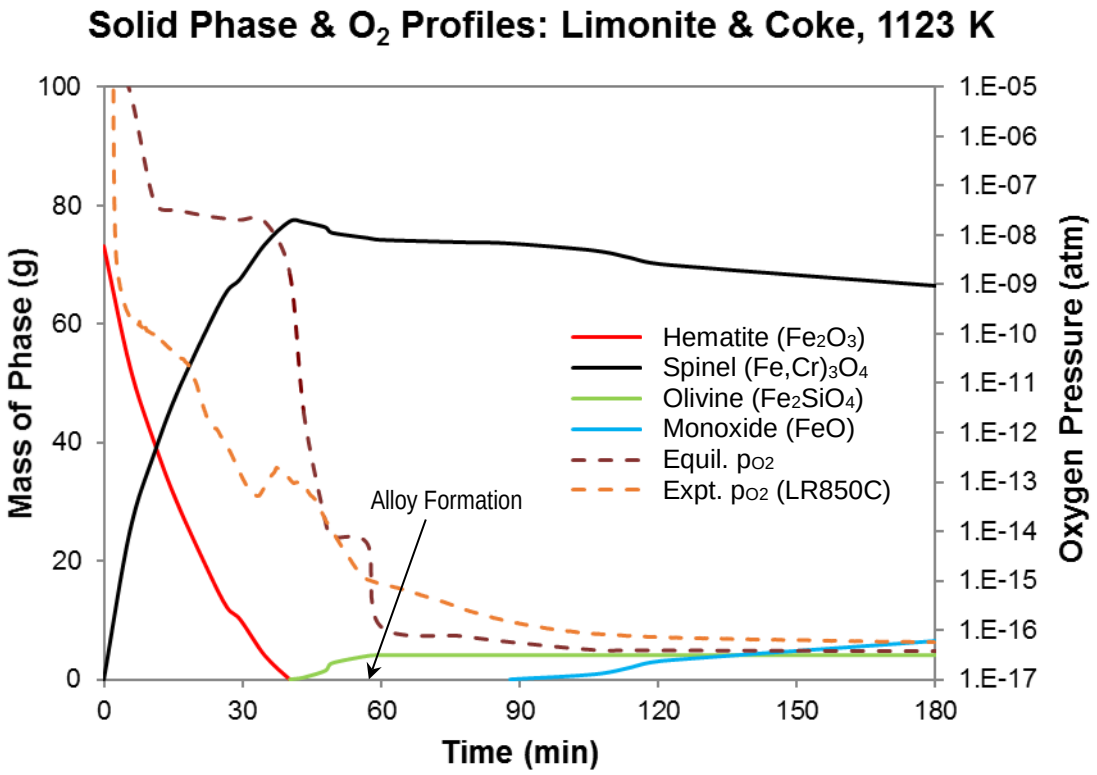

Figure B.41 Simulation: Limonite Reduction with Coke at 1123 K

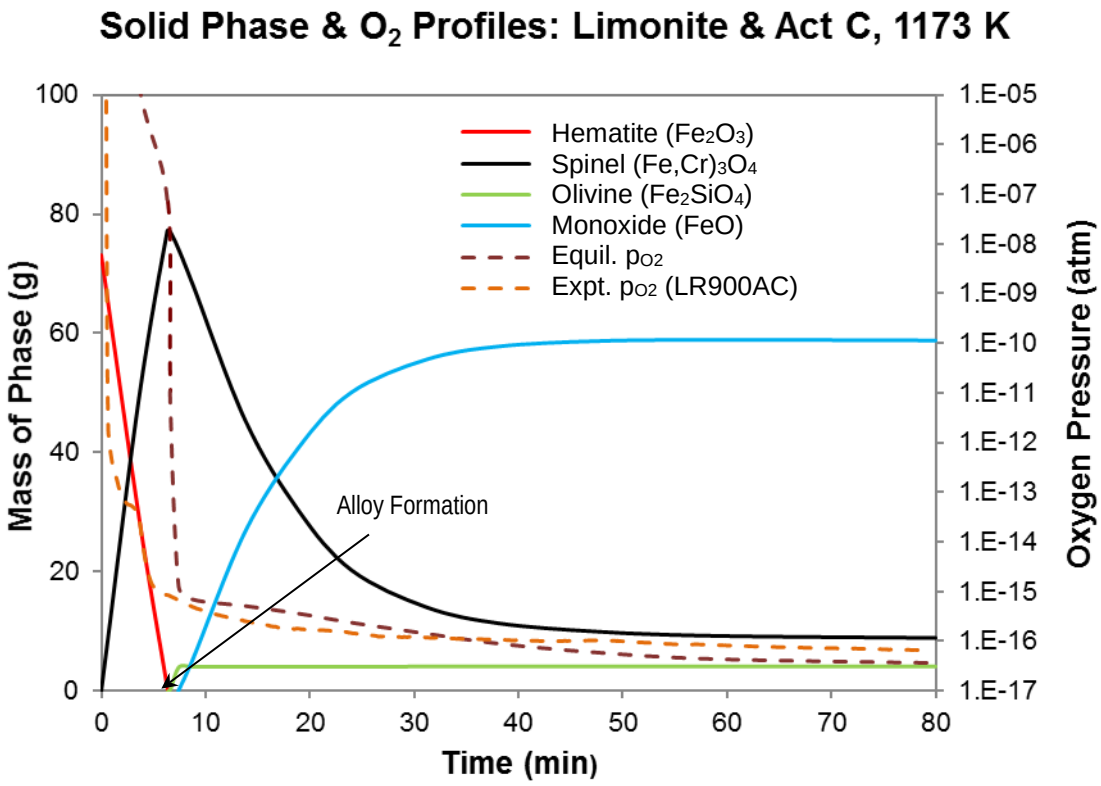

Figure B.42 Simulation: Limonite Reduction with Act C at 1173 K

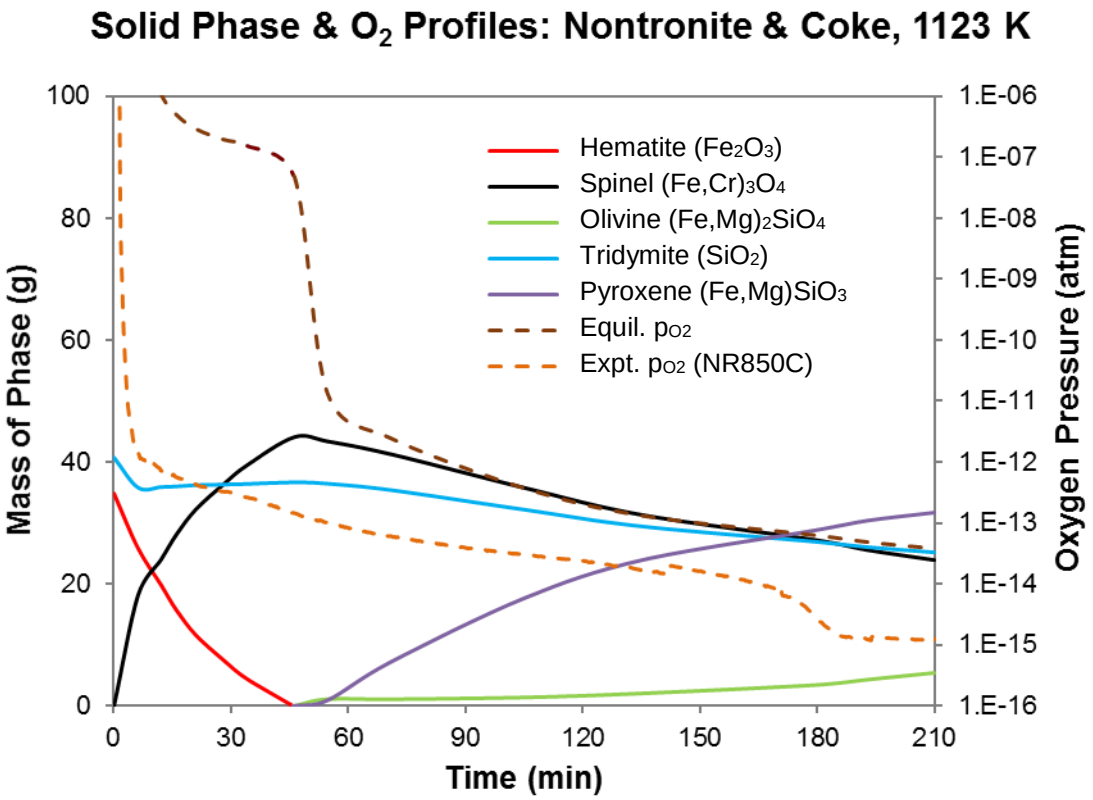

Figure B.43 Simulation: Nontronite Reduction with Coke at 1123 K

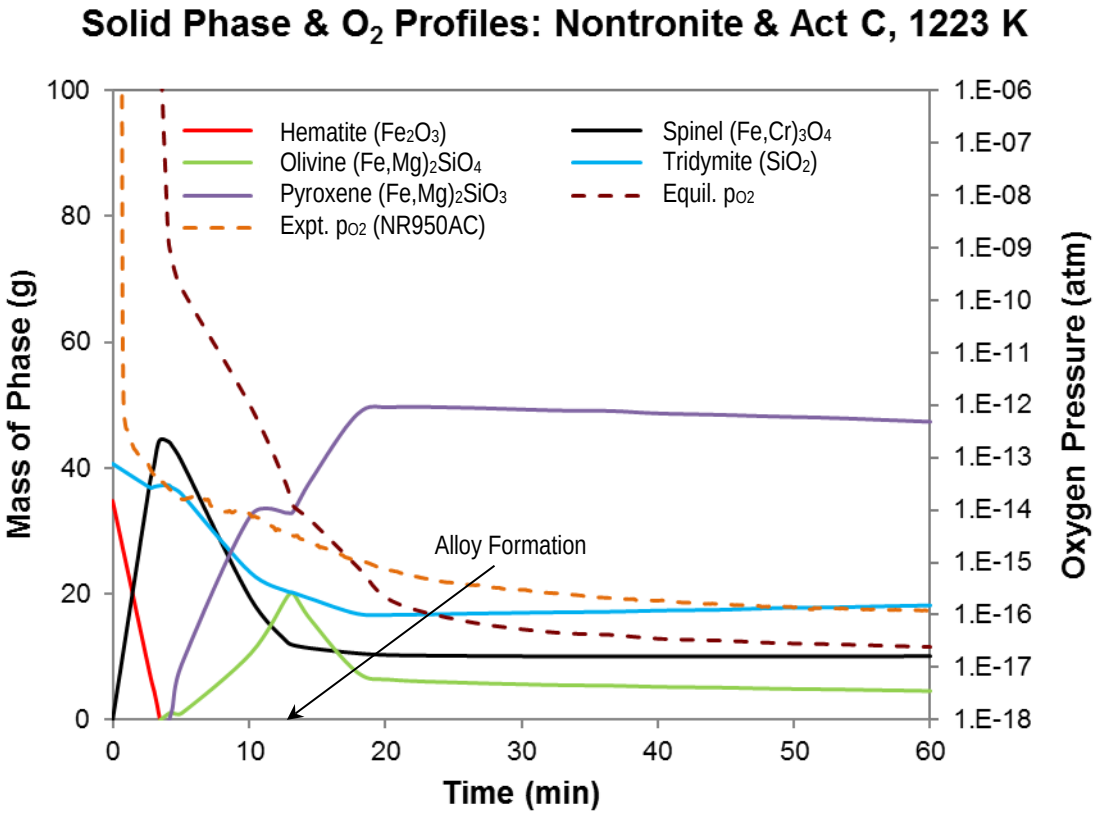

Figure B.44 Simulation: Nontronite Reduction with Act C at 1223 K

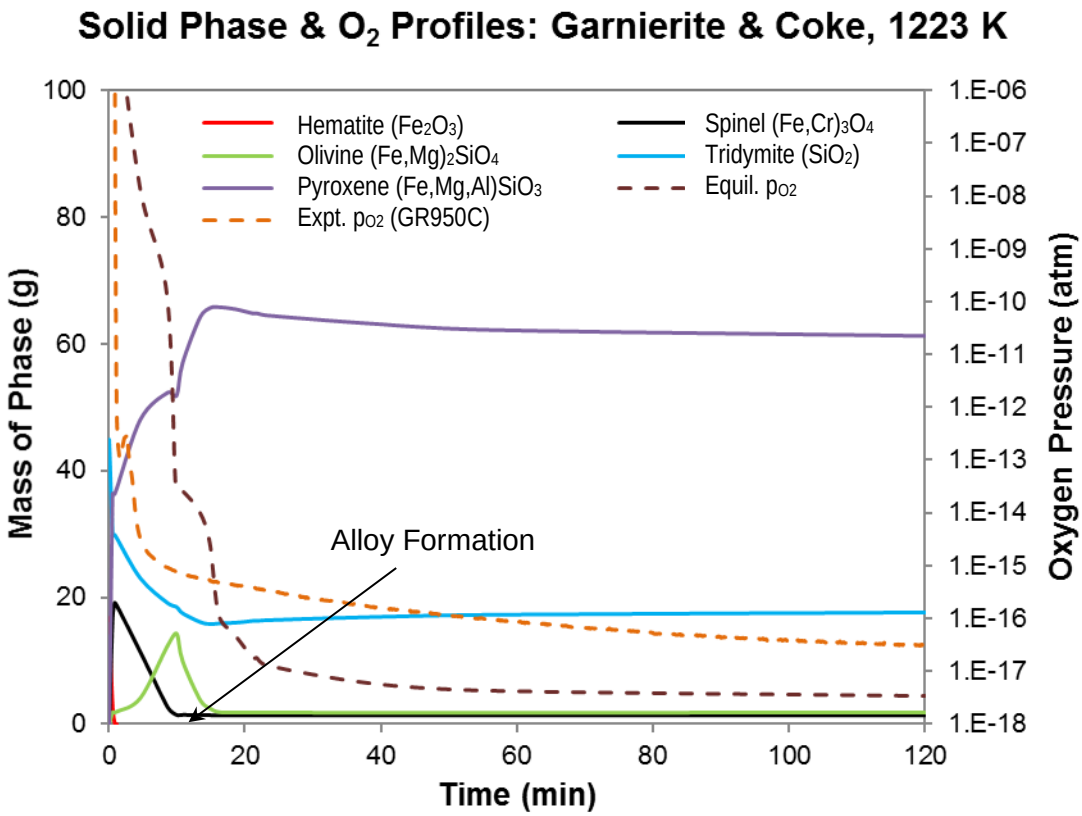

Figure B.45 Simulation: Garnierite Reduction with Coke at 1223 K

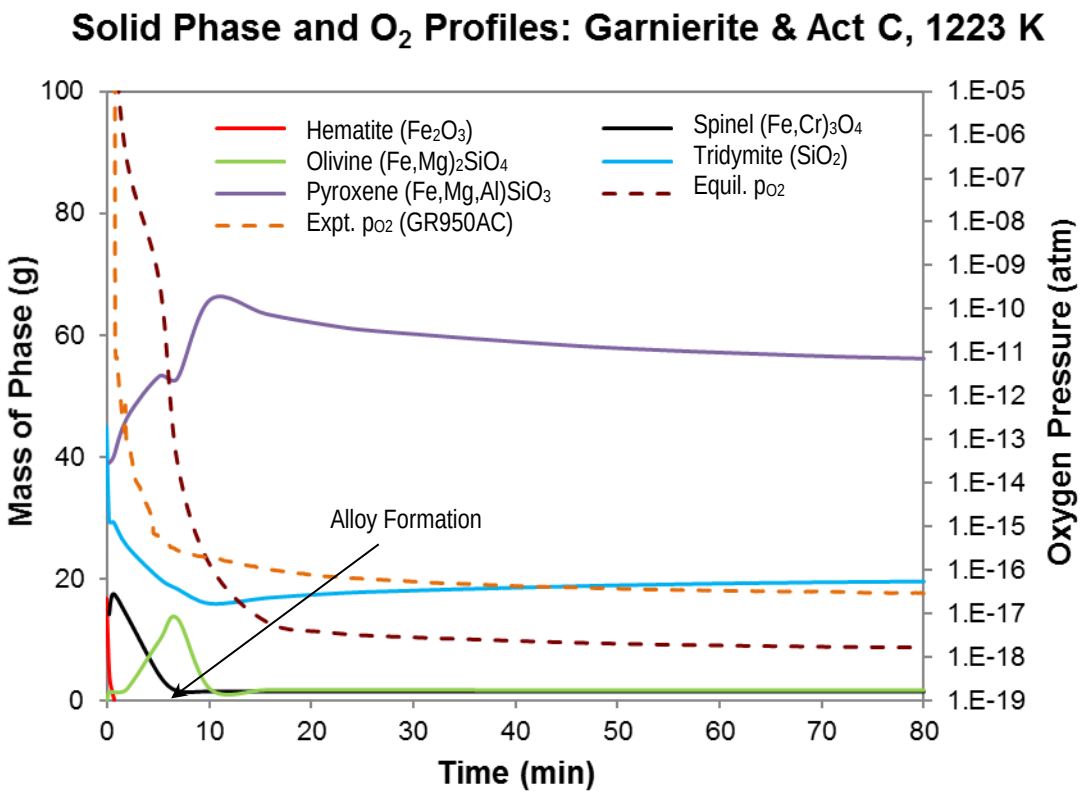

Figure B.46 Simulation: Garnierite Reduction with Act C at 1223 K

B.8 Segregation Equilibrium Simulations

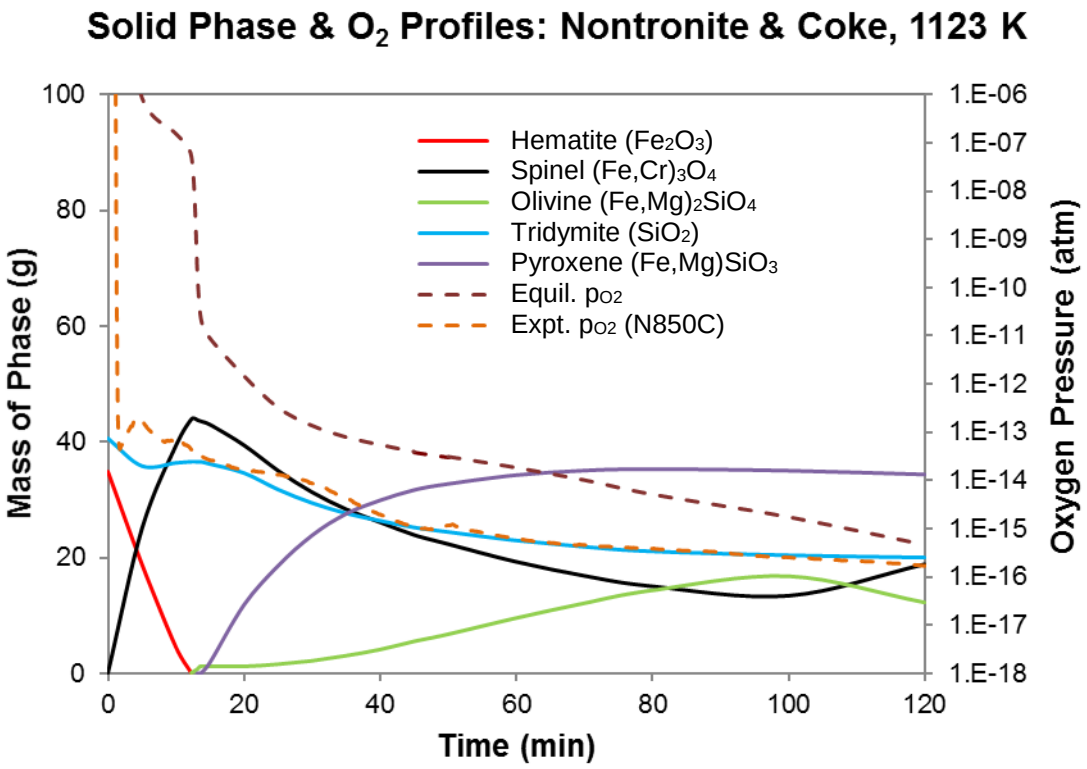

Figure B.47 Simulation: Nontronite Segregation with Coke at 1123 K

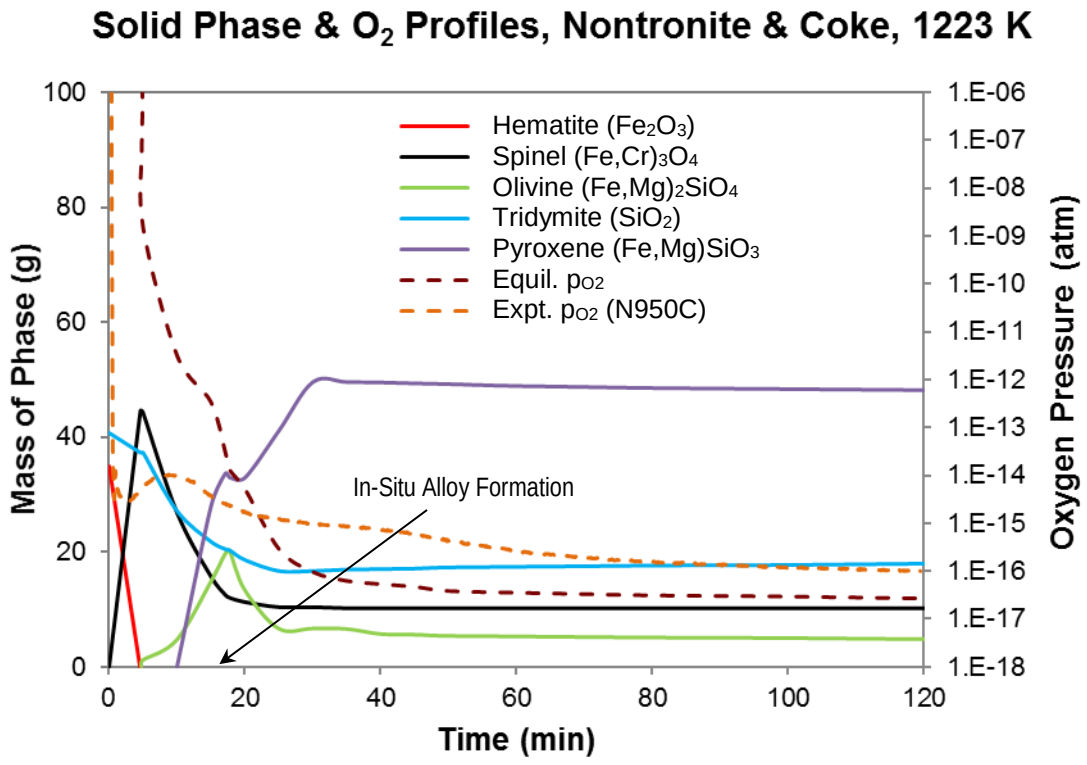

Figure B.48 Simulation: Nontronite Segregation with Coke at 1223 K

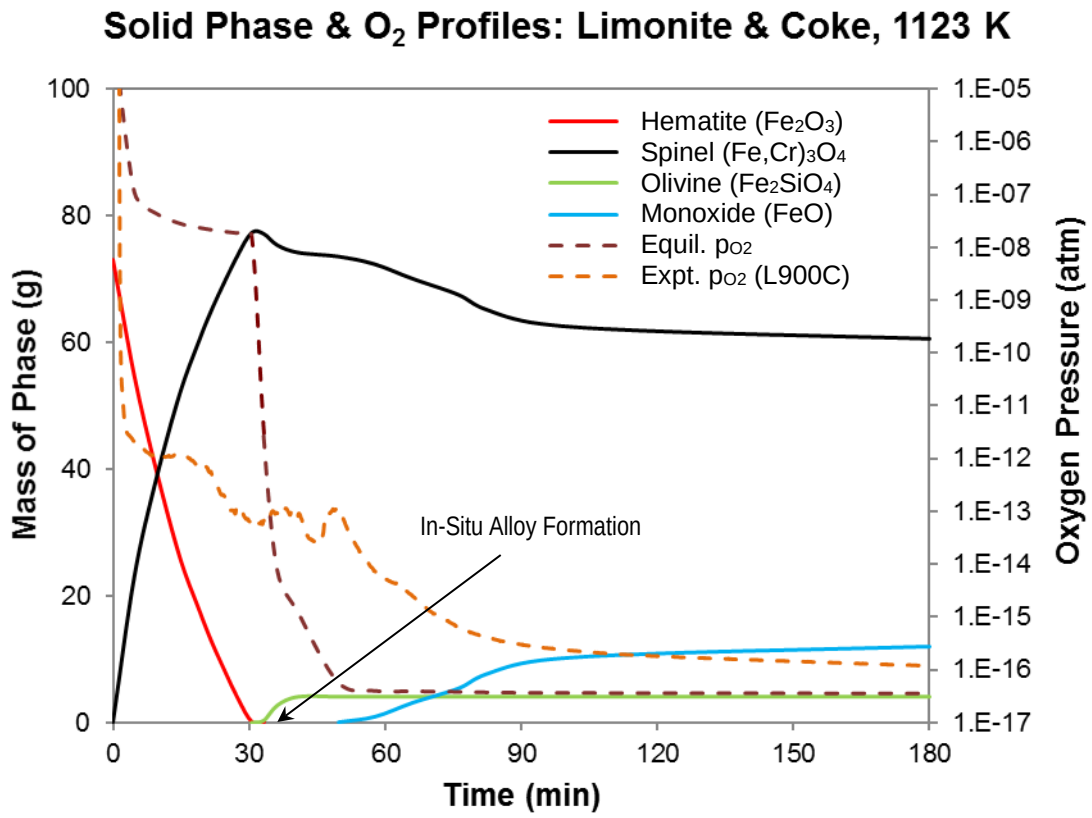

Figure B.49 Simulation: Limonite Segregation with Coke at 1123 K

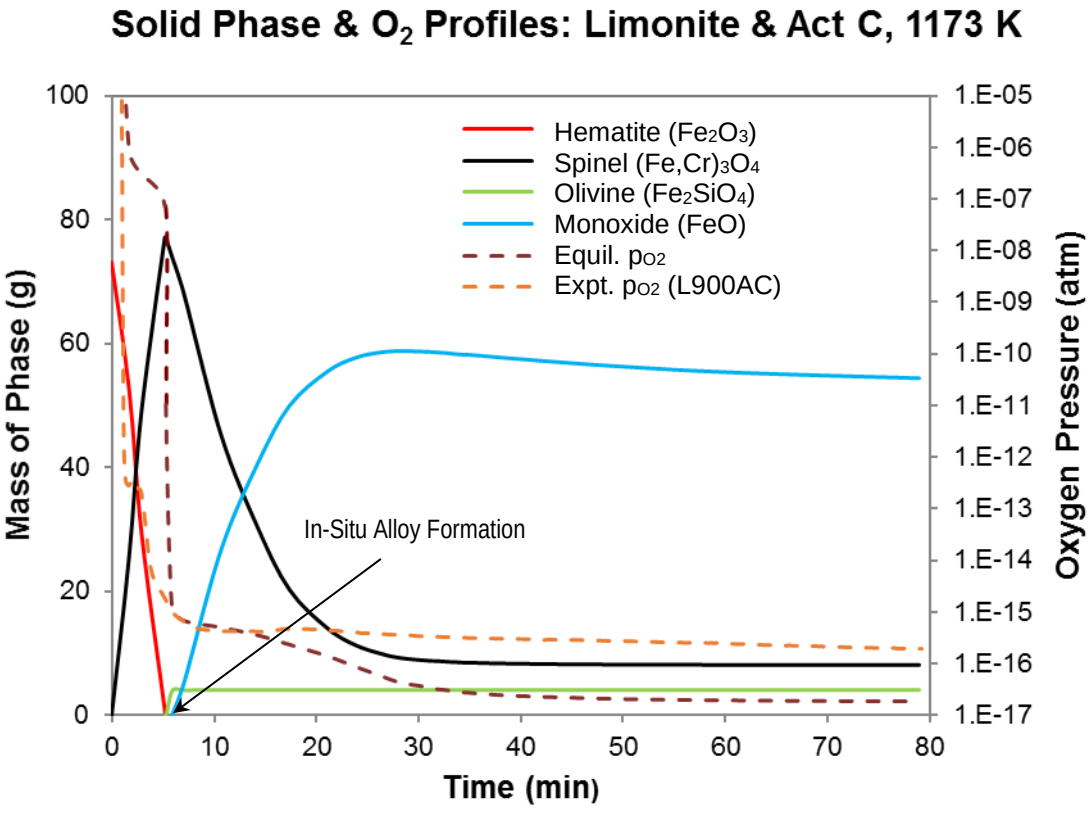

Figure B.50 Simulation: Limonite Segregation with Act C at 1173 K

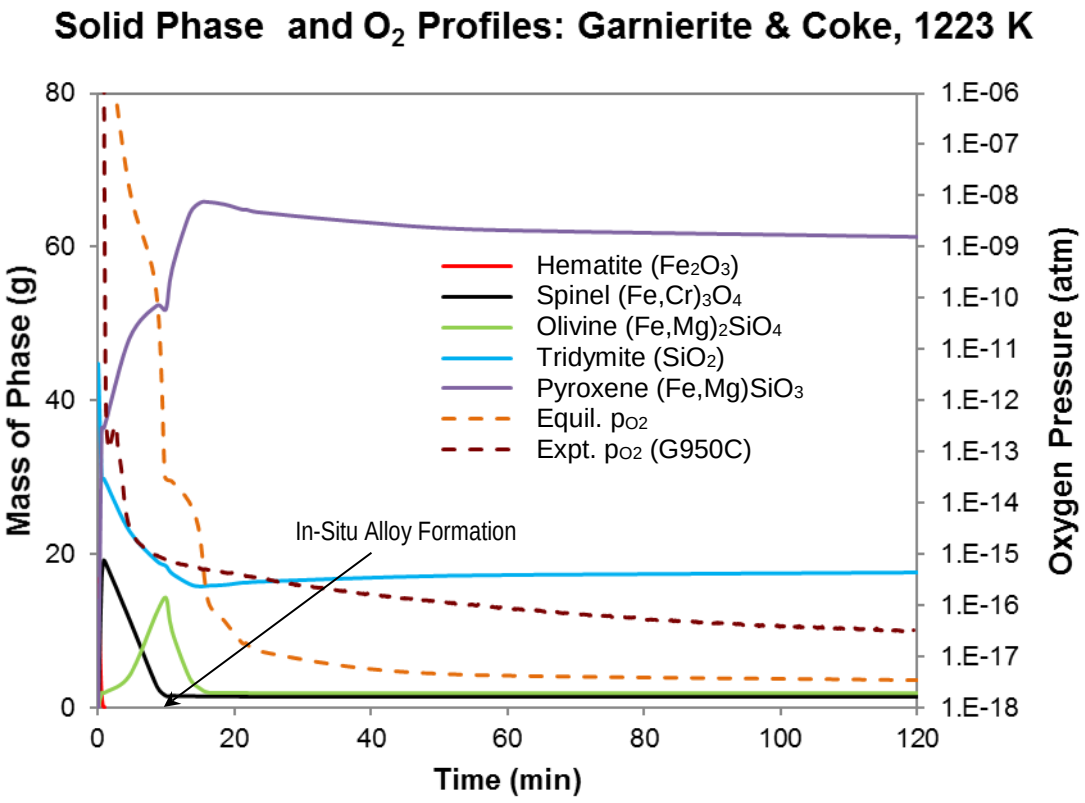

Figure B.51 Simulation: Garnierite Segregation with Coke at 1223 K

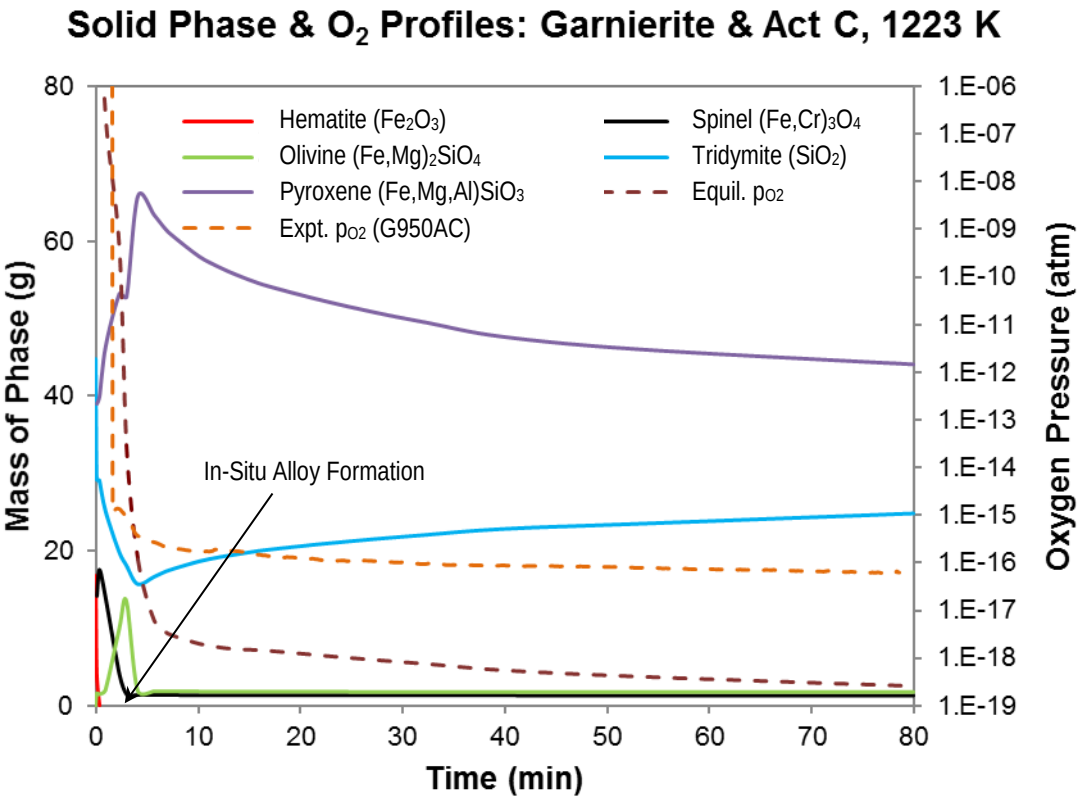

Figure B.52 Simulation: Garnierite Segregation with Act C at 1223 K

B.9 Hydrogen Chloride Evolution

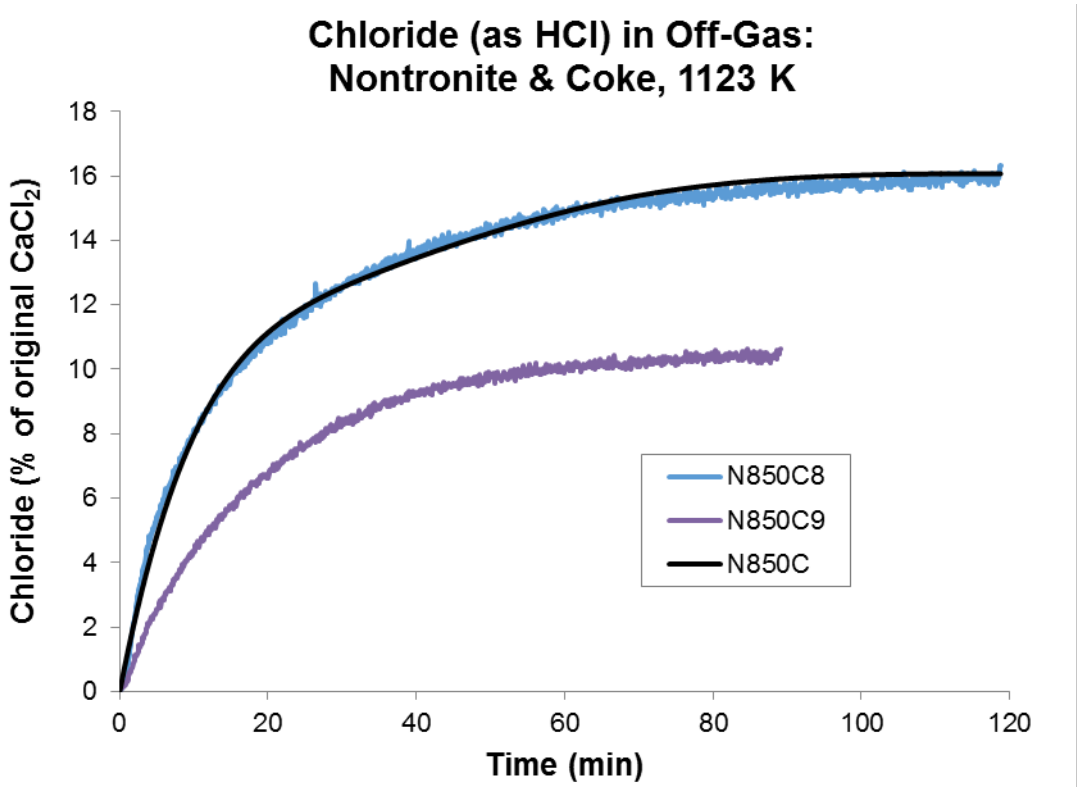

Figure B.53 HCl in Off-Gas, Nontronite with Coke at 1123 K

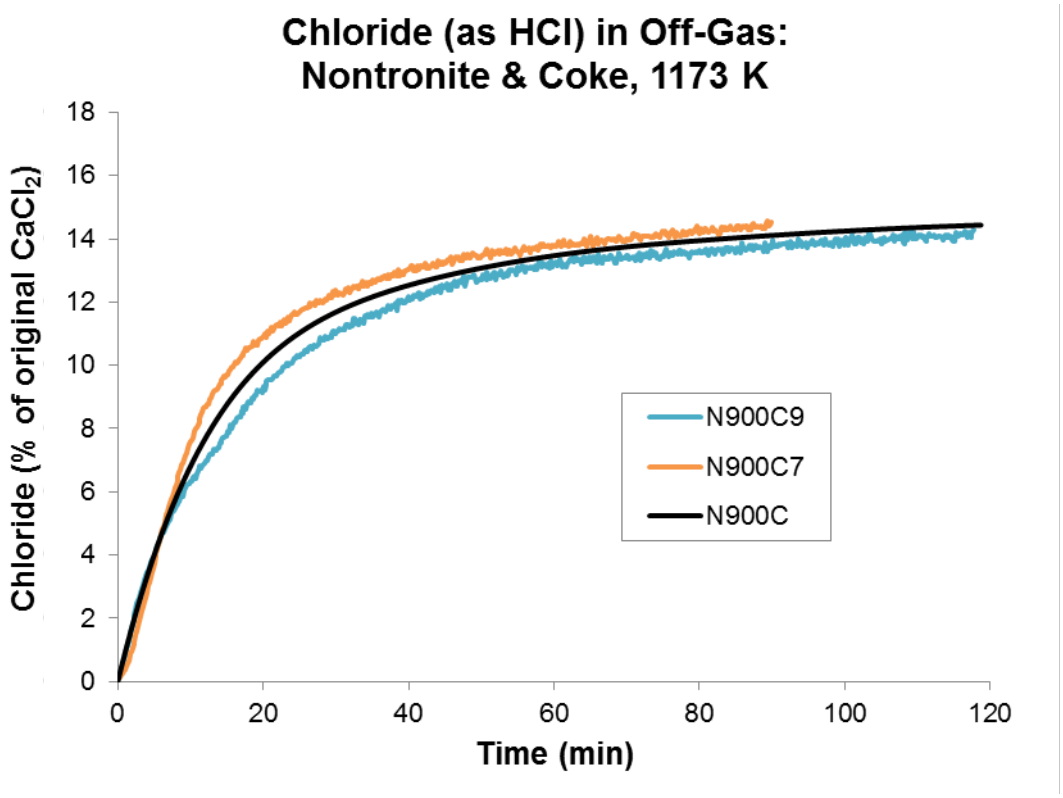

Figure B.54 HCl in Off-Gas, Nontronite with Coke at 1173 K

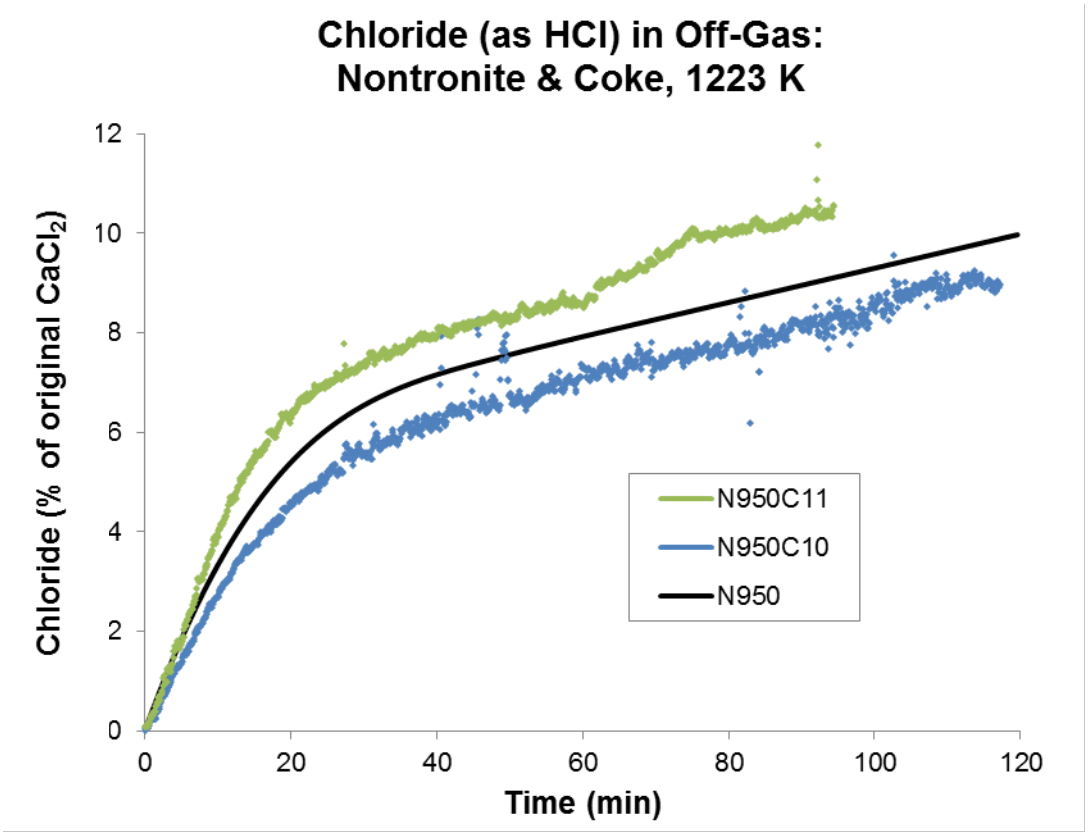

Figure B.55 HCl in Off-Gas, Nontronite with Coke at 1223 K

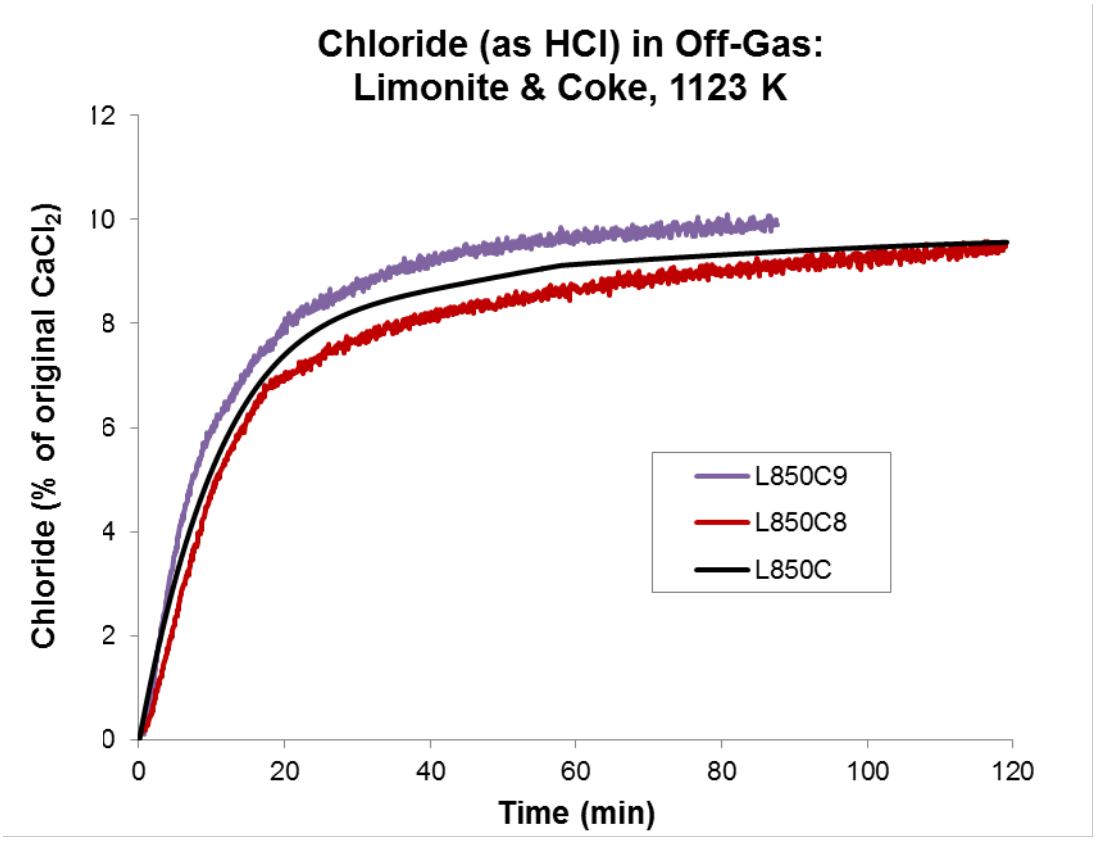

Figure B.56 HCl in Off-Gas, Limonite with Coke at 1123 K

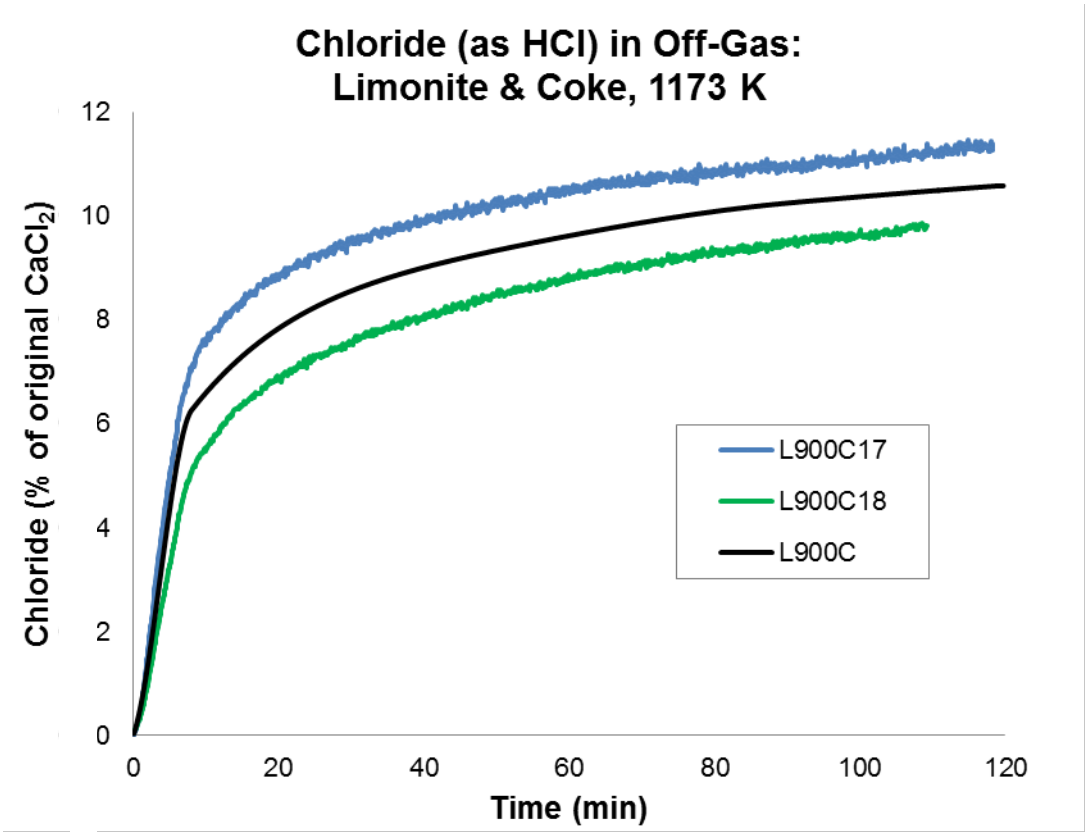

Figure B.57 HCl in Off-Gas, Limonite with Coke at 1173 K

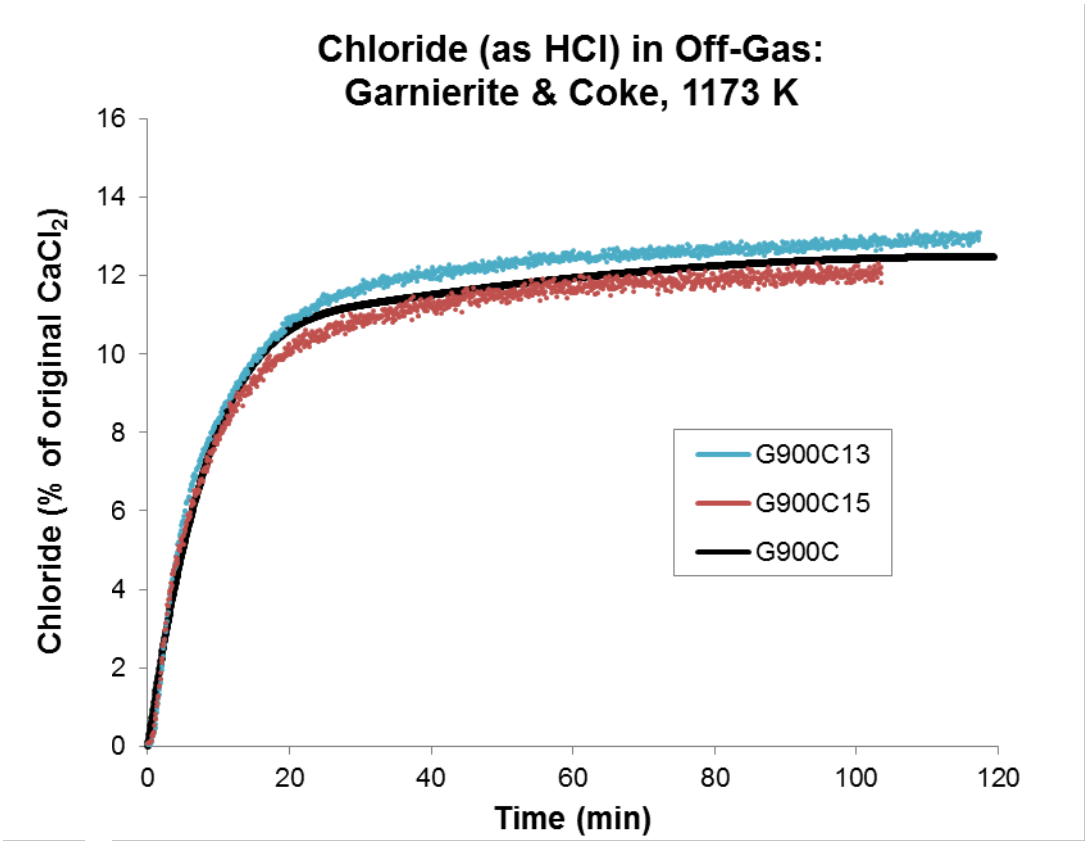

Figure B.58 HCl in Off-Gas, Garnierite with Coke at 1173 K

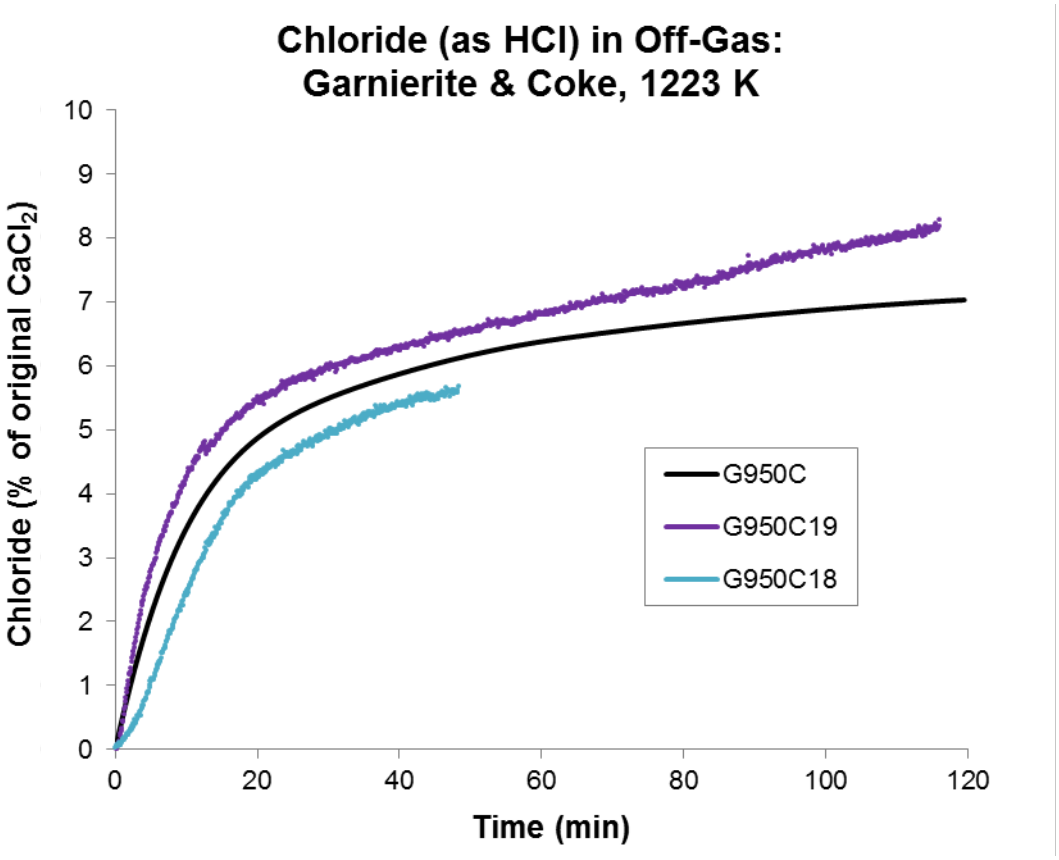

Figure B.59 HCl in Off-Gas, Garnierite with Coke at 1223 K

B.10 Soluble Chloride Data

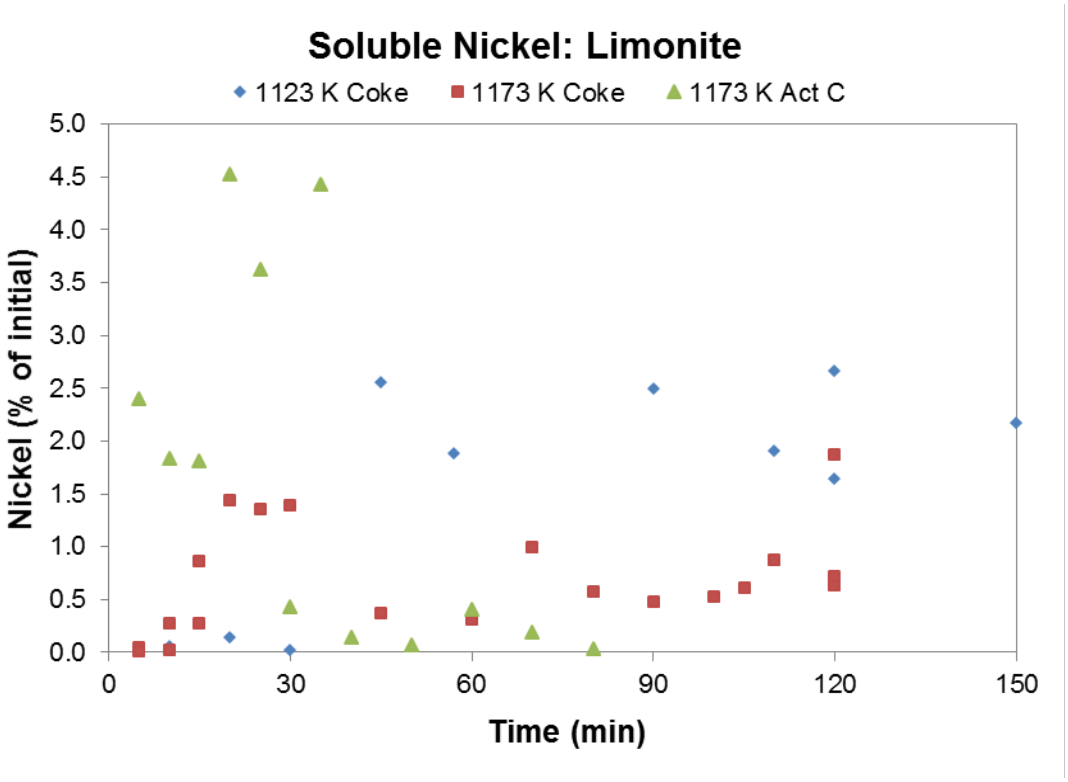

Figure B.60 Soluble Nickel, Limonite

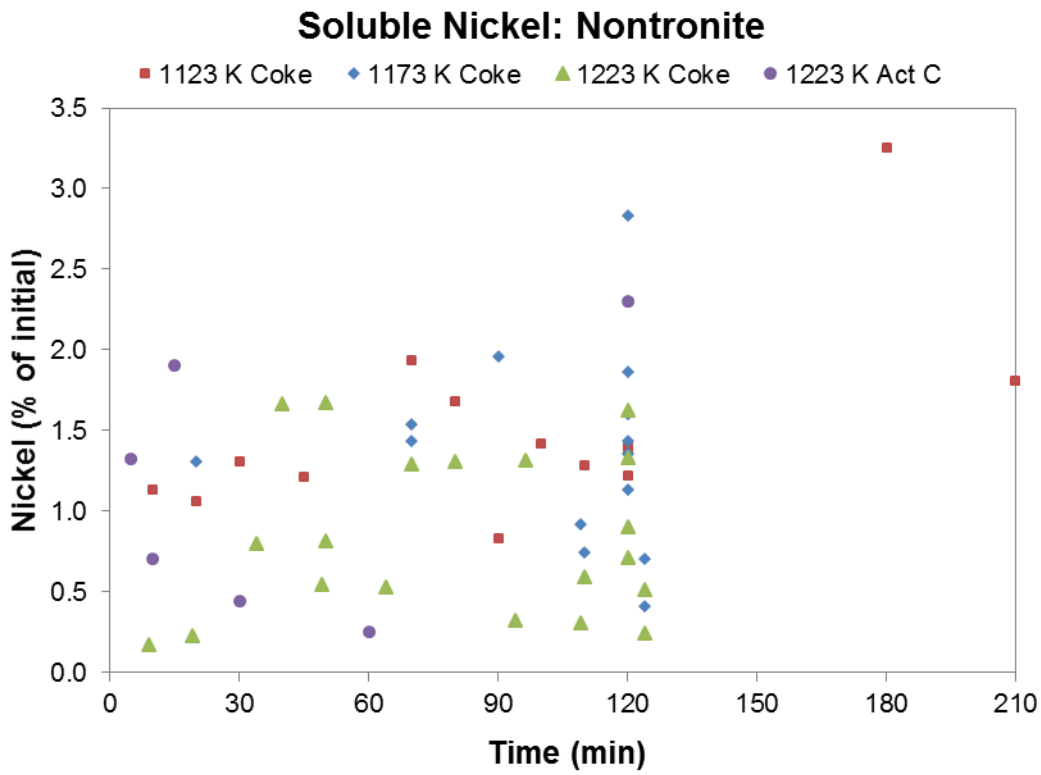

Figure B.61 Soluble Nickel, Nontronite

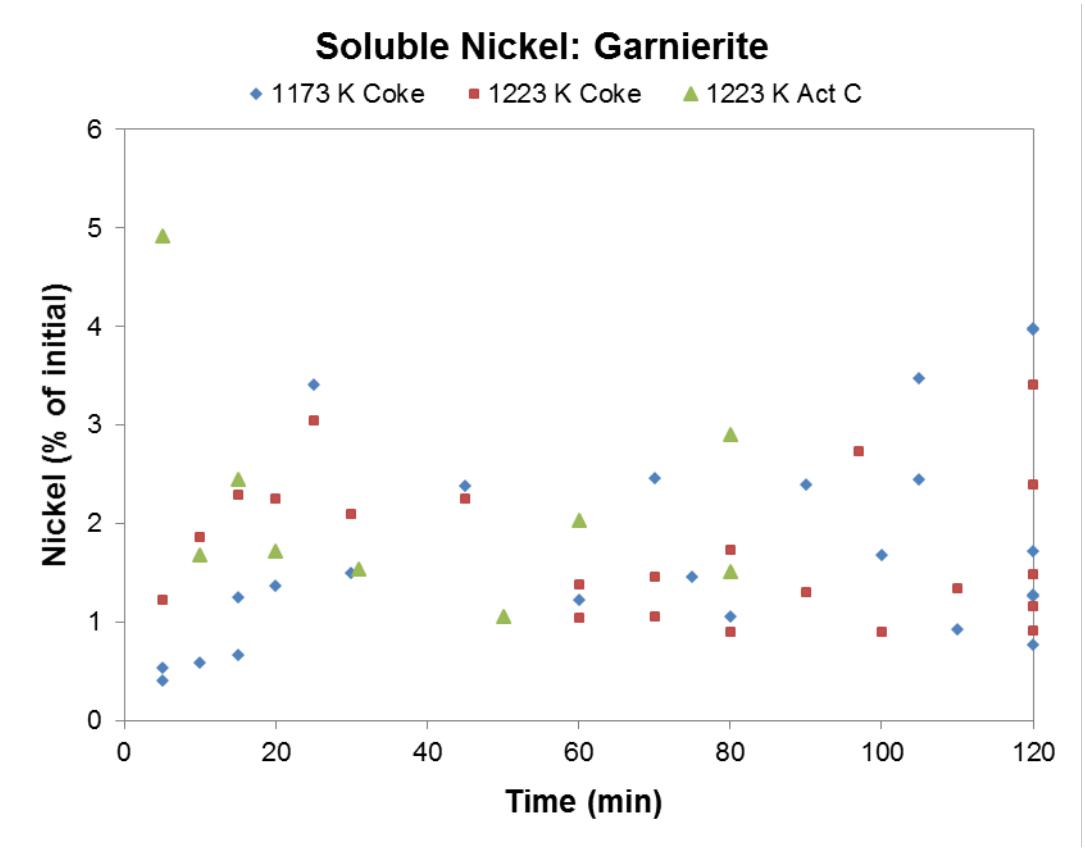

Figure B.62 Soluble Nickel, Garnierite

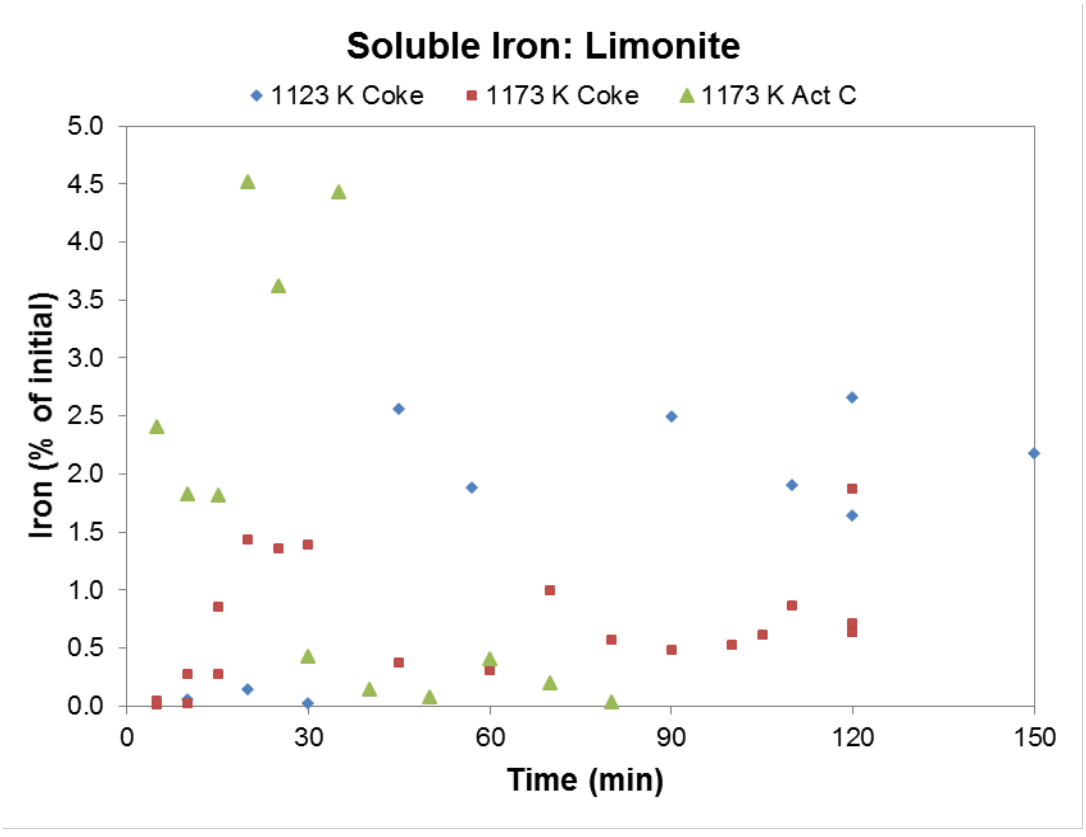

Figure B.63 Soluble Iron, Limonite

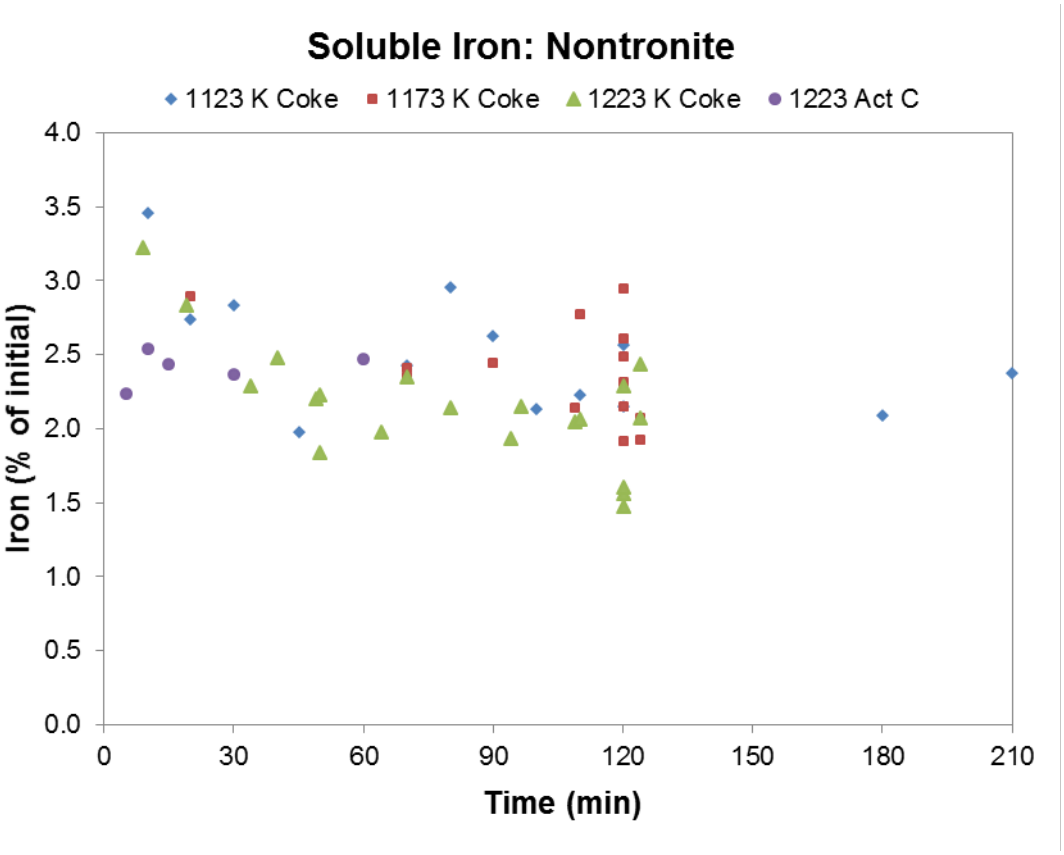

Figure B.64 Soluble Iron, Nontronite

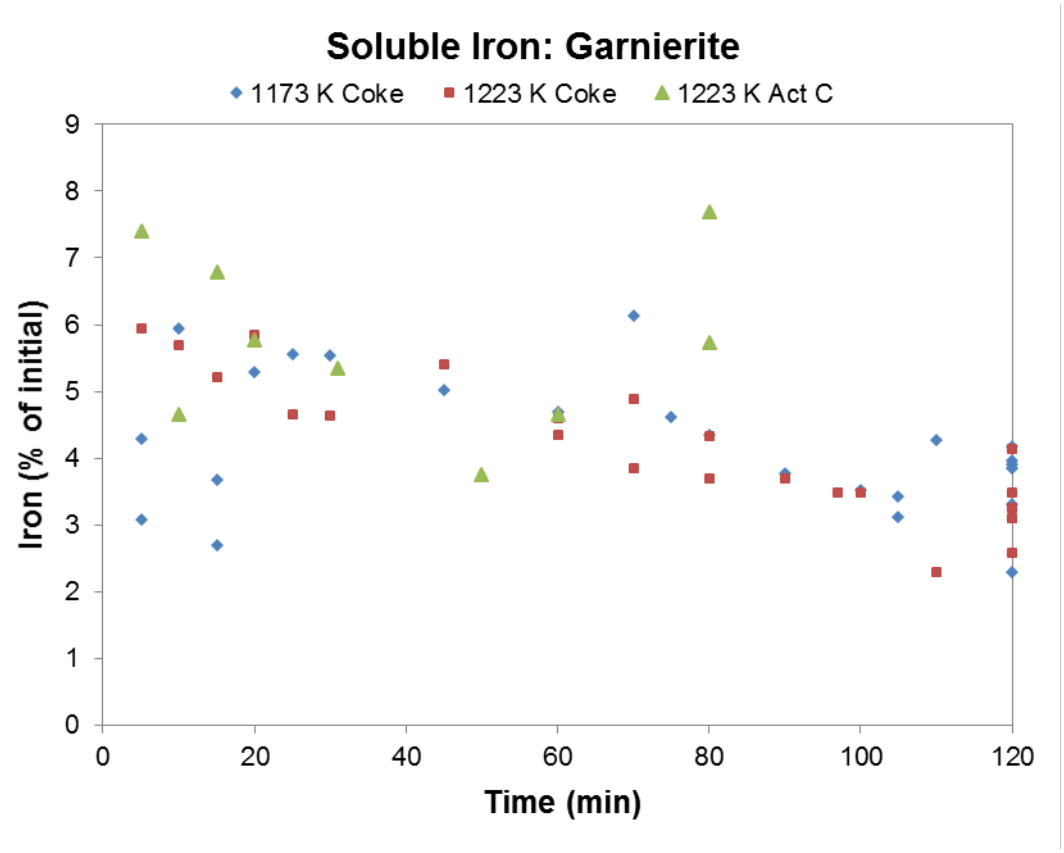

Figure B.65 Soluble Iron, Garnierite

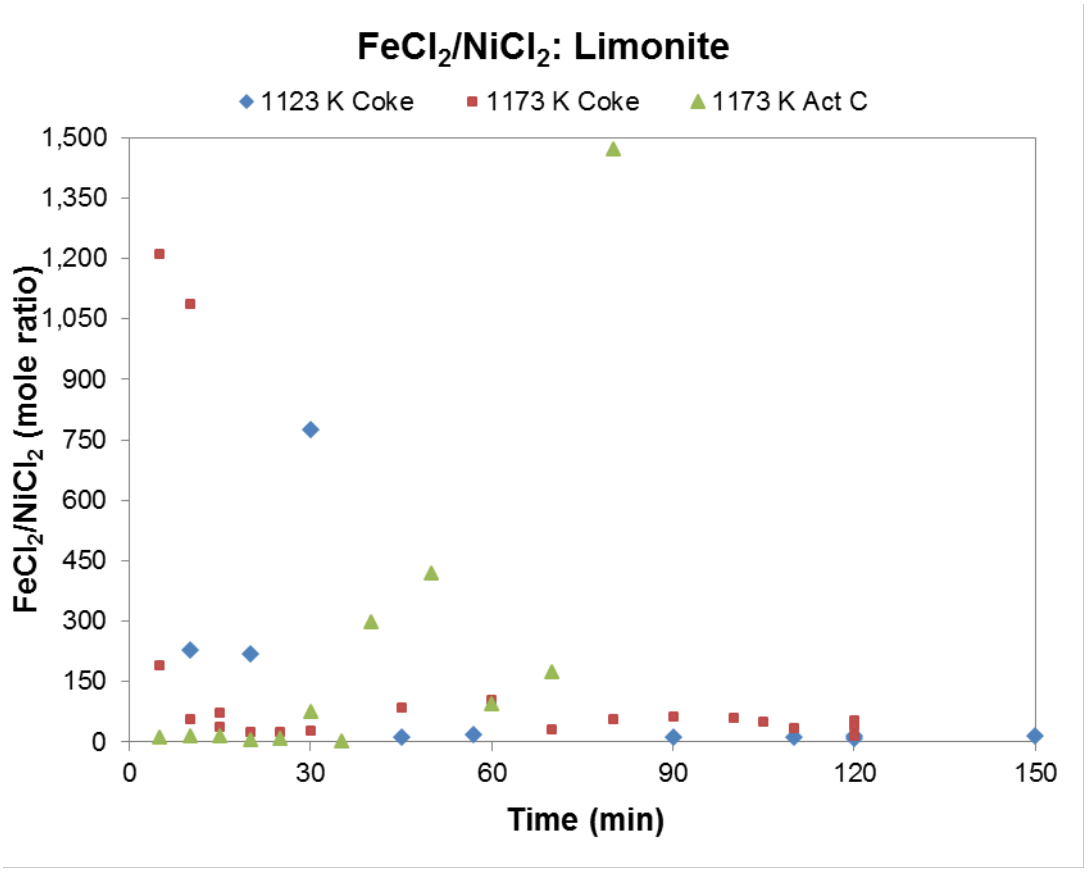

Figure B.66 $FeCl_2/NiCl_2$ Mole Ratio, Limonite

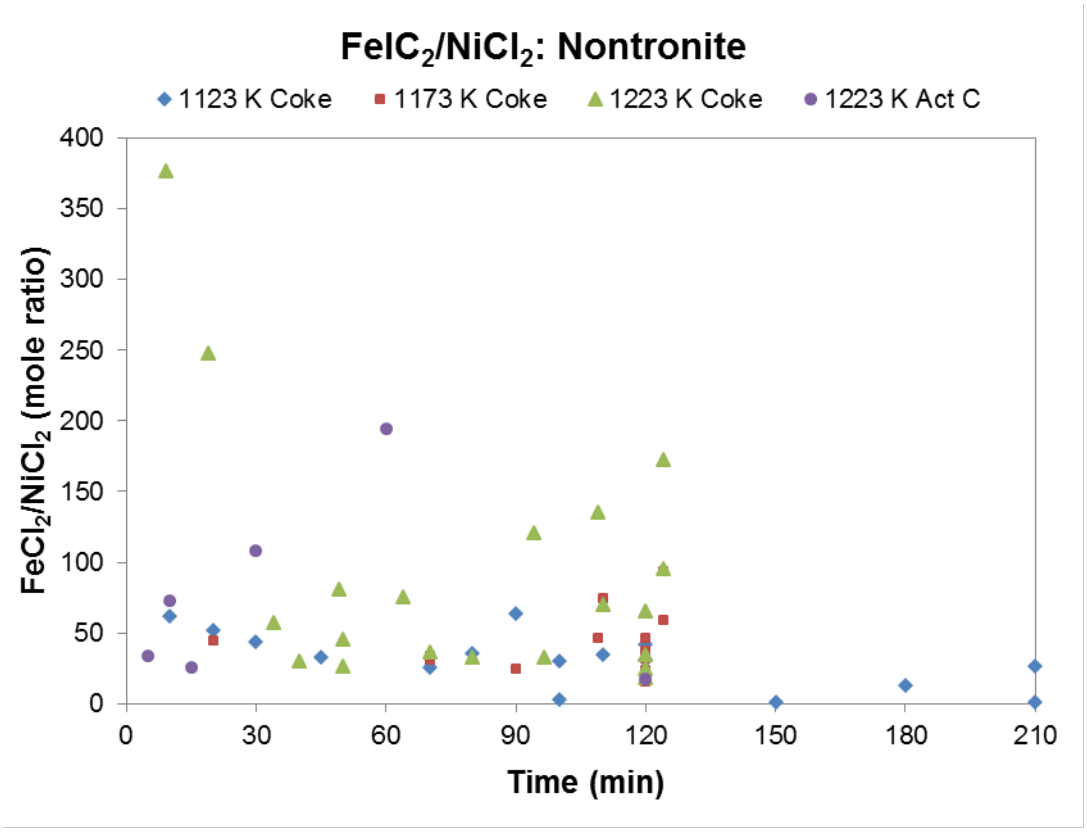

Figure B.67 $FeCl_2/NiCl_2$ Mole Ratio, Nontronite

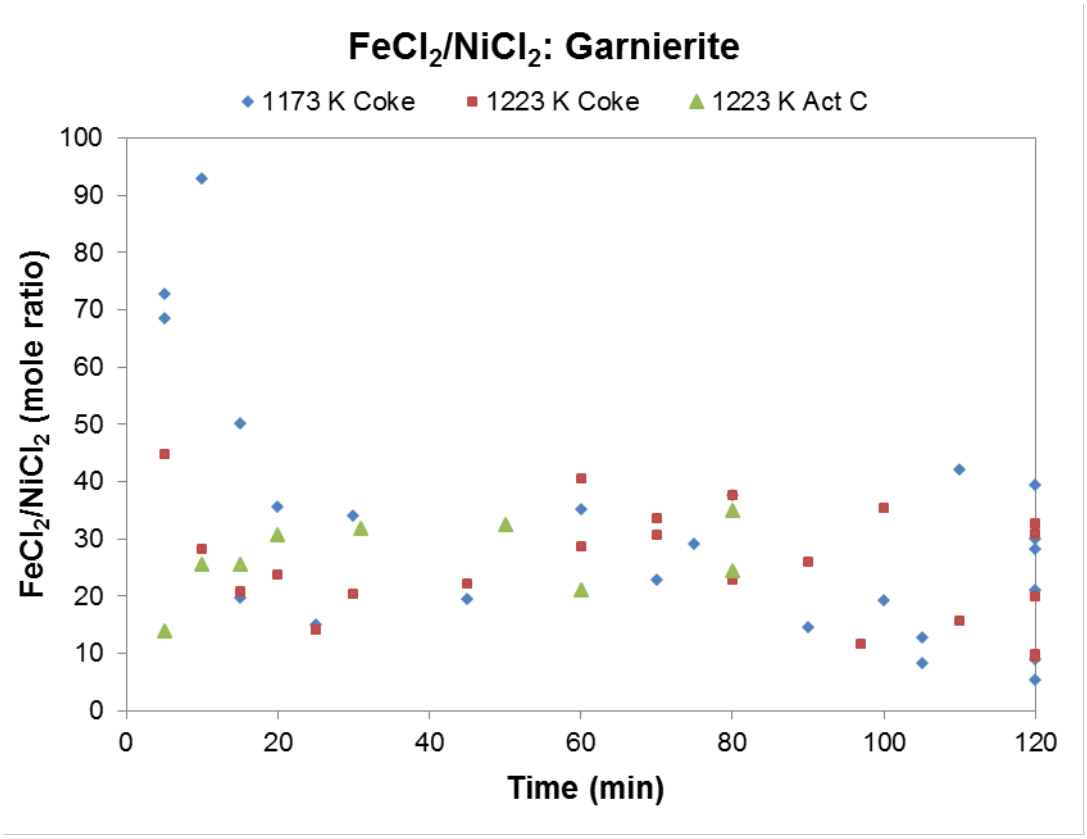

Figure B.68 $FeCl_2/NiCl_2$ Mole Ratio, Garnierite

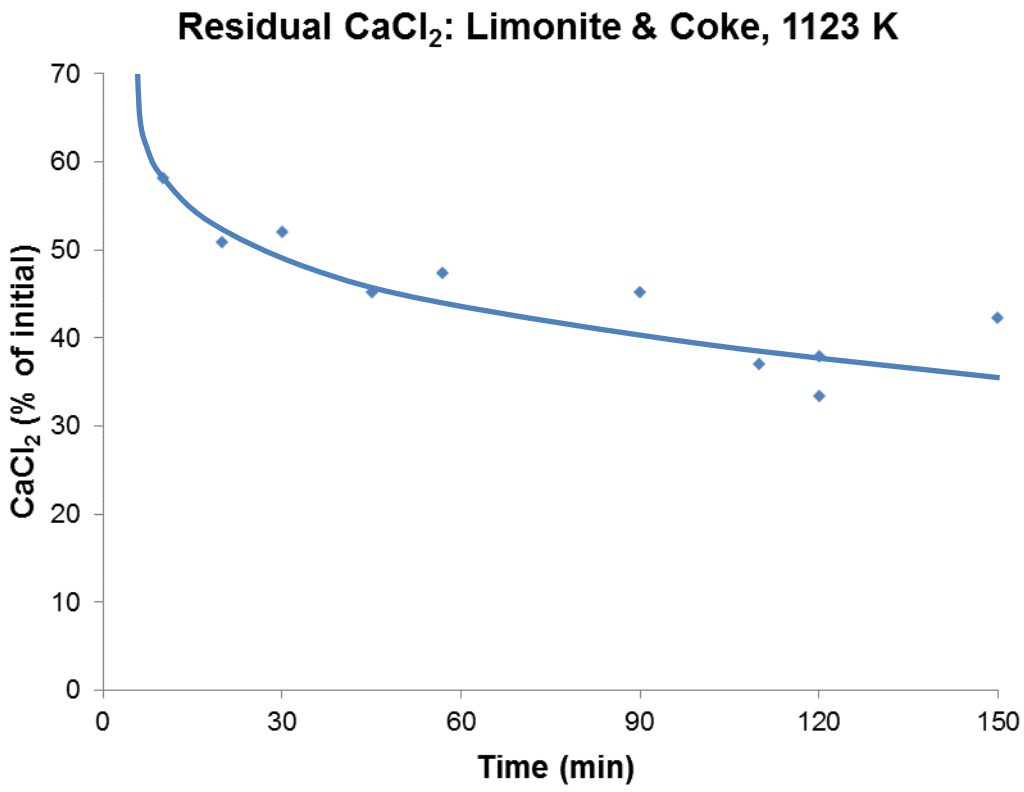

Figure B.69 Residual $CaCl_2$, Limonite with Coke at 1123 K

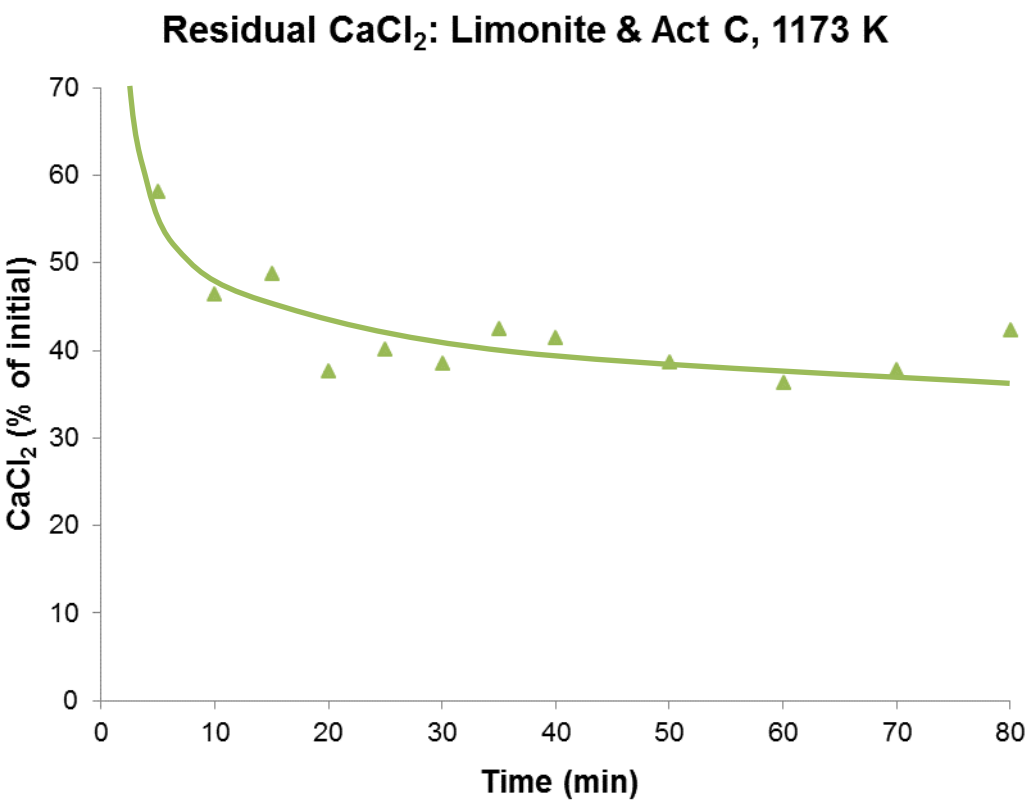

Figure B.70 Residual $CaCl_2$, Limonite with Act C at 1173 K

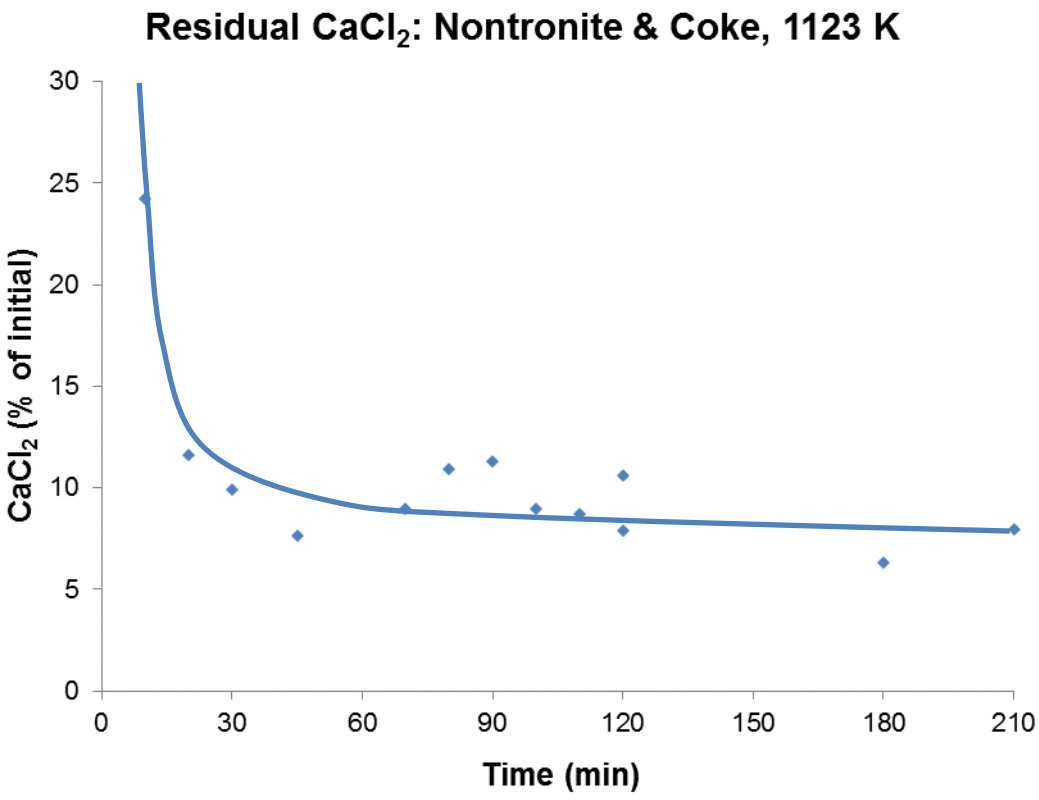

Figure B.71 Residual $CaCl_2$, Nontronite with Coke at 1123 K

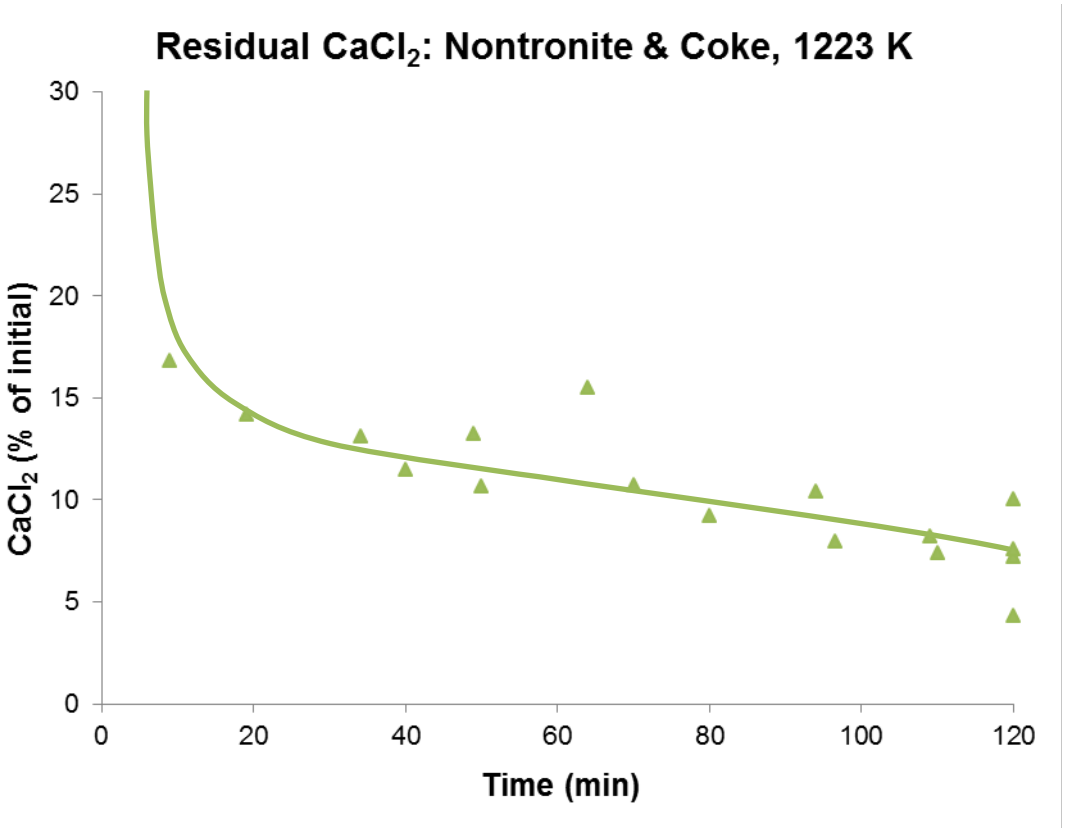

Figure B.72 Residual $CaCl_2$, Nontronite with Coke at 1223 K

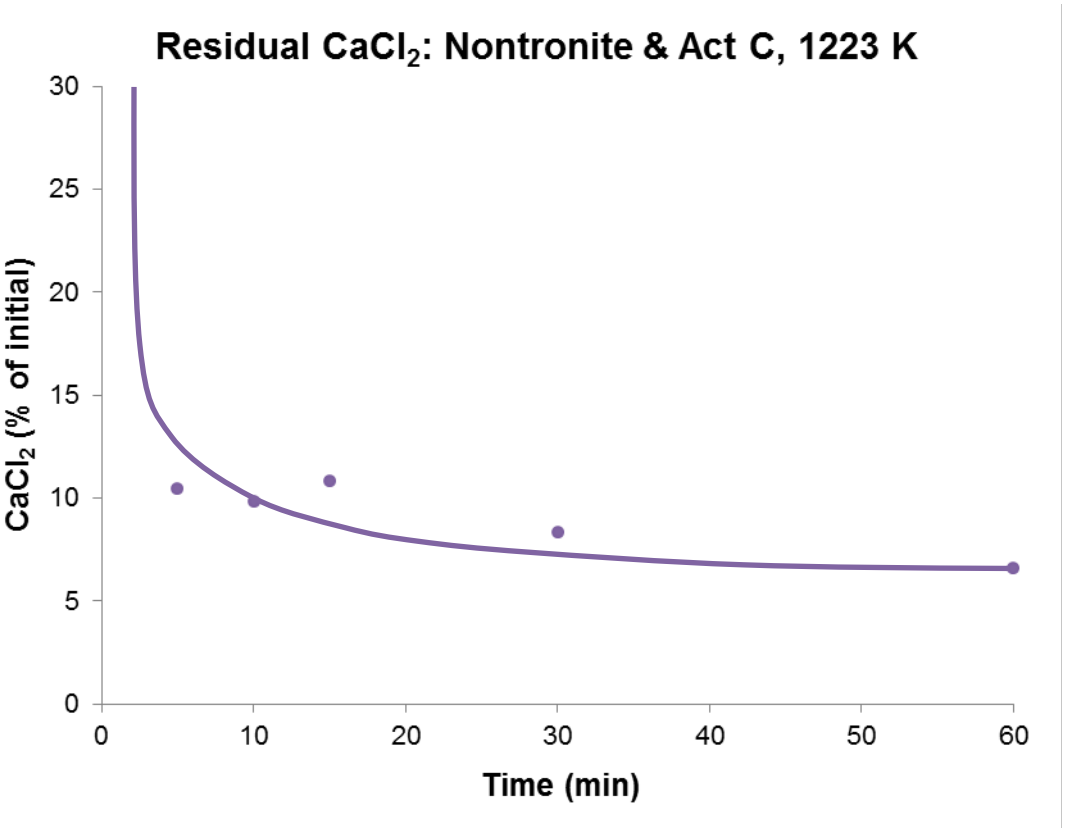

Figure B.73 Residual $CaCl_2$, Nontronite with Act C at 1223 K

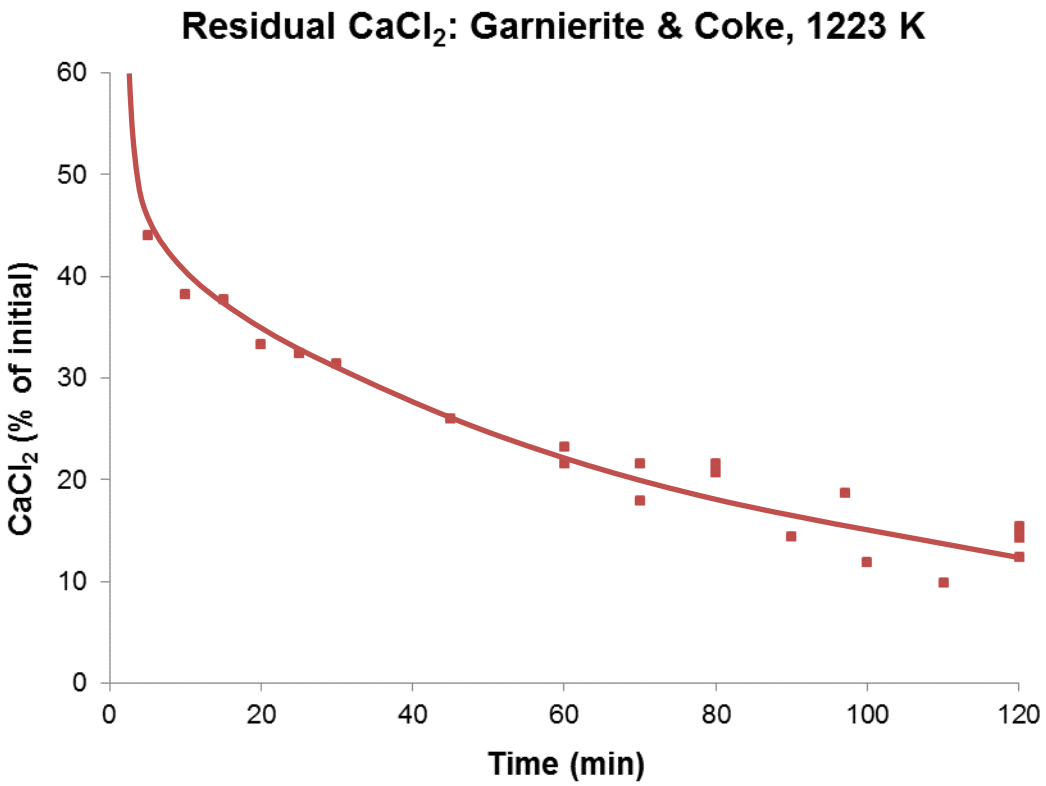

Figure B.74 Residual $CaCl_2$, Garnierite with Coke at 1223 K

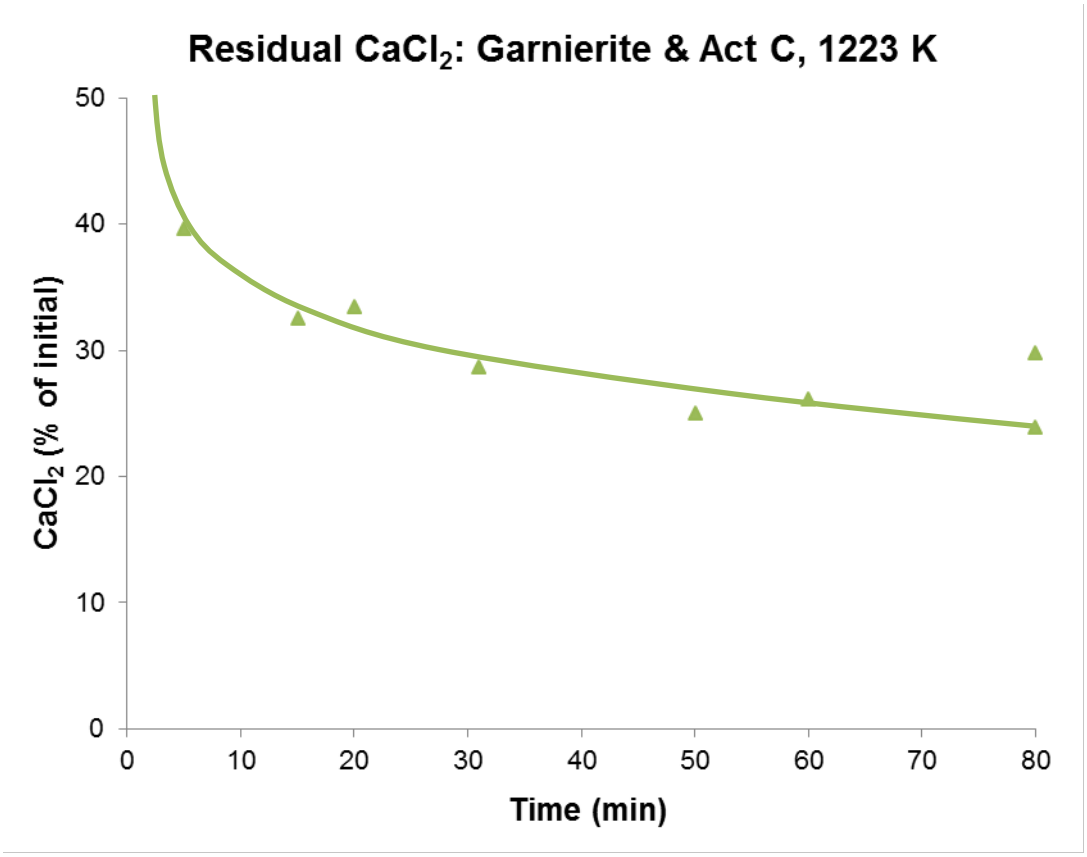

Figure B.75 Residual $CaCl_2$, Garnierite with Act C at 1223 K

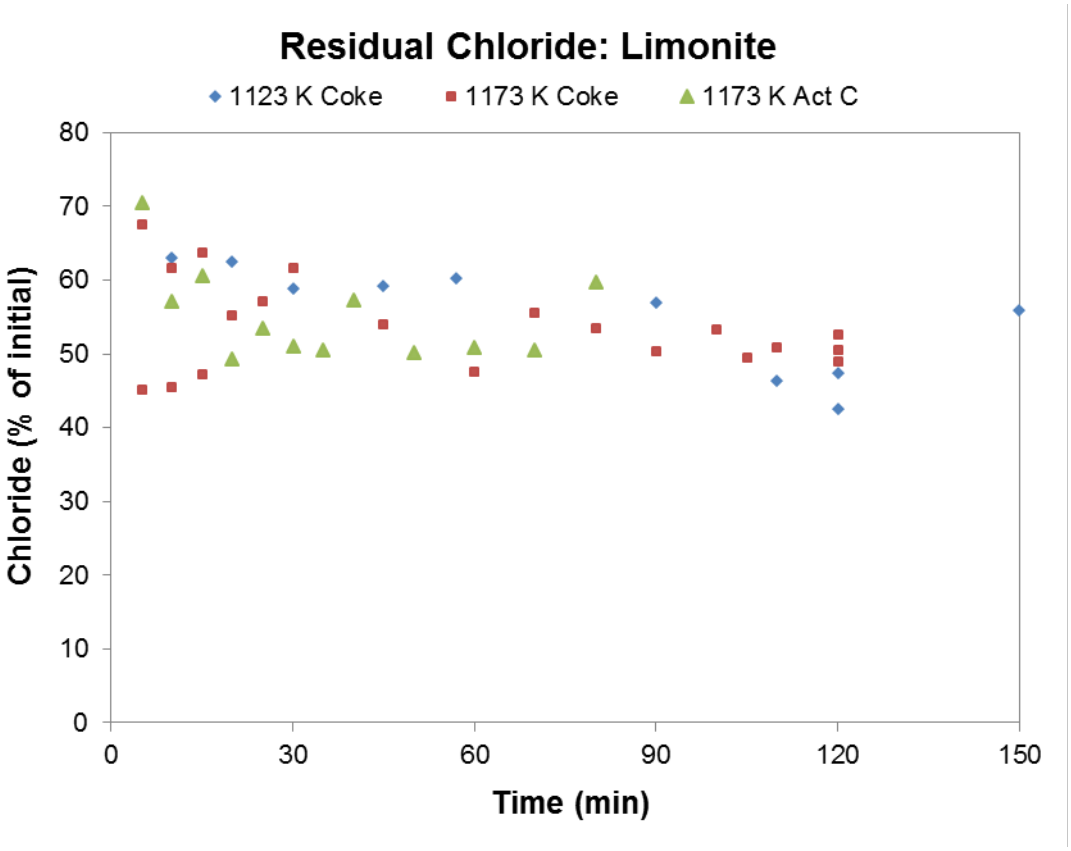

Figure B.76 Residual Chloride, Limonite

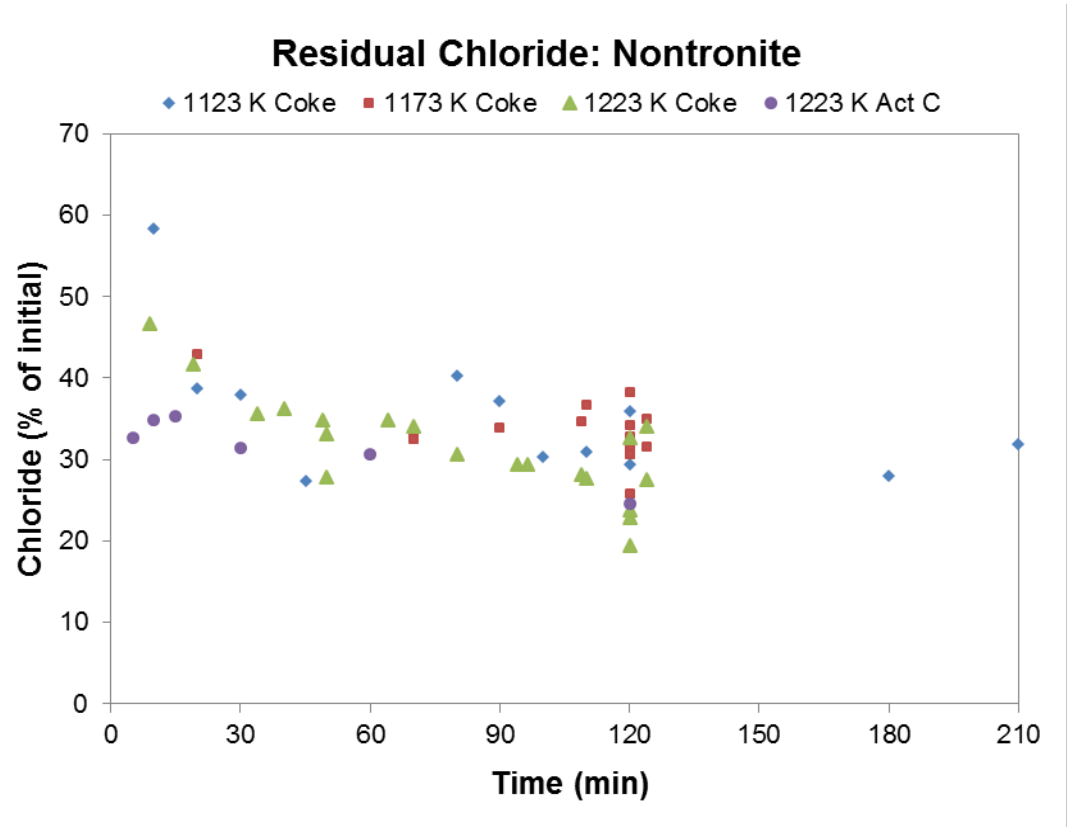

Figure B.77 Residual Chloride, Nontronite

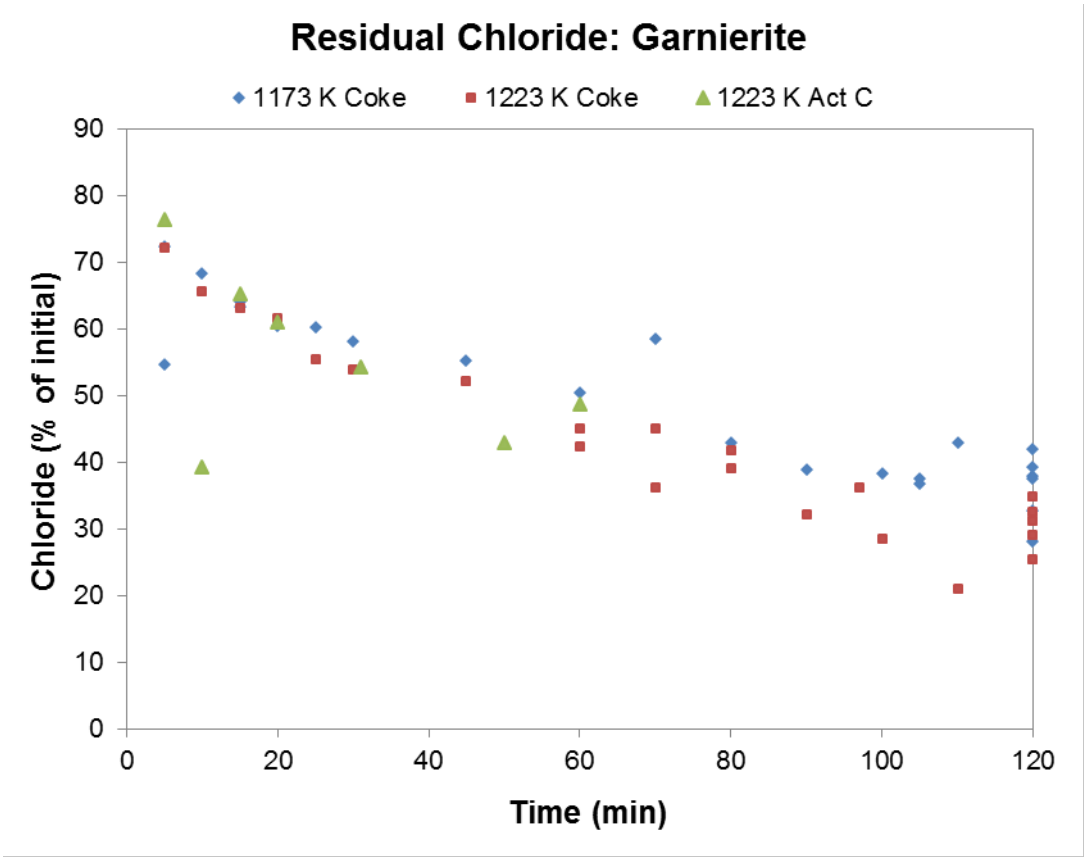

Figure B.78 Residual Chloride, Garnierite

B.11 Roast Tests: Metal Recoveries & Soluble Chloride Data

Table B.2 Limonite Roast Tests: Metal Recoveries & Soluble Chloride Data

LIMONITE												
Test Type	Test Code	Residual H_2O (mass fraction)	Recovery (%)			FeNi Ni%	Soluble Ni (%)	Soluble Fe (%)	Residual $CaCl_2$ (%)	Chloride Recovery (%)	$FeCl_2/NiCl_2$ (mole ratio)
			Ni	Fe	Co						
Rapid Heat	LPR4	$2.0x10^{-3}$	80	0.91	25	62	0.43	1.1	68	89	130
	LPR9	$1.0x10^{-3}$	65	0.56	15	68	3.2	0.85	27	46	15
	LPR17	$2.6x10^{-3}$	78	0.90	22	61	0.56	0.72	45	60	71
	LPR18	$5.1x10^{-3}$	81	1.02	26	59	0.73	0.70	44	59	53
	LPR28	$4.7x10^{-3}$	79	0.96	22	60	0.37	0.53	33	44	78
	LPR29	$5.1x10^{-3}$	82	1.05	23	59	0.09	0.53	35	46	310
	Average	$3.9x10^{-3}$	80	0.96	23	60	0.44	0.71	45	59	89
High Temp	LPR5	0	79	1.09	22	57	0.39	0.70	42	56	98
	LPR10	0	71	0.81	19	62	0.82	0.78	41	57	52
	LPR16	0	76	0.87	20	61	0.88	0.88	61	79	55
	LPR19	0	79	1.04	22	58	1.1	0.68	38	53	35
	LPR26	$6.6x10^{-3}$	79	1.09	22	57	0.12	0.42	28	37	190
	Average	$1.7x10^{-3}$	77	0.98	21	59	0.65	0.69	42	56	58
Low Temp	LPR6	$1.6x10^{-2}$	78	0.83	23	63	0.30	1.1	72	93	200
	LPR7	$1.7x10^{-2}$	76	0.82	23	63	0.34	1.1	73	96	280
	LPR11	$2.3x10^{-2}$	78	0.92	23	61	1.3	1.1	65	88	48
	LPR13	$2.3x10^{-2}$	79	0.84	23	63	0.41	1.2	74	98	160
	LPR14	$2.1x10^{-2}$	73	0.73	20	65	0.76	0.95	61	80	68
	LPR20	$2.3x10^{-2}$	83	1.0	28	60	0.79	0.66	42	55	45
	LPR22	$2.0x10^{-2}$	73	0.73	18	65	0.67	0.64	36	49	53
	Average	$2.0x10^{-2}$	77	0.84	23	63	0.65	0.96	60	80	81

Table B.3 Nontronite Roast Tests: Metal Recoveries & Soluble Chloride Data

NONTRONITE												
Test Type	Test Code	Residual H_2O (mass fraction)	Recovery (%)			FeNi Ni%	Ni in Con (%)	Soluble Ni (%)	Soluble Fe (%)	Residual $CaCl_2$ (%)	Chloride Recovery (%)	$FeCl_2/NiCl_2$ (mole ratio)
			Ni	Fe	Co							
Rapid Heat	NPR5	$9.0x10^{-3}$	59	1.3	15	69	10	3.6	2.3	8.3	32	13
	NPR6	$1.4x10^{-2}$	58	1.4	18	67	8.5	3.6	2.5	8.5	34	14
	NPR7	$2.5x10^{-3}$	55	1.3	16	68	7.8	1.9	3.5	13	48	36
	NPR10	$6.7x10^{-4}$	59	1.4	18	67	12	1.7	3.2	13	45	39
	NPR17	0	65	1.8	23	65	15	2.2	2.4	9.1	34	23
	NPR19	$5.0x10^{-4}$	66	1.8	24	64	13	2.4	2.5	9.7	35	21
	NPR22	0	65	1.8	24	64	10	2.1	2.6	9.4	36	25
	NPR16	0	56	1.2	15	71	10	0.88	2.7	10	37	62
	Average	$3.3x10^{-3}$	61	1.6	20	66	11	1.9	2.8	11	39	31
High Temp	NPR8	0	58	1.3	17	68	11	2.0	3.9	15	54	39
	NPR15	0	57	1.0	14	74	11	1.3	2.7	9.3	36	41
	NPR18	0	66	1.9	25	64	12	0.75	3.1	14	44	83
	NPR26	$8.0x10^{-4}$	63	1.6	19	66	11	1.0	2.7	11	38	53
	Average	$2.0x10^{-4}$	60	1.4	18	69	11	1.4	3.2	13	45	48
Low Temp	NPR9	$2.5x10^{-2}$	47	1.0	13	69	8.3	6.8	2.9	7.9	39	8.5
	NPR13	$2.0x10^{-2}$	44	0.73	10	75	7.5	2.8	2.3	7.0	30	16
	NPR20	$1.8x10^{-2}$	57	1.5	20	65	11	5.9	1.2	4.9	19	4.2
	NPR23	$1.8x10^{-2}$	50	1.3	16	65	8.4	2.4	1.4	4.8	20	12
	Average	$2.1x10^{-2}$	49	1.1	14	70	8.9	5.1	2.1	6.6	29	8.3

Table B.4 Garnierite Roast Tests: Metal Recoveries & Soluble Chloride Data

GARNIERITE												
Test Type	Test Code	Residual H_2O (mass fraction)	Recovery (%)			FeNi Ni%	Ni in Con (%)	Soluble Ni (%)	Soluble Fe (%)	Residual $CaCl_2$ (%)	Chloride Recovery (%)	$FeCl_2/NiCl_2$ (mole ratio)
			Ni	Fe	Co							
Rapid Heat	GPR6	$4.8x10^{-3}$	55	2.5	24	70	10	2.2	5.3	33	58	22
	GPR16	$3.1x10^{-3}$	46	2.2	22	69	10	1.8	4.9	30	54	25
	GPR17	$8.2x10^{-4}$	51	3.3	26	63	13	3.1	4.6	33	55	14
	Average	$2.9x10^{-3}$	51	2.7	24	67	11	2.3	4.9	32	56	19
High Temp	GPR7	0	58	2.5	24	71	12	3.0	5.3	35	61	16
	GPR15	0	50	2.4	21	70	12	2.3	4.5	30	51	18
	GPR23	$2.9x10^{-3}$	67	3.2	26	69	17	0.71	5.2	27	51	68
	GPR18	$5.8x10^{-4}$	51	3.3	26	63	14	3.3	4.4	32	53	12
	Average	$8.5x10^{-4}$	57	2.9	24	68	13	2.3	4.8	31	54	19
Low Temp	GPR8	$1.2x10^{-2}$	49	2.2	19	71	11	3.4	4.2	23	44	11
	GPR9	$9.9x10^{-3}$	51	2.6	22	68	10	1.9	4.3	22	43	21
	GPR11	$1.6x10^{-2}$	49	2.4	19	69	8.6	1.2	3.6	18	35	27
	GPR13	$8.1x10^{-3}$	48	2.4	20	69	9.3	2.6	4.6	21	44	16
	GPR19	$1.0x10^{-2}$	48	3.4	25	61	12	2.8	3.5	18	36	11
	Average	$1.1x10^{-2}$	49	2.6	21	67	10	2.4	4.1	20	40	16

B.12 Effect of Vibration Tests: Metal Recoveries & Soluble Chloride Data

Table B.5 Effect of Vibration Tests

Effect of vibration was tested using the same method applied for the 'Rapid Heat' roast tests (Section 6.5), with the exception being that vibration was not applied to the bed. Segregation was for 80 minutes at 1173 K with 5% coke and 5% $CaCl_2$. Two tests each were carried out with each ore, and these are compared with the average resulted from the vibrated tested below.

Ore Type	Vibration	Test	Residual H_2O (mass fraction)	Recovery (%)			FeNi	Ni in Con (%)	Soluble Ni (%)	Soluble Fe (%)	Residual $CaCl_2$ (%)	Chloride Recovery (%)	$FeCl_2/NiCl_2$ (mole ratio)
				Ni	Fe	Co	Ni%						
Limonite	No	1	$5.3x10^{-3}$	78	0.98	21	59	-	0.29	0.62	40	53	110
	No	2	$4.2x10^{-3}$	80	1.01	23	59	-	0.42	0.80	46	62	100
	Yes	Average	$3.9x10^{-3}$	80	0.96	23	60	-	0.44	0.71	45	59	89
Nontronite	No	1	$2.4x10^{-3}$	58	1.5	17	66	9.4	1.1	2.1	8.8	30	37
	No	2	$3.2x10^{-3}$	56	1.5	17	65	8.2	1.3	2.1	8.6	29	27
	Yes	Average	$3.3x10^{-3}$	61	1.6	20	66	11	1.9	2.8	11	39	31
Garnierite	No	1	$2.8x10^{-3}$	61	3.2	24	67	13	1.1	5.5	29	55	47
	No	2	$2.4x10^{-3}$	59	3.4	24	65	13	1.0	5.8	31	59	55
	Yes	Average	$2.9x10^{-3}$	51	2.7	24	67	11	2.3	4.9	32	56	19

B.13 EDS-SEM Maps: Roasted Nontronite

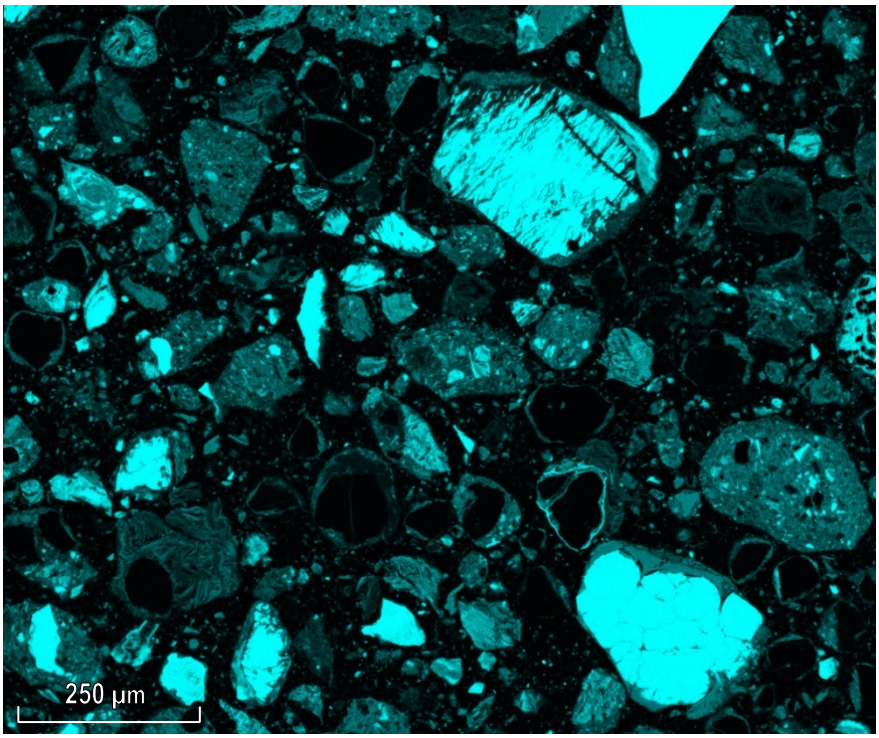

Figure B.79 Roasted Nontronite: Si Intensity Map

40.7% SiO_2 in original ore.

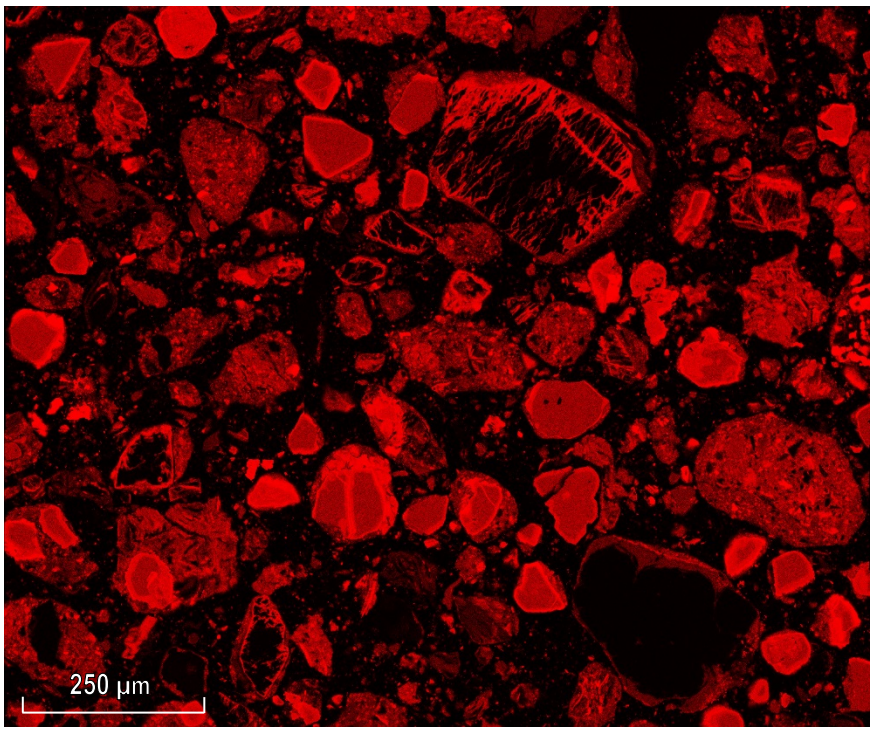

Figure B.80 Roasted Nontronite: Fe Intensity Map

24.4% Fe in original ore.

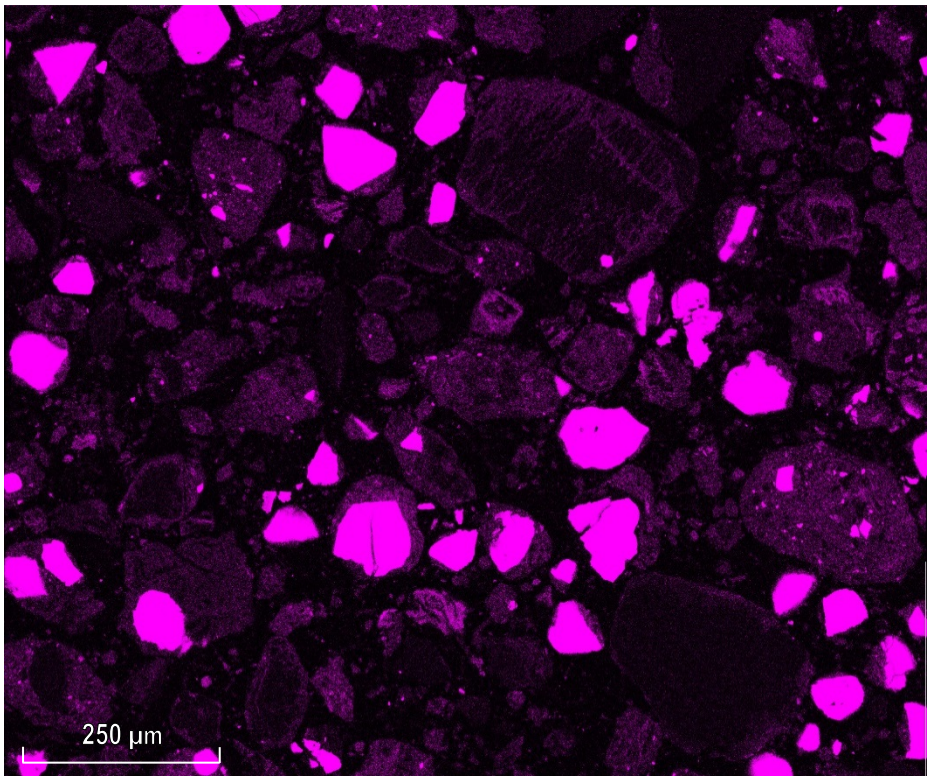

Figure B.81 Roasted Nontronite: Cr Intensity Map

4.15% Cr in original ore.

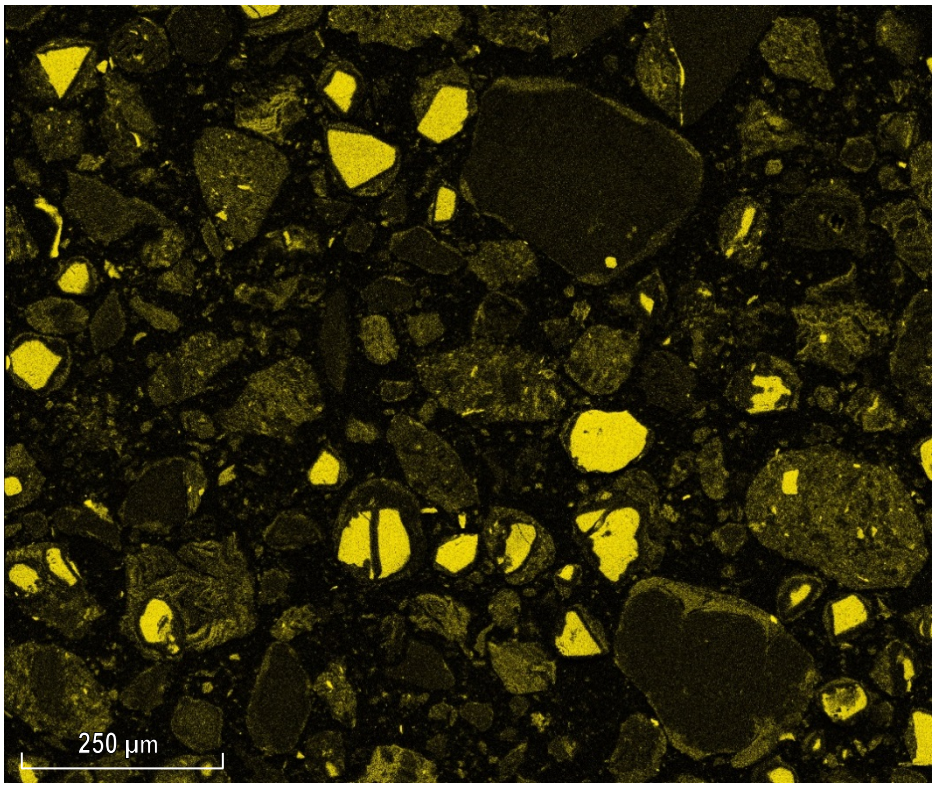

Figure B.82 Roasted Nontronite: Al Intensity Map

3.96% Al_2O_3 in original ore.

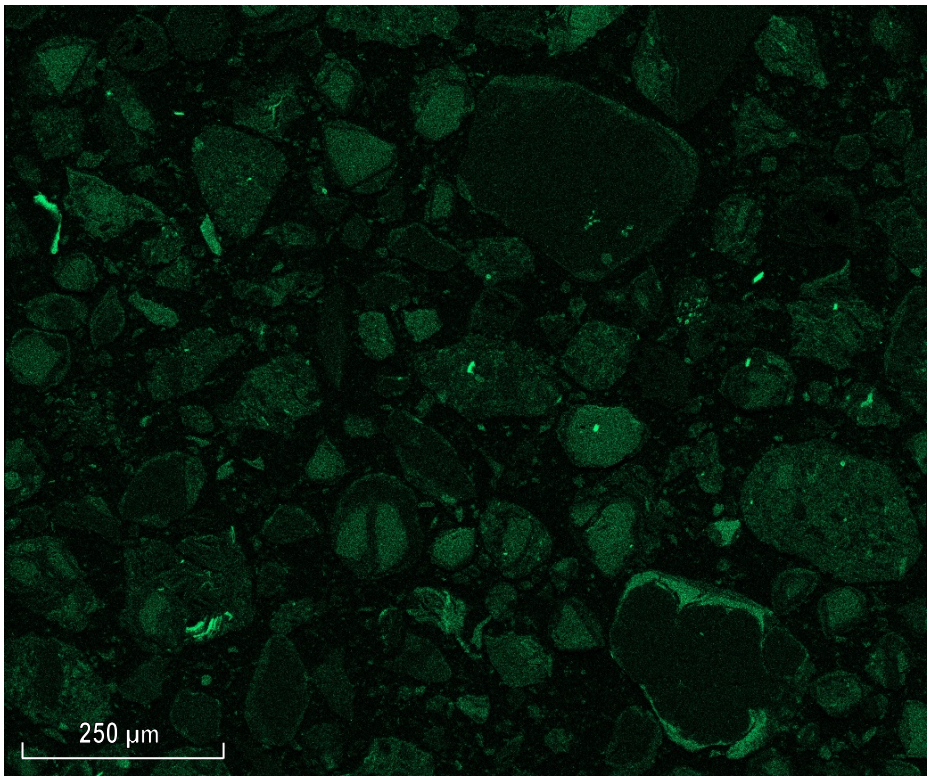

Figure B.83 Roasted Nontronite: Mg Intensity Map

2.02% MgO in original ore.

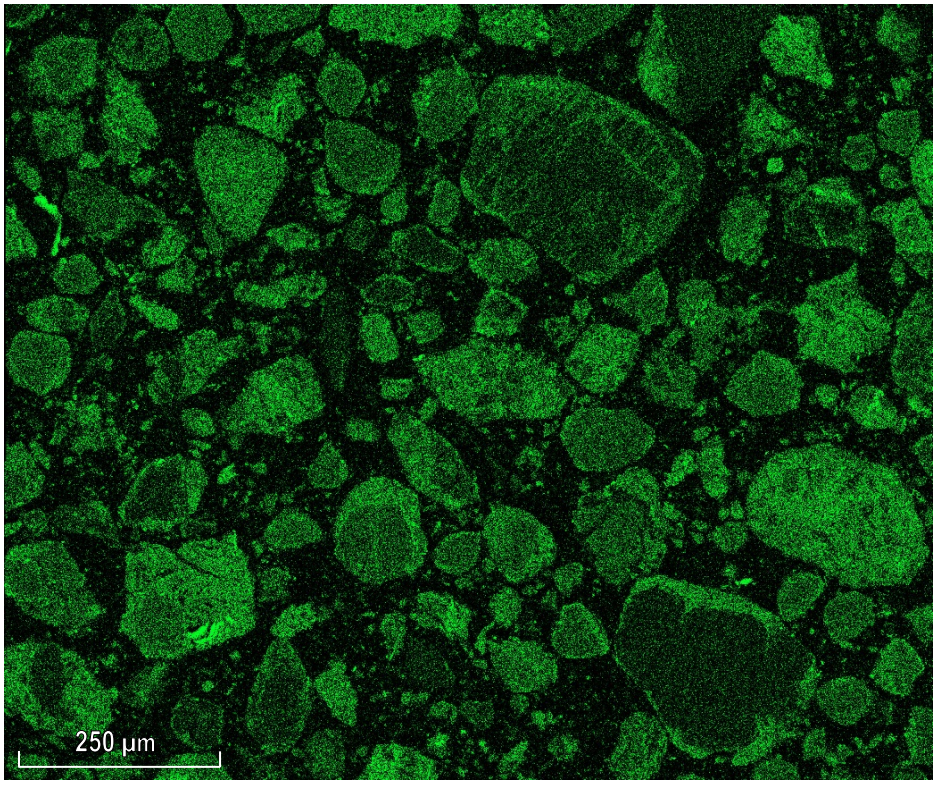

Figure B.84 Roasted Nontronite: Ni Intensity Map

1.21% Ni in original ore.

B.14 EDS-SEM Maps: Roasted Garnierite

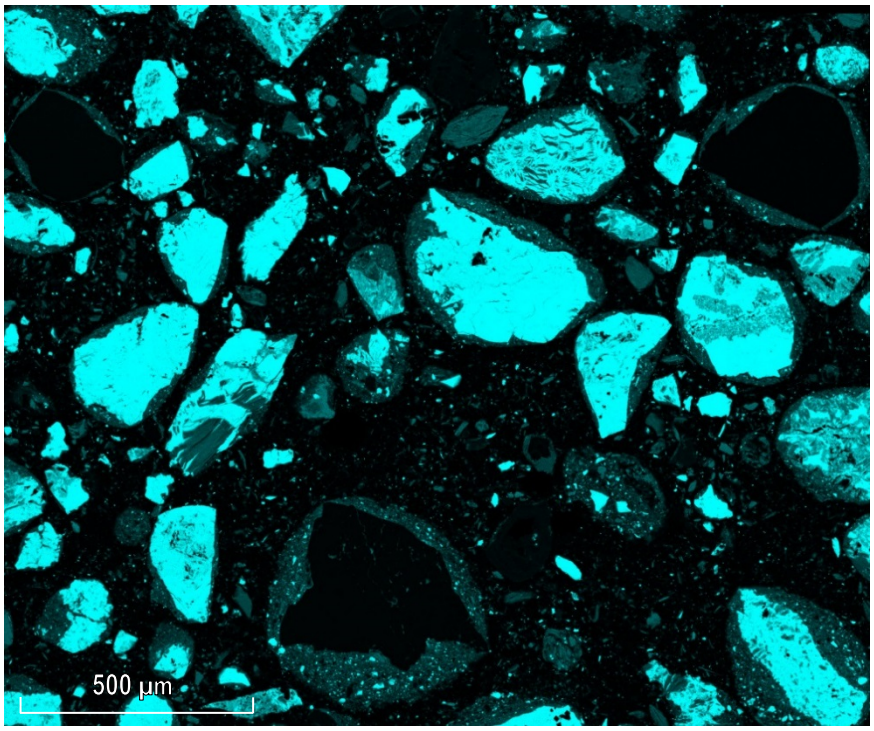

Figure B.85 Roasted Garnierite: Si Intensity Map

53.3% SiO_2 in original ore.

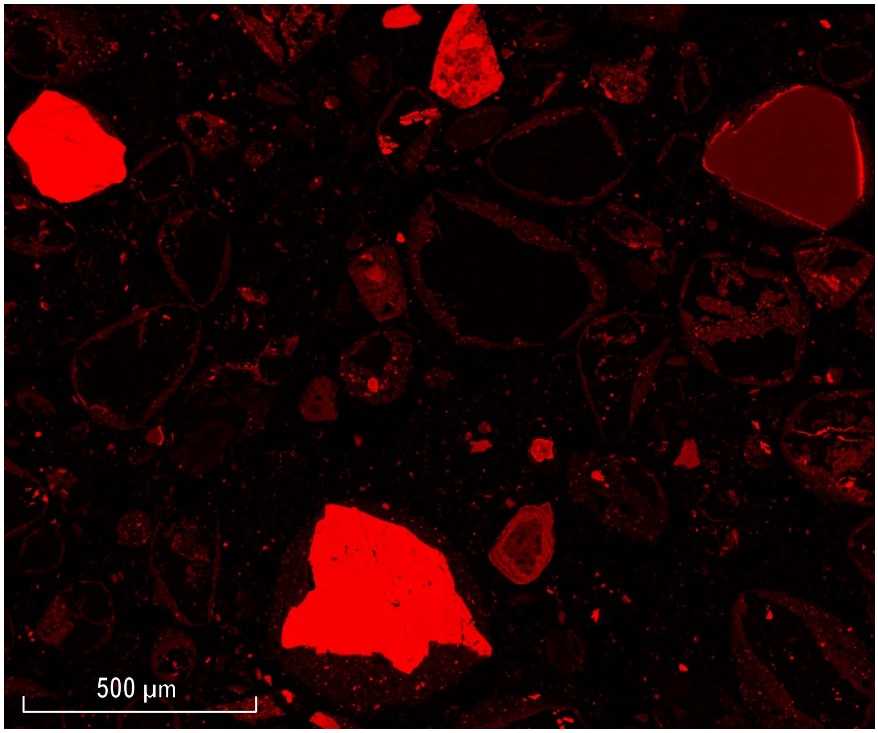

Figure B.86 Roasted Garnierite: Fe Intensity Map

11.7% Fe in original ore.

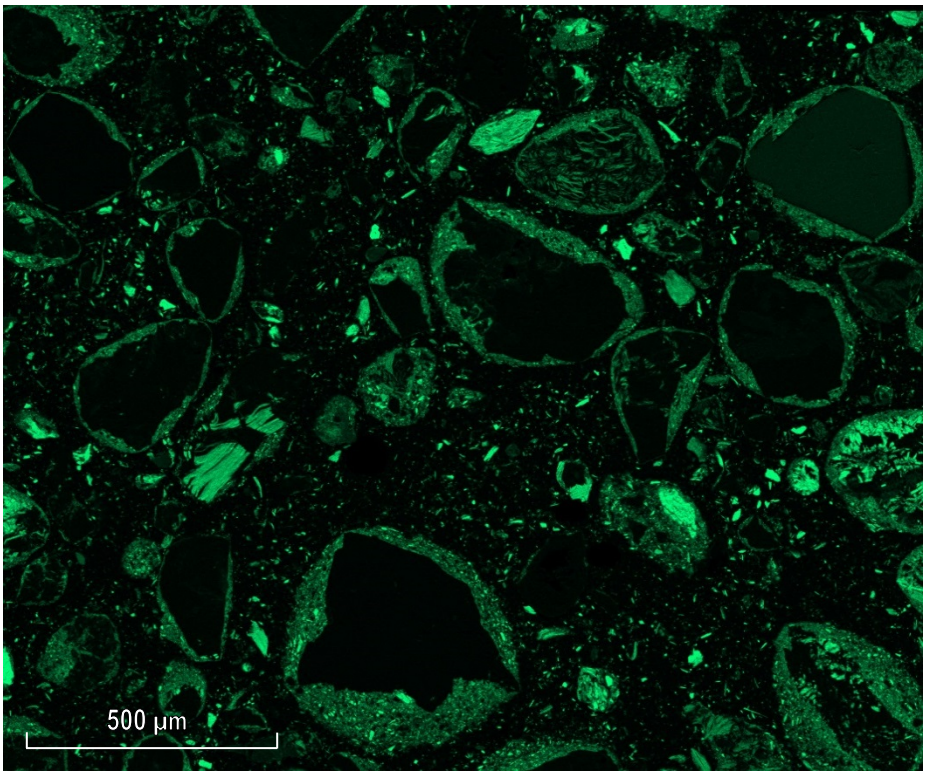

Figure B.87 Roasted Garnierite: Mg Intensity Map

14.8% MgO in original ore.

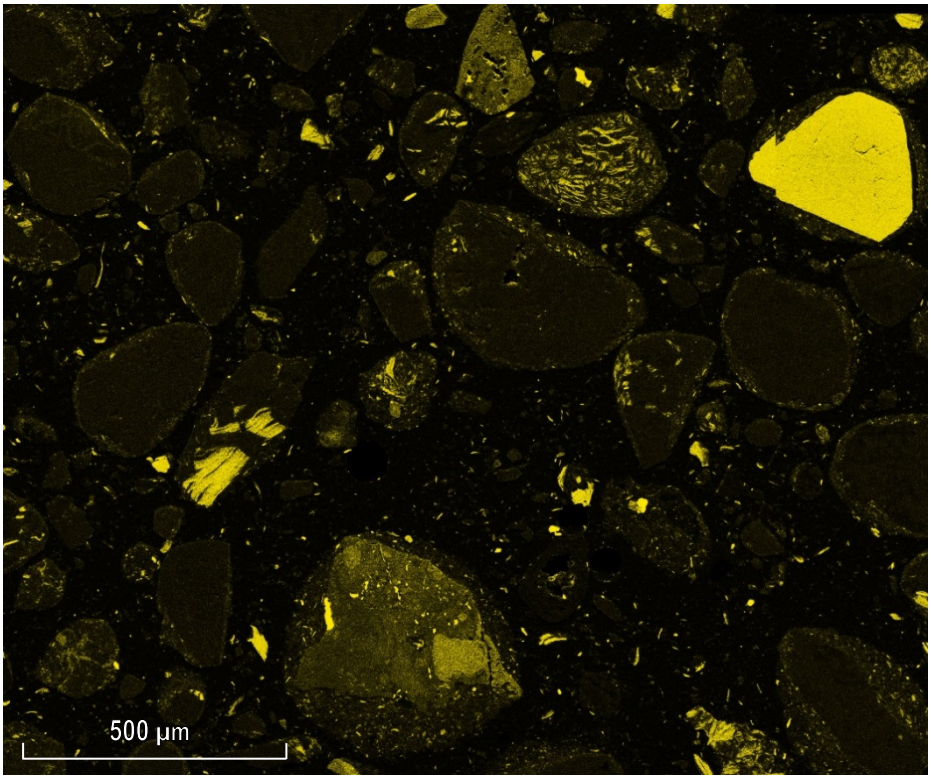

Figure B.88 Roasted Garnierite: Al Intensity Map

2.58% Al_2O_3 in original ore.

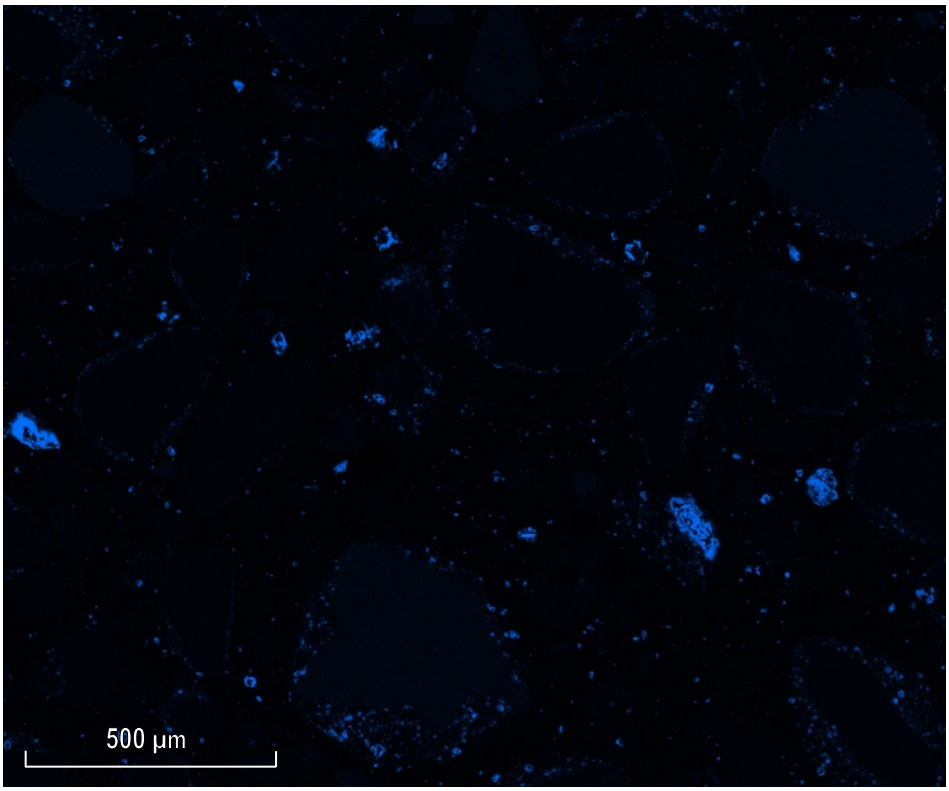

Figure B.89 Roasted Garnierite: Ca Intensity Map

1.97% CaO in original ore.

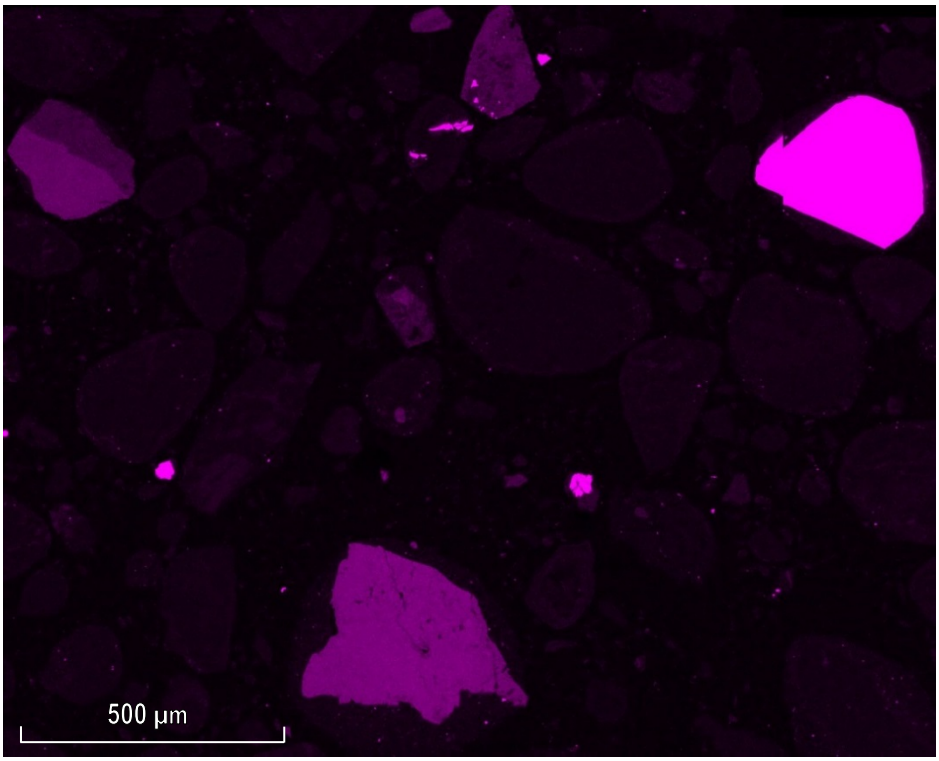

Figure B.90 Roasted Garnierite: Cr Intensity Map

0.62% Cr in original ore.

B.15 EDS-SEM Maps: Reduced Nontronite

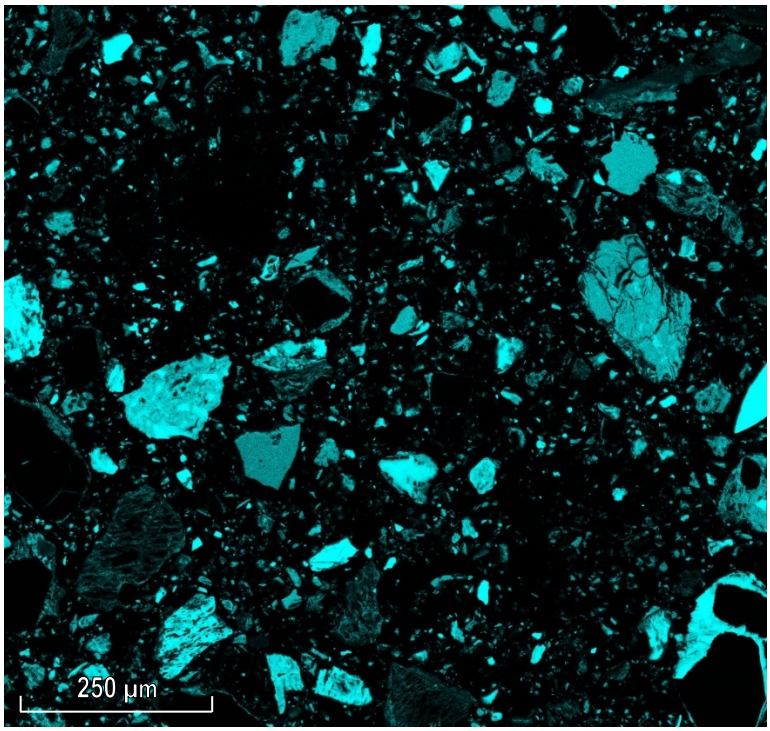

Figure B.91 Reduced Nontronite: Si Intensity Map

40.7% SiO_2 in original ore.

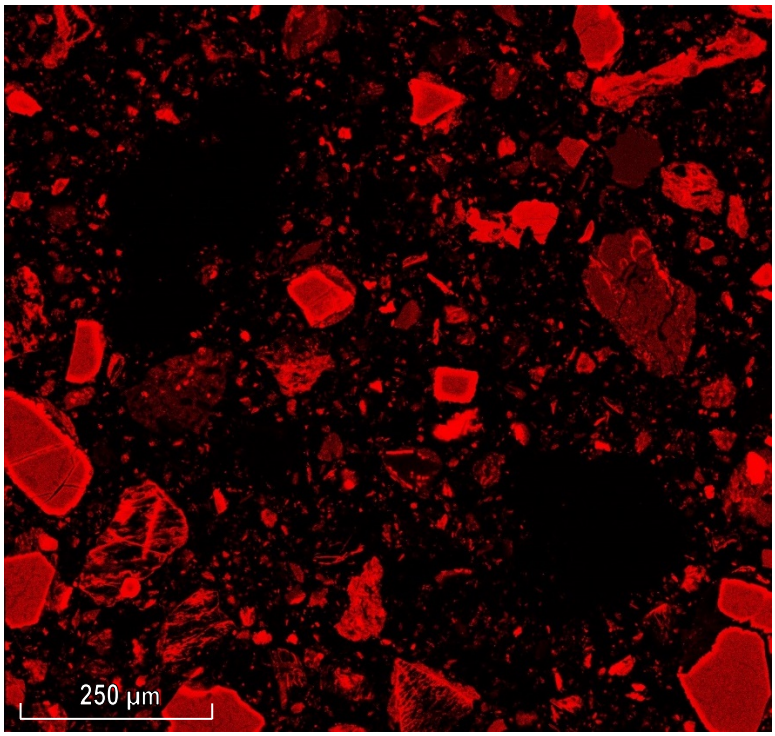

Figure B.92 Reduced Nontronite: Fe Intensity Map

24.4% Fe in original ore.

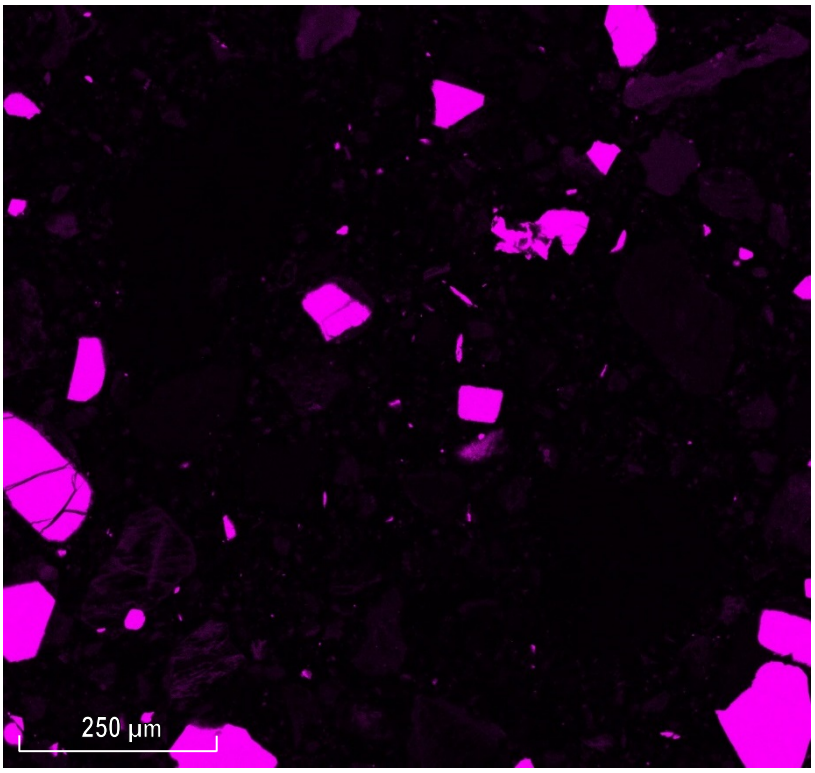

Figure B.93 Reduced Nontronite: Cr Intensity Map

4.15% Cr in original ore.

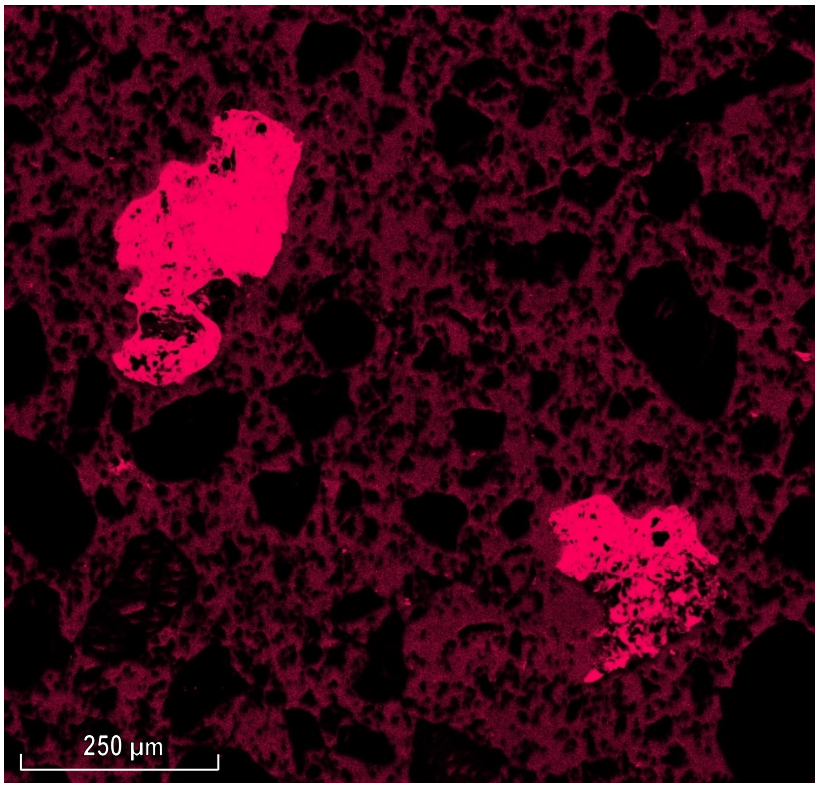

Figure B.94 Reduced Nontronite: C Intensity Map

Added at 3.91 wt% of original ore.

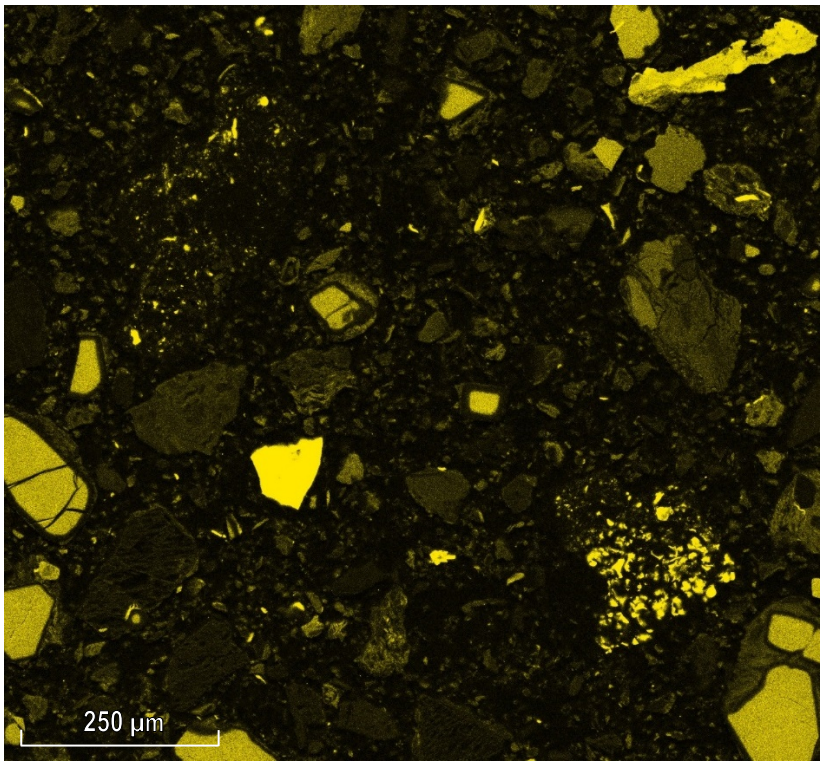

Figure B.95 Reduced Nontronite: Al Intensity Map

3.96% Al_2O_3 in original ore.

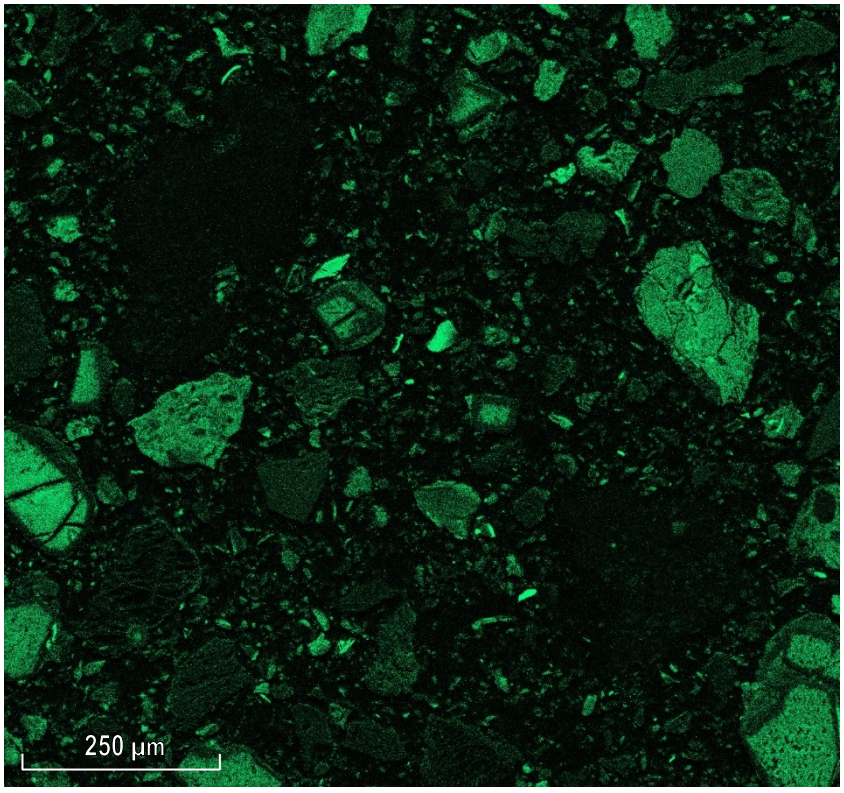

Figure B.96 Reduced Nontronite: Mg Intensity Map

2.02% MgO in original ore.

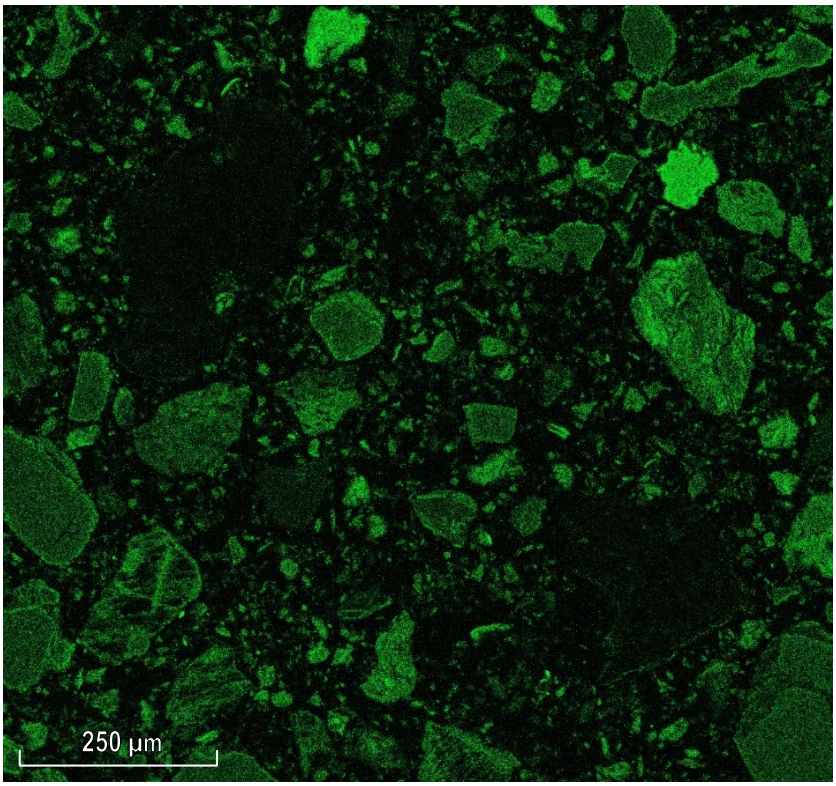

Figure B.97 Reduced Nontronite: Ni Intensity Map

1.21% Ni in original ore.

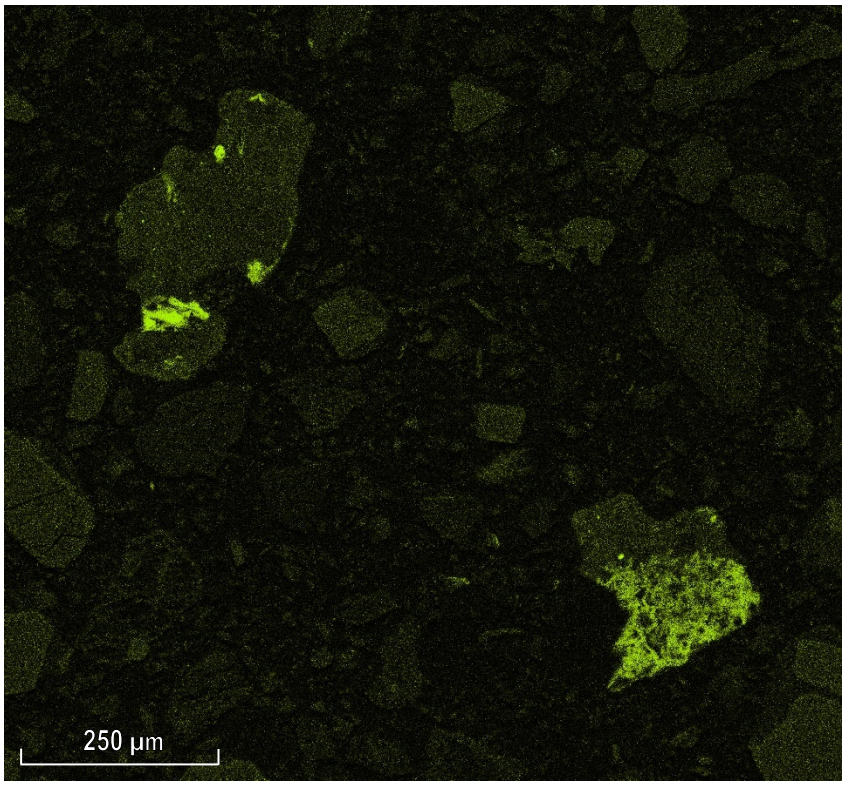

Figure B.98 Reduced Nontronite: S Intensity Map

0.21% S in original ore and 0.41% in the added coke; ~0.21% of combined feed.

B.16 EDS-SEM Maps: Reduced Garnierite

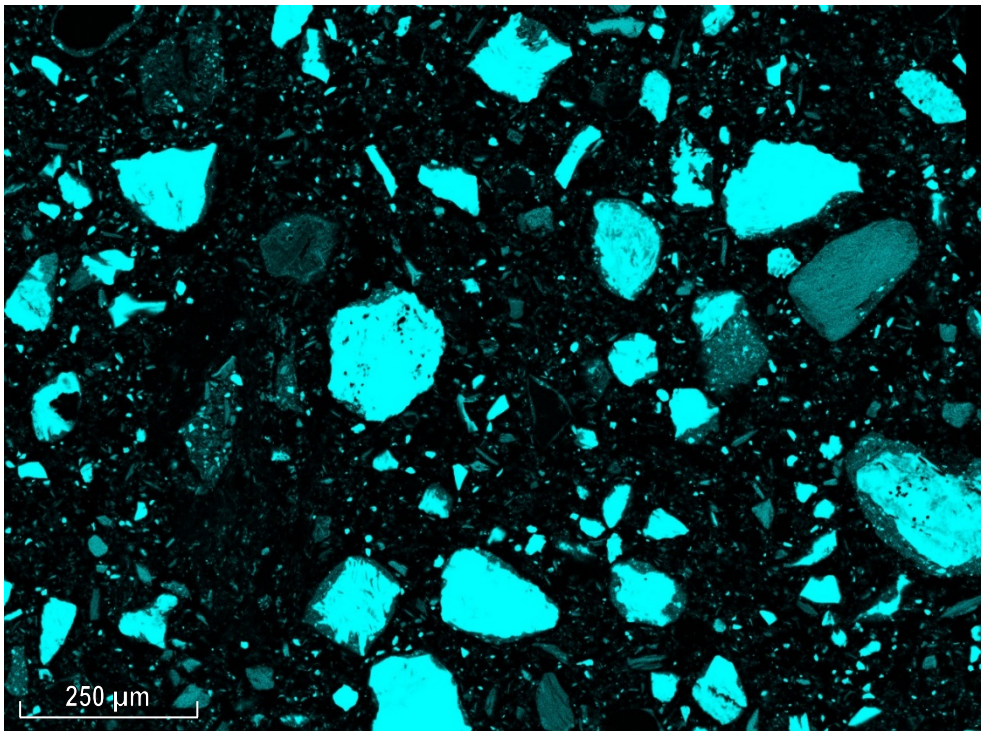

Figure B.99 Reduced Garnierite: Si Intensity Map

53.3% SiO_2 in original ore.

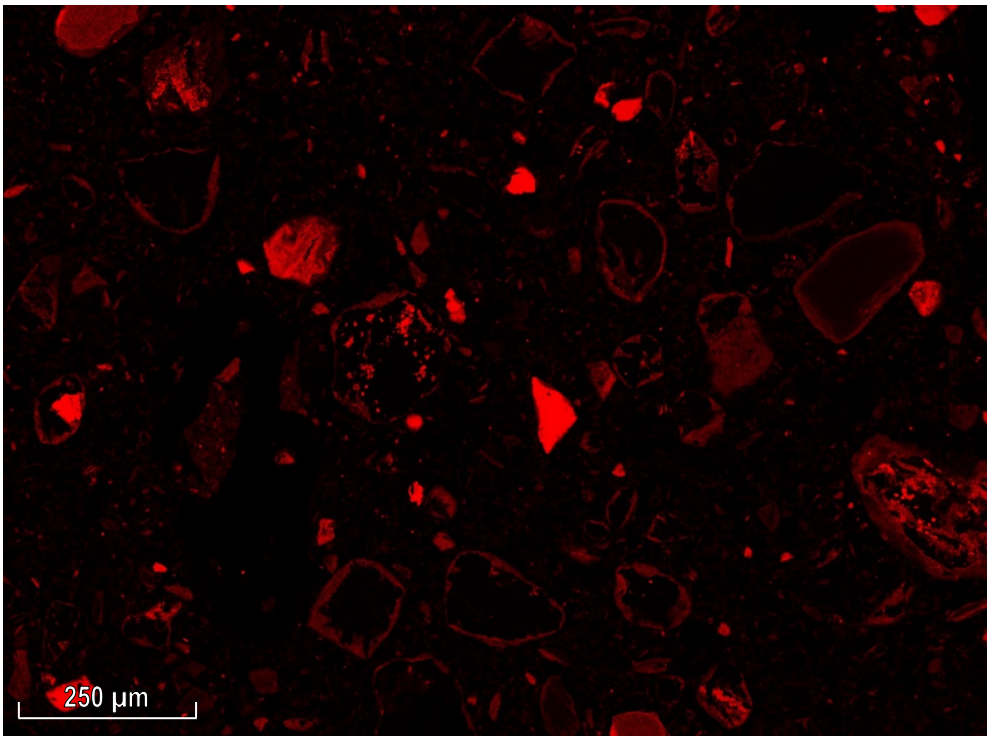

Figure B.100 Reduced Garnierite: Fe Intensity Map

11.7% Fe in original ore.

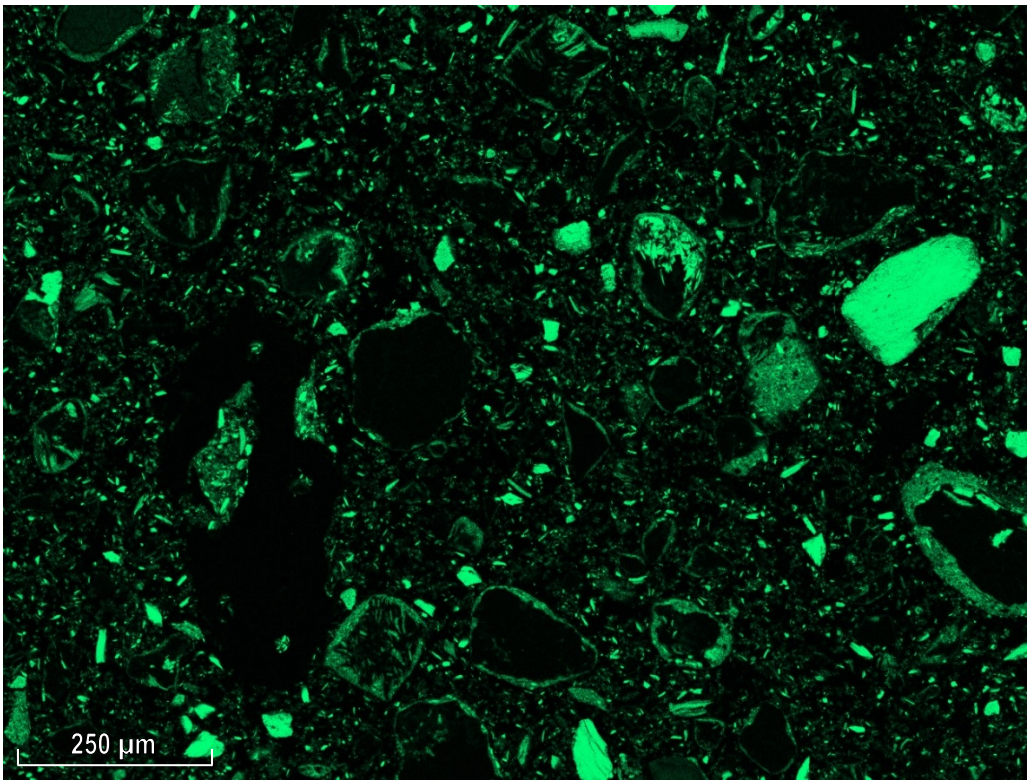

Figure B.101 Reduced Garnierite: Mg Intensity Map

14.8% MgO in original ore.

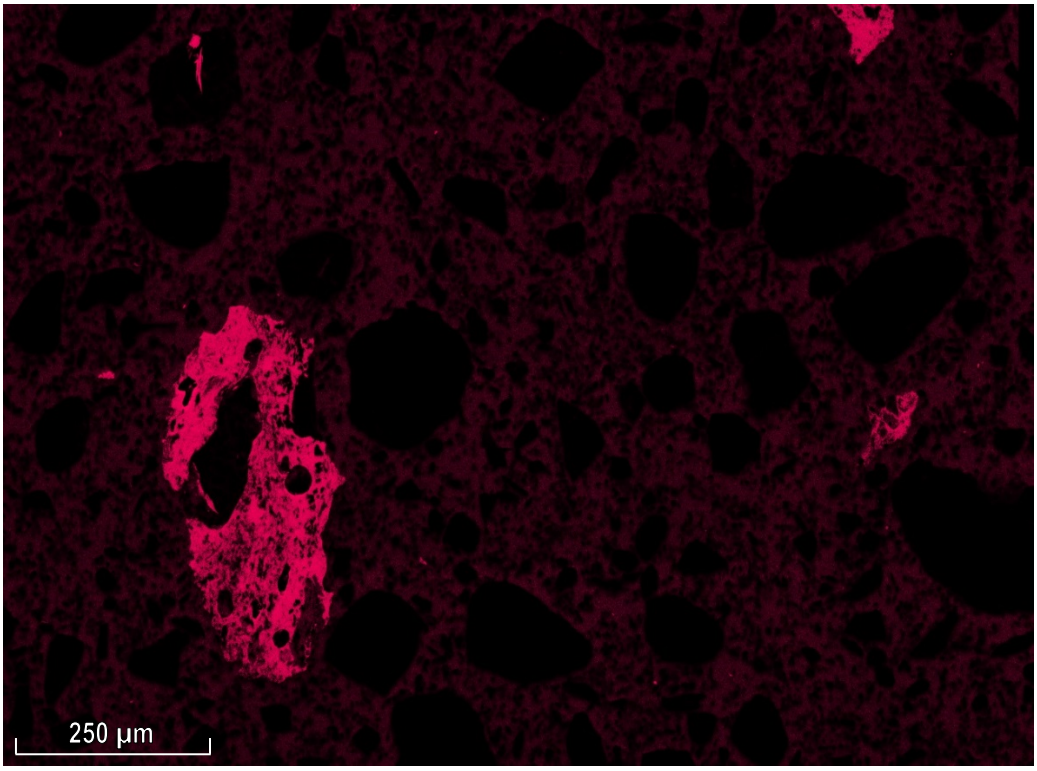

Figure B.102 Reduced Garnierite: C Intensity Map

Added at 3.91 wt% of original ore.

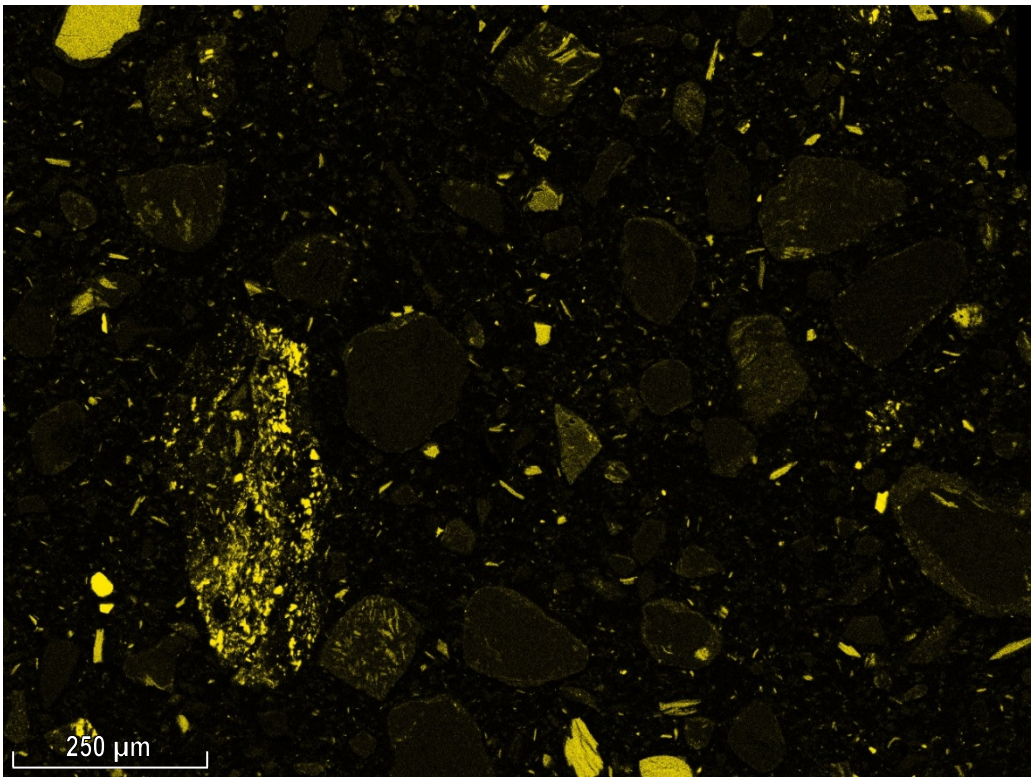

Figure B.103 Reduced Garnierite: Al Intensity Map

2.58% Al_2O_3 in original ore.

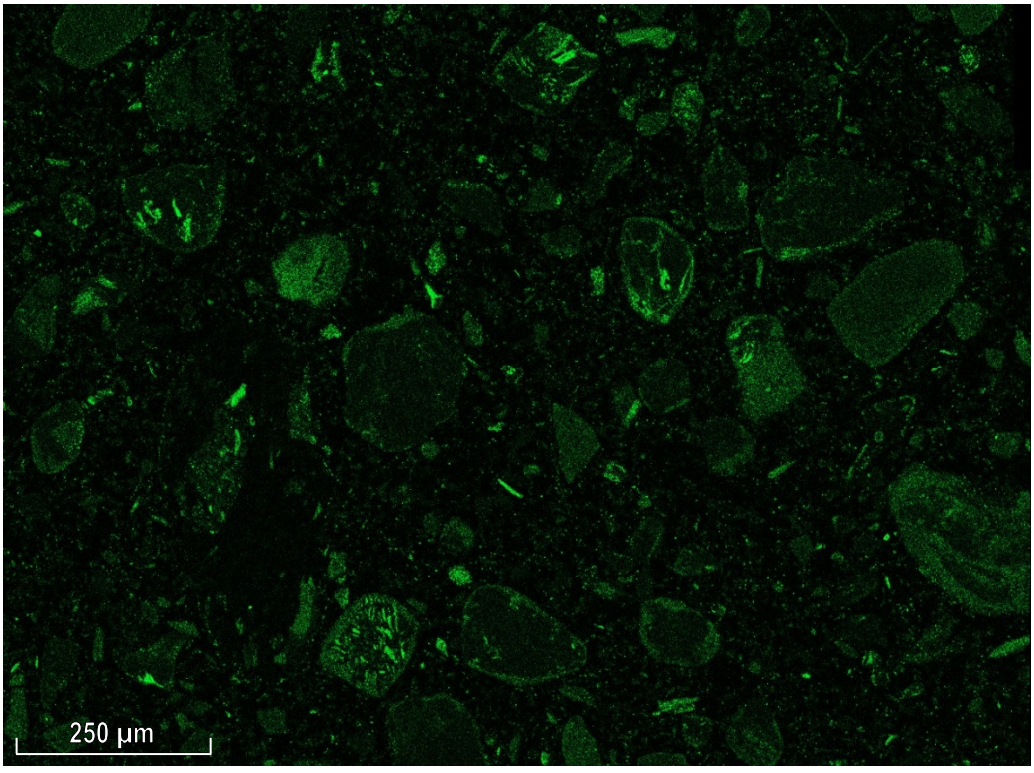

Figure B.104 Reduced Garnierite: Ni Intensity Map

1.27% Ni in original ore.

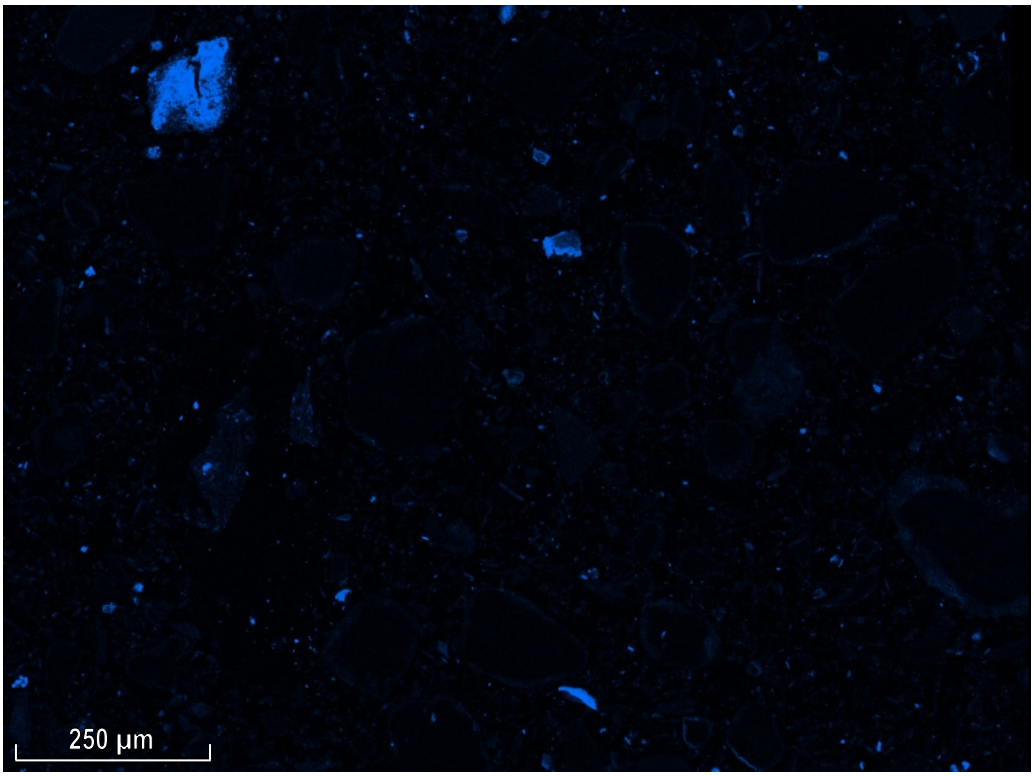

Figure B.105 Reduced Garnierite: Ca Intensity Map

1.97% CaO in original ore.

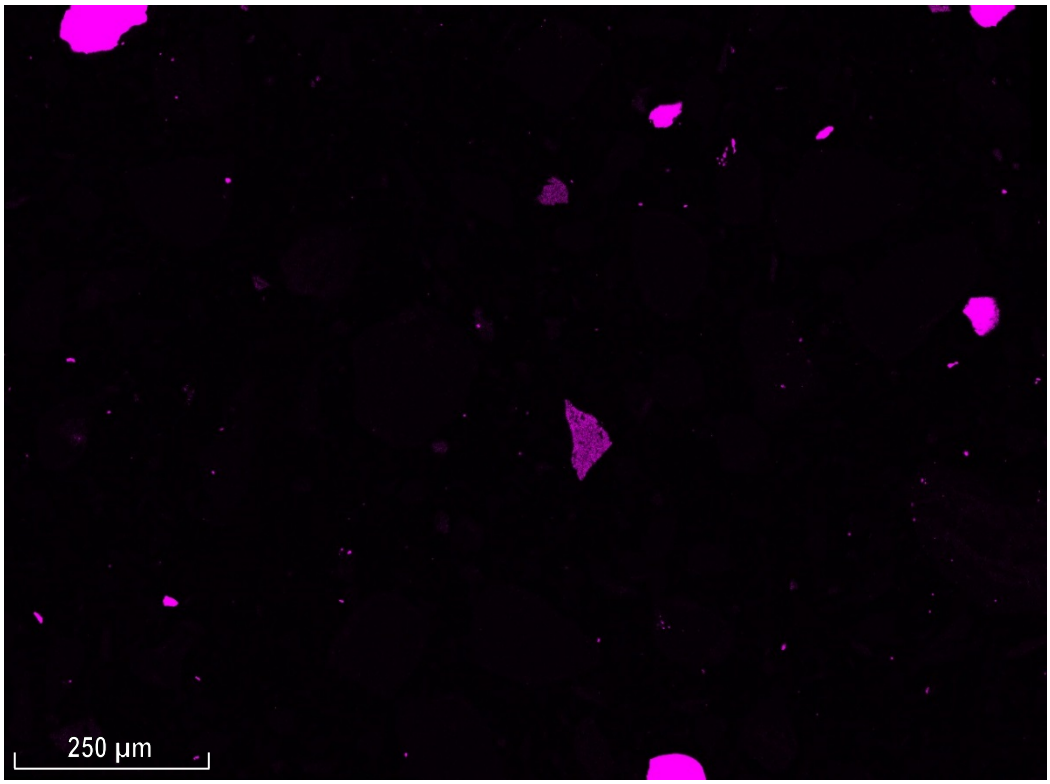

Figure B.106 Reduced Garnierite: Cr Intensity Map

0.62% Cr in original ore.

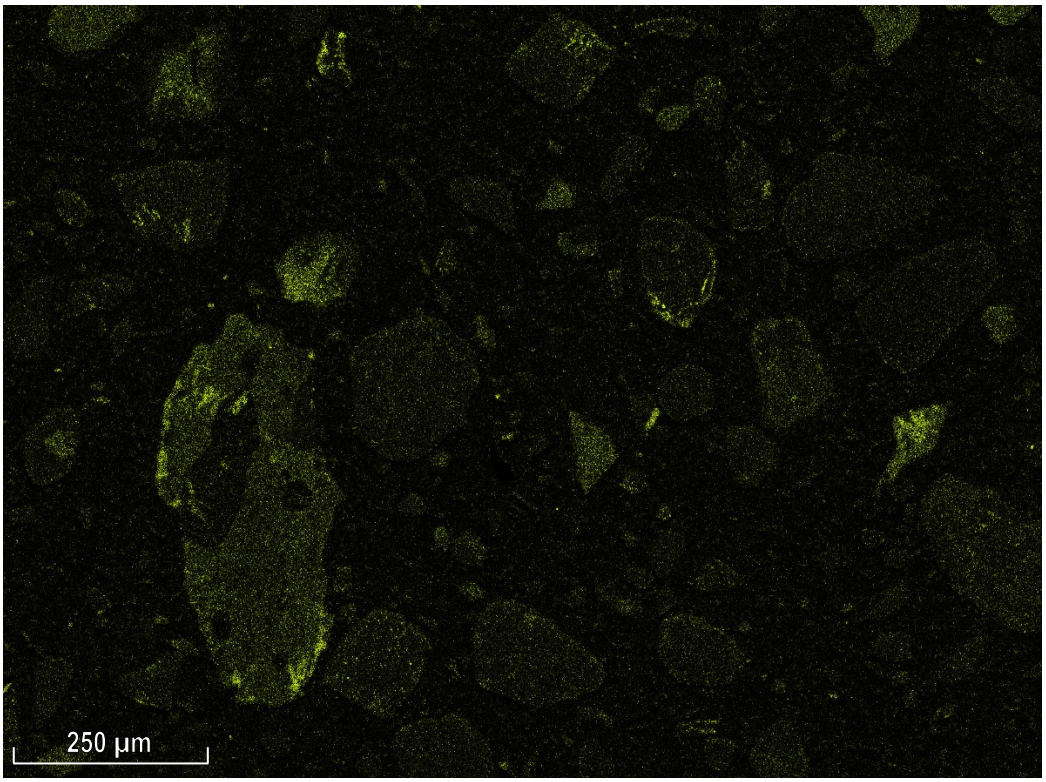

Figure B.107 Reduced Garnierite: S Intensity Map

0.06% S in original ore and 0.41% in the added coke; ~0.07% of combined feed.

B.17 EDS-SEM Maps: Segregated Nontronite

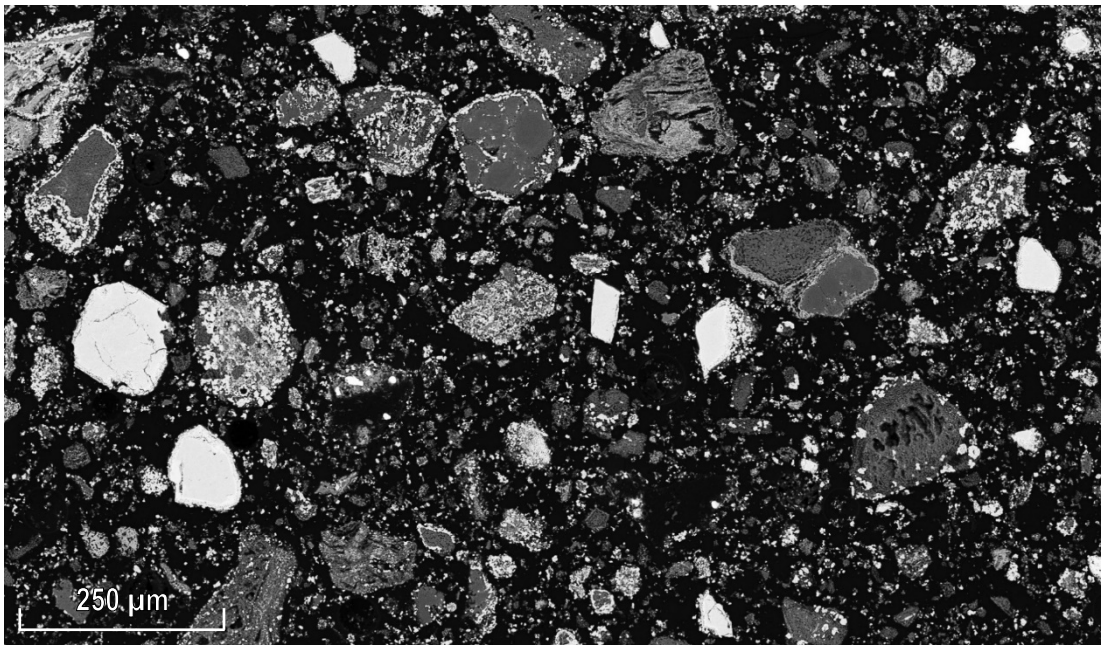

Figure B.108 Segregated Nontronite: SEM Backscattered Electron Image

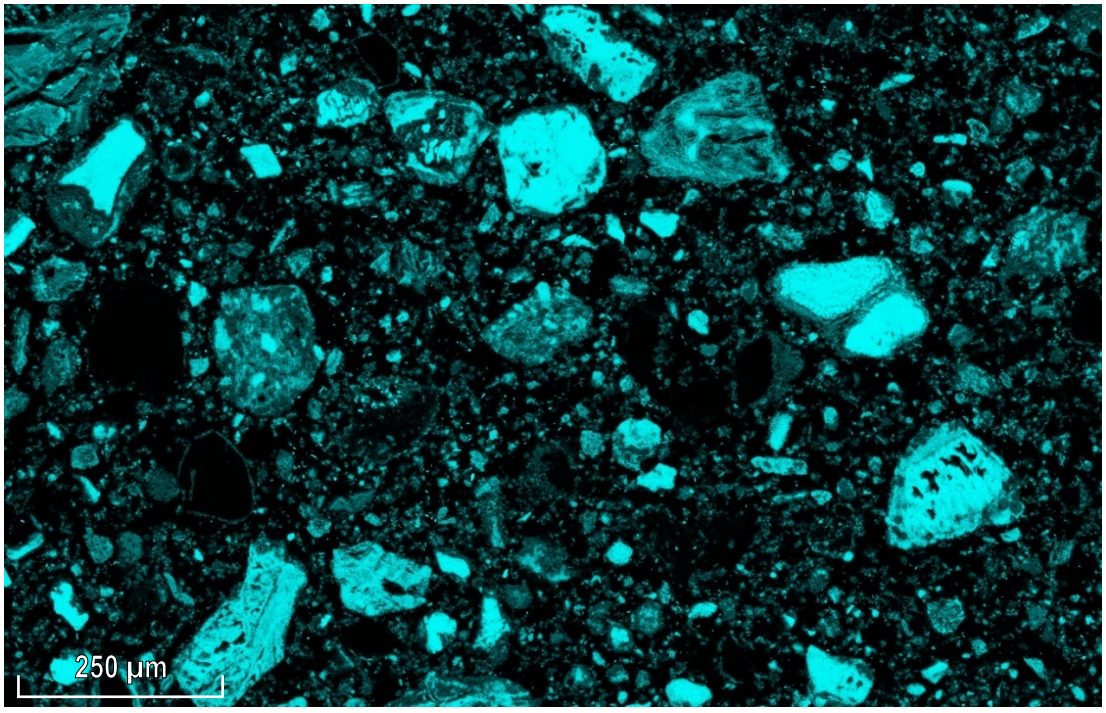

Figure B.109 Segregated Nontronite: Si Intensity Map

40.7% SiO_2 in original ore.

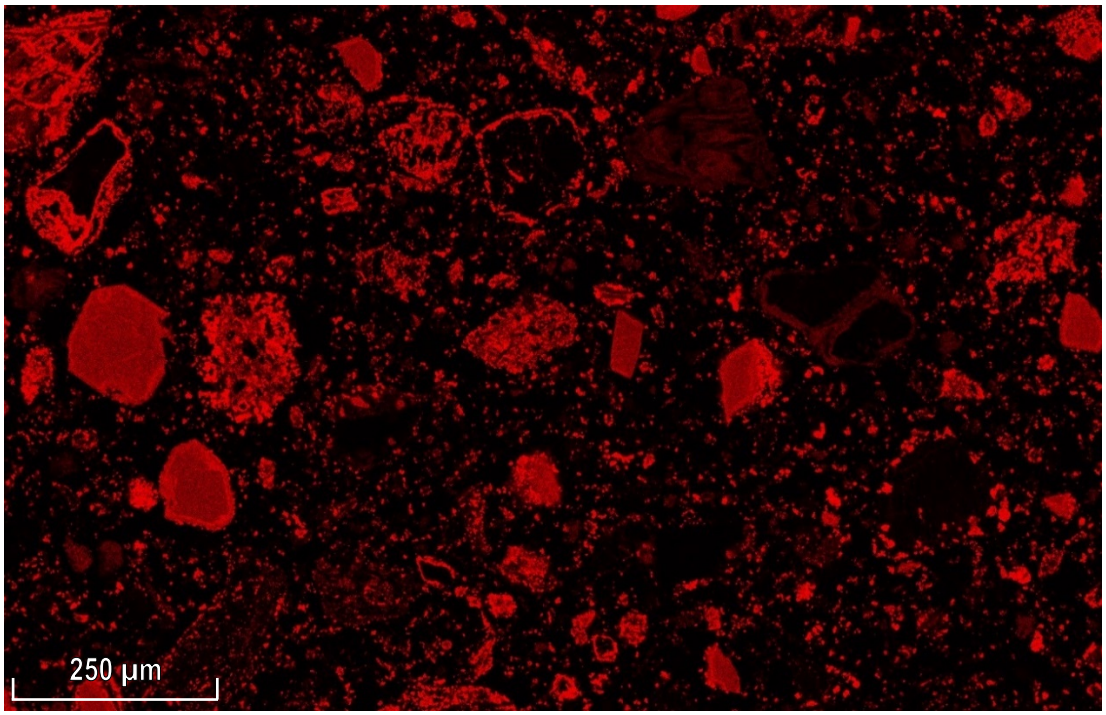

Figure B.110 Segregated Nontronite: Fe Intensity Map

24.4% Fe in original ore.

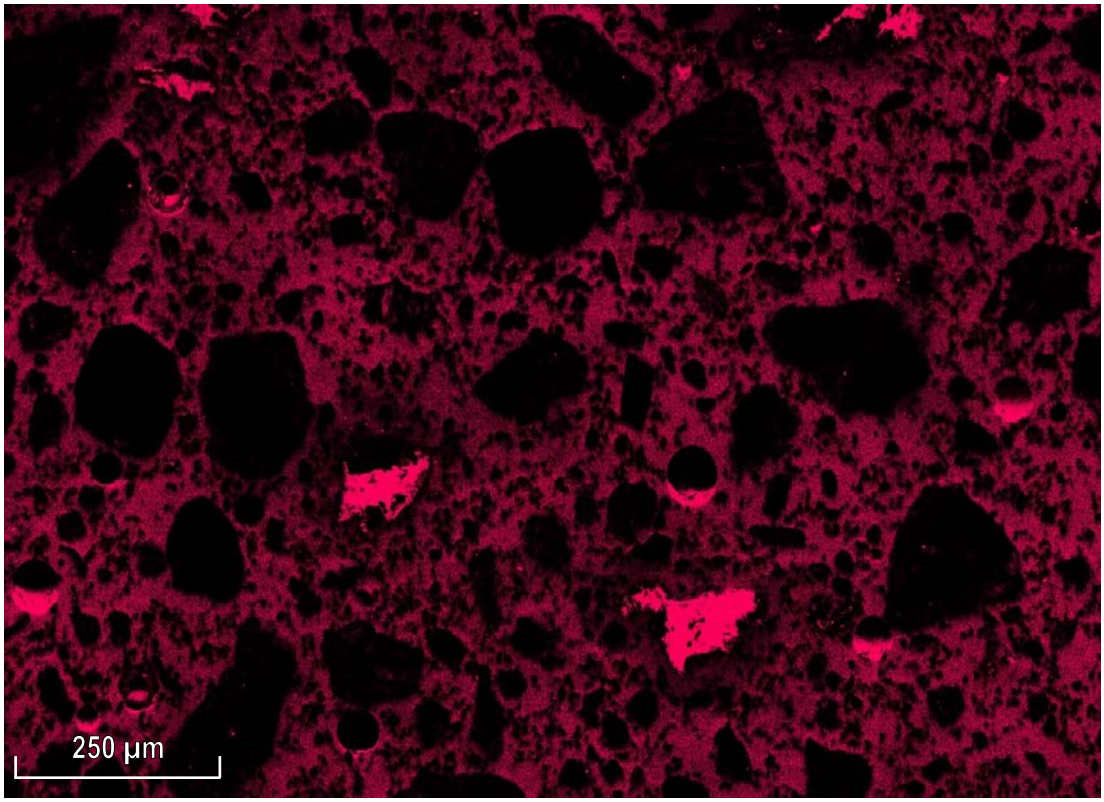

Figure B.111 Segregated Nontronite: C Intensity Map

Added at 3.91 wt% of original ore.

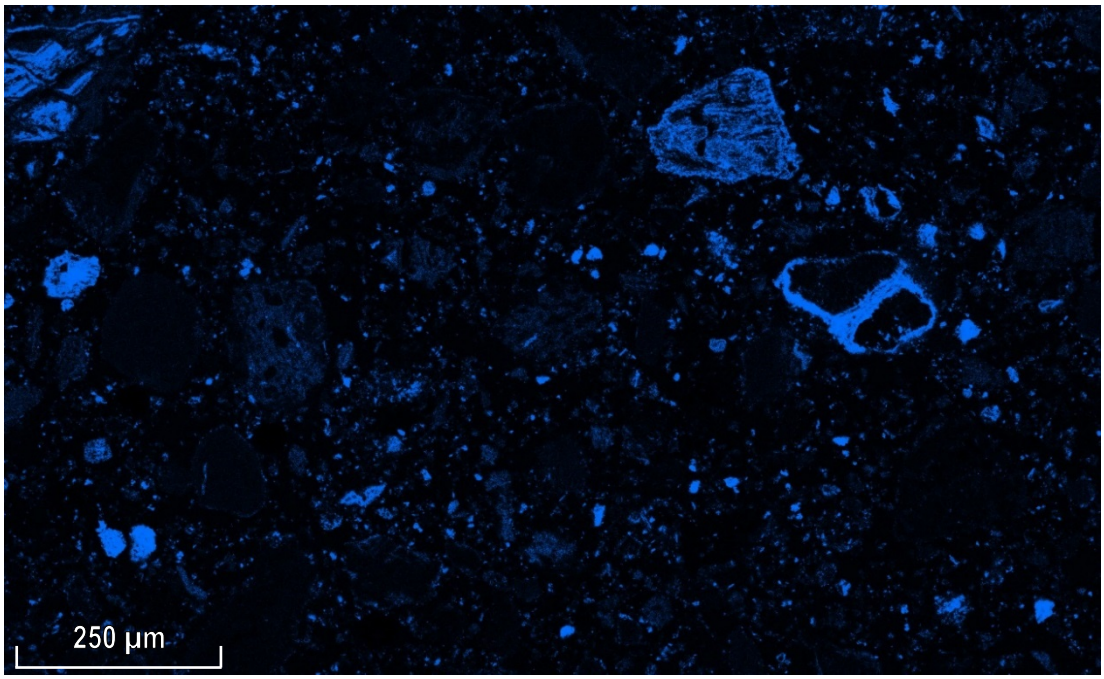

Figure B.112 Segregated Nontronite: Ca Intensity Map
Added as $CaCl_2$ at 2.67 wt% of original ore.

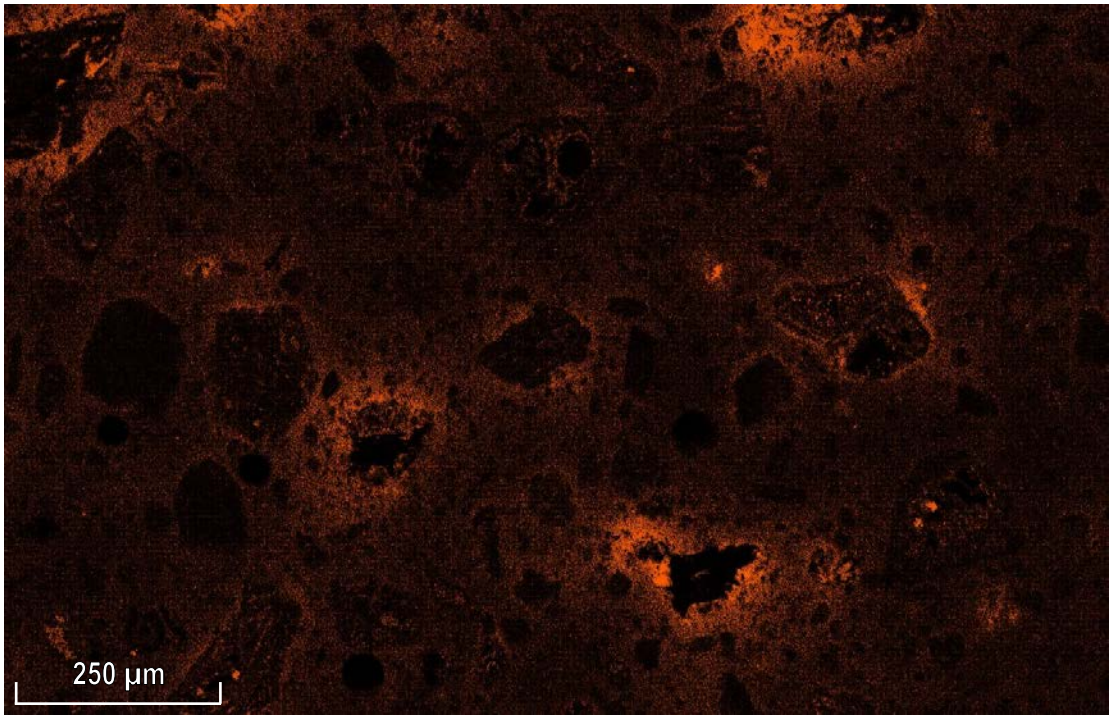

Figure B.113 Segregated Nontronite: Cl Intensity Map
Added as $CaCl_2$ at 2.33 wt% of original ore.

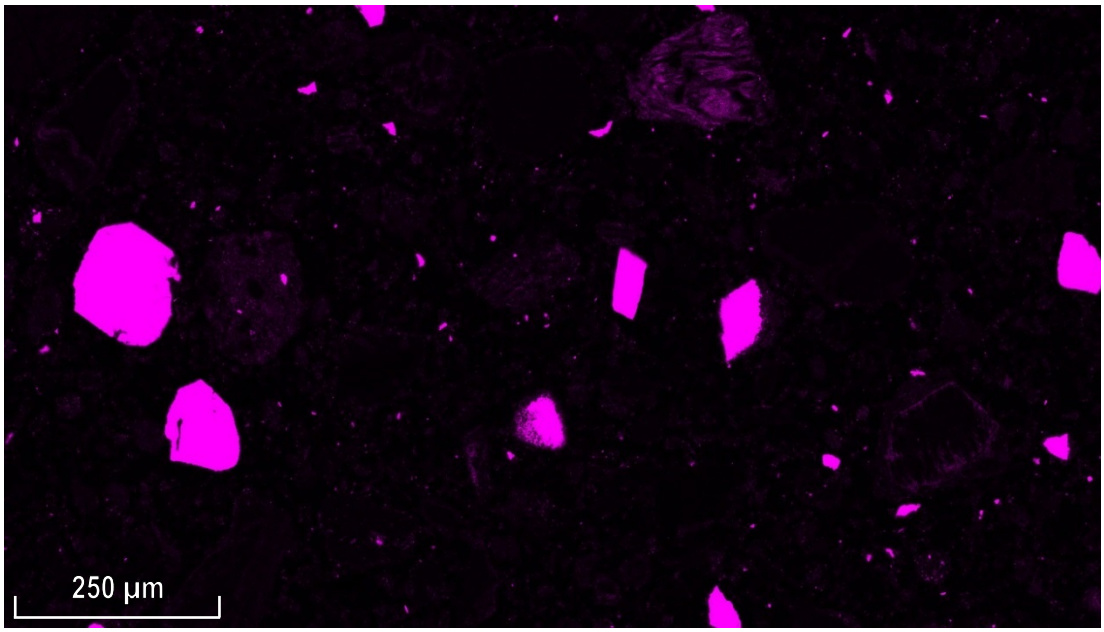

Figure B.114 Segregated Nontronite: Cr Intensity Map

4.15% Cr in original ore.

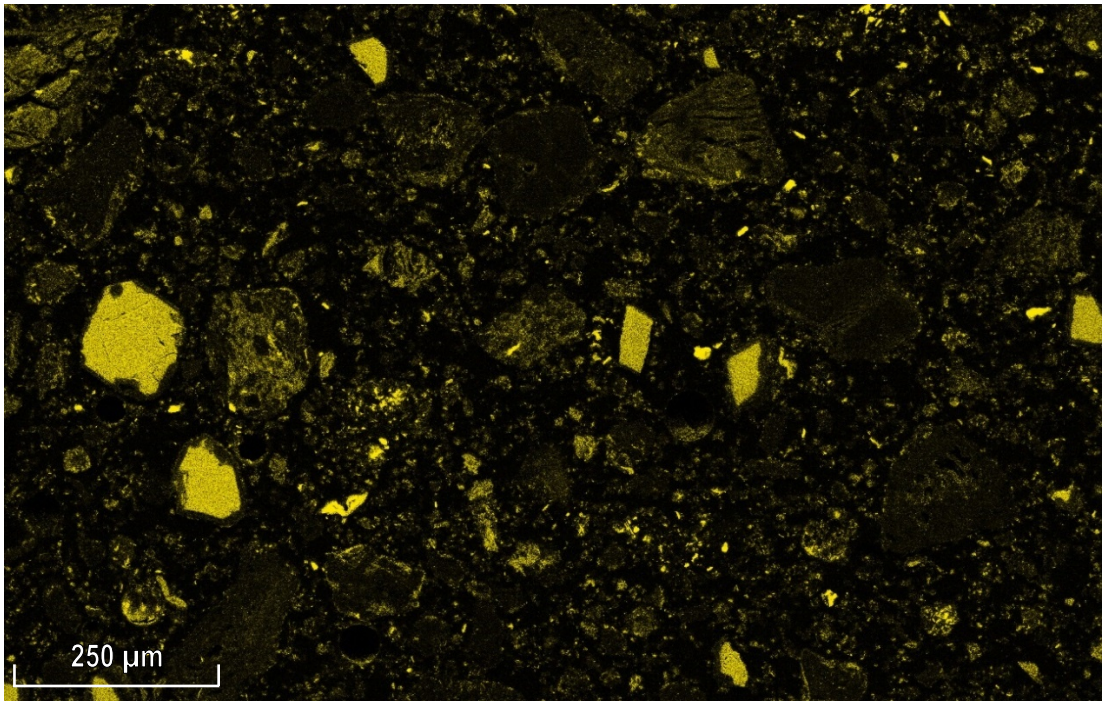

Figure B.115 Segregated Nontronite: Al Intensity Map

3.96% Al_2O_3 in original ore.

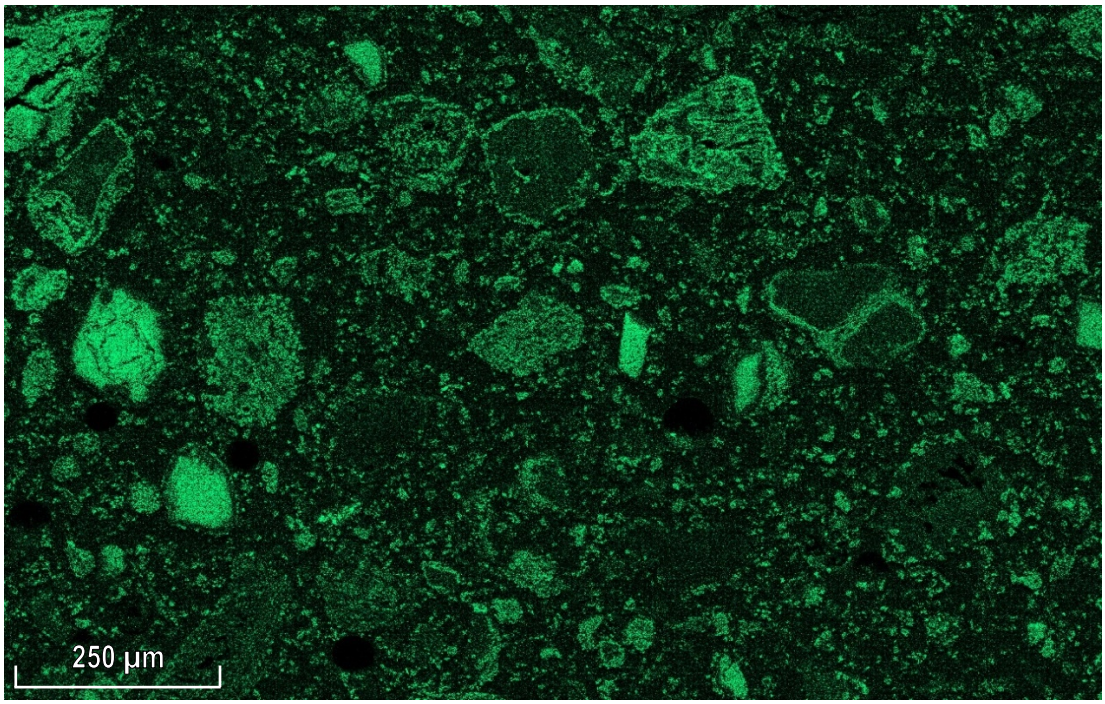

Figure B.116 Segregated Nontronite: Mg Intensity Map

2.02% MgO in original ore.

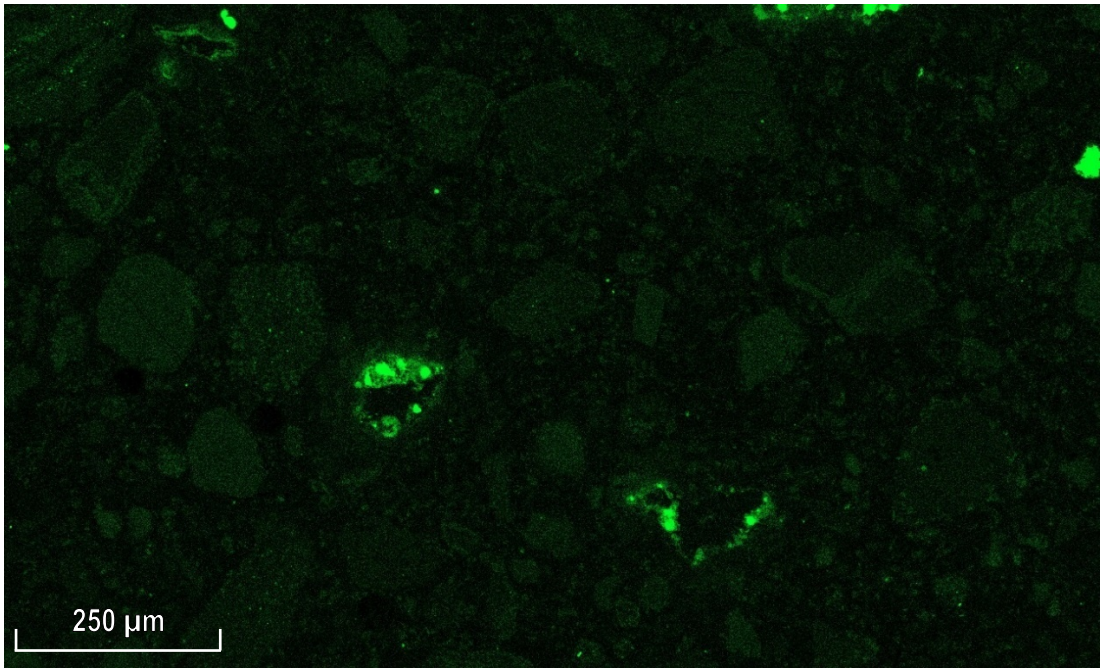

Figure B.117 Segregated Nontronite: Ni Intensity Map

1.21% Ni in original ore.

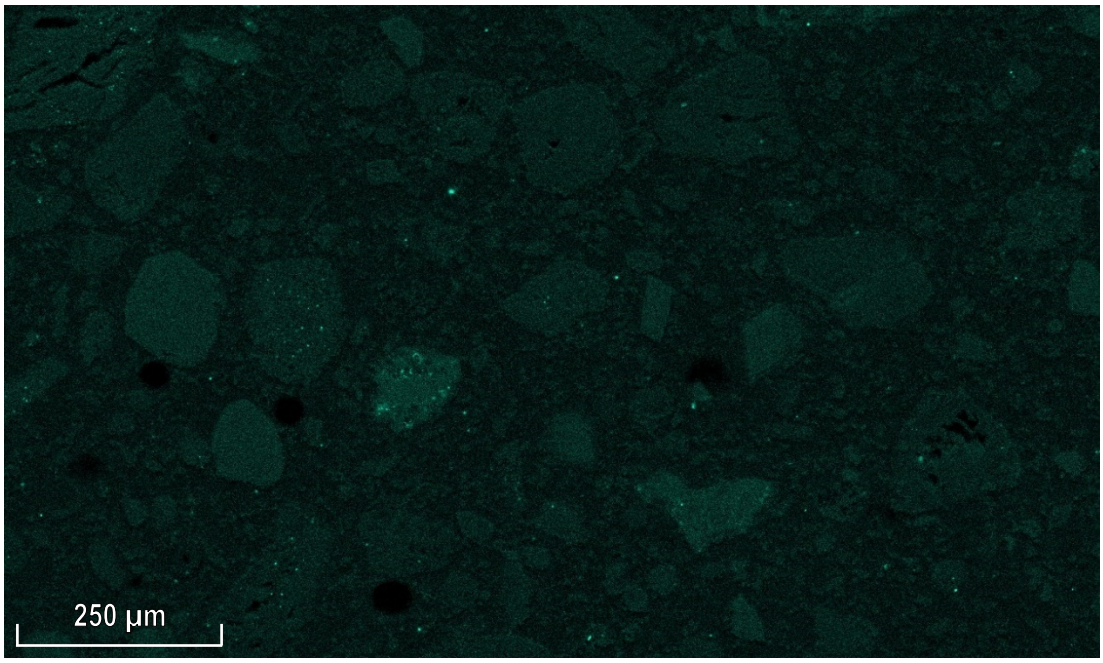

Figure B.118 Segregated Nontronite: S Intensity Map

0.21% S in original ore and 0.41% in the added coke; ~0.21% of combined feed.

B.18 EDS-SEM Maps: Segregated Limonite

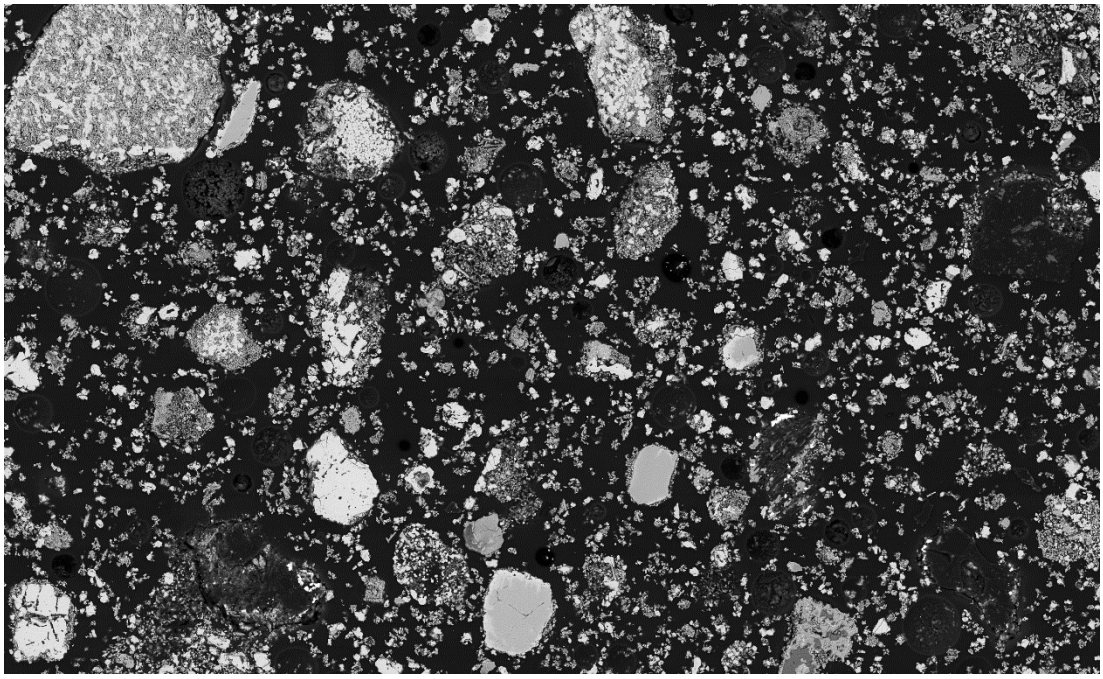

Figure B.119 Segregated Limonite: SEM Backscattered Electron Image

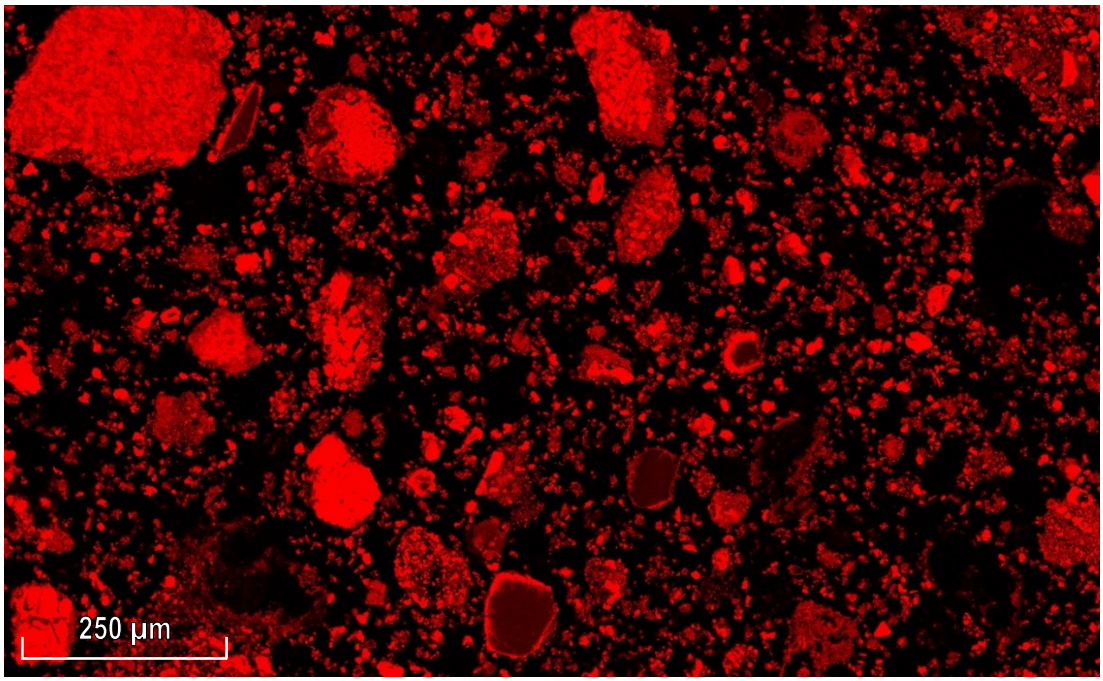

Figure B.120 Segregated Limonite: Fe Intensity Map

51.2% Fe in original ore.

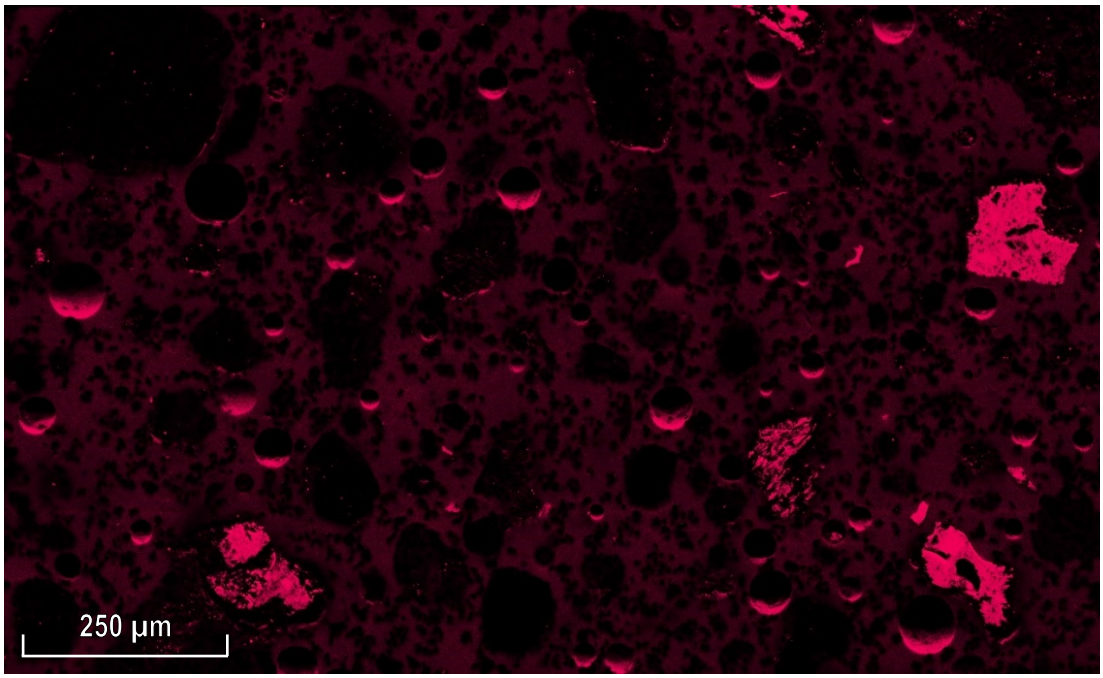

Figure B.121 Segregated Limonite: C Intensity Map

Added at 3.91 wt% of original ore.

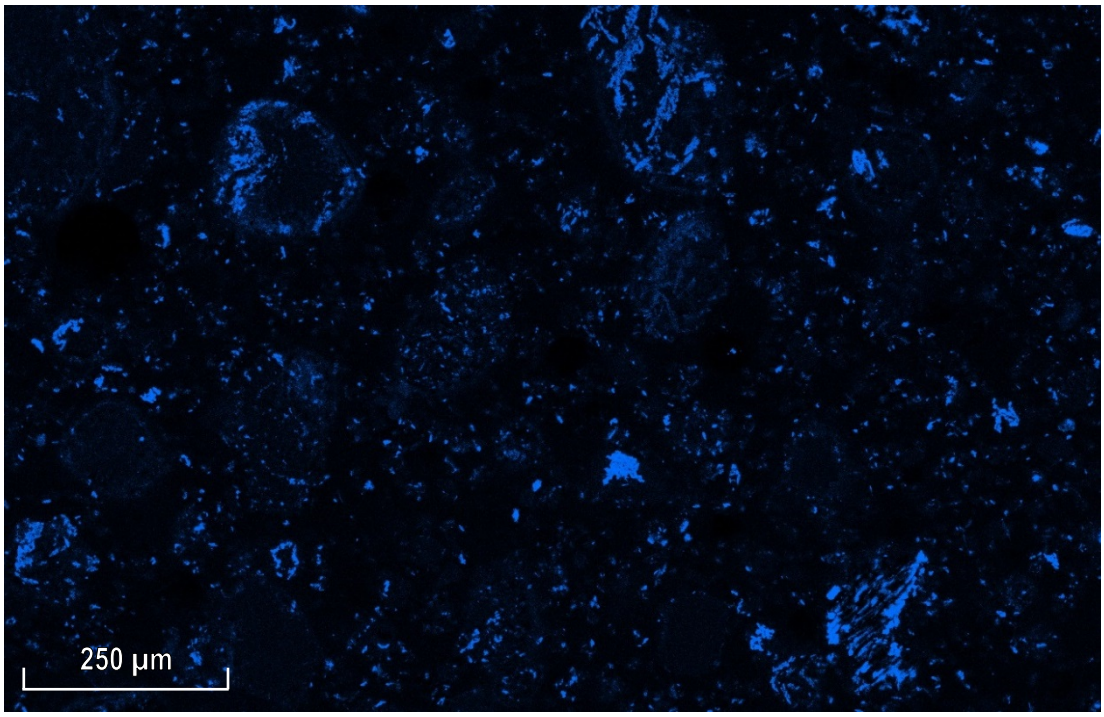

Figure B.122 Segregated Limonite: Ca Intensity Map

Added at as $CaCl_2$ at 2.67 wt% of original ore.

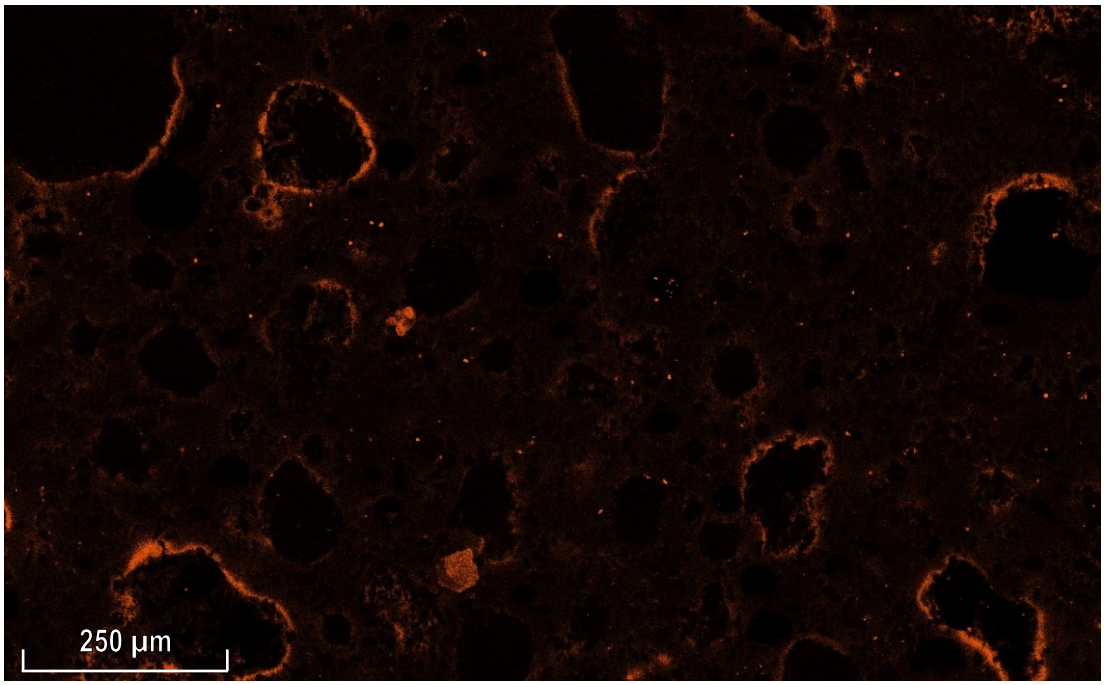

Figure B.123 Segregated Limonite: Cl Intensity Map

Added at as $CaCl_2$ at 2.33 wt% of original ore.

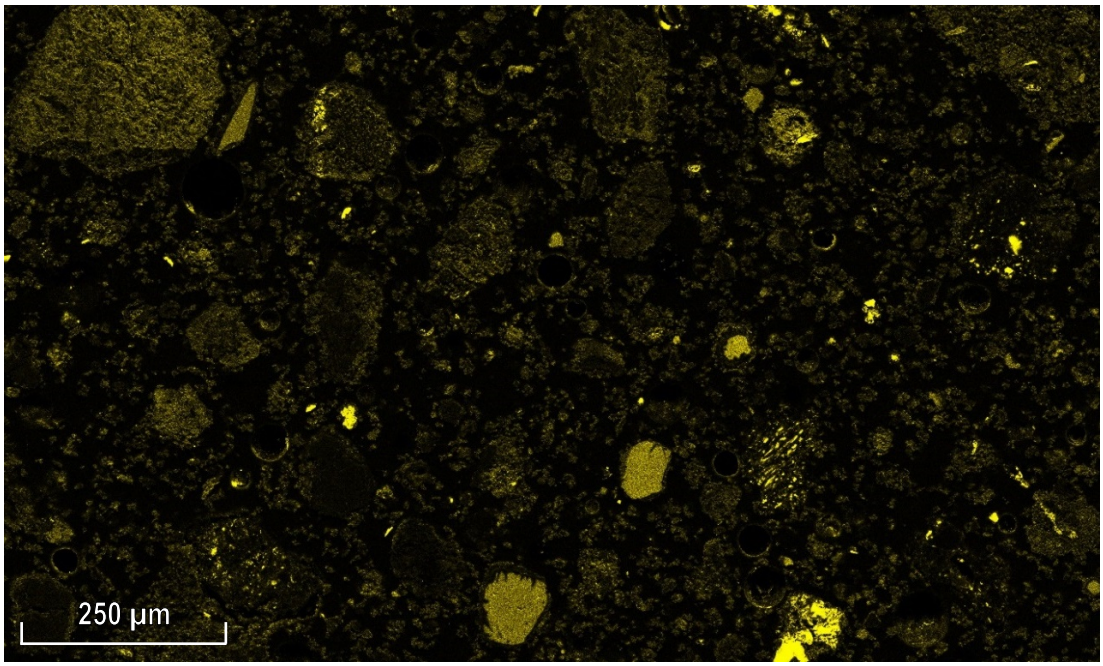

Figure B.124 Segregated Limonite: Al Intensity Map

4.47% Al_2O_3 present in original ore.

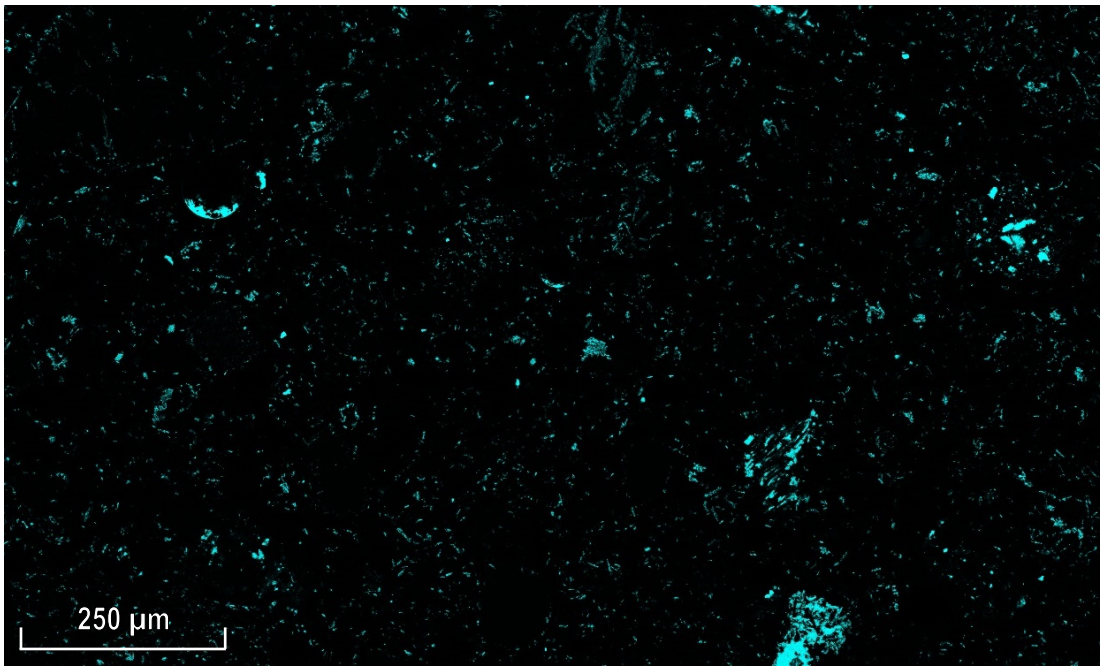

Figure B.125 Segregated Limonite: Si Intensity Map

3.11% SiO_2 present in original ore.

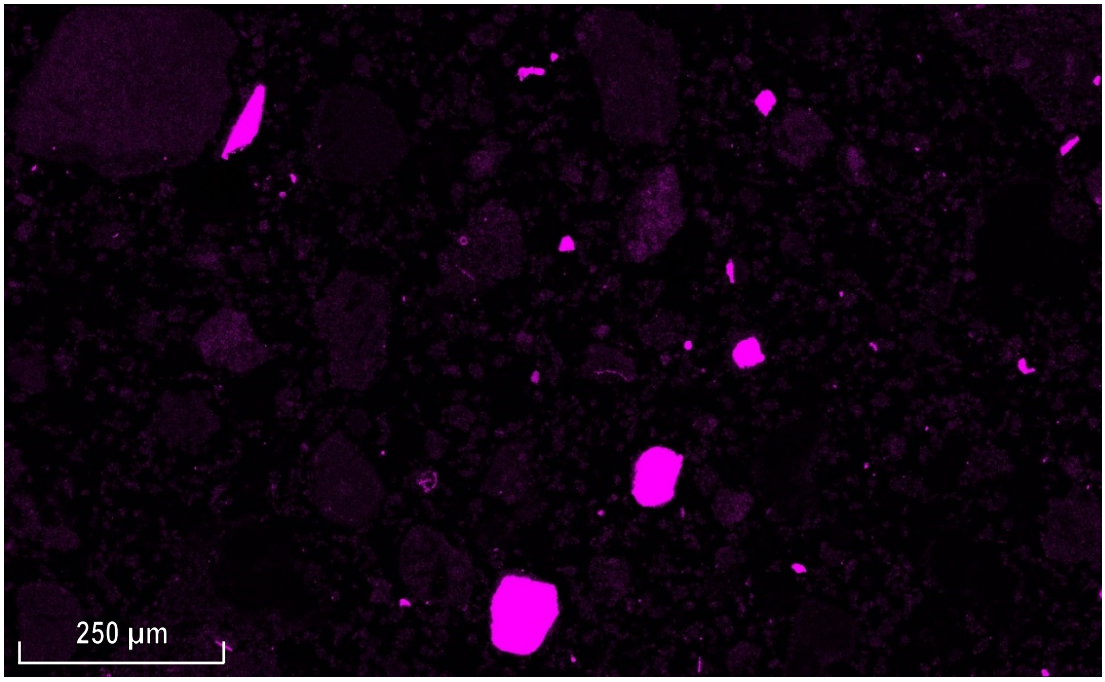

Figure B.126 Segregated Limonite: Cr Intensity Map

1.4% Cr present in original ore.

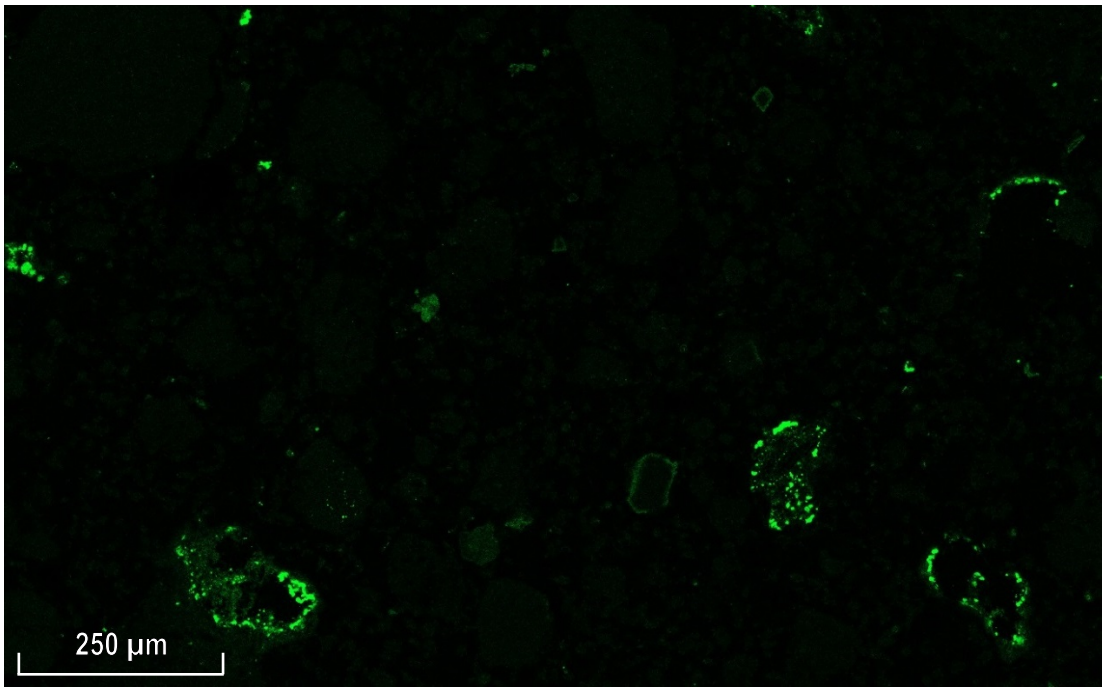

Figure B.127 Segregated Limonite: Ni Intensity Map

0.934% Ni present in original ore.

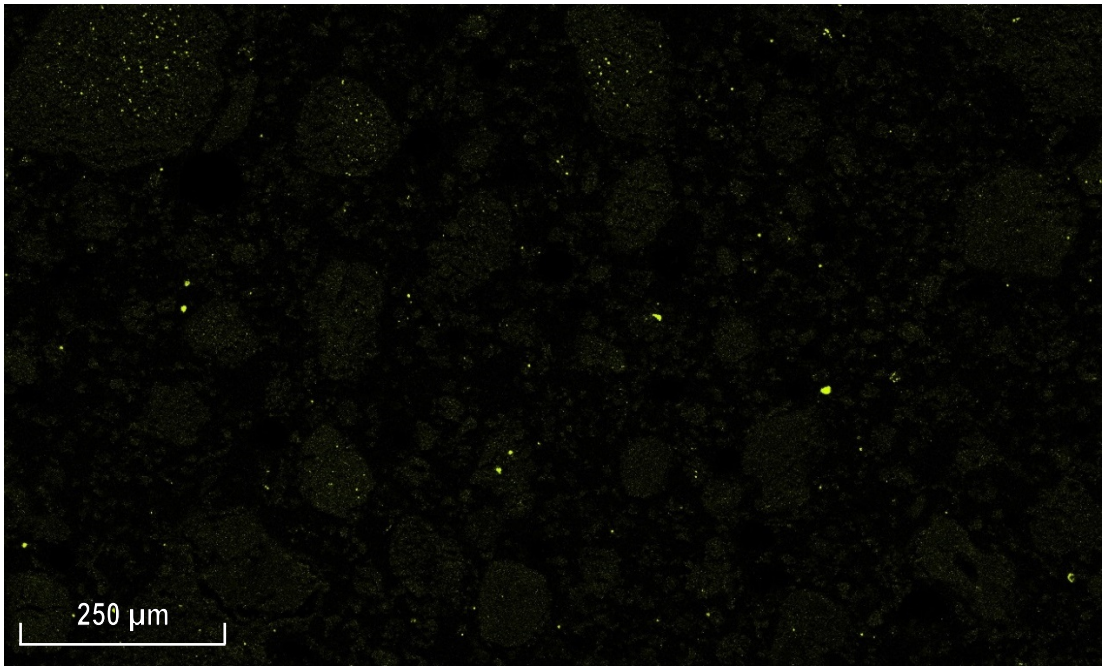

Figure B.128 Segregated Limonite: S Intensity Map

B.19 EDS-SEM Maps: Segregated Garnierite

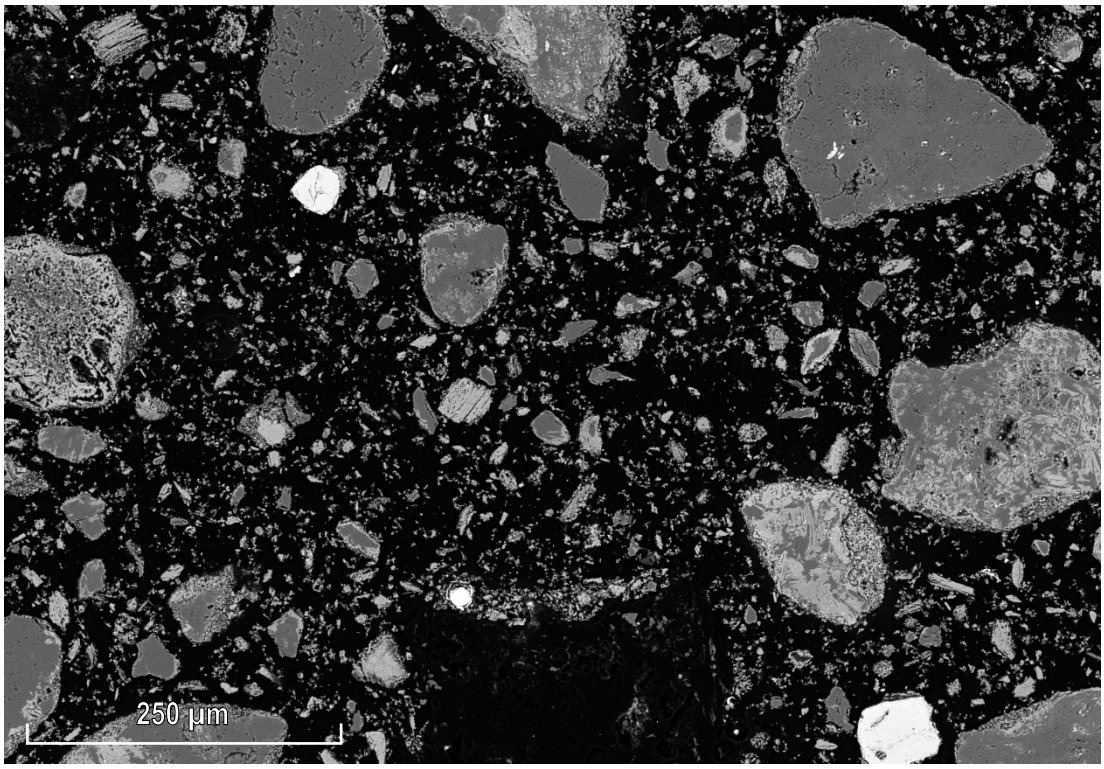

Figure B.129 Segregated Garnierite: SEM Backscattered Electron Image

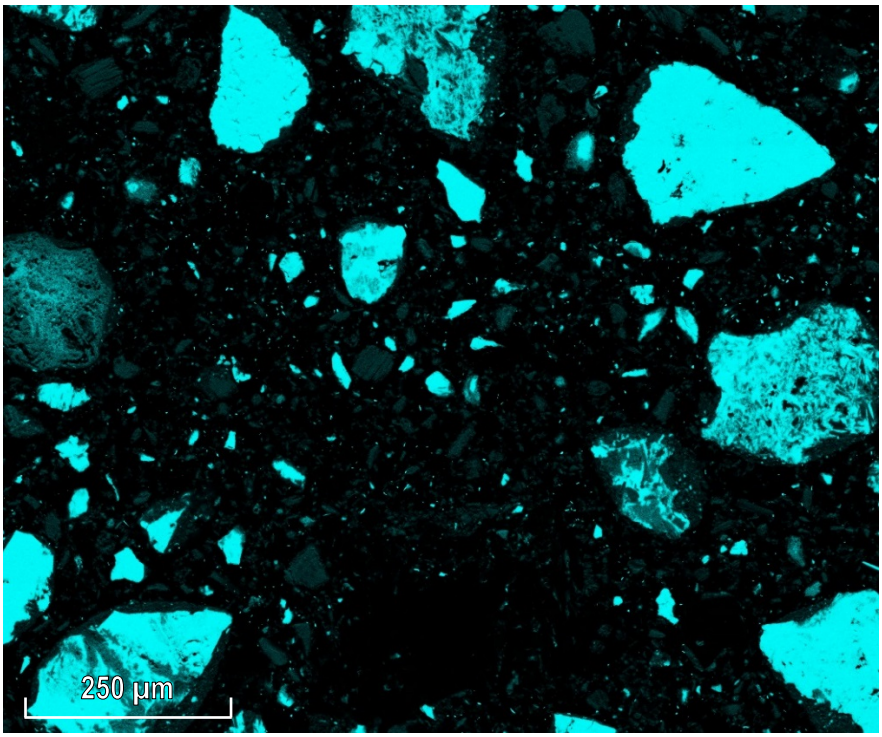

Figure B.130 Segregated Garnierite: Si Intensity Map

53.3% SiO_2 in original ore.

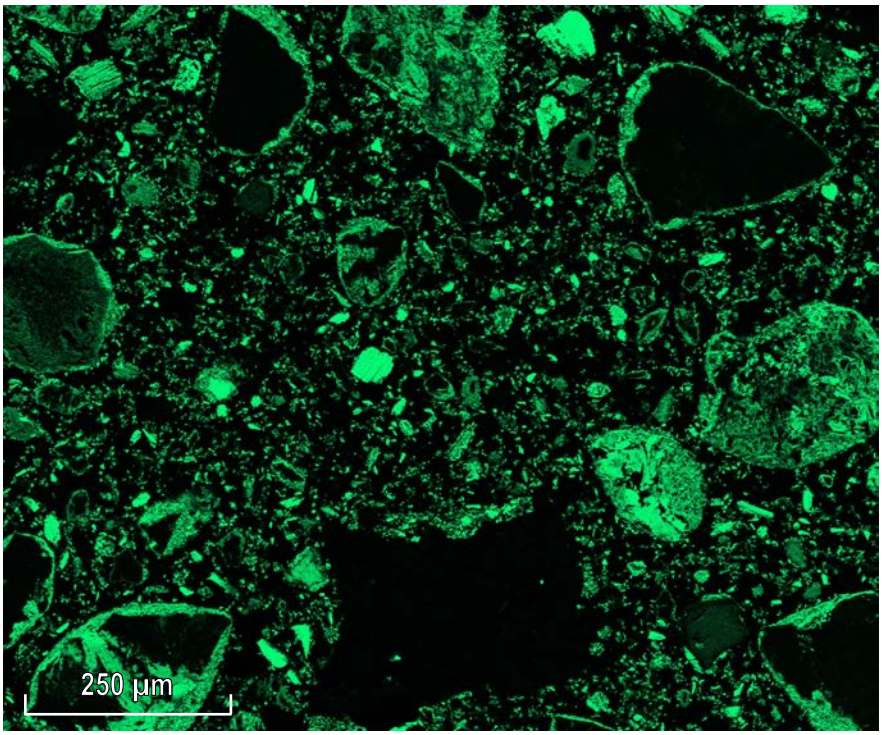

Figure B.131 Segregated Garnierite: Mg Intensity Map

14.8% MgO in original ore.

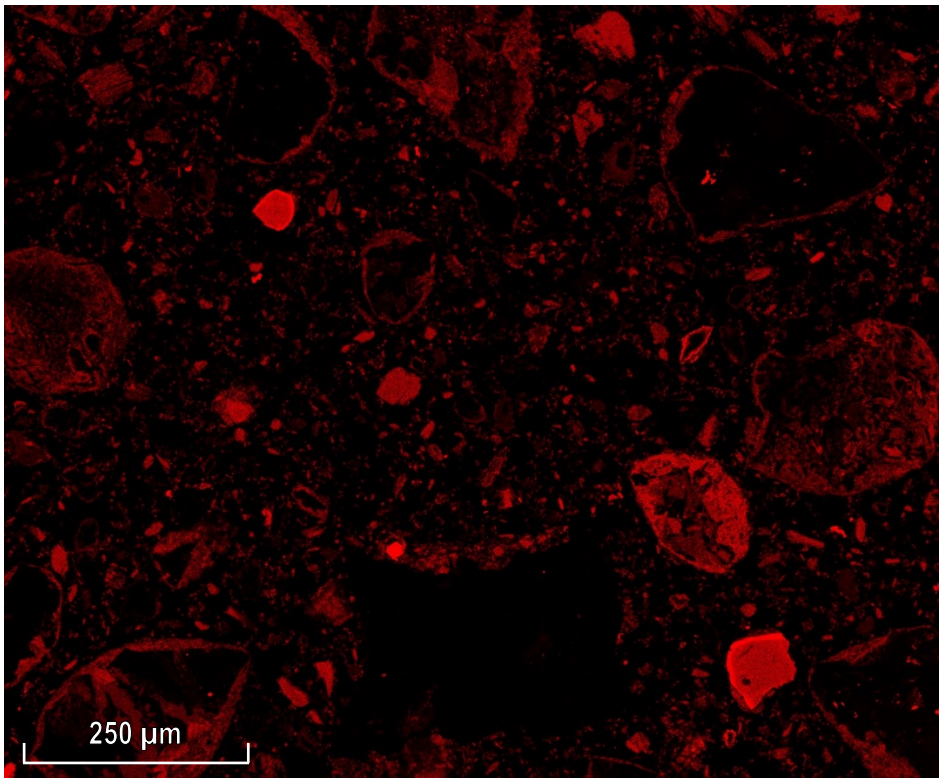

Figure B.132 Segregated Garnierite: Fe Intensity Map

Added at 11. 7% of original ore.

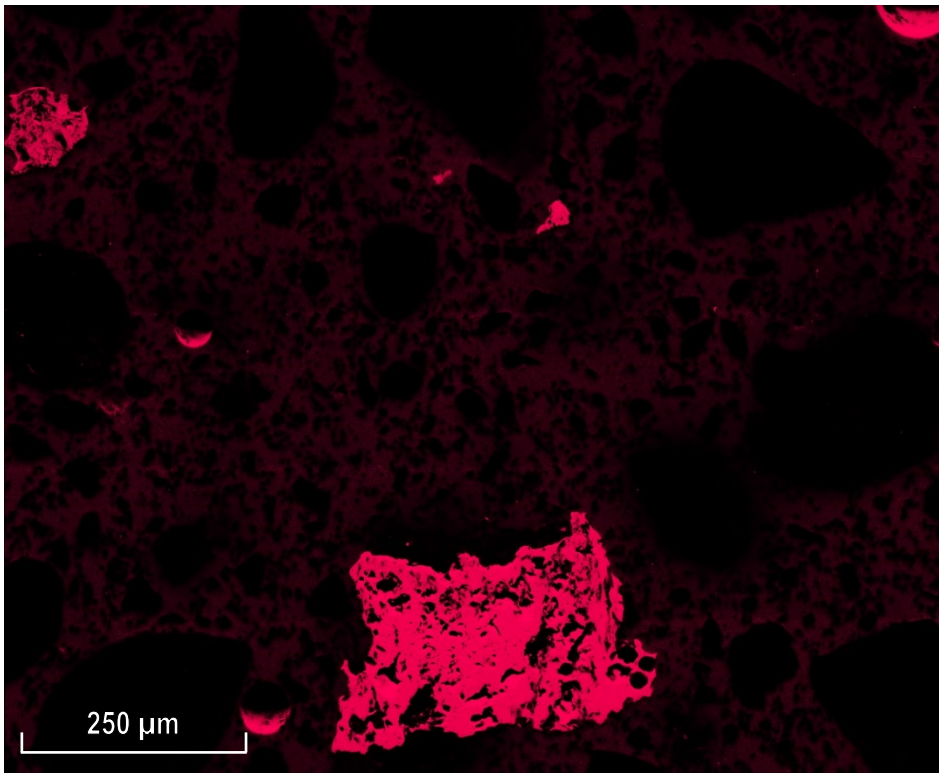

Figure B.133 Segregated Garnierite: C Intensity Map

Added at 3.91 wt% of original ore.

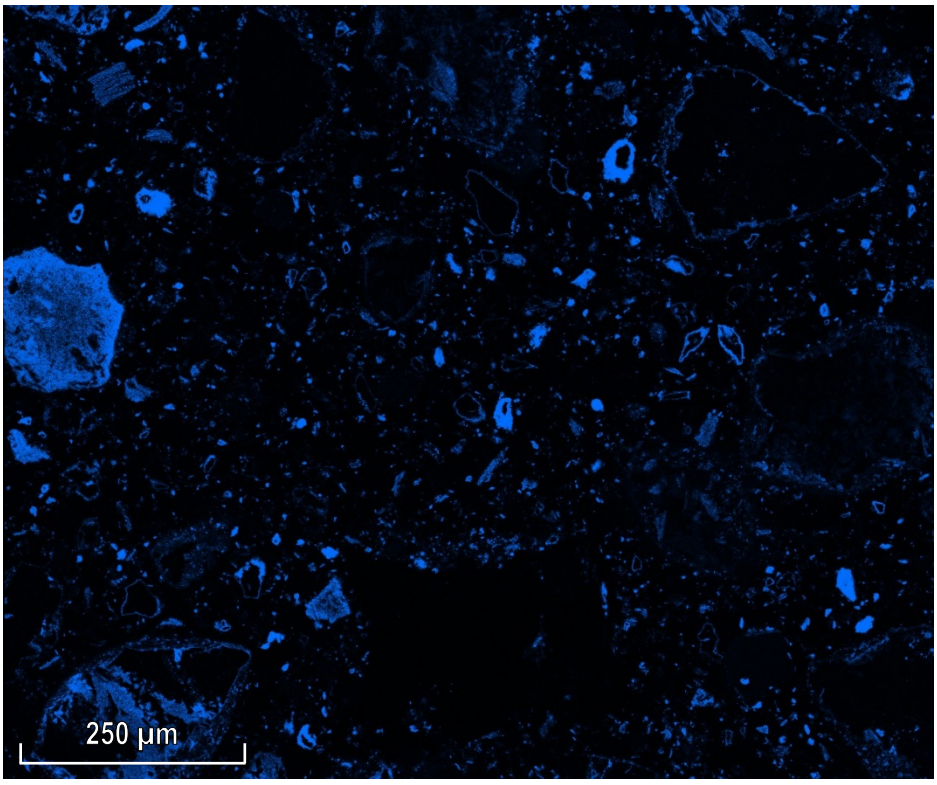

Figure B.134 Segregated Garnierite: Ca Intensity Map

Added as $CaCl_2$ at 2.67 wt% of original ore.

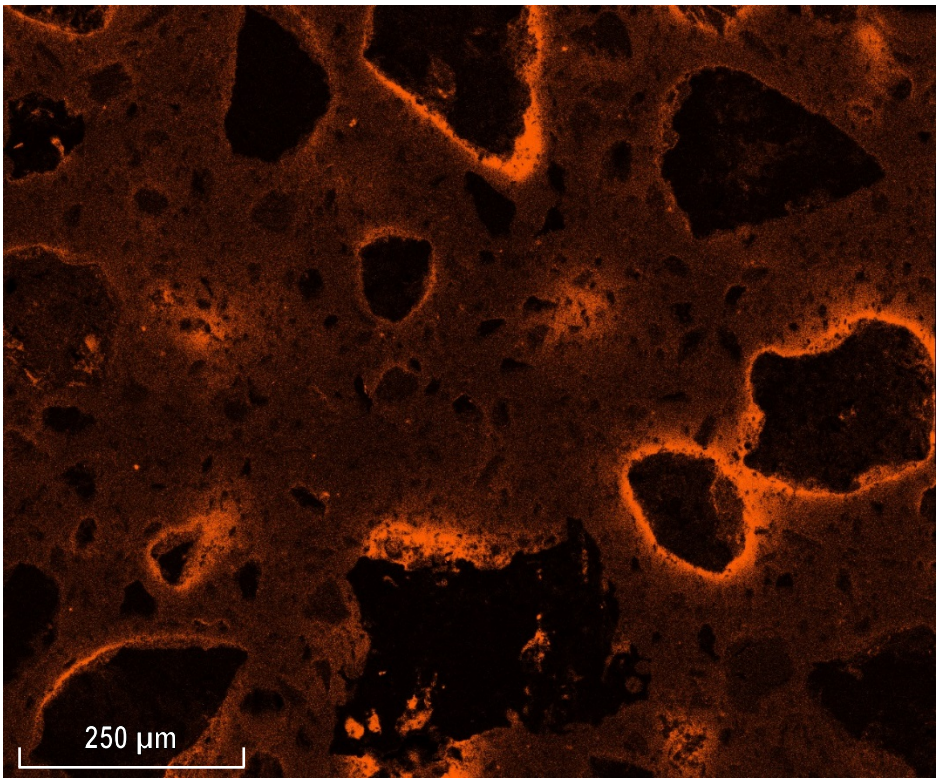

Figure B.135 Segregated Garnierite: Cl Intensity Map

Added as $CaCl_2$ at 2.33 wt% of original ore.

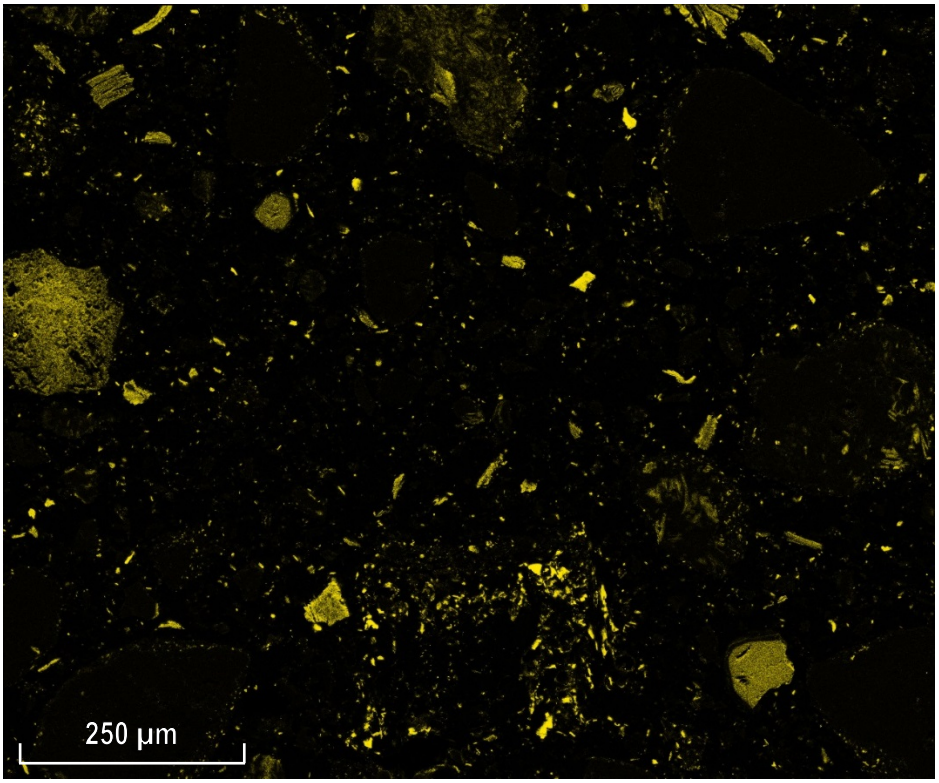

Figure B.136 Segregated Garnierite: Al Intensity Map

2.58% Al_2O_3 in original ore.

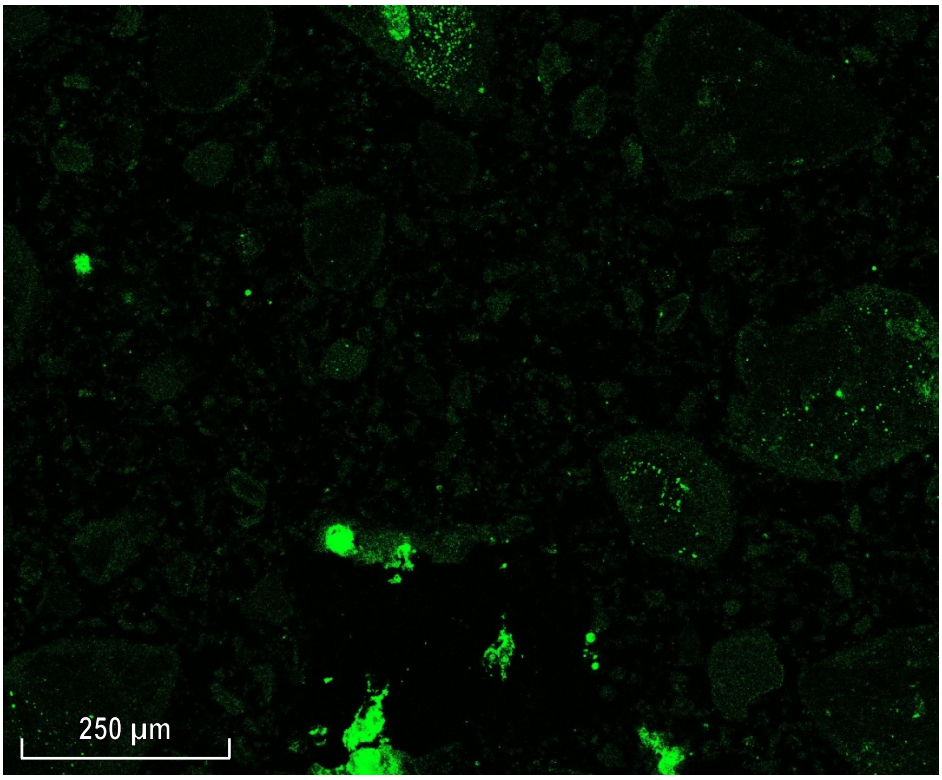

Figure B.137 Segregated Garnierite: Ni Intensity Map

1.27% Ni in original ore.

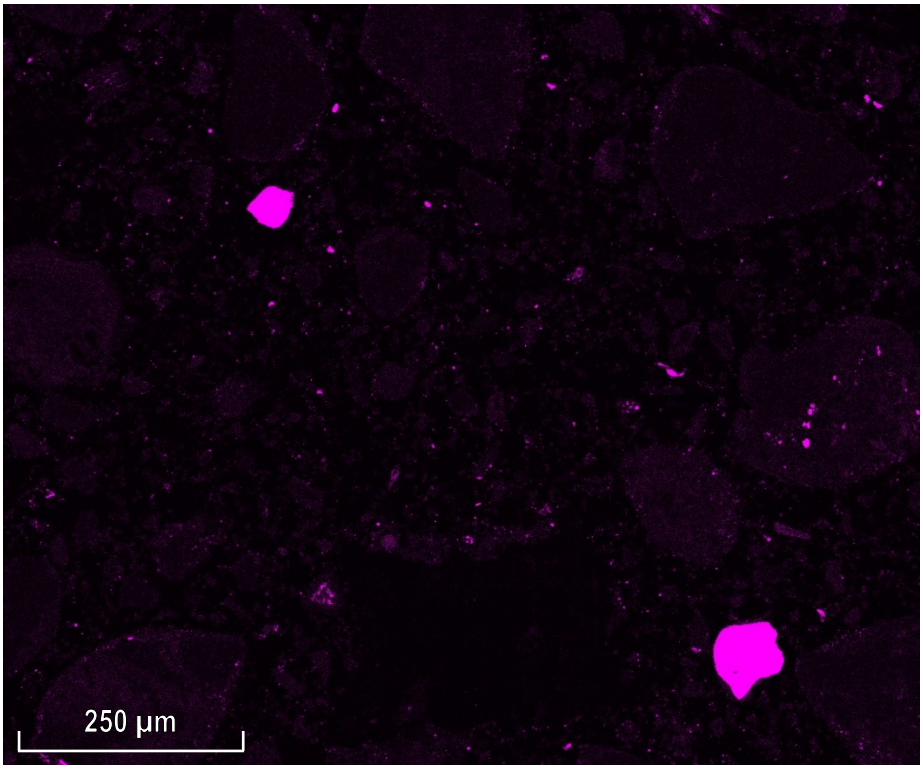

Figure B.138 Segregated Garnierite: Cr Intensity Map

0.65% Cr in original ore.

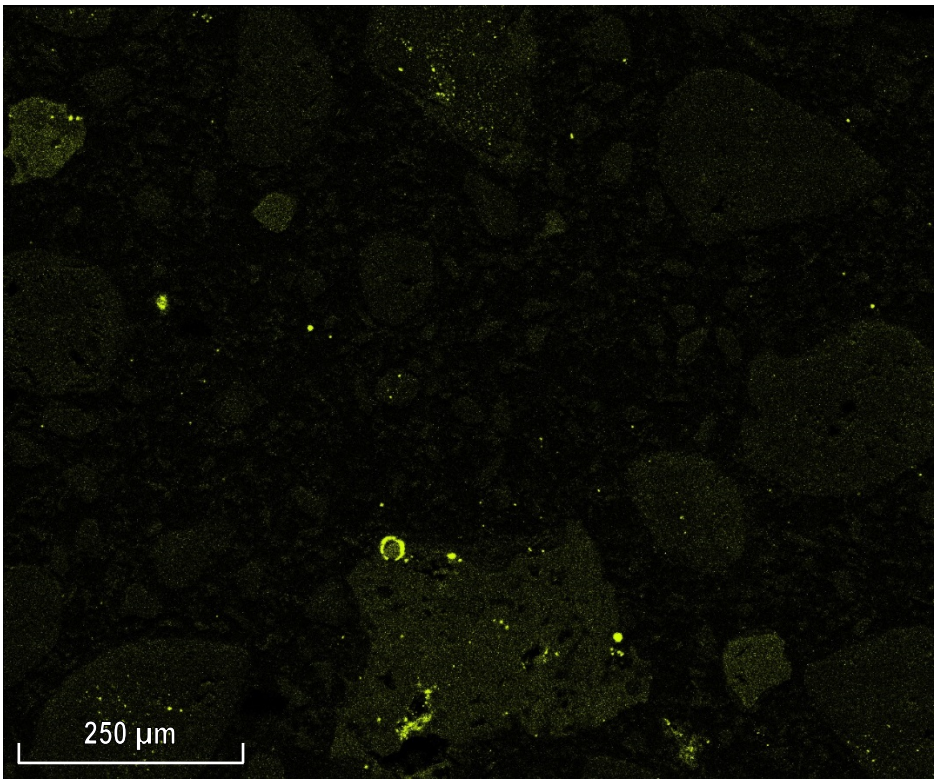

Figure B.139 Segregated Garnierite: S Intensity Map

0.06% S in original ore and 0.41% in the added coke; ~0.07% of the combined feed.

References

FORTINI, O. M. & FRUEHAN, R. J. 2005. Rate of reduction of ore-carbon composites: Part I. Determination of intrinsic rate constants. *Metallurgical and Materials Transactions B,* 36**,** 865-872.

GRIMSEY, E. J. 2012. Metallurgical Kinetics A, in Pyrometallurgy 352/561 (Pyrometallurgy Fundamentals), Curtin University.

MOOK, W. 2001. Chemistry of Carbonic Acid in Water. *Environmental Isotopes in the Hydrological Cycle - Principles and Applications.* International Atomic Energy Agency and United Nations Educational, Scientific and Cultural Organization.

ROBERTS, D. G. & HARRIS, D. J. 2006. A Kinetic Analysis of Coal Char Gasification Reactions at High Pressures. *Energy & Fuels,* 20**,** 2314-2320.